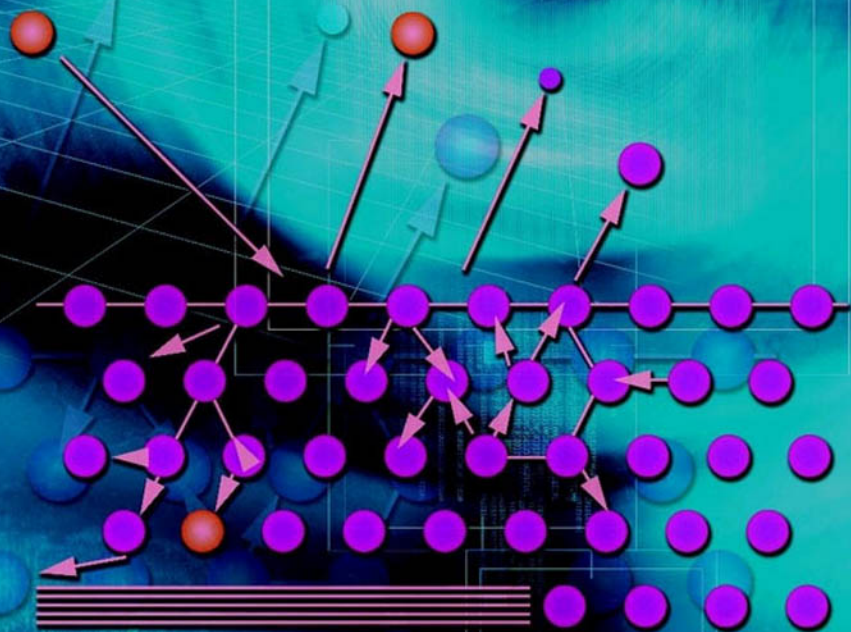


Glow Discharge Plasmas in Analytical Spectroscopy

Edited by

R. Kenneth Marcus

and **José A. C. Broekaert**



 **WILEY**



Glow Discharge Plasmas in Analytical Spectroscopy

Glow Discharge Plasmas in Analytical Spectroscopy

Edited by

R. Kenneth Marcus

Clemson University, Clemson, SC, USA

and

José A. C. Broekaert

Universität Hamburg, Hamburg, Germany



WILEY

Copyright © 2003

John Wiley & Sons Ltd, The Atrium, Southern Gate, Chichester,
West Sussex PO19 8SQ, England

Telephone (+44) 1243 779777

Email (for orders and customer service enquiries): cs-books@wiley.co.uk

Visit our Home Page on www.wileyeurope.com or www.wiley.com

All Rights Reserved. No part of this publication may be reproduced, stored in a retrieval system or transmitted in any form or by any means, electronic, mechanical, photocopying, recording, scanning or otherwise, except under the terms of the Copyright, Designs and Patents Act 1988 or under the terms of a licence issued by the Copyright Licensing Agency Ltd, 90 Tottenham Court Road, London W1T 4LP, UK, without the permission in writing of the Publisher. Requests to the Publisher should be addressed to the Permissions Department, John Wiley & Sons Ltd, The Atrium, Southern Gate, Chichester, West Sussex PO19 8SQ, England, or emailed to permreq@wiley.co.uk, or faxed to (+44) 1243 770571.

This publication is designed to provide accurate and authoritative information in regard to the subject matter covered. It is sold on the understanding that the Publisher is not engaged in rendering professional services. If professional advice or other expert assistance is required, the services of a competent professional should be sought.

Other Wiley Editorial Offices

John Wiley & Sons Inc., 111 River Street, Hoboken, NJ 07030, USA

Jossey-Bass, 989 Market Street, San Francisco, CA 94103-1741, USA

Wiley-VCH Verlag GmbH, Boschstr. 12, D-69469 Weinheim, Germany

John Wiley & Sons Australia Ltd, 33 Park Road, Milton, Queensland 4064, Australia

John Wiley & Sons (Asia) Pte Ltd, 2 Clementi Loop #02-01, Jin Xing Distripark,
Singapore 129809

John Wiley & Sons Canada Ltd, 22 Worcester Road, Etobicoke, Ontario, Canada M9W 1L1

Wiley also publishes its books in a variety of electronic formats. Some content that appears in print may not be available in electronic books.

Library of Congress Cataloging-in-Publication Data

Glow discharge plasmas in analytical spectroscopy / edited by R. Kenneth Marcus and
José A.C. Broekaert.

p. cm.

Includes bibliographical references and index.

ISBN 0-471-60699-5 (alk. paper)

1. Emission spectroscopy. 2. Glow discharges. 3. Solids — Surfaces — Spectra. I. Marcus,
R. Kenneth. II. Broekaert, J. A. C., 1948–
QD96.E46 G46 2003
543'.0858 — dc21

2002072636

British Library Cataloguing in Publication Data

A catalogue record for this book is available from the British Library

ISBN 0-471-60699-5

Typeset in 10/12pt Times by Laserwords Private Limited, Chennai, India

Printed and bound in Great Britain by TJ International, Padstow, Cornwall

This book is printed on acid-free paper responsibly manufactured from sustainable forestry in which at least two trees are planted for each one used for paper production.

Dedicated to our family, friends and colleagues
for their support through the years . . .

RKM
JACB

Contents

Preface	xi
List of Contributors	xiii
1 Introduction	1
<i>R. K. Marcus and J. A. C. Broekaert</i>	
1.1 Rationale	1
1.2 Glow Discharge Devices: Basic Operating Principles	3
1.3 Glow Discharge Devices: Scope of Application	6
1.4 Volume Outline	7
1.5 References	12
2 Optical Emission Spectrometry with Glow Discharges	15
<i>J. A. C. Broekaert</i>	
2.1 Introduction	15
2.2 Glow Discharges	16
2.3 Atomic Emission Spectrometry	36
2.4 Material Ablation	49
2.5 Analyses with Glow Discharge Atomic Emission Spectrometry ..	55
2.6 Other Methods of Analysis and Outlook	63
2.7 References	67
3 Mass Spectrometry of Glow Discharges	71
<i>W. W. Harrison, C. Yang and E. Oxley</i>	
3.1 Introduction	71
3.2 Fundamentals of Mass Spectrometry	75
3.3 Instrumentation	82
3.4 Qualitative Considerations	91
3.5 Quantitative Analysis	92
3.6 Conclusions	95
3.7 References	95

4 Radio Frequency Glow Discharges	97
<i>R. K. Marcus</i>	
4.1 Introduction	97
4.2 Radio Frequency Glow Discharge (rf-GD) Operation Principles	99
4.3 Comparisons with dc-Powered Glow Discharge Sources	101
4.4 Instrumentation	106
4.5 Analytical Applications	112
4.6 Summary	136
4.7 References	136
5 Depth Profile Analysis	141
<i>A. Bengtson</i>	
5.1 Introduction	141
5.2 Instrumentation	142
5.3 Practical Aspects and Results	144
5.4 Conclusions	153
5.5 References	154
6 Numerical Modeling of Analytical Glow Discharges	155
<i>A. Bogaerts and R. Gijbels</i>	
6.1 Introduction	155
6.2 Description of the Models	157
6.3 Results and Discussion	170
6.4 Conclusion	202
6.5 References	203
7 Application of Glow Discharge Optical Emission Spectrometry in the Steel Industry	207
<i>K. Kakita</i>	
7.1 Introduction	207
7.2 Measurement Traceability of Coating Weight and Chemical Composition by GD-OES	208
7.3 Method of Coating Analysis by GD-OES	209
7.4 Depth Profiles of Coatings by GD-OES	213
7.5 Factors Affecting Depth Profiles	217
7.6 Validation and Verification of Calibration Graphs	225
7.7 References	229
8 Surfaces, Thin Films and Coatings	231
<i>R. Payling, P. Chapon, K. Shimizu, R. Passetemps, A. Jadin, Y. Bourgeois, K. Crener, M. Aeberhard and J. Michler</i>	
8.1 Introduction	231
8.2 Surfaces	232
8.3 Thin Films	238

8.4 Coatings	243
8.5 Conclusions	251
8.6 Acknowledgements	251
8.7 References	251
9 Comparison of Glow Discharge Atomic Spectrometry with Other Surface Analysis Methods	253
<i>K. Wagatsuma</i>	
9.1 Introduction	253
9.2 Surface Analysis Methods Competitive with Glow Discharge Spectrometry	256
9.3 Analytical Examples	263
9.4 References	272
10 Analysis of Samples of Nuclear Concern with Glow Discharge Atomic Spectrometry	273
<i>M. Betti</i>	
10.1 Introduction	273
10.2 Instrumentation	274
10.3 Practical Aspects and Results	277
10.4 Conclusions	288
10.5 Acknowledgements	289
10.6 References	290
11 Analysis of Nonconducting Materials by dc Glow Discharge Spectrometry	293
<i>A. Bogaerts, W. Schelles and R. Van Grieken</i>	
11.1 Introduction	293
11.2 Use of a Conducting Host Matrix	294
11.3 Use of a Conducting Secondary Cathode	301
11.4 Conclusion	311
11.5 References	314
12 Standards and Reference Materials for Glow Discharge Spectroscopies	317
<i>M. R. Winchester</i>	
12.1 Introduction	317
12.2 Practical Aspects	318
12.3 Conclusions	331
12.4 References	332
13 Analysis of Liquid Samples Using Glow Discharge Spectroscopies	335
<i>R. K. Marcus</i>	
13.1 Introduction	335

13.2 Instrumentation	336
13.3 Practical Aspects and Applications	341
13.4 References	360
14 GC Speciation with GDMS Detection	363
<i>J. A. Caruso and L. Milstein</i>	
14.1 Introduction	363
14.2 Elemental Speciation	364
14.3 Instrumentation	364
14.4 Practical Aspects and Results	370
14.5 Conclusions	378
14.6 References	379
15 Glow Discharge Atomic Emission Spectrometry for the Analysis of Gases and as an Alternative Gas Chromatographic Detector	381
<i>R. Pereiro, N. G. Orellana-Velado and A. Sanz-Medel</i>	
15.1 Introduction	381
15.2 Instrumentation for the Analysis of Gases and Gas Chromatographic Detection by GD-AES	386
15.3 Practical Aspects and Results	392
15.4 Conclusions	399
15.5 References	399
16 Low-pressure Inductively Coupled Plasmas	401
<i>H. Evans</i>	
16.1 Introduction	401
16.2 Fundamentals	403
16.3 Instrumentation	407
16.4 Practical Aspects and Results	416
16.5 Conclusions	430
16.6 References	430
17 Multidimensional Ionization Sources for Plasma-source Mass Spectrometry	435
<i>J. P. Guzowski, Jr and G. M. Hieftje</i>	
17.1 Introduction	435
17.2 Tandem Sources in PSMS	437
17.3 Multipurpose Ionization Sources for PSMS	441
17.4 Conclusions	463
17.5 Acknowledgments	463
17.6 References	464
Index	469

Preface

Almost by definition, analytical spectroscopy is a science of problem solving. In this ever-changing world (both politically and technologically), the problems presented to the analytical chemist seem to be changing at an even greater pace. New problems generally require the development of new strategies and tools to solve. Of the modern approaches to spectrochemical analysis, the use of glow discharge (GD) devices seems to be showing some of the greatest breadth in terms of the ways that the devices are being used to solve problems. The opening lines of the Preface of a book edited by one of the present editors (R.K.M.) almost a decade ago stated that 'One of the greatest challenges remaining in the area of analytical atomic spectrometry is the development of more universal methods for the direct analysis of solid materials'. This statement remains true to this day, but the breadth of the diversity of potential applications has evolved far beyond the realm of solids elemental analysis to molecular analysis of solids, elemental analysis of gases and liquids and indeed molecular species analysis of gases and liquids.

The potential use of glow discharge sources in such diverse areas of application is really a product of the basic physics by which the devices operate. By their nature, GD sources provide means of converting solid specimens into gas-phase atoms and molecules in a controlled fashion. This quality is, of course, the basis of the still-growing use of glow discharge sources in bulk solids and depth-resolved elemental analysis. Gas-phase atoms and molecules are subsequently exposed to a plasma environment that is mild in comparison with spectrochemical sources operating at atmospheric pressure [e.g. flames, inductively coupled plasmas (ICPs) and microwave-induced plasmas (MIPs)]. Mild in this case refers to the fact that the kinetic temperatures are just above room temperature as opposed to thousands of degrees celsius. As such, gaseous molecules are not *de facto* broken down to their atomic constituents. In addition, the inert gas environment minimizes greatly the possibility of complicating side-reactions. Collisions taking place in the plasma are very effective, though, in exciting and ionizing gaseous atoms and molecules. In this way, atomic (optical) emission and atomic and molecular mass spectrometries can be employed to detect sputtered analytes.

Recent developments have now brought new sample introduction schemes to bear. Methods for analyzing liquid microsamples and flowing streams as well as a wide variety of gas-phase environments have been developed. While the types of GD instruments that are commercially available have been fairly static over the last decade, developments in these new application areas are surely going to yield very exciting new tools of high practical utility for problem solving in materials, environmental and biological chemistry.

Glow Discharge Plasmas in Analytical Spectroscopy is a multi-authored volume that hopes to capture the present state of the art of analytical applications while also highlighting the exciting new developments that will permit problem solving over an ever-expanding range of application. The chapters in the volume have been arranged first to present the basic technology and science underlying the most widely employed implementations of GD sources, then to highlight specific application areas of technological (and economic) significance. The final few chapters serve as a window to new applications of glow discharge devices in areas that are both nontraditional and also of high potential impact. As such, it is intended that the volume will be of use both to current practitioners and to those in the future. The authors of the chapters are clearly recognized world leaders in their respective fields, and in fact the entirety of analytical spectroscopy. They are leaders in both hardware development as well as application areas. Each author has been intentional in discussing their respective topic in relation to alternative methodologies, and as such the reader should gain a better understanding of the context of the work. It is intended that the content should be suitable for the technician, staff scientist and laboratory manager alike.

The Editors would like to express their appreciation to each of the authors for their thoughtful and valuable contributions. The writing of a chapter in such a volume is not a glamorous or invigorating undertaking, it is truly a service to the community as a whole. For this we are very grateful. We would also like to acknowledge the editorial staff of John Wiley & Sons who have shepherded this project from conception through to production. They have provided both a pleasurable and professional environment in which to work.

R. Kenneth Marcus
Clemson, SC, USA

J. A. C. Broekaert
Hamburg, Germany

List of Contributors

- MAX AEBERHARD
*Swiss Federal Laboratories for Materials
Testing and Research (EMPA),
Feuerwerkerstrasse 39, CH-3602 Thun,
Switzerland*
- ARNE BENGTON
*Swedish Institute for Metals Research,
Drottning Kristinas vag 48, S-111428
Stockholm, Sweden*
- MARIA BETTI
*European Commission, Joint Research
Centre, Institute for Transuranium
Elements, P.O. Box 2340, D-76125
Karlsruhe, Germany*
- ANNEMIE BOGAERTS
*University of Antwerp (UIA), Department of
Chemistry, Universiteitsplein 1, B-2610
Wilrijk, Belgium*
- YANN BOURGEOIS
*Certech, Zone Industrielle C, B-7180
Seneffe, Belgium*
- JOSÉ A.C. BROEKAERT
*University of Hamburg, Institute for
Inorganic and Applied Chemistry,
Martin-Luther-King-Platz 6, D-20146
Hamburg, Germany*
- JOSEPH A. CARUSO
*University of Cincinnati, Department of
Chemistry, P.O. Box 210037, Cincinnati,
OH 45221-0037, USA*
- PATRICK CHAPON
*Jobin-Yvon Horiba, 16–18 rue du Canal,
F-91165 Longjumeau Cedex, France*
- KARL CRENER
*Certech, Zone Industrielle C, B-7180
Seneffe, Belgium*

- HYWEL EVANS *Plymouth Analytical Chemistry Research Unit, Department of Environmental Sciences, University of Plymouth, Drake Circus, Plymouth PL4 8AA, UK*
- RENAAT GIJBELS *University of Antwerp (UIA), Department of Chemistry, Universiteitsplein 1, B-2610 Wilrijk, Belgium*
- JOHN P. GUZOWSKI, Jr *Indiana University, Department of Chemistry, Bloomington, IN 47405, USA*
- WILLARD W. HARRISON *University of Florida, Department of Chemistry, P.O. Box 117200, Gainesville, FL 32611-7200, USA*
- GARY M. HIEFTJE *Indiana University, Department of Chemistry, Bloomington, IN 47405, USA*
- ALAIN JADIN *Certech, Zone Industrielle C, B-7180 Senefte, Belgium*
- KAZUTOSHI KAKITA *Nippon Steel Technoresearch Corporation, 3-2-1-KSP A101 Sakato Takatsu-ku, Kawasaki 213-0012, Japan*
- R. KENNETH MARCUS *Department of Chemistry, Clemson University, Clemson, SC 29634-1905, USA*
- JOHANN MICHLER *Swiss Federal Laboratories for Materials Testing and Research (EMPA), Feuerwerkerstrasse 39, CH-3602 Thun, Switzerland*
- LISA MILSTEIN *RTI International, Analytical and Chemical Sciences, 3040 Cornwallis Road, Research Triangle Park, NC 27709-2194, USA*
- NESTOR G. ORELLANA-VELADO *Department of Physical and Analytical Chemistry, Faculty of Chemistry, University of Oviedo, E-33006 Oviedo, Spain*
- ERIC OXLEY *University of Florida, Department of Chemistry, P.O. Box 117200, Gainesville, FL 32611-7200, USA*

- RICHARD PASSETEMPS *Direction de l'Ingénierie des Matériaux,
Technocentre Renault, 1 avenue du Golf,
F-78288 Guyancourt Cedex, France*
- RICHARD PAYLING *Department of Physics, University of
Newcastle, Newcastle, NSW 2505,
Australia*
- ROSARIO PEREIRO *Department of Physical and Analytical
Chemistry, Faculty of Chemistry,
University of Oviedo, E-33006 Oviedo,
Spain*
- ALFREDO SANZ-MEDEL *Department of Physical and Analytical
Chemistry, Faculty of Chemistry,
University of Oviedo, E-33006 Oviedo,
Spain*
- WIM SCHELLES *University of Antwerp (UIA), Department of
Chemistry, Universiteitsplein 1, B-2610
Wilrijk, Belgium*
- KENICHI SHIMIZU *University Chemical Laboratory, Keio
University, 4-1-1 Hiyoshi, Yokohama
223-8521, Japan*
- RENÉ VAN GRIEKEN *University of Antwerp (UIA), Department of
Chemistry, Universiteitsplein 1, B-2610
Wilrijk, Belgium*
- KAZUAKI WAGATSUMA *Institute for Materials Research, Tohoku
University, Katahira 2-1-1, Sendai
980-8577, Japan*
- MICHAEL R. WINCHESTER *National Institute of Standards and
Technology, Chemical Science and
Technology Laboratory, Analytical
Chemistry Division, Gaithersburg, MD
20899, USA*
- CHENGLONG YANG *University of Florida, Department of
Chemistry, P.O. Box 117200, Gainesville,
FL 32611-7200, USA*

Glow Discharge Plasmas in Analytical Spectroscopy

Edited by

R. Kenneth Marcus

Clemson University, Clemson, SC, USA

and

José A. C. Broekaert

Universität Hamburg, Hamburg, Germany



WILEY

1

Introduction

R. K. MARCUS and J. A. C. BROEKAERT*

*Department of Chemistry, Clemson University, Clemson, SC, USA and
*University of Hamburg, Institute for Inorganic and Applied Chemistry,
Hamburg, Germany*

1.1 RATIONALE

Developments in the area of analytical chemistry have a very key role in almost all aspects of commerce, environmental science, and health science. Analytical measurements serve to confirm hypotheses as well as generate new ones. The evolution of analytical methodologies reflects a counterbalance between advances in the capabilities of basic instrumentation and its components and the demands for qualitative and quantitative information for a particular sample (analyte) system. The first of these aspects is driven by technology. The development of new optical sensors in atomic and molecular spectroscopy and high field magnets for FT-NMR or MS are examples of such advances. The other component in this process is the constant introduction of new analytical samples and the need for new types of information. For example, the development of higher density electronic devices and flat panel displays requires the ability to perform spatially resolved analyses with greater sensitivities than required of previous devices. Further, there is a need for analytical methodology for monitoring civil risks in the environment and for healthcare-related tasks, and for enabling progress in the biosciences. Eventually, analytical challenges outpace the capabilities of existing instrumentation, hence new methodologies must be developed. New challenges do not necessarily require the invention of new 'wheels'; simple retooling may produce improved capabilities. The analytical applications of glow discharge (GD) devices described herein are based on using well characterized technologies which have evolved over the last 100 years or so [1,2] to permit new capabilities for solving new problems. Specifically, low pressure, glow discharge plasmas are now

employed to address challenges in the materials, biological, and environmental chemistry arenas.

Since the early 1970s, the use of glow discharge sources has been principally focused in the area of alloy characterization. Based primarily on the design concepts first described by Grimm [3], the sources were employed as higher precision alternatives to atmospheric pressure arc and spark emission sources. The forte of the devices is their ability to allow the direct elemental analysis of materials in the solid state. The 1980s brought about a number of studies that illustrated the more substantial capabilities to perform depth-resolved elemental analysis of 'thick' metal layers such as galvanized coatings [4,5]. The scope of application in solids was brought full-spectrum with the advent of radio frequency (rf) powering schemes in the 1990s that allow the direct analysis of nonconductive coatings and bulk insulators [6]. These basic capabilities for solids analysis are now realized in steady growth in sales of commercial instrumentation.

Recent studies described in the scientific literature have suggested very new applications of glow discharge spectroscopies not imagined a decade ago, including polymer mass spectrometry, sensitive determinations of nonmetals, and very thin ($<0.1 \mu\text{m}$) film analysis. Figure 1.1 is a graph of the number of publications appearing in the literature describing the use, development, and study of glow discharge devices used in analytical spectroscopy over the decade 1991–2000. These data were compiled by the authors through queries on the Web of Science (Institute for Scientific Information) and, although some papers were surely overlooked, they should be a fair reflection of activity in the area. The data are broken down for each year according to whether the essence of the studies

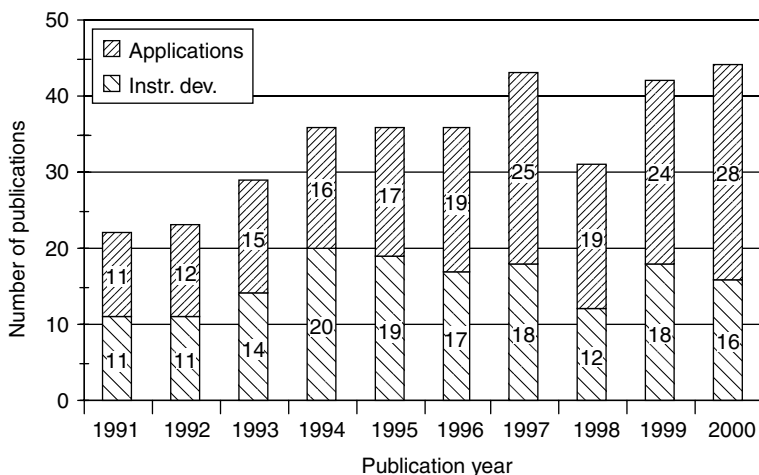


Figure 1.1 Number of publications describing instrumentation developments and applications of glow discharge sources from 1991 to 2000

was directed at the development of GD-based instrumentation or in the area of analytical applications of existing instrumentation. As can be seen, the total number of publications has nearly doubled over the last 10 years, with the lion's share of the growth in papers being carried by the applications category. This is a sign that the early-year research, taking place most often in academic laboratories, is being adopted in industrial laboratories. This is also reflective of the increase in sales of commercial instruments. While the absolute number of publications pales in comparison with those of most other atomic spectroscopic methods, the growing acceptance of GD methods is definitely being felt in many industries, as outlined throughout this book.

Certainly direct solids elemental analysis has been the 'bread and butter' of glow discharges for many decades, but there is a salient wave of application of glow discharge sources that should be noted here. The need for more extensive pieces of chemical information has led to new ways of looking at the glow discharge as an excitation and ionization source. As detailed in Chapters 13–17, the low pressure plasma has an advantageous combination of low kinetic (thermal) temperature with a high excitation temperature that affords the ability to provide both atomic and molecular species information not provided by atmospheric pressure plasmas and flames. In addition, the devices are easily coupled to many forms of gaseous sample introduction, such as gas chromatography. Creative methods of solution sample introduction have also been realized. Given the need for new methodologies for performing the so-called 'speciation' experiment, developments in this area are growing fast and are highlighted herein as a sign of their projected future impact.

Overall, it is the purpose of this book to outline the developments in analytical applications of glow discharge devices over the last decade and to highlight future trends as the techniques continue to evolve. Experts in the various applications of glow discharge devices have contributed to this volume and put their own applications into perspective with competing and complementary methods. It is hoped that the reader will begin to gain an appreciation for the fundamental processes occurring in glow discharges and also the scope of the current, and expected, analytical applications.

1.2 GLOW DISCHARGE DEVICES: BASIC OPERATING PRINCIPLES

Glow discharge devices are traditionally defined as reduced pressure, inert atmosphere, gaseous conductors [7]. The glow discharge is just one of many forms of gaseous discharges, often called plasmas. Figure 1.2 depicts the characteristic current–voltage relationships that exist for a number of diode-type discharges [8]. Each of these devices operates on the premise of having two distinct electrodes in a gaseous medium, between which electrical current is passed, the cathode having a negative potential and anode having a positive potential. In reality, these

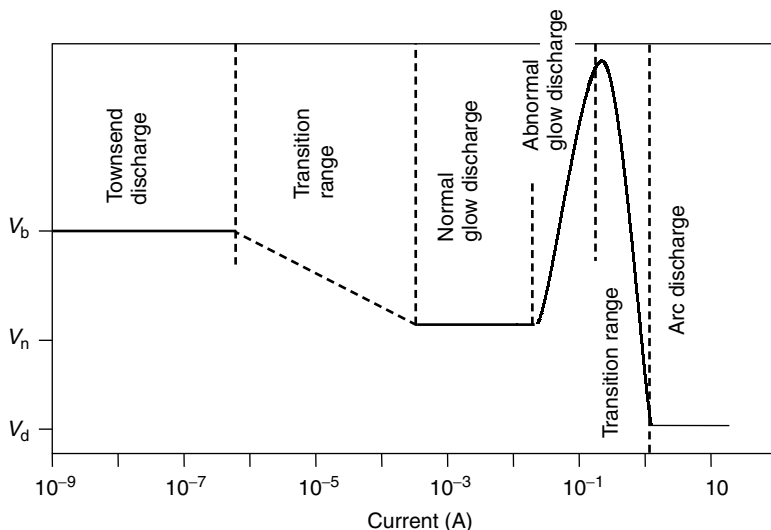


Figure 1.2 Current–voltage (i – V) characteristics of direct current (dc) electrical discharges

discharges are formed by potential differences, and so the designation of the two electrodes is simply based on relative potentials. In the figure, the increase in current (moving from left to right) can also be equated to operation pressure. Of the three major classifications, the Townsend discharge, the glow discharge, and the arc discharge, only the last two have been applied extensively in analytical chemistry. In Figure 1.2, V_b is the breakdown voltage, V_n is the normal operating voltage, and V_d is the operating voltage of arc discharge.

The electrical characteristics of a gas discharge can be best understood by beginning with the Townsend discharge regime. This discharge is generally operated in the sub-millitorr pressure regime and is characterized by having only a small degree of ion and free electron production. Following the Townsend discharge is a transition region, resulting from the increased energy exchange through collisions (due to higher gas pressures), wherein the electrical current increases while actually decreasing the required discharge maintenance voltage. This is a basic characteristic of a self-sustained discharge.

After the transition region, a luminous glow forms between the electrodes and is thus named a ‘glow discharge’. At the onset of the glow discharge regime, increases in the current do not change the current density because the cathode surface is only partially covered by the discharge; as such, no increase in voltage is required. This is classified as the ‘normal’ glow discharge regime. As the current is further increased, the discharge glow will eventually cover the entire cathode surface. At this point, any increases in discharge current will result in an increase in current density, requiring an increase in the discharge

voltage. Plasmas that display this type of increasing $i-V$ relationship are termed 'abnormal' glow discharges. It is the abnormal glow discharge mode that is used most often in atomic spectroscopy. Analytical glow discharge devices generally operate in reduced pressure (0.1–10 Torr), inert gas atmospheres and at powers of less than 100 W. At the publication of this volume, it has now become clear, in fact, that plasmas operating in the glow discharge realm of voltage and current response can exist at atmospheric pressure [9].

As the discharge current is increased further in the glow discharge, the current density becomes so high that intense heating of the cathode through bombardment by filler gas ion species causes thermal vaporization of the cathode. Under these conditions, the production of high number densities of analyte atoms perturbs the potential fields and the $i-V$ characteristics of discharge become 'normal', i.e. the current then increases while decreasing the required discharge voltage, as is the situation for a dc arc. Usually operating at atmospheric pressure, the dc arc is characterized by its large currents and bright discharge plasma. At typical operating currents, 10–1000 A, the cathode surface is heated to the point that thermionic electron emission becomes a prominent current carrying mechanism. The combination of high vaporization rates and collisionally energetic plasma has made dc arcs a mainstay in analytical spectrochemical analysis of metallurgical samples [10,11].

A depiction of the simplest source geometry and plasma structure is presented in Figure 1.3 [7]. A glow discharge is initiated by the application of a sufficiently

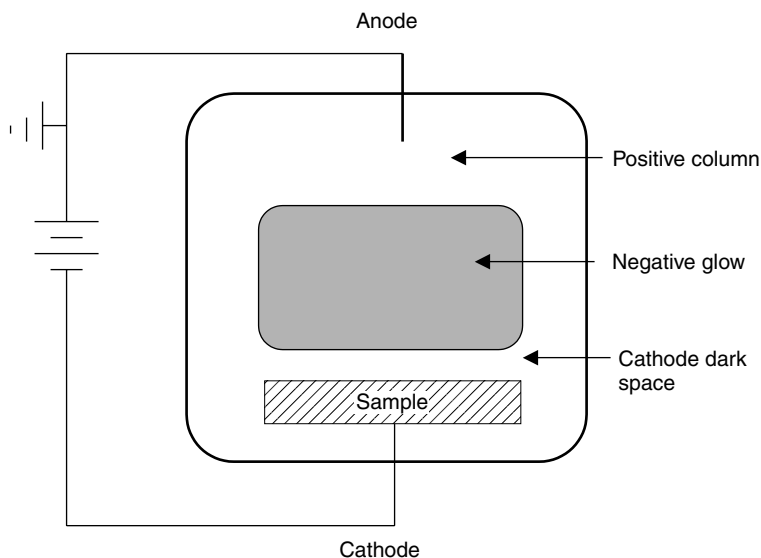


Figure 1.3 Simple diode geometry employed for glow discharge devices employed in spectrochemical analysis

high voltage between two electrodes in contact with the discharge gas (typically Ar). The potential difference (250–2000 V) causes the breakdown of the discharge gas to form positively charged ions and free electrons. The relative potentials on the cathode (–) and anode (+) result in the establishment of electric field gradients such that positively charged ions are accelerated to the cathode surface. The impinging ions transfer their momentum to the surface and lattice atoms, setting off a cathodic sputtering event. The products of the sputtering process are ejected atoms and small clusters of cathode material, ionic species, and secondary electrons. The process of cathodic sputtering is the means of solid sample atomization and the basis for depth-resolved analyses. In comparison with high vacuum sputtering of the sort employed in secondary ion mass spectrometry (SIMS), the GD source has much greater current densities (100s mA/cm² vs 1 μ A/cm²) and far lower average kinetic energies (<100 eV vs >1 keV) than typical ‘ion guns’. As a result, sample ablation rates are much higher, but with far less lattice damage for the GD sputtering. The analytical consequences of these characteristics are highlighted throughout the following chapters.

Secondary electrons emitted in the sputtering process are essential in sustaining the discharge through gas phase ionization of sputtered material and discharge gas atoms. The negative potential of the cathode surface accelerates the electrons across the cathode dark space and into the negative glow region. Beyond direct ionization events, thermalized electrons are efficient at producing excited state atoms of the sputtered and discharge gas atoms. Evidence of these electron impact collisions is seen in the characteristic luminosity of the negative glow. Depending on the means of powering the GD, electrons in the negative glow can have temperatures of >5 eV; as such, they are very effective in populating high-lying excited states of nonmetal analytes such as H, C, and S. These sorts of electron energies are much higher than those found in atmospheric pressure plasmas and flames, while at the same time existing in an environment whose kinetic temperature is typically less than 500 K. Important also in the bulk plasma ionization are Penning-type collisions between highly excited, metastable discharge gas atoms and neutral atoms of the sputtered material. The result of these collisions is the formation of ions of the sputtered atoms that can be detected mass spectrometrically. The greatly increasing application of glow discharge devices (and reduced-pressure plasmas in general) as detectors for gaseous and solution-phase samples capitalizes on these gas-phase processes and conditions rather than in the ability to convert solid specimens into gas-phase populations which is essential to solids analysis.

1.3 GLOW DISCHARGE DEVICES: SCOPE OF APPLICATION

As suggested in the previous sections, the application of glow discharge devices as spectrochemical sources is increasing in diversity. It is important to realize, as with all other things in life, that ‘one size does not fit all’. There are

a number of different discharge (electrode) geometries and powering schemes. There are also a variety of means of introducing the analytical sample depending on its state of matter: solid, liquid, or gas. In addition, analyte species within the discharge volume can be detected by many different spectroscopic methods including atomic absorption and fluorescence, optical emission, mass spectrometry, and a number of laser-based optical methods. In the case of optical emission spectrometry, the responses of component elements allows for the determination of the empirical formulae of 'molecular' analytes. Furthermore, molecular analytes can be determined directly by mass spectrometry where the spectra obtained can contain signatures representative of the molecular ion and structurally significant fragments. While this presentation may give the impression that each analysis employing a GD is unique in its own right, this is not the case. Instead, the experimental apparatus and methods can be quite routine, and this variability is simply a reflection of the inherent versatility afforded by the devices.

As described in the chapters that follow, at this stage in the evolution of analytical glow discharge sources there is a firm user base in the area of bulk and depth-resolved elemental analysis of metals and alloys by glow discharge optical emission spectroscopy (GD-OES). There are fewer actual instruments in the field of glow discharge mass spectrometry (GDMS), but the technique holds a unique place in the landscape of elemental analysis as providing sensitivity not afforded by any other conventional method of solids analysis. The scope of application of both of these methods is now being greatly expanded with the advent of rf powering schemes, wherein the direct analysis of insulating layers and bulk nonconductors is now possible. All of these sorts of applications rely on the two-step process of sputter atomization followed by gas-phase excitation/ionization. Some of the most exciting new applications employ the GD simply as an excitation/ionization source for samples introduced into the vapor phase. Strategies now exist, and are quickly evolving, wherein analytes originating in either the gaseous or solution phase can be introduced into reduced pressure plasmas, including inductively coupled plasmas. In this way, the discharges afford a great range of chemical information that is vital for applications in biological and environmental chemistry. In many respects, this well-aged source is finding many new lives to lead.

1.4 VOLUME OUTLINE

In an effort to cover the most relevant applications of glow discharge spectroscopies in the most informative way, the chapters of this volume have been written by acknowledged research and application leaders in the respective areas. It is these people who are the most up to date with literature coverage and can provide the most insight into how GD sources are designed and implemented for that particular field. The chapters have been arranged so as to build first on the

fundamentals of glow discharge operation, discuss the general application of the devices in the various atomic spectrometric modes, and then to look at specific fields of application. Most of the later chapters treat for the first time the rapidly evolving use of glow discharge and other forms of reduced pressure plasmas for solution and gaseous sample analyses. In this regard, it is hoped that the reader will gain new appreciation and insight into the next generation of glow discharge sources, that at this point have not reached the commercial market, although they most certainly will given the results demonstrated to date.

The most widespread commercial application of glow discharge devices is in the area of atomic emission spectroscopy. In Chapter 2, Professor José Broekaert (University of Hamburg) describes the fundamental aspects of emission spectroscopy in general and how GD plasmas generate useful emission spectra. Comparison of operation mechanisms and analytical characteristics are made with other solids analysis methods. Also described in the chapter is the evolution of the common Grimm-type cell geometry and its many applications in bulk solids analysis. Methods of modifying the basic design in order to optimize the source characteristics are also discussed.

Chapter 3 presents the design considerations and methodologies employed in performing mass spectrometry of glow discharge devices. Professor Willard W. Harrison (University of Florida) and co-workers review the pertinent plasma processes responsible for the ionization of sputtered atoms and the roles of plasma parameters and operating modes in producing quantitatively useful mass spectra. The particular strengths and weaknesses of the different mass analyzer types are also presented. Finally, the methods of quantification for solids elemental analysis by GDMS are described.

While the majority of GD systems sold in the 1970s and 1980s were dedicated to the analysis of metallic specimens, the types of solid samples that could benefit from GD analysis extend across many different physical and chemical forms. In Chapter 4, Professor R. Kenneth Marcus (Clemson University) describes the underlying plasma physics which accompany the use of rf powering of GD sources and permit the analysis of electrically insulating materials. The results of comparative studies performed in a number of laboratories between rf and conventional dc powering modes are presented. Practical examples of the sorts of applications that rf powering permits include glass analysis, depth profiling of oxide coatings, and direct mass spectrometric analysis of polymeric materials.

The most compelling advantage of glow discharge sources over other solids analysis methods is the inherent ability to perform depth-resolved analyses in a rapid, yet well controlled manner. Dr Arne Bengtson (Swedish Institute for Metals Research) presents in Chapter 5 the fundamental and practical aspects of performing depth profile analysis using GD sources, particularly when employing optical emission detection. Plasma operation and control functions and also data acquisition parameters are discussed in detail. The concept of the emission yield

as a fundamental quantity for performing quantitative depth profiles is presented in detail along with a discussion of the common artifacts encountered and how they are remedied.

In Chapter 6, Dr Annemie Bogaerts and Professor Renaat Gijbels (University of Antwerp, Belgium) deal with their work on the modeling of analytical glow discharges. This includes the development of a fluid model and Monte Carlo simulation and also a particle-in-cell model. For analytical glow discharges, a hybrid model is shown to be very powerful and is used surprisingly well to predict current–voltage characteristics. Potential and electrical field distributions, densities and level populations of the plasma species, energies of the plasma species, sputtering profiles and even optical spectra can be calculated, which are in good agreement with experimental data. As the influence of various operational and cell parameters can be predicted, optimization of the construction of sources may greatly benefit from this work. It is also shown, however, that the acquisition of the required plasma characteristic data is very challenging and that progress here is necessary to make the agreement between the results of modeling and experimental data better still.

Probably the largest market sector employing GD spectrometries on a routine basis is the steel industry. Early acceptance took place by virtue of the relative freedom from the matrix of GD-OES in comparison with spark emission spectroscopy. In Chapter 7, Dr Kazutoshi Kakita (Nippon Steel Technoresearch Corporation) describes the current use of GD-OES in the steel industry. Aspects of method development including traceability and eventual verification are described in detail. Specific application examples include the depth-resolved analysis of galvanized steel, aluminized steel, and galvanized steel. Practical considerations in obtaining valid profiles are presented along with examples of how GD-OES profiles can be used to explain metallurgical phenomena.

As mentioned previously, the introduction of the rf powering mode opens up many new areas of application for glow discharge analyses, particularly GD-OES. Dr Richard Payling (University of Newcastle, Australia) and co-workers from a number of industrial laboratories present the use of rf-GD-OES in the analysis of surfaces, coatings, and thin films in Chapter 8. The versatility of the method is demonstrated for a large array of applications that cut across many industrial sectors ranging from studies of alloy corrosion and hardening, to electronic multilayer materials and a variety of coating technologies. Many of the examples include the use of complementary physical and chemical analysis methods to solve the posed problems.

Of course, any discussion of the capabilities of a single analytical method cannot take place with the exclusion of the figures of merit for other techniques providing the same or complementary forms of information. Professor Kazuaki Wagatsuma (Tohoku University) presents in Chapter 9 a comparison of the attributes of glow discharge spectroscopies with a number of what might be termed ‘more traditional’ methods of surface and thin film analysis. Starting

with a baseline set of qualities for (principally) GD-OES, the most relevant of the other methods are discussed. Detailed descriptions of the underlying physics and analytical characteristics are presented for ion probe, electron probe, X-ray probe, and laser probe techniques. Finally, direct comparisons between GDS and secondary ion mass spectrometry (SIMS) and with Auger electron/photoelectron spectroscopies are made for the same samples. Actual analytical data are presented in the comparisons to highlight the respective performance characteristics of each method.

The analysis of samples of nuclear concern with glow discharge atomic spectrometry is treated in Chapter 10 by Dr Maria Betti (European Commission, JRC, Karlsruhe, Germany). For the applications of GD techniques for the determination of major and trace elements, as well as the matrix isotopic composition, dc-GDMS and rf-GD-OES instrumentation installed inside glove-boxes has been described for the handling of radioactive samples. The analysis of conductive samples has been described in addition to different approaches for the analysis of nonconductive samples. The latter includes the use of radio frequency powered sources, the use of a secondary cathode, and mixing with a binder conductive host matrix prior to briquetting. In the case of oxide-based samples, the employment of a tantalum secondary cathode acting as an oxygen getter is shown to reduce polyatomic ion formation and plasma quenching. Analysis of uranium oxide with respect to impurities and isotopic composition is reported and GDMS is shown to be competitive with TIMS.

The analysis of nonconducting materials in general is treated in Chapter 11 by Dr Annemie Bogaerts, Dr Wim Schelles and Professor René Van Grieken (University of Antwerp, Belgium). Here the features and use of the three methodologies mentioned above are discussed for a wide range of applications, referring to the respective literature. In the technique using metal powders as binder, special attention is given to the sample-to-host ratio. The influence of the particle size in the case of the analysis of powders is discussed, in addition to the presence of trapped gases in the pellets. Applications cited range from ores to glasses, vegetation to ceramic samples and meteoric residues. For the case of a conducting secondary cathode, the mechanism is discussed in detail. Attention is also paid to the material and geometry of the secondary cathode, and the discharge conditions and applications of the technique confined to GDMS work are discussed.

Driven by the highly international nature of commerce, there is an increasing need for standardization within given industrial and economic sectors. In the area of analytical chemistry, standardization can be thought of in terms of either methodology or reference materials. Dr Michael Winchester (National Institute of Standards and Technology, USA) describes both of these aspects of achieving accurate analytical results in Chapter 12. Standard methods adopted by a number of standards development organizations such as ASTM and ISO are presented for both GDMS and GD-OES. In addition, the various classifications and uses for reference materials and how they are developed are also described.

Traditionally, the development of glow discharge sources as tools for performing direct solids elemental analysis took place in parallel with developments of techniques for the analysis of solution samples including flames and atmospheric pressure plasma sources. While the kinetic temperature of a GD plasma is too low to achieve solution sample desolvation in the case of direct solution nebulization, there are a number of advantages that can be projected in using the sources for the analysis of samples originating in the solution phase. Professor R. Kenneth Marcus (Clemson University) describes in Chapter 13 the three general approaches to introducing solution samples into GD sources for subsequent analysis. Included in the discussion are two different means of introducing solutions as part of flowing streams such as encountered in liquid chromatography. The versatility of the GD source as a detector for elemental speciation is demonstrated in the analysis of a number of amino acid species.

Just as GD devices can be used to advantage as detectors for liquid chromatography, their use as detectors for gas chromatography (GC) also holds great promise. The coupling between the GC and a glow discharge is quite natural as no solvent load is imposed on the plasma and because the mobile phase is usually an inert gas that can sustain the plasma. In Chapter 14, Professor Joseph A. Caruso (University of Cincinnati) and Dr Lisa Milstein (RTI International) describe the coupling of gas chromatography with GDMS sources to effect a powerful new approach to elemental speciation of volatile organometallic molecules. The ability of the sources to achieve sub-picogram sensitivities while providing unambiguous mass spectra of species of environmental importance is demonstrated. Very important in these applications is the ability to 'tune' the fragmentation patterns of mass spectra to achieve different levels of information. Studies to date suggest that this approach holds much promise for speciation studies in environmental and biological chemistry.

In Chapter 15, Dr Rosario Pereiro, Dr Nestor G. Orellana-Velado and Professor Alfredo Sanz-Medel (University of Oviedo, Spain) treat the use of glow discharge atomic emission spectrometry as an alternative gas chromatographic detector. The favorable physical features of atomic emission spectrometry with a low-pressure discharge, such as low continuum background and high electron temperatures, indeed make it a promising spectrochemical source for the analysis of gases and volatilized analytes. Potentially, the glow discharge could offer similar and even better detection limits than other more common sources used as detectors for the direct analysis of gaseous samples or as a detector in gas chromatography. An important advantage of glow discharges when used for chromatographic detection are their low running costs. In the chapter, three approaches to the introduction of analytes into the discharge chamber in the gas phase are treated. First, the gaseous samples or liquid organic samples can be introduced after vaporization by thermal means. Second, a chemical reaction can be used to convert the analyte from a liquid sample to a volatile derivative. Finally, the glow discharge can be used as gas chromatographic detector

directly. Details about the source construction, types of cathodes and interfaces, the plasma operating conditions, and analytical performance both for dc and rf sources are discussed along with relevant examples.

Even though this book is devoted to the development and application of glow discharge sources for analytical spectroscopy, there are other means of producing low-pressure plasma sources that have favorable characteristics for speciation studies. In each of the approaches, the target plasma has very similar gas-phase characteristics to GD sources, as such very powerful ion sources for speciation studies are the result. Professor Hywel Evans (University of Plymouth) describes in Chapter 16 how a variety of powering schemes can result in analytically useful low-pressure (LP) plasma ion sources. Specifically, inductively coupled and microwave-induced plasmas can be configured to operate in the 1–10 Torr range. Rf microplasmas and flowing afterglows are also described. In comparison with their widely used atmospheric pressure cousins, MS sampling of these plasmas is easier from the instrumentation point of view. In addition, optical emission sampling is an effective means of GC detection.

In Chapter 17, Dr John Guzowski, Jr and Professor Gary Hieftje (Indiana University) treat the development of multidimensional ionization sources for plasma-source mass spectrometry and give an outlook on a very important direction of development for glow discharges. For chemical speciation, it is a common approach to couple a separation method with a selective and sensitive detection method such as mass spectrometry. Conventional atomic or molecular mass spectrometric ionization sources are ordinarily incapable of providing, by themselves, both elemental and molecular information. This limitation drastically increases the cost, time, and complexity associated with fully characterizing a sample. However, new ionization sources, among which are glow discharges, are being developed that can generate both atomic and molecular fragment ions, and have been coupled with a variety of mass spectrometers and separation techniques. The approaches being used in the development of these multidimensional ion sources are highlighted in this chapter. Ultimately, the goal is to develop a single ionization source that can provide both types of information during a single measurement, making it especially valuable as a chemical speciation and characterization tool.

In the development of this volume, it was the Editors' intention to put together a comprehensive overview of the quickly expanding area of glow discharge spectroscopies. It is hoped that the volume will be a useful reference source for those entering the field and practitioners alike.

1.5 REFERENCES

1. Paschen, F. *Ann. Phys.* 1916, **50**, 191.
2. Schuler, H. Z. *Phys.* 1929, **59**, 149.
3. Grimm, W. *Spectrochim. Acta, Part B* 1968, **23**, 443–454.

4. Belle, C. J.; Johnson, J. D. *Appl. Spectrosc.* 1973, **27**, 118–124.
5. Bengtson, A. *Spectrochim. Acta, Part B* 1985, **40**, 631–639.
6. Marcus, R. K.; Harville, T. R.; Mei, Y.; Shick, C. R., Jr. *Anal. Chem.* 1994, **66**, 902A–911A.
7. Fang, D.; Marcus, R. K. In *Glow Discharge Spectroscopies*, Marcus, R. K., Ed., Plenum, New York, 1993, Chapter 2.
8. Howason, A. M. *An Introduction to Gas Discharges*, Pergamon Press, Elmsford, NY, 1976.
9. Davis, W. C.; Marcus, R. K. *J. Anal. At. Spectrom.* 2001, **16**, 931–937.
10. Boumans, P. W. J. M. *Theory of Spectrochemical Excitation*, Hilger & Watts, London, 1966.
11. Broekaert, J. A. C. *Analytical Atomic Spectrometry with Flames and Plasmas*, Wiley-VCH, Weinheim, 2001.

2

Optical Emission Spectrometry with Glow Discharges

J. A. C. BROEKAERT

*University of Hamburg, Institute for Inorganic and Applied Chemistry,
Hamburg, Germany*

2.1 INTRODUCTION

Atomic spectrometry is the oldest instrumental method of elemental analysis and in its principle goes back to the work of Bunsen and Kirchhoff in the middle of the 19th century [1]. One makes use of the fact that owing to the element-specific energy differences between the atomic terms, every element has a specific line spectrum, where the presence of an elemental atomic line directly relates to the presence of the respective element. On the other hand, the intensity of an atomic emission line is directly related to the number density of the radiating atoms and thus finally to the concentration of the element in the sample analyzed. In atomic emission spectrometry, one accordingly makes use of a radiation source where the sample material is brought in the gas phase and excited. The radiation is spectrally resolved in a spectrometer and the intensities of the analytical lines are measured with suitable detectors after isolation from the other spectral lines with the aid of a slit. The fact that all elements brought in the radiation sources emit their element-specific spectra enables multielement determinations of virtually all elements present in the sample. Apart from optical emission spectrometry, atomic absorption was discovered at about the same time. Here one found that analyte material in the gas phase is able to absorb radiation of the same wavelength as an emitted spectral line of the same element. In this case one uses a primary source emitting the element-specific radiation. The latter is passed through an

analyte reservoir containing the sample in the atomized form and the absorption of the element-specific radiation is measured. Here the selectivity of the analysis method is realized in the primary source and the spectrometer is less important. Therefore, the approach permits monoelement determinations, essentially.

The diversity in atomic emission and atomic absorption spectrometry results from the many different radiation sources in atomic emission and atom reservoirs in atomic absorption. Here, great innovation has taken place in atomic emission spectrometry since its early beginnings with flames for the analysis of liquid samples and arcs for solids analysis; this also applies for atomic absorption in the case of the atom reservoirs. Glow discharges are one of the possible groups of radiation sources for atomic emission. Their study goes back to the early work on electrical discharges by Penning in the beginning of the 20th century [2]. Glow discharges were developed as alternatives to classical arc and spark sources (and later on lasers) for direct solids analyses or besides mainly inductively coupled plasmas for the analysis of liquids or microwave discharges for determinations in gases or vapors. The glow discharges, their fundamental properties and their nature with respect to sample volatilization and excitation as well as their analytical properties as sources for atomic emission are centrally treated in this chapter. This necessitates a treatment of the processes involved in the formation of glow discharges as well as a discussion of their plasma parameters together with ways to measure them. As mostly solids and to a much lesser extent solutions or gases are directly analyzed, there is great importance in knowing the means of sample volatilization, their relation to the plasma parameters and the relative importance of the different mechanisms of sample volatilization in the different types of glow discharge sources. The latter include sources with a flat cathode and sources with a hollow cathode where the sample is at high temperature or cooled during operation of the source. The plasma generation processes also determine the excitation of the analytes and sample matrices. Both the special nature of sample ablation and the excitation in a so-called delocalized plasma of low density and large volume mostly at reduced pressure determine the analytical properties of glow discharges. Both are important with respect to power of detection, precision, freedom of spectral and other types of interferences and the multielement capacity. The analytical capacities of glow discharges also have to be compared with other sources for atomic spectrometry allowing direct solids analysis. This is required in terms of analytical performance and also with respect to costs.

2.2 GLOW DISCHARGES

In the radiation sources for atomic spectrometry the plasma is produced by an electrical discharge. Here electrically charged particles (ions, electrons) are moved under the influence of an electric field between electrodes, where they can also recombine and lose their charge. When a voltage is provided between

two electrodes placed in a gas-filled discharge tube, free electrons and ions are formed in the vicinity of the electrode and a measurable current flows because

- the electrons gain energy from the field until they can cause ionization during the collisions;
- electrons are expelled from the electrode (cathode) through collisions with energy-rich ions (secondary emission);
- field emission starts as the binding energy of the electrons is surpassed (from 10^7 V/cm onwards);
- electrons or ions can be freed as a result of an increase in the temperature of the electrode (thermoemission).

As a result of all these processes, the gas becomes partially ionized and a so-called plasma is formed.

2.2.1 GAS-PHASE PROCESSES IN GLOW DISCHARGES

As a result of the collisions between all kinds of particles in the gas phase an energy exchange takes place. One distinguishes between different types of collisions:

- Inelastic collisions:

When a particle of mass m_1 collides with a particle of mass m_2 the fraction of the kinetic energy transferred is given by

$$\Delta E / (E_i - E_m) = 2m_1 m_2 / (m_1 + m_2)^2 \quad (2.1)$$

where ΔE is the amount of energy transferred and $E_i - E_m$ is the part of the kinetic energy of an individual particle E_i above the mean energy of the particles E_m .

When the mass of the particle m_1 is much less than the mass of the particle m_2 ,

$$\Delta E / (E_i - E_m) \sim 2m_1 / m_2 \quad (2.2)$$

and $10^{-5} < 2m_1 / m_2 < 10^{-3}$. When the masses of the colliding particles are equal, the energy transfer is a maximum and

$$\Delta E / (E_i - E_m) \sim 1/2 \quad (2.3)$$

- Charge transfer:

Here only an electron and only little kinetic energy is transferred.

- Recombination:

Slow electrons can recombine with ions and the probability therefore increases with the square of the densities and decreases with the temperature as

$$dn = -\alpha_e n^2 dT \quad (2.4)$$

The degree of interaction by collisions of particles in a plasma is determined by the cross-section of the particles and their velocity distribution. The cross-section is given by

$$\sigma(v) = 2\pi \int_0^\pi p(v, \theta)(1 - \cos \theta) \sin \theta \, d\theta \quad (2.5)$$

It is a measure for the loss of impulse of the particle with mass m and velocity v when it collides with particles with mass M including its change of direction. With respect to the impulse exchange by collisions, the particle velocity distributions are also important. In a plasma they can be given by a Maxwell function:

$$dn/n = 2/(\sqrt{\pi})\sqrt{u'}e^{-u'} \, du' \quad (2.6)$$

but also by a Druyvenstein function:

$$dn/n = 1.039\sqrt{u'} \exp(-0.548u'^2) \, du' \quad (2.7)$$

where $u' = E/kT$ and E the mean energy of the particles. Whereas most often the velocity distributions can be described with a Maxwell function, it is necessary to use a Druyvenstein function when there are strong electrical fields and lack of collisions for ensuring equilibration with respect to the energies of the different species in the plasma. When the latter is reached the population of the energy levels for each species can be described by the Boltzmann equation

$$n_q/n_0 = (g_q/g_0) \exp(-E_q/kT) \quad (2.8)$$

where n_q is the number density of the particles in the excited state, n_0 the number density of the particles in the ground state, g_q and g_0 are the statistical weights of the corresponding levels, E_q is the excitation energy of the state q , k is Boltzmann's constant (1.38×10^{-16} erg/K) and T is the absolute temperature.

When referring to the sum of the number densities in all states instead of the number density in the ground state $n = \sum_m n_m$ and the equation becomes

$$n_q/n = \{g_q \exp[(-E_q)/kT]\} / \{\sum_m g_m \exp[(-E_m)/kT]\} \quad (2.9)$$

The sum $Z = \sum_m g_m \exp[(-E_m)/kT]$ is the partition function. It is denoted Z_a in the case of neutral atoms and as Z^+ in the case of ions and it is a function of temperature. For many atoms and their ions the values of the coefficients in these functions are listed in the literature [3]. When expressing the energies in eV and k by its numerical value, the expression becomes

$$\log n_a = \log n + \log g - (5040/T)V_q - \log Z_a \quad (2.10)$$

where V_q is the excitation energy in eV.

In a state of equilibrium the number of particles leaving a state of energy equals the number of particles excited to this state and for characterizing the equilibrium all processes causing excitation and de-excitation must be known. They include:

- collisions with neutrals where atoms are excited (collisions of the first kind);
- collisions where excited atoms return to a lower level without emitting radiation (collisions of the second kind);
- excitation by collisions with electrons;
- de-excitation of excited atoms through collisions with electrons;
- excitation of atoms by absorption of radiation;
- de-excitation of atoms by spontaneous or stimulated emission of radiation.

When there are in a plasma n particles of a first kind per cm^3 , when N is the number of particles of a second kind per cm^3 ($n \ll N$) and n_e is the electron number density, several equilibria are to be considered:

$$\alpha N n_0 = \beta N n_q \quad (2.11)$$

$$\alpha_e n_e n_0 = \beta_e n_e n_q \quad (2.12)$$

$$B' \rho_\nu n_0 = (A + B \rho_\nu) n_q \quad (2.13)$$

where n_e is the electron number density, A , B and B' are the Einstein transition probabilities for spontaneous emission, stimulated emission and absorption, respectively, α_e , α , β_e and β are functions of the cross-section for the process considered and the velocity distribution for the exciting particles and ρ_ν is the radiation density for radiation with a frequency ν . When the system is in so-called thermodynamic equilibrium, all processes are in equilibrium with their inverse process and with each other. The distribution of all levels is described by a Boltzmann distribution, there are no radiation losses and the temperature is given by

$$n_q/n_0 = \alpha/\beta = (\alpha_e/\beta_e) = B'/[(A/\rho_\nu) + B] = (g_q/g_0)[\exp(-E_q/kT)] \quad (2.14)$$

In the sources used in atomic spectrometry, the radiation losses constitute only a small fraction of the total energy and the sources are in so-called local thermal equilibrium, for which

$$\alpha N n_0 + \alpha_e n_e n_0 + B' \rho_\nu n_0 = \beta N n_q + \beta_e n_e n_q + (A + B \rho_\nu) n_q \quad (2.15)$$

and

$$n_q/n_0 = [\alpha N + \alpha_e n_e + B' \rho_\nu]/[\beta N + \beta_e n_e + (A + B \rho_\nu)] \quad (2.16)$$

The excitation conditions in the source determine the values of the coefficients. In a dc arc in air, $\alpha N \gg \alpha_e n_e + B' \rho_\nu$ and $\beta N \gg \beta_e n_e + (A + B \rho_\nu)$, by which

$$n_q/n_0 = \alpha/\beta = (\alpha_e/\beta_e) = (g_q/g_0)[\exp(-E_q/kT)] \quad (2.17)$$

Accordingly, excitation here is mainly due to collisions of the first kind with neutral particles. In discharges under reduced pressure and in a noble gas atmosphere, collisions with electrons play a more important role and the absorption and emission of radiation can no longer be neglected in the energy balance. Moreover, the velocity distributions can no longer be described by a Maxwell function but have to be described by a Druyvenstein function, and such sources even are no longer in local thermodynamic equilibrium.

Excited levels are energetically unfavorable. They can decay by the emission of radiation and also by collisions with other particles. When they are allowed to decay by the emission of radiation, their lifetime is very short (10^{-8} s). When no decay by emission is allowed, as the lower levels have different multiplicity, one has so-called metastable levels which only can get rid of their energy through collisions. In the case of discharges under reduced pressure, collisions are rare and the lifetimes of the metastable levels become long (up to several seconds). This gives rise to afterglow phenomena. When energy is given off by the emission of radiation the frequency of the latter is given by Planck's law:

$$E = h\nu = hc/\lambda \quad (2.18)$$

where h is Planck's constant (6.6×10^{-27} erg s). The transition probability describes the probability that decay from an excited level occurs and is given by

$$-dN_q/dt = A_{qp}N_q \quad (2.19)$$

as the number of spontaneous transitions per unit of time is proportional to the population of the excited level. As from an excited level q different transitions are possible, one can write

$$-dN_q/dt = N_q \sum_p A_{qp} \quad (2.20)$$

where $\sum_p A_{qp}$ is the inverse value of the lifetime of the excited level. Apart from the processes for spontaneous emission, for which $-dN_q/dt = N_q \sum_p A_{qp}$, also stimulated emission, where an emission only takes place when radiation of the same frequency ν is entered and for which $-dN_q/dt = N_q B_{qp} \rho_\nu$ with p the lower level, and absorption, for which $dN_q/dt = B_{pq} N_p \rho_\nu$, can take place. A_{qp} , B_{qp} and B_{pq} are the Einstein transition probabilities for spontaneous emission, stimulated emission and absorption, respectively. The intensity of an emitted atomic spectral line then is given by

$$I_{qp} = A_{qp} n_{aq} h\nu_{qp} \quad (2.21)$$

or after substituting according to Equation 2.9

$$I_{qp} = A_{qp} h \nu_{qp} n_a (g_q/Z_a) [\exp(-E_q/(kT))] \quad (2.22)$$

When enough energy is brought into the plasma, ionization also takes place. For the equilibrium

$$n_{aj} \rightleftharpoons n_{ij} + n_e \quad (2.23)$$

one defines the Saha constant as

$$K_{n_j} = S_{n_j}(T) = (n_{ij} n_e)/n_{aj} \quad (2.24)$$

The degree of ionization is given by

$$\alpha_j = n_{ij}/n_j = n_{ij}/(n_{aj} + n_{ij}) \quad (2.25)$$

Accordingly, $n_{aj} = (1 - \alpha_j)n_j$ and $n_{ij} = \alpha_j n_j$. This allows one to write for the intensity of an atom line

$$I_{qp} = A_{qp} h \nu_{qp} (g_q/Z_{aj}) (1 - \alpha_j) n_j [\exp(-E_q)/(kT)] \quad (2.26)$$

and for the intensity of an ion line

$$I_{qp}^+ = A_{qp}^+ h \nu_{qp}^+ (g_q^+/Z_{ij}) \alpha_j n_j [\exp(-E_q^+)/(kT)] \quad (2.27)$$

The factor α_j can be written as a function of the electron number density and Saha's constant as:

$$\alpha_j/(1 - \alpha_j) = S_{nj}(T)/n_e \quad (2.28)$$

The Saha function can also be written in terms of the partial pressures as $S_{pj}(T) = (p_{ij} p_e)/p_{aj}$. From wave mechanics and differentiation of the Boltzmann equation, $S_{pj}(T)$ can be obtained as

$$(p_{ij} p_e)/p_{aj} = \{[(2\pi m)^{3/2} (kT)^{5/2}]/(h^3)\} (2Z_{ij}/Z_{aj}) [\exp(-E_{ij})/(kT)] \quad (2.29)$$

With the constants $k = 1.38 \times 10^{-16}$ erg/K, $m = 9.11 \times 10^{-28}$ g being the mass of the electron, $h = 6.67 \times 10^{-27}$ erg s and $1 \text{ eV} = 1.6 \times 10^{-12}$ erg, this becomes

$$S_{pj}(T) = 6.58 \times 10^{-7} T^{5/2} Z_{ij}/Z_{aj} \times 10 [\exp(-5040 V_{ij}/T)] \quad (2.30)$$

This equation only applies when the plasma is at least in local thermal equilibrium. When there is no thermal equilibrium, the equilibrium between

species belonging to different ionization levels is given by the so-called Corona equation [4].

With the determination of the wavelengths for the atomic spectral lines emitted by different elements in the second half of the 19th century, some empirical rules were found. Balmer found that for hydrogen the wavelengths could be given by the relation

$$\lambda = k[n^2/(n^2 - 4)] \quad (2.31)$$

where $n = 3, 4, 6$ for the lines H_α , H_β and H_γ , respectively. When using wavenumbers, Equation 2.31 transforms to

$$\nu' = 1/\lambda = R(1/2^2 - 1/n^2) \quad (2.32)$$

where ν' is the wavenumber (in cm^{-1}) and R is Rydberg's constant (109.677 cm^{-1}). For all series of the spectrum of hydrogen, it was found that

$$\nu' = 1/\lambda = R(1/n_1^2 - 1/n_2^2) \quad (2.33)$$

where n_2 is a series of integral numbers $>n_1$. $n_1 = 1, 2, 3, 4, 5$ for the Lyman, Paschen, Brackett and Pfund series, respectively. Rydberg adapted Equation 2.33 for other elements by entering the charge of the nucleus Z and found

$$\nu' = 1/\lambda = RZ^2(1/n_1^2 - 1/n_2^2) \quad (2.34)$$

Accordingly, the wavelengths can be obtained from the difference of two positive terms and the spectra consist of as many spectral lines as differences of terms are possible. These terms are the energy levels of the atoms described by the quantum theory. These atomic and ionic energy levels are related to the atomic structure itself. For an electron in a single valence electron atom with charge of the nucleus Z , the energy according to Bohr is given by

$$E = -(2\pi Z^2 e^4 \mu)/(n^2 h^2) \quad (2.35)$$

with $\mu = mM/(m + M)$, where m is the mass of the electron, M is the mass of the nucleus and n is the principal quantum number ($n = 1, 2, 3, 4, \dots$, giving the order of the energy levels possible for the electron). For the orbital angular momentum L ,

$$|L| = h/(2\pi)\sqrt{l(l + 1)} \quad (2.36)$$

where l is the orbital quantum number and has values of $0, 1, 2, \dots, (n - 1)$; $l = 0$ for a circular orbit and $l = 1, 2, \dots$, for elliptical orbits.

The possible orientations of the elliptical orbits with respect to an external electric or magnetic field defines

$$L_z = h/(2\pi)m_l \quad (2.37)$$

where L_z is the component of the orbital angular momentum along the field axis and $m_l = \pm l, \pm(l-1), \dots, 0$ is the magnetic quantum number; for each value of l it has $(2l+1)$ values.

When a spectral line source is subjected to a magnetic field, the spectral lines display hyperfine structure (Zeeman effect). In order to explain hyperfine structure it is postulated that the electron rotates around its axis with a spin angular momentum S :

$$|S| = h/(2\pi)\sqrt{[S(S+1)]} \quad (2.38)$$

The spin quantum number m_s determines the angles between the axis of rotation and the external field as

$$s_z = h/(2\pi)m_s \quad (2.39)$$

where $m_s = 1/2$. The orbital and spin angular momenta determine the total angular momentum J of the electron:

$$J = L + S \text{ with } |J| = h/(2\pi)\sqrt{[j(j+1)]} \quad (2.40)$$

where $j = l \pm s$ is the total internal quantum number.

Atomic spectral terms differ in their electron energies and can be characterized by the quantum numbers through the term symbols:

$$n^m l_j \quad (2.41)$$

where $l = 0, 1, 2, \dots$, and the corresponding terms are given the symbols s (sharp), p (principal), d (diffuse), f (fundamental), etc., relating originally to the nature of different types of spectral lines; n is the principal quantum number, m is the multiplicity ($m = 2s + 1$) and j is the total internal quantum number. The energy levels of each element can be given in a term scheme, in which it is also indicated which transitions between energy levels are allowed and which are forbidden. This is reflected by the so-called selection rules; only those transitions are allowed for which Δn has integral values and at the same time $\Delta l = \pm 1$, $\Delta j = 0$ or ± 1 and $\Delta s = 0$. The terms for an atom with one outer (valence) electron can easily be found. For Na ($1s^2 2s^2 2p^6 3s^1$) in the ground state: $3^2 S_{1/2}$ [$l = 0(s)$, $m = 2(1/2) + 1 = 2(s = 1/2)$ and $j = 1/2(|l \pm s|)$].

For atoms with more than one valence electron, especially in the case of the low-mass elements, a so-called Russell–Saunders ($L-S$) coupling applies. The

orbital moments of all electrons have to be coupled to the total orbital momentum, like the spin momentum. The fact that each electron has a unique set of quantum numbers is known as the Pauli exclusion principle. The total quantum number L is obtained as $L = \Sigma l$, $S = \Sigma s$ and $J = L - S, \dots, L + S$. The term symbol then becomes

$${}^M L_J \quad (2.42)$$

For the case of the first excited state of Mg ($1s^2 2s^2 2p^6 3s 3p$), the terms are 3^0P_1 ($L = 1$ as $l_1 = 0$ and $l_2 = 1$, $S = 0$ as $s_1 = 1/2$ and $s_2 = -1/2$ and $J = |L \pm S| = 1$), but also 3^3P_2 , 3^3P_1 and 3^3P_0 (as for the parallel spins $s_1 = 1/2$ and $s_2 = 1/2$, $S = 1$, and further $J = 0, 1, 2$). As the number of electrons increases, the coupling becomes more complex, increasing the number of spectral terms and thus the number of lines in the spectrum. The term schemes of the elements are well documented in the work of Grotrian [3]. The term scheme for Na is shown in Figure 2.1.

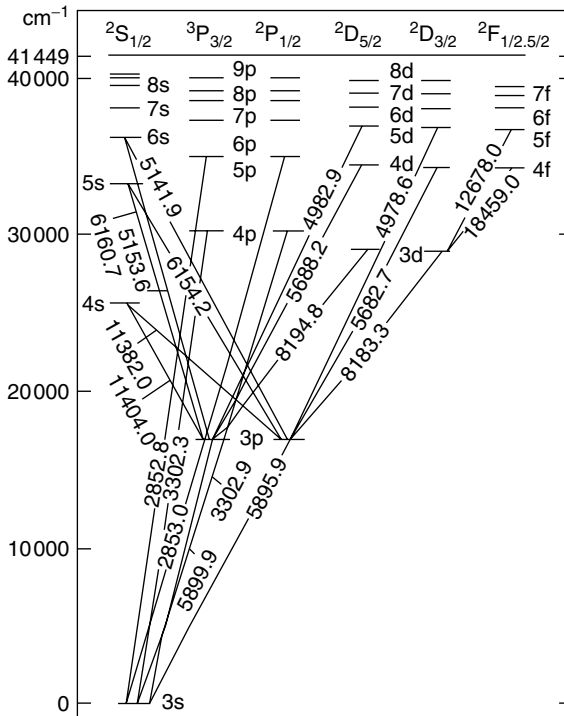


Figure 2.1 Atomic energy level diagram for the sodium atom. Reprinted from Grotrian, W., *Graphische Darstellung der Spektren von Atomen mit Ein, Zwei und Drei Valenzelektronen*, 1928, with permission from Springer-Verlag

Atomic spectral lines also have a physical width resulting from several broadening mechanisms [6]. The natural width of a spectral line results from the finite lifetime of an excited state, τ . The corresponding half-width in terms of the frequency is

$$\Delta\nu_N = 1/(2\pi\tau) \quad (2.43)$$

This corresponds with a half-width being for most spectral lines of the order of 10^{-2} pm. The Doppler or temperature broadening of a line results from the fact that the emitting species have a velocity component in the direction of observation. The half-width is

$$\Delta\nu_D = \{[2\sqrt{(\ln 2)}/c]\nu_0\{\sqrt{[(2RT)/M]}\} \quad (2.44)$$

where c is the velocity of light, ν_0 is the frequency of the line maximum, R is the gas constant and M the atomic mass. The Doppler temperature depends strongly on the gas temperature. For the Ca 422.6 nm line at 300 and 2000 K, $\Delta\nu_D$ is 0.8 and 2 pm, respectively.

The Lorentz or pressure broadening results from the interaction between emitting atoms and atoms from other elements. The half-width is given by

$$\Delta\nu_L = (2/\pi)\sigma_L^2 N \sqrt{[2\pi RT(1/M_1 + 1/M_2)]} \quad (2.45)$$

where M_1 and M_2 are the atomic masses, N the concentrations of other atoms and σ_L the cross-sections. The pressure broadening is low in the case of discharges under reduced pressure. For the Ca 422.6 nm line in the case of a gas discharge at 9 Torr and a temperature of 300 K it is only 0.02 pm [7].

Isotope and hyperfine structures and resonance broadening resulting from the interaction between emitting and nonemitting atoms of the same element and Stark broadening resulting from the interaction with electrical fields also contribute to line broadening. The natural and the Lorentz broadening can be described with a Lorentz profile, whereas the contributions of the Doppler broadening can be described with a Gauss profile. Both combine to a Voigt profile for which deconvolution is possible, as is required in determinations of the gas temperature from the Doppler broadening of spectral lines. The physical widths of spectral lines in spectrochemical radiation sources are mostly between 1 and 20 pm. In practice, however, the spectral bandwidths of spectrometers are much higher.

The radiation emitted in a source is absorbed by ground-state atoms, which are always present at high number densities. As the chance that an absorbed photon is re-emitted is small, the observed radiation is weaker than the total amount of radiation emitted, which is known as self-absorption. When $I_0 P_E(\nu)$ is the intensity distribution over the profile of a line emitted by a radiation source, where I_0 is the maximum intensity and $P_E(\nu)$ the profile function, then

the intensity distribution $I(\nu)$ obtained after the radiation has passed through a layer with n_A absorbing atoms per cm^3 is given by:

$$I(\nu) = I_0 P_E(\nu) \{ \exp - [p P_A(\nu) / P_A(\nu_0)] \} \quad (2.46)$$

where ν_0 is the frequency of the line center, $P_A(\nu)$ the absorption profile and p the absorption parameter, which increases with the transition probability. Therefore, self-absorption is strong for resonance lines being lines which end at the ground level. As the absorption profile is narrower than the emission profile, the line profile flattens as a result of self-absorption. When p becomes > 1 , one has a minimum at the line center. This can only occur when there is a strong temperature gradient in the source and when the analyte number densities in the cooler zones are still considerable. The latter is the case in strongly constricted hot discharges such as arcs and sparks but much less in glow discharges, unless for resonance lines of the matrix elements, as shown for both branches of the Cu 324.7 nm line recorded by Fourier transform optical emission spectrometry (Figure 2.2) [8].

2.2.2 DC AND RF GLOW DISCHARGES

Glow discharges are characterized by a low current density and a high burning voltage. They are strongly delocalized and, in contrast to arc and spark discharges,

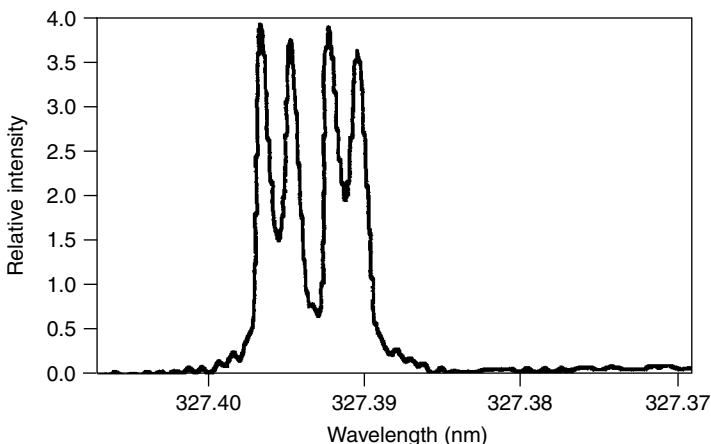


Figure 2.2 High-resolution spectral record of Cu I 327.4 nm resonance line obtained by Fourier transform spectrometry for a dc Grimm-type glow discharge. Sample, electrolytic copper plate; conventional GDS; discharge voltage, 1000 V; argon pressure, 3.5 Torr. Reprinted from Heintz, M. J., Mifflin, K., Broekaert, J. A. C. and Hieftje, G. M., *Appl. Spectrosc.* 1995, **49**, 241–246 with permission of the Society for Applied Spectroscopy

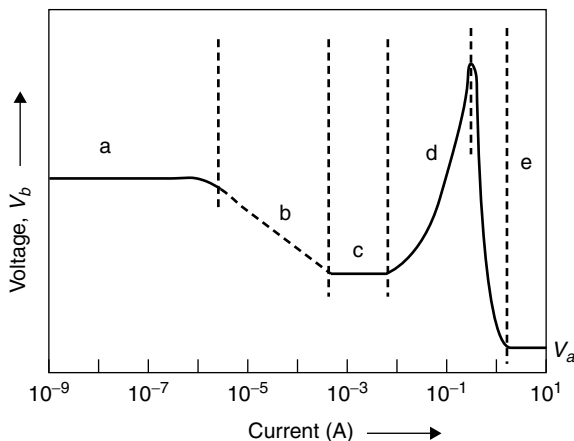


Figure 2.3 Current–voltage characteristic of a self-sustaining dc discharge. V_b , breakdown voltage; V_a , arc voltage. Reprinted from Penning, F. M., *Electrical Discharges in Gases*, 1957, p. 41 with permission of Philips Technical Library

the temperature and species number densities mostly have only low gradients. They can have both an abnormal and a normal characteristic (Figure 2.3). The former occurs when the sputtered electrode is completely covered by the discharge and the current can only be increased by increasing the current density. This range is limited by the heating of the electrode. When evaporation starts, the discharge may become normal and enter the arc regime. The latter is also the case as long as the discharge can increase the surface covered. Almost all analytical glow discharges operate in the abnormal mode.

Glow discharges can be sustained by both dc and rf electrical fields, over a range of pressure from 10^{-2} mbar to atmospheric pressure. In the case of dc glow discharges, atoms are ionized and impact with high energy on the cathode, through which material can be ablated in a purely mechanical way (cathodic sputtering) or the cathode can be heated and start to evaporate (thermal volatilization). A certain voltage is required to create enough charged particles for the sputtering process, where on the other hand the sputtered atoms which become ionized contribute to the current as well. In analytical glow discharges one can have currents of up to some 0.1 A at voltages of up to 2 kV. Here at argon pressures of a few torr, the ablation rates may be in the milligrams per minute range, by which the sputtered material in the case of complete ionization would contribute only for a few percent of the current. One mostly has a cathode and a remote anode, the latter not being analytically important in most cases. In the case of dc discharges, one distinguishes between discharges where the sample constitutes a flat cathode. Such an analytically relevant discharge was first described by Grimm in 1968 [9] (Figure 2.4). The anode is at a remote distance and one has a restrictor made of an isolator or the anode tube may come close to the cathode. A direct discharge in

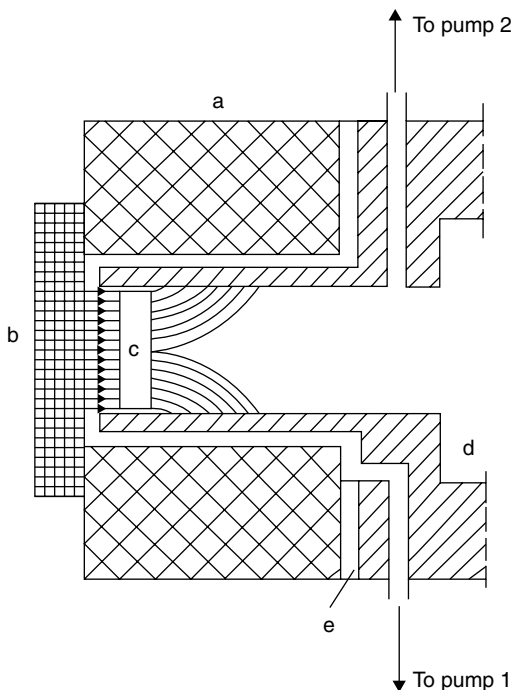


Figure 2.4 Glow discharge lamp according to Grimm. (a) Cathode block; (b) sample; (c) negative glow; (d) anode window; (e) anode–cathode interspace. Reprinted with permission from Boumans, P. W. J. M., *Anal. Chem.* 1973, **44**, 1221, Copyright 1973 American Chemical Society

the anode–cathode annular space at any case is hampered by the small distance, which is in the left wing of the so-called Paschen curve. The latter gives the breakthrough voltage as a function of the product of pressure and interelectrode distance. It has a minimum and both its left and right wings increase rapidly. In the Grimm-type lamp the cathode is cooled and is ablated by sputtering only. Owing to the form of the field, one ablates layer-by-layer, through which this type of discharge is very useful for both bulk and depth-profiling analyses. The Grimm-type glow discharge [10] is only one of many possibilities of realizing a restricted discharge with a flat burning crater. Here much work has been done, e.g. by proposing a floating restrictor or a ceramic restrictor [11]. The topic is of interest, as the residual curvature of the crater is determined by the field distribution, which depends on the way in which the restricted discharge is realized. This point is of great importance for one of the most prominent routine applications of glow discharge atomic spectrometry, namely depth profiling.

Much older than the Grimm-type glow discharge is the so-called hollow-cathode lamp, well known as a primary radiation source for atomic absorption

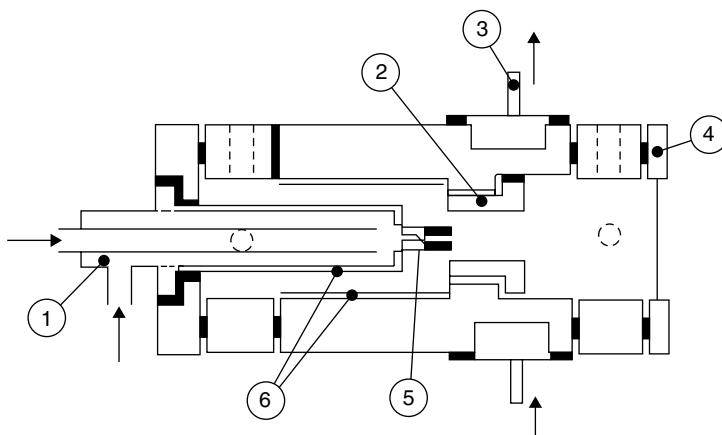


Figure 2.5 Demountable hollow cathode lamp. (1) Water-cooled, glass-shielded, electrically insulated cathode support; (2) exchangeable anode; (3) anode cooling circuit; (4) sapphire viewport; (5) graphite cathode; (6) Pyrex shields. Reprinted from Broekaert, J. A. C., *Bull. Soc. Chim. Belg.* 1976, **85**, 262 with permission of the Committee van Beheer van het Bulletin

spectrometry. This source was introduced as an emission source in the early work with glow discharges [12]. The source is demountable (Figure 2.5), so that the sample can be brought into the hollow cathode in the form of drillings, a pellet or a dry solution residue. The cathode can be shielded and cooled so that the volatilization occurs by sputtering only, while the discharge characteristic is abnormal. It also can be shielded so that thermal effects play a role, whereas the characteristic in most cases remains abnormal. In the case of a so-called hot hollow cathode, the volatilization mainly takes place by thermal effects and the characteristic becomes normal. As an atomic emission source the hollow cathode has the advantage as a source where the analyte residence times in the excitation zones are very high and accordingly the smallest absolute amounts of analyte are still detectable. Further, selective volatilization from a matrix may be very advantageous to reduce spectral interferences and matrix suppression or enhancement during excitation.

With both flat and hollow cathodes, not only dc but also rf discharges can be sustained. Here rf power is entered through an antenna. For the excitation of gases this antenna can be anywhere. Such sources are also used as primary radiation sources in atomic absorption spectrometry. When the sample is a solid to be volatilized, the rf power is often applied through the sample, as in the rf source described by Marcus and co-workers (Figure 2.6) [14]. In the case of rf discharges, frequencies in the low megahertz range are used. This field can be well followed by the electrons, but not by heavy ions. Accordingly, a bias potential in the vicinity of the sample is built up and ions accelerated through the

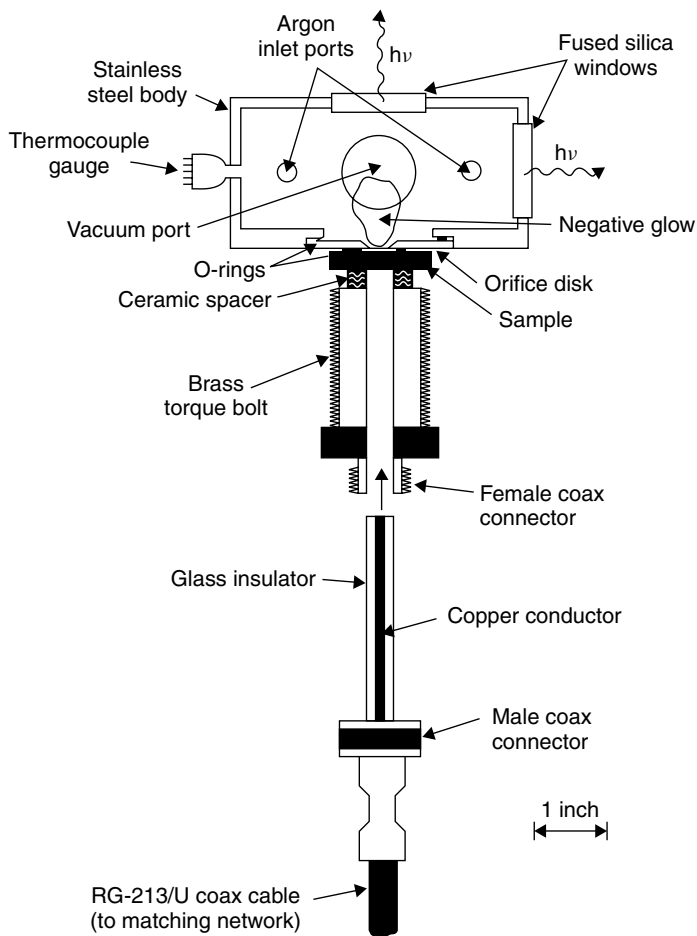


Figure 2.6 Rf glow discharge atomization/excitation source. Reprinted from Winchester, M. R., Lazik, C., Marcus, R. K., *Spectrochim. Acta, Part B* 1991, **46**, 485 with permission of Elsevier Science

dc field induced. These ions cause ablation of the sample, irrespective of whether it is electrically conductive or not, and a discharge with properties similar to dc glow discharges is formed. Also in the case of rf discharges a power of up to some 100 W can be dissipated, the gas pressure is also of the order of some torr and the sample is ablated mainly by sputtering. Also here it is ablated layer by layer; however, the crater formed depends considerably on the power and on the coupling geometry.

Other types of glow discharges are known from other fields in science and technology. This applies especially for developments in light sources and also for

coating technologies as used in microelectronics. For some of these discharges, their use for analytical purposes has also been explored or they may play an important role in emerging fields such as micro- and nanoanalytics. A source to be mentioned in this respect is the so-called barrier discharge, where power is applied through a dielectric layer coating the electrodes. This source in a miniaturized version has recently been proposed as an atom reservoir under reduced pressure for diode laser atomic absorption spectrometry [15]. Furthermore, glow discharges at atmospheric pressure, also in micro-systems, have been mentioned [16]. A special topic is the use of liquids as one of the electrodes, allowing the use of glow discharges for direct liquids analysis [17].

2.2.3 ELECTRICAL PARAMETERS OF GLOW DISCHARGES

When a voltage is applied across two electrodes in a gas atmosphere at a not too high pressure, one subsequently obtains at increasing discharge current a Townsend (a) and a corona (b) discharge (Figure 2.3). Subsequently the current increases rapidly at a nearly constant voltage, as the surface area of the electrode covered by the discharge increases in the normal glow discharge (c). One then enters the abnormal region (d), where the current can only increase at a strongly increasing voltage. The abnormal glow discharge is a self-sustaining discharge with a highly positive space charge in front of the cathode, a low current density (10^{-2} – 10^{-3} A/cm²) and a burning voltage of several hundred volts. With still further increases in the current one obtains an arc discharge (e). Here, there is thermoemission and field emission of electrons at the cathode. The positive space charge in front of the cathode drastically decreases, as does the cathode voltage drop. The burning voltage can go down to the ionization energy of the working gas. The arc discharge is characterized by a high current (several amps), a relatively low burning voltage (<100 V), a normal characteristic and intensive heat. Discharges under reduced pressure normally operate in the abnormal part of the characteristic and in the transition region between the abnormal and the normal regions. The pressure often is 1–10 Torr, the burning voltage 400–1500 V and the current 0.05–2 A. When the whole cathode is covered by the discharge, one normally has an abnormal discharge. It becomes normal when the part of the cathode covered by the discharge increases at constant current density or when working at high currents where thermal volatilization becomes considerable.

A glow discharge has a typical structure, where in different regions different species predominate and where field gradients may differ greatly (Figure 2.7). The structure of glow discharges is very similar in the case of dc and rf discharges. In the immediate vicinity of the cathode the energy of atoms and ions is very high and there are hardly any inelastic interactions and excitation is insufficient (Aston cathodic dark space). Near to it one has the cathode layer, where there is intense emission as a result of the high collision number density. Further, one has another dark space (Hittorf dark space), the negative glow and the Faraday

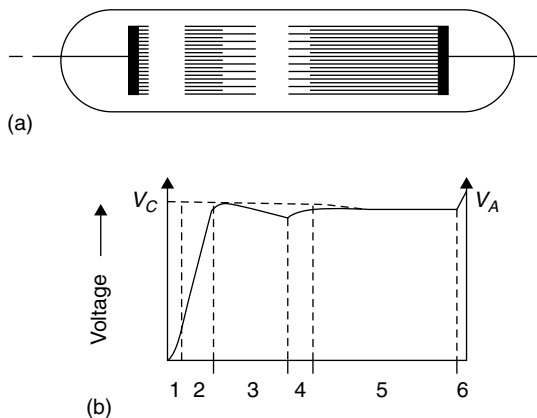
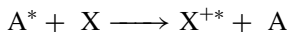


Figure 2.7 (a) Geometry and (b) potential distribution of a dc electrical discharge under reduced pressure. (1) Cathode layer and Aston dark space; (2) Hittorf dark space; (3) negative glow; (4) Faraday dark space; (5) positive column; (6) anode region

dark space. The positive column is much less intense as is the anode glow and finally there is an anode dark space. As the potential outside the cathode region hardly changes, the length of the discharge tube is almost of no importance. As one wants to obtain signals from the elements volatilized from the cathode, the negative glow is analytically very important. Here both the analyte atom number densities and the densities of the exciting species (electrons, energetic neutrals and ions) are high.

The electrons acquire much energy in the cathode fall region. Working gas atoms and ions mostly are excited through collisions of the first kind. In the case of noble gases, highly energetic metastable states are formed (e.g. for argon at 11.2 eV). They have long lifetimes, especially at low pressure (up to seconds), and may excite analyte atoms through collisions of the second kind.



The efficiency of the collisions is high when the sum of ionization and excitation energy is nearly the energy of the metastable states and little energy has to be released as kinetic energy (Penning ionization). Also, excitation through excited working gas atoms and ions is important. As highly energetic photons are also produced by photoexcitation this is important. As the pressure in glow discharges and accordingly also the number of collisions is rather low, there is no energy equilibration between different species. Also as a result of the presence of high fields, there is no Boltzmann distribution and the plasma is not in thermal equilibrium. It can be accepted that there are two groups of electrons. For one group the energy is high and so they cause excitation and ionization. The other group of slow electrons is available for recombination processes. As the pressure

and number of collisions are low the Lorentz and the Doppler broadening of spectral lines in glow discharges is low. As a consequence, the line widths in glow discharge optical emission spectroscopy (GD-OES) are relatively low and of the order of 1–2 pm.

2.2.4 PLASMA PARAMETERS AND DIAGNOSTICS

Plasmas can be characterized from their properties as sources for atomic spectrometry by a number of parameters such as temperatures and species number densities. A number of methods known from classical plasma physics can be used to determine these parameters. These methods include both spectroscopic and nonspectroscopic methods. The determination of the temperatures describing the energies of the different species (electron temperatures, gas temperatures, ion temperatures) and the determination of electron number densities and electron pressures (diagnostics) are important for characterizing the efficiency of a plasma for excitation and/or ionization of an analyte and the dependence of these processes on the sample composition.

Spectroscopic Methods

From the equations describing the intensities of atomic emission lines it becomes clear that the so-called *excitation temperature* is of paramount importance for describing the excitation efficiency. When applying Equation (2.22) to transitions from different excited states (a and b), which belong to the same level of ionization, one obtains in the notations used by Boumans [18]:

$$I_a/I_b = [(gA)_a/(gA)_b](\nu_a/\nu_b)\{\exp[-(E_a - E_b)/(kT)]\} \quad (2.47)$$

or

$$T = [5040/(V_a - V_b)]/[\log[(gA)_a/(gA)_b] - \log(\lambda_a/\lambda_b) - \log(I_a/I_b)] \quad (2.48)$$

where T is the excitation temperature, which can be determined with high precision and accuracy with thermometric species such as Zn, which have a high ionization energy. This procedure is known as the two-line method. Further, the excitation energies of the excited terms used should differ widely, the ratio $(gA)_a/(gA)_b$ must be large and the wavelengths of the lines should not differ too much so as to minimize the influence of the spectral response of the detector. The transition probabilities should also be well known. The excitation temperature can be determined even more precisely by using a large number of atomic emission lines of the element in the same state of ionization. Indeed, from Equation 2.22 one obtains

$$\ln[I_{qp}/(g_q A_{qp} \nu_{qp})] = \ln(h\nu/Z) - E_q/(kT) \quad (2.49)$$

where n is the thermometer species number density. By plotting for a number of lines $\ln[I_{qp}/(g_q A_{qp} \nu_{qp})]$ versus E_q (Boltzmann plot), one obtains a straight line and from the slope T can be determined.

One also can write Equation 2.49 as

$$\ln\{I[\lambda/(gA)]\} = \ln[hc(n/Z)] - E_q/(kT) \quad (2.50)$$

for which the $\lambda/(gA)$ values for a large number of elements can be found in tables.

The excitation temperature is physically meaningful only when the plasma is at least in low-temperature equilibrium (LTE). In the case of glow discharges, excitation temperatures therefore can only be used to describe the population of excited levels. In plasmas where there is a large deviation of LTE one also has to determine the so-called *gas temperature*, which describes the kinetic energy of neutrals and heavy particles in general.

The gas temperature is usually similar for neutrals and radicals. Therefore, it can often be approximated by the so-called rotational temperature describing the population of the terms in molecular spectroscopy. Molecules and radicals, such as those stemming from working gases (CN, NH, NO, OH, N₂ or N₂⁺) or from thermally stable oxides of sample constituents (such as AlO⁺, TiO⁺, YO⁺, etc.), have different electronic states (¹Σ, ²Σ, ²Π, etc.). The latter have a vibrational fine structure ($\nu = 0, 1, 2, \dots$) and a rotational hyperfine structure ($J = 0, 1, 2, 3, \dots$). The total energy of a state is given by

$$E = E_{el} + E_{vibr} + E_{rot} \quad (2.51)$$

E_{el} is of the order of 1–10 eV, the difference between two vibrational states of the same electronic level is ca 0.25 eV and between two rotational states only 0.005 eV. When a transition between two rotational levels occurs, a rotational line is emitted. When both levels belong to the same electronic level, the line is in the infrared region. When they belong to different electronic levels, however, its wavelength is in the UV or visible region. Such transitions are characterized by $n', \nu', j' \rightarrow n'', \nu'', j''$. All lines emitted as a result of transitions between rotational levels belonging to different vibrational levels of two electronic states form a band: $n'\nu' \rightarrow n''\nu''$. Transitions are subject to the selection rules: $\Delta j = j' - j'' = \pm 1, 0$. For $j'' = j' + 1$ one has the P-branch, for $j'' = j' - 1$ the R-branch and for $j' = j''$ the Q branch. The line for $j' = j'' = 0$ is the zero line of the branch. When also $\nu' = \nu'' = 0$ it is the zero line of the system. The difference between the wavenumber σ of a rotational line and that of the zero line for the case of the P, Q and R branch is a different function of the rotational quantum number j and of linear combinations of the rotational constants for which

$$E_j/(hc) = B_v j(j+1) \quad (2.52)$$

These functions are quadratic and describe the so-called Fortrat parabola. The molecular and radical spectra consist of different electronic series, which consist of different vibrational bands. These bands often consist of many nonresolved rotational lines. The intensity of a rotational line I_{nm} emitted for a transition of the higher level m to a lower level n is given by

$$I_{nm} = N_m A_{nm} h \nu_{nm} [1/(2\pi)] \quad (2.53)$$

where N_m is the population of the excited level and ν_{nm} the frequency of the emitted radiation. The transition probability for dipole radiation is given by

$$A_{nm} = [(64\pi^4 \nu_{nm}^3)/(3k)](1/g_m) \sum |R_{nimk}|^2 \quad (2.54)$$

where i and k are degenerate levels of the higher (m) and lower (n) states. R_{nimk} is a matrix element of the electrical dipole moment and g_m is the statistical weight of the upper state. N_m is given by the Boltzmann equation (Equation 2.10), in which E_r is the rotational energy for the excited electronic and vibrational level and is given by

$$E_r = hc B_{v'} J'(J' + 1) \quad (2.55)$$

$B_{v'}$ is the rotational constant and J' the rotational quantum number of the upper state. For a (${}^2\Sigma - {}^2\Sigma$) transition, $\sum |R_{nimk}|^2$ is equal to $J' + J'' + 1$ and

$$I_{nm} = [(16\pi^3 c N \nu_{nm}^4)/3Z(T)](j' + J'' + 1) \{ \exp[hc B_{v'} J'(J' + 1)] / (kT) \} \quad (2.56)$$

or

$$\ln[I_{nm}/(J' + J'' + 1)] = \ln[(16\pi^3 c N \nu_{nm}^4)/(3Z(T))] - \{ [hc B_{v'} J'(J' + 1)] / (kT) \} \quad (2.57)$$

When plotting for a number of rotational lines $\ln[I_{nm}/(J' + J'' + 1)]$ versus $J'(J' + 1)$, one obtains the rotational temperature. In the case of glow discharges one can accept LTE for molecules and radicals, and rotational temperatures in the range 300–1200 K are found, as shown, e.g., for argon and helium hollow-cathode sources [19].

The gas temperature can also be determined from the Doppler width of a spectral line (see Equation 2.44). Therefore, it is necessary to separate the Lorentz and the Doppler contributions of the linewidth, which is possible with the aid of deconvolution programs [6].

A further important diagnostic characteristic is the *electron number density*. It can be calculated from the line intensity ratio for an atom and an ion line of the same element (see Equations 2.26 and 2.27) as

$$\begin{aligned} \log[\alpha_j/(1 - \alpha_j)] = & \log(I_{qp}^+/I_{qp}) - \log[(g_q^+ A_{qp}^+ \nu_{qp}^+) / (g_q A_{qp} \nu_{qp})] \\ & + (5040/T)(V_q^+ - V_q) + \log(Z_{ij}/Z_{aj}) \end{aligned} \quad (2.58)$$

This method only delivers correct values for α when the plasma is in LTE, as the temperature must be known. In this way one can also determine the electron pressure by combining with the Saha equation (Equation 2.30) as

$$\log[\alpha_j/(1 - \alpha_j)] = \log S_{pj}(T) - \log p_e \quad (2.59)$$

so that

$$\begin{aligned} \log p_e = & -\log(I_{qp}^+/I_{qp}) + \log[(g_q^+ A_{qp}^+ \nu_{qp}^+)/ (g_q A_{qp} \nu_{qp})] \\ & - (5040/T)(V_{ij} + V_q^+ - V_q) + (5/2) \log T - 6.18 \end{aligned} \quad (2.60)$$

Through $p_e = n_e kT$ one obtains the electron number density. Also here the plasma must be in LTE to permit correct calculations.

Irrespective of the existence of LTE, one can determine the electron number density from the Stark broadening of the hydrogen β (H_β) or of argon lines. This line broadening contribution is mainly determined by the interaction of the electrons in the plasma and is the predominant one in the case of the H_β and some argon lines, from which the n_e can be determined as described by Mermet for inductively coupled plasmas (ICPs) [20]. In the case of Grimm-type glow discharges, Human and co-workers determined n_e values and found values of the order of 10^{-11} cm^{-3} [21]. From these n_e and p_e values and Equation 2.60, one can also calculate a temperature which describes the energy of the electrons and is called the *ion temperature*. The energy of the electrons is described by the *electron temperature*. It can be determined from the background continuum intensities, which are determined by the interaction of free with free electrons (bremsstrahlung) and the interaction of free and bound electrons (recombination continuum). Electron temperatures in the case of glow discharges may range from 5000 K for the slow electrons to several 10 000 K for the high-energy electrons. Irrespective of the existence of LTE, gas temperatures, electron temperatures and electron number densities can be determined by laser scattering and measurements of the Rayleigh and Thomson scattering, as discussed by Hieftje [22]. The low number densities in glow discharges, however, present a particular challenge for this method.

Nonspectroscopic Measurements

Electron number densities can also experimentally be determined by measurements with Langmuir probes, as shown by Marcus for rf glow discharges, as discussed in Chapter 4.

2.3 ATOMIC EMISSION SPECTROMETRY

Atomic emission spectroscopy as a method of instrumental analysis has a high selectivity and therewith a high multielement capacity. The fact that the occurrence

of the spectral lines of an element is unequivocal proof of its presence in the sample makes it a strong approach for qualitative analysis. As the intensities of atomic spectral lines directly relate to the analyte number densities in the source and indirectly also in the sample and all these relations are known, one should be able to calculate the concentrations from the intensities measured. However, through lack of precise atomic constants and lack of knowledge on the losses of radiation in the spectrometer, one uses optical emission spectrometry as a relative method, and not as an absolute method. Calibration then needs to be done with samples of known analyte content and a matrix composition similar to that of the samples to be analyzed.

2.3.1 BASIC PRINCIPLES

The relation between atomic line intensities I and analyte concentrations c can be formulated as

$$I = ac^b \quad (2.61)$$

where a and b are constants. Absolute intensities are only used in flame and ICP atomic emission, but also in glow discharge atomic emission as these sources are very stable. Often, however, the intensity ratio of an analyte line intensity to a reference signal is used, which goes back to early arc emission spectrometry work. This leads to calibration functions of the form

$$I/I_R = a'c^{b'} \quad (2.62)$$

The inverse calibration function is the analytical evaluation function:

$$c = c_R(I/I_R)^\eta \quad (2.63)$$

or

$$\log c = \log c_R + \eta \log(I/I_R) \quad (2.64)$$

In trace analysis, the slope of the analytical evaluation curve (in logarithmic form) is usually 1; at higher concentrations η may become >1 as a result of self-reversal. In the case of glow discharge atomic spectrometry, this has been found to be the case for resonance lines at high concentrations or when they are the matrix element. In this case they cannot be used as reference lines. In trace analysis by atomic emission spectrometry, the intensity of the spectral background is often taken as a reference and the calibration equation then becomes

$$c = c_U(I_x/I_U)^\eta \quad (2.65)$$

where $c_U = [(I_x/I_U)(1/c)]^{-1}$ is the background equivalent concentration (BEC) and c is the concentration for which a line to background intensity ratio I_x/I_U is measured.

In atomic emission spectrometry one has to be aware of the fact that the atomic spectra as a result of the high number of terms are very line-rich. This may lead to coincidences of lines in the registered spectra. This risk is still increased by the fact that the temperatures in the atomic emission sources should be high so as to reach a sufficiently high population of the excited states. This is necessary to obtain high line intensities. For classical sources, such as the spark and arc, the 92 naturally occurring elements produce more than 200 000 spectral lines between 200 and 400 nm, as tabulated in the MIT spectral line tables. It should be emphasized that still many more spectral lines are emitted by these sources. According to the concentrations of the respective elements, these lines occur in the spectra with a certain line to background intensity ratio. Apart from atomic spectral lines, band emission also occurs. This may be due to molecules and radicals stemming from the working gases or from breakdown products of salts, which is the case for, e.g., oxides MO^+ . In the case of glow discharges, the optical atomic spectra are relatively poor in spectral lines in comparison with arcs and sparks. Mostly, the atomic resonance lines are strong, but then also suffer from self-reversal in the case of atom lines. The latter effect hampers their use as analytical lines for high concentrations. Furthermore, the linewidths are low (1–2 pm), which again lowers the risk of spectral interferences. Also band emission is limited. Indeed, one often works under a noble gas atmosphere at reduced pressure. The use of pure noble gases is required so as to keep the risks for quenching of the excitation or excited species low. Therefore, GD-OES can be characterized by low risks of interferences from molecular bands.

The spectral background in atomic spectrometry sources stems from several contributions. Apart from stray light in the spectrometer, the intensity of which is proportional to the total amount of radiation emitted in the source, there are several contributions to be considered. The intensity of the continuum background radiation in discharges under reduced pressure is low, as the electron number densities are low. They have been found to be of the order of 10^{11} cm^{-3} , which is at least a factor of 10^4 lower than in arc, spark or ICP sources. Furthermore, the intensities of the wings of matrix lines, which may be very broad, have to be considered as contributors to the spectral background. This is especially the case when the matrix elements have very sensitive resonance lines, such as calcium and magnesium. This contribution in the case of glow discharges is considerably lower than in sources operated at atmospheric pressure. This also applies for contributions from band emission spectra. They are low when the glow discharge is operated with pure noble gases. Here, however, one often has to provide for in-line gas purification systems or systems where the sample is entered into the source through an air-lock. In atomic emission spectrometry, provisions in any case must be made to free the analytical signals from contributions of interfering spectral lines and from changes in spectral background intensity. As glow discharges are very stable sources, one can therefore subtract the intensities at the analytical wavelengths, which one obtains for blank samples, from the

measured intensities. In the case of solids analysis, one often has no suitable blank samples. Here one has to make an estimate of the spectral background intensity at the analytical wavelength from the intensities measured besides the analytical lines. This is often possible through the rather flat nature of the spectral background and through the high stability of glow discharges.

2.3.2 INSTRUMENTATION FOR GLOW DISCHARGE EMISSION SPECTROMETRY

The instrumentation for glow discharge atomic spectrometry includes a discharge source with the required vacuum and gas supply, an electrical power supply, a spectrometer and the required illumination system, as well as radiation measurement and data readout systems. Both the discharge source and its parameter settings and the data acquisition are often controlled by appropriate computer facilities.

As atomic spectrometers, both monochromators especially designed for high-resolution work and spectrometers using either classical photomultipliers or advanced multichannel detectors are used. Photomultipliers consist of a photocathode, where the incoming photons as a result of the Compton effect free photoelectrons. The ratio of the photoelectrons produced per incoming photon determines the quantum efficiency (mostly between 10 and 20%). The photoelectrons enter a dynode chain, where each dynode is kept at a certain potential with respect to the preceding dynode or the photocathode, respectively. As a result, a photoelectron frees several secondary electrons at the first dynode and each of them several electrons at the following dynode. With dynode voltages of 100 V and up to 10 dynodes, multiplication factors of 10^5 can be obtained. Accordingly, with photon fluxes of 100 000 photons/s, which are often obtained through the exit slit, cathode currents of 10^{-14} A [$100\,000 \times 1.6 \times 10^{-19}$ (charge of the electron in Coulomb)] can be obtained. Subsequent to amplification, anode currents of 10^{-9} A can be obtained, which can be measured with sufficiently high signal-to-noise ratios. Photomultipliers can be used in a wide spectral range (with an S 20 photocathode certainly from below 200–500 nm and with bialkali cathodes at longer wavelengths). They have a high linear dynamic range, being defined as the range within which the signal linearly changes with the photon flux, which is of the order of five orders of magnitude. The lower limit of the dynamic range is set by the dark current, being the signal obtained in the absence of plasma radiation, as a result of cosmic radiation and imperfections in the amplifiers and transmission lines. The dark current of photomultipliers is often in the 0.1 pA range (10^{-10} A). Photomultipliers are very useful for single-channel detection within a wide linear dynamic and spectral range and with high ratios of signal-to-dark current.

With semiconductor detectors, simultaneous measurements even at a high number of so-called pixels are possible. Specifically, charge-coupled and charge-injection devices [23] are now in use. They unify the simultaneous parallel input

capacity of photographic plates, used since the early beginnings of atomic spectrometry but suffering from laborious readout and lack of adequate precision and spectral range coverage, and the high precision of photomultiplier detectors. Through the action of incoming photons in microstructures, electron–hole pairs are produced, which have a certain lifetime and can be read out also after integration at the local pixels. Accordingly, even low level simultaneous, but locally differing, radiation intensities of spectral features can be detected with high signal-to-noise ratios and a dynamic range now encompassing more than three orders of magnitude. Detectors with dimensions of 1×1 in and as many as 1000 pixels in both directions are now available from several manufacturers. To increase the sensitivity of new detectors, so-called microchannel plates are very useful. They are made of semiconductor materials in which many equidistant and small-sized parallel channels are provided, which all act as photomultipliers when a high voltage is supplied between the two sides of the plates. The electron multiplication is very efficient and these devices can be well combined with phosphors and linear diode arrays and two-dimensional charge-coupled device (CCD) detectors. As two-dimensional detectors, so-called image dissection tubes [24] have also been proposed. In these devices an aperture is provided between the photocathode and the dynode chain. The photoelectrons leaving different locations of the photocathode can be directed selectively through the aperture with the aid of electrical or magnetic fields. Detectors of the size of 1×1 in have been constructed, with dynamic range, sensitivity and signal-to-noise ratios similar to those of photomultipliers.

Both sequential and simultaneous spectrometers use an illumination system consisting of several lenses, allowing entry of radiation from a preselected zone in the discharge with a suitable space angle through the entrance slit into the spectrometer. One often uses a three-lens illumination system, with which the radiation from a well-defined zone in the source is selected at the intermediate image of the field lens with the aid of a diaphragm. At the diaphragm a second lens is used to image the field lens on the slit and a lens in front of the slit to fill the entrance collimator of the spectrometer, from which a parallel beam of the incoming radiation is produced and directed on to the dispersive element of the spectrometer. This system allows it to select the observation zone and to fill the entrance slit of the spectrometer homogeneously with radiation. Additionally, a fiber with a defined entrance angle can be combined with a small lens with short focal length to bring the radiation flexibly on the entrance slit where it again illuminates the entrance collimator through a lens so that stray radiation in the spectrometer is avoided. As monochromators, mostly Czerny–Turner and Ebert geometries are used. Both have a turnable reflection grating illuminated by the entrance collimator having a focal length of 0.3–1 m. The Czerny–Turner monochromator has a separate exit collimator imaging the spectrum in the exit camera, where a photomultiplier is located behind the exit slit. As the entrance and exit collimator may have slightly different focal lengths and entrance angles,

coma aberrations are minimized and a straight exit slit can be used. In an Ebert monochromator the same mirror is used as entrance and exit collimator, and often a curved exit slit must be used. Entrance and exit slit widths are kept small (10–20 μm) to keep the spectral bandwidths of the monochromator small and to allow high practical spectral resolution ($\lambda/\Delta\lambda$). In the case of a grating with low line density (1/1200 to 1/3600 mm) and a sufficient width (60–90 mm), a high theoretical resolving power (100 000 and more) is obtained. With small slit widths, 10 and 20 μm for the entrance and exit slit, respectively, the practical resolution in the case of 1 m spectrometers may be 40 000 or more. As such, spectral lines with wavelength differences of 0.02 nm at 200 nm, for example, can still be resolved. The practical resolution is limited by the slit widths, which cannot be made too narrow, as then diffraction limits the practical resolution and the transmission of the spectrometer also becomes low. Moreover, the exit slit should always be considerably wider than the entrance slit so as to minimize the effects of mechanical drift. Monochromators equipped with photomultipliers especially are of interest for high-resolution work; however, they do not permit simultaneous recording of the intensities of lines and the adjacent spectral background or of different spectral lines.

Simultaneous spectrometers mostly use a so-called Paschen–Runge mounting, where the entrance slit, the curved grating and different detectors are aligned along the Rowland circle. In the case of photomultipliers and exit slits, many detector units can be aligned along the focal curve. For example, in a 1 m Paschen–Runge spectrometer the number can amount to 30 or more. Further, CCDs have become so cheap that one may mount up to 20 CCDs along the focal curve and cover the whole analytically important spectral range continuously. In the CIROS instrument (Spectro Analytical GmbH), this has been done. The use of diode-array spectrometers, where one makes very efficient use of the parallel input capacity of a 1024 pixel array through the use of a segmented spectrometer, has already shown to be very useful. This has been shown for spectra from a glow discharge for steel samples recorded with a diode-array spectrometer, where several atomic emission lines together with the adjacent background structures could be measured simultaneously [25]. A further possibility for simultaneous electronic detection lies in the use of Echelle spectrometers. Here with a crossed dispersion system the wavelengths are separated with an Echelle grating, having a low line density but being used at high orders, and the orders are separated with a prism. Through the two-dimensional arrangement, high spectral resolution can be obtained with apparatus of low focal length, which improves the thermal stability. Parts of the spectrum may be measured with separate spectral systems inside the main spectrometer in both cases. In the case of the Echelle spectrometer, a large number of spectral lines are accessible together with the adjacent wavelength ranges so as to permit background correction.

In addition to dispersive spectrometers, nondispersive spectrometers may also be used. Here the Fourier transform spectrometer using a Michelson interferometer

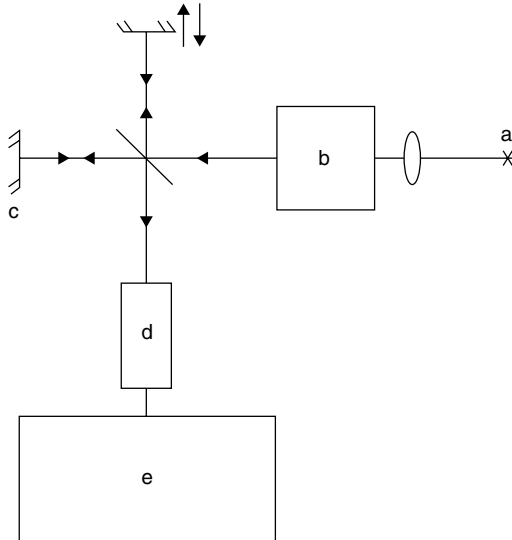


Figure 2.8 Principle of Fourier transform emission spectrometry. (a) Source; (b) pre-dispersion; (c) interferometer; (d) detector; (e) FT in computer

[26] is most important (Figure 2.8). With the aid of a beamsplitter, the radiation is split into two parts, each of which is directed to a mirror. Shifting the mirror in one of the side-arms gives an interference for each wavelength:

$$I(x) = B(\sigma)[1 + \cos(2\pi\sigma x)] \quad (2.66)$$

where x is the optical path difference, I the intensity measured with the detector and B the radiation density of the source. A polychromatic radiation source gives an interferogram where the intensity of each point is the sum of all values resulting from Equation 2.66. The central part contains the low-resolution information and the ends contain high-resolution information. The resolution depends on the recording time, the spectral bandwidth and the number of scans. By applying a Fourier transform to the signal for each point of the interferogram:

$$\begin{aligned} I(x) &= \int_{-\infty}^{+\infty} B(\sigma) d\sigma + \int_{-\infty}^{+\infty} B(\sigma) \cos(2\pi\sigma x) d\sigma \\ &= C + \int_{-\infty}^{+\infty} B(\sigma) \cos(2\pi\sigma x) d\sigma \end{aligned} \quad (2.67)$$

where C is a constant which must be subtracted before the transformation. The end result is

$$B(\sigma) = \int_{-\infty}^{+\infty} I(x) \cos(2\pi\sigma x) dx \quad (2.68)$$

By digitizing the interferogram, rapid Fourier transformation is possible with a powerful computer. For complex spectra, this is possible by small, but highly accurate, stepwise displacements of the side-arm. Repetitive scanning intensifies the image, and a reference laser is used to make the mirror positioning reproducible. The technique has been used for decades in infrared spectroscopy but since the end of the 1980s also in the visible and UV regions. Fourier transform atomic emission spectrometry is suitable for sources with a low radiance and with a high-stability detector to avoid detector noise. Wavelength calibration must be very accurate to achieve maximum resolution. Reasonable signal-to-noise ratios are only achieved with low-noise sources. Owing to the low radiation output and high stabilities of glow discharges, the use of Fourier transform atomic emission spectrometry is very suitable. As shown in Figure 2.2, even the self-reversal of copper atomic emission resonance lines in the case of a Grimm-type glow discharge used for copper samples can be studied in detail for both wings of the Cu I 324.7 nm line [8]. From measurements with a boosted Grimm-type glow discharge lamp, it was found that the self-reversal is due to the high density of ground-state atoms in front of the plasma. Indeed, when using cross-excitation, e.g. with a microwave discharge, the self-reversal decreases considerably [27]. From measurements of linewidths, it was found that most spectral lines have widths in the 1–2 pm range unless they are prone to large Stark broadening or have hyperfine structure [28]. In the case of Fourier transform atomic spectrometry with a Grimm-type glow discharge, a detection limit for molybdenum in steel of as low as 30 $\mu\text{g/g}$ could be obtained without much optimization [28]. In Fourier transform atomic emission spectrometry, the resolution achievable is very high and so is the wavelength precision. The instrument is ideally suited for recording spectra as required for wavelength tables and atlases.

Nowadays in atomic emission spectrometry of compact solid samples, mostly systems with a flat cathode are used, as described earlier (see Section 2.2.2). Special developments have taken place both for increasing the material volatilization and the specific radiation output. The first aim can be achieved by using gas jet-assisted sputtering [29] and also by constricting the plasma with the aid of magnetic fields [8] in the case of both dc and rf discharges. A considerable increase in the specific radiation output can be reached by applying cross-excitation. This can be obtained with a dc discharge [30]. However, a high-frequency discharge [31] and a microwave discharge [32] can also be used. Whereas the high-frequency energy easily can be coupled into the plasma with the aid of an antenna, the use of microwaves for boosting is most effective, when providing a cavity such as the TM_{010} resonance cavity according to Beenakker in front of the glow discharge, as shown in Figure 2.9.

A further instrumental development in the field of glow discharges for atomic spectrometry is the introduction of gases for analysis. For this aim, classical lamps can be easily used and one simply provides a plate with an aperture at the location of the compact solid sample. Here it is advantageous to use helium as working

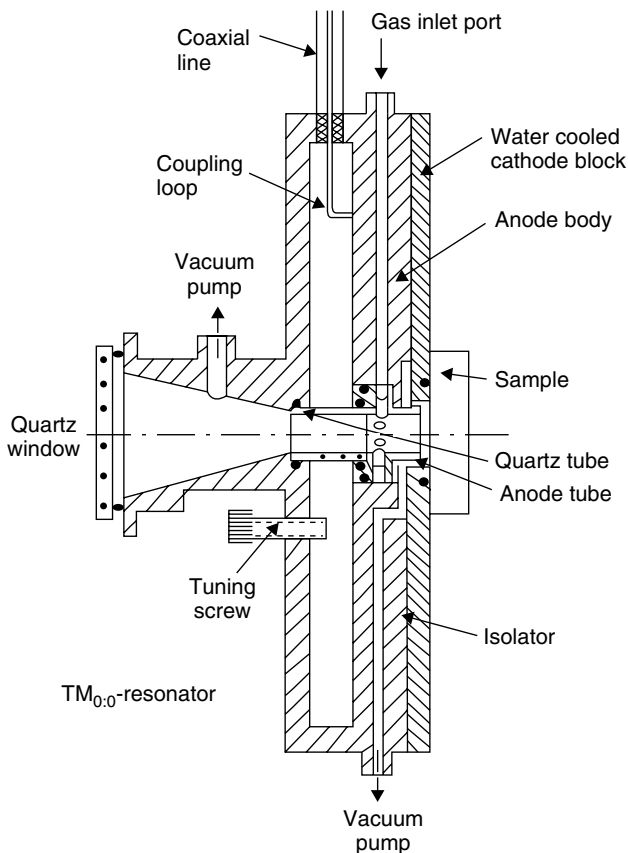


Figure 2.9 Glow discharge lamp with integrated microwave cavity for atomic emission spectrometry. Reprinted from Leis, F., Broekaert, J. A. C. and Laqua, K., *Spectrochim. Acta, Part B* 1987, **42**, 1170 with permission of Elsevier Science

gas as then the sputtering activity is low and the excitation efficiency for elements with high excitation potential, such as the halogens and chalcogens, is high. It was found, however, that the form of the aperture has a considerable influence on the spatial distribution of the line intensities [33]. In a helium discharge, it was possible to break down halogenated hydrocarbons so far that the elemental ratios can be derived from the ratios of atomic emission line intensities. This was found to be true both for classical Grimm-type glow discharges [33] and for hollow-cathode discharges [34], when introducing halogenated hydrocarbons. For the analysis of gas mixtures, so-called gas sampling glow discharges can also be used. In the case of hydride generation, it was found that argon, helium and neon can also be used as discharge gases [35] and that in all cases both elemental and, as shown by mass spectra, molecular information can be extracted, depending on

the working conditions. The possibility of highly sensitive elemental detection in the gas phase makes glow discharges very suitable for performing empirical formula determinations, being very useful for peak identification, when using glow discharges for element-specific detection in gas chromatography. This area is rapidly expanding, as microdischarges, which are very small and have low gas and power consumption, are now becoming available. This is the case for dielectric barrier discharges as described by Miclea *et al.* [15].

From the instrumentation point of view, the vacuum system used is very important. Indeed, because of the high power of detection of glow discharges, impurities in the source may be very unfavorable. This applies especially for molecular gases, remaining after bringing the source back to atmospheric pressure for sample change. This is especially true when these elements are to be determined or they give rise to spectral interferences, also as a result of molecular bands. Precautions have to be taken including baking of the lamp body, purification of the gas, the use of getters, *etc.* Furthermore, back-diffusion from the pumping system used must be controlled. Here one now mostly uses turbomolecular pumps instead of oil pumps. The latter also may influence the discharge stability as a result of pump ripple. As working parameters, not only the gas pressure but also the gas flow through the lamp is important. For the pressure measurements, being necessary in the range 0.1–10 mbar, depending on the gas used, one mostly makes use of capacitance manometers. The gas pressure measurement is critical, as one hardly can measure the pressure in the discharge itself. Further, it is important to avoid turbulence inside the discharge source space, as this gives rise to additional noise, hampering the achievable precision and power of detection. Special attention also has to be paid to the radiation sampling. First the glow discharge, being operated at reduced pressure, is mostly separated by an observation window from the spectrometer. This must be made of quartz when including UV measurements down to 150 nm and for the VUV region MgF₂ optics are required. To keep the deposition of sputtered material on the window low, which is necessary so as to maintain maximum transmittance, the gas flows entering the lamp should be directed away from the window. To sample the maximum amount of radiation, one has to tune the observation angle of the optics and the discharge source. In most cases this is no problem, apart from the case of microbore hollow cathodes with long cavities.

2.3.3 FIGURES OF MERIT

The analytical figures of merit of spectrochemical procedures include the analytical precision determined by the different sources of noise, the power of detection, the linear dynamic range and the matrix effects in terms of the different sources of interferences.

For a series of analytical signal measurements for a sample with a well-defined analyte concentration, a statistical uncertainty exists, which stems from

fluctuations in the analytical system. The *precision* achievable is an important figure of merit of an analytical procedure. In the case where the measurements have a Gaussian or normal distribution, the precision of a measurement procedure is expressed in terms of the standard deviation:

$$\sigma = \sqrt{\{[\Sigma(Y_m - Y_i)^2]/(n - 1)\}} \quad (2.69)$$

where $Y_m = \Sigma(Y_i/n)$ is the mean value, Y_i is an individual measurement and n is the number of measurements. In the case of glow discharges, relative standard deviations of better than 0.01% can be achieved as both the material volatilization and the discharge itself and accordingly the excitation are very smooth and of stable nature. The precision of a certain measurement system depends on the noise in the system. Different types of noise can be distinguished [36]:

- Fundamental or random noise: this is statistically distributed and its amplitude as a function of frequency can be written as a sum of sinusoidal functions. This type of noise is related to the discrete nature of matter and cannot be completely eliminated.
- Nonfundamental, flicker or excess noise: here the sign or the magnitude can correlate with well-defined phenomena. In the case of glow discharges, moisture included in the sample can give rise to discharge spikes appearing as flicker noise.
- Interference noise: this is observed at well-defined frequencies and mostly stems from components in the system. In the case of a glow discharge source of which the vacuum includes a rotary vane pump, the pump frequency often can be observed. This component can be eliminated by fitting a throttling valve between the pump and the source [28].

Both nonfundamental and interference noise can often be eliminated by appropriate filtering. In a noise power spectrum (NPS) the noise amplitude is plotted as a function of frequency [37]. White noise occurs over all frequencies and is almost always fundamental in origin, whereas for $1/f$ noise the amplitude decreases with the frequency and it is nonfundamental in origin. Discrete noise bands with well-defined causes may also occur. These may stem from the power supply source or from the vacuum system or the gas supply. Noise spectra are a powerful diagnostic tool to trace the sources of noise, and to study instrumental limitations to the power of detection. In atomic spectrometry, it is important to determine if noise from the detector is predominant; if so, it can be described by a Poisson distribution:

$$\sigma^2 = n \quad (2.70)$$

where n is the number of events per unit time and σ the standard deviation. In the case of glow discharges, detector noise limitations, especially in the case

of diode-array detection, may be limiting at wavelengths below 220 nm. Here the background continuum spectral radiances become very low. Indeed, in the case of a dc Grimm-type glow discharge and a high-luminosity 0.3 m McPherson monochromator, the photocurrent of a 1P28 photomultiplier for the spectral background at ~ 200 nm is 2.8×10^{-9} A, being hardly above the dark current of 2×10^{-9} A [28]. In other cases, the background noise of the source may be much more important, as is the case at wavelengths of ~ 400 nm, where background signals were 4×10^{-9} A [28] or flicker noise or frequency-dependent noise are predominant. In the latter case, overtones often occur.

For the precision of an analytical method, not only the reproducibility of single measurements but also calibration errors have to be considered. This is a complex problem, as depending on the nature of the noise, the precision may vary considerably with concentration. In glow discharge atomic spectrometry, at concentrations sufficiently above the detection limit, the relative standard deviations may be fairly constant over a considerable range of concentration.

When a linear regression is performed of the form $Y = ac + b$, where c is concentration, the standard deviation of the regression can be defined as

$$s(Y) = \sqrt{[\Sigma(Y_i - Y)^2 / (n - 2)]} \quad (2.71)$$

where Y_i is the signal obtained for a standard sample with concentration c from the regression equation. The latter is calculated by a least-squares procedure from the pairs (c, Y) , where Y are the measured signals and n is the total number of measurements. The standard deviation for the concentration of the analytical sample c_X can be calculated through a propagation of error:

$$s_r(c_X) = \ln_{10} s(c_X) = \ln_{10} a' s(Y) \quad (2.72)$$

where a' is the slope of the calibration curve. The magnitude of the concentration of the analytical sample with respect to those of the standard samples has to be considered, and can be included in the equation as follows:

$$s_r(c_X) = \ln_{10} a' s(Y) \sqrt{\{(1/n) + (1/m) + (c_X - c_m)^2 / [\Sigma(c - c_m)^2]\}} \quad (2.73)$$

where m is the number of replicates for the analytical sample and c_m is the mean of all the standard concentrations measured.

Here one assumes that the precision with which the concentrations of the standard samples are known is much better than the precision of the analytical procedure, which is often not the case. Then the error on the standard samples has to be included in the analytical error. The influence of this uncertainty on the analytical error in the case of a calibration with one external calibration sample can be calculated by a propagation of error. When weighing an amount of analyte — there is a weighing error σ_M and when mixing this amount of analyte

with a diluent up to a mass M' , there is an additional uncertainty $\sigma_{M'}$ on the mass to be taken into account. The resulting standard deviation of the concentration $\sigma_{r,c}$ can be calculated as

$$\sigma_{r,c} = \sqrt{[(\sigma_M/M)^2 + (\sigma_{M'}/M')^2]} \quad (2.74)$$

When calibrating with one synthetic calibration sample with concentration c_S , the concentration of the unknown sample can be calculated as

$$c_X = (Y_X/Y_S)c_S \quad (2.75)$$

and

$$\sigma^2(c_X) = (\delta c_X/\delta Y_X)^2 \sigma^2(Y_X) + (\delta c_X/\delta Y_S)^2 \sigma^2(Y_S) + (\delta c_X/\delta c_S) \sigma^2(c_S) \quad (2.76)$$

with

$$\delta c_X/\delta Y_X = \delta/\delta Y_X [(Y_X/Y_S)c_S] = c_S/Y_S \quad (2.77)$$

$$\delta c_X/\delta Y_S = \delta/\delta Y_S [(Y_X/Y_S)c_S] = -(Y_X c_S)/(Y_S^2) \quad (2.78)$$

$$\delta c_X/\delta c_S = \delta/\delta c_S [(Y_X/Y_S)c_S] = Y_X/Y_S \quad (2.79)$$

and

$$\sigma^2(c_X) = (c_S/Y_S)^2 \sigma^2(Y_X) + [-(Y_X c_S)/Y_S^2]^2 \sigma^2(Y_S) + (Y_X/Y_S) \sigma^2(c_S) \quad (2.80)$$

Accordingly, analysis results can be made traceable to amounts of substance with an uncertainty including both measurement uncertainties and uncertainties in the concentrations of the calibration samples.

The calibration functions are valid only for a limited concentration range, known as the *linear dynamic range*. This range is limited at the upper end by physical phenomena, such as self-absorption and detector saturation, and at the lower end by the limit of determination. In the case of glow discharges, especially for the lower end of the dynamic range at low wavelengths, detector noise limitations can be limiting and at the high end of the dynamic range self-reversal may limit the linearity of calibration curves. The limit of determination is a characteristic of a given analytical procedure and is the lowest concentration at which a determination can be performed with a certain precision. This figure of merit is clearly to be distinguished from the *limit of detection*. For 99.86% certainty, and provided that the fluctuations of the limiting noise source can be described by a normal distribution, the lowest detectable net signal Y_L is three times the relevant standard deviation σ^* :

$$Y_L = 3\sigma^* \quad (2.81)$$

The net signal is determined from the difference between a background signal and a signal including analyte and background contributions, so a factor of $\sqrt{2}$ has to be introduced. In many cases the limiting standard deviation is often the standard deviation obtained for a series of blank measurements [38]. From the calibration function the detection limit can be written as

$$c_L = a'(3\sqrt{2})\sigma \quad (2.82)$$

The detection limit is therefore closely related to the signal-to-background and the signal-to-noise ratios. It is the concentration for which the signal-to-background ratio is $3\sqrt{2}$ times the relative standard deviation of the spectral background intensity, or at which the signal-to-noise ratio is $3\sqrt{2}$. The signal-to-noise ratio itself is related to the types of noise occurring in the analytical system. From a knowledge of the limiting noise sources, well-established measures can improve the signal-to-noise ratio and hence the power of detection. Procedures for the calculation of the limits of detection in the case of glow discharge atomic spectrometry are described by Marcus in Chapter 4.

The analytical signals measured often include contributions from constituents other than the analyte (e.g. matrix constituents). This is known as spectral interference and can be corrected by subtracting contributions calculated from the magnitude of interference and the concentration of the interfering species. A special type of interference influences the background signal on which the analyte signals are superimposed; a number of correction methods exist. As in glow discharge optical emission spectrometry the physical widths of the lines are low and the spectra are often not so rich in lines as is the case with other sources, the risks of spectral interferences are often low. As influences of matrix constituents on analyte volatilization and excitation often are also low, multiplicative interferences often are low.

2.4 MATERIAL ABLATION

For direct solids analysis, the sample has to be brought into the vapor phase, so that the composition of the latter is representative of the sample or the analyte is brought up to a reproducible fraction in the vapor phase. This can be done by thermal volatilization methods, by sputtering action and also by laser or electroerosion through sparks and arcs. In the case of glow discharges, thermal volatilization and sputtering are very important for the case of solids. For liquids, dry solution residue volatilization, a nebulization process followed by a moisture removal, so as to avoid influences of the latter on the excitation processes in the plasma, and vapor generation techniques such as hydride generation can be used. Thermal volatilization and sputtering are treated here more in detail, whereas for the other techniques reference is made to the respective chapters.

2.4.1 THERMAL VOLATILIZATION

Thermal volatilization is important where the sample is heated, as a result of atom or ion bombardment, without providing external cooling. This may be the case where the plasma is present in a well-defined space such as in the so-called hollow cathode, being positioned freely in the discharge chamber without providing a cooling. Here, in the case of a graphite cathode temperatures of above 2000 K can easily be obtained at discharge currents above 100 mA and discharge voltages even above 1 kV in the case of argon. Under such conditions the analytes can evaporate according to their boiling-points, even making it possible to leave behind a less volatile matrix. This approach has been found very successful for the determination of volatile elements such as As, Se, S, P, etc. in high-temperature alloys [39]. In the case of refractory powders even volatile compound formation may be useful, such as in the case of Ti and Fe by adding halogens. The approach may be useful for obtaining the highest power of detection for the volatile analytes or so as to avoid spectral interferences from the matrix. Anyhow, thermal volatilization normally does not lead to signals that are constant in time, which makes calibration difficult. In practice, well-designed glow discharge sources with flat cathodes are cooled to eliminate thermal volatilization.

2.4.2 ABLATION BY SPUTTERING

In this case, the sample is ablated layer by layer as a result of impacting species removing the analyte atoms from their lattice sites by impulse transfer. When the sample is taken as a cathode, positive ions gain energy and impact with high energy on the sample. However, when the ions through collisions are transformed into neutrals, the latter can also give rise to cathodic sputtering. Cathodic sputtering not only occurs in dc discharges. In rf discharges a barrier layer and a bias potential are built up in the vicinity of the sample as a result of the different mobilities of electrons and ions in the rf field. Accordingly, the energy situation becomes similar to that of dc discharges and similar sputtering phenomena can occur. The models developed for cathodic sputtering start from ideal solids, i.e. single, perfect crystals, whereas real samples in atomic spectrochemical analysis are polycrystalline or even chemically heterogeneous. The available models developed for high-vacuum sputtering are valid only for monoenergetic beams of neutrals impacting on the sample, whereas in fact both ions and atoms of widely different energies impact at different angles.

The ablation is characterized by a sputtering rate q ($\mu\text{g/s}$) and a penetration rate w ($\mu\text{m/s}$) [10]. The latter is the thickness of the layer removed per unit time and related to the sputtering rate by

$$w = (10^{-2}q)/(\rho s) \quad (2.83)$$

where s is the target area (cm^2) and ρ is the density (g/cm^3). The sputtering yield indicates the number of sputtered atoms per incident particle:

$$S = (10^{-6}qN_Ae)/(MI^+) \quad (2.84)$$

where N_A is Avogadro's constant, e the charge of an electron (in coulombs), M the atomic mass and I^+ the ion current (in amps).

As treated in textbooks (see, e.g., Ref. [40]), classical sputtering experiments with a monoenergetic ion beam in high vacuum show that the sputtering yield first increases with increasing mass of the incident ions and the pressure, but then decreases. For polycrystals, it is maximized at an incident angle of 30° . For single crystals, it is maximum in the direction perpendicular to a densely packed plane. The results of these experiments can only be explained by the impulse theory. According to this theory, a particle can be removed from a lattice site when the displacement energy E_d (the sum of the covalent or electrostatic binding energies) is delivered by momentum transfer from the incident particles. The maximum fraction of the energy transferrable from an incident particle is

$$E_{\text{max}}/E = (4mM)/(m + M) \quad (2.85)$$

The ablation rate is thus proportional to the number of particles which deliver an energy equal to the displacement energy. It should be taken into account, however, that some incident particles are reflected (f_r) or adsorbed at the surface. Particles of low mass can penetrate into the lattice and be captured (f_p). Other particles enter the lattice and cause a number of collisions until their energy is below the displacement energy. The overall sputtering yield accounting for all of the processes mentioned is

$$S = [(\alpha E)/E_d]^{1/2}(f_p + Af_a)\varphi \quad (2.86)$$

with $\alpha = (2mM)/(m + M)^2$ and $\varphi = f(m, M)$.

Accordingly, cathodic sputtering increases with increasing energy of the incident particles and is inversely proportional to the displacement energy E_d . It is a maximum when $m = M$. This explains why sputtering by analyte species which diffuse back to the target is very efficient. The dependence of the sputtering yield on the orientation of the target with respect to the beam can be easily explained. In a single crystal, there is a focusing of momentum along an atom row in the direction of dense packing. If D_{hkl} is the lattice constant and d the smallest distance between atoms (or ions) during a collision, the angle θ_1 , at which particles are displaced from their lattice sites, relates to the angle θ_0 , between the direction of the atom row and the line between the displaced atom and its nearest neighbor in the next row, according to the equation

$$\theta_1 = \theta_0(D_{hkl}/d - 1) \quad (2.87)$$

This focusing of momentum, referred to as Silsbee focusing, takes place when

$$f = \theta_{n+1}/\theta_n \text{ or } D_{hkl}/d < 2.$$

2.4.3 ABLATION RATES

The model described for the cathodic sputtering is very helpful for optimizing glow discharges with cooled cathodes [10]. When sample volatilization by sputtering occurs, it should be noted that some features can be realized only when working at sputtering equilibrium. On initiating a discharge, the burning voltage is normally high in order to break through the layer of oxides and of gases adsorbed at the electrode surface. When these species are sputtered off and the breakdown products are pumped away, the burning spot (crater) can start to penetrate with a constant velocity into the sample, so that the composition of the ablated material in the plasma may become constant. The time required to reach sputtering equilibrium (burn-in time) depends on the nature and pretreatment of the sample and also on the filler gas used and its pressure. All measures which increase the ablation rate will shorten the burn-in times. Burn-in times are usually up to 30 s for metals (at 90 W in argon: zinc 6 s, brass 3–5 s, steel 20 s, Al 40 s), but depend on the sputter conditions (shorter at high burning voltage, low pressure, etc.), on the fact whether dc or rf powering is used and on the powering scheme in rf operation.

The topography of the burning crater depends on the solid-state structure of the samples. It reflects its graininess, chemical homogeneity and degree of crystallinity. Inclusions and defects may locally disturb the sputtering. These effects can be observed on micrographs, comparing the craters obtained with a glow discharge and a spark (Figure 2.10) [41]. The roughness of the burning crater can be measured with sensing probes; it imposes the ultimate limitation of the depth resolution obtainable when applying sputtering to study variations of sample composition with depth from the sample surface. The structure of the burning crater depends on the material structure and on inclusions. Also, the electrical field may induce a small curvature, especially in the classical glow discharge lamp [11]. It stems from changes of the electrical field across the sample surface but is also influenced by the pumping. The latter causes a wall to be built up around the burning spot, as a result of the deposition of sputtered material entrained into the vacuum line. Field inhomogeneities seem to be lower in the case of a floating restrictor or a restrictor made of electrically nonconducting material and a remote anode.

Achievable ablation rates depend on the sample composition and the discharge gas and its pressure. In glow discharge optical emission spectrometry, one mostly works at ablation rates in the mg/min range. Normally a noble gas is used as filler gas. With nitrogen or oxygen, chemical reactions at the sample surface occur and disturb the sputtering, as electrically insulating oxide or nitride layers are formed.

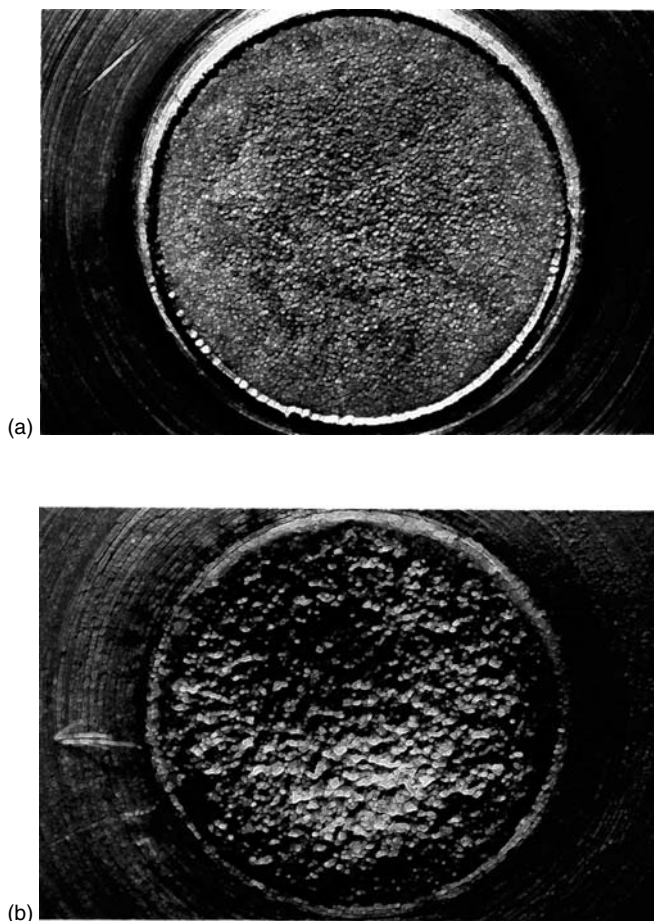


Figure 2.10 Burning spots obtained with (a) a Grimm-type dc glow discharge and (b) a medium-voltage spark. Sample, aluminum. Reproduced by permission by the Royal Chemical Society from Broekaert, J. A. C., *J. Anal. At. Spectrom.* 1987, **2**, 539

Reactions with the ablated material would further produce molecular species which emit band spectra in optical atomic spectrometry, or produce cluster ion signals in mass spectrometry. In both cases, severe spectral interferences could hamper the measurement of the analytical signals. The relation between ablation rates and sample composition can be understood from the impulse theory. In most cases argon ($m = 40$) is used as sputtering gas, and the sequence of the ablation rates follows the mass sequence $C < Al < Fe < \text{steel} < Cu < \text{brass} < Zn$.

For solids analysis, helium is not suitable as working gas, as its small mass renders its sputtering efficiency negligible. The sputtering rates further increase in the sequence $Ne < Ar < Kr < Xe$. The last two gases are rarely used because

of their price. Neon is attractive because of its high ionization potential and may be used in mass spectrometry when argon causes spectral interferences. The gas pressure has a very important influence on the electrical characteristics, as discussed already. At low gas pressure the burning voltage is high, as is the energy of the incident particles. At high pressure, the number density of potential charge carriers is higher and the voltage decreases. The number of collisions also increases, so the energy of the incident particles decreases. The resulting decrease in sputtering rate with increasing gas pressure for a Grimm-type glow discharge with planar cathode and abnormal characteristic [42] can be described as

$$q = c/\sqrt{p} \quad (2.88)$$

where c is a constant and p the pressure.

In bulk analysis, the sputtering rate is important in order to come rapidly to a sputtering equilibrium, but also to sample enough material per unit time to compensate for sample inhomogeneities, which otherwise would decrease the analytical precision. For depth-profile analysis, one should work at high pressure so as to obtain sufficient depth resolution. First, working at relatively high pressure has the advantage of resulting in low sputtering rates and moreover the luminosity per unit penetration into the sample is high. Both are good for obtaining high signal-to-background rates and precision, as detector noise will be less dominant, and accordingly the power of detection will be high. Several approaches have been followed to increase the sputtering rate, especially in bulk analysis, as finally the line intensities are proportional to the amount of sample ablated per unit time. By the application of a magnetic field, which is possible even through metallic samples of 1–2 mm thickness by providing a strong permanent magnet in a cooled holder behind the sample, the ablation rates already can be increased by a factor of three, while keeping the pressure and the voltage at the same value [8]. In this case the current was found to increase slightly. The discharge as a result of the magnetic field, however, was found to become more ring-shaped, which also was observed back in the more concave form of the burning crater. Through the use of gas jets directed on the sample surface, the ablation rates can also be enhanced considerably [29]. This could be shown for the case of a Grimm-type glow discharge, where channels with a width of 0.2–0.5 mm were drilled under an angle of 45° and a gas flow of ca 200 ml/min was directed on the burning spot of an argon discharge operated at 60 W. Through the jets an increase in burning voltage was implied and also in sputtering rate. The latter in the case of copper was found to be increased from 1.4 to ~ 5 mg/min. As shown for the case of brass, turbulence in the plasma can occur, through which even selective sputtering and/or deposition could occur. This could be shown by electron microprobe line scans across the burning spot. It was also found that the intensities of resonance lines do not increase, in contrast with the intensities of nonresonance lines, e.g. for copper. This again testifies to the importance of

self-reversal as the result of the presence of a highly dense cloud of ground-state atoms in front of the plasma.

Whereas in bulk analysis the form of the crater profile is not very important, it is extremely important in depth profiling analysis, as together with the roughness of the burning crater bottom it is the ultimate limitation of the depth resolution. For dc discharges in the case of jet-assisted sputtering through narrow channels the burning crater profile becomes so irregular that depth profiling is no longer possible. It is a question if with increased gas flows through the anode–cathode interspace there also would be increased sputtering without making the burning profile irregular. With a magnetic field the curvature of the burning crater becomes concave and accordingly also here the depth resolution decreases. With rf discharges, it could be found that especially when the discharge spot becomes very large, the ring shaping of the plasma as a result of a magnetic field can become extreme. Further, both concave and convex burning profiles can be obtained as a result of combined influences of the burning spot diameter, the gas flows and the power dissipated in the source.

2.5 ANALYSES WITH GLOW DISCHARGE ATOMIC EMISSION SPECTROMETRY

Glow discharge atomic emission spectrometry is now a standard method used for the analysis of metals and metallurgical samples, with respect to both bulk and in-depth composition, the analysis of nonconducting powders subsequent to mixing with metal powder, direct analysis of compact electrically nonconducting samples through the use of rf discharges, dry solution residue analysis and the analysis of gases.

2.5.1 BULK ANALYSIS OF METAL SAMPLES

Metal samples can be analyzed with GD-OES using flat cathodes with high powers of detection, precision and accuracy and the linear dynamic range is excellent. The preburn times are longer than in spark emission spectrometry and accordingly the method is less suitable for in-line production control applications. After discharge initiation preburn-times up to 30 s must be used to come to stable ablation. In this time adsorbed species and the oxide layers are sputtered off and a constant crater surface in terms of sputtering and re-deposition is formed. Both the structure and the composition of the samples influence the preburn times required. In the case of large crystals they may be longer and for matrices such as Cu and Zn they are much smaller than for Al, which in addition to its mass has the drawback of easy oxide layer formation. Through applying high power (> 100 W) and especially high voltage through reducing the pressure, the material ablation can be increased often by a factor of up to three, thus reducing the preburn times to the same extent.

The achievable limits of detection in GD-OES are limited by the background continuum intensities or detector noise, especially at low wavelengths. Owing to the very low background intensities, high line-to-background ratios are obtained and, as the stability of the discharges is excellent, this results in low detection limits. For most elements and types of metal samples they are in the $\mu\text{g/g}$ range. This is well documented by the detection limits for steel samples listed in Table 2.1 [32]. Here also elements such as B, P, S, O, N and H can be included, provided that the blank contributions are kept low and that for a number of elements VUV lines are used.

The analytical precision achievable with GD-OES, as a result of the absence of flicker noise, is very favorable and relative standard deviations (RSDs) even for absolute line intensities may be of the order of 1%. When ratioing to a matrix line and performing simultaneous measurements of analytical and internal standard line intensities, one first realizes the full precision in analytical atomic spectrometry. Indeed, when I_X is the intensity of the analytical line of the analyte X and I_R the intensity of the reference line of an element R, the ratio can be written as

$$I_X/I_R = \{[n_{(X)}A_X\nu_Xg_XQ_{(R)}]/[n_{(R)}A_R\nu_Rg_RQ_{(X)}]\}[\exp(E_R - E_X)/(kT)] \quad (2.89)$$

In order to compensate efficiently for fluctuations in sample ablation and in excitation temperature, the volatilities, the excitation energies E_R and E_X , and the partition functions Q should be similar. In any case, either two atom or two ion lines should be selected, as otherwise ionization differences would falsify the

Table 2.1 Detection limits ($\mu\text{g/g}$) for steels in spark and glow discharge OES.

Element	Spark OES ^a	GD-OES ^b
Al	0.5	0.1
B	1	0.3
Cr	3	0.05
Cu	0.5	0.3
Mg	2	0.9
Mn	3	0.2
Mo	1	0.8
Nb	2	0.6
Ni	3	0.1
Si	3	0.4
Ti	1	0.6
V	1	1
Zr	2	1.5

^aSpark discharge in argon using polychromator [43].

^bGrimm-type glow discharge with 1 m Czerny–Turner monochromator [32].

number densities of the radiating analytical or reference species. For the same reason, the ionization energies of both should be as similar as possible. With an internal standard one easily comes to RSDs below 0.1% over a considerable working range.

Glow discharge atomic emission spectra have narrow lines as a result of the low Doppler and pressure broadening. However, matrix lines are numerous and band emission from molecular impurities in the working gases also occurs, requiring high-purity gases and eventually gas purifiers. Then spectral interferences as a limiting factor for the analytical accuracy become low. Interferences also can arise as a result of differences in the sputtering of samples. Here the metallographic sample structure may play an important role, also when one works at sputtering equilibrium conditions. This has been found when analyzing cast and rolled iron samples. For this type of interference the use of internal standards again may be very helpful. In the case of aluminum samples, early atomic emission work showed the superiority of glow discharges in terms of low matrix effects as compared with spark emission spectrometry. In the case of the latter, one even comes to different calibration curves for the same family of samples (Figure 2.11) [44]. Through improvements in the knowledge of sparks and better approaches for using the spectral information through a careful selection of the observation zone, spark emission spectrometry has become much improved in this respect.

In the meanwhile, both dc and rf Grimm-type glow discharges have been used for the analysis of metal samples. One often states that in the case of rf glow discharges the detection limits are lower, as the sputtering may be more intense and the excitation by electrons through the long residence time for electrons in the negative glow as major excitation zone may also be high. In metal analysis with GD-OES one uses a flat cathode rather than a pin-type geometry. Indeed, as in glow discharge atomic emission work high ablation rates are used and sputtering equilibrium is required, especially in flexible but sequential multielement determinations, the flat cathode geometry is advantageous. Moreover, with the flat cathode the high optical guidance required for high radiation throughput is more easily realized than with a pin-type geometry.

Hollow cathodes have also been used for metals analysis. The cooled hollow cathode has the advantage of having lower detection limits than Grimm-type glow discharges. This is due to the high analyte residence times inside the cathode cavity, as already discussed by Mandelstam and Nedler [45]. However, the source cannot be operated in sputtering equilibrium, which is a serious drawback with respect to the possibility of sequential multielement determinations. Hot hollow cathodes have long been used very successfully for the determination of volatile elements or volatile compound-forming elements in metal samples. These applications go back to the work of Thornton [39] and Thelin [46]. When one uses a hollow cathode operated in the normal range in helium and graphite as cathode material, elements such as As, Bi, Se, P and S can be evaporated

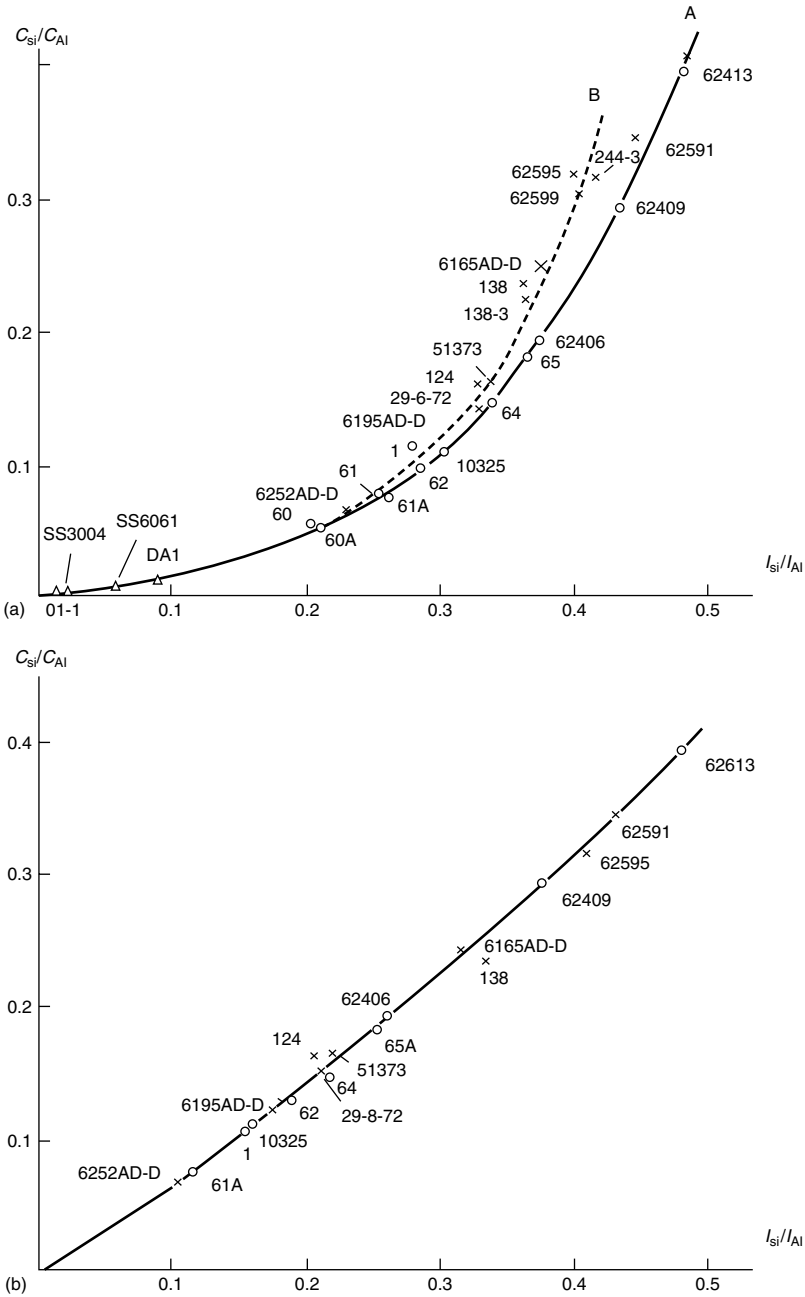


Figure 2.11 Determination of Si in Al alloys with (a) medium-voltage spark OES and (b) OES using a Grimm type glow discharge [44]

selectively from refractory metals and alloys. This has the advantage that the line-rich matrix is left behind, decreasing the risks of spectral interferences and so the analytes appear matrix-free in the excitation zones. In the case of helium as discharge gas, elements with high excitation potential can be excited very efficiently. Accordingly, one obtains detection limits in the sub- $\mu\text{g/g}$ range, which for these types of samples otherwise only can be obtained with glow discharge mass spectrometry, which is much more time intensive and sophisticated and much more expensive with respect to instrumentation.

Apart from bulk analysis, GD-OES now is especially used for depth-profiling analysis in the case of metals. From an industrial point of view this area of applications has become very important for industrialized countries, being more and more active in the production of surface-improved metallurgical products. This is necessary to meet the requirements for corrosion-resistant steels, hardened steels with lower mass, etc. The feasibility of a glow discharge for depth-profile analysis has already been mentioned in early glow discharge atomic spectrometry work and now the sputtering crater profiles even can be predicted as a result of modeling work [47]. Indeed, when the penetration rate is known or has been determined as a result of calculations or measurements for known metal samples, the time axis can be converted into a depth axis, whereas after calibration with pure metal samples the intensity axis can be converted into a concentration axis. Accordingly, the intensity versus time curve provides information both on the thickness of individual layers for a multitude of elements and on variations of the concentrations with the penetration depth in the sample, as shown exemplarily for a coated aluminum sample in Figure 2.12 [48]. In depth profiling, one normally works at constant current, voltage and power, which have to be described in the analytical prescription for the procedure. The analytical figures of merit of depth resolution, power of detection and achievable precision are interrelated and strongly dependent on the working parameters. The power of detection and the depth resolution are optimum at fairly high pressure. Indeed, under these conditions the burning voltage and accordingly also the sputtering rate are low. Therefore, the radiant output per unit of penetration rate is high, as the excitation efficiency through the large number of collisions is high. This also favors the precision, as the risks of detector noise limitations then are minimal. For a copper or steel matrix, depth resolutions of 0.1 nm are easily achieved and then a precision of a few percent in terms of the RSD and a concentration detection limit at least of 0.01% can be obtained [48]. The ultimate limiting factor of the depth resolution is often the roughness of the burning crater, which is the result of the metallographic structure of the sample and of preferential orientations for sputtering and also redeposition. Further, the field distribution across the burning crater is often a limitation, especially at high burning voltages. This effect can be substantially eliminated when working with a floating restrictor and remote anode. Also the gas flow dynamics are important as the entrainment of sputtered material with the working gas flow into the vacuum line here also has

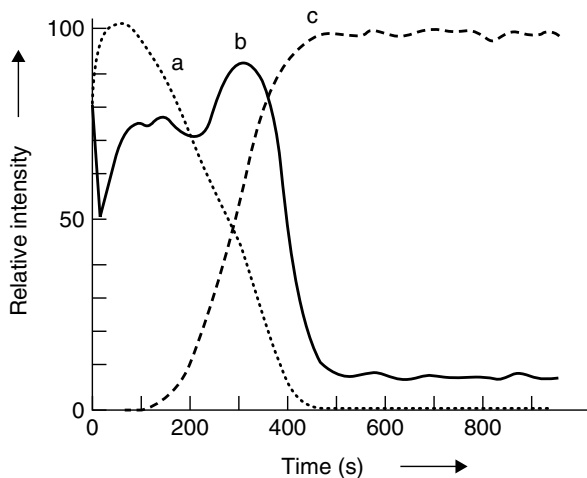


Figure 2.12 Depth profile through a galvanized steel sheet surface. The Zn coating is $\sim 18 \mu\text{m}$ thick and the Al concentration in the bulk is 0.049%. Line intensity tracings for (a) Zn, (b) Al and (c) Fe. The voltage U increases from 510 V in the Zn to 740 V in the bulk steel. Reprinted from Bengston, A., *Spectrochim. Acta, Part B* 1985, **40**, 631 with permission of Elsevier Science

an influence. Here it should be mentioned again that devices using jet-assisted sputtering or magnetically enhanced glow discharges, as a result of the influences of these measures on the burning profile, as a rule are not suitable for depth-profiling work.

2.5.2 ELECTRICALLY NONCONDUCTIVE POWDER SAMPLES

Dc glow discharges can also be used very well for the analysis of electrically non-conducting powders, such as ores and minerals or also of ceramic powders (see Chapter 11). These materials, however, have to be mixed with a host matrix and from the mixture a mechanically stable, heat conductive and vacuum-tight pellet has to be briquetted, as described in early work on glow discharges (see ref. [49]). As host materials, copper and silver powder have frequently been used for several reasons. These metal powders are available at reasonably high purity, hence blank limitations often are at a tolerable level. Moreover, their atomic emission spectra are not too line rich, so that the limitations arising from spectral interferences are kept within limits. Also, with both copper and silver, mechanically stable pellets can be obtained when using pressures up to 9 t/cm^2 , which can be realized with a press of reasonable size. These pellets have a good heat conductance and are vacuum tight when sample to host matrix ratios of 1:4 are used.

Materials which contain crystal water have to be dried prior to pressing, otherwise the release of water during the glow discharge will lead to the liberation of water vapor, by which the vacuum will be deteriorated and the excitation in the plasma will become especially poor. To obtain suitable pellets one can bring the sample–host mixture into a bed of pure host powder. The pellet then can have outer dimensions of 30 mm diameter and 2 mm thickness while a spot of about 12 mm diameter and 1 mm thickness in the center is provided on top of the sample. In this case the sample consumption is low and the ring of pure host ensures good vacuum tightness and heat conduction. For some materials, such as SiO₂, it is difficult to obtain stable pellets because of risks from swelling. Further, the particle size of the material to be analyzed has a large influence on the discharge stability and accordingly the precision but also on the pre-burning times required. The latter are always longer than in the case of metal samples and easily amount to up to 1 min. The influence of the sample graininess can be understood from sputtering profiles. Here, one finds towers of sample material in the burning crater, as the host is sputtered more rapidly and the insulating sample can only be sputtered after being covered with electrically conductive host material [49]. Despite the limitations mentioned, the use of glow discharge atomic emission spectrometry for the analysis of electrically nonconductive powders remains attractive. Indeed, in contrast with X-ray fluorescence spectrometry, here also light elements such as Be, Li and B can be determined with detection limits at the $\mu\text{g/g}$ level.

2.5.3 COMPACT ELECTRICALLY NONCONDUCTIVE SAMPLES

For the direct analysis of electrically nonconductive samples such as glasses, ceramics and even plastics, rf glow discharges can well be used, as is discussed in several other chapters in detail. Other than in mass spectrometry, the use of grids or secondary cathodes in front of the sample in atomic emission does not allow sufficient sputtering and analyte radiation densities to make it an analytically useful approach. Rf glow discharges can be used for bulk analysis after sputtering equilibrium is obtained but depth profiling is also possible. The curvature of the burning crater is again one of the limitations of the depth resolution. All kinds of parameters such as the sample matrix, the power applied and the working pressure and certainly the use of magnetic fields which may transform the plasma into a ring can severely influence the crater profiles and accordingly the depth-profiling possibilities, as shown exemplarily by the results in Figure 2.13.

2.5.4 DRY SOLUTION RESIDUES

Dry solution residue analysis is especially useful for the analysis of micro-samples. In the case of Grimm-type glow discharges, one could even think of

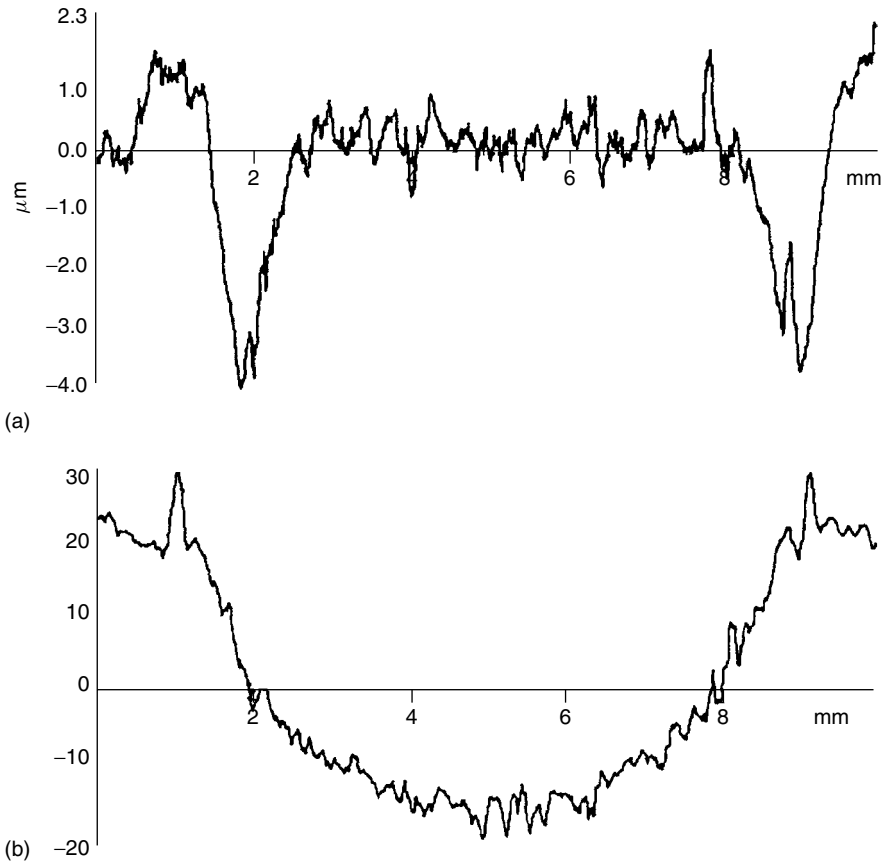


Figure 2.13 Influence of a magnetic field on the crater profiles of an rf discharge. (a) Sample, quartz; argon pressure, 2 Torr; and (b) sample, electrolytic copper plate; argon pressure, 2 Torr. Reprinted from Heintz, M. J., Broekaert, J. A. C. and Hieftje, G. M., *Spectrochim. Acta, Part-B* 1997, **52**, 589 with permission of Elsevier Science

briquetting a mixture of naphthalene and graphite, after which the naphthalene is sublimed. In this way a porous electrode is obtained, which also could take up salt-loaded solutions such as diluted serum samples. These samples could be sputtered reproducibly. Dry solution residue analysis has been applied especially in hollow-cathode atomic emission spectrometry, as also mentioned by Harrison and Prakash [51] and in many papers by Zilbershtein and colleagues (see references cited in Ref. [52]). Here, thin layers of trace concentrate can be deposited inside steel electrodes or graphite cups can be soaked with the analyte solution. Dry solution residue analysis with hot hollow cathodes is a technique with extremely low absolute detection limits, down to the femtogram

level. However, its significance has decreased through the availability of plasma mass spectrometric methods.

2.5.5 GASES AND AEROSOLS

Glow discharges are also very suitable for gas analysis, as will be treated in a separate chapter including their use for element-specific detection in gas chromatography. In the case of helium as the discharge gas, elements such as O, N, C, S and the halogens can be well determined. As treated in a special chapter on gas sampling, both normal Grimm-type glow discharges [33], hollow cathodes [34] and special gas sampling glow discharges (see, e.g., Ref. [53]) can be used. The use of all noble gases is possible, as sputtering is not an issue. In this case, argon and the heavier noble gases are even less suitable so as to avoid sputtering at higher working currents and voltages. Also, breakdown of small molecules is easily possible, as was shown when coupling hydride generation to a gas sampling glow discharge [35], but also as the determination of empirical formulae is possible [33]. For the analysis of aerosols and airborne dust glow discharges can also be used. This is possible in an off-line mode through the use of suitable sampling procedures. When using a graphite cup as air filter the trapped particulate material can be directly analyzed when using the cup as cathode in a hollow cathode. In this way lead and cadmium could be determined down to the sub- $\mu\text{g}/\text{m}^3$ level in air, which is convenient for air pollution monitoring [54].

2.6 OTHER METHODS OF ANALYSIS AND OUTLOOK

Glow discharge optical atomic spectrometry for direct solids analysis is an alternative to other methods for direct solids analysis in different respects (Table 2.2).

2.6.1 POWER OF DETECTION

The detection limits of glow discharge atomic emission spectrometry are similar to those of arc and spark atomic emission work in the case of bulk analysis. For a number of elements such as the halogens and chalcogens glow discharges are favorable when using the noble gases with higher ionization potentials, namely helium and neon. In the first case, however, one should use mixtures of argon and helium as otherwise the sputtering rates are too low. This is not the case when using glow discharges for gas analysis, where no atomization has to be performed. Even for the cleavage of molecular bonds, the helium discharge is suitable. For direct solids analysis the power of detection achievable with glow discharges can possibly still be increased. The approach followed, and where there is still room for more innovation, lies in measures which increase the sputtering rate and in those improving the excitation efficiency. For increasing the sputtering rate both

Table 2.2 Analytical figures of merit of direct solids analysis methods^a.

Method ^b	Power of detection	Depth profiling	Precision	Accuracy	Linear dynamic range	Costs
Dc arc OES	++	—	+	+	+	++
Spark OES	+	—	++	++	+	++
GD-OES	++	+++	+++	+++	+++	++
GD-MS	+++	+++	++	++	++	+
Laser ablation	++	++	++	++	+++	++
ICP-OES						
Laser ablation ICP-MS	+++	+++	++	++	+++	+
SIMS	+++	+++	++	+	+	+
SNMS	+++	+++	++	++	+	++
XRF	+	+	+++	+++	++	+

^a+, Rather unfavorable; ++, favorable; +++, very favorable.

^bDc arc OES, direct current arc optical emission spectrometry; GD-OES, glow discharge optical emission spectrometry; GD-MS, glow discharge mass spectrometry; laser ablation ICP-OES/MS, laser ablation inductively coupled plasma optical emission spectrometry/mass spectrometry; SIMS, secondary ion mass spectrometry; SNMS, sputtered neutrals mass spectrometry; XRF, X-ray fluorescence.

the use of gas jet-assisted sputtering and an increase in the plasma density through the use of magnetic fields have been used successfully. Both measures, however, are not completely understood with respect to the change in the processes taking place. In the first case the changes in the energetic possibilities of sputtering agents certainly have to be investigated in more detail, whereas in the second case changes in the plasma parameters also have to be studied. In the case of both measures it was also found that the ground-state atom concentrations increase considerably, but not necessarily the radiation output. This is especially true for the case of resonance lines, which then suffer from self-reversal. Here an increase in the excitation efficiency especially is required. For this aim, the use of boosted discharges for improving the power of detection achievable is very interesting. Apart from dc discharges, the use of superimposed rf or microwave discharges through including cavities in the lamp construction or the use of an antenna has been proposed and shown to be effective. Here, there is certainly room for still better combinations of the glow discharge sputtering and the cross-excitation, which certainly still has to be studied in more detail with respect to its implications for discharge conditions and plasma parameters. A further way to improve the signal-to-noise ratio and the power of detection lies in the use of pulsed discharges, including measurements in the afterglow period, for which diagnostics are still very incomplete. Certainly, the cathode form remains an important point with respect to power of detection also. Hollow cathodes are and will remain the most powerful sources in atomic emission work in this

respect. However, they suffer from an absence of sputtering equilibrium, making sequential multielement determinations impossible and the analytical precision remains modest. They will therefore remain of less importance to direct solids analysis, unless for special applications as discussed above.

Whereas for direct solids analysis and for gas analysis glow discharges are already fairly well developed, this is not the case for liquids analysis, of which the state of the art is given in a separate chapter. Here one should especially be aware of the fact that moisture considerably influences the energetic and excitation properties of the discharge. As such, techniques for aerosol formation known from atmospheric pressure plasma sources, such as pneumatic and ultrasonic nebulization cannot be used directly. Here aerosol desolvation is helpful and electrothermal and gas generation methods, as shown by the example of hydride generation, can also be well used. The use of molecular beams, as treated elsewhere in this work, is also very useful.

With respect to power of detection, GD-OES is as powerful as X-ray fluorescence methods, but has the advantage of also giving access to all light elements. Therefore, when working in the total reflection mode, X-ray fluorescence spectrometry has a higher power of detection. With respect to power of detection, GD-OES is similar to spark emission techniques. Generally, however, among the methods for direct solids analysis, glow discharge mass spectrometry certainly has superior power of detection.

2.6.2 ANALYTICAL PRECISION

The analytical precision achievable with glow discharges in terms of the RSDs of measured intensities in the case of flat cathodes is excellent compared with other spectrochemical sources. Indeed, compared with atmospheric pressure plasma sources, the influence of gas flow dynamics is much lower. Also flicker noise is remarkably low. Therefore, one must ensure that noise components from the power or vacuum supply system do not occur. In the low wavelength range, detector noise limitations can occur, which especially with diode-array detection may limit the power of detection in the case of low-UV and VUV analytical lines.

2.6.3 LINEAR DYNAMIC RANGE

In GD-OES the low fluctuations together with the optically thin character of the plasma guarantee a high linear dynamic range compared with other methods of direct solids analysis such as spark emission techniques. In the latter case sample volatilization, which here partly occurs by evaporation, is less favorable than in the case of glow discharges with a cold and flat cathode. In comparative studies with X-ray fluorescence, glow discharges also have good precision, when including the errors in the calibration and selecting a larger concentration range even in the case of the major elements [55]. The linear dynamic range in the

case of resonance lines is also lower, as a result of self-reversal. Here progress still could be made by applying side-on observation.

2.6.4 ANALYTICAL ACCURACY

The analytical accuracy finally is limited by influences of the sample structure and matrix composition on the material volatilization and of concomitants on the analyte excitation and on spectral line coincidences. The influence of the sample structure in the case of Grimm-type glow discharges is well known from analyses of steels of different qualities, leading to different calibration curves in the case of differences in metallographical structure. However, the sample surface pretreatment can introduce differences, as shown by switching from polishing to turning samples with a cutting diamond. In the case when one works in sputtering equilibrium, the latter differences practically vanish. The influence of the matrix composition and structure on the sample sputtering can also be substantially eliminated by using a suitable reference element and internal standard line. The influence of concomitants on the material excitation cannot easily be eliminated by using an internal standard as the plasma is not in LTE. The matrix effects arising from this point are especially strong in hollow cathodes, where both the sample volatilization and material excitation are influenced by concomitants. On the other hand, selective volatilization here can just eliminate the presence of concomitants during analyte excitation. Spectral interferences in the case of glow discharges are low compared with atmospheric pressure plasma sources because of less band emission, narrower lines and usually a smaller number of atomic emission lines in the spectra. The last point especially is true when use is made of selective volatilization.

2.6.5 DEPTH PROFILING

With respect to depth profiling, glow discharge atomic spectrometry has the special advantage of being very useful for routine applications in an industrial environment. The depth resolution certainly is lower than in the established surface analytical methods such as secondary ion mass spectrometry (SIMS), sputtered neutrals mass spectrometry (SNMS) and Auger electron spectroscopy. Therefore, qualitative and quantitative characterization of the thickness and composition of coating layers now is possible, and commercial instrumentation for this purpose is available.

2.6.6 COSTS OF ANALYSIS

Glow discharge atomic spectrometry, as opposed to inductively coupled plasma spectrometry also with direct solids sampling provisions, does not suffer from

high argon consumption. For new applications such as element-specific detection both in process analysis and in gas and eventually also in liquid chromatography, glow discharges have a strong future. This certainly will be fostered by the availability of microplasmas both for molecular emission, as introduced by Manz and co-workers [56], but especially for elemental detection as proposed recently by Blades [16]. In this respect, glow discharges can have a similar scope to miniaturized plasmas at atmospheric pressure and the analytical features will have to be critically compared so as to achieve the optimum solution for the analytical problem to be solved.

2.7 REFERENCES

1. Kirchhoff, G. R.; Bunsen, R. Chemical Analysis by spectrum-observation, *Philos. Mag.* 1860, **20**, 89–98.
2. Penning, F. M. *Electrical Discharges in Gases*. Philips Technical Library, Philips, Eindhoven, 1957, p. 41.
3. de Galan, L.; Smith, R.; Winefordner, J. D. The electronic partition functions of atoms and ions between 1500 K and 7000 K, *Spectrochim. Acta, Part B* 1968, **23**, 521–525.
4. Elwert, G. Über die Ionisations- und Rekombinationsprozesse in einem Plasma und die Ionisationsformel der Sonnenkorona, *Z. Naturforsch., Teil A* 1952, **7**, 432–439.
5. Grotrian, W. *Graphische Darstellung der Spektren von Atomen mit Ein, Zwei und Drei Valenzelektronen*, Springer, Berlin, 1928.
6. Junkes, J.; Salpeter E. W. Linienbreiten in der photographischen Spektralphotometrie II. Das optische Linienprofil, *Ric. Spettrosc.* 1961, **2**, 255–483.
7. Bruce, C. F.; Hannaford, P. On the width of atomic resonance lines from hollow cathode lamps, *Spectrochim Acta, Part B* 1971, **34**, 73–84.
8. Heintz, M. J.; Mifflin, K.; Broekaert, J. A. C.; Hieftje, G. M. Investigations of a magnetically enhanced Grimm-type glow discharge source, *Appl. Spectrosc.* 1995, **49**, 241–246.
9. Grimm, W. Eine neue Glimmentladungslampe für die optische Emissionsspektalanalyse, *Spectrochim. Acta, Part B* 1968, **23**, 443–454.
10. Boumans, P. W. J. M. Sputtering in a glow discharge for spectrochemical analysis, *Anal. Chem.* 1973, **44**, 1219–1228.
11. Ko, J. B. New designs of glow discharge lamps for the analysis of metals by atomic emission spectrometry, *Spectrochim. Acta, Part B* 1984, **39**, 1405–1423.
12. Paschen, W. Die Funkenspektren des Aluminium, *Ann. Phys. (Leipzig)* 1923, **71**, 142–161
13. Broekaert, J. A. C. Emission spectrographic determination of all rare earths in solutions by hollow cathode excitation, *Bull. Soc. Chim. Belg.* 1976, **85**, 261–270.
14. Winchester, M. R.; Lazik, C.; Marcus, R. K. Characterization of a radio frequency glow discharge emission source, *Spectrochim. Acta, Part B* 1991, **46**, 483–499.
15. Miclea, M.; Kunze, K.; Musa, G.; Franzke, J.; Niemax, K. The dielectric barrier discharge—a powerful microchip plasma for diode laser spectrometry, *Spectrochim. Acta, Part B* 2001, **56**, 37–43.
16. Blades, M. W. Radio frequency capacitively-coupled microplasmas—an efficient route to a plasma on a chip, Paper presented at FACSS, Detroit, MI, 2001.
17. Lee, J. W.; Kim, H. J.; Yang, S. Y.; Gee, B. Y.; Cserfalvi, T.; Meisel, P. Fundamental and analytical applications of electrolyte cathode atomic glow discharge (ELCAD)

as a new source for on-line monitoring of metals in flowing water, Poster presented at the XXXI Colloquium Spectroscopicum Internationale, Ankara, September 5–10, 1999, Book of Abstracts, p. 15.

18. Boumans, P. W. J. M. *Theory of Spectrochemical Excitation*, Hilger & Watts, London, 1966.
19. Broekaert, J. A. C. Determination of rotational temperatures in a transitional type hollow cathode glow discharge, *Bull. Soc. Chim. Belg.* 1977, **86**, 895–906.
20. Mermet, J. M. Spectroscopic diagnostics: basic concepts, in Boumans P. W. J. M. (ed.), *Inductively Coupled Plasma Emission Spectroscopy, Part II*, Wiley-Interscience, New York, 1987, pp. 353–386.
21. Ferreira, N. P.; Human, H. G. C.; Butler, L. R. P. Kinetic temperatures and electron densities in the plasma of a side view Grimm-type glow discharge, *Spectrochim. Acta, Part B* 1980, **35**, 287–295.
22. Hieftje, G. M. Plasma diagnostic techniques for understanding and control, *Spectrochim. Acta, Part B* 1992, **47**, 3–25.
23. Billhorn, R. B.; Epperson, P. M.; Sweedler, J. V.; Denton, M. B. Charge transfer device detectors for analytical optical spectroscopy—operation and characteristics, *Appl. Spectrosc.* 1987, **41**, 1114–1124.
24. Danielson, A.; Lindblom, P.; Södermann, E. The IDES spectrometer, *Chem. Scr.* 1974, **6**, 5–9.
25. Hieftje, G. M.; Brushwyler, K. R. Glow-discharge atomic emission spectrometry with a spectrally segmented photodiode-array spectrometer, *Appl. Spectrosc.* 1991, **45**, 682–691.
26. Faires, L. M. Fourier transforms for analytical atomic spectroscopy, *Anal. Chem.* 1986, **58**, 1023A–1043A.
27. Steers, E. B. M.; Leis, F. Excitation of the spectra of neutral and singly ionized atoms in the Grimm-type discharge lamp, with and without supplementary excitation, *Spectrochim. Acta, Part B* 1991, **46**, 527–537.
28. Broekaert, J. A. C.; Brushwyler, K. R.; Monnig, C. A.; Hieftje, G. M. Fourier-transform-atomic emission spectrometry with a Grimm-type glow-discharge source, *Spectrochim. Acta, Part B* 1990, **45**, 769–778.
29. Broekaert, J. A. C.; Bricker, T.; Brushwyler, K. R.; Hieftje, G. M. Investigations of a jet-assisted glow discharge lamp for optical emission spectrometry, *Spectrochim. Acta, Part B* 1992, **47**, 131–142.
30. Lowe, R. M. A modified glow-discharge source for emission spectroscopy, *Spectrochim. Acta, Part B* 1978, **31**, 257–261.
31. Ferreira, N. P.; Strauss, J. A.; Human, H. G. C. Developments in glow discharge emission spectrometry, *Spectrochim. Acta, Part B* 1983, **38**, 899–911.
32. Leis, F.; Broekaert, J. A. C.; Laqua, K. Design and properties of a microwave boosted glow discharge lamp, *Spectrochim. Acta, Part B* 1987, **42**, 1169–1176.
33. Broekaert, J. A. C.; Starn, T. K.; Wright, L. J.; Hieftje, G. M. Studies of a helium-operated gas-sampling glow discharge for the atomic emission spectrometric determination of chlorine in halogenated hydrocarbon vapors, *Spectrochim. Acta, Part B* 1998, **53**, 1723–1735.
34. Schepers, C.; Broekaert, J. A. C. The use of a hollow cathode glow discharge (HCGD) as an atomic emission spectrometric element specific detector for chlorine and bromine in gas chromatography, *J. Anal. At. Spectrom.* 2000, **15**, 51–65.
35. Broekaert, J. A. C.; Pereiro, R.; Starn, T. K.; Hieftje, G. M. A gas-sampling glow discharge coupled to hydride generation for the atomic spectrometric determination of arsenic, *Spectrochim. Acta, Part B* 1993, **38**, 899–911.
36. Ingle, Jr, J. D.; Crouch, S. R. *Spectrochemical Analysis*, Prentice-Hall, Englewood Cliffs, NJ, 1988.

37. Hieftje, G. M. Signal-to-noise enhancement through instrumental techniques, *Anal. Chem.* 1972, **44**, 81A–88A.
38. Kaiser, H.; Specker, H. Bewertung und Vergleich von Analysenverfahren, *Z. Anal. Chem.* 1956, **149**, 46–66.
39. Thornton, K. The use of a high temperature hollow cathode lamp for the spectrographic analysis of steels, high temperature alloys and related materials for trace elements, *Analyst* 1969, **94**, 958–967.
40. Kaminsky, M. *Atomic and Ionic Impact Phenomena on Metal Surfaces*, Springer, Berlin, 1965.
41. Broekaert, J. A. C. State-of-the-art of glow discharge lamp spectrometry, *J. Anal. At. Spectrom.* 1987, **2**, 537–542.
42. Dogan, M.; Laqua, K.; Massmann, H. Spektrochemische Analysen mit einer Glimmentladungslampe als Lichtquelle I. Elektrische Eigenschaften, Probenabbau und spektraler Charakter, *Spectrochim. Acta, Part B* 1972, **26**, 631–649.
43. Slickers, K. *Die automatische Atom-Emissions-Spektralanalyse*, Brühlsche Universitätsdruckerei, Giessen, 1992.
44. Ko, J. B.; Laqua, K. Vergleich verschiedener Anregungsverfahren bei der emissionsspektrometrischen Analyse von Aluminium-Legierungen. In *Proceedings of the XVIII Colloquium Spectroscopicum International*, Vol. II, GAMS, Paris, 1975, pp. 549–556.
45. Mandelstam, S. L.; Nedler, V. V. On the sensitivity of emission spectrochemical analysis, *Spectrochim. Acta* 1961, **17**, 885–894.
46. Thelin, B. The use of a high temperature hollow cathode lamp for the determination of trace elements in steels, nickel-base alloys and ferroalloys by emission spectrometry, *Appl. Spectrosc.* 1981, **35**, 302–307.
47. Bogaerts, A.; Gijbels, R. Calculation of crater profiles on a flat cathode in a direct current glow discharge, *Spectrochim. Acta, Part B* 1997, **52**, 765–777.
48. Bengtson, A. A contribution to the solution of the problem of quantification in surface analysis work using glow discharge atomic emission spectroscopy, *Spectrochim. Acta, Part B* 1985, **40**, 631–639.
49. Brenner, I.; Laqua, K.; Dvorachek, M. Application of the Grimm glow discharge lamp (GDL) for the analysis of geological and related materials, *J. Anal. At. Spectrom.* 1987, **2**, 623–627.
50. Heintz, M. J.; Broekaert, J. A. C.; Hieftje, G. M. Analytical characterization of a planar magnetron radio frequency glow-discharge source, *Spectrochim. Acta, Part B* 1997, **52**, 579–591.
51. Harrison, W. W.; Prakash, N. J. Trace element analysis of solutions by hollow cathode excitation, *Anal. Chim. Acta* 1970, **49**, 151–159.
52. Caroli, S. *Improved Hollow Cathode Lamps for Atomic Spectrometry*, Ellis Horwood, Chichester, 1985.
53. Starn, T. K.; Pereiro, R.; Hieftje, G. M. Gas-sampling glow discharge for optical emission spectrometry. Part I: Design and operating characteristics, *Appl. Spectrosc.* 1993, **47**, 1555–1561.
54. Broekaert, J. A. C. Application of hollow cathode excitation coupled to vidicon detection to the simultaneous multielement determination of toxic elements in airborne dust—A unique sampling-analysis procedure for lead and cadmium, *Bull. Soc. Chim. Belg.* 1976, **85**, 755–761.
55. Broekaert, J. A. C.; Klockenkämper, R.; Ko, J. B. Emissionsspektrometrische Präzisionsbestimmung der Hauptbestandteile von Cu/Zn Legierungen mittels Glimmlampe und ICP, *Fresenius' Z. Anal. Chem.* 1983, **318**, 851–853.
56. Eijkel, J. C. T.; Stoeri, H.; Manz, A. A molecular emission detector on a chip employing a direct current microplasma, *Anal. Chem.* 1999, **71**, 2600–2606.

3

Mass Spectrometry of Glow Discharges

W. W. HARRISON, C. YANG and E. OXLEY

University of Florida, Department of Chemistry, Gainesville, FL, USA

3.1 INTRODUCTION

The very nature of low-pressure gas discharges requires the presence of ions for a plasma to be sustained and, where ions are present, mass spectrometry may be a useful analytical technique. The attention to ions, as opposed to other measurement species (e.g., atoms, photons), offers many advantages, but also some experimental obstacles. One only need consider the striking growth of mass spectrometry in the past two decades to realize that the advantages have been found to outweigh by far the instrumental complexities.

The fundamental considerations inherent in the mass spectrometric sampling of a gas discharge are illustrated in Figure 3.1. As in the case of any glow discharge (GD), an external source of power is required to break down the discharge. The normally insulating volume of gas is subject to Nature's own ionizing events, such as γ -rays creating random electrons, which then are rapidly accelerated by the electric field, and an ionization cascade is effected. Gas inlet and vacuum connections maintain the discharge environment, and ion transport from the low-pressure discharge into a high-vacuum mass spectrometer occurs by successive stages through a sampler and skimmer arrangement (Figure 3.1). The normally low power conditions of a GD result in only a low level of net ionization, but fortunately mass spectrometry needs few ions to achieve sensitive measurements.

In comparison with other GD analytical methods, mass spectrometry is physically invasive, in that ions must be transported (sampled) from the plasma by means of a small orifice, into a lower pressure adjacent chamber. The ions, both from the analytical sample and from the discharge gas, are then sorted in a

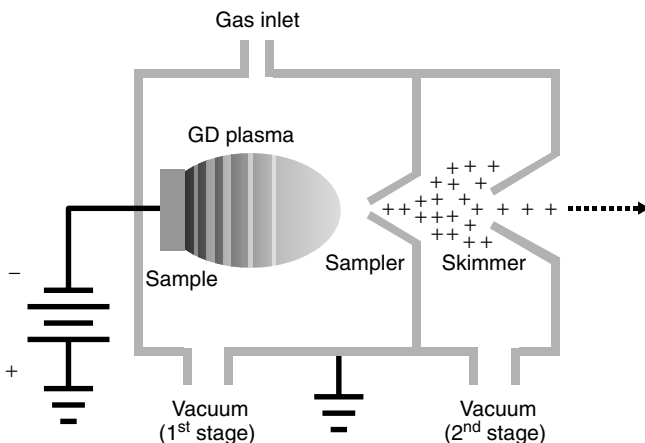


Figure 3.1 Schematic diagram of a glow discharge source and associated ion sampling configuration

mass spectrometer according to some characteristic property, such as mass/charge ratio (m/z) or velocity. Ideally, the extracted ion beam faithfully represents the composition of the sample under consideration.

Mass spectrometry's popularity in general, and for glow discharges in particular, arises from its inherent ability to provide qualitative and quantitative information rapidly and accurately. In trace element analysis, mass spectrometry permits the coverage of essentially the entire periodic table. The spectra are much simpler than optical emission spectra, and because the spectral background can be very low, detection limits are usually 2–3 orders of magnitude better by mass spectrometry than for optical atomic emission. It is little wonder that glow discharge mass spectrometry (GDMS) has become a powerful tool for the direct elemental analysis of solids.

3.1.1 HISTORICAL

Glow discharges are direct descendents of the electric discharge discoveries over 100 years ago by Goldstein [1], who showed that low-pressure, high-voltage gas discharges produced copious quantities of 'kanalstrahlen' for experimentation. By exploring the effect of magnetic and electric fields on these species, it was determined by Wien, Thomson and others [1] that these intense streams of particles were positively charged and became known as positive rays [2]. Thomson discovered that gas discharges produced both negative rays and neutral rays, but neither of these was of particular interest at the time. Figure 3.2 shows a representation of a typical early discharge chamber in which these ions were formed and extracted through a cathode slit for registration and identification

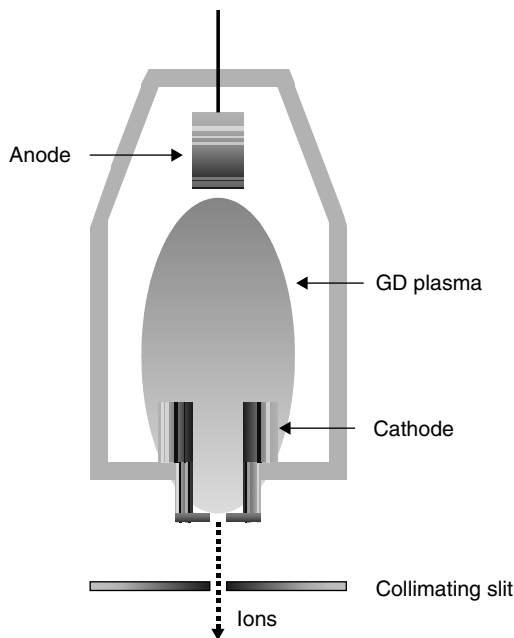


Figure 3.2 Representation of early gas discharge ion source. Modified with permission from White, F. A., *Mass Spectrometry in Science and Technology*, John Wiley & Sons, Inc., New York, 1968, Copyright John Wiley & Sons, Inc.

by ion-sensitive detectors, such as photoplates. The sample of interest could be packed into the anode and vaporized by high electron currents, or cathodic sampling was also possible, initially by thermal evaporation methods, and later by cathodic sputtering when this phenomenon became better known. The discharge chamber in Figure 3.2 would be easily recognized today as an ion source that could be coupled to a modern mass spectrometer.

Although low-pressure gas discharges were widely used over the first several decades of the 20th century to characterize elements and to study isotopic distributions, no real use was made for purposes of analytical chemistry. Indeed, as the increasingly powerful new technique of mass spectrometry developed at mid-century, it was organic substances that were of greatest interest, sparked by support from the petroleum industry, where the problem solving advantages of mass spectrometry drew special attention. As a result, new types of ion sources were developed that were much more conducive to carbon-based materials, which usually exhibited sufficient vapor pressure to allow lower energy sources, such as electron impact ionization. Organic mass spectrometry became a widespread tool for identification and structure determination, but its inorganic counterpart lagged far behind. The high-voltage vacuum spark discharge, a highly sensitive

but erratic ion source, did find some limited application for the elemental analysis of solid samples [3].

Meanwhile, glow discharges were used to some minor extent in optical emission measurements [4,5] owing to their stable operation, low background and sharp-line spectra. Hollow cathode discharges, in particular, showed good elemental sensitivity for minor and trace elements in more specialized applications. In this same time period, Knewstubb and Tickner showed the value of mass spectrometry for the examination of low pressure flames [6,7] by measuring species that were inaccessible by optical methods, and quadrupole mass analyzers were beginning to find application for monitoring discharge gases used in deposition methods by the electronics industry. In the early 1970s, Coburn and co-workers, in groundbreaking papers, showed that glow discharges could be sampled successfully by mass spectrometry [8,9]. About the same time, Harrison and co-workers, who had been using glow discharges for optical emission analyses, found strong ion emission lines in hollow cathode discharges, and set about to develop a glow discharge alternative [10,11] to the high-voltage vacuum spark discharge for elemental mass spectral analysis. Coburn and Harrison reviewed the initial development stage of what became known as glow discharge mass spectrometry [12].

The availability of commercial instrumentation about 1985 permitted a broad expansion of glow discharge mass spectrometry, and over the years it has become a mature product, widely used for the elemental analysis of solids.

3.1.2 CURRENT STATUS

Although the sampling of glow discharges by optical methods remains overall a simpler approach and still finds considerable favor, particularly in Europe, mass spectrometric sampling is now recognized as having strong advantages of sensitivity, scope, versatility, and spectral simplicity. The ability to obtain isotopic information across the periodic table, down to ppb detection limits, makes GDMS a powerful analytical tool. In addition, the development of new, improved mass spectrometers with more reliable data acquisition and control systems has lowered the threshold of concern in the transfer of GDMS from the research laboratory to the routine applications arena.

Glow discharges have been shown to couple well to all types of mass spectral equipment, from the most sophisticated multi-sector instruments to simple quadrupole units. Although glow discharges produce a relatively low degree of ionization [13], the ability of mass spectrometers to acquire and measure these small populations with highly accuracy is a key factor in the growth of GDMS. The prospect is that this mode of sampling gas discharges, including glow discharges, will form the basis for much of the growth aspect of glow discharges in analytical chemistry.

3.2 FUNDAMENTALS OF MASS SPECTROMETRY

3.2.1 GAS-PHASE ION CHEMISTRY/PHYSICS

The glow discharge is an unusual device that offers unique opportunities for the examination of atomic gas-phase processes, and mass spectrometry is one of the most versatile means of exploring the ionized plasma species. However, other analytical methods can complement mass spectrometry in probing the discharge. Ground-state atoms (the bulk of the plasma constituents) can be probed by atomic absorption or fluorescence, and excited atoms may be examined by optical emission methods, but mass spectrometry provides excellent sensitivity to measure and catalog the ionic contributions to a glow discharge. As a result, glow discharge mass spectrometry is now well established as a valuable tool for the elemental analysis of solids.

In principle, because of the 'inert' nature of analytical glow discharges, they could be considered as atomic physics processes. The sputtering step to produce atoms in the glow discharge is a physical phenomenon, and the gas-phase collisions of analyte atoms with rare gas (usually argon) atoms have no significant chemical activity. Indeed, we would wish this to be so for GDMS, but glow discharges always contain some traces of reactive impurities (e.g., water, O₂, N₂, oil vapors), and the discharge itself serves to break these molecules down to their very reactive atomic states. Hence there are always chemical reactions taking place in a glow discharge, including the formation of what would normally be unstable metal-rare gas adducts that are sufficiently long-lived to be detected by mass spectrometry, and these are potentially troublesome interferences for elemental analysis. The analyst should be aware of the many facets of atomic physics and chemistry manifested in a glow discharge.

3.2.2 IONIZATION MODES

The ability to ionize sputtered sample atoms is one of the critical features that makes the glow discharge useful for analytical applications in mass spectrometry. Although ionization is a result of many processes, sputtered sample atoms are ionized in the negative glow region of the discharge mainly by two processes: electron impact and Penning ionization. Charge exchange ionization may also occur, depending on the discharge conditions. Table 3.1 lists some of the possible ionization mechanisms occurring in the glow discharge [14].

Electron Impact Ionization

Electron impact ionization is one of the most important and best known processes in the glow discharge. Electron impact ionization occurs when an atom collides effectively with an electron whose energy is higher than the ionization energy

Table 3.1 Ionization mechanisms in the glow discharge.^a

1. Primary ionization processes
A. Electron impact
$M^0 + e^- \rightarrow M^+ + 2e^-$
B. Penning ionization
$M^0 + X^{m*} \rightarrow M^+ + X^0 + e^-$
2. Secondary ionization processes
A. Charge transfer
1. Nonsymmetric
$X^+ + M^0 \rightarrow M^+ + X^0$
2. Dissociative
$X^+ + MO \rightarrow M^+ + O + X^0$
B. Associative ionization
$X^{m*} + M \rightarrow XM^+ + e^-$
C. Photoionization
$M^* + h\nu \rightarrow M^+ + e^-$
D. Cumulative ionization
$M^0 + e^- \rightarrow M^* + e^- \rightarrow M^+ + 2e^-$

^aM⁰-sputtered atom; X⁰-gas atom; M^{*}-excited sputtered atom; X^{m*}-metastable gas atom.

Reproduced with permission from White, F. A., *Mass Spectrometry in Science and Technology*, John Wiley & Sons, Inc., New York, 1968, Copyright John Wiley & Sons.

of the atom. There are two principal sources of electrons in the negative glow: primary electrons and secondary electrons. Primary electrons are emitted from the cathode surface and accelerated by the electric field across the dark space, where most enter the negative glow at high velocity. The kinetic energy of these electrons can be as high as the entire potential dropped across the cathode fall and thus have the potential of ionizing any element. However, they have low probability of an ionizing collision owing to their short interaction time. Secondary electrons are the by-product of ionization reactions, and their energy varies with the excess energy available after ionization. The energy of these electrons assumes a quasi-Maxwell-Boltzmann distribution with a mean energy of approximately 4 eV [15]. These secondary electrons are responsible for most of the electron ionization in the negative glow region [15].

Penning Ionization

Penning ionization is another important mechanism within the discharge. This occurs as the result of a collision between a metastable gas atom and an atomic species with an ionization energy below the energy of the excited metastable state of the gas atom. Argon as a discharge gas has metastable atoms with energies

of 11.55 and 11.72 eV, sufficient energy to ionize most atoms of the periodic table. Penning ionization is generally a nonselective process for most elements, excluding such higher ionization potential elements as O, N, etc. Since Penning ionization is strongly related to the number density of metastable species, the population of these energy levels determines the ionization efficiency. It has been suggested that Penning ionization is the dominant ionization process in low-pressure discharges [16].

Asymmetric Charge Exchange Ionization

Asymmetric charge exchange (or transfer) can be an additional contributor to ionization in the glow discharge. Unlike electron impact and Penning ionization, asymmetric charge transfer is a selective mechanism for ionization of certain elements. The collision between an analyte atom and a discharge gas ion can lead to the transfer of an electron from the atom to the ion. A condition of this transfer is a small difference in energy between the gas ion ground state and the energy levels of the resulting analyte ion. Therefore, asymmetric charge transfer will only occur between specific energy levels. Bogaerts and Gijbels have reviewed the occurrence of asymmetric charge transfer in the glow discharge [17].

3.2.3 GLOW DISCHARGE ION SOURCES

Given the diverse applications of the glow discharge, numerous configurations have been investigated as ion sources. The major considerations in ion source design are (a) convenient and reproducible introduction of the sample and (b) effective and efficient sampling of the sample ions. The most commonly used sources involve some type of direct insertion probe to insert the sample into an internal GD cell. Alternatively, the Grimm-type source finds some favor owing to its convenience of external sample placement. Although several models of GD ion sources have been successful, the optimum model awaits development.

Diode Geometry

Most GD ion sources, particularly the commercial versions, have used a direct insertion probe that permits certain flexibility in sample shape, although pins or discs are normally used. As shown in Figure 3.3 [18], the samples are introduced through a vacuum interlock into the GD cell. In this configuration, the sample serves as the cathode of the glow discharge system and the cell housing as the anode. Ions are sampled from the negative glow region through an ion exit orifice (see Figure 3.1). Typical discharge conditions are voltages of 500–1000 V, currents of 1–5 mA for the dc mode and 0.4–2.0 Torr argon gas. This versatile

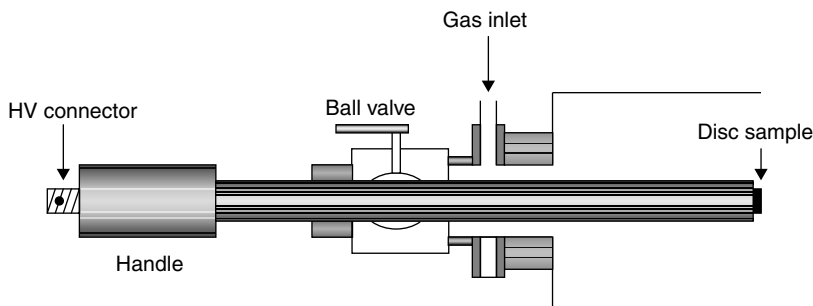


Figure 3.3 Conventional means of introducing a sample into a glow discharge ion source by a direct insertion probe

source can be used with all types of mass spectrometers and has become the 'industry standard' for GDMS.

Grimm Geometry

A Grimm-type glow discharge is the most widely applied source for atomic emission spectrometry (AES). By proper modification to permit ion extraction, it can also serve as a glow discharge ion source. In this source, the discharge is realized by a special cylindrical anode tube placed close to the surface of the sample, as shown in Figure 3.4. This permits stable operation, restricting the burning spot of the discharge to a well-defined area on the sample surface. Advantages of the source include capabilities for both surface and in-depth analysis by controlling the discharge parameters to obtain planar sputtering. The downside is that a very flat, smooth sample surface is required. Investigators have achieved results [19–21] with the Grimm ion source that show promise as an alternative to the more conventional GD sources (e.g., diode source). Voltages from 500 to 1500 V, currents of 3–30 mA for the dc mode and 1–6 Torr argon gas are typical for the Grimm-type source.

Hollow Cathode

A long known, but rarely used ion source is the hollow cathode discharge. In a hollow cathode configuration [14], the sputtering and the discharge plasma are concentrated into a hollow cathode cavity (conditions are about 0.1–10 Torr pressure, 200–500 V and 10–100 mA), which results in high atom densities and more effective ionization in the negative glow. Therefore, hollow cathode discharges can yield more ions than other types of sources and could benefit from reconsideration as an ion source. However, hollow cathodes suffer from sampling difficulties in extracting ions, since the 'well' of ions in the hollow cathode plasma

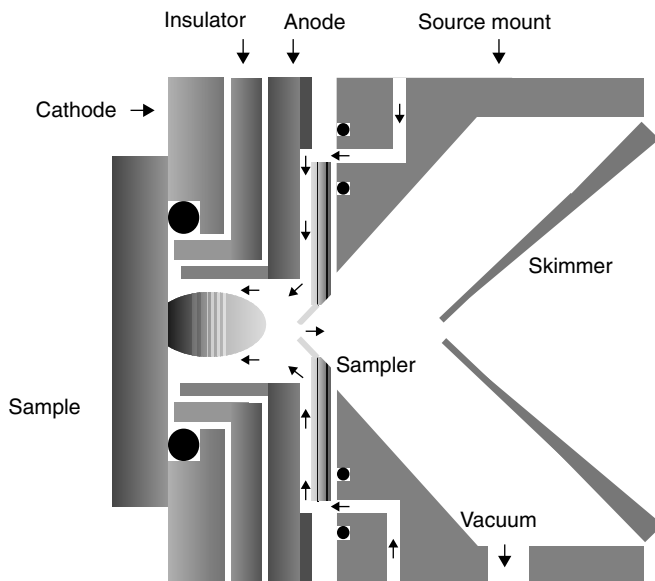


Figure 3.4 Grimm-type glow discharge ion source

is concentrated at some distance from an ion exit orifice. A further disadvantage of this source is the machining required to make hollow cathodes from samples and, of course, many sample types are not compatible with this configuration. However, the intense plasma conditions that can be generated in a hollow cathode may provide impetus for further investigations [22].

Operating Modes of the Glow Discharge

The glow discharge is amenable to several different modes of operation, including direct current (dc), radio frequency (rf) and pulsed power mode. The dc discharge is the most commonly used discharge in mass spectrometry because it is inexpensive, simple, and produces a stable, steady-state source of ions suitable for extraction into a variety of mass spectrometers. Figure 3.5 shows a representative mass spectrum for a dc glow discharge with a NIST brass sample, indicating the major spectral constituents and illustrating the relatively simple spectra typical of GD ion sources. The primary ion signals arise from the discharge gas and the matrix element(s). At higher sensitivities, constituents present at lower concentrations become apparent, as indicated for tin at 0.43% in the inset in Figure 3.5, and detection limits in the ppb range are readily achievable.

Despite the high level of acceptance of the dc mode, some limitations are found. Most importantly, it cannot be used for the direct analysis of nonconducting materials. Increasing interest in the characterization of nonconductors,

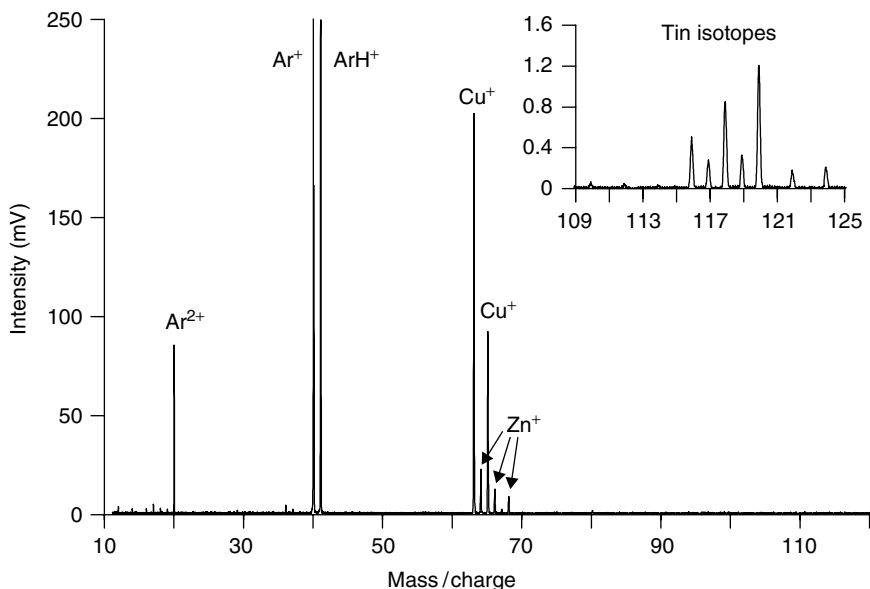


Figure 3.5 Typical dc glow discharge mass spectrum showing the major ion components (matrix elements and discharge gas), along with an inset of a minor element, Sn, at 0.43%. Sample is NIST SRM 1104 Brass

such as glasses and ceramics, has led to explorations of the rf discharge [23,24]. Compared with the dc mode, rf discharges are more complex in terms of the power coupling to the sample, and the mechanisms responsible for excitation and ionization within the rf discharge are not as well understood (see Chapter 2). However, the fundamental promise shown by an rf source to handle both conducting and nonconducting samples makes developments in this area of considerable interest.

In addition to dc and rf modes, the pulsed glow discharge mode is attracting interest from several groups [25–29]. Pulsed operation offers advantages of enhanced sputter atom yield and greater excitation and ionization by application of high, short-term power. Even though the instantaneous power can be higher than several hundred watts, the average power remains fairly low, as determined by the duty cycle of the pulse (ratio of the pulse width and pulse interval). A limitation of the pulsed GD is that it requires a gated detector to extract the information signal as a function of time.

Another advantage of a pulsed glow discharge is the temporal separation of discharge gas ions and analyte ions, particularly with a time-of-flight mass spectrometer. As shown in the series of mass spectra in Figure 3.6, taken at increasing delays after pulse termination, argon ions are formed immediately when the glow

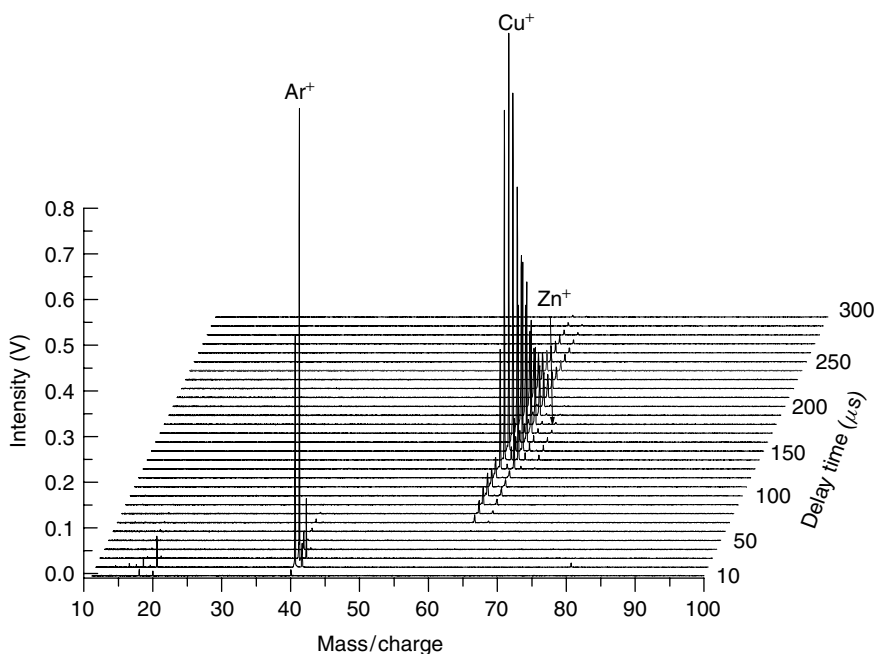


Figure 3.6 Temporally resolved mass spectra taken with a pulsed glow discharge source and time-of-flight mass spectrometer, showing the effect of delay time on the species observed. Sample is NIST SRM 1104 Brass

discharge is initiated, whereas the sample ions are observed only after a characteristic time delay. Thus, sputtered particles and discharge gas species can be temporally separated. When the spectrum is recorded after a delay of several hundred microseconds, it is dominated by ions of the sputtered material, and gas-related interferences are minimized, achieving temporal resolution not possible with conventional discharge modes.

3.2.4 MASS TRANSPORT PHENOMENA

Unlike the case of optical spectrometry wherein the discharge can be sampled as a closed, sealed-off system, mass spectrometry requires sampling ions of from the plasma and physically transporting them to the mass analyzer. Interfacing a glow discharge to a mass spectrometer requires proper recognition of the critical operating differences between the discharge source and the spectrometer. The glow discharge source typically operates in the 0.1–10 Torr range. However, mass spectrometers need a vacuum of less than 10^{-5} Torr to avoid disrupting collisions in the ion flight path. Differential pumping is required to permit this

coupling (as represented previously in Figure 3.1). Three vacuum regions are employed in GDMS: the glow discharge source at ~ 1 Torr, the intermediate vacuum region at $\leq 10^{-4}$ Torr and the analyzer region at $\sim 10^{-6}$ Torr. Since the sputtered sample atoms are ionized in the negative glow region of the discharge, the sampler (an orifice of ~ 1 mm) is placed in this region to produce a rapidly expanding beam of gas and ions from the higher-pressure source into the intermediate chamber. The skimmer, with an orifice id of ~ 1 mm, is positioned several millimeters after the sampler, and serves as the interface to the high-vacuum segment of the mass spectrometer, extracting from the sampler beam a central solid angle of ions for transmission to the ion optics and mass separation system. For GDMS, an isolation valve between the discharge ion source and the mass spectrometer is desirable in order to protect the high vacuum system during sample interchange.

Although GDMS is now a mature technique, few fundamental studies have examined the overall process of sampling ions from the glow discharge source and transmitting these ions to the mass spectrometer. Hang *et al.* reported certain theoretical and practical considerations for glow discharge source interfacing to a mass spectrometer [28]. In a typical GDMS ion source, the transition flow of atoms and ions becomes transformed into what is normally termed molecular flow (atom flow in the GD) as the plasma passes through the sampler orifice. Shock wave fronts are thought not to occur in the supersonic expansion of the GD ion source [28], which permits greater flexibility for skimmer design. Ions of different masses have similar initial kinetic energies in the GD source; thus, the angle of the skimmer cone is not normally a critical parameter for optimal ion beam extraction.

3.3 INSTRUMENTATION

The glow discharge ion source has been interfaced to most of the standard mass spectrometer types. Ions formed in the GD plasma have generally low kinetic energies (2–5 eV) owing to the formation/collision processes, so they present no extraordinary problem for ion optics. As a ‘high-pressure’ source, special pumping needs must be met to effect a transition from the 1–10 Torr ion source to the high-vacuum transport sections. Because the GD ion source is used primarily for elemental analysis, the associated mass spectrometer is required to cover a mass range encompassing only up to about 250 Da. Like all ion sources, spectral interferences are always present to some degree in the GD source, so resolution considerations must be taken into account.

3.3.1 SECTORS

Magnetic Sector Analyzers

The first mass spectrometric instrument, a mass spectrograph developed by Aston [30], was a prototype spectrograph that laid the foundation for the

principles found in today's single-focusing magnetic deflection spectrometers. The magnetic sector analyzer employs an electromagnetic field to disperse ions of different m/z spatially across a focal plane. An illustration of a typical single-focusing magnetic sector instrument is shown in Figure 3.7.

Ions exiting the ion source are accelerated into the magnetic sector analyzer by applying a potential to the entrance slit. The loss of potential energy for the ions is equal to their gain in kinetic energy, which is summarized as follows:

$$KE = zeV = 1/2mv^2 \quad (3.1)$$

where z is the number of charges on the ion of mass m , e is the charge of an electron, V is the accelerating voltage and v is the velocity of the ion. The path the ions follow in the sector is affected by two forces: (1) a centripetal force pulling ions inward and (2) a centrifugal force impelling them outward. The centripetal force, F_M , arises from the magnetic field and is given by

$$F_M = Bzev \quad (3.2)$$

The centrifugal force (F_c), resulting from the acceleration potential, is given by

$$F_c = (mv^2)/r \quad (3.3)$$

where r is the radius of curvature of the magnetic sector. Ions of different mass can be scanned across the exit slit by varying the field strength of the magnet (B) or the accelerating potential (V). In order for an ion to traverse the circular path completely, these two forces must be equal. Thus, combining Equations 3.2 and 3.3 yields the equation of motion for an ion traveling through a magnetic field:

$$Bzev = (mv^2)/r \quad (3.4)$$

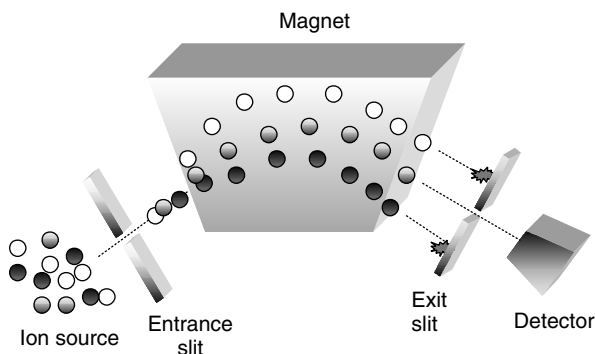


Figure 3.7 Single focusing magnetic sector analyzer

This equation assumes that all ions having the same charge (z) have the same kinetic energy after acceleration, regardless of their mass. However, this is not an accurate assumption since prior to acceleration the ions possess a distribution of velocities, which can result in a spread in the radius of accelerated ions. Rearranging Equation 3.4 yields the basic mass spectrometer equation (in terms of m/z ratio):

$$m/z = (B^2 r^2 e)/2V \quad (3.5)$$

From this equation, it can be seen that a mass spectrum can be obtained by varying one of the three variables (B , V or r) while holding the other two constant.

Double Focusing Magnetic Sector Analyzer

It may be deduced from the previous discussion that a magnetic sector instrument is a momentum analyzer, rather than a true 'mass' analyzer. As a result, ions of the same mass but of different translational energy are not focused. This can lead to broadening of the ion beam reaching the detector and a subsequent loss of resolution. Improving the resolution is achieved by correcting the directional and energy distributions of ions leaving the source. Double focusing magnetic sector analyzers, which add an electrostatic field to the pre-existing magnetic field, are capable of such correction through velocity focusing. The magnetic sector separates ions by their m/z ratio, with the electrostatic analyzer being used to focus the ions according to energy. A representation of a double focusing sector device is shown in Figure 3.8. An ion that enters the electrostatic field travels in a circular path (radius r) such that the electrostatic force balances the centrifugal force. The equation of motion of an ion traveling through an electrostatic field is

$$mv^2/r = ezE \quad (3.6)$$

where E is the electrostatic field strength. The path of an ion in the electrostatic field is dependent on its energy, as seen from Equation 3.6. The arrangement in Figure 3.8 is the Nier–Johnson geometry, in which the electrostatic analyzer precedes the magnetic analyzer. Alternatively, the magnetic analyzer may precede the electrostatic analyzer, forming the reverse Nier–Johnson geometry.

Although several commercial glow discharge optical emission spectrometers are currently available, the only commercial glow discharge mass spectrometer at this time is the VG9000 (Thermo Elemental). This system employs a reverse Nier–Johnson geometry to achieve double focusing. Introduced in the mid-1980s, the VG9000 has found broad application, including the quantitative analysis of high-purity materials and the determination of dopants and impurities in semiconductors, metal alloys and superconductors. Additional applications include the bulk analysis of oxide powders and nonconductive matrices, and also the

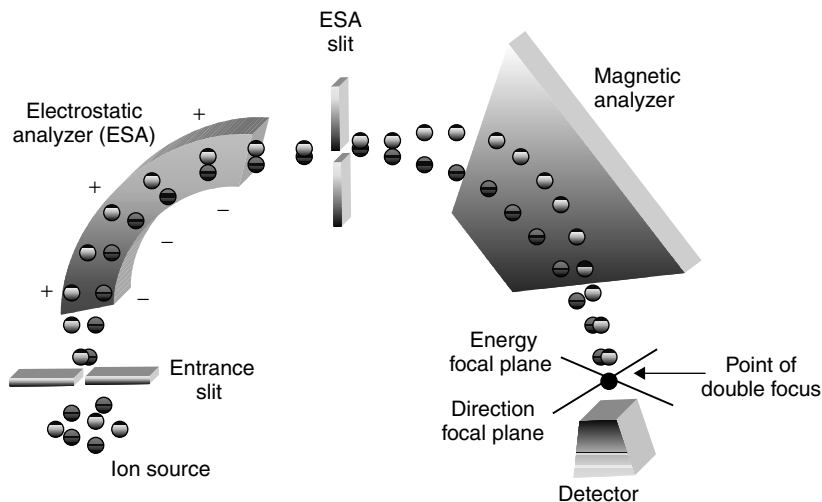


Figure 3.8 Double focusing magnetic sector analyzer

quantitative depth profile analysis of layered materials. Flexibility in the amenable sample types is afforded through the ability to analyze both pin and flat sample geometries [31]. The VG9000 is capable of resolution near 10 000, although it operates more commonly in the 3000–4000 range. The considerable cost of this magnetic sector instrument has limited to some degree the more widespread use of GDMS as a routine analysis tool.

3.3.2 QUADRUPOLE MASS FILTERS

Just as magnetic sector spectrometers are analogous to optical monochromators, quadrupole mass analyzers are analogous to optical bandpass filters [13]. Where a magnetic sector instrument simultaneously disperses all ions as a function of their m/z ratio, a quadrupole at any given instant transmits ions only within a small range of m/z ratios corresponding to a set of operating conditions. Other ions entering a quadrupole (i.e., ions outside of the chosen range) are filtered out, leaving only ions within the selected range to be detected. Controlling and varying the potentials of the quadrupole allows a range of m/z values to be transmitted, permitting spectral scanning. Often, quadrupole spectrometers are referred to as mass filters owing to their ability to transmit particular ions.

The quadrupole consists of four parallel rods, which serve as the electrodes, arranged symmetrically about the z -axis (Figure 3.9). Ions exiting the ion source are accelerated into the quadrupole by a small potential, typically 10–20 V.

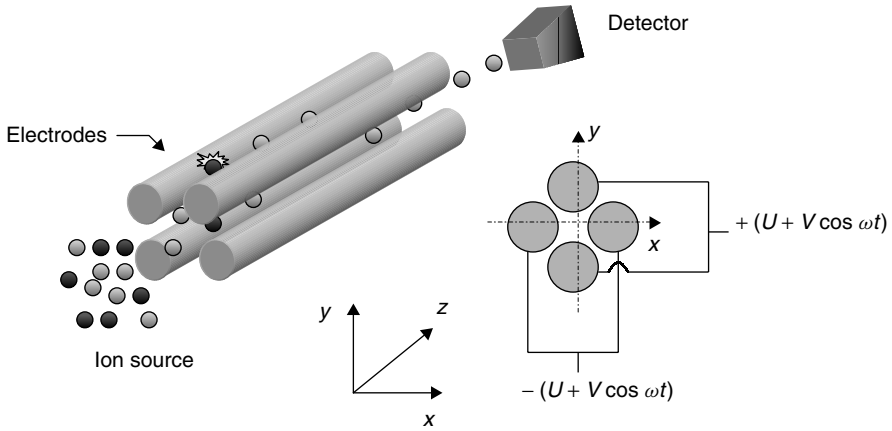


Figure 3.9 Quadrupole mass filter

A voltage consisting of a dc component (U) and a radio frequency (rf) component [$V_0 \cos(\omega t)$] is applied between adjacent rods. Opposite pairs of electrodes are electrically connected to each other. One electrode pair has a positive dc potential applied along with an rf potential, and the other electrode pair has a negative dc potential along with an rf potential that is out of phase compared with the positive electrode pair rf potential. The oscillating electric fields across the electrode pairs, along with the small accelerating voltage, cause the ions to oscillate in the x and y directions, creating a helix-type oscillation pattern as they travel through the filter.

A more rigorous explanation better defines the quadrupole's ability to transmit only certain ions [32]. The electrical potential (Φ) at time (t) of a quadrupole is given by

$$\Phi = [U + V \cos(\omega t)](x^2 - y^2)/2r_0^2 \quad (3.7)$$

where U is the dc potential, V is the rf potential of angular frequency ω , x and y are the linear displacements along the respective axes and r_0 is the radius encompassed by the four electrodes. Further treatment of Equation 3.7 leads to mathematical descriptions of the path of an ion through the electric field. The reader wanting a more detailed description of this derivation is encouraged to consult the original reference [32]. From this derivation, the parameters a , q and Φ are defined:

$$a = 8eU/m\omega^2r_0^2 \quad (3.8)$$

$$q = 4eV_0/m\omega^2r_0^2 \quad (3.9)$$

$$\Phi = \omega t/2 \quad (3.10)$$

The first two parameters help define the oscillations that the particle will follow and the last deals with the electrical potential. After rearrangement of these three equations, they can be substituted into Equation 3.7, yielding a Mathieu differential equation of the form

$$d^2u/d\Phi^2 + (a + 2q \cos 2\Phi)u = 0 \quad (3.11)$$

This equation is solved for values of a and q , under the conditions that $0 < u < r_0$. Under these conditions, the ion is never outside the radius (r_0) bounded by the electrodes. For certain values of a and q the oscillations performed by the ions are stable (i.e., finite amplitude). All other values of a and q result in oscillations that are unstable, leading to an infinite amplitude.

Quadrupole mass spectrometers are typically more compact and less expensive than magnetic sector instruments. As a consequence, quadrupoles have become one of the most popular types of mass spectrometers, at least in the research laboratory, to complement the glow discharge source. The combination of a quadrupole mass filter and a glow discharge source for analytical purposes was described by Harrison and colleagues in the 1970s [33], showing GDMS to be a useful alternative to spark source mass spectrometry for trace element analysis of conducting solid samples. An rf-GD source was also coupled by Marcus and co-workers to a quadrupole mass spectrometer for the analysis of nonconducting sample types [23]. A third type of glow discharge source, the pulsed GD, has also been coupled to the quadrupole [34].

3.3.3 ION TRAP

The quadrupole mass filter, described in the previous section, comprises four parallel conducting rods. The ion trap, which is similar in operation to the quadrupole, can be thought of as connecting two opposing rods of the quadrupole, while the other two rods are converted into hyperbolic end caps. The trap is roughly the size of a tennis ball, and normally its size is inversely proportional to its versatility. The components of an ion trap, a ring electrode positioned between two end cap electrodes, are illustrated in Figure 3.10.

Initial designs of the ion trap had a trapping principle similar to that of the quadrupole mass spectrometer. In this mode of operation, termed the mass-selective 'stability' mode, the rf and dc potentials applied to the ring electrode are ramped at a constant ratio which allows stability (i.e., storage) of a single m/z value within the trap. The potentials were increased and ions of increasing m/z values were stabilized and ejected, one m/z value at a time.

Unlike their initial designs, current ion trap mass spectrometers are based on the mass-selective 'instability' trapping mode of operation. This mode of operation allows ions of all m/z values to be stored within the trap, rather than ions of a single m/z value. Operating parameters similar to those of the

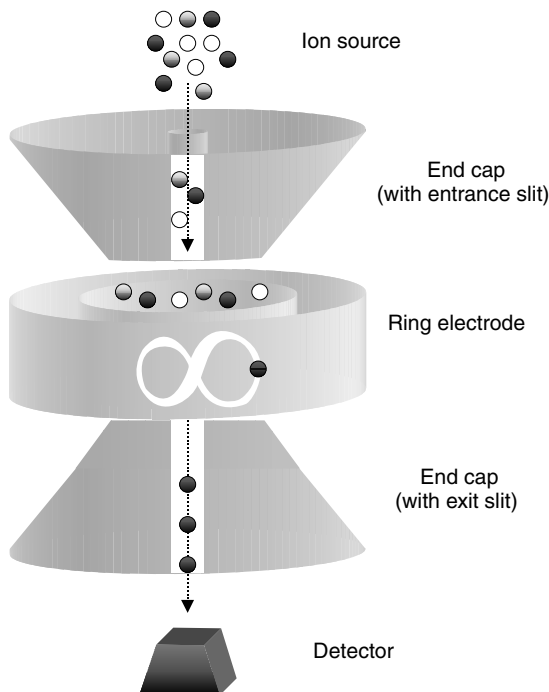


Figure 3.10 Ion trap mass analyzer

quadrupole mass spectrometer are key components in the description of the ions' stability:

$$a = -8eU/m\omega^2r_0^2 \quad (3.12)$$

$$q = -4eV/m\omega^2r_0^2 \quad (3.13)$$

These parameters are modified, with respect to those for the quadrupole, and added to the same Mathieu stability equation (Equation 3.11). Mass analysis is obtained by scanning the regions of ion instability, rather than scanning ion stability as done in previous designs. In this mass-selective instability mode, the dc component is held at zero while the rf frequency and initial amplitude are chosen so that all ions with an m/z value greater than a particular threshold value are stored [35]. As the rf amplitude is increased the motion of the ions becomes more energetic, eventually resulting in unstable trajectories. Ions of increasing m/z value leave the trap through a hole in one of the end caps where they are detected and a mass spectrum is obtained.

Although many applications of ion traps involve creating ions inside the trap for *in situ* analysis [36], combining a glow discharge with the ion trap requires transporting the ions from the external glow discharge source into the

ion trap [37]. This eliminates the need to induce electron impact or chemical ionization in the chamber of the ion trap, thereby allowing the trap to focus only on trapping the ions inside the chamber.

Ion trap instruments are more compact and, in principle, less costly than sector or quadrupole instruments. Although glow discharge ion trap instruments have found only limited applications up to this point amongst the glow discharge community, the promise of such a combination remains. The first reported glow discharge ion trap mass spectrometer was developed in the early 1990s [38], showing a reduction in argon gas interferences through the use of rapid electron- and proton-transfer reactions in the trap.

3.3.4 TIME-OF-FLIGHT MASS SPECTROMETERS

The time-of-flight mass spectrometer (TOFMS), shown in Figure 3.11, has found broad glow discharge application. Unlike the previously discussed mass spectrometers, the TOF instrument is based on a 'dispersion-in-time' principle [39]. Ions produced by the GD source are accelerated by an electric field pulse (typically 10^3 – 10^4 V). Since the ions have ideally the same kinetic energies after this acceleration pulse, they can be separated according to their velocity, which is characteristic of the m/z . Via measurement of the time taken for an ion to traverse a flight path to the detector, a mass spectrum can be compiled. The time

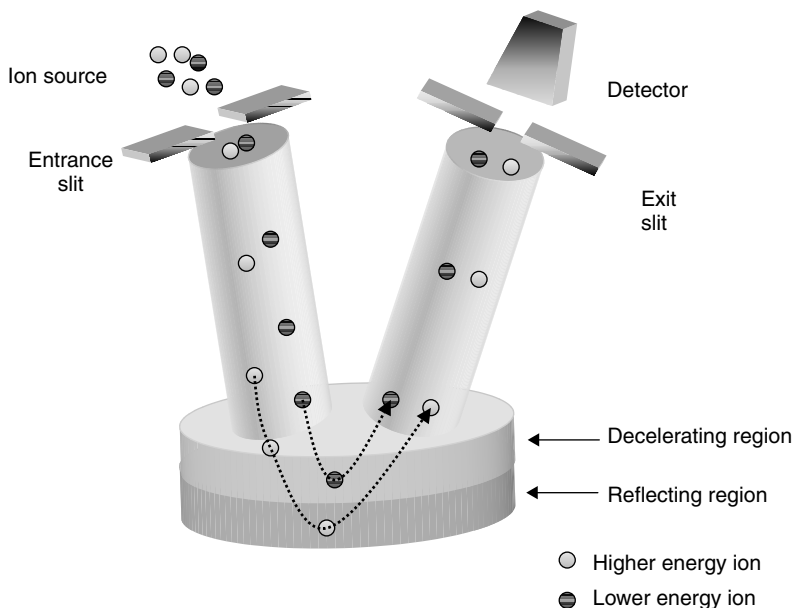


Figure 3.11 Time-of-flight mass analyzer

required for an ion of mass m to travel this pathlength L can be calculated from the following equation:

$$t = (m/2zeV)^{1/2}L \quad (3.14)$$

where z is the number of charges on the particular ion of interest, e is the charge of an electron and V is the accelerating voltage. Either orthogonal or axial ion extraction methods are suitable for selection of the ion package delivered to the TOF flight tube.

A significant development in the area of TOF mass spectrometry was the addition of a reflectron, first described by Mamyrin and Shmikk [40] in the 1970s, which affords better resolution through compensation for different flight times of ions with somewhat dissimilar kinetic energies. Figure 3.11 is an illustration of a TOF instrument employing the reflectron principle. After traversing the first stage of the overall flight tube, ions enter a retarding field and are reflected through a second stage of the flight tube. An ion with a higher energy will penetrate the retarding field more deeply and will spend more time in this field, allowing it to approximate more closely the velocity of a slower ion (of the same mass) so that both reach the detector nearly simultaneously. Since multiple ions can reach the detector at virtually the same time, only with the development of fast electronics has TOFMS become a reliable method of increasing choice.

An important characteristic of the TOF spectrometer is the transient nature by which it accepts ions. This is a special advantage for a pulsed GD source in that it allows maximum efficiency of ion sampling and temporal resolution. As the sample is atomized and ionized by successive pulses of the GD, the TOF accelerates these 'ion packets' into the flight tube. By optimizing the pulse timing (see Figure 3.6), important temporal resolution can be achieved [25]. This is seen through the discrimination of interfering ions (i.e., background gas ions) from analyte ions by controlling the delay time in which the ion packets are accelerated.

Since its first introduction in the mid-1990s, the combination of a GD source with TOFMS, particularly with a pulsed ion source, has shown marked promise. A comparison of dc and microsecond pulsed glow discharge sources coupled to TOF has been reported [27], as has the coupling an rf-GD to a TOF instrument [41].

3.3.5 FOURIER TRANSFORM ION CYCLOTRON RESONANCE

In a Fourier transform ion cyclotron resonance mass spectrometer (FT-ICR-MS), ions are typically formed, detected and analyzed internally in a single cell located within the solenoid of a superconducting magnet [35]. A schematic diagram of a typical FT-ICR-MS is shown in Figure 3.12. Ions that are transported into the cell from an external ion source are trapped and constrained to move in a circular path perpendicular to a strong magnetic field through application of small voltages. The frequency (ω) of these circular oscillations can be represented by

$$\omega = 1.537 \times 10^7 (zB/M) \quad (3.15)$$

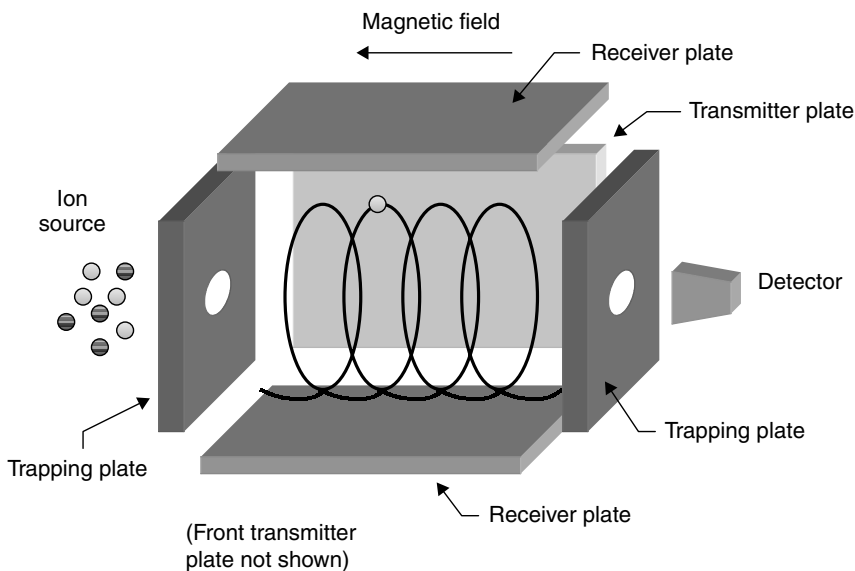


Figure 3.12 Ion cyclotron resonance cell used in Fourier transform mass analysis

where z is the number of charges on the particular ion, B is the magnetic field strength and M is the atomic mass. After trapping the ions, an rf voltage with the same frequency (ω) is applied to the transmitter plates (shown in Figure 3.12) of the spectrometer. Ions of the same frequency will absorb this energy, leading to an increase in orbital radius and velocity but no change in frequency. All ions that have absorbed this energy will move together in a coherent fashion. The cyclotron motion of these ions induces image currents that are detected as a time-domain signal which is subsequently converted to a frequency-domain spectrum by the application of fast Fourier transformation (FFT).

FT-ICR-MS is a high-resolution technique that for GD purposes is directed more towards specialized applications. Its high resolution can help separate certain isobaric interferences shown to be problems in lower resolution glow discharge mass spectrometric techniques (e.g., quadrupole, TOF). The first reported glow discharge FT-ICR-MS was assembled in the late 1980s [42].

3.4 QUALITATIVE CONSIDERATIONS

An elemental mass spectrum offers a significant advantage in that its very simplicity permits easier qualitative interpretation compared with the line-rich optical emission spectra. Elements have generally many fewer isotopes than emission lines, so a GD mass spectrum of iron, for example, will feature four main spectral

peaks, while an iron emission spectrum can exhibit hundreds of lines, depending upon the measurement sensitivity. Multi-isotopic elements provide a spectral pattern that can be used for identification and confirmation of an element's presence in a sample. Of course, mono-isotopic elements present a problem in this respect, so an observed line at m/z 27 or 59, for example, cannot be taken as unambiguously representing aluminum or cobalt, respectively. It is also necessary to recognize typical GD mass spectral interferences that may have a negative impact on the analysis, such as N_2^+ and N_2H^+ on silicon isotopes.

GD mass spectra provide information across the periodic table and serve as a ready overview of a sample's elemental constituents. In applications wherein the indicated presence or absence of a given element(s) may suffice, GD mass spectra can be particularly valuable. The analyst with a practiced eye and experience with common sample matrices may extract much valuable information from a GD mass spectrum.

3.5 QUANTITATIVE ANALYSIS

The mass spectrum obtained by GDMS can be used directly for a semi-quantitative measurement of the sample composition. Many factors influence the signal intensity of the plasma species, including sample composition, matrix type, discharge power, cathode geometry, cooling effects, discharge gas, source pressure, ion sampling and transmission, the type of mass spectrometer and the detection system. Simple comparisons of the elemental signal intensities of the analytes will lead to incorrect concentrations compared with the actual concentrations. Therefore, quantitative analysis requires the use of standards for calibration, for which there are two possibilities. One is the construction of a calibration curve, based on a set of similar standards, and the other is the analysis of a reference material as similar as possible in composition and behavior to the unknown, which allows the calculation of the relative sensitivity factors (RSFs). Of course, suitable certified standards are not always available. For powdered samples, an added (or doped) element of known concentration sometimes serves as internal standard.

3.5.1 CALIBRATION CURVE

In a GD mass spectrum, a measurable peak observed at a specific m/z position indicates the possible presence of the corresponding element in the sample. When a set of samples containing different concentrations of an element of interest and differing as little as possible in chemical composition has been measured under the same experimental conditions, a calibration curve can be obtained. The unknown elemental concentrations of interest in a sample of the same matrix type can then be determined by measuring the elemental ion intensities and determining the corresponding concentration value from the calibration curves.

Because quantitative analysis is dependent on the specific operating conditions selected, these should be re-established whenever adjustments or modifications are made to instrument operating parameters.

In practice, even when standards are available, a calibration curve approach is problematic in GDMS owing to the difficulty of reproducing the experimental conditions (e.g., sample position) and to the large number of elements (and, thus calibration curves) that are often of interest in a given sample. Therefore, GDMS has inherited from its predecessor, spark source mass spectrometry, the use of internal standardization for quantitative analysis. With internal standardization, any drift in signal intensity with time is compensated significantly. The use of an internal standard also compensates for matrix effects.

By using an ion source that allows precise sample placement, good calibration curves can be obtained. Using a Grimm-type source (Figure 3.4), rapid, reproducible results can be obtained, as shown in Figure 3.13 [21], where the reproducibility of sample-to-sample runs is better than 5%. Taking one of the standards as an 'unknown', the accuracy of elemental determinations was found to be in the 6–8% range. The stability and reproducibility of a Grimm GD source are such that the analyst can prepare and trust the use of standard calibration curves, as opposed to the normal need for an internal standard in GDMS. As a result, the use of a Grimm-type source with GDMS offers new opportunities as a truly quantitative method.

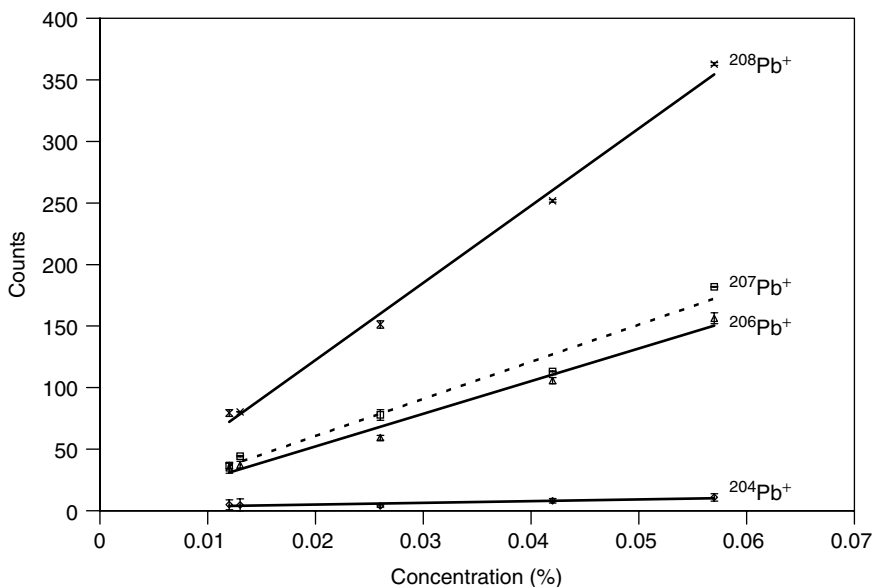


Figure 3.13 Calibration curve showing the linearity attainable with external standards using a Grimm-type ion source

3.5.2 INTERNAL STANDARDIZATION (RSF)

Quantitative analysis of unknown samples by GDMS is usually performed by applying RSFs to the measured ion beam ratios. RSFs are not uniformly calculated, but they focus on the factors that influence ion intensities, such as sample matrix, source atomization, ionization, sampling and detection [43]. RSFs are ideally obtained by the analysis of a reference material as close as possible in composition and behavior in the GD to the unknown sample. The RSFs can be broadly defined as the ratio of the elemental sensitivity of an analyte to the elemental sensitivity of a reference element [44], as is seen in the equation

$$\text{RSF} = (I_x/C_x)/(I_r/C_r) \quad (3.16)$$

where I and C are the signal intensity and the concentration of the analyte (x) and the reference element (r), respectively. This expression does not directly take into account the isotopic abundance of the selected isotopes, or the atomic weight differences that will influence numbers of atoms and ions per weight percent, which means that it relates less to relative sensitivity than to empirical correction. The RSFs are significantly influenced by the relative ionization in the GD plasma and are minimally dependent on matrix material, since the sputtering process of elements from a multi-component solid is relatively nonselective.

RSFs can be obtained by measuring a material with certified concentrations [44]. When the concentration of one element is known, quantitative analysis of an unknown sample can be done using Equation 3.16 or a variation thereof. Table 3.2 shows the results obtained for the quantitative analysis of the reference uranium oxide sample Morille with the VG 9000 GDMS, based on the RSFs calculated using the other certified uranium oxide sample, Chantarelle [44]. These

Table 3.2 Quantitative analysis of the Morille reference sample based on the RSFs obtained for the Chantarelle reference sample ($\mu\text{g g}^{-1} \pm \text{SD}$) [44].

Element	GD-MS value	Certified value	Element	GD-MS value	Certified value
¹⁰⁷ Ag	10.2 ± 1.04	10.4 ± 1.6	²⁶ Mg	19.4 ± 1.3	19.3 ± 1.5
²⁷ Al	84 ± 4	99 ± 6	⁵⁵ Mn	29.3 ± 1.07	24.5 ± 0.5
¹¹ B	3.5 ± 1.2	3.8 ± 1.6	⁹⁷ Mo	144 ± 8.7	147 ± 5
⁹ Be	3.8 ± 0.3	3.4 ± 0.6	⁶⁰ Ni	142 ± 3.3	147 ± 3
²⁰⁹ Bi	20.9 ± 1.4	24.4 ± 1.96	²⁰⁸ Pb	103 ± 7.2	101 ± 3
⁴⁴ Ca	94 ± 7	93 ± 8	²⁸ Si	93 ± 4.6	100 ± 8
¹¹¹ Cd	5.0 ± 0.3	4.9 ± 0.7	¹¹⁷ Sn	20.8 ± 2.3	18.5 ± 5.6
⁵⁹ Co	11.1 ± 0.68	9.8 ± 2	⁴⁹ Ti	48.6 ± 6.2	49.2 ± 2.6
⁵² Cr	101.6 ± 4	99 ± 2	⁵¹ V	47 ± 1.1	48.7 ± 2.8
⁶³ Cu	52.1 ± 3.3	50.2 ± 1	¹⁸³ W	106 ± 9	100 ± 9
⁵⁶ Fe	207.2 ± 8.4	211.6 ± 6.5	⁶⁸ Zn	102 ± 8	98.6 ± 5.5
¹¹⁵ In	10.4 ± 0.4	9.4 ± 1.1	⁹⁰ Zr	64 ± 7	59.9 ± 4.1

results, compared with the certified values, demonstrate the utility of GDMS for quantitative analysis.

3.6 CONCLUSIONS

Mass spectrometry remains one of the most dynamic and rapidly growing analytical methods today, showing little signs of slowing a development that has been exploding in prominence for several decades. That the sampling of glow discharges by such a technique would become important was certainly expected and is finding realization. There is no question that mass spectrometry can provide extensive elemental and perhaps even structural information from glow discharges. The ability to obtain full periodic table coverage, including isotopic information, with high sensitivity attracts well-deserved attention. Missing at the moment is adequate commercial instrumentation of reasonable cost that will permit more analysts to take advantage of these strengths. In the overall scope of glow discharge spectroscopy, mass spectrometry serves as a valuable complementary method to optical emission, and will likely take on a greater role with time.

3.7 REFERENCES

1. Aston FW, *Mass Spectra and Isotopes*, Arnold, London, 1942.
2. Thomson JJ, *Rays of Positive Electricity and Their Application to Chemical Analysis*, Longmans, Green, New York, 1913.
3. Hannay NB, Ahearn AJ, *Anal. Chem.* **26**, (1954) 1056–1058.
4. McNally JR, Harrison GR, Rowe E, *J. Opt. Soc. Am.* **37**, (1947) 93–98.
5. Birks FT, *Spectrochim. Acta* **6**, (1954) 169–179.
6. Knewstubb PF, Tickner AW, *J. Chem. Phys.* **36**, (1962) 674–683.
7. Knewstubb PF, Dawson PH, Tickner AW, *J. Chem. Phys.* **38**, (1963) 1031–1032.
8. Coburn JW, Kay E, *Appl. Phys. Lett.* **18**, (1971) 435–438.
9. Coburn JW, Taglauer E, Kay E, *J. Appl. Phys.* **45**, (1974) 1779–1786.
10. Harrison WW, Magee CW, *Anal. Chem.* **46**, (1974) 461–464.
11. Donohue DL, Harrison WW, *Anal. Chem.* **47**, (1975) 1528–1531.
12. Coburn JW, Harrison WW, *Appl. Spectrosc. Rev.* **17**, (1981) 95–164.
13. King FL, Harrison WW, Glow Discharge Mass Spectrometry, in *Glow Discharge Spectroscopies*, Marcus RK, Editor, Plenum Press, New York, 1993. Chapter 5.
14. Harrison WW, Glow Discharge Mass Spectrometry, in *Inorganic Mass Spectrometry*, Adams F, Gijbels R, Van Grieken R, Editors, John Wiley & Sons, Inc., New York, 1988. Chapter 3.
15. Anderson JM, *J. Appl. Phys.* **31**, (1960) 511–515.
16. Levy MK, Serxner D, Angstadt AD, Smith RL, Hess KR, *Spectrochim. Acta, Part B* **46**, (1991) 253–267.
17. Bogaerts A, Gijbels R, *Spectrochim. Acta, Part B* **53**, (1998) 1–42.
18. Gendt S, Grieken RV, Hang W, Harrison WW, *J. Anal. At. Spectrom.* **10**, (1995) 689–695.
19. Jakubowski N, Stuewer D, Vieth W, *Fresenius' J. Anal. Chem.* **31**, (1988) 145–149.

20. Hoffmann V, *EC Thematic Network on Glow Discharge Spectroscopy for Spectrochemical Analysis*, Autumn Newsletter, 1999.
21. Yang CL, Mohill M, Harrison WW, *J. Anal. At. Spectrom.* **15**, (2000) 1255–1260.
22. Yang CL, Harrison WW, *Spectrochim. Acta, Part B* **56**, (2001) 1195–1208.
23. Shick CR, DePalma PA, Marcus RK, *Anal. Chem.* **68**, (1996) 2113–2121.
24. Shick CR, Marcus RK, *Appl. Spectrosc.* **50**, (1996) 454–466.
25. Harrison WW, Hang W, *J. Anal. At. Spectrom.* **11**, (1996) 835–840.
26. Steiner RE, Lewis CL, King FL, *Anal. Chem.* **69**, (1997) 1715–1721.
27. Hang W, Yang PY, Wang XR, Yang CL, Su YX, Huang BL, *Rapid Commun. Mass Spectrom.* **9**, (1994) 590–594.
28. Hang W, Yan WM, Wayne DM, Olivares JA, Harrison WW, Majidi V, *Anal. Chem.* **71**, (1999) 3231–3237.
29. Majidi V, Moser M, Lewis C, Hang W, King FL, *J. Anal. At. Spectrom.* **15**, (2000) 19–25.
30. Aston FW, *Isotopes*, 2nd edn, Longmans, Green, New York, 1924.
31. *VG 9000 Product Literature*, TJA Solutions, Franklin, MA.
32. Dawson PH, *Quadrupole Mass Spectrometry and Its Applications*, Elsevier Scientific, New York, 1976.
33. Bruhn CG, Bentz BL, Harrison WW, *Anal. Chem.* **50**, (1978) 373–375.
34. Hang W, Harrison WW, *Anal. Chem.* **69**, (1997) 4957–4963.
35. Chapman JR, *Practical Organic Mass Spectrometry*, 2nd edn, John Wiley & Sons, Inc., New York, 1993.
36. Davis WM, Wise MB, Furey JS, Thompson CV, *Field Anal. Chem. Technol.* **2**, (1998) 89–96.
37. Todd JFJ, *Mass Spectrom. Rev.* **10**, (1991) 3–52.
38. McLuckey SA, Glish GL, Duckworth DC, Marcus RK, *Anal. Chem.* **64**, (1992) 1606–1609.
39. Cotter RJ, *Time-of-Flight Mass Spectrometry*, American Chemical Society, Washington, DC, 1994.
40. Mamyrin BA, Shmikk DV, *Zh. Eksp. Teor. Fiz.* **76**, (1979) 1500–1505.
41. Myers DP, Heintz MJ, Mahoney PP, Li G, Hieftje GM, *Appl. Spectrosc.* **48**, (1994) 1337–1346.
42. Shohet JL, Phillips WL, Lefkow ART, Taylor JW, Bonham C, Brenna JT, *Plasma Chem. Plasma Process.* **9**, (1989) 207–215.
43. Vieth W, Huneke JC, *Spectrochim. Acta, Part B* **46**, (1991) 137–153.
44. Betti M, *J. Anal. At. Spectrom.* **11**, (1996) 855–860.
45. White FA, *Mass Spectrometry in Science and Technology*, John Wiley & Sons, Inc., New York, 1968.

4

Radio Frequency Glow Discharges

R. K. MARCUS

Department of Chemistry, Clemson University, Clemson, SC, USA

4.1 INTRODUCTION

Although the vast majority of glow discharge (GD) applications described in this volume deal with the analysis of solid-state specimens, one must keep in mind that not all solids are alike. Differences among specimens occur not only in chemical composition, but also in physical characteristics. The most important of these differences with regard to GD analyses is the electrical conductivity of the specimen. Here we speak not only of the electrical properties of the bulk specimen, but also in the region of the sample surface. If the surface (or bulk) of the analytical specimen is electrically insulating, there is no chance for charge movement within the sample matrix and so the simple electrical circuit (akin to a diode) cannot be completed. In nonconducting samples, a positive charge accumulates on the surface under ion bombardment up to the point where the applied potential is insufficient to maintain the discharge. In the case where a discharge can at least be ignited (i.e. a source of ions and electrons exists in the gas phase) the process is analogous to the charging and discharging of a capacitor. The negative potential initially placed on the sample surface to initiate the discharge is effectively neutralized as positive ions arrive there. Thus, it is clear that while a conventional direct current (dc) potential is effective in igniting and maintaining a GD plasma at the surface of a conductive sample, this is not a viable approach for analysis of materials that are nonconductive in part or in whole.

In the context of solids elemental analysis, it is easy to identify those types of samples which would be amenable to analysis by conventional dc-GD analysis.

The analysis of bulk and layered metallic specimens is an important industrial undertaking and has been the forte of GD methods for decades. By the same token, the variability of materials that are electrically insulating is incredibly large, and is in fact growing as new materials of unique chemical and physical properties are being developed.

Winchester, Duckworth, and Marcus have reviewed the general approaches available for the analysis of nonconductive materials by GD spectroscopies [1]. More recently, Marcus has addressed this issue as it specifically applies to glow discharge mass spectrometric (GDMS) analyses [2]. The three basic approaches to nonconductor analysis include (1) making the sample conductive, (2) placing a conductive metal layer on the sample surface, and (3) using potentials in the radio frequency portion of the electromagnetic spectrum to maintain the plasma. In the first case, the specimen is ground, the resulting powder mixed intimately with a conductive powder, and the sample cathode is formed by pressing under high pressure [3–5]. This approach *de facto* precludes the ability to perform a depth-resolved analysis of the original sample. The physical nature of the sample can also affect the ability to grind the mixture to a fine enough size to ensure a stable sample disk and plasma. In addition, the amount of adventitious water that is introduced through the process has been shown often to have deleterious consequences [6,7].

In the second approach for nonconductor analysis, which is used almost exclusively in the field of GDMS, a secondary (metallic) cathode having a circular orifice in its center is placed on top of the analytical specimen. When the discharge is initiated, the sputtering process is naturally concentrated at the inner edge of the conductive electrode, and a metallic layer is eventually produced on the sample surface [8,9]. This electrically conductive layer promotes sputtering of the sample, and the continuous deposition of the metallic layer allows extended plasma operation times. This approach does put limitations on the geometry of the sample and tends to be complex in terms of optimization of the discharge conditions that balance sputtering of the sample and the secondary cathode. Interestingly, the straightforward approach of using a wire mesh (as used in ion beam etching) has not been described for GD methods.

The third approach to nonconductive specimen analysis is the use of radio frequency (rf) potentials to power the plasma. It is the only method wherein the sample does not need to be chemically modified. In addition, there is no risk of contamination by the addition of a secondary source of signal-producing species (i.e. metal powders and disks). The first two approaches are discussed in greater detail in Chapter 11. Described here are the basic operation principles of rf-powered GD devices, the physical characteristics of the plasmas, and a series of topical applications of the methodology. It should be stated clearly that, although the impetus for developing rf-GD technology is the analysis of nonconductive materials, there are fundamental advantages arguing for rf powering even in the analysis of bulk conductive samples.

4.2 RADIO FREQUENCY GLOW DISCHARGE (RF-GD) OPERATION PRINCIPLES

The application of a negative potential to an insulating electrode to initiate a plasma can be similar to the charging and discharging of a capacitor, as described in Section 4.1. In an effort to develop methods to quantify better the ion beam sputtering yields of insulating materials in high vacuum, Wehner and co-workers recognized in the early 1960s that the application of a high-frequency alternating potential could effect two processes that circumvent the observed capacitor-like phenomena [10]. First, the continuous application of high voltages at frequencies higher than the characteristic time constant of the capacitive response ($\sim 1 \mu\text{s}$) produces a series of short, distinct discharges much like a spark source. Second, there is a period of time during which a positive potential exists on the sample surface, a flow of electrons to the surface to maintain the negative potential on the sample so that the discharge itself does not extinguish. Within the duration of a typical analytical measurement, having sampling times ranging down to 0.1 ms, the plasma processes (atomization/excitation/ionization) and the resultant analytical responses are continuous. In practice, it is the combination of the high-frequency potentials and the alternating polarity that results in the inherent analytical utility of rf-GD source operation, enabling the establishment of a dc-bias potential on the surface of an insulating sample [11].

The establishment of a negative dc-bias potential can be easily understood on a first-principles basis. In the vicinity of the sample surface, ions and electrons accelerated by the cathode fall potential (depending on the instantaneous polarity) should have similar kinetic energies, in the range of eV . The velocity (v) of the charged particles under the influence of a potential difference is given by

$$v = (2eV/m)^{1/2} \quad (4.1)$$

where eV is the product of the electric charge (e) and the potential difference (V) and m is the mass of the particle. This velocity is not actually achieved owing to elastic collisions taking place when the particles cross the cathode dark space [11,12]. The kinetic energy of the argon ion population is further reduced as a result of charge exchange collisions, producing 'new' argon ions that do not experience the total cathode fall potential [12]. As a net result, the velocity of the electrons moving to the cathode surface will be much higher during the positive portion of the potential waveform than that of argon ions arriving at the cathode during the negative portion. More succinctly, the total charge per unit time is greater for the electron flow. As such, the potential present at the cathode surface will become offset toward negative values to the point where for the vast majority of the rf cycle ($\sim 90\%$), a negative voltage exists and therefore ion sputtering is taking place. In the remainder of the time, a slightly positive potential exists to compensate for the buildup of positive charge. After a short period of time (< 0.5 ms), the applied potential results in an alternating potential

on the cathode surface that is offset about a mean negative value, known as the dc bias potential.

Figure 4.1 illustrates the establishment of the dc bias potential for the case of rf-GD sputtering of a 2 mm thick ceramic (Macor) specimen. Lazik and Marcus used thin metal wire probes to measure the applied and realized surface potentials with the aid of a digital storage oscilloscope [13]. These waveforms are electronically aliased, and as such the individual 13.56 MHz alternating cycles cannot be registered. As shown in Figure 4.1a, the applied potential at the back of the sample reaches its full peak-to-peak value (~ 1500 V) in a period of 0.2 ms. In the same time frame, the potential at the cathode surface (Figure 4.1b), which sustains the discharge and the sputtering process, leads to a dc-bias potential of about -40 V. Specifically, the establishment of the dc bias is limited by the switching time of this particular generator to come to full power. Therefore, it can be understood that the plasma reaches a steady-state situation in a very short period of time and as such rf-GD sources can be used effectively in surface analysis applications.

The value of the developed dc-bias is a function of the relative ratio of the anode-to-cathode surface areas [14–16], the applied rf power and discharge gas

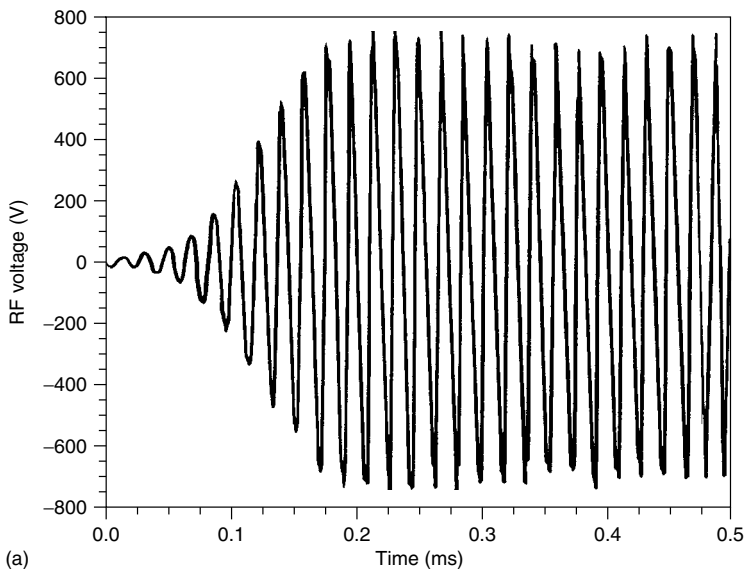


Figure 4.1 Transients signals recorded on an oscilloscope for the application of an rf potential to the back of a 2 mm thick ceramic (Macor) specimen which illustrates the establishment of a dc-bias potential at the surface of the sample. (a) Applied potential measured at the back of sample; (b) potential measured at the sample surface with the aid of a wire probe assembly. Discharge pressure = 6 Torr Ar, rf power output = 25 W. Reprinted from Lazik, C., and Marcus, R. K., *Spectrochim. Acta, Part B*, 1993, **48**, 1673–1689, Copyright 1993, with permission from Elsevier Science

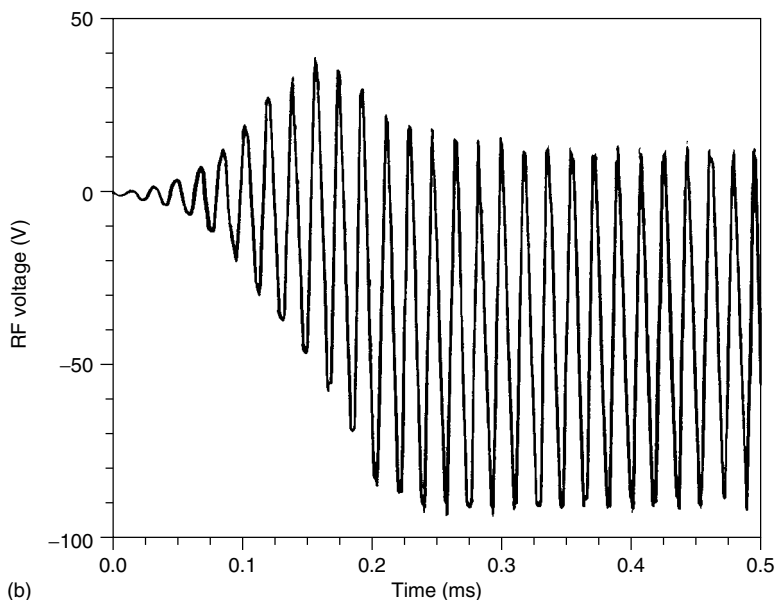


Figure 4.1 (continued)

pressure [13,16,17], and the efficiency of the rf power coupling. Clearly, the value of the dc-bias potential will control the rate of cathode sputtering (i.e. ion energy and flux) and the gas-phase electron characteristics (i.e. energies and number densities), and thus the sensitivity of the device. This multiplicity of variables and their possible effects have necessitated stringent standardization in the use of rf glow discharges in semiconductor manufacturing [18]. Marcus has described how the principles developed in the electronics industry can be applied in the design of 'analytical' rf-GD sources [19]. It is important to point out that the establishment of a dc-bias is also accomplished for conductive sample matrices via the inherent capacitance of the impedance matching networks employed in almost all rf plasma devices.

4.3 COMPARISONS WITH dc-POWERED GLOW DISCHARGE SOURCES

The advent of new analytical methodologies calls for direct comparisons with existing technologies. A new method must *at the minimum* provide equivalent analytical performance to existing instruments for like applications in order to gain acceptance. In addition, there must be some other obvious advantages, such as cost, speed, or versatility. In the case of the rf-powered glow discharges, comparisons with the widely accepted dc-powered devices are required. These

exercises can take place from the points of view of both the analytical characteristics and the fundamental processes. As with the early generation developments of any analytical apparatus, there are a number of different implementations that have been described for the rf-GD sources, which make comparisons difficult. Rather than going into detail on the specific attributes of the different rf source designs, we will discuss the general findings of studies comparing rf and dc powering of the same plasma source and leave it to the reader to make direct comparisons between the specific designs. It must be emphasized, though, that *not all rf-GD sources are alike!* In addition, it must be realized that with a proper design of an rf-GD source, the use of dc power becomes unnecessary as both conductive and nonconductive specimens can be analyzed directly. This premise has been supported as rf powering has been recognized in recent ISO standards in the use of GD-OES methodologies. In fact, of the more than 10 published comparisons of rf- and dc-GD powered source operation (via experimentation and modeling), each demonstrated a common set of attributes for all of the rf mode studies, in the case of basic metals analysis [20–32]. These features include more rapid plasma stabilization, better long-term stability, higher signal-to-background ratios for analyte species, and more energetic gas-phase processes. The equivalency in analytical performance of rf sources and dc devices has also been acknowledged in each of the ISO TC 201 documents issued to date (see Chapter 12).

The earliest comparison between the rf and dc powering modes was in an area which would be expected to be the most stringent test, the quantification of depth profiles. Payling *et al.* [20] postulated that, since the rf and dc discharges operate under the same basic mechanisms (physics) and conditions, quantification methods developed for dc powering could be extendable to the rf mode. They found that the same source operating in the two powering schemes provided very similar sensitivity factors and background equivalent concentrations. In addition, while the respective qualitative (i.e. analyte intensity vs time) depth profiles were completely different, the fully quantified profiles were highly similar for layered metal samples. The extended range of application of the rf source to painted coatings was also demonstrated in a quantitative fashion. Hoffmann and co-workers [21] came to the same conclusions for an rf-GD-OES source which employed a free-running rf generator. They obtained depth resolving powers for the rf and dc powering modes that were the same within the error of the experiments. Finally, the similarity in operation for the rf and dc sources was shown by Bengtson and Hånström [26], who also found that the general responses of Si (I) emission yields to changes in discharge parameters in the two modes paralleled each other.

Marcus and co-workers investigated both the analytical responses and the fundamental plasma characteristics for dc and rf operation with the same device [27], namely a laboratory-built Marcus-type source combined with a sequential (scanning) optical spectrometer. The discharge operating conditions were adjusted for each mode to give optimal optical responses [highest signal-to-background

Table 4.1 Comparison of analytical performance for rf- and dc-GD-OES powering modes for elements in NIST SRM 1252 Phosphorized Copper.

Analyte	λ (nm)	Certified value (ppm)	S (intensity)		S/B		S/N	
			rf	dc	rf	dc	rf	dc
Ag (I)	338.29	166.6	23 125	28 531	55.2	21.4	2 843	2 118
Ni (I)	361.94	128	5 295	6 434	18.3	11.3	799	541
Co (I)	384.55	90	37 662	47 102	48.0	53.0	1 925	2 864
Mn (I)	403.08	17 ^a	4 634	6 944	12.1	8.5	457	461

^aValue not certified.

Reproduced by permission of the Royal Society of Chemistry from Pan, X., Hu, B., Ye, Y. and Marcus, R. K., *J. Anal. At. Spectrom.* 1998, **13**, 1159–1165.

(S/B) ratio] for a number of trace level analytes in a NIST SRM 1252 Phosphorized Copper specimen. In Table 4.1 the optical responses obtained in the respective powering modes are presented. In all cases, the raw signal intensities (S) are higher for the dc powered sources, while the analytically more relevant signal-to-background (S/B) and signal-to-noise (S/N) ratios are generally superior in the case of the rf-powered source. With regard to long-term stability (important for both bulk analysis and depth profiling applications), the rf source showed a factor of $\sim 2\times$ lower variations than the dc source, although the repeatabilities on a sample-to-sample basis were comparable. Finally, the limits of detection for the two methods were comparable, as suggested by the intensity and precision data.

Of course, the analytical characteristics of a spectroscopic source are the result of both the sample introduction rates and the fundamental plasma characteristics of the device. In Table 4.2, the respective atomization and charged particle characteristics of the rf- and dc-powered plasmas are listed [27]. As can be seen, the sputtering rate of the dc source is over 50% larger than in the rf case, meaning that there are more analyte atoms available to excite and to be detected by optical

Table 4.2 Comparison of plasma parameters for rf- and dc-GD-OES powering modes using NIST SRM 1252 Phosphorized Copper.

Mode	Plasma conditions	Te (eV)	$\langle \varepsilon \rangle$ (eV)	n_i ($\times 10^{10} \text{ cm}^{-3}$)	n_e ($\times 10^{10} \text{ cm}^{-3}$)	Average depth ^a (μm)	Penetration rate ($\mu\text{m}/\text{min}$)
rf	25 W, 10 Torr	5.13	10.64	1.89	6.31	10.2 ± 0.6	2.0
dc	600 V, 12 Torr	1.54	4.13	0.66	2.88	16.6 ± 0.4	3.3

^a $n = 3$.

Reproduced by permission of the Royal Society of Chemistry from Pan, X., Hu, B., Ye, Y. and Marcus, R. K., *J. Anal. At. Spectrom.* 1998, **13**, 1159–1165.

emission. The lower atom flux resultant from rf sputtering is countered, though, by a plasma environment with much higher energy electrons. The electron and ion number densities also tend to be higher for the rf plasma than for the dc discharge. These plasma characteristics fit well with the observed analytical performance (Table 4.1) and can be directly attributed to the oscillating nature of the discharge potentials and their effect on the charged particle motion in the rf-GD environment [11]. Similar studies of the analytical and plasma characteristics for rf- and dc-powered plasmas obtained for the same discharge source have been performed by the groups of Kim [23], Wagatsuma [24], and Sanz-Medel [25,28]. Each of these reports points to the same trends, according to which the rf sources have lower sputtering rates but have higher excitation efficiencies than dc sources.

In a comparative study of mass spectrometry sources, Harrison and co-workers [29] compared rf and dc powering according to different criteria. A NIST iron standard was first used to evaluate the characteristics for conducting samples. Discharge conditions that produced similar analyte ion signals were employed for rf and dc powering, though these conditions were a compromise with respect to optimum rf analyte signal intensities. Otherwise, very few analytical differences were found to exist for the two powering schemes, including relative sensitivity factors, stability (<5% RSD), and sample-to-sample reproducibility (<20% RSD). Interestingly, the rf plasma produced much higher residual water signals than the dc plasma when no cryogenic cooling was utilized. This is of no analytical consequence, as cooling is now the norm in all GDMS analyses. Comparison of the rf and dc discharges was made for nonconductor analysis using Ag (a very weak getter) as binding matrix for La_2O_3 as a model oxide, with the discharge conditions again set to yield similar La^+ signals. A relatively low rf power of 8 W was employed as higher powers produced sputtering conditions under which the sampling orifice tended to clog, presumably due to higher sputtering rates. Under such conditions, the R value ($R = \text{M}^+ / \text{M}^+ + \text{MO}^+$) from dc powering was 98% vs 75% for the rf mode. Operation of the rf discharge at higher powers was expected to produce more comparable values (i.e. lower oxide intensities). Analysis of a mixture of rare earth elements (REEs) indicated that the degree of atomic ion production was again very sensitive to sampling conditions (i.e. position of sampler, pressure, and power) in the case of the rf mode, and not so much so for the dc mode. In fact, the R values of the REEs varied with the rf conditions, but not with the dc conditions, which apparently depend on the M–O bond strengths. Relative sensitivity factors for the rf and dc plasmas were found not to be appreciably different under controlled conditions. However, the rf source showed very good stability ($\sim 5\%$ RSD) and reproducibility (<15% RSD). Comparable precision data for dc-GDMS analysis were not provided.

The experimental results described above have been supported very well through computational modeling as described by Bogaerts and Gijbels [30–32]. This group has employed its extensive background in the modeling of various

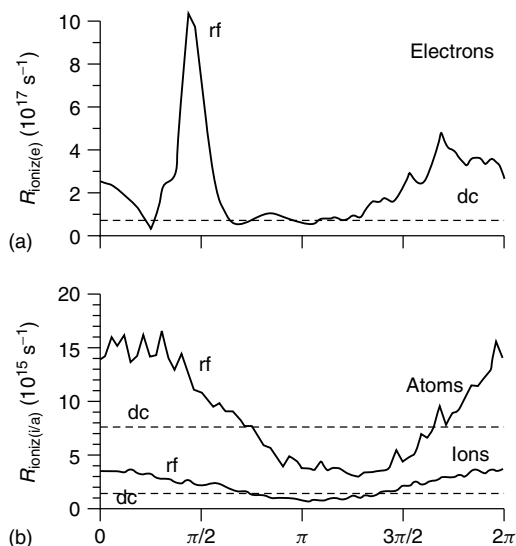


Figure 4.2 Ionization rate of argon due to electron impact (a) and argon ion and atom impact (b), integrated over the entire discharge region, both calculated for the rf-mode (as a function of time in the rf cycle, solid lines) and for the dc mode (dashed lines) ($p = 5.775$ Torr, $P = 10.2$ W rf and 10.45 W dc). Reprinted from Bogaerts, A., Gijbels, R., and Goedheer, W., *Spectrochim. Acta, Part B*, 1999, **54**, 1335–1350, Copyright 1999, with permission from Elsevier Science

dc-powered glow discharge devices to understand the operation of rf sources used in chemical analysis and materials processing applications. In a first set of calculations, they found that the rate of argon atom ionization was much higher in an rf plasma than in one powered by a dc potential at the same nominal power [30]. As a consequence of this enhanced ionization, the operating voltages for the rf plasma are appreciable lower. One of the more interesting aspects of the developed models is the output of information on a time-resolved basis during the course of a single rf cycle. In Figure 4.2, this sort of information is shown for the ionization rate of argon atoms through electron impact in the top portion and by metastable collisions and charge exchange at the bottom [30]. It can easily be seen that electron impact ionization is much more prominent in the rf plasma and is a function of the position in the rf cycle. The authors also found that although most of the argon atom ionization in dc plasmas is due to γ -ionization (i.e. via secondary electrons from the cathode surface), electrons in the negative glow of the rf plasma can gain sufficient energy to account for almost 25% of the ionization (termed α -ionization). In a subsequent paper [31], the respective excitation characteristics of 64 Ar (I) excited states were described, confirming the conclusions cited in the work of Sanz-Medel and co-workers [28]. The authors found that the rf-GD models predicted a more efficient excitation of the highest

Ar (I) excited states in comparison with dc plasmas. In addition, the calculated spatial distribution for the excited-state emission showed a distinct maximum in the region of the negative glow–cathode dark space interface [31]. Interestingly, this is the location of highest analyte ion intensities as measured by mass spectrometry by Duckworth and Marcus [33,34]. The additional ‘heating’ of electrons in the rf plasma also resulted in Ar (I) emission contours that showed greater diffusion away from the cathode region in the rf plasmas as compared with the dc mode. This means that the negative glow is larger for the rf plasma [31].

In the third paper in the series, Bogaerts and Gijbels modeled the most analytically relevant aspects of the rf sources operating for optical emission spectroscopy [32]. First, the flux of sputtering species (i.e. Ar^+ , Ar^0 , and Cu^+) were calculated for the rf and dc sources. While it turns out that the sputtering species densities are higher for the rf plasmas, the computed sputtered atom densities are larger for the dc case. The lower sputtered atom densities in the rf mode in fact have been confirmed in all of the experimental studies. The reason for the lower ‘yield’ of atoms is explained by the lower acceleration voltages in the rf plasmas. Further, the computed optical emission spectra for the two sources are very similar for the case of sputtering a copper target. The authors found that the atomic line intensities for the dc discharge should be lower than those for an rf source by an order of magnitude, whereas in the case of ionic lines they are lower by 20%. These calculations are in general agreement with the experimental results of Hoffmann and co-workers [21]. However, this contradicts experimental findings of others [23–25,27,28] who observed that the raw signals of the dc source are larger. This discrepancy is probably due to the different source geometries employed and is not representative of a flawed model. The calculations presented to date may be concluded to present a very valid and useful picture of rf and dc glow discharge source operation.

4.4 INSTRUMENTATION

4.4.1 GENERAL CONSIDERATIONS

There are certain aspects that make the design and construction of rf-powered sources easier than dc devices, and some that are more difficult. In terms of the actual source construction, the applied potentials are usually much lower in the case of rf sources and so the demands on the electrical insulation between the source components are less stringent. On the other hand, potential leakage via skin effects can easily occur. A direct consequence of the use of lower potentials is less heating of the sample, which is probably the reason for the higher S/B ratios mentioned above as a result of fewer cathode-originating photons. Because most rf sources operate in a constant power mode, the compensation between applied voltage and current appears to be less critical than with dc sources and accordingly the rf sources tend to show better stability.

When designing an rf-powered GD source, the efficient coupling of power and the minimization/elimination of electromagnetic radiation (EMR) are primary concerns [18,19]. Both criteria are optimized by considering simple electricity and magnetism effects. In terms of efficiency, the output impedance of the rf generator, which is usually operating at 13.56 MHz, although other frequencies have been investigated [35,36], must be matched to the compounded discharge source and plasma impedance. Commercial rf power systems achieve this through the use of variable L–C circuitry, so-called matching boxes. In addition to impedance matching, which is really not a guarantee of efficient power coupling, the minimization of stray radiation paths and the use of high-quality couplings are imperative. Hoffmann and co-workers [21] have described the use of a free-running generator for rf-GD-OES, but this approach has not been widely exploited. Finally, in order to minimize EMR, good electrical practices including complete coaxial protection of rf high-voltage transmission lines are required. Stray EMR can cause a number of problems with the spectrometer system, the detector electronics, and the computer controller system. Although they appear to be complex, each of these design aspects is straightforward in practice.

4.4.2 OPTICAL EMISSION SPECTROSCOPY

The use of glow discharge sources (in general) for the analysis of solid materials by optical emission spectroscopy (GD-OES) is far more prevalent in terms of the number of users than glow discharge mass spectrometry (GDMS) for a number of very simple reasons: (1) the basic cost of instrumentation and support personnel, (2) the speed of analysis, (3) the acceptance of common sample forms/shapes without modification, and (4) the procedures for thin-film analysis by GD-OES are much more developed than those for mass spectrometry. (A complementary list will be presented in Section 4.4.3 in favor of mass spectrometry.) None of these attributes listed should be lost in the development of rf-powered GD-OES sources.

There are two basic geometries that have been applied in rf-GD-OES, with a great deal of confusion existing in their designation. Figure 4.3 depicts the general features of these designs. On the left, the traditional Grimm-type [37] lamp design is shown with rf powering to the cathode block, which by contact transmits the rf potential to the surface of the sample cathode. This approach has been pursued to minimize the loss of rf energy as the potential is applied to the back of the sample (as in the Marcus-type source) [13,17,25]. In the case of conductive specimens, the electrical contact with the cathode block brings the discharge voltage to the sample. On the other hand, a ‘skin effect’ mechanism is invoked as the means of generating the plasma at the sample surface in the case of an insulating specimen, although no data has been published to substantiate this assumption. The dual-vacuum pumping of this design, according to which the bulk of the discharge volume and the cathode dark space region are

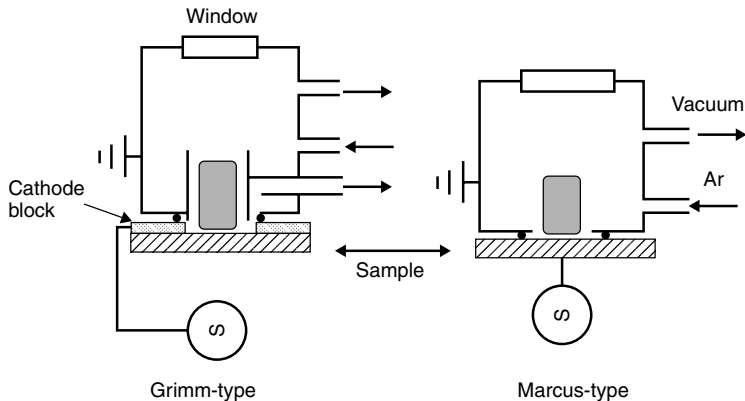


Figure 4.3 Diagrammatic representations of Grimm- and Marcus-type rf glow discharge OES sources

evacuated separately, is advantageous for producing flat craters in depth profiling (see Chapter 5). The Grimm-type design also removes any requirement for having a sample with a flat back surface. Although rf-powered Grimm-lamps are commercially available from some vendors, there has actually been just a single publication in the refereed scientific literature describing the use of a device of this geometry and powering scheme [26].

The most common mode of rf powering is shown at the right-hand side of Figure 4.3, and is known as the ‘Marcus-type’ source [13,17]. The fundamental difference between this geometry and the former one lies in the fact that the discharge potential is applied directly to the ‘back-side’ of the sample rather than to the front through contact with the cathode block as in the Grimm lamp. In fact, there is no cathode block in this geometry. Further, in this geometry the cell volume and the anode, which can be either a cylindrical tube or just the mounting plate, are electrically grounded. The rationale for this approach is that it permits coaxial shielding of the rf potential to the point of application of the high voltage to the cathode, thus minimizing power losses and excess stray electromagnetic radiation interference. Another aspect of this approach is the fact that a single source can be used for either conductive or insulating samples, rather than in the case of the rf Grimm lamp where the source components must be changed according to the sample type. Whereas the source shown in Figure 4.3 has a single pump arrangement, commercial versions of the Marcus-type lamp incorporate a pumping system similar to that of the Grimm-type lamp, where a grounded annular anode is employed together with a second pump to evacuate the region near the sample surface. This geometry seems to have the advantages of better stability and crater shapes compared with the original source described by Marcus and co-workers [13,17]. Many other papers in the literature describe the use of an ‘rf Grimm lamp’, where in fact the potential is applied

directly to the sample cathode and not to the cathode block and where no use is made of the 'skin effect' [38–43]. On the other hand, they do employ the dual pumping strategy described originally by Grimm [37]. To alleviate confusion of the powering scheme–geometry nomenclature, the author proposes to refer to this most widely employed geometry for rf-GD-OES as an 'external power application, dual pumping source'.

4.4.3 MASS SPECTROMETRY

Historically, glow discharge mass spectrometry (GDMS) is one of the oldest instrumental analytical methods, dating back to the first generation mass spectrometers developed in the early 1900s (see Chapter 3). In comparison with GD-OES, mass spectrometric sampling provides (1) isotopic composition information for all elements, (2) much lower limits of detection, and (3) the possibility of obtaining molecular species information rather than simple elemental analysis. It would be expected that implementation of rf powering would allow the extension of these capabilities to a much wider range of materials than dc discharges. On the other hand, the fundamental differences between photon sampling for OES and charged particle extraction for MS analysis place far greater constraints on source designs.

The design of rf-GDMS sources must incorporate the basic concepts of shielding and effective power coupling as described in the previous two sections. There are two very important points that make GDMS source designs that make them more complicated than the designs of GD sources for optical emission. First, all commercial GDMS systems require the transport of the sample to a cell volume located within the primary vacuum chamber, by which the sample must pass through some form of vacuum interlock. Second, in the case of most magnetic sector instruments (which are by far the most common commercial systems) the ion source must be 'floated' at the acceleration potential of the instrument (typically 4000–10 000 V). Figure 4.4 depicts two basic rf source designs that have been used for the analysis of small (<5 mm diameter) pin or disk-type samples and a so-called 'flat cell' used for the analysis of disks having >5 mm diameter surfaces.

Studies of the plasma chemistry and physics occurring in rf plasmas used in the manufacture of electronic circuitry and devices was well established in the 1970s [44]. The first analytical use of rf powering for elemental analysis was reported in the use of a hollow cathode geometry by Donohue and Harrison in 1975 [45]. In that work, rf potentials produced by a spark source generator were used to power a hollow cathode discharge for the analysis of solution residues. Duckworth and Marcus reintroduced the concept of rf-GDMS for direct solids analysis in 1989 [33]. A simple diode source was used for the analysis of 0.5 in diameter sample disks, including metals, solid glass, and metal oxide powders compacted without binder. Data were presented which indicated a more complex

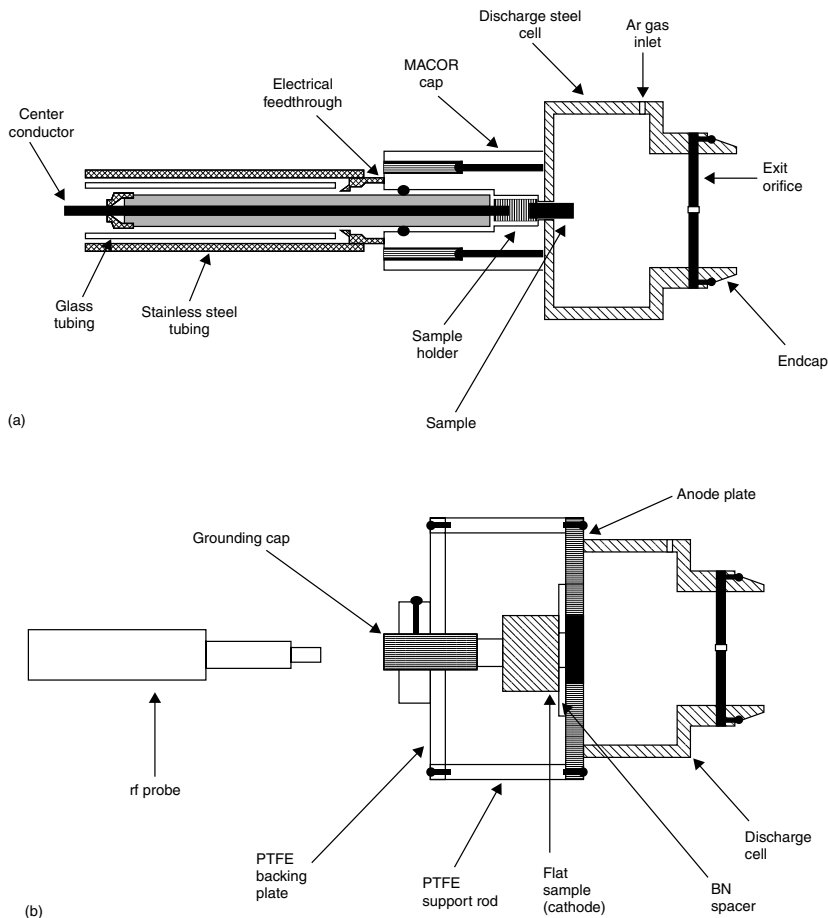


Figure 4.4 Diagrammatic representations of DIP-mounted rf-GDMS ion sources for the VG GloQuad instrument employing the (a) pin-type [56] and (b) flat sample holder geometries. Reprinted from Shick, C. R., Jr, and Marcus, R. K., *Appl. Spectrosc.*, 1996, **50**, 454–466, with permission of the Society of Applied Spectroscopy

relationship between discharge conditions and ion sampling position than had been seen for dc-GDMS. The need to optimize the ion sampling position and discharge conditions, along with a need for efficient sample interchange, led to the implementation of more user-friendly designs based on ~ 0.5 in diameter direct insertion probes (DIP) [34]. Figure 4.4 illustrates the general approaches used in rf-GDMS source design as implemented at Clemson University. The use of a DIP provides a means of mounting the sample, providing electrical contact, sampling position optimization, and introduction through a vacuum interlock, as is practiced in commercial GDMS systems. All subsequent rf-GDMS sources have

employed some sort of DIP approach. Depending on the diameter of the probe, sample holders for pin-shape and small disc samples are relatively easy to implement (Figure 4.4a). A number of groups have described such designs [46–48]. While each of these designs is somewhat different based on the ion source and spectrometer geometries (and also investigators' preferences), trends in the optimization of discharge and sampling positions are remarkably similar.

Given the wide diversity of solid sample forms and the particular difficulty of machining oxide (e.g. glass and ceramic) samples to a fixed form, rf-GD ion sources which allow for the analysis of flat, disk-type samples have been developed for mounting on the end of DIP devices (Figure 4.4b). This is also the way in which layered specimens can be analyzed. The analysis of disk samples is accomplished with either suitable mounts on the end of a DIP or the use of the probe to engage the sample against the body of the ionization volume (anode) [49–51]. In this way, an obstructed discharge geometry is obtained. In some implementations of this geometry, the authors use the phrase 'Grimm-type' geometry by analogy with the common GD-OES source [50,51]. Although the Grimm-type discharge does indeed employ an obstructed electrode arrangement, most GDMS sources are not truly of this geometry as auxiliary pumping between the cathode and anode is not employed, nor is there a cathode block assembly as in the case of OES.

In the discussion of source geometries for rf-GDMS, a number of studies involving the use of magnetic plasma enhancement methods cannot be ignored [52–55]. These 'magnetron' arrangements have their roots in the deposition science and engineering literature [11]. Magnetron GD sources generally employ concentric permanent magnets (100s G field strength) located behind the cathode/target, and thus not exposed to the plasma. Magnetic fields permeating through the cathode trap plasma electrons in helical orbits close to the sample surface. Accordingly, the atom–electron mean free paths decrease, by which the overall plasma ionization efficiencies increase. As a result, magnetron enhanced GD sources operate at pressures that are 2–3 orders of magnitude lower than standard rf-GD ion sources (single vs 100s of mTorr). This greatly reduces the vacuum pumping requirements for the entire system. Lower operating pressures would seem to hold the promise of lower signals for molecular ion species in the spectra and perhaps higher ion fluxes as larger differential pumping apertures could be employed. Of particular note in this area have been developments by Becker and co-workers [55], which will be described in subsequent sections.

As a final comment, it must be pointed out that although no commercial source exists for a complete rf-GDMS system, the devices have been sampled by a very wide range of mass analyzer types. The list of mass analyzers include single quadrupole [33,46,56], double quadrupole [57], ion trap [58,59], Fourier transform ion cyclotron resonance (FT-ICR) [60], time-of-flight (TOF) [61], and double focusing instruments [48,49].

4.5 ANALYTICAL APPLICATIONS

Although there has been a large growth in the number of publications dealing with the study of 'analytical' rf-GD sources, the number dealing with source optimization and plasma physics is probably still greater than those describing actual analytical results. These more fundamental studies, which are indeed crucial for proper analytical implementation, are beyond the scope of this presentation. Relevant works have involved optimization of discharge conditions for depth profiling [49,62–66], the use of mixed gas plasmas [67–70], and alternative power/control modes [40,71–74]. These papers are cited here to provide the reader with a starting point to learn more about fundamental operation of the devices beyond simple source design. Presented in the following sections are just a few summaries of published applications of rf-powered sources. These topics are given simply to illustrate the potential scope and possible benefits of the sources. Given the rapid increase in device sales, the list of applications will continue to grow for many years.

4.5.1 OPTICAL EMISSION SPECTROMETRY

Bulk Elemental Analysis

Even though the primary purpose for developing rf powering strategies is the realization of devices for the analysis of insulating materials directly, one is not likely to accept such a new technology at the expense of current capabilities. With this in mind, and given the fact that the rf technology was still evolving, early work in bulk analysis by rf-GD-OES focused on the analysis of metals and alloys. This also provided the most effective means of benchmarking the technique with dc-GD-OES and also other methods such as spark source optical emission and X-ray fluorescence spectrometry (XRF). Harville and Marcus [75] described a systematic approach for the selection of appropriate analytical lines for the determination of selected elements in copper and aluminum alloys. It is important to realize that as described in Section 4.3, rf-GD plasmas have a more energetic negative glow region than dc sources, and so any assumption that the same elemental lines are optimum is incorrect. Line selection based on a comparison of raw intensity (S), S/B ratio, S/N ratio, and eventually linearity and scattering of the calibration was performed for a handful of elements. Internal (steady-state) and external (sample-to-sample) precisions were found to be excellent, with values of <0.5% and <4% RSD, respectively, for elements ranging in concentration from 6 to 800 ppm in the solid. These values are all the more impressive given the fact that a laboratory-built source was being used in combination with a scanning monochromator and not with a simultaneous monitoring polychromator as used in virtually all commercial instruments. The use of low-intensity lines of the sample matrix element (i.e. Cu and Al) for internal standardization purposes was also evaluated. Table 4.3 summarizes the

Table 4.3 Calibration characteristics obtained for the determination of target analytes in a range of matrices by rf-GD-OES analysis.

Matrix	Analyte	Certified value (ppm)	λ (nm)	R^2 (raw)	Error (%) (raw)	R^2 (ratio)	Error (%) (ratio)
Cu ^a	Cr	7.4	360.53	1.000	2.6	0.986	13.3
	Ni	128	349.30	0.996	3	0.972	10
	Fe	(330)	385.99	0.998	6	0.994	20
	Zn	350	334.50	0.950	19	0.958	12
Al ^b	Cr	320	359.35	1.000	12	0.993	5
	Ni	200	341.38	0.996	15	0.999	2
	Fe	2 000	385.99	1.000	11	0.999	1
	Zn	10 300	334.50	0.991	21	0.985	6
Au ^c	Zn	20.9	481.05	1.000	17	0.999	5
	Sn	27.2	303.41	0.981	2.9	0.987	13
	Pd	19.8	340.46	1.000	4.1	0.998	0.1
	Ag	49.7	328.29	0.994	9.6	0.991	3.4
	Pt	40.8	299.80	1.000	0.1	1.000	4.6
	Si	9.0	288.16	1.000	10	1.000	10
	Bi	34.0	306.77	0.972	35	0.941	3
	Pb	21.9	405.78	0.978	16	0.994	8.7
	Mn	58.9	403.08	0.997	5	0.998	7.1
	Ni	14.6	352.45	0.958	14	0.994	8.8
Ag ^c	Fe	27	385.99	0.731	26	0.972	3.8
	Au	45	242.79	0.987	4.3	0.988	21
	Pb	38.8	405.78	0.971	16	0.990	5.4
	Zn	165	481.05	0.955	15	0.976	3
	Ni	57.0	352.45	0.969	47	0.994	5
Pt ^c	Rh	445	369.24	0.999	6.3	0.996	15
	Au	85	267.59	1.000	1.2	1.000	2.4
	Pd	115	340.46	1.000	1.7	0.994	12
	Ir	115	380.01	1.000	0.2	0.997	21

^aAnalyte/Cu (I), 515.3 nm internal standard.

^bAnalyte/Al (I), 390.1 nm internal standard.

^cRatio values calculated as S/B.

Reprinted with permission from Harville, T. R. and Marcus, R. K., *Anal. Chem.* 1993 **65**, 3636–3643 and 1995, **67**, 1271–1277, Copyright 1993 and 1995 American Chemical society.

figures of merit of calibration for elements in the two matrices for both the raw intensity and ratioed data. This basic methodology was extended by Harville and Marcus for the determination of trace elements in the precious metals gold, platinum, silver, and sterling silver [76]. In addition to the use the matrix element as internal standards, this work illustrated the use of the S/B ratio for calibration. This is done under the assumption that differences in sputtering rates within

related families are the result of differences in dc-bias, which in turn affects the amount of broadband spectral background emission coming from the sample surface. Table 4.3 also includes the figures of merit of the calibration and results of analyses of the Au, Ag, sterling Ag and Pt samples [76].

Extension of the use of rf-GD-OES analyses for bulk analyses of nonconductors such as glasses and ceramics requires different sets of discharge conditions than for the case of alloys, generally lower discharge gas pressures, and higher powers [13,17,77]. These conditions are needed to affect the highest dc-bias potentials on the insulating surface and thus to enhance sputtering. The dielectric nature of such samples is such that capacitive losses are experienced as the rf potential applied to the back of the sample (Marcus-type source). Therefore, the thickness of the sample/nonconductive coating will effect the bias and thus the sputtering rates [13,17]. As noted previously, this is the initial reason for the use of a surface application of the rf power via a Grimm-type configuration. (At the time of this writing, no papers illustrating the successful implementation of this strategy to bulk nonconductors have been published in the refereed literature.) As suggested previously, the relationship between dc-bias and the sputtering rate must then be exploited to correct for differences in response due to different thickness of standards/samples. These corrections (based on either direct measurement of dc-bias [13,17] or the intensity of the Ar (I) emission [77,78]) have been shown to be effective for samples having a thickness of up to 5 mm. In fact, all commercial GD-OES systems now employ some form of voltage correction to normalize responses for samples of different material/thickness, including metals, alloys, and thin insulating coatings!

In addition to the determinations of metals as described here, there is every indication that rf-GD-OES should perform exceptionally well for the determination of nonmetals, which tend to have high excitation energies. In fact, many of these elements emit strongly in the vacuum-UV region of the spectrum. These elements are growing in importance in a wide range of new materials, and also tend to be difficult to determine by other conventional methods of direct solids analysis (particularly when atmospheric pressure sources are used). The reason for the enhanced detectability via rf-GD-OES lies in the much higher electron energies in the negative glow region as compared with dc-powered sources [27]. Hartenstein and Marcus have described the basic procedure for ensuring low blank/background levels for atmospheric species that may interfere in determination of nonmetals [79]. Using their commercial rf-GD-OES system, they were able to obtain detection limits for nitrogen in steel specimens at the level of 1 ppm. (Lower values have since been achieved.) Similarly, although not necessarily a problematic ubiquitous element, Winchester obtained detection limits for phosphorus at the single ppm level using an in-house built system [80]. In that work, analytical responses for a number of alloys were normalized through the use of the relative sputtering rates. Obviously, the inherent capability for

rf-GD sources to analyze nonconductive specimens makes the determination of nonmetals a key application area.

Anfone and Marcus have described the use of a laboratory-built rf-GD source combined with a sequential spectrometer for the analysis of solid glass samples [77]. Discharge conditions were optimized for a number of analytes with respect to S/B ratios and relative standard deviations of the spectral background (RSDB). In addition, the use of an auxiliary argon bath gas was described to lower contributions from atmospheric gases introduced by imperfect vacuum seals that are common on the rough surface of oxides. Use of the Ar bath gas results in the introduction of ambient Ar instead of N₂, O₂, H₂O, etc., and consequently specific molecular band interference and broadband emission are diminished [81]. The bath gas also decreased the plasma stabilization times (<30 s) and improved the long-term stability (<10% RSD). Glass samples with a thickness ranging from 1 to ~5 mm were employed to assess the use of Ar (I) emission as a means of correcting for thickness-based differences in the analyte signals. While the raw responses for each analyte varied by up to three orders of magnitude for identical samples of the different thickness, ratioing to the corresponding Ar (I) intensities resulted in variations of <1% RSD for the suite of analytes/thickness. By using the Ar (I) normalization, calibration curves with $R^2 > 0.99$ were obtained. The studies were extended to the analysis of oxide/glass powders by Pan and Marcus [82], who used a simple hydraulic press to form oxide disks without the use of a metal or graphite powder binder. As might be expected, the extent of powder drying and the particle size distribution effect the robustness of the pressed disk and also the plasma stability. Once the procedure had been optimized, the operation characteristics were very similar to those for bulk glass specimens. Calibration curves were evaluated when using the Si (I) emission line and the analyte S/B ratio as the analytical signals. As in the case of the precious metals analysis described above [76], the use of S/B ratios produced better calibration curves. There was no need for corrections by referring to the dc-bias or Ar (I) line intensities here as all of the compacted disks had the same thickness.

As mentioned in previous sections, the basic characteristics of rf-GD optical emission, such as high levels of temporal stability and high S/B ratios, should result in very low limits of detection (LOD). The concept of detection limits and their actual assessment is complicated in the area of solids analysis where matrix matching can be difficult and no spectroscopic blank is available. A very useful means of establishing limits of detection (LODs) in solids was described in detail by Boumans and Vrakking [83]. Developed more specifically as a means of comparing LODs between different instruments or techniques, the use of the 'SBR-RSDB' approach is a very versatile means for assessing the detection limit for a given element in a specific matrix. The equation takes the form

$$\text{LOD} = \frac{(0.01)^3 (\text{RSDB}) m}{\text{S/B}} \quad (4.2)$$

where RSDB is the percentile relative standard deviation for the background, m is the concentration of the test element in the specimen, S/B is the signal-to-background ratio, and the multiplier 3 is used so as to give a 99% confidence limit. The RSDB could in fact be the variation at one spectral wavelength in time or the variation in values across an adjacent spectral region. As with all procedures for calculating LOD values, there are caveats to consider, and a comparison between computation methods is hazardous at best. Table 4.4 lists some of the elemental detection limits of rf-GD-OES for a range of elements, matrices, and instruments. While specific comparisons are required in evaluating a new method, in general, the rf-GD-OES method presents more new opportunities for sensitive analysis than limitations due to a degradation in the power of detection.

A final comment is needed regarding the methods of quantification in rf-GD-OES. As in the case of dc-GD-OES, the interplay of the discharge parameters (current, voltage, power, and gas pressure) provides a number of modes of discharge control and means of compensating for atomization/excitation efficiencies [20,84–86]. In fact, each of the manufacturers employs their own strategy for control/normalization. Depending on one's point of view, the number of parameters can be more or less complicating in the use of rf-GD sources. For example, as described in the previous paragraphs, one can use dc-bias, applied power, Ar (I) line intensities, S/B ratios, or weight losses as means of performing quantification. Variations in applied power, dc-bias, or discharge pressure can be used in the course of analysis to normalize responses. As such, each of the current rf-GD-OES manufacturers has their own control strategies. At the end, it is the performance of these procedures in the case of real world samples that will determine their suitability.

Depth Profiling of Painted Coatings

One of the most outstanding applications of the unique capabilities of rf-GD sources is the depth-resolved analysis of organic (painted) coatings on metallic substrates. This type of specimen is prevalent in the automotive and structural materials industries. These layered systems pose very large challenges to more established methods of analysis, for a number of reasons. First and foremost, the painted coatings are nonconductive by nature and exist at thicknesses in excess of 150 μm . This combination makes any sort of charged particle method difficult to apply, perhaps requiring multiple hours to obtain a single profile, if possible at all. Second, there may exist a number of layers within the coatings that have different physical and chemical properties. Finally, in the case of organic coatings, information about the chemical identity of the organic matrix is required. There, quantitative determinations of C, H, N, etc., are required, which are problematic with many 'surface' methods. These very formidable challenges create a natural fit for the features of rf-GD-OES.

Table 4.4 Limits of detection obtained for a number of elements in various matrices by rf-GD-OES.

Matrix	Analyte	λ (nm)	Certified value (ppm)	LOD (ppm)
Cu	Cr	360.53	2.8	0.018
	Ni	346.16	22	0.086
	Fe	385.99	35	0.12
	Zn	334.50	8	0.12
Al	Cr	360.53	11	0.085
	Ni	346.16	6	0.056
	Fe	385.99	790	2.2
	Zn	334.50	510	2.0
Au	Zn	481.05	20.9	0.04
	Sn	303.41	27.2	0.06
	Pd	340.46	19.8	0.01
	Ag	328.29	49.7	0.01
	Pt	299.80	40.8	0.2
	Bi	306.77	34.0	0.4
	Pb	405.78	21.9	0.05
	Ni	352.45	14.6	0.01
Ag	Fe	385.99	27	0.04
	Au	242.79	45	0.09
	Pb	405.78	38.8	0.3
	Zn	481.05	165	0.1
	Ni	349.30	57.0	0.06
	Cu	327.40	61.6	0.04
	Pd	340.46	5.1	0.04
	Sn	303.41	46.1	0.5
	Pt	306.47	12.3	0.07
	Bi	306.77	83.5	1
Pt	Rh	369.24	445	0.02
	Au	267.59	85	0.1
	Pd	40.46	115	0.01
	Ir	380.01	115	0.07
	Ag	328.07	5	0.02
	Cr	425.45	1	0.03
	Cu	327.40	1	0.05
	Fe	371.99	16	0.1
Cu	P	185.89	1300	1.6
Steel	N	174.2	20	1.5

As described in previous sections, one of the very early applications of the newly evolving method, as described by Payling *et al.* [20], was the analysis of pigmented polymer coatings. In a more detailed study, laboratory-synthesized specimens were prepared from polyester polymers reacted with melamine–formaldehyde cross-linker resins [87]. Different inorganic pigments, a TiO_2 -based white, a $\text{TiO}_2/\text{Fe}_2\text{O}_3$ red, and combinations of the two, were evaluated to determine both the general depth profiling capabilities of the method and the ability to provide accurate stoichiometric information regarding the organic and inorganic components. One of the important challenges revealed in the work was the fact that these types of soft materials could not be polished to provide very flat sample surfaces. Another key aspect of this work was the complementary use of cross-sectional SEM–EDX maps of the metal species compositions in the coatings. This provided information on the morphology (porosity, etc.) of the layers and allowed an independent measure of the actual layer thickness.

Depth profiling of the organic coatings was part of a detailed evaluation of the quantification capabilities of rf-GD-OES relative to the use of dc-GD sources [37]. Of course the transition between the nonconductive coatings and the metallic supports would be expected to be a very great challenge. In Figure 4.5, the qualitative (intensity vs time) and quantitative depth profiles for a commercial silicon-modified polyester–metallic coated steel sample are shown. There are definite differences in the both the shapes and measured depths for the qualitative and quantitative profiles. In some instances, such as this, the qualitative profiles show more exaggerated features than exist in reality. Clearly observed are the strontium chromate primer and the hydrogen-rich region between the Al/Zn coating and the ferrous base. Use of a quantification model in which the sputtering rates are corrected yields the appropriate compositions. The authors very nicely showed, even in this relatively early study of the method, that while uncorrected layer thickness were generally found to have an error of $>20\%$ as compared with optical metallography, the errors were reduced to $<5\%$ after use of the developed model.

Sanz-Medel and co-workers have looked at the optimization of plasma conditions for depth profiling of painted coatings using a Marcus-type source [62]. As would be expected, increases in applied rf power increase the measured sputtering rates. Interestingly, increases in pressure (up to 10 Torr Ar) also lead to higher sputtering rates. In this instance, the sputtering of the painted coating responds more like that of a metal than the sputtering of a bulk insulator, such as a glass specimen. After using chilled water (2°C) to cool the back of the sample and also the limiting orifice plate, it could be concluded that there is no evidence for thermal degradation of the polymer. Correction of the obtained temporal profiles for the sputter rates of paint components allows one to obtain ‘quantitative’ profiles that were very similar to SEM–EDX data obtained for a cross-section of the specimen. Some disagreement was still observed for the region of the paint/galvanneal substrate interface. Monitoring of the optical emission lines of

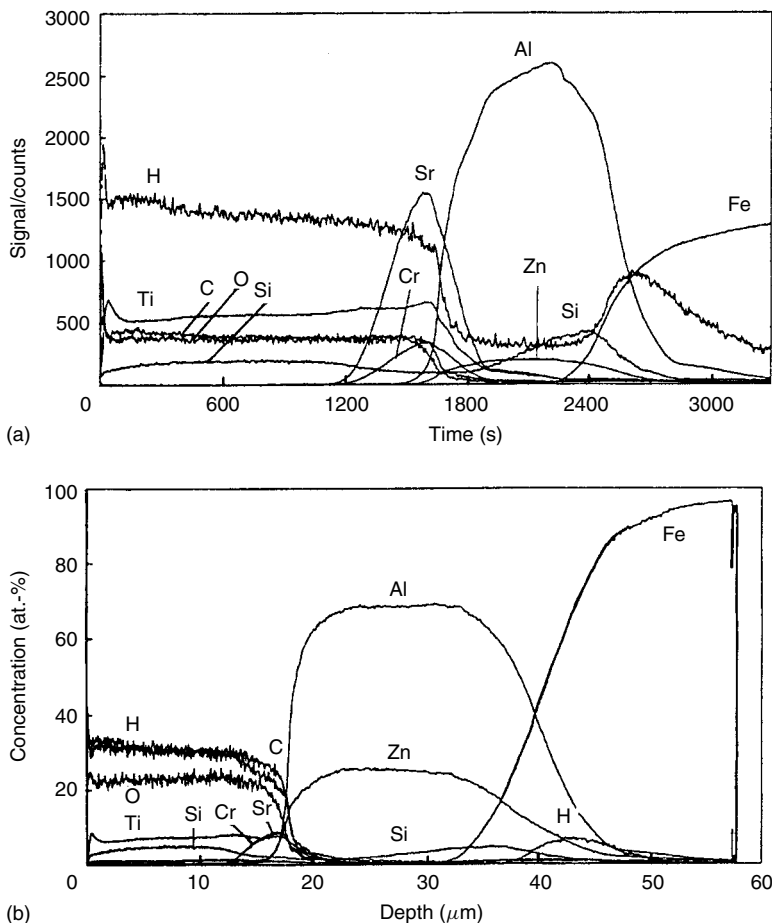


Figure 4.5 Depth profiles of commercial silicon-modified polyester-metallic coated steel sample: (a) qualitative and (b) quantitative. Reproduced by permission of The Royal Society of Chemistry from Jones, D. G., Payling, R., Gower, S. A., and Boge, E. M., *J. Anal. At. Spectrom.*, 1994, **9**, 369–373

the Ar discharge gas species as a function of time (depth) revealed that there was a change in the discharge excitation conditions as the new matrix was entered. As in other applications cited here, these authors also suggested the use of Ar emission lines as internal standards for the plasma excitation conditions.

Depth Profiling of Very Thin (<1 μm) Layers

The application of GD-OES to the analysis of ‘thick’ coatings was realized very early after the introduction of the Grimm-type lamp (see Chapters 2 and 5).

It remains the prime application area of commercial GD-OES systems (see Chapter 5). Distortions in crater shapes observed when analyzing thick layers ($>5 \mu\text{m}$), suggested that profiling of layers of less than $1 \mu\text{m}$ would not be useful. The fact that for sample types accessible to dc-powered systems (e.g. galvanized coatings) the layer thicknesses are usually beyond the $5 \mu\text{m}$ level also limited exploration into thinner layers and coatings. The advent of rf powering with the ability to sputter nonconductive coatings pushed the technology into more shallow depth regimes where oxides are of key importance. The work of Shimizu, Thompson, and co-workers has opened up entirely new ways of thinking about glow discharge spectroscopies and their application in areas traditionally serviced by high-vacuum methods such as SIMS, X-ray photoelectron spectroscopy (XPS), and the like [88–90]. Paramount in the use of any analytical method in applications where chemical information at the nanometer scale is desired is the ability to sample the material accurately. In the case of a glow discharge device, this relates to the question of how rapidly the plasma conditions reach a steady state. For example, in a material with a sputtering rate of $1 \mu\text{m}/\text{min}$, a depth of 25 nm is reached in 1.5 s ! Despite data of the sort depicted in Figure 4.1, some users of rf-GD-OES have not achieved stability on this time scale. Clearly, plasma start-up and stabilization times depend on the actual discharge source geometry, power supply capabilities, and the cleanliness of the discharge.

Shimizu and co-workers [88–90] have published a number of papers illustrating the use of a Marcus-type source for the analysis of a wide range of aluminum oxide coatings, covering a thickness range from tens of nanometers to many micrometers. Typical of these sorts of analyses is the profile depicted in Figure 4.6. This profile is obtained from an anodic film formed electrochemically in a mixture of chromate ion and phosphoric acid on an aluminum substrate. The film was further anodized in a solution of ammonium pentaborate to generate a film having a thickness of 358 nm as determined by transmission electron microscopy [90]. The basic structure of the film is depicted in cartoon form in Figure 4.6a, with the corresponding depth profile shown in Figure 4.6b. As seen in the profile, a very distinct structure is produced for Cr, B, and P incorporated into the aluminum oxide film. The distribution shows that Cr is incorporated in a very thin region, whereas the B diffuses fairly uniformly into the surface layer. The phosphate anion, as indicated by the P response, segregates toward the oxide/metal interface. A very finite step function is seen at the onset of sputtering of the Al substrate. Two other points warrant mention here. First, the temporal response for the B (I) line shows the depth-related interference effects first described by Hoffmann *et al.* [91]. Second, the very fast stabilization of the rf-GD plasma is proven by the intensity of the Al (I) line response in the oxide coating.

With the evolving capability of performing very thin film analyses by rf-GD-OES, one is pressed to wonder how the method compares with ‘traditional’ thin film methods such as SIMS. Shimizu *et al.* performed such a comparison

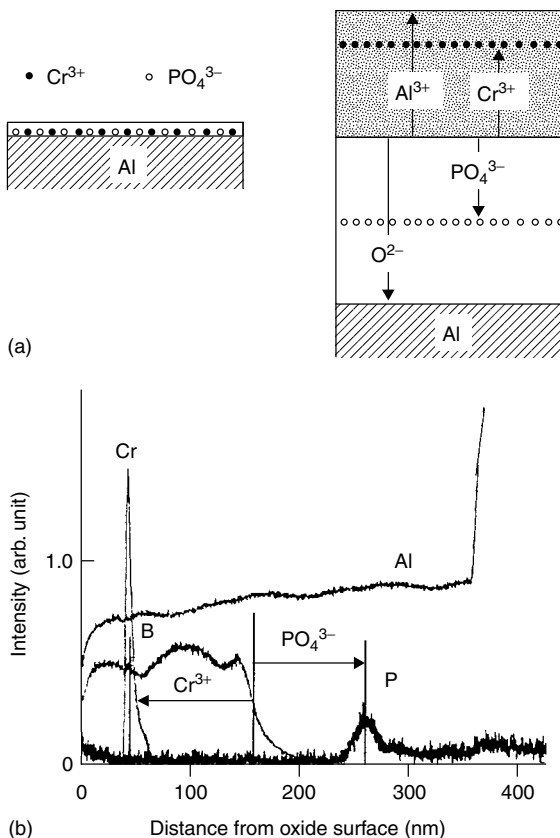


Figure 4.6 Analysis of an aluminum oxide coating by rf-GD-OES. (a) Depiction of the structure of the Al_2O_3 coating after electropolishing in a 20 g/l CrO_3 –35 ml/l H_3PO_4 solution and after anodization in 0.1 M ammonium pentaborate and (b) the resultant depth profile of the final anodic film obtained by rf-GD-OES. Reproduced with permission from Shimizu, K., Brown, G. M., Habazki, H., Kobayashi, K., Skeldon, P., Thompson, G. E., and Wood, G. C., *Surf. Interface Anal.*, 1999, 27, 24–28. Copyright John Wiley & Sons

for the case of a barrier-type aluminum oxide film that had been exposed to Na_2CrO_3 [90]. As described in the previous paragraph, Cr ions tend to segregate in very thin layers just below the oxide surface in these systems. Figure 4.7a presents the rf-GD-OES profile of the Cr and Al components in an ~ 140 nm thick oxide film. Transmission electron microscopy indicated that the nominal depth of the Cr layer was ~ 15 nm below the surface, with a primary bandwidth of 7 nm. Clearly, rf-GD-OES using this Marcus-type source yields analytically relevant information for very thin film systems. The corresponding SIMS depth profile for the same material is shown in Figure 4.7b. The agreement between the two profiles is excellent. Given the relative experimental simplicity and short

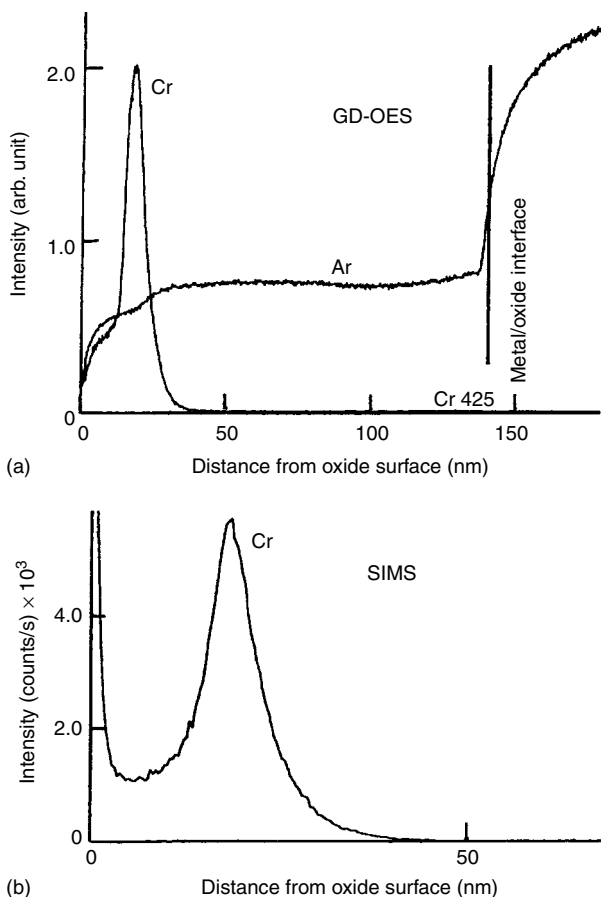


Figure 4.7 Depth profiles of anodic films formed in NaCrO_3 solution by (a) rf-GD-OES and (b) SIMS. Reproduced with permission from Shimizu, K., Brown, G. M., Habazki, H., Kobayashi, K., Skeldon, P., Thompson, G. E., and Wood, G. C., *Surf. Interface Anal.*, 1999, 27, 24–28. Copyright John Wiley & Sons

analysis times for the rf-GD method, one must conclude that the technique is a truly applicable for ‘thin film’ analysis. As a second example of the potential of rf-GD-OES for analyses that are usually thought to be only the domain of methods using high-vacuum apparatus, Figure 4.8 depicts the depth profile for the NIST SRM 2137 Boron Implant in Silicon standard [92]. This material is certified with respect to the distribution of B and is used for depth profiling applications in the semiconductor industry. As can be seen, the distribution obtained by rf-GD-OES is virtually identical in shape with that of the SIMS data provided with the material certificate. Certainly, much work remains to develop the quantitative potential of the rf-GD method to be truly competitive with SIMS, but the inherent

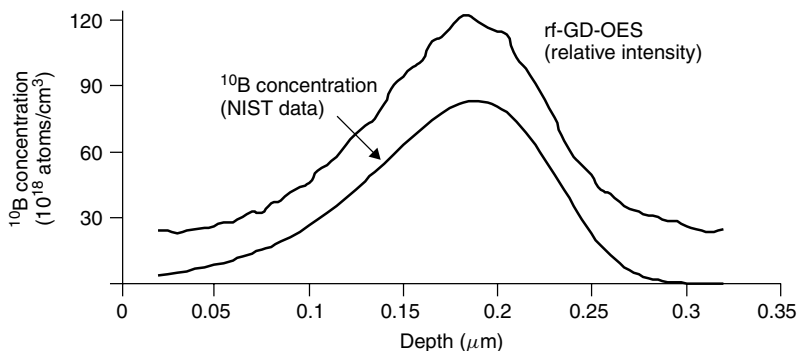


Figure 4.8 rf-GD-OES depth profile of NIST SRM 2137 Boron Implant in Silicon standard for calibration of concentration in a depth profile [92]

sampling and sensitivity capabilities are evident. While glow discharge sources will never be able to compete with ion and electron beam methods for the case of lateral microdistributional analyses, it may be that they will be competitive for in-depth analyses.

4.5.2 MASS SPECTROMETRY

In the discussion of the analytical applications of rf-GDMS sources, it should be noted that in a number of the cited works it has been suggested that the performance of rf-GD sources for metallic, conductive samples is equal to or better than that of dc-GDMS. A significant difficulty in making definite statements about the two modes, however, is the fact that most of the practitioners of the method are using **very** different types of mass analyzers, of which some are commercial and some are laboratory-built. Great differences also exist in the designs of the actual sources as described in Section 4.4.3, whereas in rf-GD-OES there are only two prominent designs. The lack of any commercial provider of an rf-GDMS system has also limited the development of the methodologies and the applications. In the following discussion, general features of the use of rf-GDMS are presented for a number of potential applications, as described by different researchers, which will hopefully justify commercial adoption.

Bulk Elemental Analysis

The analysis of bulk conductive and nonconductive materials by rf-GDMS has been undertaken much more with the aim of source development and characterization, rather than for quantitative analyses within specific analytical areas. For the most part, studies by Marcus and co-workers have demonstrated general analytical figures of merit that can be realized for given source geometries for the case of commercial quadrupole GDMS (GloQuad, VG, Winsford, UK) [56,93]

and magnetic sector mass spectrometer (VG Model 9000) [48]. As such, the analytical results are somewhat benchmarks relative to dc source operation given the fact that the same cryogenic cooling and mass analyzer were employed. Throughout these studies, a few general observations can be made, which are for the most part consistent with the rf-GDMS literature cited in this section. The basic trends include the facts that (1) lower operating pressures relative to dc-powered systems (100s mTorr vs Torr), (2) higher degree of signal and spectral responsivity to changes in discharge conditions and ion sampling position, and (3) faster plasma stabilization times are found for metallic sample analysis relative to dc discharges (single vs tens of minutes).

Pin-type and flat sample source geometries developed for the VG GloQuad system have been evaluated for the analysis of metals and bulk nonconductors [56,93]. Frankly, the machining of pin-type specimens from bulk insulating materials (oxides, glasses, etc.) is difficult, and so only limited studies of this sort have been pursued. In Table 4.5, the accuracy and precision (stability) are presented for the analysis of NIST SRM 1259 Aluminum Alloy with the pin-type source [56]. In general, stable plasmas were obtained after <5 min of sputtering, with the short-term stability of the raw signal values typically occurring in the range 1–8% RSD for 15 min analysis times. In contrast to GD-OES, where traditional analytical (calibration) curves are used for quantification, in GDMS the most widely applied approach to determine concentration values is based on the use of relative sensitivity factors (RSFs) (see Chapter 3). As shown in Table 4.5, the RSF-based analyte concentrations show excellent agreement with

Table 4.5 Internal stability in the analysis of NIST SRM 1259 Aluminum Alloy by rf-GDMS.

Element	Certified value	Determined value		RSD (%) of rf-GloQuad values	
		Short-term ^a	Long-term ^b	Short-term	Long-term
Be	2.5 ppm	24.6 ppm	25.6 ppm	1.91	2.16
Mg	2.48%	2.48%	2.47%	0.07	0.30
Al	Matrix	89.37%	89.60%	0.05	0.05
Si	0.18%	0.184%	0.179%	0.99	0.60
Ti	(400 ppm)	385 ppm	436 ppm	1.68	5.99
Cr	0.173%	0.175%	0.172%	1.19	0.62
Mn	790 ppm	770 ppm	856 ppm	1.76	5.59
Fe	0.205%	0.217%	0.204%	0.12	1.04
Ni	630 ppm	645 ppm	718 ppm	2.69	9.49
Cu	1.60%	1.63%	1.61%	0.65	0.59
Zn	5.44%	5.48%	5.46%	0.51	0.39
Ga	(220 ppm)	210 ppm	243 ppm	1.85	7.11

^a15 min.

^b45 min.

Reproduced by permission of The Royal Society of Chemistry from Shick, C. R., Jr, Raith, A. and Marcus, R. K., *J. Anal. At. Spectrom.* 1993, **8**, 11043–1048.

the certified values in the case of both short- and long-term (45 min) analysis regimes. There was no appreciable benefit in using extended analysis times for the elements studied. The precision of the measurements (actually of the determined values) was up to $\sim 2.7\%$ RSD for the short-term regime, with most of the values degrading when using extended analysis times. Degradation of the precision, necessitating the use of an internal reference in the RSF method, indicates element-specific drift and suggests that isobaric interferences likely due to residual gas species are probably occurring. The variations in the analysis values for the same elements determined from five separate analyses of the specimen (external precision) yielded results that are almost identical with those of the long-term precision, again suggesting isobaric interferences from residual gases. A brief evaluation of the operating characteristics for a NIST glass reference material (cut into a 3 mm diameter, 3 mm thick disk) showed that precision values of 2–10% RSD can be obtained for a 30 min sputtering cycle.

As stated in Section 4.4.2, one of the driving forces for the early acceptance of the Grimm-type geometry in GD-OES is the possibility of analyzing flat disk samples. Shick and Marcus [93] described a detailed evaluation of the roles of source geometry and operation conditions for a flat-type sample holder. As with the pin-type source, the analyte ion signals were found to stabilize rapidly as compared with dc source operation. Pre-burn times for metals were found to be less than 5 min, whereas for bulk glasses the analyte signals required up to 15 min to stabilize. Once stable, both types of samples could be analyzed over extended periods of time with better than 10% RSDs for the raw ion signal intensities. The internal precision and accuracy were determined for NIST SRM 1104 Free Cutting Brass and NIST SRM 610 Trace Elements in Glass specimens by triplicate analyses over 15 and 45 min periods, respectively. External precision and accuracy were evaluated for five replicate analyses of each specimen. Table 4.6

Table 4.6 Analysis of NIST SRM 1104 Free Cutting Brass standard by rf-GDMS (discharge conditions: rf power = 35 W, Ar flow rate = 2.50 sccm; orifice diameter = 10 mm; cell = 10 mm).

Element	Certified value	RSF	Internal ($n = 3$)			External ($n = 5$)		
			Av. conc.	RSD (%)	Error (%)	Av. conc.	RSD (%)	Error (%)
Cu	61.33%	1.00	60.10%	0.1	2.1	61.39%	1.4	0.1
Zn	35.31	0.499	36.39	0.2	3.1	34.78	3.1	1.5
Sn	0.43	0.795	0.44	1.0	2.3	0.46	7.7	7.0
Pb	2.77	9.72	2.92	1.7	5.4	2.86	6.9	3.4
Fe	880 ppm	0.0124	962 ppm	3.4	9.3	838 ppm	5.8	4.8
Ni	700	0.187	720	0.8	2.9	680	6.0	2.9

Reproduced from Shick, C. R. and Marcus, R. K., *Appl. Spectrosc.* 1996, **50**, 454–466, with permission of The Society for Applied Spectroscopy.

presents the data obtained for the analysis of the NIST brass standard where the ^{63}Cu isotope is used as the internal standard for RSF calculations. For each of the test elements, very good precision and accuracy are obtained. Interestingly, the accuracy of the data for the replicate analyses was better than the precision, which of course is the virtue of the RSF approach in GDMS analyses. Table 4.7 presents the corresponding precision and accuracy data for the NIST glass reference material. In this particular matrix, there are a few elements certified at the percentage concentration level and a large number of dopant elements present at the 500 ppm level and below. A few important observations can be made when comparing the data for the metal and glass matrix standards. First, there is no sacrifice in precision or accuracy on moving to the nonconductive matrix. Second, the presence of large amounts of oxygen in the plasma leads to a degradation of the precision and accuracy for the data of iron, as the signals for ^{56}Fe isotope are interfered with by the $^{40}\text{Ar}^{16}\text{O}$ molecular ion. Third, the external precision of the analytical results for the case of the glass samples is poorer than for the metal. This is not unexpected, as the glass matrix and its target analytes are likely more susceptible to interferences due to the presence of residual gases, the levels of which change from sample to sample. In any case, an error of $>10\%$ occurs only for Fe in the analytical determinations. The repeatability values presented here are very good and do not differ significantly from those achieved in conventional dc-GDMS analysis of alloys in the case of using this instrument. By the same token, the limits of detection obtained for trace elements in glass matrix materials are not appreciably different from those for alloys.

As in the case of rf-GD-OES using the Marcus-type geometry, the thickness of an insulating sample has a pronounced effect on the analyte signal levels in rf-GDMS using the flat cell geometry [93]. The observed decrease in sensitivity is directly related to the specimen thickness and can be compensated on a first principles basis. In this case, signal intensities were plotted as function of sample thickness (1–3 mm) and the resulting equation of the line was used to compensate for the role of thickness, with the corrections for the analytes tested (Ag and Mn) yielding responses that were in agreement by better than 5% absolute. Detection limits were also determined for the case of NIST SRM 616 Trace Elements in Glass. The dopant concentrations in this matrix were at the sub-ppm level, yielding a relatively clean mass spectrum. Even so, the determined limits of detection (1–280 ppb) were excellent given the limited resolution and sensitivity of the quadrupole mass spectrometer. Figure 4.9 further illustrates the sensitivity achievable in the analysis of glass samples by rf-GDMS for the lead isotopes present in a NIST SRM 612 Trace Elements in Glass sample generated by a flat-type rf-GDMS source mounted on a VG 9000 magnetic sector mass spectrometer. Based on the observed signal-to-noise characteristics, the detection limit for the ^{204}Pb isotope (504 ppb in sample) can be calculated to be 16 ppb. This value is very competitive with that achieved in metals analysis under similar

Table 4.7 Analysis of NIST SRM 610 Trace Elements in Glass standard by rf-GDMS (discharge conditions: rf power = 35 W, Ar flow rate = 2.00 sccm; orifice diameter = 10 mm; cell = 10 mm).

Element	Certified value	RSF	Internal ($n = 3$)			External ($n = 5$)		
			Av. conc.	RSD (%)	Error (%)	Av. conc.	RSD (%)	Error (%)
O	50.37%	2.43	50.39%	1.5	1.9	52.10%	11.3	1.4
Na	5.19	0.658	5.19	0.4	0.1	4.78	13.6	7.9
Al	0.53	0.273	0.55	2.0	3.4	0.52	10.4	2.4
Si	33.66	1.00	33.99	0.4	1.0	32.99	4.9	2.0
Ca	8.58	0.00443	9.07	1.0	5.7	8.95	2.9	4.3
Ti	437 ppm	0.00625	453 ppm	0.1	3.7	431 ppm	4.7	1.3
Mn	485	1.29	492	0.3	1.5	497	2.7	2.5
Fe	458	0.00262	555	6.6	21.3	546	14.2	19.2
Co	390	1.25	394	0.6	1.1	398	3.2	2.0
Ni	459	0.0971	469	0.7	2.3	466	6.4	1.5
Zn	433	0.168	418	1.2	3.4	408	5.8	5.9
Rb	426	1.28	440	0.9	3.4	435	2.5	2.2
Sr	516	2.08	531	0.7	3.0	517	4.9	0.3
Ag	254	2.54	262	1.8	3.2	243	5.7	4.5
Ce	450	6.68	457	0.7	1.5	437	6.3	3.0
Eu	450	4.21	433	1.3	3.8	434	3.1	3.5
Au	25	1.72	24	0.3	2.2	23	10.6	8.0
Tl	61.8	9.34	65	1.7	5.8	59	10.9	4.5
Pb	426	6.92	429	1.2	0.7	415	6.8	2.7
Th	457.2	51.42	447	2.3	2.3	423	8.9	7.6
U	461.5	66.59	447	1.4	3.1	427	8.3	7.4

Reprinted from Shick, C. R. and Marcus, R. K., *Appl. Spectrosc.* 1996, **50**, 454–466, with permission of The Society of Applied Spectroscopy.

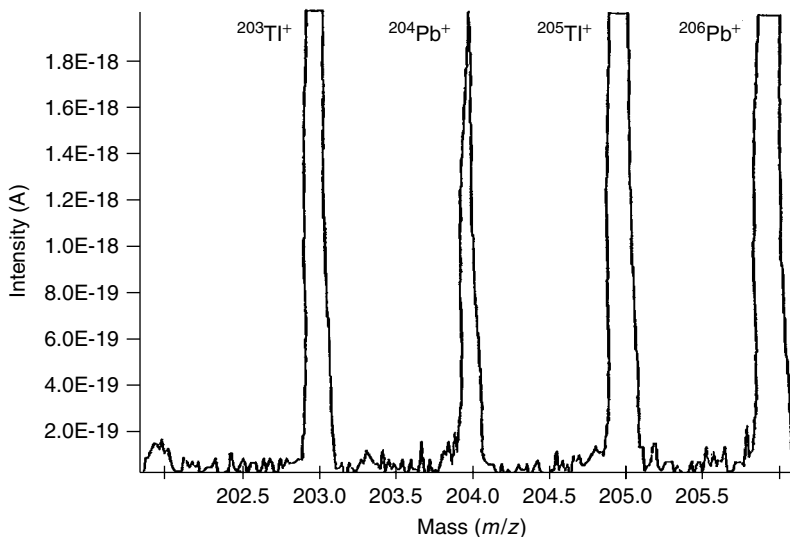


Figure 4.9 rf-GDMS spectrum of lead components of an NIST SRM 612 Trace Elements in Glass taken on a VG 9000 spectrometer (Duckworth, D. C., unpublished results)

acquisition conditions when using dc power, which is also a consistent finding with quadrupole analyzer work.

As mentioned in Section 4.4.3, Becker and co-workers [52,55] used a magnetron enhanced rf-GDMS source that was similar in structure to that developed by Duckworth *et al.* [48]. However, instead of a commercial GDMS mass analyzer, the authors modified a double-focusing spark source mass spectrometer that operated with photoplate detection [49,94]. Parametric studies of sputtering crater shapes and ion signals were very similar to that for the flat cell source both with the VG GloQuad and VG 9000, though the mass analyzer system limited the analytical utility of the system. Subsequent combination of the source with a Finnigan MAT (Bremen, Germany) Element instrument provided a far more powerful platform [55,95]. The initial source was modified to operate in a magnetron mode, permitting lower discharge pressures and higher sputtering rates than the 'conventional' rf-GD source [52]. Table 4.8 summarizes the results obtained for the analysis of NIST SRM 613 Trace Elements in Glass when using mass resolutions ($m/\Delta m$) of 3000 and 300 [55]. The internal precision of the measurements was found to be in the range 4–10% RSD, while the external precision on changing samples yielded values of 6–18% RSD. As found by Duckworth *et al.* [48], the RSF values for the elements were just as uniform as in the case of dc-GDMS, with values calculated relative to Sr (present at 78.4 ppm in the standard) ranging from 0.2 and 3. Thus, one could expect that semi-quantitative analyses without the aid of RSF are possible to within an order

Table 4.8 Analysis of NIST SRM 613 Trace Elements in Glass by rf-GDMS at mass resolution values of $m/\Delta m = 3000$ and 300.

Resolution ($m/\Delta m$)	Element	Certified value, C_0 ($\mu\text{g/g}$)	Measured value, C ($\mu\text{g/g}$)	RSF (C/C_0)	LOD ($\mu\text{g/g}$)
3000	B	(32)	6.5 ± 1.0	0.2	0.07
	Ti	50.1 ± 0.8	42 ± 7.8	0.84	0.08
	Mn	39.6 ± 0.8	55.8 ± 9.0	1.4	0.04
	Fe	51 ± 2	43.5 ± 4.8	0.85	0.06
	Ni	38.8 ± 0.2	15.8 ± 2.3	0.4	0.2
	Co	35.5 ± 1.2	47.6 ± 6.6	1.4	0.05
	Cu	37.7 ± 0.9	13.8 ± 2.4	0.37	0.25
	Rb	31.4 ± 0.4	38.3 ± 3.8	1.2	0.1
	Sr	78.4 ± 0.2	Internal standard	1.0	0.1
	Ag	22.0 ± 0.3	27.2 ± 2.1	1.2	0.2
	Ba	(41)	30.1 ± 5.6	0.75	0.3
	Au	(5)	2.5 ± 0.36	0.5	0.5
	Tl	15.7 ± 0.3	40 ± 4.8	2.5	0.1
	Pb	38.6 ± 0.2	77.6 ± 7.6	2.0	0.2
	Th	37.8 ± 0.8	6.7 ± 0.95	0.18	1
	U	37.4 ± 0.08	10.0 ± 1.4	0.27	0.9
300	Rb	31.4 ± 0.4	31.4 ± 3.2	1.0	0.02
	Sr	78.4 ± 0.2	Internal standard	1.0	0.015
	Ag	22.0 ± 0.3	23.1 ± 2.2	1.05	0.02
	Au	(5)	2.4 ± 0.4	0.48	0.06
	Tl	15.7 ± 0.3	34.3 ± 7.8	2.2	0.02
	Pb	38.6 ± 0.2	65.6 ± 6.4	1.7	0.03
	Th	37.8 ± 0.08	3.8 ± 0.52	0.1	0.2
	U	37.4 ± 0.08	7.9 ± 1.2	0.21	0.1

Reprinted from Saprykin, A. I., Becker, J. S. and Dietze, J.-H., *Fresenius' J. Anal. Chem.* 1997, **359**, 449–453, with permission from Springer-Verlag.

of magnitude. The calculated concentrations are, of course, better than those based on RSFs generated from the same material. One would expect better accuracy in GDMS analyses than seen here, but the low concentration of the Sr internal standard likely affects the performance. However, for a laboratory-built source/instrument, the performance is encouraging. Table 4.8 also presents the detection limits obtained at the two resolution settings. As expected, the LODs are better for the low-resolution mode as the wider slit settings yield higher beam currents. Of course, the spectral complexity in the case of oxide materials (which often yield small molecules such as oxides) makes the use of a high-resolution spectrometer almost imperative for the low-mass (<70 Da) elements. The increase in spectral resolution was of little consequence for the high-mass analytes in terms of the removal of interferences. Although the performance of the magnetron rf-GD source showed many positive attributes, the irregular

crater shape resulting from all magnetron sputtering sources ultimately limits the application of such sources to bulk analyses.

Analysis of Oxide Materials

The analysis of nonconductive oxide (usually powder) samples is relevant to a very diverse set of industrial applications ranging from geological specimens to precious metal-containing automotive catalysts. The analysis of oxides such as ceramics is a great analytical challenge for all GD methods because of high levels of moisture and adsorbed gases that are brought into the plasma (see Chapter 11). These species quench the plasma atomization and ionization processes and also lead to the formation of molecular ions, such as oxides and hydroxides. Extensive studies by Harrison and co-workers [96,97], in particular, have shown that compaction of such samples with a powdered ‘getter’ metal such as Ti or Ta minimizes these deleterious effects. The analysis of samples that are present in powder form does not benefit to the extent that one might expect from rf powering. The reason is straightforward: although the use of rf powering permits the analysis of pressed oxide materials without the need to use a conductive metal binder (as required for dc-GD operation), the benefits of the use of ‘gettering’ binders are lost. Thus, the mass spectra of directly compacted samples are inherently complicated owing to adventitious water and gases trapped during the pressing process. In this case, direct comparison and use of dc powering for getter-bound compacted samples is a reasonable endeavor.

Harrison and co-workers have described an evaluation of the operating characteristics of rf-GDMS for oxide powders [98] and the comparison of this method with the use of metal binders for dc-GDMS analysis [29]. As mentioned previously, the direct compaction of geological materials in this case leads to very complex mass spectra, including signals for many molecular species related to water and trapped gases. This situation was remedied to an appreciable extent by the insertion of a liquid nitrogen cold finger in the plasma region for periods of longer than 30 min prior to analysis [98]. The same profound improvement of a 70–100% reduction in gaseous ions was found for bulk nonconductors, such as Macor. A detailed evaluation of the roles of discharge power and pressure and ion sampling distance on the signal responses of analyte, residual gas, and argon-related species provided very interesting and useful insights into plasma processes and optimization of the spectral responses [98]. While sets of discharge conditions that provide very good sensitivity and high S/N are readily identified, the sensitivity to variations in conditions is profound, which could be problematic. Relative sensitivity factors were compared for a number of analytes and oxide materials, with the span of values for most elements being fairly well defined and not out of line with literature values. In fact, semi-quantitative analysis of a firebrick standard, based on simple ion beam ratios, was within a factor of two. Direct analyses of compacted oxides by rf-GDMS produced very stable plasmas

(<5% RSD for 1 h), which is advantageous for quantitative determinations. It should be pointed out that these results are comparable to those of Pan and Marcus [82] (see Section 4.5.1, first sub-section) in the evaluation of the use of rf-GD-OES for the analysis of glass powder samples without the use of a binder material.

Perhaps the most forward-looking application of rf-GDMS for oxide material analyses has been described by Becker and co-workers in their extensive studies of the characterization of solid oxide fuel cells (SOFC) [95,99]. The rf-GDMS source described previously was employed together with both a converted spark source mass spectrometer having photoplate detection capabilities and a commercial double-focusing instrument (Element, Finnigan MAT). The rf-GD source was advantageously applied owing to its relatively high sputtering rates and capabilities for nonconductor analysis compared with SIMS and the related secondary neutral mass spectrometry (SNMS). Figure 4.10 illustrates the use of rf-GDMS

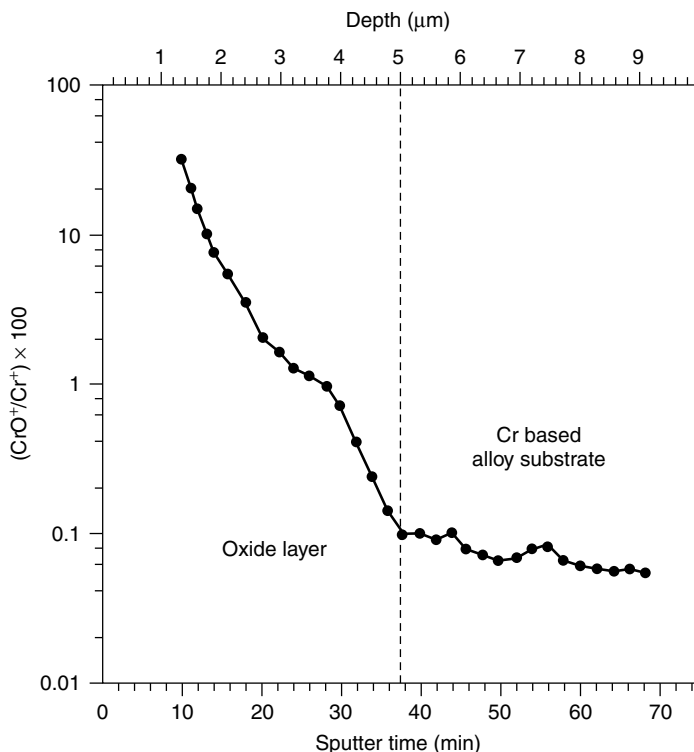


Figure 4.10 Dependence of the CrO^+/Cr^+ ion signal ratio on sputtering time for rf-GDMS analysis of an oxide layer on a chromium-based alloy (stabilization of parameters after 10 min). Reprinted from Saprykin, A. I., Becker, J. S., and Dietze, J.-H., *Fresenius' J. Anal. Chem.*, 1997, **358**, 145–147, with permission from Springer-Verlag

to profile the presence of a Cr_2O_3 coating formed by thermal cycling (to 950°C) of a Cr alloy, which is used as the interconnector for the ceramic anode and cathode components. The temporal profile of the CrO^+/Cr^+ ratio clearly identifies the formation of a favorably conductive and thermomechanically effective oxide layer on the surface of the Cr base alloy. Similar studies indicated that Ni and Co components in the alloy were taken up into the formed oxide layer to the same extent. A sputtering rate of $\sim 0.15 \mu\text{m}/\text{min}$ suggests that the thickness of the oxide coating was $4.5\text{--}5 \mu\text{m}$. Detection limits in the analysis of these types of SOFC materials, obtained with the commercial mass spectrometer system, were in the low-ppm to ppb range [55].

Analysis of Polymeric Materials

One area where the sputtering characteristics of rf-GD sources are used to particular advantage is in the analysis of organic (polymeric) coatings, as described for rf-GD-OES in Section 4.5.1, second sub-section. The ability to gain elemental information on thick layers within a relatively short period of time can be used in many applications. Almost unexpectedly, the analysis of such coatings (and in fact bulk polymers) by rf-GDMS provides a wealth of additional chemical information. As will be shown subsequently, the analysis of polymers by rf-GDMS is a simple method providing elemental, backbone, and end-group information. Coburn *et al.* reported the production of molecular fragment mass spectra of fluoro- and hydrocarbon polymers by rf-GDMS in the mid-1970s [100]. Early rf-GDMS work at Clemson University revealed a number of unexpected spectral features when analyzing small glass samples mounted on the DIP with the aid of double-sided adhesive tape. Upon further study, it was shown that these species were in fact related to the composition of the tape. This observation has been exploited in the use of rf-GDMS as a tool that provides highly sensitive determinations of the composition of polymers, during both bulk and depth-resolved analyses [101–104].

Early studies on the application of rf-GDMS to polymer analysis focused on assessing the influence of discharge conditions on the product mass spectra. The first studies by this group involved an evaluation of the discharge parameters and their respective roles in the structure and intensity of mass spectra derived from fluorohydrocarbon polymers [101]. The spectra were found to be nearly identical with those obtained by SIMS, as shown in Figure 4.11 for a 1 mm thick specimen of polytetrafluoroethylene-co-perfluoromethyl vinyl ether (PTFE-co-PFA); however, with ion beam currents that were six orders of magnitude more intense (10^{-9} vs 10^{-15} A) [101]. The polymer fragment ion signal levels are in fact similar to those obtained in metals analysis by rf-GDMS. By the same token, the plasma stabilization times and overall stability are of the same quality as presented in Table 4.6 for metals. The structure of the mass spectra for all polymers studied to date seems to be insensitive to the applied rf power, with high discharge pressures

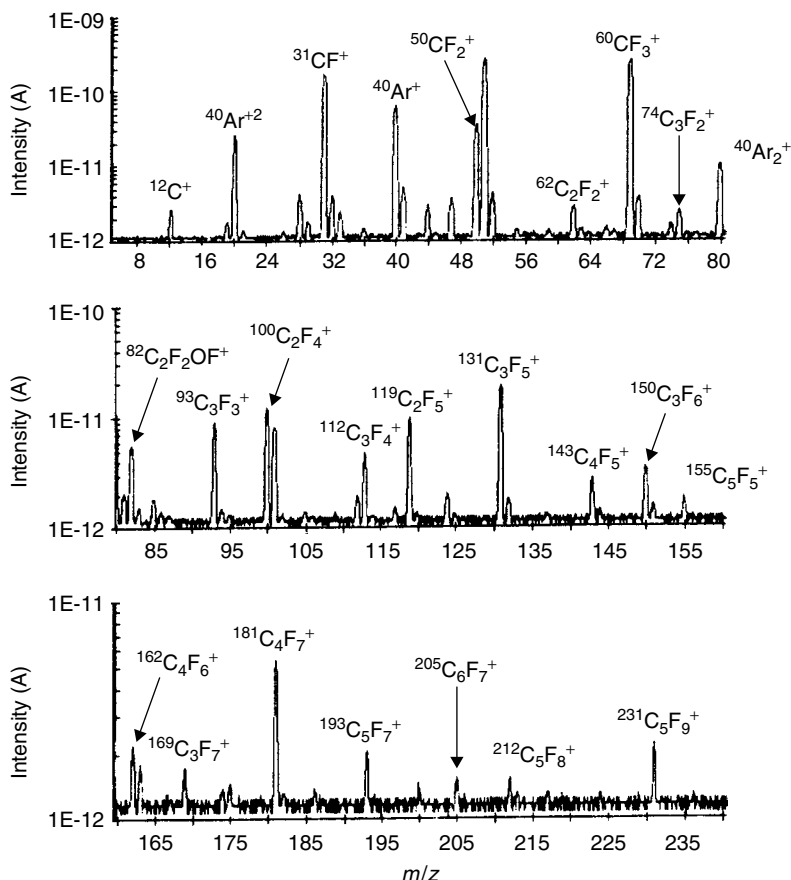


Figure 4.11 Mass spectrum of a 3.0 mm thick PTFE-co-PFA specimen obtained by rf-GDMS on a VG GloQuad spectrometer (logarithmic scale) (rf power = 20 W, argon pressure = 0.075 mbar). Reprinted with permission from Shick, C. R., Jr, DePalma, P. A., Jr, and Marcus, R. K., *Anal. Chem.*, 1996, **68**, 2113–2121, Copyright 1996 American Chemical Society

generally yielding spectra with strong signals for smaller sized polyatomics (i.e. fragments having few atoms). As such, there does exist some level of ‘tunability’, enhancing the potential use of the method for polymer identification. Use of well-regulated discharge conditions in fact allows the unambiguous identification of polymeric isomers such as low-density polyethylene (LDPE), linear low-density polyethylene (L-LDPE), and high-density polyethylene (HDPE) [104].

One of the key areas where rf-GDMS may be used to particular advantage is the depth profiling of polymeric systems. Two specific source modifications developed in this laboratory increase the utility for these applications [103,104].

First, one must recognize that organic coatings are far more thermally sensitive during sputtering than metals or even oxides. While melting or even pyrolysis can be easily envisioned to occur, exposure to heat in many polymer systems can cause species migration and the destruction of finite interface structures. Any of these thermally-induced changes can render an analysis useless. Gibeau and Marcus modified the rf-GD probe of a VG GloQuad system to use the liquid nitrogen supplied to cool the ion source also to cool the flat sample holder [103]. This modification not only allowed effective analysis of polymers having low melting-points, but also yielded greater temporal stability in all polymer analyses. The release of adsorbed water in the polymer sample matrix was also alleviated so that fewer protonated fragments were formed. As such, the ratios of characteristic fragment ion signals were found to be more reproducible and unique for the polymers examined after this implementation. As a result, ion signal ratios in the fingerprint region of the mass spectra can be effectively employed to distinguish polymers of the same (or related) chemical formula. By the same token, the

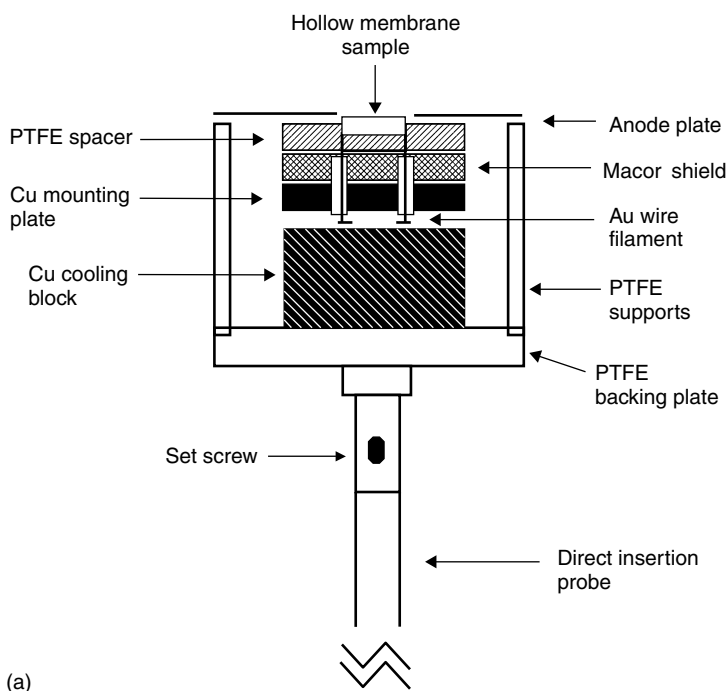


Figure 4.12 Analysis of hollow fiber polymer specimens by rf-GDMS. (a) Diagrammatic representation of the filament-type sample holder and (b) rf-GDMS temporal profile of characteristic ions produced in the analysis of a fouled PVDF hollow fiber membrane (rf power = 25 W, argon pressure = 0.1 mbar). Reproduced by permission of The Royal Society of Chemistry from Marcus, R. K., *J. Anal. At. Spectroms*, 2000, **15**, 1271–1277

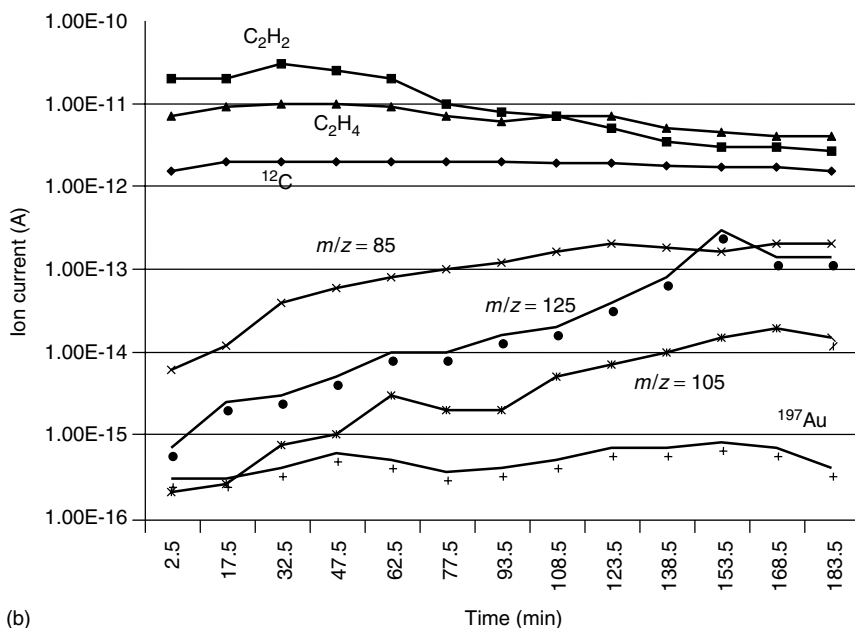


Figure 4.12 (continued)

shapes of the sputtered craters for polymers samples were found to be very similar to those of metals and oxides [66].

The second source modification of particular relevance to polymer material analysis allows the mounting and uniform sputtering of hollow fibers and or tubes [104]. These sorts of structures are commonly used in chemical separations and membrane science. In these systems, one often desires to follow the decomposition of the material or the transport of species into and out of the hollow. As such, a 'radial' depth profile, from the outer surface to the inner surface, is desired. As shown in Figure 4.12a, an assembly wherein the specimen is mounted on a metal filament, and to which the rf potential is applied, sets up the desired situation wherein the plasma is established around the circumference of the fiber [104]. Sputtering proceeds from this outer surface toward the center effectively to generate a depth profile of the membrane. Figure 4.12b illustrates the depth profile obtained in the sputtering of a 1.3 mm o.d., 0.7 mm i.d. poly(vinylidene fluoride) (PVDF) membrane which had been used in the filtration of bacteria from natural waters. Such membranes are cleaned with caustic solutions and eventually fail, meaning that the pores in the walls collapse over time. The temporal profiles of the characteristic rf-GDMS fragments of PVDF show an appreciable change from the outer to inner surfaces. Specifically, fragments separated by 20 Da increase in time/depth. This experiment provided the first,

direct evidence of the dehydrofluorination (i.e. loss of HF units) from the PVDF polymer backbone structure over the course of repeated cleanings. This sort of depth profile, coupled with the ability to profile flat layered systems rapidly, indicates that rf-GDMS could become a very important tool in basic polymer chemistry.

4.6 SUMMARY

Although the glow discharge has had a long history in fundamental studies of atomic structure and in the bulk analysis of metals and alloys, the advent of rf powering schemes has totally revolutionized the potential scope of application. Dc powering yields what can at best be termed a 'so-so' technique, as evidenced by the volumes of scientific publications and commercial sales. On the other hand, rf glow discharges yield information simply not available from other methods, without compromising the analytical characteristics of traditional dc-powered sources. Although certainly a biased opinion, it seems very clear that single-source systems will replace dc-only or dual-source instruments, yielding instruments of incredible versatility that are required in the materials analysis laboratory of the 21st century.

4.7 REFERENCES

1. Winchester, M. R.; Duckworth, D. C.; Marcus, R. K. Analysis of Nonconducting Sample Types, in *Glow Discharge Spectroscopies*, Marcus, R. K., Ed., Plenum, New York, 1993, Chapter 7.
2. Marcus, R. K. Analysis of Nonconducting Sample Types by Glow Discharge Mass Spectrometry, in *Inorganic Mass Spectrometry: Fundamentals and Applications*, Barshick, C. M.; Duckworth, D. C.; Smith, D. H., Eds, Marcel Dekker, New York, 2000, Chapter 7.
3. Dogan, M.; Laqua, K.; Massman, H. *Spectrochim. Acta, Part B* 1972, **27B**, 65–88.
4. Caroli, S.; Alimonti, A.; Zimmer, K. *Spectrochim. Acta, Part B* 1985, **38**, 625–631.
5. Loving, T. J.; Harrison, W. W. *Anal. Chem.* 1983, **54**, 1523–1526.
6. Tong, S. L.; Harrison, W. W. *Spectrochim. Acta, Part B* 1993, **48**, 1237–1245.
7. Mei, Y.; Harrison, W. W. *Anal. Chem.* 1993, **65**, 3337–3342.
8. Milton, D. M. P.; Hutton, R. C. *Spectrochim. Acta, Part B* 1993, **48**, 39–52.
9. Van Grieken, R.; Schelles, W.; De Gendt, S.; Muller, V. *Appl. Spectrosc.* 1995, **49**, 939–944.
10. Anderson, G. S.; Mayer, W. N.; Wehner, G. K. *J. Appl. Phys.* 1962, **33**, 2991–2992.
11. Chapman, B. N. *Glow Discharge Processes*, Wiley-Interscience, New York, 1980.
12. Davis, W. D.; Vanderslice, T. A. *Phys. Rev.* 1963, **131**, 219–228.
13. Lazik, C.; Marcus, R. K. *Spectrochim. Acta, Part B* 1993, **48**, 1673–1689.
14. Kohler, K.; Coburn, J. W.; Horne, D. E.; Kay, E.; Keller, J. H. *J. Appl. Phys.* 1985, **57**, 59–66.
15. Koenig, H. R.; Maissel, L. I. *IBM J. Res. Dev.* 1970, **14**, 168–171.
16. Lazik, C.; Marcus, R. K. *Spectrochim. Acta, Part B* 1992, **47**, 1309–1324.
17. Parker, M. Marcus, R. K. *Spectrochim. Acta, Part B* 1995, **50**, 617–638.

18. Hargis, P. J.; Greenberg, K. E.; Miller, P. A.; Gerardo, J. B.; Torczynski, J. R.; Riley, M. E.; Hebner, G. A.; Roberts, J. R.; Olthoff, J. K.; Whetstone, J. R.; Van Brunt, R. J.; Sobolewski, M. A.; Anderson, H. M.; Splichal, M. P.; Mock, J. L.; Bletzinger, P.; Garscadden, A.; Gottscho, R. A.; Selwyn, G.; Dalvie, M.; Heidenreich, J. E.; Butterbaugh, J. W.; Brake, M. L.; Passow, M. L.; Pender, J.; Lujan, A.; Elta, M. E.; Graves, D. B.; Sawin, H. H.; Kushner, M. J.; Verdeyen, J. T.; Horwath, R.; Turner, T. R. *Rev. Sci. Instrum.* 1994, **65**, 140–154.
19. Marcus, R. K. *J. Anal. At. Spectrom.* 1993, **8**, 935–943.
20. Payling, R.; Jones, D. G.; Gower, S. A. *Surf. Interface Anal.* 1993, **20**, 959–966.
21. Prässler, F.; Hoffmann, V.; Schumann, J.; Wetzig, K. *J. Anal. At. Spectrom.* 1995, **10**, 677–680.
22. De Gendt, S.; Van Grieken, R.; Hang, W.; Harrison, W. W. *J. Anal. At. Spectrom.* 1995, **10**, 689–695.
23. Cho, W. B.; Woo, Y. A.; Kim, H. J.; Kim, I. J.; Kang, W. K. *Appl. Spectrosc.* 1997, **51**, 1060–1066.
24. Wagatsuma, K.; Suzuki, S. *Fresenius' J. Anal. Chem.* 1997, **358**, 581–584.
25. Perez, C.; Pereiro, R.; Bordel, N.; Sanz-Medel, A. *Spectrochim. Acta, Part B* 1998, **53**, 1541–1551.
26. Bengtson, A.; Hänström, S. *J. Anal. At. Spectrom.* 1998, **13**, 437–441.
27. Pan, X.; Hu, B.; Ye, Y.; Marcus, R. K. *J. Anal. At. Spectrom.* 1998, **13**, 1159–1165.
28. Perez, C.; Pereiro, R.; Bordel, N.; Sanz-Medel, A. *J. Anal. At. Spectrom.* 1999, **14**, 1413–1418.
29. De Gendt, S.; Van Grieken, R.; Hang, W.; Harrison, W. W. *J. Anal. At. Spectrom.* 1995, **10**, 689–695.
30. Bogaerts, A.; Gijbels, R.; Goedheer, W. *Spectrochim. Acta, Part B* 1999, **54**, 1335–1350.
31. Bogaerts, A.; Gijbels, R. *Spectrochim. Acta, Part B* 2000, **55**, 263–278.
32. Bogaerts, A.; Gijbels, R. *Spectrochim. Acta, Part B* 2000, **55**, 279–297.
33. Duckworth, D. C.; Marcus, R. K. *Anal. Chem.* 1989, **61**, 1879–1886.
34. Duckworth, D. C.; Marcus, R. K. *J. Anal. At. Spectrom.* 1992, **7**, 711–715.
35. Lazik, C.; Marcus, R. K. *Spectrochim. Acta, Part B* 1994, **49**, 649–693.
36. Heintz, M. J.; Hieftje, G. M. *Spectrochim. Acta, Part B* 1995, **50**, 1125–1141.
37. Grimm, W. *Spectrochim. Acta, Part B* 1968, **23**, 443–454.
38. Kawaguchi, H.; Tanaka, T.; Fukaya, H. *Anal. Sci.* 1991, **7**, 537–540.
39. Woo, J.-C.; Cho, K. H.; Tanaka, T.; Kawaguchi, H. *Spectrochim. Acta, Part B* 1994, **49**, 915–924.
40. Wagatsuma, K. *Surf. Interface Anal.* 1999, **27**, 63–69.
41. Hoffmann, V.; Uhlemann, H.-J.; Prässler, F.; Wetzig, K.; Birus, D. *Fresenius' J. Anal. Chem.* 1996, **355**, 826–830.
42. Wagatsuma, K. *Fresenius' J. Anal. Chem.* 1999, **363**, 333–338.
43. Wagatsuma, K.; Matsuta, H. *Anal. Sci.* 2001, **17**, 313–318.
44. Coburn, J. W.; Harrison, W. W. *Appl. Spectrosc. Rev.* 1981, **17**, 95–164.
45. Donohue, D. L.; Harrison, W. W. *Anal. Chem.* 1975, **47**, 1528–1531.
46. De Gendt, S.; Van Grieken, R.; Ohorodnik, S. K.; Harrison, W. W. *Anal. Chem.* 1995, **67**, 1026–1033.
47. Giglio, J. J.; Caruso, J. A. *Appl. Spectrosc.* 1995, **49**, 900–906.
48. Duckworth, D. C.; Donohue, D. L.; Smith, S. H.; Lewis, T. A.; Marcus, R. K. *Anal. Chem.* 1993, **65**, 2478–2484.
49. Saprykin, A. I.; Melchers, F.-G.; Becker, J. S.; Dietze, H.-J. *Fresenius' J. Anal. Chem.* 1995, **363**, 570–574.
50. Tanaka, T.; Matsuno, M.; Kawaguchi, H. *Bunseki Kagaku* 1997, **46**, 351–355.

51. Woo, J. C.; Moon, D. M.; Tanaka, T.; Matsuno, M.; Kawaguchi, H. *Anal. Sci.* 1996, **12**, 459–464.
52. Saprykin, A. I.; Becker, J. S.; Dietze, J.-H. *Fresenius' J. Anal. Chem.* 1996, **355**, 831–835.
53. Heintz, M. J.; Myers, D. P.; Mahoney, P. P.; Li, G.; Hieftje, G. M. *Appl Spectrosc.* 1995, **49**, 945–954.
54. Hecq, M.; Molle, C.; Wautelet, M.; Dauchot, J.-P. *J. Anal. At. Spectrom.* 1995, **10**, 1039–1045.
55. Saprykin, A. I.; Becker, J. S.; Dietze, J.-H. *Fresenius' J. Anal. Chem.* 1997, **359**, 449–453.
56. Shick, C. R., Jr; Raith, A.; Marcus, R. K. *J. Anal. At. Spectrom.* 1993, **8**, 1043–1048.
57. Duckworth, D. C.; Marcus, R. K. *Appl. Spectrosc.* 1990, **44**, 649–655.
58. McLuckey, S. A.; Glish, G. L.; Duckworth, D. C.; Marcus, R. K. *Anal. Chem.* 1992, **64**, 1606–1609.
59. Eanes, R. C.; Marcus, R. K. *Spectrochim. Acta, Part B* 2000, **55**, 403–428.
60. Marcus, R. K.; Cable, P. R.; Duckworth, D. C.; Buchanan, M. V.; Pochkowski, J. M.; Weller, R. R. *Appl. Spectrosc.* 1992, **46**, 1992.
61. Myers, D. P.; Heintz, M. J.; Mahoney, P. P.; Li, G.; Hieftje, G. M. *Appl. Spectrosc.* 1994, **48**, 1337–1346.
62. Fernandez, M.; Bordel, N.; Pereiro, R.; Sanz-Medel, A. *J. Anal. At. Spectrom.* 1997, **12**, 1209–1214.
63. Pisonero, J.; Perez, C.; Pereiro, R.; Sanz-Medel, A. *J. Anal. At. Spectrom.* 2001, **16**, 370–375.
64. Payling, R.; Aeberhard, M.; Delfosse, D. *J. Anal. At. Spectrom.* 2001, **16**, 50–55.
65. Parker, M.; Hartenstein, M. L.; Marcus, R. K. *Anal. Chem.* 1996, **68**, 4213–4220.
66. Gibeau, T. E.; Marcus, R. K. *J. Anal. At. Spectrom.* 1998, **13**, 1303–1311.
67. Christopher, S. J.; Hartenstein, M. L.; Marcus, R. K.; Belkin, M.; Caruso, J. A. *Spectrochim. Acta, Part B* 1998, **53**, 1181–1196.
68. Belkin, M.; Caruso, J. A.; Christopher, S. J.; Marcus, R. K. *Spectrochim. Acta, Part B* 1998, **53**, 1197–1208.
69. Hartenstein, M. L.; Christopher, S. J.; Marcus, R. K. *J. Anal. At. Spectrom.* 1999, **14**, 1039–1048.
70. Tanaka, T.; Matsuno, M.; Woo, J.-C.; Kawaguchi, H. *Anal. Sci.* 1996, **12**, 591–595.
71. Winchester, M. R.; Marcus, R. K. *Anal. Chem.* 1992, **64**, 2067–2074.
72. Parker, M.; Marcus, R. K. *Appl. Spectrosc.* 1996, **50**, 366–376.
73. Wagatsuma, K.; Matsutua, H. *Spectrochim. Acta, Part B* 1999, **54**, 527–535.
74. Wagatsuma, K. *Spectrochim. Acta, Part B* 2000, **55**, 833–838.
75. Harville, T. R.; Marcus, R. K. *Anal. Chem.* 1993, **65**, 3636–3643.
76. Harville, T. R.; Marcus, R. K. *Anal. Chem.* 1995, **67**, 1271–1277.
77. Anfone, A. B.; Marcus, R. K. *J. Anal. At. Spectrom.* 2001, **16**, 506–513.
78. Parker, M.; Hartenstein, M. L.; Marcus, R. K. *Spectrochim. Acta, Part B* 1997, **52**, 567–578.
79. Hartenstein, M. L.; Marcus, R. K. *J. Anal. At. Spectrom.* 1997, **12**, 1027–1032.
80. Winchester, M. R. *J. Anal. At. Spectrom.* 1998, **13**, 235–242.
81. Marcus, R. K. Radio Frequency Glow Discharges: Challenges and Opportunities from Aluminum to Zeolites, presented at the 1996 Winter Conference on Plasma Spectrochemistry, Fort Lauderdale, FL, January 8–13, 1996.
82. Pan, X.; Marcus, R. K. *Mikrochim. Acta* 1998, **129**, 239–250.
83. Boumans, P. J. W. M.; Vrakking, J. J. A. M. *Spectrochim. Acta, Part B* 1987, **42**, 819–840.
84. Bengtson, A. *Spectrochim. Acta, Part B* 1994, **49**, 411–429.
85. Marshall, K. A. *J. Anal. At. Spectrom.* 1999, **14**, 923–928.

86. Payling, R. *Surf. Interface Anal.* 1995, **23**, 12–21.
87. Jones, D. G.; Payling, R.; Gower, S. A.; Boge, E. M. *J. Anal. At. Spectrom.* 1994, **9**, 369–373.
88. Shimizu, K.; Habazaki, H.; Skeldon, P.; Thompson, G. E.; Wood, G. C. *Surf. Interface Anal.* 1999, **27**, 998–1002.
89. Shimizu, K.; Habazaki, H.; Skeldon, P.; Thompson, G. E.; Wood, G. C. *Surf. Interface Anal.* 1999, **27**, 1046–1049.
90. Shimizu, K.; Brown, G. M.; Habazaki, H.; Kobayashi, K.; Skeldon, P.; Thompson, G. E.; Wood, G. C. *Surf. Interface Anal.* 1999, **27**, 24–28.
91. Hoffmann, V.; Kurt, R.; Kammer, K.; Thielsch, R.; Wirth, Th.; Beck, U. *Appl. Spectrosc.* 1999, **53**, 987–990.
92. Anfone, A. B.; Marcus, R. K. Clemson University, unpublished results, 2001.
93. Shick, C. R., Jr; Marcus, R. K. *Appl. Spectrosc.* 1996, **50**, 454–466.
94. Saprykin, A. I.; Becker, J. S.; Dietze, J.-H. *J. Anal. At. Spectrom.* 1995, **10**, 897–901.
95. Saprykin, A. I.; Becker, J. S.; Dietze, J.-H. *Fresenius' J. Anal. Chem.* 1997, **358**, 145–147.
96. Mei, Y.; Harrison, W. W. *Anal. Chem.* 1993, **65**, 3337–3342.
97. Ohorodnik, S. K.; De Gendt, S.; Tong, S. L.; Harrison, W. W. *J. Anal. At. Spectrom.* 1993, **8**, 859–865.
98. De Gendt, S.; Van Greiken, R.; Ohorodnik, S. K.; Harrison, W. W. *Anal. Chem.* 1995, **67**, 1026–1033.
99. Becker, J. S.; Breuer, U.; Westheide, J.; Saprykin, A. I.; Holzbrecher, H.; Nickel, H.; Dietze, J.-H. *Fresenius' J. Anal. Chem.* 1996, **355**, 626–632.
100. Coburn, J. W.; Eckstein, E. W.; Kay, E. *J. Vac. Sci. Technol.* 1975, **12**, 151–154.
101. Shick, C. R., Jr; DePalma, P. A., Jr; Marcus, R. K. *Anal. Chem.* 1996, **68**, 2113–2121.
102. Gibeau, T. E.; Hartenstein, M. L.; Marcus, R. K. *J. Am. Soc. Mass Spectrom.* 1997, **8**, 1214–1219.
103. Gibeau, T. E.; Marcus, R. K. *J. Appl. Polym. Sci.* 2000, **76**, 954–961.
104. Marcus, R. K. *J. Anal. At. Spectrom.* 2000, **15**, 1271–1277.

5

Depth Profile Analysis

A. BENGSTON

Swedish Institute for Metals Research, Stockholm, Sweden

5.1 INTRODUCTION

The sputtering process in a glow discharge typically erodes the sample surface rather evenly, more or less ‘atomic layer by layer’. At every instant of the sputtering process, the most recently removed atomic layers are present in the plasma, giving rise to analytical signals in the form of optical emission from element-specific spectral lines, or ion currents for mass spectrometry. The very rapid diffusion and re-deposition processes ensure that the analytical signals are essentially instantaneous, and there are practically no ‘memory’ effects from previous atomic layers. As a consequence, depth profile analysis can be accomplished in glow discharge spectroscopy by recording the analytical signals as a function of time from the initiation of the discharge. Greene and Whelan published the first work on depth profile analysis using a glow discharge in 1973 [1]. The application was GaAs thin films. In the same year, Belle and Johnson [2] first demonstrated glow discharge depth profiling of metal alloys. Their work was also the first on depth profiling where the Grimm-type source [3] was employed. This type of source was originally designed as an alternative to the classical spark source for bulk analysis, featuring easily interchangeable flat samples and a hollow anode. This geometry gives rise to a homogeneous electrical field in front of the sample surface, with a very even sputtering crater as a result. Therefore, the Grimm source is both practical to use and well suited for depth profile analysis, and is to date the most commonly used source type for this purpose by far. An additional reason for the popularity of this source is the relatively high sputtering rates, typically in the range 1–10 $\mu\text{m}/\text{min}$. The credit for the most important initial development work on GD-OES depth profile analysis using the Grimm source goes to Berneron and co-workers of the research institute IRSID in France [4,5].

The majority of published depth profile work to date has been done with optical emission (OES) and the Grimm-type source, but mass spectrometry and other source types have also been used to a limited extent. The predominant OES spectrometer types are multichannel instruments based on the designs of Rowland or Paschen–Runge. In general, while high plasma power is beneficial for sensitivity and speed of analysis, the practical limits are set by the material to be analysed. The flatness of the sputtered crater bottom and thereby the depth resolution are also affected by the discharge parameters. Depending on the surface layer thickness and the depth penetration rate, the data acquisition speed must be set in order to obtain a reasonable size of the data files without loss of depth information. The data from a depth profile analysis can be presented as intensity vs time diagrams, so-called qualitative depth profiles. Quantification techniques based on the concept of emission yield, defined as the analytical signal per unit weight of the analyte, have been successfully developed and commercialized by several manufacturers. It has been shown that the emission yields are nearly matrix-independent, provided that the discharge conditions are reasonably constant. The calibration provides the sputtered mass per element, allowing concentrations and sputtered depth to be calculated if elements making up nearly 100% of the sample composition are included.

A similar concept for quantification has been successfully tested for mass spectrometry, but a commercial breakthrough is still lacking. The major reason for this is probably the fact that commercial GDMS instruments are slow and cumbersome to operate compared with the GD-OES instruments. To date, most depth profile work has been carried out with optical emission instrumentation (GD-OES). There are a number of technical reasons for this, primarily connected with analysis speed. However, a substantial amount of interesting depth profile work has also been carried out using mass spectrometers (GD-MS). With the development of faster GD-MS systems, such as that recently developed by Dorka *et al.* at the IFW in Dresden [6], it is anticipated that MS will become more frequently used for depth profile analysis in the future.

This chapter presents the experimental aspects and underlying plasma physics that have led to the growing use of glow discharge sources in depth profiling applications. Examples of applications to industrial products, including metallic coatings, surface oxides, nitriding, carburizing and paints, are presented to illustrate the potential range of applications.

5.2 INSTRUMENTATION

As was mentioned in the previous section, the majority of depth profiling work to date has been carried out using glow discharge optical emission (GD-OES) and sources based on the design of Grimm from 1967. The principal layout and function of this source are presented in Chapter 2.

With a relatively high current density of 50–500 mA/cm², the depth penetration rate in a Grimm-type GD is typically in the range 1–10 μm/min. The homogeneous electric field distribution in the plasma region ensures that the sample surface is sputtered fairly evenly, resulting in a crater with a nearly flat bottom (Figure 5.1). In order to make full use of the vast amount of analytical information provided from the glow discharge, the spectrometer must be able to sample the emission signals at a rate of at least 100 times per second per spectral channel. As a consequence, so-called multichannel spectrometers are most commonly used. A spectrometer of this type has a fixed grating, and is equipped with individual photomultiplier detectors for up to 60 analytical spectral lines (wavelengths), determined by exit slits in fixed positions. The optical design is based on those of Rowland or Paschen–Runge employing focusing gratings (see Chapter 2). Depending on the analytical applications, spectral lines for the elements of interest are selected for the data acquisition. In order to accommodate sensitive spectral lines for some of the light elements (C, S, P, N, O), the spectrometer optics must be in vacuum or a purged gas atmosphere, since the most sensitive lines for these elements are found in the vacuum UV spectral region below 200 nm. For increased flexibility, a complete spectrometer system often incorporates some scanning device, e.g. an additional monochromator with fixed detector and a movable grating.

In commercially available GD-OES systems, the source is normally fixed to the spectrometer to form one integrated unit. A schematic diagram of a GD-OES spectrometer system, based on a Grimm-type source, is shown in Figure 5.2.

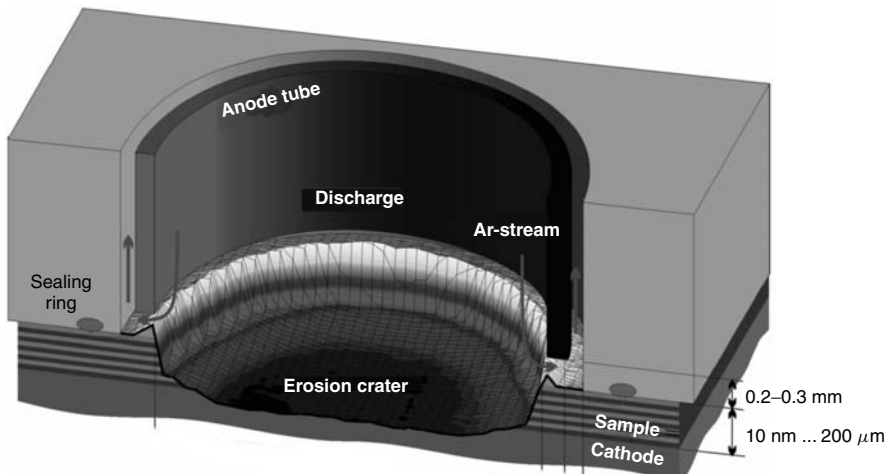


Figure 5.1 A sputtering crater in front of the hollow anode of a Grimm-type glow discharge source

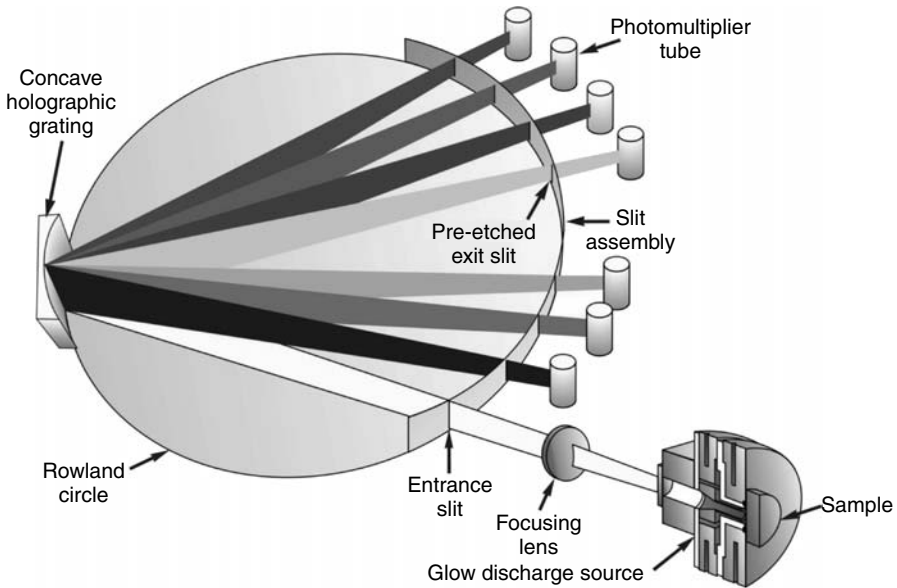


Figure 5.2 Principal layout of a GD-OES spectrometer system. Reproduced by permission of Leco Corporation

Another class of spectrometer systems seeing increased use is compact spectrometers equipped with charged-coupled device (CCD) detectors instead of photomultipliers. These spectrometers do not have the same performance as the larger multichannel spectrometers in terms of spectral resolution and acquisition speed, but they can be manufactured at considerably lower cost. Commercial GD-OES instruments with CCD spectrometers have recently become available from the companies Spectruma Analytik and Leco Corporation. An advantage with such spectrometers is that complete spectra can be recorded depending on the design, which is very useful for method development and diagnostic work. A disadvantage is that the detector gain is the same for all lines, which limits the dynamic range in that many intense lines become saturated if the gain has to be set for weak lines. Furthermore, if the low cost advantage is to be retained, these spectrometers are designed for low to moderate spectral resolution.

5.3 PRACTICAL ASPECTS AND RESULTS

5.3.1 INSTRUMENTAL SETTINGS

When performing depth profile analysis, there are a number of practical considerations in addition to those common to bulk analysis of solids. In most depth profile applications, the samples can only sustain a limited amount of heat, and

this fact restricts the setting of the discharge parameters (power, voltage and current). On the other hand, a high depth penetration rate is often desired in the interest of sample throughput and signal intensity. Optimization of the discharge parameters is therefore to a large extent the search for maximum sustainable input power. This value is in turn instrument-dependent, mainly owing to differences in sample cooling systems.

Concerning differences in power input, special attention must be paid to rf systems as opposed to dc systems. In a dc source, the applied power is identical with the plasma power, and optimized settings for one source type can be transferred to another of different manufacture. This is not the case for rf sources, where a substantial part of the input power is lost in cables, connectors, etc. These losses vary to a large extent between sources of different manufacture, and are typically in the range 10–60% of the applied power (see Chapter 4). As an example, an applied power of, e.g., 40 W can give the same plasma (effective) power as 15 W in another source. Consequently, determination of the maximum sustainable applied power must be carried out individually for each rf source type.

In terms of analytical figures of merit, the depth resolution is normally of primary importance. It is well known that the shape of the sputtering crater is affected by the discharge parameters. General recommendations valid for several applications are not available, since the optimum conditions are highly material dependent. If the user has a profilometer device available, it is recommended to carry out tests at different voltage–current (or power–pressure) combinations to determine the best settings for a flat crater bottom, compatible with the other restrictions. A profilometer is a device that determines the shape and roughness of a surface on a micrometer scale, using a fine mechanical needle or a laser beam to probe the surface. Alternatively, a coated sample can be run at different conditions and the depth profile interface examined for selection of the best conditions. The best conditions are usually when the transition from the coating to the substrate appears as sharp as possible, but the signal-to-noise ratio must also be considered.

In addition to suitable discharge parameters, data acquisition parameters must be selected. While it was stated previously that a speed of at least 100 measurements per second per channel was required for a good system, it is seldom meaningful to use such high speeds throughout the depth profile, since that leads to excessively large data files loaded with redundant information. In several applications, a high speed during the first few seconds in order to see rapid transients in the top atomic layers is useful, then the speed can be progressively decreased to the order of one measurement cycle per second at depths exceeding a few micrometers.

5.3.3 PRESENTATION AND INTERPRETATION OF DATA

As was mentioned in the Introduction, the primary data obtained are in the form of intensities from the elemental detectors as a function of sputtering time. This

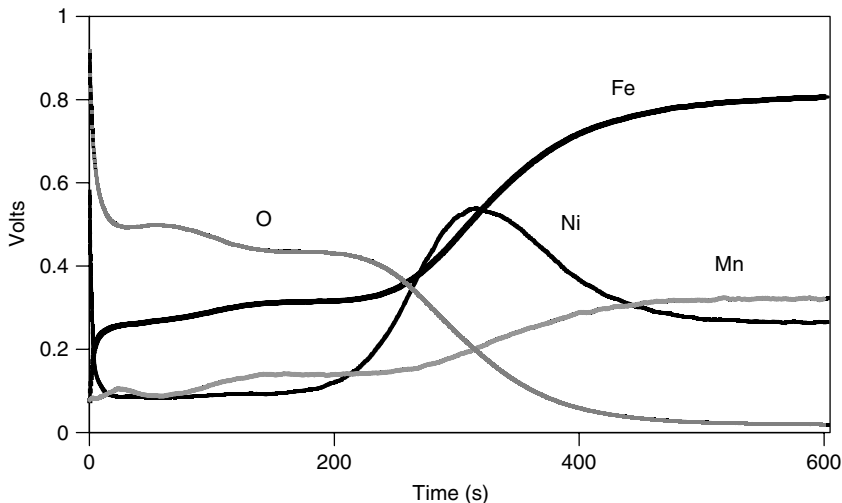


Figure 5.3 Qualitative depth profile through the oxide layer of a hot rolled steel

information is normally presented in diagrams on the computer screen and/or on paper, which in a qualitative way represent elemental depth profiles through the corresponding surface layers (Figure 5.3). The word *qualitative* is used in order to emphasize the fact that the data presented in this way are not quantified into concentration vs depth, which normally is the desired information. However, for many applications a qualitative depth profile is sufficient. This can be the case when, for example, the analytical problem is simply to compare ‘good’ samples with ‘bad’ for troubleshooting in a production process. In order to extract full analytical information from the data, however, quantification is necessary. The quantification problem can be separated into two parts: (i) elemental concentrations and (ii) sputtered depth. As we shall see in the following sections, there is a connection between these two aspects of depth profile quantification that can be effectively exploited.

The Emission Yield Concept as a Basis for Quantification in Optical Emission

Experimentally, it is easy to show that the emission intensities of analytical lines in GD-OES are proportional not just to the concentration of the corresponding element, but also to the sputtering rate of the sample. Intuitively, this observation is easy to accept; the emission intensity should be proportional to the sample atom density in the plasma, which in turn should be proportional to the sputtering rate. If we allow the voltage, current and pressure to vary, the situation becomes more complex. However, as long as the excitation conditions remain at

least nearly constant, the sputtering rate–intensity proportionality provides for an elegant solution to the quantification problem based on the concept of the emission yield [7,8], which can be defined as the emitted light per unit of sputtered mass of an element. The emission yield is an element- and instrument-dependent quantity, which must be determined independently for each spectral line and instrument. The assumption which forms the basis for this quantification technique is that the integrated signal intensity from one element (and spectral line) is proportional to just the sputtered mass of that element, which implies that the emission yield is independent of the sample matrix. This has been investigated by several authors [9,10], and is now widely accepted to be valid, at least to a first approximation. Mathematically, the relation described above can be expressed as

$$R_{nm} = I_{nm}\delta t/\delta w_n \quad (5.1)$$

where δw_n is the sputtered mass of element n during time increment δt , I_{nm} is the emission intensity of spectral line m of element n and R_{nm} is the emission yield of spectral line m of element n , which is an atomic- and instrument-dependent quantity.

Equation 5.1 is equivalent to

$$I_{nm} = c_n q_b R_{nm} \quad (5.2)$$

where c_n is the concentration of element n in sample segment b and $q_b (= \delta w_n/\delta t)$ is the sputtering (mass loss) rate in sample segment b .

Calibration is effected by determining the emission yields by means of calibration samples. These samples may be of bulk type with known concentrations, in which case it is necessary to determine the sputtering rate of each calibration sample. Alternatively, samples with coatings of known composition and thickness may be used. The crucial difference compared with a bulk calibration of traditional type is that the calibration samples, owing to the matrix independence of emission yields, do not have to be of very similar composition to the unknown samples that are to be measured. This fact increases enormously the practical applicability of the emission yield quantification method over methods requiring matrix-matched calibration samples. As an example, a set of calibration samples consisting of low-alloy steels, high-alloy steels, cast irons, a few different aluminium alloys, a few different brasses and a high-purity copper will cover a wide range of depth profile applications. Depending on the intended applications, this ‘basic’ set of calibration samples needs to be supplemented with ‘high’ samples for O, N and preferably H. Such calibration samples are not readily available, and in-house samples are often used.

In practical analytical work, the most commonly used calibration function is the following rewritten version of Equation 5.2:

$$c_n q_b = k_{nm} I_{nm} - b_{nm} \quad (5.3)$$

where k_{nm} is a calibration constant (equal to the inverse of the emission yield) and b_{nm} is the background signal expressed in the same units as the mass loss rate.

Equation 5.3 is often augmented by a second-order term to handle any nonlinearity of the calibration curves. For several sensitive spectral lines, nonlinearity occurs as a result of self-absorption. Not shown here, the calibration function normally also includes so-called line interference corrections to compensate for spectral line overlaps.

In a slightly different approach, a quantification method developed by SIMR is often referred to as the ‘intensity normalization’ technique [11]. The basic calibration function is the following:

$$c_n = k_{nm} I_{nm} q_{\text{ref}} / q_b - b_{nm} \quad (5.4)$$

where q_{ref} is the sputtering rate of a commonly used type of calibration material (e.g. low-alloy steel) of well determined sputtering rate (the reference matrix). The rationale for using Equation 5.4 is that it closely resembles the normal calibration function in bulk analysis, where concentrations of the calibration samples are plotted as a function of intensity. The only difference is that the raw intensities are first normalized to the sputtering rate of the reference matrix.

If the calibration function in Equation 5.3 is used, the primary data obtained when measuring an unknown sample is the sputtered mass of each element per time increment. The total sputtered mass of the sample is obtained as the sum of all elements, and the concentrations are easily calculated as fractions of the sum. If the calibration function in Equation 5.4 is used, the primary data obtained are sputter rate-adjusted concentrations. If the sputtering rate is higher than that of the reference matrix, the sum of all concentrations will be >100% and vice versa. The correct concentrations are calculated by sum normalization to 100%. The sputtering rate is then easily calculated from the normalization factor and the sputtering rate of the reference matrix. It is a fairly straightforward exercise to show that the two calculation approaches described above are equivalent.

Determination of Sputtered Depth

The effective sputtering rate is obtained in units of mass loss, i.e. $\mu\text{g/s}$. The density must also be known in order to convert this information to depth. The density can only be estimated from the elemental concentrations, since no other information is available from the analysis. In the original SIMR method, the density is calculated as a weighted average of the density of the pure elements, according to their concentrations in atomic (not weight!) percent. This rather crude method is essentially based on the simplified assumption that all atoms, regardless of mass, occupy the same volume in a solid. With the exception of a few unusually large atoms, this is a reasonable first-order approximation. An alternative calculation algorithm described by Takimoto *et al.* [9], summing over

the fractional volumes of each element, is almost functionally equivalent to the SIMR method. Both methods give very accurate results for all types of metal alloys. Compounds containing light and gaseous elements as majors (oxides, nitrides, carbides, etc.) are more problematic. For example, it is well known that the volume occupied by oxygen atoms in different metal oxides varies considerably owing to the differences in the electronic and lattice structures of the oxides. The densities assigned to these elements have to be taken as averages based on measured densities of several materials. Fitted to the SIMR calculation model, these densities turn out to be surprisingly high, 4.2 g/m³ for O and 4.7 g/m³ for N. The calculated densities for oxides, nitrides, etc., are generally accurate to within 10%, but deviations up to 30% have been observed in a few cases. An inaccurate density will translate into a corresponding systematic error in the determined sputtered depth. However, given the state of the art of quantitative depth profile analysis, the uncertainty in the density estimate can still be regarded as a second-order problem.

Compensation for Variations in Excitation Conditions

As was mentioned in Section 5.1, the approximation of constant emission yields is only valid for constant excitation conditions in the source. Source current, voltage and pressure determine the excitation conditions. From practical experience with GD-OES systems, it is well known that different applications require different settings of these parameters. Furthermore, at least one of these parameters will normally vary during the course of an analysis. In state-of-the-art dc systems, the two electrical parameters can be controlled by means of an active pressure regulation system, i.e. the pressure is allowed to vary. In systems without active pressure regulation, one of the electrical parameters will normally vary instead. The reason for these variations is that different sample materials give different plasma impedance, the sample being the cathode. For these reasons, it was considered necessary in the development of the SIMR quantification method to be able to compensate for variations in the excitation parameters. Experimentally, intensities from a large number of reference samples were measured while systematically varying the voltage and current. The results were fitted to different mathematical models, leading eventually to the empirical intensity expression [12]

$$I_{nm} = k_{nm} c_n C_{qb} i^{A_m} f_m(U) \quad (5.5)$$

where k_m is an atomic- and instrument-dependent constant characteristic of spectral line m , A_m is a matrix-independent constant, characteristic of spectral line m only, U is the voltage and $f_m(U)$ is a polynomial of degree 1–3, also characteristic of spectral line m .

Equation 5.5 embodies both the sputtering-rate intensity dependence from Equation 5.2 and the direct influence of voltage and current on the excitation

processes. The current dependence is exponential; experimentally determined values of A_m are in the range 1.0–2.5, with a remarkably large proportion relatively close to 2.0. Since this is a quadratic function, and the sputtering rate increases linearly with increase in current, this shows that the emission yield increases approximately linearly with the current. The voltage dependence is most conveniently modelled by a polynomial. Experimentally, it has been found that, for a large number of analytical lines, the intensity increases approximately as the square root of the over-voltage ($U - U_0$), where U_0 is the lower threshold voltage for sputtering to occur [13]. This in turn shows that the emission yield actually decreases with voltage, since the sputtering rate increases linearly with increasing over-voltage. Constants A_m and polynomials $f_m(U)$ for a large number of analytical lines have been measured by several laboratories. Tables of these constants are made available by manufacturers of GD-OES spectrometers. In the SIMR quantification model, Equation 5.5 is used to compensate for voltage–current variations by normalizing the measured intensities to those used for the calibration measurements. This added feature is to date unique for the SIMR model.

It should be noted that equation (5) does not include the pressure as a parameter. While pressure changes will always affect the emission yields indirectly by changes in at least one of the electrical parameters (due to the plasma impedance change), it is still a matter of some controversy whether there is any substantial direct influence of pressure on the emission yields. Experimentally, it is difficult to investigate this in detail because the three plasma parameters cannot be varied independently: if any two are fixed the third is determined by the sample material. In two investigations where different types of sample materials were used, and all three source parameters were measured [14,15], it was found that the direct influence of pressure was at least considerably smaller than that of the electrical parameters. Whether this holds true in general for all elements and spectral lines remains to be further investigated.

Quantification Using Radio Frequency-powered Sources

Over the last few years, radio frequency (rf)-powered glow discharge sources have found more widespread use, also for depth profile analysis. While the original motivation for the development of rf sources was the need to analyse non-conducting materials, it can be used equally well for conductive materials. In terms of quantification, it has been found that the basic emission yield concept functions in the same way as for direct current (dc)-powered sources [16]. A complication compared with dc sources is that the electrical parameters in the plasma cannot be well controlled or measured, at least not with the technology in currently commercially available instruments. Therefore, it is necessary to be more cautious in ensuring that the excitation conditions do not change excessively for different sample types when using rf sources.

Quantification Using GDMS Techniques

In the case of GDMS, no generally accepted method of quantification of depth profiles has emerged. In most cases, standard bulk methods have been used for the determination of elemental concentrations. The sputtered depth has then been calibrated against direct measurements of sputtering rates of the materials analysed. However, Jacobowski and Steuwer successfully used a quantification method very similar to the emission yield technique [17].

Artefacts to be Considered

A qualitative depth profile is always more or less distorted with respect to the true profile, in basically two respects. First, variations in the sputtering rate have the effect that the depth is not linear with the time scale. Second, since the emission intensity is proportional to the sputtering rate, these variations also cause a distortion in the apparent concentrations. An example of these types of nonlinearity is Zn-based coatings on steel sheet, where the sputtering rate in the coating is substantially higher than in the steel. In many applications, this effect is not so obvious, since the elements that make up one coating often are nearly nonexistent in other layers or the substrate material. The example in Figure 5.4, ZnFe on steel, shows both effects in a very illustrative manner. In the intensity vs time diagram, the substantially higher sputtering rate in the coating compared to the steel gives the impression that the coating is thinner than the sputtered depth in the steel substrate, and the Fe concentration in the coating is very high, on the average approaching 50%. The concentration vs depth diagram gives the correct picture of the profiled depth of the sample.

Even as quantified, there are certain artefacts from the sputtering process that must be considered when interpreting a depth profile. First, the sputtering process fundamentally limits the depth resolution. Starting with a minimum 'information depth' of the order of 1 nm on the top surface [18], the relative depth resolution (apparent interface width/sputtered depth) is fairly constant and typically 10–15% [19]. This means that at, e.g., 10 μm depth, an 'infinitely sharp' interface will appear as approximately 1 μm thick. This is typical of any depth profiling technique based on sputtering, and it must be kept in mind when, e.g., concentration levels in interface regions are estimated. A very narrow peak of high concentration will be 'smeared out', with the effect that the determined peak concentration may appear considerably lower than the true value. However, the integrated elemental mass under such a peak, as expressed in, e.g., g/m^2 , remains correct and is not affected by depth resolution. A more difficult form of artefact to deal with in depth profile analysis is what is known as 'preferential sputtering'. This occurs if the sample has a coarse microstructure with relatively large grains of different phases [20]. An example is aluminium oxide particles on a Zn surface. Owing to the very large difference in sputtering rates of these

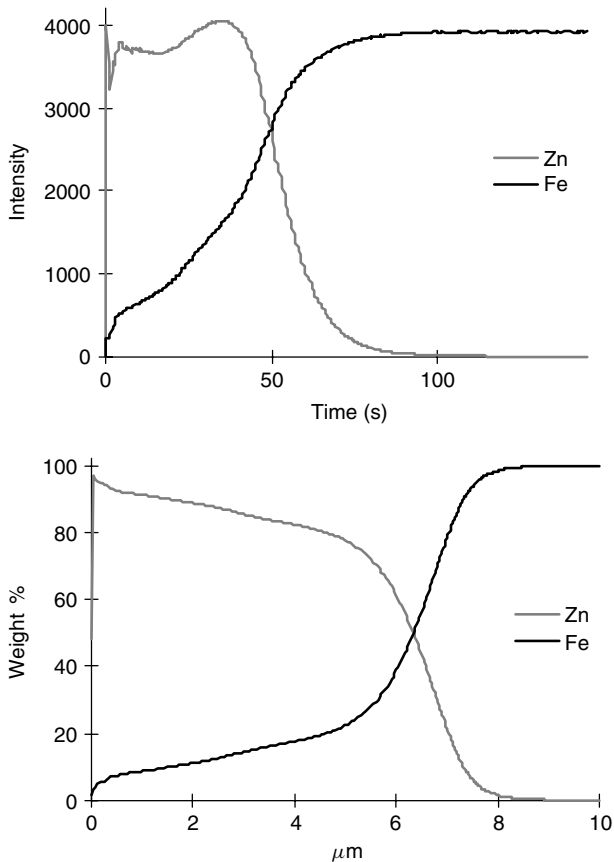


Figure 5.4 Qualitative and quantitative depth profiles of a ZnFe coating on steel

materials, the oxide appears to penetrate deeper into the Zn layer than it actually does. An example of distortion due to both the effects of limited depth resolution and preferential sputtering is shown in Figure 5.5. In this depth profile (recorded with an rf source) of a painted and galvanized steel sheet, the AlZn metallic coating appears to be alloyed into the steel in the interface, as evidenced by long ‘tails’ of Zn, Al and Si extending into the steel substrate. However, these ‘tails’ are due to a combination of crater bottom curvature and preferential sputtering in the rather complex AlZn coating material.

In more recent years, it has been discovered that a type of ‘matrix’ effect, primarily from hydrogen, can also affect the quantification of GD-OES depth profiles [21]. It has been shown that the emission yields of spectral lines from other elements can be rather dramatically affected even by very minute concentrations of hydrogen in the plasma. The hydrogen can originate from the sample

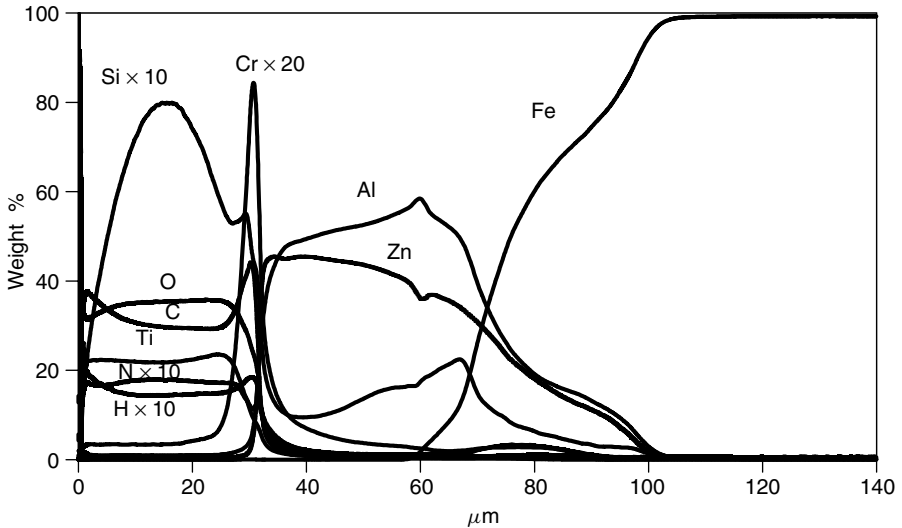


Figure 5.5 Quantitative depth profile of a polyester-coated Aluzinc on steel

itself, contamination due to adsorbed water and pumping oil inside the source, or small vacuum leaks. Both enhancement and suppression effects can be observed for one element depending on the emission line used, showing that it is the excitation probability of excited levels that are affected rather than ‘plasma chemical’ reactions at work. While source contamination and leaks should be minimized by improved source design, owing to the number of applications where the hydrogen is found in the sample itself, it has become necessary to introduce matrix correction algorithms to deal with these effects [22]. At present, such algorithms are being introduced into software from major instrument manufacturers.

5.4 CONCLUSIONS

Depth profile analysis by glow discharge spectroscopy has emerged in the last two decades as a very useful and practical analytical technique. In optical emission (GD-OES), depth profiling has arguably become more important in terms of industrial applications than conventional bulk analysis of solids. A major reason for this is that efficient and accurate methods of quantification have been developed, and in this respect GD-OES outperforms several other depth profiling techniques (see Chapter 9). Another important reason for the industrial interest in the depth profiling technique is the high sputtering rates combined with true multielement analysis, providing exceptionally high sample throughput. In recent years, the field of applications of GD-OES has been dramatically expanded by the introduction of the rf technique, allowing nonconductive layers and materials

to be analysed. Examples of current industrially important applications for depth profile analysis are metallic coatings, surface oxides, nitriding and carburizing, paints, etc. As the methodologies and instrumentation evolve, an even greater range of applications can be imagined.

5.5 REFERENCES

1. Greene, J. E.; Whelan, J. M. *J. Appl. Phys.* 1973, **44**, 2509–2513.
2. Belle, C. J.; Johnson, J. D. *Appl. Spectrosc.* 1973, **27**, 118–124.
3. Grimm, W. *Spectrochim. Acta, Part B* 1968, **23**, 443–454.
4. Berneron, R. *Spectrochim. Acta, Part B* 1978, **33**, 665–673.
5. Berneron, R.; Charbonnier, J.-C. *Surf. Interface Anal.* 1981, **3**, 134–141.
6. Dorka, R.; Hoffmann, V.; Kunstär, M. Presented at the European Winter Conference on Plasma Spectrochemistry, Hafjell, Norway, 2001, Poster PA-31.
7. Takadoum, J.; Pivin, J. C.; Pons-Corbeau, J.; Berneron, R.; Charbonnier, J. C. *Surf. Interface Anal.* 1984, **6**, 174–183.
8. Suzuki, K.; Nishizaka, K.; Ohtsubo, T. *Trans. ISIJ* 1984, **24**, B-259.
9. Takimoto, K.; Nishizaka, K.; Suzuki, K.; Ohtsubo, T. *Nippon Steel Tech. Rep.* 1987, **33**, 28–35.
10. Naoumidis, A.; Guntur, D.; Mazurkiewicz, M.; Nickel, H.; Fischer, W. In *Proceedings of the 3rd User-Meeting Analytische Glimmentladungs-Spektroskopie*, Jülich, 1990, pp. 138–153.
11. Bengtson, A. *Spectrochim Acta, Part B* 1994, **49**, 411–429.
12. Bengtson, A.; Eklund, A.; Lundholm, M.; Saric, A. *J. Anal. At. Spectrom.* 1990, **5**, 563–567.
13. Boumans, P. W. J. M. *Anal. Chem.* 1972, **44**, 1219–1228.
14. Payling, R. *Surf. Interface Anal.* 1995, **23**, 12–21.
15. Bengtson, A.; Hänström, S. *J. Anal. At. Spectrom.* 1998, **13**, 437–441.
16. Jones, D. G.; Payling, R.; Gower S. A.; Boge, E. M. *J. Anal. At. Spectrom.* 1994, **9**, 369–373.
17. Jakubowski, N.; Steuwer, D. *Appl. Spectrosc.* 1992, **7**, 951.
18. Hoffmann, V.; Praessler, F.; Wetzig, K. *Nachr. Chem. Techn. Lab.* 1998, **46**, 535–538.
19. Payling, R. *Glow Discharge Optical Emission Spectrometry*, John Wiley & Sons Ltd, Chichester, 1997, pp. 27–28.
20. Klang, H.; Nilsson, J.-O.; Österholm, L.-H.; Karlsson, J.; Hörnström, S.-E. In *Progress of Analytical Chemistry in the Iron and Steel Industry*, Luxemburg, ed. Tomellini, R., office for Official Publications of the European Communities, Brussels, 1996, pp. 317–324.
21. Bengtson, A. and Hänström, S. In *Progress of Analytical Chemistry in the Iron and Steel Industry*, Luxemburg, ed. Tomellini, R., office for Official Publications of the European Communities, Brussels, 1999, pp. 47–54.
22. Bengtson, A.; Hänström, S.; Hocquaux, H.; Meilland, R.; Zchetti, N.; Lo Piccolo, E.; Hoffmann, V.; Prässler, F.; Österholm, L.-H.; Homman, P. *Technical Steel Research, Report EUR 18919 EN, European Commission, Brussels, 1999.*

6

Numerical Modeling of Analytical Glow Discharges

ANNEMIE BOGAERTS and RENAAT GIJBELS

University of Antwerp, Department of Chemistry, Wilrijk, Belgium

6.1 INTRODUCTION

In order to improve the analytical capabilities of glow discharges, and to study the relation between plasma properties and analytical results, a good insight into the plasma processes is desirable. This can be obtained by, among others, numerical simulations of the behavior of the various plasma species.

There are a large number of papers in the (plasma physics) literature about glow discharge modeling (e.g. [1–14]), but these models were generally developed for other application fields. Indeed, glow discharges and related plasmas are not only used in analytical spectrometry, but also find application in a large number of other fields, e.g. in the semiconductor industry (for etching of surfaces or for the deposition of thin films), in materials technology (for the deposition of protective coatings), as gas lasers, light sources, flat plasma display panels, etc. The models referred to apply generally to other discharge conditions and setups. They focus on different aspects in the plasma (e.g. mainly the electrical characteristics, or plasma instabilities, etc.), and they do not consider the analytically important characteristics (such as sputtered atoms and ions, optical emission intensities, erosion rates, etc.). Nevertheless, these models have appeared to be very useful as a basis to start the numerical modeling of analytical glow discharges. The list of models for analytical glow discharges is rather limited. In addition to the work carried out in our group (e.g. [15,16] and references cited therein), a number of

other groups have performed modeling work for analytical glow discharges, but only to a limited extent [17–21]. Therefore, the data presented in this chapter will mainly stem from our work.

Table 6.1 gives an overview of the different modeling approaches in the literature to describe glow discharge plasmas, with their specific features and drawbacks. A so-called *analytical model* [1,2] is based on deriving suitable equations to describe the plasma behavior. This approach is very fast and can easily predict trends in the behavior of glow discharges. However, it is only a rough approximation, valid for a limited range of conditions. A *fluid model* [3,4] makes use of the first velocity moments of the Boltzmann equation (i.e. continuity equations of particle density, momentum density and energy density) usually coupled to Poisson's equation to obtain a self-consistent electric field distribution. This means that the electric field calculated from Poisson's equation based on the electron and ion charge densities is used in turn to calculate the behavior of these charged plasma species. It is in principle also fairly simple and fast, although it can be tricky to solve the set of coupled differential equations, but it is also approximative. Indeed, it assumes that the plasma species are more or less in equilibrium with the electric field, which means that the energy they gain from the electric field is roughly balanced by the energy they lose due to collisions. This is, for example, not true for the fast electrons in the cathode dark space (CDS). In this region adjacent to the cathode, characterized by a strong electric field, they gain more energy from the electric field than they lose by collisions. Solving the *full Boltzmann equation* [5,6] takes into account the nonequilibrium behavior of the plasma species, but this approach can become

Table 6.1 Different models used in the (plasma physics) literature to describe glow discharge plasmas, with their specific features and limitations.

Model	Short description	Advantage	Disadvantage
Analytical	Simple equations	Simple, fast	Approximation
Fluid	Momentum equations of Boltzmann equation	Simple, fast, self-consistent	Approximation (thermal equilibrium)
Boltzmann	Full Boltzmann equation	Nonequilibrium	Complex
Monte Carlo	Newton's laws + random numbers	Accurate	Long calculation time, not self-consistent
Particle-in-cell	As above + Poisson equation	Accurate + self-consistent	Long calculation time
Hybrid	Combination of above models	Accurate + self-consistent, reduced calculation time	—

mathematically very complicated, especially in more than one dimension. In contrast, *Monte Carlo simulations* [7,8] are mathematically very simple. Indeed, a large number of plasma particles are followed, one after the other. Their trajectories are calculated with Newton's laws and their collisions are treated with random numbers. If a large number of particles are followed in this statistical way, their behavior can be simulated. Because this modeling approach describes the plasma species at the lowest microscopic level, it is very accurate. However, in order to obtain sufficient statistics, a large number of particles have to be simulated, which leads to a long calculation time, especially for slow-moving particles. Moreover, the Monte Carlo model on its own requires the electric field distribution as input value, and therefore is not self-consistent. The latter problem is overcome in the *particle-in-cell method* [9,11], which couples Monte Carlo simulations for the behavior of electrons and ions to the Poisson equation for a self-consistent electric field. However, this approach is even more time consuming than the Monte Carlo approach.

As a method for analytical glow discharges we use a so-called *hybrid model* [12–14], which benefits from the advantages of the various models, and does not suffer so much from the disadvantages. Indeed, it is very accurate since it applies the most accurate Monte Carlo models where needed, namely for fast plasma species, such as fast electrons and ions, and it benefits from a reduced computation time by using faster (fluid) models where possible. This is the case for slow plasma species, such as slow electrons and ions, which are practically in equilibrium with the electric field. Moreover, when the fluid model also incorporates Poisson's equation, the hybrid model also yields self-consistent results. In this chapter, we will give an overview and a brief description of the different models that we have developed for the various plasma species, and discuss some typical results, mainly for direct current (dc), but also radio frequency (rf) and microsecond pulsed discharges.

6.2 DESCRIPTION OF THE MODELS

6.2.1 GENERAL OVERVIEW

The various collision processes in the plasma, described in our hybrid model, are summarized in Table 6.2. It is clear that not all these processes take place to the same extent, but the table tries to give a complete overview, and can be used as a reference when the processes are mentioned later in this paper. A schematic picture of the most important plasma processes can be found elsewhere [22].

Table 6.3 gives an overview of the plasma species considered in our simulations, as well as the different models used to describe these species. We assume that the discharge gas is pure argon and that the cathode is made of pure copper. The argon gas atoms are usually assumed to be at rest, uniformly distributed throughout the discharge, and in general no model is used to describe

Table 6.2 Overview of the collision processes in the plasma described in the models.^a

Electrons: elastic collisions with argon atoms	$e^- + \text{Ar}^0 \rightarrow e^- + \text{Ar}^0$
Electrons: ionization of argon atoms or copper atoms or ions (in the ground state or in excited levels)	$e^- + X \rightarrow X^+ + 2e^-$ ($X = \text{Ar}^0, \text{Ar}^*, \text{Cu}^0, \text{Cu}^*, \text{Cu}^+ \text{ or } \text{Cu}^{+*}$)
Electrons: two-electron ionization of argon atoms	$e^- + \text{Ar}^0 \rightarrow \text{Ar}^{2+} + 3e^-$
Electrons: ionization of Ar^+ ions	$e^- + \text{Ar}^+ \rightarrow \text{Ar}^{2+} + 2e^-$
Electrons: excitation of argon atoms or copper atoms or ions (in the ground state or in excited levels)	$e^- + X \rightarrow e^- + X^{**}$ ($X = \text{Ar}^0, \text{Ar}^*, \text{Cu}^0, \text{Cu}^*, \text{Cu}^+ \text{ or } \text{Cu}^{+*}$)
Electrons: de-excitation of argon atomic or copper atomic or ionic excited levels	$e^- + X^* \rightarrow e^- + X^{*/'} \text{ or } X^0$ ($X^* = \text{Ar}^*, \text{Cu}^*, \text{ or } \text{Cu}^{+*}$)
Electrons: Coulomb scattering with other electrons	$e^- + e^- \rightarrow e^- + e^-$
Argon ions: elastic collisions with argon atoms	$\text{Ar}^+ + \text{Ar}^0 \rightarrow \text{Ar}^+ + \text{Ar}^0$
Argon ions: symmetric charge transfer with argon atoms	$\text{Ar}_i^+ + \text{Ar}_s^0 \rightarrow \text{Ar}_i^0 + \text{Ar}_s^+$
Argon ions: ionization of argon atoms (in the ground state or in excited levels)	$\text{Ar}^+ + \text{Ar}^0 \text{ (or } \text{Ar}^*) \rightarrow \text{Ar}^+ + \text{Ar}^+ + e^-$
Argon ions: excitation of argon atoms (in the ground state or in excited levels)	$\text{Ar}^+ + \text{Ar}^0 \text{ (or } \text{Ar}^*) \rightarrow \text{Ar}^+ + \text{Ar}^{**}$
Argon ions: de-excitation of argon excited levels	$\text{Ar}^+ + \text{Ar}^* \rightarrow \text{Ar}^+ + \text{Ar}^{*/'} \text{ or } \text{Ar}^0$
Argon ions: Ar^+ to Ar_2^+ conversion	$\text{Ar}^+ + 2\text{Ar}^0 \rightarrow \text{Ar}_2^+ + \text{Ar}^0$
Argon atoms: elastic collisions with argon atoms	$\text{Ar}^0 + \text{Ar}^0 \rightarrow \text{Ar}^0 + \text{Ar}^0$
Argon atoms: ionization of argon atoms (in the ground state or in excited levels)	$\text{Ar}^0 + \text{Ar}^0 \text{ (or } \text{Ar}^*) \rightarrow \text{Ar}^0 + \text{Ar}^+ + e^-$
Argon atoms: excitation of argon atoms (in the ground state or in excited levels)	$\text{Ar}^0 + \text{Ar}^0 \text{ (or } \text{Ar}^*) \rightarrow \text{Ar}^0 + \text{Ar}^{**}$
Argon atoms: de-excitation of argon excited levels	$\text{Ar}^0 + \text{Ar}^* \rightarrow \text{Ar}^0 + \text{Ar}^{*/'} \text{ or } \text{Ar}^0$
Electron– Ar^+ ion radiative recombination	$e^- + \text{Ar}^+ \rightarrow \text{Ar}^0 \text{ (or } \text{Ar}^*) + h\nu$
Electron– Ar^+ (or Ar^{2+} or Cu^+ or Cu^{2+}) ion three-body recombination with an electron as third body	$e^- + X^+ + e^- \rightarrow X^0 \text{ (or } X^*) + e^-$ ($X = \text{Ar}, \text{Ar}^+, \text{Cu} \text{ or } \text{Cu}^+$)
Electron– Ar^+ ion three-body recombination with an argon atom as third body	$e^- + \text{Ar}^+ + \text{Ar}^0 \rightarrow \text{Ar}^0 \text{ (or } \text{Ar}^*) + \text{Ar}^0$
Electron– Ar_2^+ ion dissociative recombination	$e^- + \text{Ar}_2^+ \rightarrow \text{Ar}^0 \text{ (or } \text{Ar}^*) + \text{Ar}^0 \text{ (or } \text{Ar}^*)$

Table 6.2 (continued)

Radiative decay of argon atom, copper atom or ion excited levels	$X^* \rightarrow X^0$ (or $X^{*'} + h\nu$) ($X = \text{Ar}, \text{Cu}$ or Cu^+)
Argon metastable atom–metastable atom ionization	$\text{Ar}_m^* + \text{Ar}_m^* \rightarrow \text{Ar}^+ + \text{Ar}^0 + e^-$
Argon metastable atom–metastable atom associative ionization	$\text{Ar}_m^* + \text{Ar}_m^* \rightarrow \text{Ar}_2^+ + e^-$
Hornbeck–Molnar associative ionization (for $\text{Ar}^{**} > 14.6$ eV)	$\text{Ar}^{**} + \text{Ar}^0 \rightarrow \text{Ar}_2^+ + e^-$
Two-body collisions of argon metastable atoms with Ar atoms	$\text{Ar}_m^* + \text{Ar}^0 \rightarrow \text{Ar}^0 + \text{Ar}^0$
Three-body collisions of argon metastable atoms with Ar atoms	$\text{Ar}_m^* + 2\text{Ar}^0 \rightarrow \text{Ar}_2^+ + \text{Ar}^0$
Cu (sputtered) atoms: elastic collisions with argon atoms \rightarrow until thermalized	$\text{Cu}_f^0 + \text{Ar}^0 \rightarrow \text{Cu}^0 + \text{Ar}^0$
Cu atoms: Penning ionization by argon metastable atoms	$\text{Ar}_m^* + \text{Cu}^0 \rightarrow \text{Ar}^0 + \text{Cu}^+ + e^-$
Cu atoms: asymmetric charge transfer with Ar^+ ions	$\text{Ar}^+ + \text{Cu}^0 \rightarrow \text{Ar}^0 + \text{Cu}^+$
Cu atoms: two-electron asymmetric charge transfer with Ar^{2+} ions	$\text{Ar}^{2+} + \text{Cu}^0 \rightarrow \text{Ar}^0 + \text{Cu}^{2+}$
Cu ions: elastic collisions with argon atoms	$\text{Cu}^+ + \text{Ar}^0 \rightarrow \text{Cu}^+ + \text{Ar}^0$

^a Ar^* , Ar_m^* , $\text{Ar}^{*'}$, and Ar^{**} denote argon atoms in excited levels, in the metastable levels, in lower excited levels and higher excited levels, respectively. The subscripts f and s indicate fast and slow atoms or ions, respectively. The other symbols are straightforward.

Table 6.3 Overview of the different plasma species considered in the simulations, and the various models used to describe these species.

Plasma species	Model
Ar gas atoms	No model (uniformly distributed + at rest) or gas heating model (dc case)
Fast electrons	Monte Carlo model
Slow electrons	Fluid model
Ar^+ , Ar^{2+} , Ar_2^+ ions	Fluid model
Ar^+ ions in CDS	Monte Carlo model
Fast Ar_f^0 atoms in CDS	Monte Carlo model
Ar atoms in various excited levels	Collisional-radiative model
Sputtered Cu atoms: thermalization	Monte Carlo model
Cu atoms and ions in ground state + excited levels	Collisional-radiative model
Cu^+ ions in CDS	Monte Carlo model

their behavior. Nevertheless, we recently developed a model to describe argon gas heating in dc glow discharges, and we calculated a nonuniform gas temperature and hence a nonuniform argon gas density throughout the discharge. The other plasma species are described by either a Monte Carlo, a fluid or a collisional-radiative model. The electrons are split up into a fast and a slow group, depending on their energy. The electrons are called ‘fast’ when they have enough energy to produce inelastic collisions (i.e. ionization and excitation). The fast electrons, which are not in equilibrium with the electric field, are described with a Monte Carlo model, whereas the slow electrons, which can be considered to be in equilibrium with the electric field, are treated with a fluid approach, together with the argon ions (Ar^+ , Ar^{2+} and Ar_2^+). Moreover, this fluid model incorporates also the Poisson equation, for self-consistent electric field results. Since the Ar^+ ions are not in equilibrium with the strong electric field in the CDS, they are also handled with a Monte Carlo model in this region. Moreover, the fast argon atoms, Ar_f^0 , which are created in collisions from the Ar^+ ions, are also simulated with a Monte Carlo model in the CDS. The argon atoms in various excited levels are described with a so-called collisional-radiative model. This is actually a kind of fluid model, which consists of a set of balance equations (one for each excited level) with different production and loss terms. The name ‘collisional-radiative’ model stems from the fact that the production and loss processes are typically due to collisions or radiative decay (see below).

The sputtering of copper atoms at the cathode is calculated with an empirical equation for the sputtering yield as a function of energy of the bombarding particles, multiplied with the flux energy distributions of the bombarding particles. Immediately after sputtering from the cathode the sputtered copper atoms undergo a thermalization as a result of collisions with the argon gas atoms. This is described with a Monte Carlo model. The further behavior of copper atoms, their ionization and excitation and the behavior of the corresponding copper ions and excited copper atoms and ions is described with a collisional-radiative model. Finally, because the copper ions are not in equilibrium with the electric field in the CDS, they are also described with a Monte Carlo model in this region.

All the models mentioned above are coupled to each other because of the interaction processes between the species, i.e. the output of one model is used as input for the next model, and so on. The models are solved iteratively until final convergence is reached, to obtain an overall picture of the glow discharge. The Monte Carlo models are developed in three dimensions. The fluid and collisional-radiative models, however, are only two-dimensional. Indeed, the glow discharge cells under investigation in our work are assumed to be cylindrically symmetrical. Hence the three dimensions can then be reduced to two dimensions (axial and radial direction). In the following, the various models will be explained in more detail.

6.2.2 MONTE CARLO MODEL FOR FAST ELECTRONS

The behavior of the fast electrons is simulated by following a large number of electrons, one after the other, during successive time steps. During each time step, the trajectory of an electron is calculated with Newton's laws:

$$\begin{aligned}
 z &= z_0 + v_{z_0} \Delta t + \frac{q E_{\text{ax}}(z, r, t)}{2m} (\Delta t)^2 \\
 x &= x_0 + v_{x_0} \Delta t + \frac{q E_{\text{rad}}(z, r, t) \cos(\alpha)}{2m} (\Delta t)^2 \\
 y &= y_0 + v_{y_0} \Delta t + \frac{q E_{\text{rad}}(z, r, t) \sin(\alpha)}{2m} (\Delta t)^2 \\
 v_z &= v_{z_0} + \frac{q E_{\text{ax}}(z, r, t)}{m} \Delta t \\
 v_x &= v_{x_0} + \frac{q E_{\text{rad}}(z, r, t) \cos(\alpha)}{m} \Delta t \\
 v_y &= v_{y_0} + \frac{q E_{\text{rad}}(z, r, t) \sin(\alpha)}{m} \Delta t
 \end{aligned} \tag{6.1}$$

where z_0, x_0, y_0 and z, x, y are the position coordinates before and after Δt , $v_{z_0}, v_{x_0}, v_{y_0}$ and v_z, v_x, v_y are the velocities before and after Δt . E_{ax} and E_{rad} are the axial and radial electric field, as a function of axial and radial position and time (obtained from the argon ion–slow electron fluid model, see below), α is the azimuthal angle of the radial position (i.e. the angle of the radial position coordinates with respect to the x -axis), and q and m are the electron charge and mass, respectively.

The probability of collision during that time step, $\text{Prob}_{\text{coll}}$, is calculated and compared with a random number between 0 and 1:

$$\text{Prob}_{\text{coll}} = 1 - \exp\{-\Delta s \Sigma[n\sigma_{\text{coll}}(E)]\} \tag{6.2}$$

where Δs is the distance traveled during Δt and n and $\sigma_{\text{coll}}(E)$ are the densities of the target particles and the cross-sections of the different collision types of the electron with energy E . If the probability is lower than the random number, no collision occurs, and the Monte Carlo solver continues with the next electron during that time step. If the probability is higher, a collision takes place. The collisions taken into account in the model are elastic collisions with argon ground-state atoms, electron impact ionization, excitation and de-excitation for all argon atom levels, copper atom and copper ion levels, as well as electron impact ionization from Ar^+ ions and two-electron impact ionization from Ar^0 to Ar^{2+} . Finally, electron–electron Coulomb scattering is also taken into account. To determine which collision takes place, the partial collision probabilities of

the various collisions are calculated, and the total collision probability, which is equal to one, as it is the sum over all partial collision probabilities, is subdivided in intervals with lengths corresponding to these partial collision probabilities. A second random number between 0 and 1 is generated, and the interval in which the random number falls determines the collision that takes place. Then, the new energy and direction after collision are also defined by random numbers, based on energy and angular differential cross-sections.

This procedure is repeated for the next electron during that time step, and so on, until all electrons are followed. Then, the Monte Carlo procedure is repeated during the next time step, again for all electrons, and so on, until a steady state is reached. However, the electrons can also be removed from the Monte Carlo model, when they undergo recombination at the cell walls, or (at least in the dc discharge) when they are transferred to the slow electron group. The latter occurs when they reach energies lower than the threshold for inelastic collisions. Indeed, these ‘slow’ electrons are only important for carrying the electrical current and for providing negative space charge, and they can as well be described with a fluid model (see below), to save calculation time. However, when we want to calculate the detailed excitation and de-excitation between the various excited argon and copper levels for the collisional-radiative models (see below), all electrons, also the slow ones, are simulated with the Monte Carlo model, because low-energy electrons can cause de-excitation or excitation to nearby levels. More information about this model can be found elsewhere [23–27].

6.2.3 FLUID MODEL FOR ARGON IONS AND SLOW ELECTRONS

As mentioned in the Introduction, a fluid model consists generally of the (first three) velocity moments of the Boltzmann equation: continuity of particle density, of momentum density and of energy density. In our model, the energy balance equation is generally not solved, because the energy of the fast electrons and of the argon ions in the CDS is calculated with a Monte Carlo model, and the slow electrons and argon ions in the negative glow (NG) can be considered to be thermalized. Moreover, the momentum equations for argon ions and electrons are reduced to the transport equations based on diffusion and migration in the electric field. The latter is justified when the collision mean free path is much smaller than the typical cell dimensions, which is definitely the case for most analytical glow discharges, where the pressure is typically in the range 0.5–5 Torr.

As argon ionic species, Ar^+ , Ar^{2+} and Ar_2^+ ions are taken into account in this model. The continuity equations and transport equations for the three types of argon ions and for the slow electrons are coupled to Poisson’s equation to obtain a self-consistent electric field distribution, which is used later on in the electron and argon ion Monte Carlo models to calculate the trajectory by Newton’s laws.

This yields the following equations:

$$\begin{aligned}
 \frac{\partial n_{\text{Ar}^+}(z, r, t)}{\partial t} + \bar{\nabla} \cdot \overline{j_{\text{Ar}^+}}(z, r, t) &= R_{\text{prod,Ar}^+}(z, r, t) - R_{\text{loss,Ar}^+}(z, r, t) \\
 \frac{\partial n_{\text{Ar}^{2+}}(z, r, t)}{\partial t} + \bar{\nabla} \cdot \overline{j_{\text{Ar}^{2+}}}(z, r, t) &= R_{\text{prod,Ar}^{2+}}(z, r, t) - R_{\text{loss,Ar}^{2+}}(z, r, t) \\
 \frac{\partial n_{\text{Ar}_2^+}(z, r, t)}{\partial t} + \bar{\nabla} \cdot \overline{j_{\text{Ar}_2^+}}(z, r, t) &= R_{\text{prod,Ar}_2^+}(z, r, t) - R_{\text{loss,Ar}_2^+}(z, r, t) \\
 \frac{\partial n_{\text{e,slow}}(z, r, t)}{\partial t} + \bar{\nabla} \cdot \overline{j_{\text{e,slow}}}(z, r, t) &= R_{\text{prod,e,slow}}(z, r, t) \\
 &\quad - R_{\text{loss,e,slow}}(z, r, t) \\
 \overline{j_{\text{Ar}^+}}(z, r, t) &= \mu_{\text{Ar}^+} n_{\text{Ar}^+}(z, r, t) \bar{E}(z, r, t) \\
 &\quad - D_{\text{Ar}^+} \bar{\nabla} n_{\text{Ar}^+}(z, r, t) \\
 \overline{j_{\text{Ar}^{2+}}}(z, r, t) &= \mu_{\text{Ar}^{2+}} n_{\text{Ar}^{2+}}(z, r, t) \bar{E}(z, r, t) \\
 &\quad - D_{\text{Ar}^{2+}} \bar{\nabla} n_{\text{Ar}^{2+}}(z, r, t) \\
 \overline{j_{\text{Ar}_2^+}}(z, r, t) &= \mu_{\text{Ar}_2^+} n_{\text{Ar}_2^+}(z, r, t) \bar{E}(z, r, t) \\
 &\quad - D_{\text{Ar}_2^+} \bar{\nabla} n_{\text{Ar}_2^+}(z, r, t) \\
 \overline{j_{\text{e,slow}}}(z, r, t) &= -\mu_{\text{e,slow}} n_{\text{e,slow}}(z, r, t) \bar{E}(z, r, t) \\
 &\quad - D_{\text{e,slow}} \bar{\nabla} n_{\text{e,slow}}(z, r, t) \\
 [\nabla^2 V(z, r, t) + (e/\varepsilon_0)[n_{\text{Ar}^+}(z, r, t) + n_{\text{Ar}^{2+}}(z, r, t) + n_{\text{Ar}_2^+}(z, r, t) - n_{\text{e,slow}}(z, r, t) \\
 &\quad - n_{\text{e,fast}}(z, r, t)] = 0; \bar{E} = -\bar{\nabla} V
 \end{aligned} \tag{6.3}$$

n and j , respectively, are the densities and fluxes of the argon ionic species and electrons, R_{prod} and R_{loss} are the production and loss rates (see Table 6.2 for the reaction mechanisms). Production of Ar^+ ions is due to electron impact ionization, which is calculated in the electron Monte Carlo model above, as well as Ar^{2+} -electron recombination. Loss of Ar^+ ions is due to Ar^+ -electron recombination, atomic to molecular ion conversion from Ar^+ to Ar_2^+ and electron impact ionization from Ar^+ to Ar^{2+} . The production processes for the Ar^{2+} ions include electron impact ionization from Ar^0 and from Ar^+ , as calculated in the Monte Carlo model above. The loss processes are Ar^{2+} -electron recombination and two-electron asymmetric charge transfer with Cu^0 , being a resonant process [28]. Production of Ar_2^+ ions is caused by associative ionization of argon atoms (Hornbeck-Molnar process or due to the collision of two argon metastable atoms), as well as by atomic ion to molecular ion conversion (see above). Loss of Ar_2^+ ions is assumed to occur entirely due to dissociative recombination. Finally, production of the slow electrons is due to electron transfer to the slow electron group

(calculated in the above electron Monte Carlo model), whereas loss of these electrons is due to various electron–argon ion recombination mechanisms. Further, \bar{E} is the electric field and V is the electric potential. D and μ , respectively, are the diffusion coefficients and mobilities of the argon ionic species and electrons.

The four transport equations can be inserted into the four continuity equations, leading to a set of five coupled differential equations, including Poisson's equation, with boundary conditions: $V = -V_c$ at the cathode [or $V(t) = V_{dc} + V_{rf} \sin(\omega_{rf}t)$ in the rf discharge, where V_{dc} is the dc bias voltage, V_{rf} is the applied rf voltage and ω_{rf} is the rf frequency] and $V = 0$ at the anode; $n_{e,slow} = 0$ at all walls and all times because electron–ion recombination at a conducting surface is assumed to be infinitely fast, and $\bar{\nabla}n_{Ar^+}$, $\bar{\nabla}n_{Ar^{2+}}$, $\bar{\nabla}n_{Ar_2^+} = 0$ at all walls and all times. The latter means that the ion fluxes at the walls are only due to migration. This forces a nonzero ion density at the electrodes, although it is expected that the ion density is zero or close to zero, owing to Auger neutralization. Hence this boundary condition is not completely correct, but it is used to avoid numerical difficulties due to a very thin ion diffusion boundary layer.

Owing to the severe nonlinearity and strong coupling of the equations, solving this model is a difficult numerical problem. The method we used was developed by Passchier and Goedheer [4], and is based on the Scharfetter–Gummel exponential scheme for the transport equations [29,30]. The basic idea is that the particle fluxes are assumed constant between mesh points, instead of the densities. The advantage of this scheme is its ability to switch between situations where either the migration component or the diffusion component of the particle flux is dominant, namely in the high and low electric field, sheath region (CDS) and bulk plasma (NG), respectively. More details about this model can be found in the literature [24–27,31,32].

6.2.4 MONTE CARLO MODEL FOR ARGON IONS AND FAST ARGON ATOMS IN THE CDS

As mentioned before, the argon ions are not really in equilibrium with the strong electric field in the CDS, and the fluid model is, therefore, only an approximation for the argon ions in this region. Therefore, the argon ions are also simulated with a Monte Carlo method in this region, which enables us to calculate the argon ion energy distribution at the cathode, needed to calculate the amount of sputtering (see below). Only the Ar^+ ions are treated with this Monte Carlo model, because the Ar^{2+} and Ar_2^+ ions have a lower density and flux, and they play only a minor role in the sputtering process [32]. However, in addition to the Ar^+ ions, also the fast argon atoms (Ar_f^0), which are created by collisions of the argon ions, are described with this Monte Carlo model, since it was found that they play a dominant role in the sputtering process [23].

The argon ion and fast argon atom Monte Carlo model is similar to the electron Monte Carlo model. Indeed, during successive time steps, the trajectory of the

ions and atoms is calculated by Newton's laws, and the occurrence of a collision, the nature of the collision and the new energy and direction after collision are determined by random numbers. The collision processes taken into account are elastic scattering collisions with argon ground-state atoms, for both ions and atoms, symmetric charge transfer for argon ions (which is actually also a form of elastic collisions, because there is no change in kinetic energy), and ion and atom impact ionization, excitation and de-excitation for all argon atom levels.

The ions are followed until they bombard the cathode. Then, the 'fast' (i.e. nonthermal) argon atoms created by collisions of the ions, are also followed, until they collide at the walls or until they are again thermalized by collisions. More information about this Monte Carlo model can be found in the literature [23,33,34].

6.2.5 HEAT TRANSFER MODEL FOR ARGON GAS ATOMS

In most cases, we have assumed in our model that the argon gas atoms are at rest, uniformly distributed throughout the discharge, and that no specific model is applied to describe their behavior. However, recently we have developed a model for the dc discharge to calculate gas heating, and consequently the gas temperature distribution, which yields, when the gas pressure is constant, a nonuniform gas density distribution. The gas temperature is calculated as a function of z and r position with the heat conduction equation:

$$\frac{\partial^2 T_g}{\partial z^2} + \frac{1}{r} \frac{\partial}{\partial r} \left(r \frac{\partial T_g}{\partial r} \right) = -\frac{P}{\kappa} \quad (6.4)$$

where T_g is the argon gas temperature, P is the power input and κ is the thermal conductivity ($= 1.8 \times 10^{-4} \text{ W cm}^{-1} \text{ K}^{-1}$ for argon). The power input in the argon gas is calculated in the ion and atom Monte Carlo models, based on collisions and subsequent energy transfer of the argon ions, fast argon atoms and copper atoms (see below) to the argon gas atoms. A detailed description of this model can be found in Bogaerts *et al.* [35].

6.2.6 COLLISIONAL-RADIATIVE MODEL FOR ARGON ATOM EXCITED LEVELS

Figure 6.1 shows a schematic energy diagram of the argon atomic levels taken into account in our model. Sixty-four argon atomic excited levels are considered; most of them are effective levels, i.e. a group of individual levels with comparable excitation energy and quantum numbers. The four 4s levels, being two metastable levels and two resonant levels, are, however, treated separately. The behavior of these levels is described with 64 coupled balance equations,

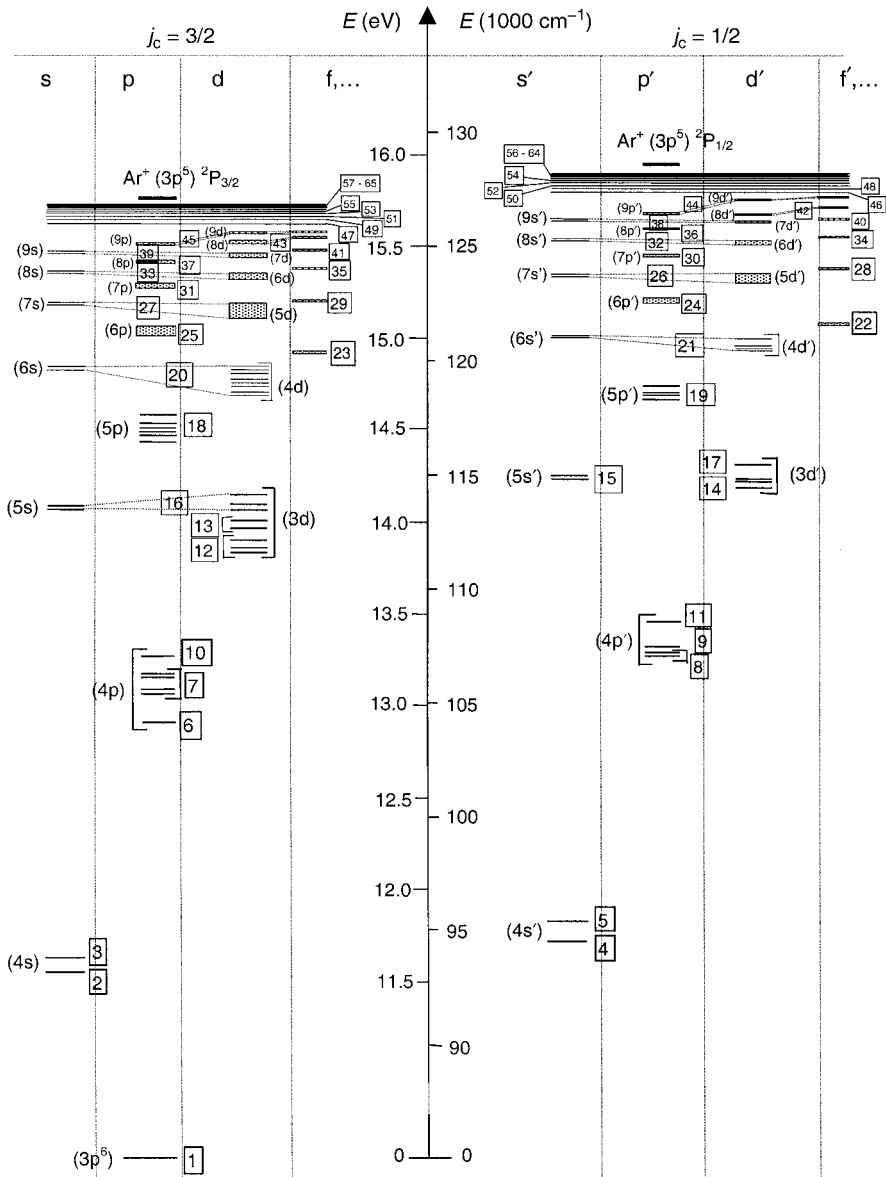


Figure 6.1 Argon atom energy level scheme, illustrating all the effective levels incorporated in the model. Reproduced by permission of The American Institute of Physics from Bogaerts, A., Gijbels, R., and Vlcek, J., *J. Appl. Phys.* 1998, **84**, 121–136

taking into account a large number of populating and depopulating collisional and radiative processes:

$$\begin{aligned} \frac{\partial n_{\text{Ar}^*}(z, r, t)}{\partial t} - D_{\text{Ar}^*} \frac{1}{r} \frac{\partial}{\partial r} \left[r \frac{\partial n_{\text{Ar}^*}(z, r, t)}{\partial r} \right] - D_{\text{Ar}^*} \frac{\partial^2 n_{\text{Ar}^*}(z, r, t)}{\partial z^2} \\ = R_{\text{prod}}(z, r, t) - R_{\text{loss}}(z, r, t) \end{aligned} \quad (6.5)$$

The production and loss processes taken into account are electron, argon ion and atom impact ionization from all levels, excitation and de-excitation between all these levels, and electron–ion three-body and radiative recombination to all levels, in addition to radiative decay between the levels and Hornbeck–Molnar associative ionization (for Ar^* levels with excitation energy above 14.7 eV). Moreover, some additional processes are incorporated for the 4s metastable levels, namely metastable atom–metastable atom collisions, Penning ionization of the sputtered copper atoms, and two-body and three-body collisions with argon ground state atoms (see Table 6.2 for the reaction mechanisms).

Transport occurs by diffusion; the latter plays only a role for the 4s levels, because the higher excited levels decay more rapidly to the ground state by emission of radiation than they could move due to diffusion. Furthermore, when the two non-metastable 4s levels decay to the ground state, a large fraction of the emitted radiation is re-absorbed by the ground level, leading again to formation of this 4s level. This phenomenon of ‘radiation trapping’ is accounted for by means of ‘escape factors’ which express the fraction of photons which can really escape without being re-absorbed [36,37].

The 64 balance equations are coupled to each other, because higher and lower levels affect each other owing to radiative decay, excitation and de-excitation. The boundary conditions for these equations are $n_{\text{Ar}^*} = 0$ at all walls, because the excited levels will de-excite upon collision at the walls. More information about this model can be found elsewhere [38,39].

6.2.7 SPUTTERING AT THE CATHODE AND THERMALIZATION OF THE SPUTTERED ATOMS

The flux of sputtered copper atoms is calculated from the flux energy distribution functions of the argon ions, fast argon atoms and copper ions (see below) bombarding the cathode, $f(0, r, t, E)$, calculated in the Monte Carlo models. It is multiplied with an empirical equation for the sputtering yield as a function of the bombarding energy (Y), adopted from Matsunami *et al.* [40]:

$$\begin{aligned} J_{\text{sput}}(0, r, t) = - \int_E \{ Y_{\text{Ar-Cu}}(E) [f_{\text{Ar}^+}(0, r, t, E) + f_{\text{Ar}^0}(0, r, t, E)] \\ + Y_{\text{Cu-Cu}}(E) f_{\text{Cu}^+}(0, r, t, E) \} dE \end{aligned} \quad (6.6)$$

When the copper atoms are sputtered from the cathode, they have energies of the order of 5–10 eV. However, they lose these energies almost immediately in the first few millimeters from the cathode, by collisions with argon gas atoms, until they are thermalized. This thermalization process is described with a Monte Carlo model, similar to the electron Monte Carlo model (see above), except that the electric field does not come into play for the neutral atoms, and that only elastic collisions with argon atoms are incorporated. Indeed, collisions with other plasma species can be neglected, owing to the lower densities of these species. This Monte Carlo model is employed until all atoms are thermalized, and it results in a so-called thermalization profile, F_T , i.e. the number of atoms thermalized as a function of position from the cathode. More details can be found elsewhere [41].

The product of J_{sput} and F_T will be used as source term for the copper atoms, described in the next model.

6.2.8 COLLISIONAL-RADIATIVE MODEL FOR THE COPPER ATOMS AND IONS

The further behavior of the thermalized sputtered copper atoms (i.e. transport, ionization and excitation) and the behavior of the excited copper atoms and of the copper ions, both in the ground state and in excited levels, are described with a collisional-radiative model. Eight copper atom levels, seven copper ion (Cu^+) levels and the Cu^{2+} ions are considered (see the energy level scheme in Figure 6.2). Some of the Cu atom and ion levels are grouped into effective levels. The behavior of all the levels is again described with a set of coupled balance equations with various production and loss terms, i.e. electron impact ionization from all levels, excitation and de-excitation between all levels, radiative decay between all levels, electron–ion three-body recombination to the upper copper atom and copper ion levels, Penning ionization by argon metastable atoms, and asymmetric charge transfer between copper atoms and argon ions (see Table 6.2). Moreover, an additional production term for the copper ground-state atoms is the product of J_{sput} and F_T , as is described above.

The transport occurs by diffusion for the atoms, and by diffusion and migration for the ions. The equations are also coupled owing to the effect of higher and lower levels on the other levels, and they are solved until a steady state is reached. More information about this model is available [42,43].

6.2.9 MONTE CARLO MODEL FOR COPPER IONS IN THE CDS

As mentioned before, the copper ions are also treated with a Monte Carlo model in the CDS, because they are not in equilibrium with the strong electric field in this region. The procedure is again comparable to the electron Monte Carlo model,

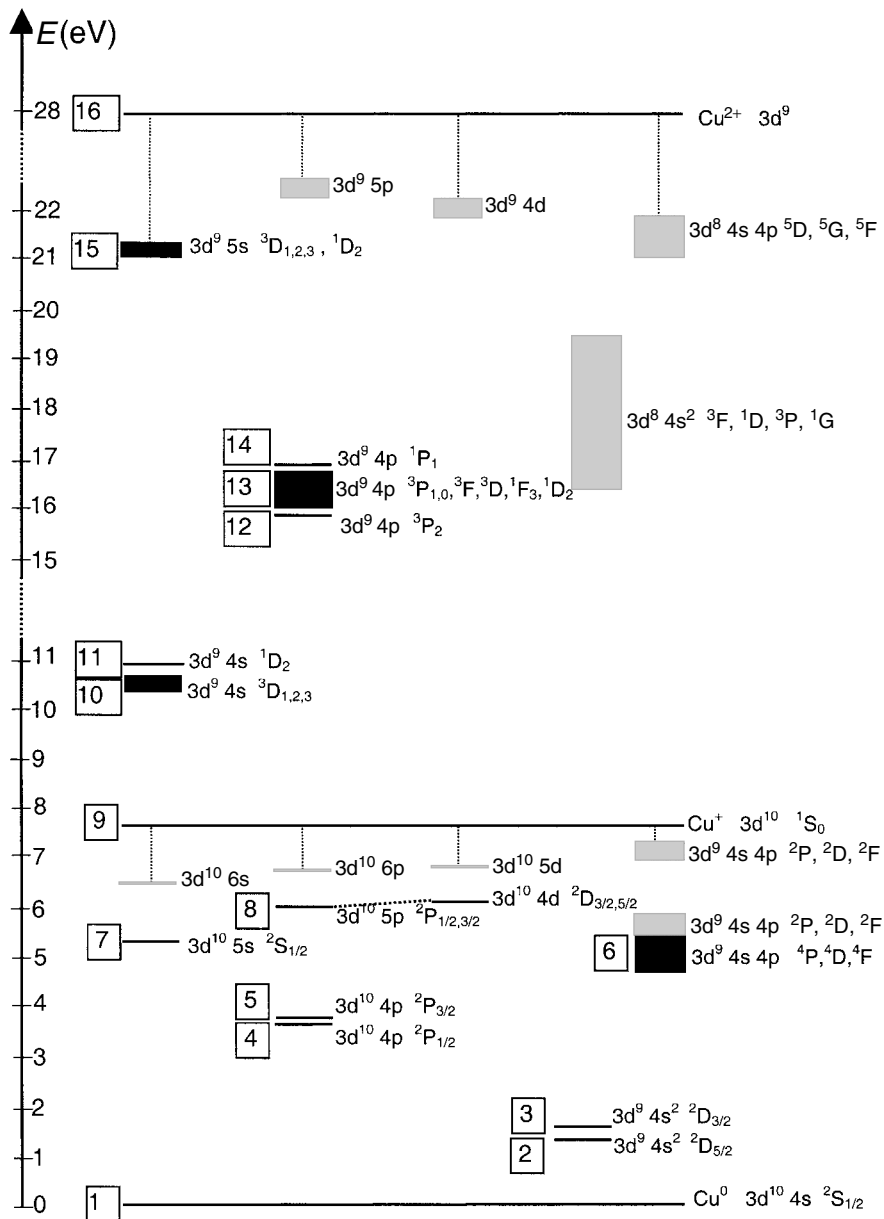


Figure 6.2 Copper atom and ion energy level scheme, with the effective level number (left) and the designation according to Moore (right of the levels). The levels considered in the model are presented in black. Reprinted from Bogaerts, A., Gijbels, R., and Carman, R. J., *Spectrochim. Acta, Part B*, 1998, **53**, 1679–1703, with permission of Elsevier Science

and includes calculation of the trajectory by Newton's laws, and treatment of the collisions by random numbers (for more information, see earlier papers [44,45]).

6.3 RESULTS AND DISCUSSION

An overview of the typical quantities that have been calculated with our models is given in Table 6.4. Comparison is made with experimental data, when available. More details about the calculation results and the comparison with experiments can be found in the references mentioned. In the following, some of the calculation results will be discussed in more detail, to illustrate the possibilities and limitations of our models. Calculations have mainly been performed for dc glow discharges, under both GDMS and GD-OES (Grimm-type) conditions; therefore, most results presented below apply to dc glow discharges. Nevertheless,

Table 6.4 Overview of the typical results obtained with our models, and comparison with experimental data, if available.

Calculated quantities (+ ref. for more information)		Comparison with experimental data (+ ref.)	
<i>Electrical characteristics:</i>			
Current as a function of voltage and pressure (dc)	[33,46,47]	Measured for VG 9000 cell	[33,46]
Rf amplitude and dc bias voltage (rf)	[31,48,49]	Measured for Grimm-type cell	[49]
Voltage, current, power as a function of time (μ s-pulsed)	[27]	Measured for Grimm-type cell	[50]
<i>Potential, electric field distributions:</i>			
3D potential distributions	[24–27,31,46]	—	
3D axial and radial electric field distributions	[24–27,31,46]	—	
Value of the plasma potential	[24–27,31,46]	—	
Lengths of the different regions (CDS, NG)	[24–27,31,46]	Length of CDS as function of pressure and current: empirical equation of Aston	[46,51]
<i>3D density profiles of:</i>			
Argon atoms (gas heating)	[35]	—	
Argon ions	[24–27,31,46]	—	
Fast argon atoms	[23,46]	—	
Argon metastable atoms	[38,39,45,46,52]	Measured (for dc discharge) by laser induced fluorescence (LIF)	[53]

Table 6.4 (continued)

Calculated quantities (+ ref.for more information)		Comparison with experimental data (+ ref.)	
Other argon excited levels	[38,39]	—	
Fast electrons	[23–25,46]	—	
Thermalized electrons	[24–27,31,46]	Measured by Langmuir probe (dc)	[54]
Atoms of the cathode material	[42–46]	Measured by LIF (dc)	[55]
Ions of the cathode material	[42–46]	Measured by LIF (dc)	[55]
Atoms + ions of the cathode material, in excited levels	[42,43]		
<i>Ion fluxes</i> of argon and cathode ions at the exit slit of the cell to the mass spectrometer (dc)	[56,57]	Ratio in qualitative agreement with ratios in dc GD mass spectra	[56]
<i>Ionization degrees</i> of argon and cathode atoms	[44–46]	Based on the LIF results (see above)	[55]
<i>3D energy distributions and mean energies of:</i>			
Electrons	[22,24,26,31,46]	—	
Argon ions	[22,34,46]	Measured at cathode for dc GDMS	[58]
Fast argon atoms	[23,34,46]	—	
Cathode ions	[44,46]	Measured at cathode for dc GDMS	[58]
<i>Information about collision processes:</i>			
3D collision rates of the different collision processes of electrons, argon ions and fast argon atoms and relative importances of these collision processes	[23–27,31,33,46]	—	
3D rates of Penning ionization, asymmetric charge transfer and electron impact ionization and relative contributions to the total ionization of sputtered atoms	[42–46]	—	

(continued overleaf)

Table 6.4 (continued)

Calculated quantities (+ ref. for more information)		Comparison with experimental data (+ ref.)	
3D rates and relative contributions of the various populating and depopulating processes (see text) of the metastable and other excited argon levels	[38,39,45,46,52]	—	
3D rates and relative contributions of the various populating and depopulating processes (see text) of the excited cathode atom + ion levels	[42,43]	—	
<i>Information about sputtering:</i>			
Sputtering (erosion) rates at the cathode	[43–47,59]	Values for GDMS, GD-OES, dc, rf	[49,60–62]
Thermalization profiles of the sputtered atoms	[41,46]	—	
Amount of redeposition on the cathode by backscattering or back-diffusion	[41,46,59]	—	
Relative contributions of argon ions, fast argon atoms and cathode ions to the sputtering process	[23,43–46]	—	
2D crater profiles due to sputtering at the cathode	[59]	Profiles obtained for GDMS	[60]
<i>Emission spectra and emission spatial distributions</i> due to radiative decay from the excited levels (for argon and cathode atoms + ions)	[39,43,63–65]	Data from the literature	[66–68]
Effect of cell geometry on the calculated quantities	[56,57]	—	
Prediction of variations in relative sensitivity factors for GDMS	[69]	Data from the literature	[17]

calculations have also been carried out for rf and microsecond-pulsed discharges, and some of these results will also be discussed below.

6.3.1 ELECTRICAL CHARACTERISTICS

The only input parameters in the model are the cell geometry, the kind of discharge gas and the corresponding cross-sections, and also in general the discharge voltage, gas pressure and gas temperature. The electric current, which is another macroscopic quantity, follows self-consistently from the calculation results, as the sum of the microscopic fluxes of charged plasma species. Since this parameter is, hence, one of the final results of the model, as it is summed over the various charged species, and since it is also experimentally available, it can be used to check the validity of the model. Indeed, when a realistic value for this calculated current is obtained, it can be expected that the other calculated microscopic plasma quantities (fluxes, densities, etc.) are also more or less realistic.

Figure 6.3 presents the calculated dc electrical current as a function of voltage and pressure, for the VG 9000 glow discharge cell (Thermo Elemental; solid lines, left axis). Current–pressure–voltage characteristics were also measured for the same cell, and the results are also included in Figure 6.3 (dashed lines, right axis). The agreement between theory and experiment is reasonable, in so far that the current increases in a similar way with pressure and voltage. Indeed, at higher pressures, there are more gas atoms, and therefore more ionization collisions and hence the creation of more ions and electrons, which means that more current will

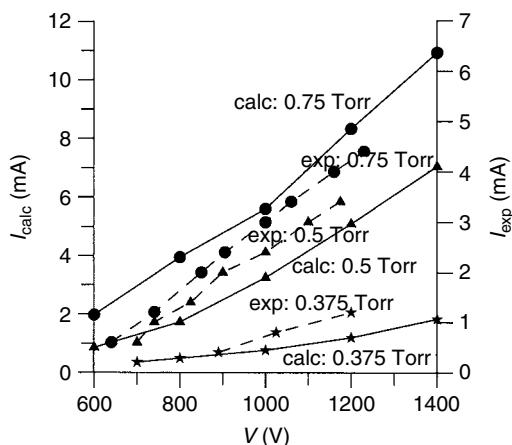


Figure 6.3 Electrical current as a function of voltage at three pressures in a dc discharge (standard VG 9000 flat cell). The calculation results are presented by the solid lines (left axis), whereas the experimental values [72] are shown with dashed lines (right axis; note the different vertical scale)

flow through the discharge cell. The effect of the voltage is explained as follows. At low voltages (below 600 V), the electrons have low energies (below the maximum in the electron impact ionization cross-section, at ca 100 eV) [70], and increasing the voltage means that the electrons will reach more suitable energies for ionization, leading to more electrons and ions, hence yielding a higher current. At voltages above 600 V, the electrons have too high energies for efficient ionization, and increasing the voltage means that the amount of electron impact ionization will decrease again. However, at these high voltages, other processes such as argon ion and atom impact ionization come into play. The cross-sections of these processes reach their maximum at much higher energies (1000 eV and more) [71], allowing a further increase in current with rising voltage. Indeed, in the model described by Bogaerts *et al.* in 1995 [24], argon ion and atom impact ionization were not yet incorporated, and the correct current–voltage behavior could therefore not yet be predicted.

Exact quantitative agreement between the experimental and calculated current–voltage relations is, however, not yet reached (note the different scales on the y-axis), and can, in fact, at present not yet be expected. Indeed, the pressure can in principle not directly be measured in the VG 9000 glow discharge cell. In order to obtain current–voltage characteristics at specific pressures, the pressure was measured with a thermocouple [72], but these measured pressures in Figure 6.3 are subject to uncertainties. More recently, Venzago and co-workers have proposed a pressure measurement in the VG 9000 cell, with the aid of a Baratron capacitance manometer, which might be more reliable [73]. Moreover, the exact gas temperature in the discharge cell is not known. We assumed a gas temperature of 300–380 K (rising with pressure and voltage), because this is a reasonable value, in so far as it is expected that the gas temperature in the discharge is higher than room temperature at the present conditions, and it yields realistic current values. For the sake of simplicity, we assumed uniform values throughout the discharge. However, our gas heating calculations [35] predict some temperature gradients in the discharge (see below). Since small variations in the gas temperature had already a significant effect on the electrical current (e.g. 30% variation in gas temperature yields a change in electrical current by as much as 100%) [46], the quantitative results of the model have to be considered with caution.

Since the gas temperature is such a critical input parameter, we have tried to calculate this value for a dc glow discharge with the heat transfer equation. The resulting two-dimensional distributions, both for the VG 9000 GDMS cell and a Grimm-type cell, are presented in Figure 6.4, for typical dc GDMS and GD-OES operating conditions. The cathode is found at the left end of both parts of the figure, whereas the other borders of the figure represent the anode cell walls (grounded). The black rectangles in Fig. 6.4a symbolize the insulating ring (from $z = 0$ to 0.05 cm) and anode front plate (from $z = 0.05$ to 0.15 cm). In Figure 6.4b, not the entire Grimm cell geometry, but only the first 1.5 cm from

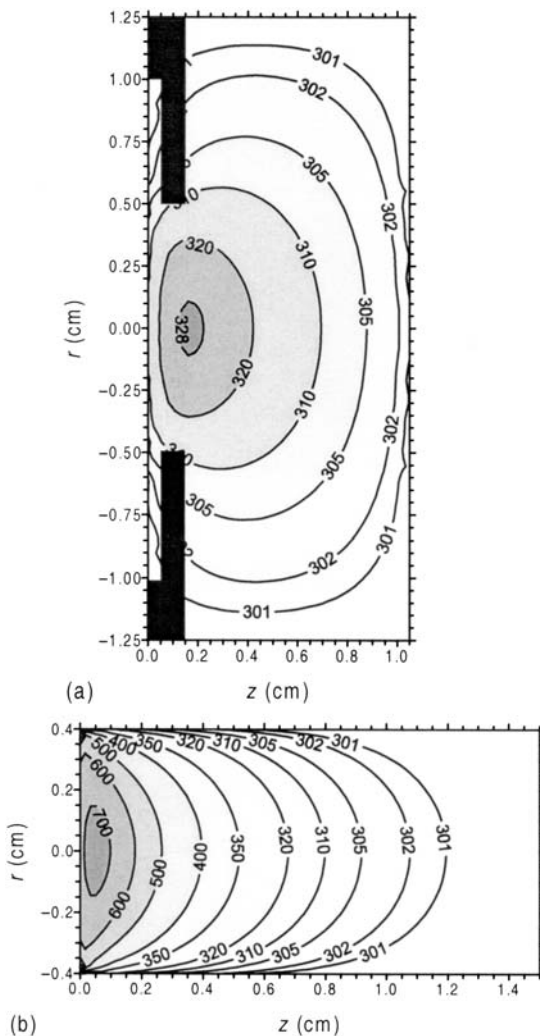


Figure 6.4 Calculated two-dimensional gas temperature profiles in a dc discharge, (a) in the VG 9000 cell at 1000 V, 0.5 Torr and 3.5 mA and (b) in a Grimm-type cell at 800 V, 3 Torr and 52 mA. The cathode is found at the left end of both parts, whereas the other borders of the figures represent the anode cell walls (grounded). The black rectangles in (a) symbolize the insulating ring (from $z = 0$ to 0.05 cm) and anode front plate (from $z = 0.05$ to 0.15 cm). In (b), not the entire cell geometry but only the first 1.5 cm from the cathode is shown, because the gas heating was found to be negligible at larger distances from the cathode. Reproduced by permission of the American Institute of Physics from Bogaerts, A., Gijbels, R., and Serikov, V. V., *J. Appl. Phys.*, 2000, **87**, 8334–8344

the cathode is shown, because the gas heating was found to be negligible at larger distances away from the cathode. It is clear that the temperature in the VG 9000 cell rises only moderately, whereas a considerable increase in gas temperature was computed for the Grimm-type cell. The reason is, of course, that the Grimm-type cell is operated at much higher electrical powers, yielding a much higher power input into the argon gas. It should be mentioned, however, that the calculated gas temperatures are still subject to considerable uncertainties, owing to some input parameters in the heat transfer equation which are unknown, such as the thermal accommodation coefficient at the cell walls, and the cathode temperature. The latter affects the calculated gas temperature to a large extent. Hence this seems to shift the problem of unknown gas temperature to the problem of unknown cathode temperature. The situation might be further complicated when the glow discharge cell is cooled with liquid nitrogen, as is the case with the VG 9000 cell. Nevertheless, the spatial distributions of the calculated gas temperatures, and also their qualitative rise with respect to the cathode temperature, are expected to be fairly realistic.

The importance of the gas temperature as input in the model has also been demonstrated [27] for a microsecond-pulsed glow discharge. Indeed, it was found that when the gas temperature was assumed to be constant in time, the model could not predict the experimental electrical current and power behavior as a function of time in the microsecond-pulsed discharge. Figure 6.5 shows the applied voltage, and also the resulting electrical current and power, and the gas temperature assumed in the model, as a function of time during and after the pulse. The values used as input (i.e. voltage and gas temperature) or calculated (i.e. current and power) in the model are represented by the solid lines, whereas the experimental data are plotted with dashed lines. The gas pressure was measured to be 3 Torr and assumed to be constant in time. A voltage of 1500–2000 V is applied during 10 μs , and then it drops exponentially, reaching zero at about 40 μs after initiation of the pulse (see Figure 6.5a). The electrical current (Figure 6.5b), and hence also the power (Fig. 6.5c), appear to rise significantly to values of almost 1 A and 1.5 kW, respectively, at 1.5–2 μs , and then they drop almost as rapidly to ‘plateau values’ of about 100 mA and 200 W, respectively, which are more or less maintained from 4 to 10 μs . After the pulse, the current and power decay to zero at about 20 μs after the start of the pulse. This experimental behavior of current and power could only be predicted with our model if a time-varying gas temperature (see Figure 6.5d) was assumed. Indeed, at the start of the pulse, the gas is at room temperature. However, the gas temperature will increase rapidly as a function of time, owing to the high electrical power, and hence high power input into the argon gas. When the power has dropped to a plateau value of ca 200 W, the gas temperature will not increase further, but on the other hand, the power is still high enough to maintain the high gas temperature. Only when the power has dropped further, after the pulse, does the gas temperature decrease exponentially. It was found to reach room temperature again around 200 μs [27],

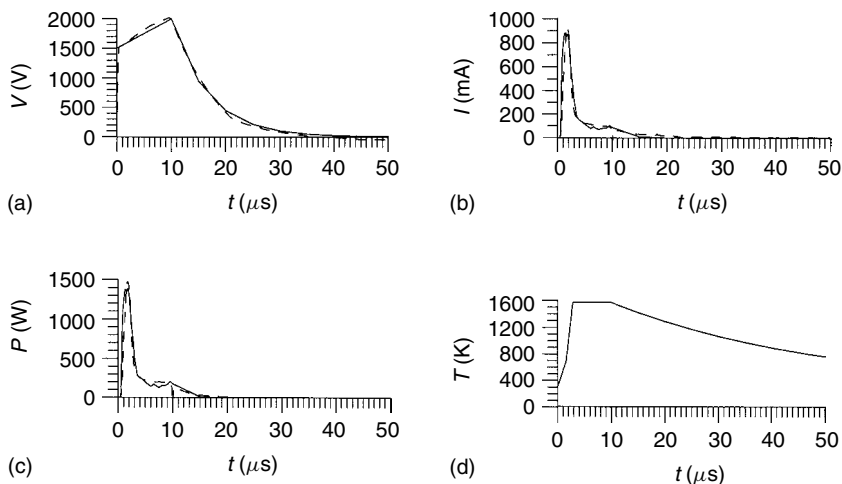


Figure 6.5 Calculated electrical characteristics as a function of time during and after the pulse, in a microsecond-pulsed glow discharge at a gas pressure of 3 Torr, an applied voltage of 2 kV, a pulse width of 10 μs and a pulse repetition frequency of 200 Hz. The data used as input or calculated in the model are represented by solid lines: (a) applied voltage assumed in the model; (b) calculated electrical current; (c) calculated electrical power; (d) gas temperature assumed in the model. The experimental data in (a)–(c) are plotted with dashed lines

hence well before the next pulse will be applied, at the pulse repetition frequency of 200 Hz used in the experiment. The time evolution of the gas temperature presented in Figure 6.5d was used as a kind of fitting parameter in our model, to obtain reasonable agreement with the experimental behavior of voltage, current and power as a function of time. Nevertheless, the assumed values have also been checked, at least qualitatively, with a time-dependent heat transfer equation, and it was illustrated that the fitted time evolution of the gas temperature was indeed realistic [27].

In our model for rf glow discharges, not the voltage but the power is used as an input value in addition to the gas pressure and temperature. The applied voltage at the rf electrode and the dc bias voltage are then calculated, based on the conditions that (i) the power dissipated by electrons and ions in the discharge should be equal to the applied rf power, (ii) the product of rf voltage and current, averaged over time, should be equal to the applied rf power and (iii) the total current towards the rf electrode, integrated over one rf cycle, should be zero, as it is imposed by the capacitive coupling of both electrodes. Figure 6.6a shows the calculated voltage at the rf electrode as a function of time in the rf cycle (thick solid line), at an electrical power of 37 W and a gas pressure of 5 Torr. The voltage is negative during most of the rf-cycle, except around $\omega t = \pi/2$. This is attributed to the highly negative dc bias voltage of -519 V (see thin

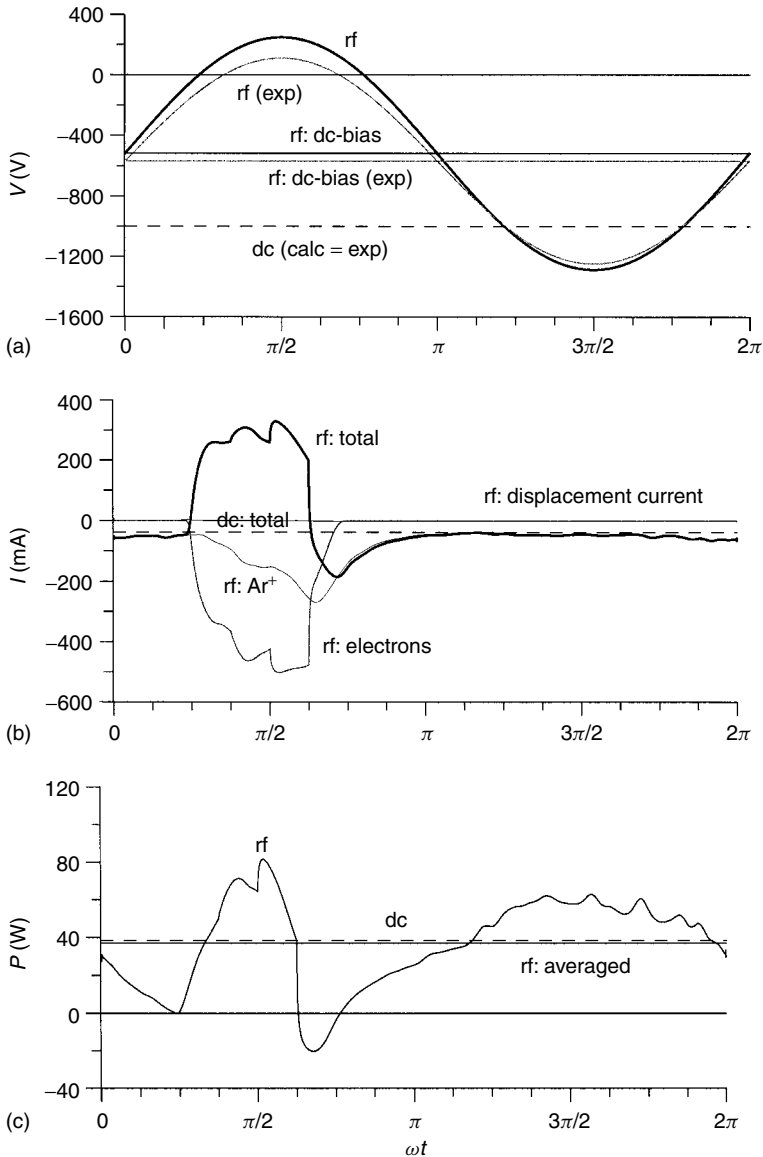


Figure 6.6 Calculated electrical characteristics as a function of time in the rf cycle, in the rf discharge (solid lines) and in a dc discharge (constant in time; dashed lines), at a gas pressure of 3 Torr and an electrical power of 37–38 W. (a) Voltage (the experimental values are also presented, in gray lines); (b) current, including the contributions of ion and electron current and displacement current at the rf electrode, in the rf case (in thinner lines); (c) electrical power. Reprinted from Bogaerts, A., and Gijbels, R., *Spectrochim. Acta, Part B*, 2000, **55**, 263–278, with permission of Elsevier Science

solid line), which arises from the large difference in size between the rf-powered and grounded electrode, in combination with the capacitive coupling of both electrodes. The experimental rf voltage as a function of time and the experimental dc bias voltage are also illustrated in Figure 6.6a (gray lines) [49]. It appears that our calculated amplitude for the rf voltage was slightly too high and our dc bias voltage was too low, but in general, the agreement with experiments was considered satisfactory. The voltage obtained in the dc case, for the same values of power and pressure, is also presented in Figure 6.6a (dashed line). There was excellent agreement with the experimental value, as demonstrated in the figure.

The electrical current flowing towards the rf electrode is plotted against time in the rf cycle in Figure 6.6b (thick solid line), together with the individual contributions of electron and argon ion currents and the rf displacement current at the rf electrode. The latter arises from the moving of the rf sheath as a function of time, which gives rise to a variation of charge in the sheath as a function of time, and hence to an electrical current (since $I = dq/dt$, where I is the current, q is the charge and t is the time). It appears that for the conditions under study here, the displacement current makes only a minor contribution to the total current, as is expected since the rf sheath does not move considerably with time owing to the large dc bias voltage. It should be mentioned, however, that the displacement current can play a dominant role in rf discharges used for technological applications [74,75], which are mostly characterized by two electrodes of similar size and which operate at lower pressures. It is clear from Figure 6.6b that the total electrical current at the rf electrode is mainly due to argon ions. Only around $\omega t = \pi/2$, where the rf voltage is positive, is a large electron current observed at the rf electrode. It contributes to the total current with an opposite sign, so that the total current to the rf electrode, integrated over the rf cycle, is equal to zero, as is imposed by the capacitive rf coupling. The current in the dc discharge, under the same conditions of power and pressure, is also presented in Figure 6.6b (dashed line; constant in time). It is slightly lower than the rf current, which is of course necessary when the voltage is higher and the electrical power is the same.

The product of voltage and current gives rise to the electrical power, which is presented as a function of time in Figure 6.6c. The time-averaged value is also illustrated, in addition to the dc value (dashed line; constant in time). The fact that these values are equal to the input values in the model illustrates that the time evolution of voltage and current is correctly calculated in our model.

6.3.2 POTENTIAL AND ELECTRIC FIELD DISTRIBUTIONS

As mentioned before, the model is completely self-consistent, i.e. the potential and the electric field distributions used to calculate the trajectories of the charged plasma species in the Monte Carlo models are in their turn obtained from the

calculated densities of these plasma species, via Poisson's equation in the slow electron–argon ion fluid model.

In Figure 6.7, the two-dimensional potential distribution is illustrated for a dc discharge, calculated for the VG 9000 cell at 1000 V, 0.5 Torr argon gas pressure and 3.5 mA current. The potential is equal to -1000 V at the cathode and increases very rapidly towards zero at about 0.24 cm from the cathode. This position where the potential crosses zero is defined as the interface between cathode dark space (CDS) and negative glow (NG). In the NG, the potential is slightly positive (approximately 10 V for these discharge conditions and cell geometry). This value is called the 'plasma potential'. It drops again to zero at the anode walls, which are grounded. The value of the plasma potential does not depend

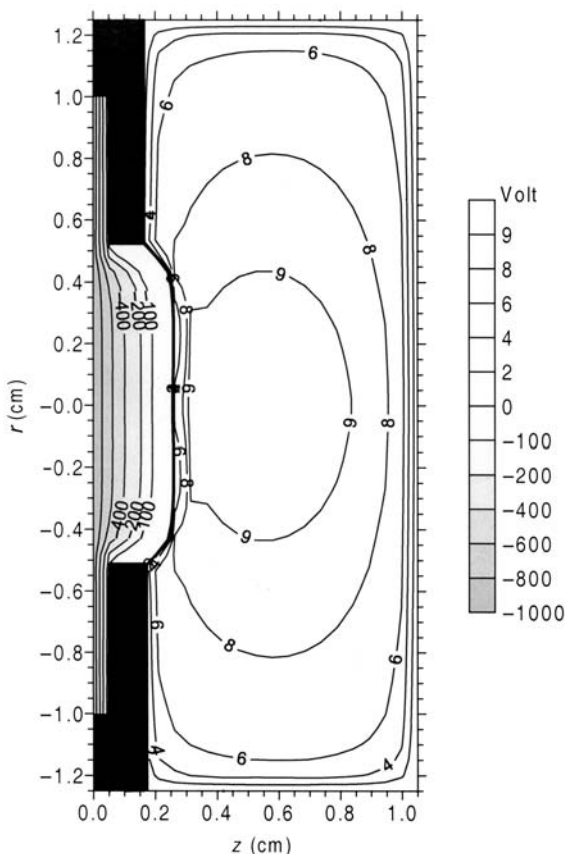


Figure 6.7 Calculated two-dimensional potential distribution in a dc discharge, in the VG 9000 cell at 1000 V, 0.5 Torr and 3.5 mA. Reprinted with permission from Bogaerts, A., Gijbels, R., and Goedheer, W. J., *Anal. Chem.*, 1996, **68**, 2296–2303, Copyright 1996 American Chemical Society

strongly on the discharge conditions, but it varies with the cell dimensions, ranging from about 1 V in large cells (diameter of a few centimeters) [56] to several tens of volts in small cells (diameter of a few millimeters) [47]. The length of the CDS, on the other hand, does not depend on the cell dimensions, but it varies strongly with the discharge conditions [33,46,47]. It rises with decreasing voltage and more significantly with decreasing pressure, ranging from about 0.5 mm at 5.25 Torr [47] to almost 8 mm at 0.375 Torr [33].

The electric field distribution can easily be derived from the potential distribution, by taking the spatial gradient. This leads to a strongly negative electric field in the CDS, which is responsible for the significant energy gain of electrons and ions in this region. In the NG, a weak electric field, both positive and negative, depending on the position, is found.

The potential and electric field distributions in the rf- and in the microsecond-pulsed discharge were calculated to be very similar to the dc potential distributions. They are characterized by a strongly negative value at the cathode (or rf electrode), a steep drop to zero in the CDS (or rf sheath) and a nearly constant, slightly positive value in the NG (or bulk plasma) [26,27,31]. Only the potential distribution around $\omega t = \pi/2$ in the rf discharge is significantly different [26,31]. This means that the potential is clearly positive at the rf electrode and has a value of about 250 V (see Figure 6.6a). It drops gradually to zero at the grounded cell walls. This gives rise to a considerable electric field in the bulk plasma around this time.

6.3.3 DENSITIES AND LEVEL POPULATIONS OF THE PLASMA SPECIES

Figure 6.8 presents the two-dimensional argon ion density profiles, for Ar^+ , Ar^{2+} and Ar_2^+ ions, in the dc case, at the same discharge conditions and cell geometry as in Figure 6.7 [32]. For all three ionic species, the densities are low and fairly constant in the CDS, but they increase rapidly in the NG and reach a maximum at about 5 mm from the cathode. They decrease again to low values at the anode walls. Comparing the absolute values in the three figures tells us that the $\text{Ar}^{2+}/\text{Ar}^+$ and $\text{Ar}_2^+/\text{Ar}^+$ ratios are of the order of a few percent. This appeared to be the case for all discharge conditions investigated [32]. Moreover, the ratios of the fluxes of these ionic species at the anode backwall, where the exit slit is located in the cell of the VG 9000 mass spectrometer, were also found to be of the order of 1–10%. This is in reasonable agreement with measured intensity ratios in the glow discharge mass spectrum for $\text{Ar}^{2+}/\text{Ar}^+$ and $\text{Ar}_2^+/\text{Ar}^+$, as shown in Figure 6.9 [76].

The density of slow electrons (not shown here) is characterized by nearly the same profile as the Ar^+ ion density profile, except that it is zero in the CDS. This gives rise to a positive space charge in the CDS and nearly charge neutrality in the NG, which results in the typical potential distribution shown in Figure 6.7.

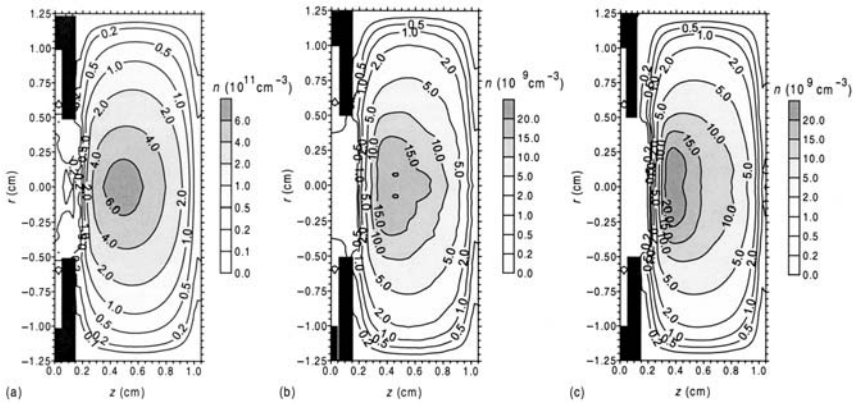


Figure 6.8 Calculated two-dimensional density profiles of the (a) Ar^+ , (b) Ar_2^+ and (c) Ar_2^+ ions in a dc discharge, in the VG 9000 cell at 1000 V, 0.5 Torr and 3.5 mA. Reproduced by permission of the American Institute of Physics from Bogaerts, A., and Gijbels, R., *J. Appl. Phys.*, 1995, **78**, 6427–6431

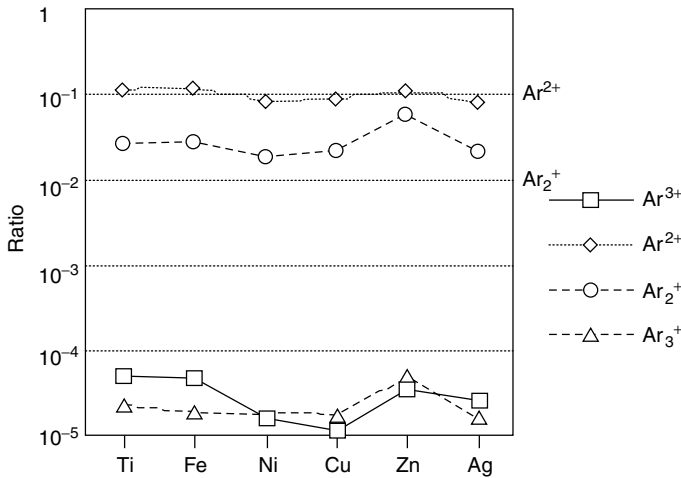


Figure 6.9 Measured intensity ratios in the VG 9000 glow discharge mass spectrum (dc discharge), for different Ar ionic species relative to Ar^+ ions, for different cathode materials [76]. Reproduced by permission of the American Institute of Physics from Bogaerts, A., and Gijbels, R., *J. Appl. Phys.*, 1995, **78**, 6427–6431

To check our calculation results for the electron densities, we performed Langmuir probe measurements in a dc Grimm-type glow discharge, under typical GD-OES discharge conditions [54]. It should be mentioned that the argon ion densities presented in Figure 6.8 were obtained at typical GDMS conditions, and that GD-OES operates generally at clearly higher pressures and currents

than GDMS, namely 3–7 Torr compared with ca 1 Torr gas, and 10–50 mA compared with 1–10 mA electrical current. Hence higher electron densities are therefore expected at the GD-OES conditions. In Figure 6.10, the electron densities, calculated for the Grimm-type glow discharge, and taken at the maximum of their profile (solid lines, left axis), are compared with the experimental values for the same cell (dashed lines, right axis). The results are in satisfactory agreement, in so far as both calculated and experimental values rise to nearly the same extent with voltage and pressure. Quantitatively, we found a factor of about two difference (note the different scales on the y-axes). This is, however, still reasonable because it is well below the expected errors of both the model calculations (e.g. uncertainties in input data, such as gas pressure and temperature and collision cross-sections; small variations in these input data can yield significant variations in the calculation results) and the experimental data (e.g. possible disturbance of the plasma by the Langmuir probe, possible contamination due to deposition on this probe, approximations in the Langmuir probe theory).

Figure 6.11a shows the calculated two-dimensional density profile of the sputtered cathode atoms in the case of tantalum (the reason for taking tantalum as an example is given below), for a six-way cross glow discharge cell (approximated to be cylindrically symmetrical) and dc conditions of 1000 V, 1 Torr and ca 2 mA [55]. The cathode is found at the left-hand side of the figure, whereas the other borders of the figure are anode walls. The tantalum atom density reaches

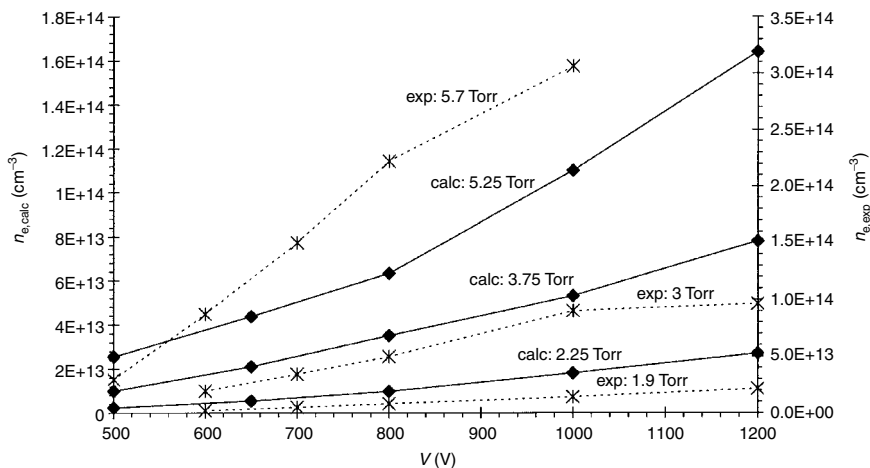


Figure 6.10 Electron number densities (at the maximum of their profiles) in a dc Grimm-type glow discharge cell, as a function of voltage at several pressures. The values calculated with our model [47] are depicted with the solid lines (left axis) whereas the Langmuir probe results [54] are represented with the dashed lines (right axis; note the different vertical scale). Reproduced from Bogaerts, A., and Gijbels, R., *Spectrochim. Acta, Part B*, 1998, **53**, 437–462, with permission of Elsevier Science

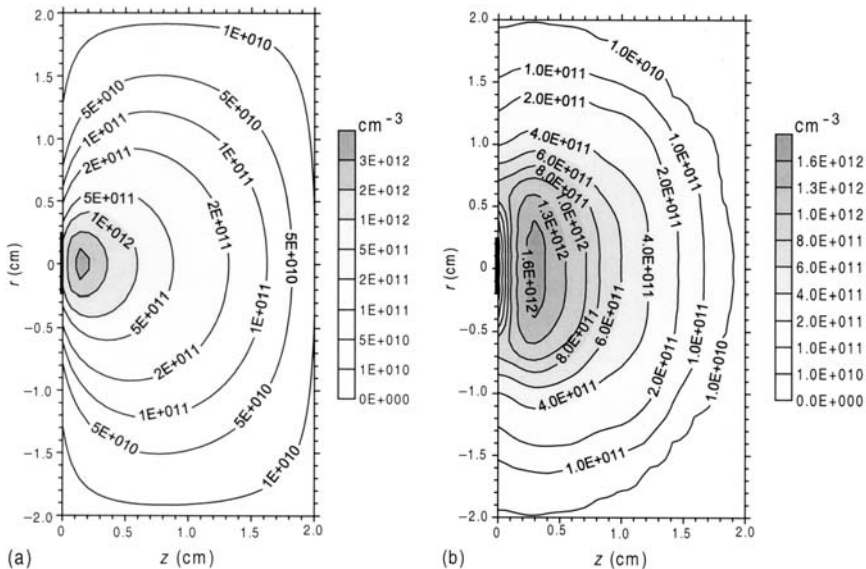


Figure 6.11 Two-dimensional density profiles of the sputtered tantalum atoms in a cylindrically symmetrical (six-way cross) glow discharge cell, at the dc conditions of 1000 V, 1 Torr and 2 mA, (a) calculated with our model and (b) measured with laser induced fluorescence (LIF). The black line at $z = 0$ indicates the cathode; the anode is formed by the other borders of the figure. Reprinted from Bogaerts, A., Wagner, E., Smith, B. W., Winefordner, J. D., Pollmann, D., Harrison, W. W., and Gijbels, R., *Spectrochim. Acta, Part B*, 1997, **52**, 205–218, with permission of Elsevier Science

a maximum at ca 1 mm from the cathode and decreases towards the cell walls. It is of the order of 10^{12} cm^{-3} under the discharge conditions under investigation, which is about four orders of magnitude lower than the argon gas atom density at 1 Torr.

The tantalum atom density has also been measured in the same cell and at the same discharge conditions as in the model, both by laser induced fluorescence (LIF) and by a combination of LIF, to obtain the relative profile, and atomic absorption spectrometry (AAS) to put an absolute number on this profile. Tantalum was used as the cathode material, because it has fluorescent lines which are in the suitable wavelength range of the laser available for the experiment [55]. The result of the LIF measurements is depicted in Figure 6.11b; the combined LIF + AAS experiments yielded values which were generally a factor of three lower [55]. The latter indicates that the experimental uncertainties can be fairly large, i.e. at least a factor of three. Comparison of Figure 6.11a and b shows that the calculated and measured tantalum atom densities are in fairly good agreement with each other. The different behavior near $z = 0$ is due to an approximation in the model, i.e. the cell used for the experiments was open at $z = 0$ (the cathode was mounted on an insertion probe), whereas the model assumed a wall at $z = 0$.

Quantitatively, the results are in very good agreement; more precisely, the calculated values lie between the LIF and the combined LIF + AAS results. Hence we can conclude that the calculated and experimental results are equal to each other within the experimental uncertainty.

The corresponding tantalum ion density, calculated for the same cell and under the same dc discharge conditions, is presented in Figure 6.12a [55]. We found that the tantalum ion and argon ion densities are characterized by the same relative profile, but the tantalum ion density is more than two orders of magnitude lower. However, as mentioned above, the ratio of tantalum atom to argon atom density was about 10^{-4} , which indicates that the tantalum atoms are more efficiently ionized in the glow discharge than the argon atoms. Indeed, in addition to electron impact ionization, the tantalum atoms can also be ionized by Penning ionization (due to argon metastable atoms) and by asymmetric charge transfer with argon ions, and the last two processes are absent for the argon atoms. Under the discharge conditions under consideration, the degree of ionization was calculated to be of the order of 10^{-5} – 10^{-3} for argon, whereas for the sputtered atoms (tantalum, copper, etc.) typical values of about 10^{-4} – 5×10^{-2} were obtained [46,47,55].

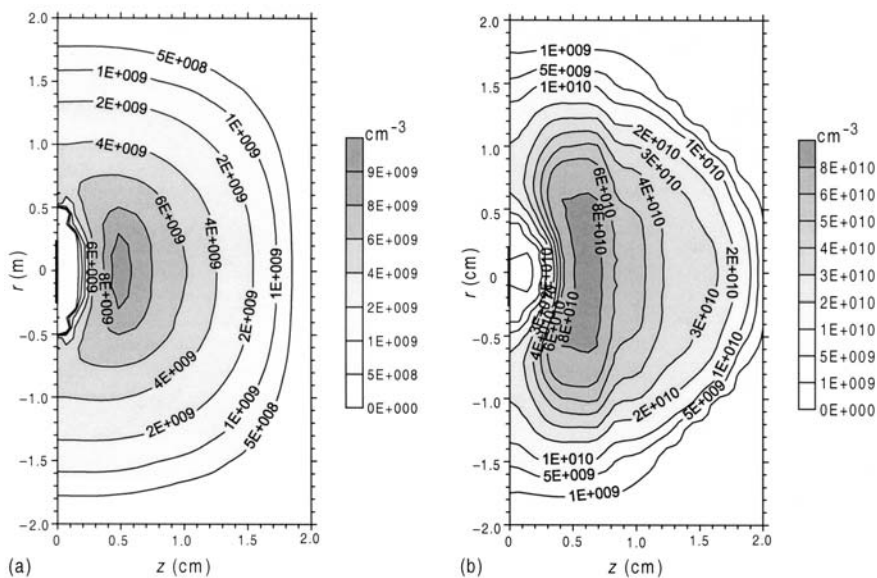


Figure 6.12 Two-dimensional density profiles of the tantalum ions in a cylindrically symmetrical (six-way cross) glow discharge cell, at the dc conditions of 1000 V, 1 Torr and 2 mA, (a) calculated with our model and (b) measured with laser induced fluorescence (LIF). Reprinted from Bogaerts, A., Wagner, E., Smith, B. W., Winefordner, J. D., Pollmann, D., Harrison, W. W., and Gijbels, R., *Spectrochim. Acta, Part B*, 1997, **52**, 205–218, with permission of Elsevier Science

To check the results of the modeling, the tantalum ion density has also been measured by LIF, and the result is shown in Figure 6.12b [55]. Calculated and experimental results qualitatively are in good agreement, but the quantitative agreement is poor. Indeed, the calculated results are a factor of almost 10 smaller than the experimental values. Since the tantalum atom densities were in fairly good agreement, this may indicate that the calculated ionization is too low, either because an important ionization mechanism is not incorporated, or because the rate coefficients for Penning ionization and asymmetric charge transfer used in the calculations are too low. The latter can indeed be the case, because these rate coefficients are very difficult to find in the literature, and the values we assumed are subject to large uncertainties. On the other hand, the experimental results are also prone to some errors, as illustrated already for the tantalum atoms (see above). Probably, the observed discrepancy is a combination of uncertainties and approximations in the model and in the experiment (e.g. conversion of LIF intensities into ion number densities). After all, the difference of a factor of 10 is maybe not so bad if one realizes that, to the authors' knowledge, such model calculations and experiments have never been carried out and confronted before.

Not only ground-state densities have been calculated with the models, also the level populations for various excited states can be obtained. Figure 6.13 illustrates the level population profiles (in one dimension) of the four lowest excited

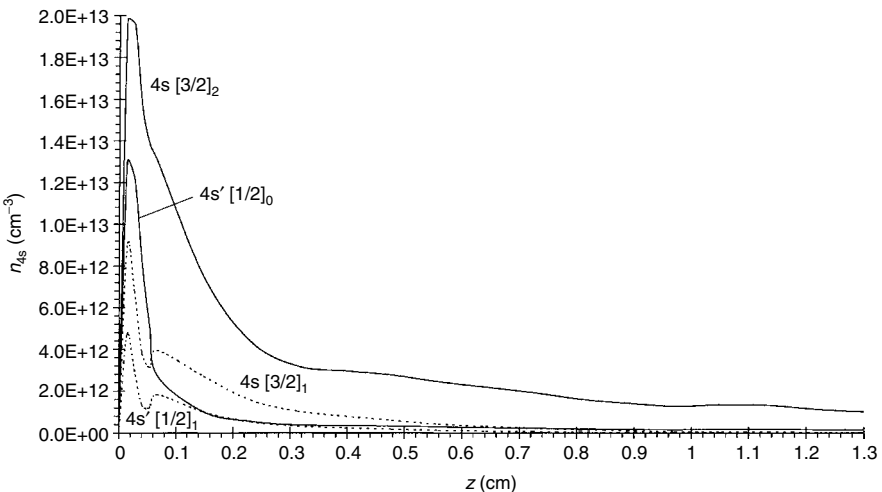


Figure 6.13 Calculated one-dimensional density profiles (at the cell axis) of the argon atoms excited to the four 4s levels, in a dc Grimm-type glow discharge cell, at 800 V, 3.75 Torr and 28 mA (solid lines, 4s metastable levels; dashed lines, 4s resonant levels). Reprinted from Bogaerts, A., and Gijbels, R., *Spectrochim. Acta, Part B*, 1998, **53**, 437–462, with permission of Elsevier Science

states of argon atoms, i.e. the 4s metastable and resonant levels, computed for the case of a Grimm-type glow discharge, under the dc conditions of 3.75 Torr, 800 V and 28 mA [47]. Only the first 1.3 cm is shown, where the densities were found to be appreciable. The two metastable levels ($4s[3/2]_2$ and $4s'[1/2]_0$; solid lines) have a slightly higher density than the two resonant levels ($4s[3/2]_1$ and $4s'[1/2]_1$; dashed lines). This is as expected, since the resonant levels can decay to the ground state by emission of radiation, whereas the metastable levels cannot decay (optically forbidden transitions). However, a large fraction of the emitted radiation from the resonant levels will again be absorbed by the ground state, leading to re-excitation. In practice, only a fraction of about 10^{-3} – 10^{-4} of the emitted photons can really escape from the plasma under the discharge conditions under investigation [47], so that the 4s resonant levels also have a fairly high population density in comparison with other higher excited levels [47]. All 4s levels are characterized by a pronounced peak adjacent to the cathode, which is due to fast argon ion and atom impact excitation [38,47]. Indeed, the latter processes are important close to the cathode where the ions and atoms reach high energies, especially at the high voltages typical of analytical glow discharges. One-dimensional density profiles of the argon $4s[3/2]_2$ metastable levels have been measured in a Grimm-type source with AAS by Ferreira *et al.* [77]. They also found a pronounced maximum adjacent to the cathode, followed by a rapid decrease. Depending on the discharge conditions, a second maximum sometimes was observed at about 4 mm from the cathode. A similar second maximum appeared sometimes in our modeling results (e.g. [52,53]) depending on the discharge conditions and cell geometry. The value of the maximum in the experimental density profiles of Ferreira *et al.* [77] was also of the order of 10^{13} cm $^{-3}$, which is in excellent agreement with the results of our calculations. In Figure 6.14 the level populations for various excited copper atom and ion levels, at the maximum of their profiles, are plotted against the excitation energy of these levels, for the same dc Grimm-type conditions as in Figure 6.13 [42]. Since some of the excited levels were grouped together into effective levels (see above) with hence a much larger statistical weight, we divided the level populations by the corresponding statistical weights, to exclude this effect. It is clear that the ground-state densities of both copper atoms and ions are higher than the excited level populations, and the latter generally decrease with excitation energy. It appears that the $\text{Cu}^+ 3d^9 4p \ ^3P_2$ level is exceptionally high compared with the other excited levels. The reason is that this level can be selectively excited by asymmetric charge transfer with argon ions, owing to good energy overlap [42]. The latter is also experimentally demonstrated, since the lines originating from this level are extremely high in comparison with other emission lines [78], which validates our calculation results.

Finally, it should be mentioned that the densities for the various plasma species calculated for an rf- and a microsecond-pulsed discharge were found to be similar to those for dc discharges [26,27,31,39,43]. The density profiles are more or

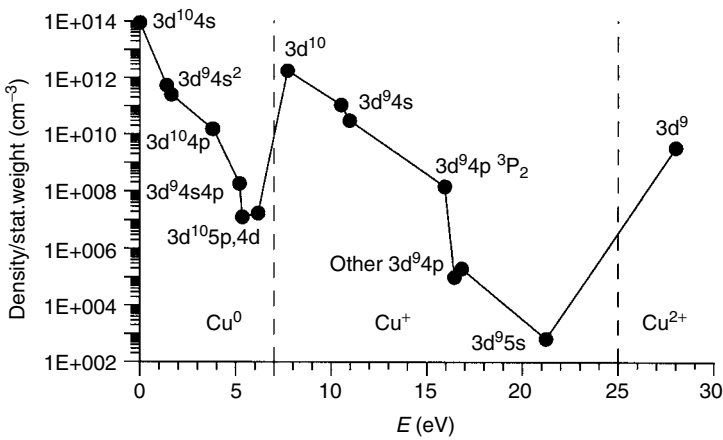


Figure 6.14 Calculated level populations at the maximum of their profiles, divided by the statistical weights of the levels, for various Cu^0 and Cu^+ levels and also for the Cu^{2+} ions, as a function of their excitation energy, in a dc Grimm-type glow discharge cell, at 800 V, 3.75 Torr and 28 mA [42]

less the same; only the absolute values can differ somewhat, depending on the discharge conditions.

6.3.4 ENERGIES OF THE PLASMA SPECIES

As mentioned before, the fluid models and collisional-radiative models are applied to the plasma species which are assumed to be in thermal equilibrium with the electric field, such as the argon atoms and copper atoms and ions in the ground state and also in excited levels, and also the slow electrons in the NG. Hence no equations are included to calculate the energy of these species, because they are assumed to have thermal energy. The plasma species which are not in hydrodynamic equilibrium, on the other hand, are described explicitly with a Monte Carlo model, and the energy distributions of these species can be computed.

Figure 6.15 presents the flux energy distribution of the electrons, at various positions from the cathode, in the VG 9000 cell at 1000 V, 0.5 Torr and 3.5 mA (dc discharge)[15,46]. The electrons leave the cathode ($z = 0$, not indicated in the figure) with low energy (assumed to be 4 eV on average [79]), but they gain energy from the electric field as they move in the CDS towards the NG. At the same time, however, they lose energy owing to collisions, so that their energy distribution spreads out from zero energy toward the maximum energy, with all energy values being more or less of equal probability. At the CDS–NG interface, being 0.24 cm away from the cathode (see Figure 6.7), this maximum energy is equal to the total discharge voltage of 1000 V. In the NG, however, the electrons

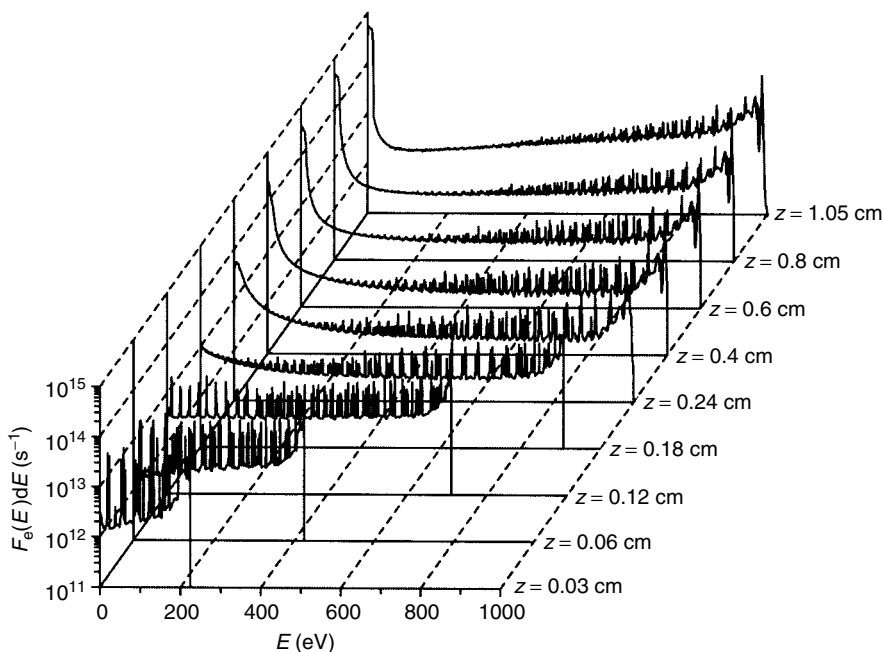


Figure 6.15 Calculated flux energy distribution of the electrons, as a function of distance from the cathode, in the VG 9000 cell, under the dc conditions of 1000 V, 0.5 Torr and 3.5 mA. Reproduced by permission of the Royal Society of Chemistry from Bogaerts, A., and Gijbels, R., *J. Anal. At. Spectrom.*, 1998, **13**, 945–953

do not gain much energy any longer from the weak electric field, but they lose their energy very efficiently owing to collisions. Hence the energy distribution shifts towards lower energies. Nevertheless, even at the end of the discharge cell, there is still a peak at maximum energy, which indicates that there are still some electrons which have traversed the entire discharge without collisions, under the discharge conditions under investigation. The present flux energy distribution of electrons is in reasonable qualitative agreement with experimental results obtained with a retarding field analyzer in the NG of a helium glow discharge at pressures of 10–15 Torr and a few hundred volts discharge voltage [80]. Indeed, it was found that most electrons have low energies, but a small peak is observed at maximum energy. This shows that our calculation results can be considered to be realistic.

In contrast to the electron flux energy distribution, the energy distribution of the argon ions is not characterized by a peak at maximum energy. This appears from Figure 6.16a, where the calculated flux energy distribution of the argon ions is depicted for several distances from the cathode in the CDS, under the same discharge conditions as in Figure 6.15 [15,46]. The argon ions are assumed

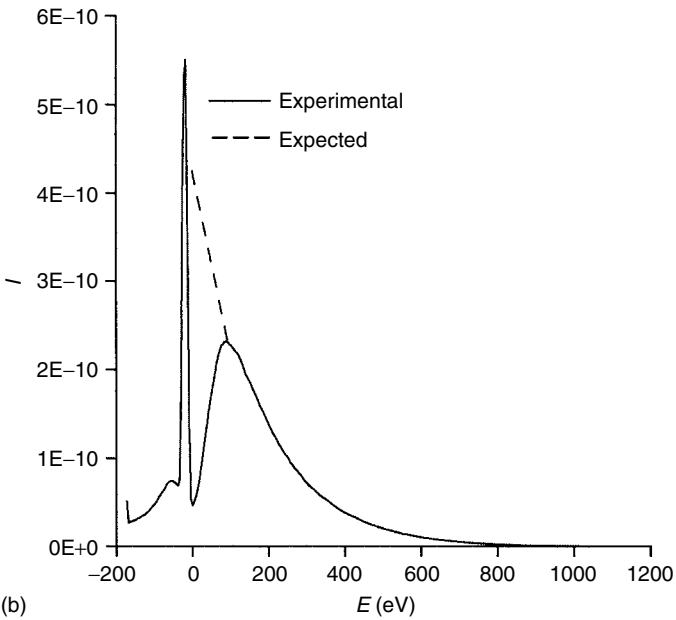
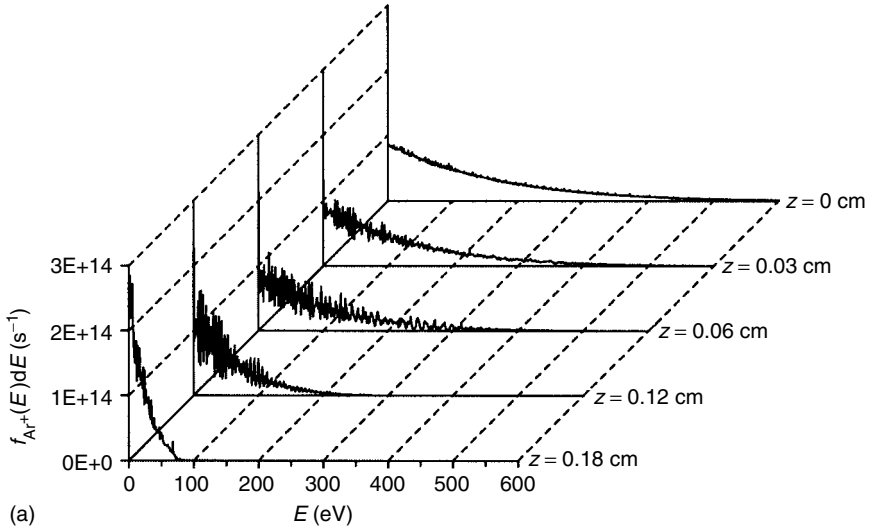


Figure 6.16 Flux energy distributions of the argon ions in a dc discharge, in the VG 9000 cell: (a) calculated in the CDS, as a function of distance from the cathode, for 1000 V, 0.5 Torr and 3.5 mA; (b) measured at the cathode, at 1000 V and 3 mA (pressure unknown). Reproduced by permission of the Royal Society of Chemistry from Bogaerts, A., and Gijbels, R., *J. Anal. At. Spectrom.*, 1998, **13**, 945–953

to have thermal energies in the NG, but when they enter the CDS they gain energy from the electric field. However, they also lose energy owing to collisions. It appears that the collisions of the ions, which mainly are elastic scattering and symmetric charge transfer collisions, are more frequent and more efficient for losing energy than the collisions of the electrons (mainly ionization and excitation), because most argon ions have fairly low energies when they arrive at the cathode ($z = 0$ cm).

The energy distribution of the argon ions bombarding the cathode has been measured in a similar cell, in reversed geometry so that the ions are sampled through a hole in the cathode, and under similar discharge conditions to those used for the calculations [58]. These measurements were performed with the VG 9000 double focusing glow discharge mass spectrometer, by keeping the magnetic field constant and varying the acceleration voltage. The results are shown in Figure 6.16b [15,46]. A dip was obtained at low energy and a peak at negative energy, which were probably the results of experimental artifacts; it was suggested that low-energy ions were subject to charge transfer collisions (for which the cross-section is, indeed, larger at low energies) immediately outside the discharge cell, in the acceleration region of the mass spectrometer. This gives rise to some loss for low-energy ions, explaining the dip, because the ions disappear from the energy distribution, as well as some production (i.e. a peak) at negative energy, because these ions have not attained the maximum acceleration voltage. Therefore, the expected 'real' energy distribution is indicated by the dashed line in Figure 6.16b, which agrees qualitatively with the calculated results.

As mentioned earlier in this chapter, the collision processes of the argon ions with thermal argon atoms in the CDS can give rise to the production of 'fast' (i.e. nonthermal) argon atoms, due to exchange of energy. These fast argon atoms can continue in the same direction as the ions, towards the cathode, or they can be scattered in another direction, but at least a fraction of them will be able to arrive at the cathode before again being thermalized owing to collisions. Because these fast argon atoms can, themselves, also create new fast argon atoms due to energy exchange in elastic collisions, the flux of fast argon atoms traveling through the CDS is fairly high. This can be seen in Figure 6.17, where the calculated flux energy distributions of the fast argon atoms in the CDS, at various positions from the cathode, are presented [15,46]. The flux is, indeed, more than an order of magnitude higher than the argon ion flux. The energy distribution qualitatively looks very similar to the argon ion energy distribution, but it is shifted towards lower energies (note that the energy scale is cut at 100 eV), because the argon atoms cannot gain energy from the electric field; they can only lose their energy in collisions.

In addition to the argon ions and fast argon atoms, also the ions of the cathode material travel through the CDS and can bombard the cathode. Figure 6.18a shows the calculated energy distribution of the cathode copper ion flux in the CDS, at various positions from the cathode, for the same discharge conditions

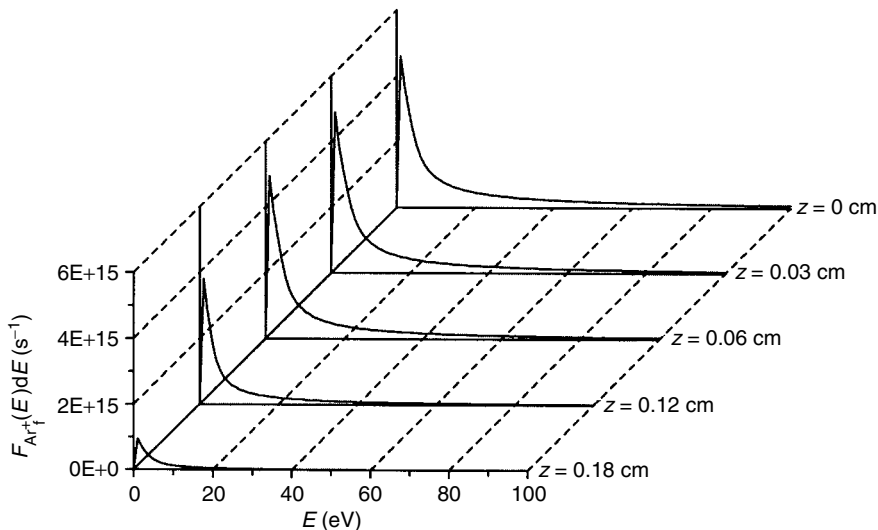


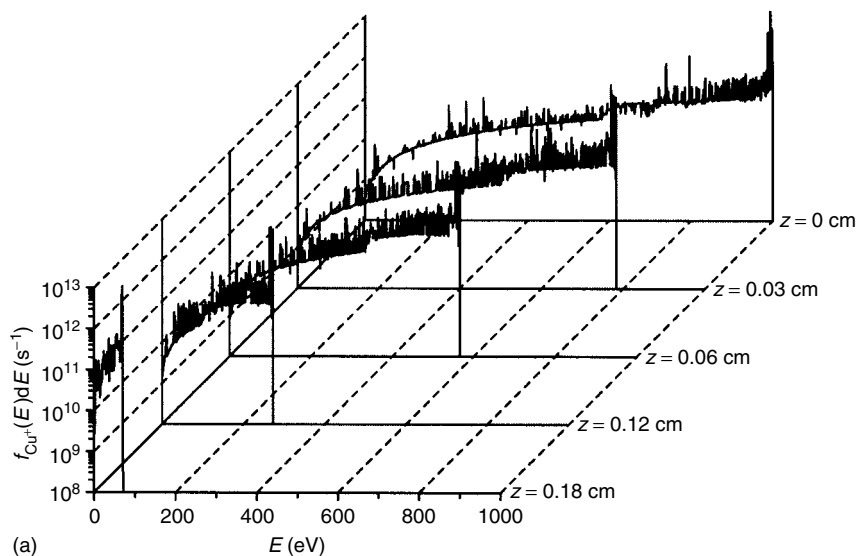
Figure 6.17 Calculated flux energy distribution of the fast argon atoms in the CDS, as a function of distance from the cathode, in the VG 9000 cell, at the dc conditions of 1000 V, 0.5 Torr and 3.5 mA. Reproduced by permission of the Royal Society of Chemistry from Bogaerts, A., and Gijbels, R., *J. Anal. At. Spectrom.*, 1998, **13**, 945–953

as in Figure 6.16 [15,46]. The copper ions also have thermal energy in the NG, where most of them were formed, but when they diffuse into the CDS they gain energy from the electric field and are accelerated towards the cathode. In contrast to the argon ions, they do not lose their energy very efficiently in collisions. Therefore, they are characterized by a pronounced peak at maximum energy.

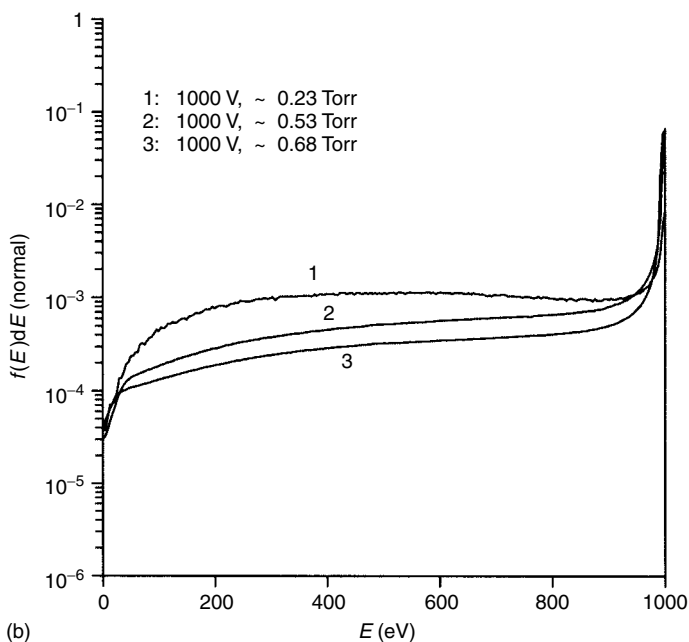
This pronounced peak is also experimentally observed (Figure 6.18b) [58]. These experiments were performed with the same technique as explained above. Since the pressure could actually not be measured inside the glow discharge cell of this mass spectrometer, three estimated pressure values are indicated for the three experimental energy distributions. Exact quantitative comparison therefore cannot be carried out, but qualitative agreement between calculated and experimental results, at least, is reached.

6.3.5 INFORMATION ABOUT COLLISION PROCESSES IN THE PLASMA

Since the Monte Carlo models describe the behavior of the plasma species explicitly, they can give information about the individual collision processes in the plasma. The various collision rates of the plasma species (i.e. ionization, excitation, elastic collisions, charge transfer, etc.) have been calculated as a function of the position in the discharge; the results (in one and in two dimensions) have been



(a)



(b)

Figure 6.18 Flux energy distributions of the copper ions in a dc discharge, in the VG 9000 cell: (a) calculated in the CDS, as a function of distance from the cathode, for 1000 V, 0.5 Torr and 3.5 mA; (b) measured at the cathode, at 1000 V and three pressure values. Reproduced by permission of the Royal Society of Chemistry from Bogaerts, A., and Gijbels, R., *J. Anal. At. Spectrom.*, 1998, **13**, 945–953

presented many times in our previous papers (e.g. [23–27,31,33,38,39,42–47,52]), and will therefore not be repeated here. Instead, some data will be given concerning the relative importance of these processes. Moreover, ionization will be discussed in somewhat more detail, since it is considered to be the most important process in the glow discharge.

Ionization of the argon gas atoms is the process which makes the glow discharge self-sustaining. The ionization occurs mainly by electron impact; at high discharge voltages (ca 1000 V), however, fast argon ion and atom impact ionization play a non-negligible role [33]. Figure 6.19 presents the ionization rates according to these three mechanisms, in the VG 9000 cell under the same dc conditions as in Figure 6.7 [25]. Electron impact ionization is especially important in the NG, whereas fast argon ion and atom impact ionization occur only adjacent to the cathode. Integrated over the entire discharge region, the relative contributions of electron, ion and atom impact ionization were calculated to be typically about 90, 2 and 8%, respectively. Hence electron impact ionization is still clearly dominant, because it can take place throughout the entire discharge, whereas ion and atom impact ionization occur only close to the cathode, where these species can reach high energies. Nevertheless, it was found really necessary to incorporate the latter processes in our models, in order to be able to reproduce the correct current–pressure–voltage relations at high voltages (see the

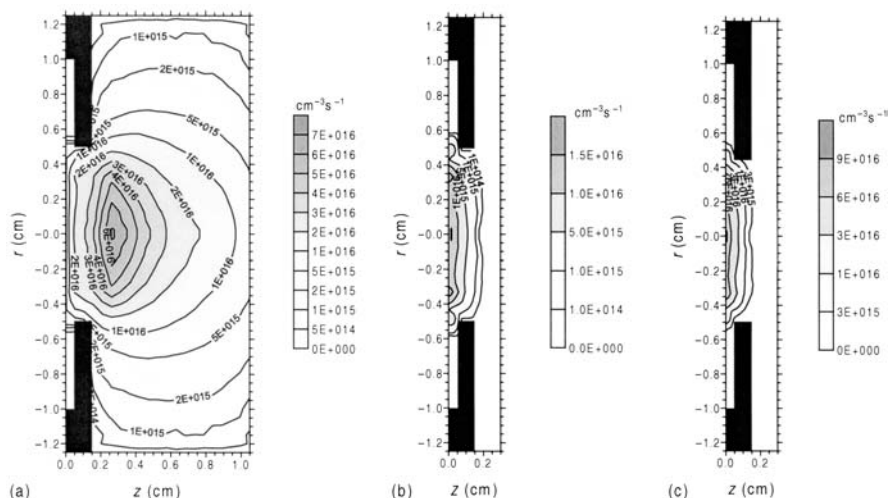


Figure 6.19 Calculated ionization rates of the argon atoms in the VG 9000 cell, under the dc conditions of 1000 V, 0.5 Torr and 3.5 mA: (a) by electron impact ionization in the entire discharge; (b) by fast argon ion impact ionization in the CDS; (c) by fast argon atom impact ionization in the CDS. Reprinted with permission from Bogaerts, A., Gijbels, R., and Goedheer, W. J., *Anal. Chem.*, 1996, **68**, 2296–2303, Copyright 1996 American Chemical Society

discussion concerning Figure 6.3). On the other hand, stepwise electron impact ionization from the metastable levels and metastable atom–metastable atom collisions leading to the ionization of one of the atoms were found to be generally negligible under the discharge conditions under investigation. Their contribution is estimated to be lower than 1%.

As far as the sputtered atoms are concerned, electron impact ionization also takes place, but it is of minor importance compared with Penning ionization and asymmetric charge transfer, as explained above. The ionization rates due to these three mechanisms are presented in Figure 6.20 [45], for the same conditions and cell geometry as in Figure 6.19. Integrated over the total discharge region, the three ionization processes contribute typically about 2–4% (electron impact), 40–85% (Penning ionization) and 10–60% (asymmetric charge transfer). These values depend fairly strongly on the cell geometry, the kind of sputtered material (i.e. for some elements whose ions have no energy levels overlapping with the argon gas ions, asymmetric charge transfer is absent) and the discharge conditions. Penning ionization is clearly dominant at low pressures, whereas asymmetric charge transfer gains importance at higher pressures.

The model predicts also the relative contributions of the different populating and depopulating processes for the argon atom and copper atom and ion excited levels, such as electron, ion and atom impact excitation, de-excitation and ionization for all levels, electron–ion radiative and three-body recombination, radiative decay, etc. [38,39,42,43].

For the argon excited levels [38,39], radiative decay was calculated to be dominant, both as production and loss process for the low-lying levels, although

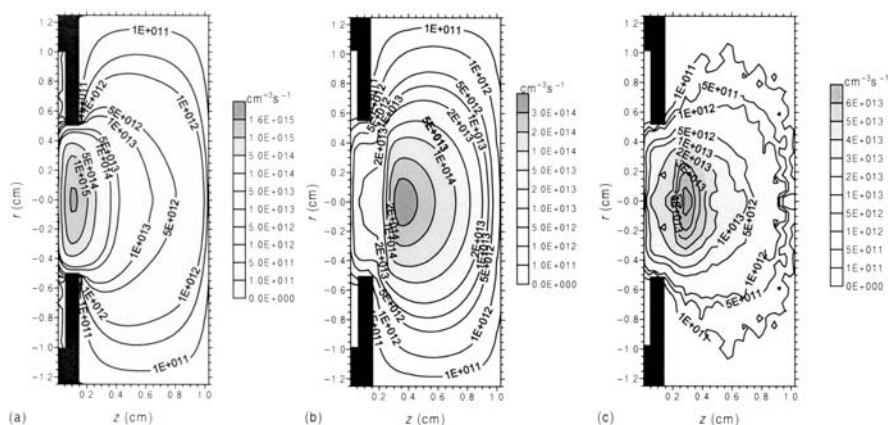


Figure 6.20 Calculated ionization rates of the sputtered copper atoms in the VG 9000 cell, under the dc conditions of 1000 V, 0.5 Torr and 3.5 mA: (a) by Penning ionization; (b) by asymmetric charge transfer; (c) by electron impact ionization. Reproduced with permission from Bogaerts, A., and Gijbels, R., *Anal. Chem.*, 1996, **68**, 2676–2685, Copyright 1996 American Chemical Society

electron, fast argon ion and fast argon atom impact excitation from the ground state were also found to be important production processes. The 4s metastable levels, which cannot decay to the ground state by emission of radiation, are mainly destroyed by metastable atom–metastable atom collisions, by Penning ionization of sputtered atoms, by electron impact excitation to the nearby 4s resonant levels and also by diffusion and subsequent de-excitation at the cell walls [38]. The highly excited levels, on the other hand, appear to be primarily populated and depopulated by electron, argon ion and atom impact excitation and de-excitation from and towards nearby levels.

In the case of the copper atoms [42,43], it was found that sputtering from the cathode is the dominant production process for the copper ground-state atoms, whereas depopulation is mainly caused by ionization (especially Penning ionization and asymmetric charge transfer) and by excitation to copper atom excited levels. The copper atom excited levels are mainly formed by electron impact excitation from the copper atom ground state and by radiative decay from higher excited levels. The major loss process for the copper atom excited levels is found to be radiative decay to lower levels. The copper ions, both in the ground state and in the $3d^9 4s$ metastable levels, are predominantly formed by Penning ionization. Loss of the copper ion ground state occurs by electron impact excitation to higher levels, and also by electron impact ionization to Cu^{2+} and by electron–ion three-body recombination. The copper ion metastable levels are mainly depopulated by electron impact de-excitation to the ground state. The $\text{Cu}^+ 3d^9 4p \ ^3P_2$ level appears to be almost exclusively created by asymmetric charge transfer, whereas the other $3d^9 4p$ levels are formed by electron impact excitation from the $\text{Cu}^+ 3d^9 4s$ metastable levels and the copper ion ground state. The highly excited copper ion levels were found to be primarily depopulated by radiative decay to the lower levels. More information about the relative importance of the various populating and depopulating processes of argon and copper excited levels can be found in the literature [38,39,42,43].

The results presented above for the dc mode are in general, at least qualitatively, similar for the rf and pulsed operation modes, except that the collision processes will vary as a function of time.

6.3.6 INFORMATION ABOUT SPUTTERING AT THE CATHODE

In addition to making predictions about collision processes in the plasma, the models can also give more information about the sputtering process at the cathode. Indeed, the energy distributions of the species bombarding the cathode, namely argon and cathode ions and fast argon atoms, (see Figures 6.16, 6.17 and 6.18) are calculated over the entire cathode surface. When combining these flux energy distributions with an equation for the sputtering yield as a function of bombarding energy and type of bombarding particle, the flux of sputtered atoms,

as a function of radial position, can be calculated. From this, the crater profile at the cathode, after a certain time of sputtering, can be obtained [46,59].

A typical calculated crater profile, calculated for the VG 9000 cell at 1000 V, 0.5 Torr and 3.5 mA (dc conditions), is shown in Figure 6.21a. For good depth-profiling analysis, it is logical that flat crater profiles are desirable; if not, sample atoms originating from different depths enter the plasma simultaneously and the depth resolution of the analysis is worsened. The crater profile presented in Figure 6.21a is therefore not ideal for depth profiling. Indeed, it is much deeper at the edges than in the center (so-called ‘crater edge effect’), the crater walls are not steep and the crater bottom is not flat. Moreover, there is a small rim outside the crater profile. This calculated result is, however, often encountered in glow discharge depth profiling with the VG 9000 cell, which is actually not designed for concentration depth profiling, but for sensitive trace analysis of homogeneous samples. Figure 6.21b illustrates a typical measured crater profile, obtained in the VG 9000 cell, under similar discharge conditions as in Figure 6.21a [60]. The crater profile also displays the crater edge effect, the crater walls are not very steep, although not so pronounced as in the calculated result, and there

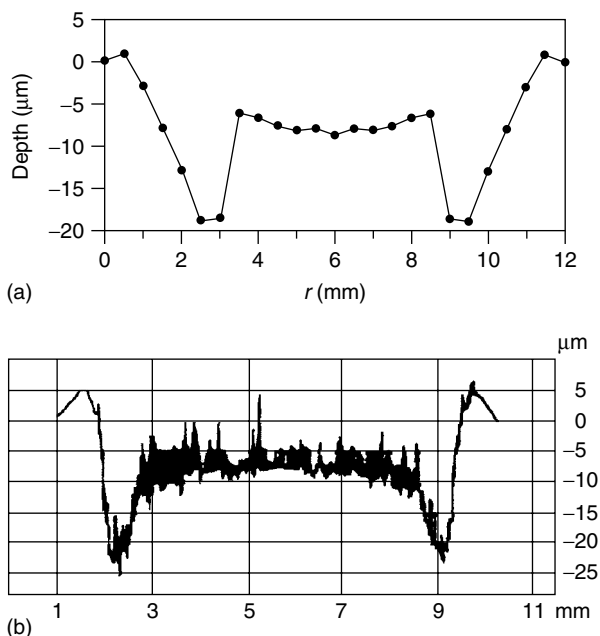


Figure 6.21 Crater profiles after 45 min of sputtering on a copper cathode, in a dc discharge, in the VG 9000 cell, (a) calculated at 1000 V, 0.5 Torr and 3.5 mA and (b) measured at 1000 V and 3 mA (pressure unknown). Reproduced by permission of the Royal Society of Chemistry from Bogaerts, A., and Gijbels, R., *J. Anal. At. Spectrom.*, 1998, **13**, 945–953

is also a rim outside the crater profile. Hence the calculated and experimental crater profiles are in reasonable qualitative agreement. Moreover, the absolute values on the y -axis show that the results are also in satisfactory quantitative agreement. This example demonstrates that the model is able to make predictions about crater profiles to be expected for a specific cell geometry and certain discharge conditions. By applying some modifications to this geometry and/or to the discharge conditions, the crater profile could be optimized. In practice, this optimization procedure is commonly performed by trial and error. This can be expensive and time consuming, and often leads to disappointing results. However, the optimization can now in principle also be simulated with the model, prior to building the new cell, which is much cheaper and more efficient.

From the energy distributions of the argon ions, fast argon atoms and copper ions bombarding the cathode, the relative contributions of these species to the sputtering process can be calculated. From the large flux of fast argon atoms, it can be expected that they have a dominant role in sputtering, in spite of the lower bombarding energies. Indeed, their contribution to the sputtering amounts to about 40–70% (increasing with decreasing pressure and voltage). The argon ions generally contribute about 20–40%. The role of the copper ions (called ‘self-sputtering’) is of minor importance at low voltages and pressures, but they can have a contribution of as much as 50% at the highest voltages and pressures investigated (i.e. 5 Torr, 1200 V, ca 100 mA) [47]. Indeed, as was shown in Figure 6.18a and b, the copper ion energy distribution has a distinct peak at maximum energy, and since the sputtering efficiency increases with rising energy of the bombarding species, it can indeed be expected that the copper ions have a non-negligible contribution in spite of their lower flux. This was also suggested earlier, based on experimental results [58].

The above crater profiles are shown for the VG 9000 cell, because we had experimental data available, but it should be mentioned that glow discharge depth profiling is more often performed with the Grimm-type cell, under GD-OES conditions (at higher pressure and current), where much higher erosion rates are obtained. We calculated erosion rates for typical GD-OES discharge conditions [47], and found that the absolute values are in reasonable agreement with experimental data found in the GD-OES literature [61,62]. Hence this suggests that our models present a realistic picture of the sputtering in a glow discharge.

Our calculations for the rf mode indicated that there is slightly more sputtering than in the dc mode for the same conditions of power and pressure [43]. The latter was in excellent agreement with experiment data [49]. In the microsecond-pulsed mode, the calculated net amount of erosion during one pulse was also found to be in good correspondence with the experimental values. Moreover, we found that the fast argon atoms play the most important role for sputtering in the first 1–3 μs of the pulse, whereas the copper ions appear to become dominant after 3 μs (so-called self-sputtering).

6.3.7 OPTICAL EMISSION INTENSITIES

From the collisional-radiative models which describe the behavior of various excited levels of argon atoms, copper atoms and copper ions [38,39,42,43] we were able to calculate optical emission intensities in the glow discharge (i.e. the product of the level populations and the Einstein transition probabilities for radiative decay) [64–66].

Figure 6.22a presents the calculated argon atomic optical emission spectrum for a Grimm-type glow discharge, integrated over the discharge axis, to simulate end-on observation. It is clear that the lines in the region of 700–1000 nm (i.e. the so-called red lines, corresponding to $4p \rightarrow 4s$ transitions) dominate in the spectrum. Figure 6.22b depicts the argon atomic spectrum, found in the literature [67] and measured in a hollow cathode glow discharge at a current of 150 mA and a pressure of 1 Torr. In spite of the completely different discharge conditions, both spectra have a similar appearance. Indeed, the intensities of the various lines are comparable. This is not straightforward, in view of the large number of populating and depopulating processes taking place for the various levels, and the uncertainties in the cross-sections and transition probabilities used in the model. In the near future, we plan to perform a detailed comparison between calculated and measured optical emission spectra under exactly the same conditions, both for the dc mode and the rf mode (in the framework of an EC Thematic Network on Glow Discharge Spectrometry).

In order to study the relative importance of various excitation mechanisms, we have also compared our calculated spectral line intensities, as a function of distance from the cathode, with measurements at exactly the same discharge conditions and cell geometry [66]. Figure 6.23a shows the calculated spatial distributions of some selected Ar I, Ar II and Cu I lines, at 0.6 Torr and five different currents and voltages, and the corresponding experimental results [81] are plotted in Figure 6.23b. It appears that very good agreement has been reached, which suggests that our model takes into account the correct excitation mechanisms and uses realistic cross-sections, and that it can therefore give more or less reliable predictions for GD-OES.

6.3.8 PREDICTION OF THE EFFECT OF THE CELL GEOMETRY

The models can be applied to various kinds of cell geometries, such as shown above for the VG 9000 flat cell, a Grimm-type cell, a six-way cross glow discharge cell or other types of cell geometries, as long as the cell is cylindrically symmetrical. For example, Figure 6.24a and b show the calculated copper atom density distribution for an arbitrary cell, with a flat and a pin-type of cathode [57]. In the cell with a flat cathode, the plasma is most intense in front of the cathode, whereas in a cell with a pin cathode, the plasma forms a kind of ring around

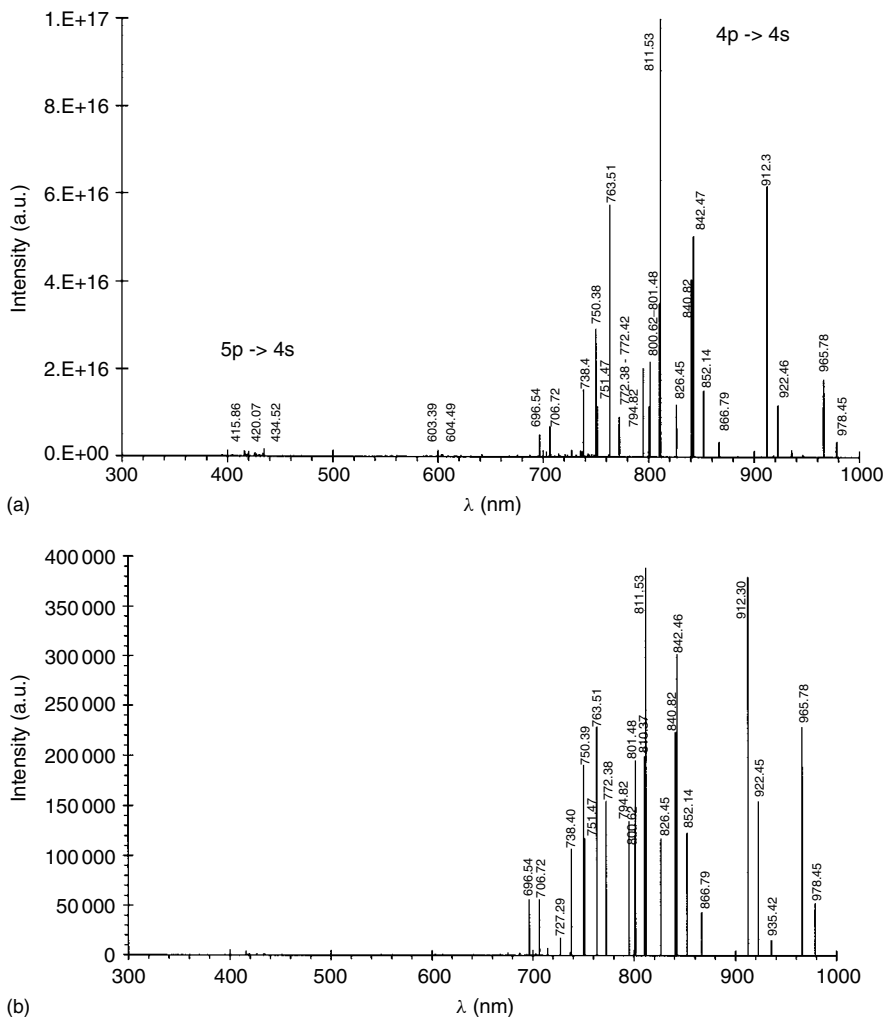


Figure 6.22 Optical emission spectra of the argon atoms, in a dc discharge: (a) calculated in a Grimm-type glow discharge cell, integrated over the entire cell axis to simulate end-on observation, at 800 V, 3.75 Torr and 28 mA; (b) measured in a hollow cathode glow discharge at 150 mA and 1 Torr. Reprinted from Bogaerts, A., Gijbels, R., and Vlcek, J., *Spectrochim. Acta, Part B*, 1998, **53**, 1517–1526, with permission of Elsevier Science

the pin. In that work [57], the ion fluxes bombarding the exit slit to the mass spectrometer were calculated for the above two cell designs, which gives an idea about the ion intensities in the mass spectrum. This illustrates that the models can in principle be applied to predict the effect of cell geometry, as a help for the design of new cells.

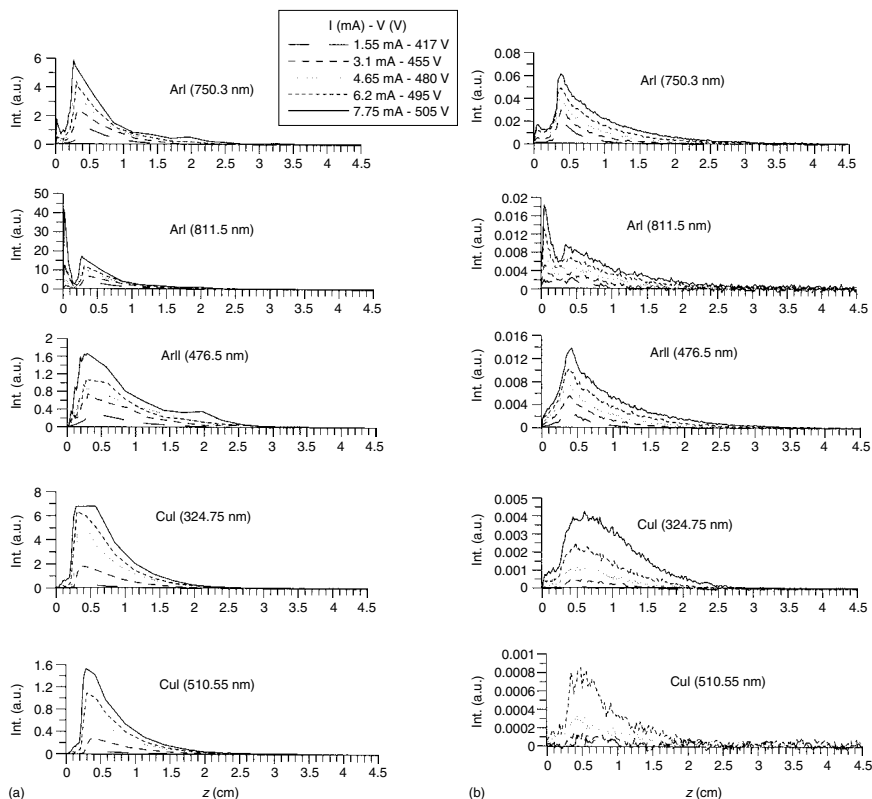


Figure 6.23 Optical emission intensities as a function of distance from the cathode, in a dc cylindrically symmetrical glow discharge cell, at a pressure of 0.6 Torr and five different currents and voltages, for the lines Ar I (750.3 nm), Ar I (811.5 nm), Ar II (476.5 nm), Cu I (324.75 nm) and Cu I (510.55 nm). (a) Calculated and (b) measured values [66]

6.3.9 PREDICTION OF RELATIVE SENSITIVITY FACTORS IN GDMS

Finally, as a spin-off, we have used our models to explain experimentally observed differences in relative sensitivity factors (RSFs) in GDMS [69]. Since the cross-sections of asymmetric charge transfer ionization of different elements are not available in the literature, a model was developed for calculating RSFs based on transport and Penning ionization only, since electron impact ionization is of minor importance (see above), to test the influence of asymmetric charge transfer. A systematic investigation for 42 elements showed that a correlation exists between the discrepancy between calculated and experimental RSFs on the one hand, and the availability of suitable energy levels for asymmetric charge transfer on the other.

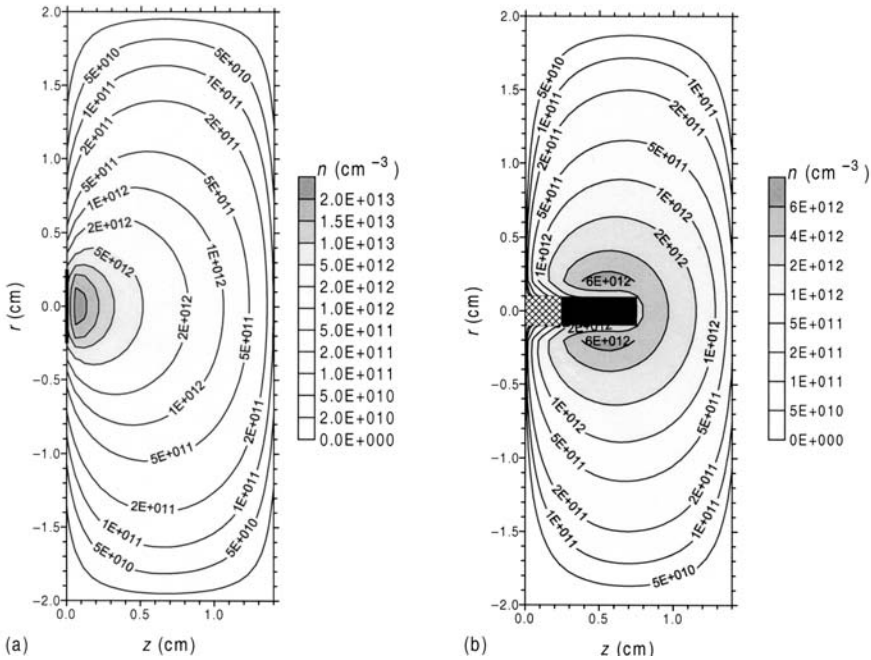


Figure 6.24 Calculated two-dimensional density profiles of the sputtered copper atoms, in a dc discharge (a) with flat cathode (at 1000 V, 2.2 mA and 1 Torr) and (b) with pin-type of cathode (at 1000 V, 2.2 mA and 0.7 Torr). Reprinted from Bogaerts, A., and Gijbels, R., *J. Am. Soc. Mass Spectrom.*, 1997, **8**, 1021–1029, with permission of Elsevier Science

This strongly suggests that, in addition to transport and Penning ionization, especially the occurrence or nonoccurrence of asymmetric charge transfer can explain the differences in RSFs among different elements. More information about this investigation can be found elsewhere [69].

6.4 CONCLUSION

It has been illustrated with some typical examples what can be calculated with the models described for the case of several types of glow discharges. In general, it can be concluded that the models present a realistic picture of the glow discharge and can predict qualitative trends. Exact quantitative predictions, however, cannot yet be expected, because there are too many uncertainties in the input data, such as the cross-sections. Therefore, exact computer prediction of an analytical measurement is not yet realistic, but the models can certainly give a better insight into what is important in the plasma, which might also help to improve the analytical performance of glow discharges.

6.5 REFERENCES

- [1] Berezhnoi, S. V.; Kaganovich, I. D.; Tsendin, L. D.; Schweigert, V. A. *Appl. Phys. Lett.*, 1996, **69**, 2341–2343.
- [2] Lee, Y. T.; Lieberman, M. A.; Lichtenberg, A. J.; Bose, F.; Baltès, H.; Patrick, R. *J. Vac. Sci. Technol. A*, 1997, **15**, 113–126.
- [3] Boeuf, J.-P. *J. Appl. Phys.*, 1988, **63**, 1342–1349.
- [4] Passchier, J. D. P.; Goedheer, W. J. *J. Appl. Phys.*, 1993, **73**, 1073–1079.
- [5] Yachi, S.; Kitamura, Y.; Kitamori, K.; Tagashira, H. *J. Phys. D*, 1988, **21**, 914–921.
- [6] Loffhagen, D.; Winkler, R. *J. Comput. Phys.*, 1994, **112**, 91–101.
- [7] Kushner, M. J. *IEEE Trans. Plasma Sci.*, 1986, **14**, 188–196.
- [8] Donko, Z.; Rozsa, K.; Tobin, R. C. *J. Phys. D*, 1996, **29**, 105–114.
- [9] Surendra, M.; Graves, D. B. *IEEE Trans. Plasma Sci.*, 1991, **19**, 144–157.
- [10] Smith, H. B.; Charles, C.; Boswell, R. W.; Kuwahara, H. *J. Appl. Phys.*, 1997, **82**, 561–565.
- [11] Yan, M.; Goedheer, W. J. *IEEE Trans. Plasma Sci.*, 1999, **27**, 1399–1405.
- [12] Surendra, M.; Graves, D. B.; Jellum, G. M. *Phys. Rev. A* 1990, **41**, 1112–1125.
- [13] Huang, F. Y.; Kushner, M. J. *J. Appl. Phys.*, 1995, **78**, 5909–5918.
- [14] Donko, Z. *Phys. Rev. E*, 1998, **57**, 7126–7137.
- [15] Bogaerts, A.; Gijbels, R. *J. Anal. At. Spectrom.*, 1998, **13**, 945–953.
- [16] Bogaerts, A.; Gijbels, R. *J. Anal. At. Spectrom.*, 2000, **15**, 1191–1201.
- [17] Vieth, W.; Huneke, J. C. *Spectrochim. Acta, Part B*, 1991, **46**, 137–153.
- [18] Valles-Abarca, J. A.; Gras-Marti, A. *J. Appl. Phys.*, 1984, **55**, 1370–1378.
- [19] Mason, R. S.; Pichilingi, M. J. *J. Phys. D.*, 1994, **27**, 2363–2371.
- [20] Fiala, A.; Pitchford, L. C.; Boeuf, J. P.; Baude, S. *Spectrochim. Acta, Part B*, 1997, **52**, 531–536.
- [21] Ganeev, A. A.; Vergizova, V. S.; Voronov, M. V.; Slyadnev, M. N.; Sholupov, S. E.; Stroganov, A. A., Glow discharge pulse ionization of residue in thin-walled metallic hollow cathode with time-of-flight spectrometry. Experimental and modeling investigation. Poster at 2000 Winter Conference on Plasma Spectrochemistry, Fort Lauderdale, FL, January 2000.
- [22] Bogaerts, A.; Gijbels, R. *Anal. Chem.*, 1997, **69**, 719A–727A.
- [23] Bogaerts, A.; van Straaten, M.; Gijbels, R. *Spectrochim. Acta, Part B*, 1995, **50**, 179–196.
- [24] Bogaerts, A.; Gijbels, R.; Goedheer, W. J. *J. Appl. Phys.*, 1995, **78**, 2233–2241.
- [25] Bogaerts, A.; Yan, M.; Gijbels, R.; Goedheer, W. J. *Anal. Chem.*, 1996, **68**, 2296–2303.
- [26] Bogaerts, A.; Gijbels, R.; Goedheer, W. J. *Jpn. J. Appl. Phys.*, 1999, **38**, 4404–4415.
- [27] Bogaerts, A.; Gijbels, R. *J. Anal. At. Spectrom.*, 2000, **15**, 895–905.
- [28] Jogwisch, M.; Huber, B. A.; Wiesemann, K. *Z. Phys. D*, 1990, **17**, 171–179.
- [29] Gummel, H. K. *IEEE Trans. Plasma Sci.*, 1964, **11**, 455–465.
- [30] Scharfetter, D. L.; Gummel, H. K. *IEEE Trans. Electron. Devices*, 1969, **16**, 64–77.
- [31] Bogaerts, A.; Yan, M.; Gijbels, R.; Goedheer, W. J. *J. Appl. Phys.*, 1999, **86**, 2990–3001.
- [32] Bogaerts, A.; Gijbels, R. *J. Appl. Phys.*, 1999, **86**, 4124–4133.
- [33] Bogaerts, A.; Gijbels, R. *J. Appl. Phys.*, 1995, **78**, 6427–6431.
- [34] Bogaerts, A.; Gijbels, R. *IEEE Trans. Plasma Sci.*, 1999, **27**, 1406–1415.
- [35] Bogaerts, A.; Gijbels, R.; Serikov, V. V. *J. Appl. Phys.*, 2000, **87**, 8334–8344.
- [36] Holstein, T. *Phys. Rev.*, 1951, **83**, 1159–1168.
- [37] Walsh, P. J. *Phys. Rev.*, 1959, **116**, 511–515.
- [38] Bogaerts, A.; Gijbels, R.; Vlcek, J. *J. Appl. Phys.*, 1998, **84**, 121–136.
- [39] Bogaerts, A.; Gijbels, R. *Spectrochim. Acta, Part B*, 2000, **55**, 263–278.
- [40] Matsunami, N.; Yamamura, Y.; Itikawa, Y.; Itoh, N.; Kazumata, Y.; Miyagawa, S.; Morita, K.; Shimizu, R.; Tawara, H. *At. Data Nucl. Data Tables*, 1984, **31**, 1–80.

- [41] Bogaerts, A.; van Straaten, M.; Gijbels, R. *J. Appl. Phys.*, 1995, **77**, 1868–1874.
- [42] Bogaerts, A.; Gijbels, R.; Carman, R. J. *Spectrochim. Acta, Part B*, 1998, **53**, 1679–1703.
- [43] Bogaerts, A.; Gijbels, R. *Spectrochim. Acta, Part B*, 2000, **55**, 279–297.
- [44] Bogaerts, A.; Gijbels, R. *J. Appl. Phys.*, 1996, **79**, 1279–1286.
- [45] Bogaerts, A.; Gijbels, R. *Anal. Chem.*, 1996, **68**, 2676–2685.
- [46] Bogaerts, A. *PhD Dissertation*, University of Antwerp, 1996.
- [47] Bogaerts, A.; Gijbels, R. *Spectrochim. Acta, Part B*, 1998, **53**, 437–462.
- [48] Bogaerts, A.; Gijbels, R.; Goedheer, W. *Spectrochim. Acta, Part B*, 1999, **54**, 1335–1350.
- [49] Bogaerts, A.; Wilken, L.; Hoffmann, V.; Gijbels, R.; Wetzig, K. *Spectrochimica Acta Part B*, 2002, **57**, 109–119.
- [50] Yang, C.; Harrison, W. W. Personal communication.
- [51] Aston, F. W. *Proc. R. Soc. London, Ser. A*, 1907, **79**, 80.
- [52] Bogaerts, A.; Gijbels, R. *Phys. Rev. A*, 1995, **52**, 3743–3751.
- [53] Bogaerts, A.; Guenard, R. D.; Smith, B. W.; Winefordner, J. D.; Harrison, W. W.; Gijbels, R. *Spectrochim. Acta, Part B*, 1997, **52**, 219–229.
- [54] Bogaerts, A.; Quentmeier, A.; Jakubowski, N.; Gijbels, R. *Spectrochim. Acta, Part B*, 1995, **50**, 1337–1349.
- [55] Bogaerts, A.; Wagner, E.; Smith, B. W.; Winefordner, J. D.; Pollmann, D.; Harrison, W. W.; Gijbels, R. *Spectrochim. Acta, Part B*, 1997, **52**, 205–218.
- [56] Bogaerts, A.; Gijbels, R. *J. Anal. At. Spectrom.*, 1997, **12**, 751–759.
- [57] Bogaerts, A.; Gijbels, R. *J. Am. Soc. Mass Spectrom.*, 1997, **8**, 1021–1029.
- [58] van Straaten, M.; Bogaerts, A.; Gijbels, R. *Spectrochim. Acta, Part B*, 1995, **50**, 583–605.
- [59] Bogaerts, A.; Gijbels, R. *Spectrochim. Acta, Part B*, 1997, **52**, 765–778.
- [60] Jonkers, C. *PhD Dissertation*, University of Antwerp, 1995.
- [61] Bogaerts, A.; Wilken, L.; Hoffmann, V.; Gijbels, R.; Wetzig, K. *Spectrochim. Acta Part B*, 2001, **56**, 551–564.
- [62] Hocquaux, H. Thin film analysis, in Marcus, R. K. (Ed.), *Glow Discharge Spectroscopies*, Plenum, New York, 1993, p. 346.
- [63] Bogaerts, A.; Gijbels, R. *J. Anal. At. Spectrom.*, 2001, **16**, 239–249.
- [64] Bogaerts, A.; Gijbels, R.; Vlcek, J. *Spectrochim. Acta, Part B*, 1998, **53**, 1517–1526.
- [65] Bogaerts, A.; Gijbels, R. *J. Anal. At. Spectrom.*, 1998, **13**, 721–726.
- [66] Bogaerts, A.; Donko, Z.; Kutasi, K.; Bano, G.; Pinhao, N.; Pinheiro, M. *Spectrochim. Acta, Part B*, 2000, **55**, 1465–1479.
- [67] Gray, D. E. *American Institute of Physics Handbook*, 3rd Edition, McGraw-Hill, New York, 1972.
- [68] Rozsa, K.; Gallagher, A.; Donko, Z. *Phys. Rev. E*, 1995, **52**, 913–918.
- [69] Bogaerts, A.; Gijbels, R. *J. Anal. At. Spectrom.*, 1996, **11**, 841–847.
- [70] Peterson, L. R.; Allen, J. E., Jr. *J. Chem. Phys.*, 1972, **56**, 6068–6076.
- [71] Phelps, A. V. *J. Phys. Chem. Ref. Data*, 1991, **20**, 557–573.
- [72] van Straaten, M., unpublished results.
- [73] Born, S.; Venzago, C.; Stojanik, B. *Appl. Spectrosc.*, 1998, **52**, 1358–1360.
- [74] Graves, D. B.; Jensen, K. F. *IEEE Trans. Plasma Sci.*, 1986, **14**, 78–91.
- [75] Passchier, D. *PhD Dissertation*, University of Utrecht, 1994.
- [76] Kennis, P. *PhD Dissertation*, University of Antwerp, 1996.
- [77] Ferreira, N. P.; Strauss, J. A.; Human, H. G. C. *Spectrochim. Acta, Part B*, 1982, **37**, 273–279.

- [78] Steers, E. B. M.; Fielding, R. J. *J. Anal. At. Spectrom.*, 1987, **2**, 239–244.
- [79] Hagstrum, H. D. *Phys. Rev.*, 1954, **96**, 325–335.
- [80] Gill, P.; Webb, C. E. *J. Phys. D*, 1977, **10**, 299–311.
- [81] Donko, Z.; Bano, G.; Szalai, L.; Kutasi, K.; Rosza, K.; Pinheiro, M.; Pinhao, N. *J. Phys. D.*, 1999, **32**, 2416–2425.

7

Application of Glow Discharge Optical Emission Spectrometry in the Steel Industry

K. KAKITA¹, K. SUZUKI¹ AND S. SUZUKI²

¹*Nippon Steel Technoresearch Corporation, Kawasaki, Japan*

²*Nippon Steel Corporation*

7.1 INTRODUCTION

Glow discharge optical emission spectroscopy (GD-OES) is a technique that is rapidly gaining acceptance in the steel industry. It is the unique ability of the GD method to perform depth-resolved analyses which distinguishes it from the bulk analysis methods of spark emission or X-ray fluorescence (XRF) spectrometry. Depth profiles of surface layers on steel can be often measured using GD-OES, by which the sputtering rate is higher than the high-vacuum ion beam milling used in surface analytical techniques such as Auger electron spectroscopy (AES), X-ray photoelectron spectroscopy (XPS) and secondary ion mass spectrometry (SIMS). The depth profiles measured by GD-OES can be quantitatively analyzed based on a calibration method. With these advantages, GD-OES is frequently applied in the steel industry, in which surface layers on steel such as coatings and oxide scales are required to be analyzed. Typically, zinc- and aluminum-based coatings are widely processed on to the surface of steel sheets and thereby the surface properties such as corrosion resistance are improved for use in automobiles, for example. On the other hand, steel sheets are processed by tin or chromium plating for use in food and beverage cans. Since the properties of

these coatings are strongly influenced by the process conditions, characterization of the coatings is indispensable. Standardization of GD-OES methods for analysis is in now progress [1–4].

This chapter describes the practical application of GO-OES for the analysis of zinc- and aluminum-based coatings, which are important products in the steel industry [4–11]. For instance, suitable measurement conditions of GD-OES and influences of various types of coating matrices on the analytical measurements are shown from the viewpoint of the traceability of measurement. Furthermore, the chemical composition and thickness of coatings obtained by GD-OES should be compared with those obtained by chemical analytical methods. The high sensitivity of GD-OES allows us to investigate the distribution behavior of small amounts of alloying elements and also major elements. Related to such distribution behavior, the microstructure has also been investigated with electron microscopy and other imaging methods. Thus, the total characteristic features of coatings analyzed by these different methods are discussed along with the results of GD-OES.

7.2 MEASUREMENT TRACEABILITY OF COATING WEIGHT AND CHEMICAL COMPOSITION BY GD-OES

The thickness and composition of coatings are obtained in quantitative depth analysis by GD-OES, but assurances must be in place regarding traceability and validation of the methods. The SI units of thickness and composition are length (m) and mass (kg), respectively, and can be measured by other chemical and physical techniques to assess the quality of the proposed GD methods. The composition or weight of elements can be directly measured by gravimetry, which is one of the most fundamental methods in chemical analysis, a so-called primary method. Inductively coupled plasma atomic emission spectrometry (ICP-AES) and flame atomic absorption spectrometry (FAAS), which are traceable to gravimetry, are used in practice to confirm the composition. In order to establish a measurement traceability of thickness or coating weight, a physical measurement is necessary. The thickness of coatings is measured by the use of a profilometer after discharging and/or observing the cross-section of coatings using an optical or electron microscope. Figure 7.1 summarizes the traceability of the chemical composition and thickness of zinc and aluminum coatings, which are analyzed by several kinds of analytical methods. Although the chemical composition and thickness of coatings are obtained in quantitative GD-OES, the traceability should be considered in all analytical practices.

In general, calibration graphs in GD-OES are established by measuring a variety of bulk reference materials which may not always be matrix-matched to the coating samples to be measured. It is the fact that the GD-OES method is less prone to matrix effects that allows greater flexibility in the calibration procedures than spark emission or XRF methods. Even so, these calibration graphs should be

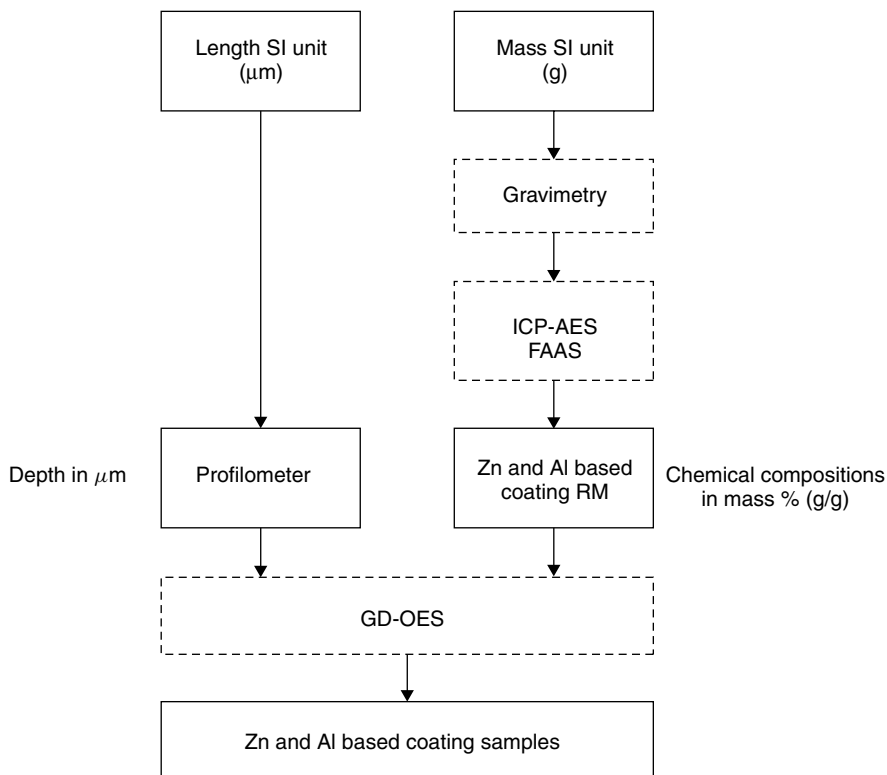


Figure 7.1 Measurement traceability of the chemical composition and thickness of zinc and aluminum coatings which are analyzed by different methods

validated using metallic coating reference materials characterized and assigned by referee methods such as ICP-AES and FAAS from the viewpoint of traceability.

7.3 METHOD OF COATING ANALYSIS BY GD-OES

7.3.1 EMISSION YIELD METHOD

As described in Chapter 5, quantification of coatings by GD-OES is generally performed under the assumption that the emission yield of a spectral line of an element, which is given as the product of the optical emission intensity and the sputtering rate, is constant. Figure 7.2a–c show the composition dependence of the intensities of iron and zinc, the sputtering rate, and the emission yields for those elements in an iron–zinc system, respectively. Both the intensity and

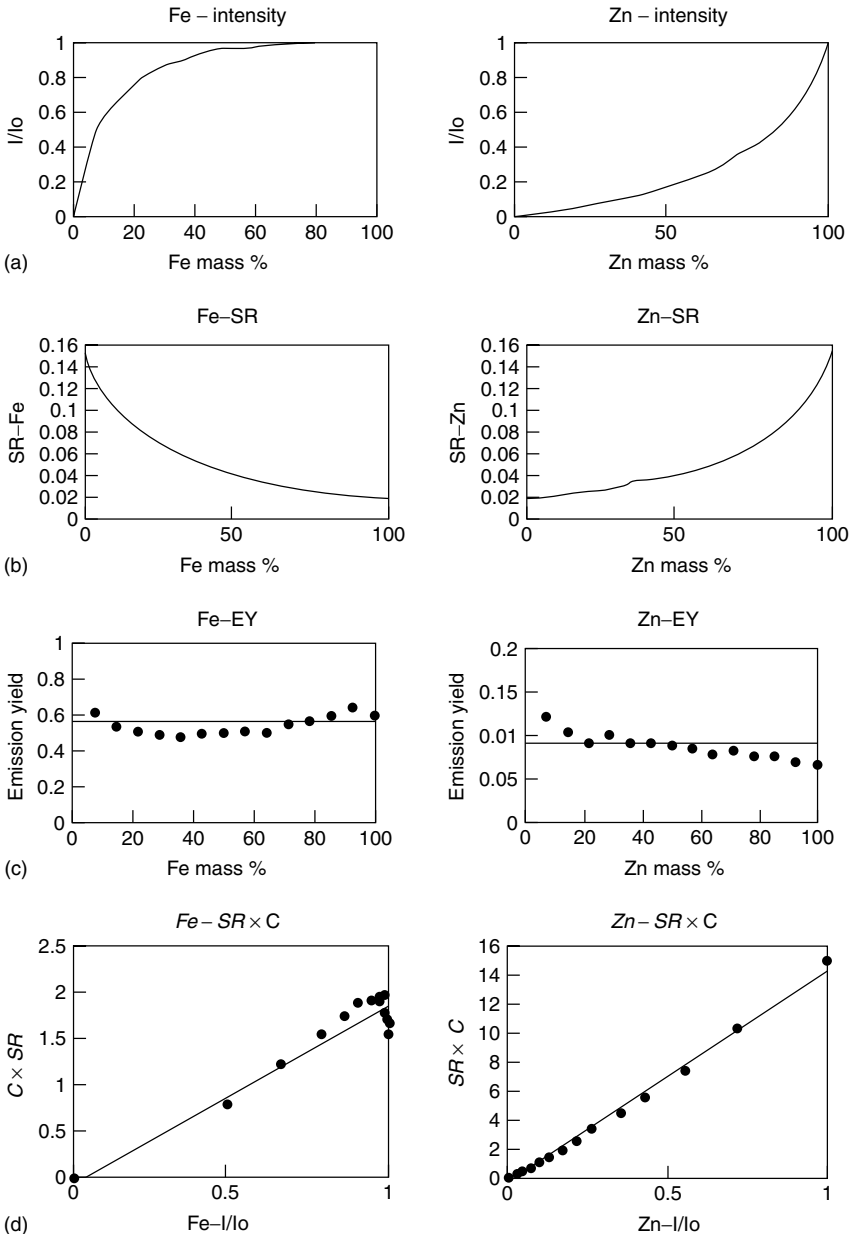


Figure 7.2 Composition dependence of (a) intensity of iron and zinc, (b) the sputtering rate, (c) emission yield in an iron–zinc system, and (d) the relationship between the product of the measured emission intensities with the sputtering rate for iron and zinc

sputtering rates increase significantly with increase in the concentration of zinc, as they are mutually correlated (i.e. greater numbers of atoms produce more photons). This phenomenon is related to the high sputtering rate of zinc. The relationship between the product of the chemical composition and the sputtering rate ($SR \times C$) and intensity for the iron and zinc constituents is shown in Figure 7.2d. A nearly linear relationship is easily seen (particularly for Zn), which is the underlying principle of quantification [5]. If a large deviation from a linear relationship were to be found, then some higher order terms would need to be accounted for in the quantification.

Figure 7.3a exemplifies the relationship between the nickel composition and the Ni I emission intensity obtained for very different matrices, Ni–Zn alloy coatings and a stainless steel. When the effect of the sputtering rates on the observed intensities is taken into account, the relationship between the emission

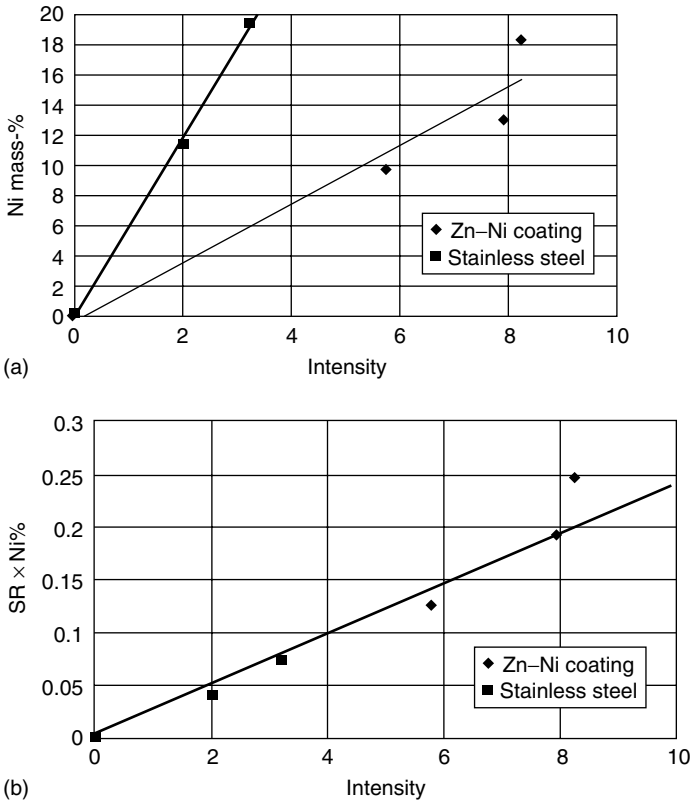


Figure 7.3 (a) The relationship between the nickel composition and measured emission intensity of nickel in Ni–Zn alloy and stainless-steel plates and (b) the relationship between the product of the sputter rate and composition and the measured intensity

Operating conditions		EY ratio						Tested samples A and B	
		Zn 90%	Al 80%	Zn 40%	Ni 10%	Ni 20%	A(RM)	B(CRM)	EY ratio
I, V constant	50 mA, 600 V	100.01	86.35	76.95	86.87	76.87	Zn90Fe10	Zn95Al5	EY A/EY B
	30 W, 8 Torr	77.94	88.12	69.76	90.65	81.77	Zn20Al80	Casted	EY A/EY B
	30 W, 9 Torr	94.98	89.04	81.99	87.92	82.09	Zn40Fe60	Electr. coat	EY B/EY A
I constant	30 W, 10 Torr	62.48	89.27	72.04	91.25	86.31	Ni 10%	Fe73Cr17Ni10	EY A/EY B
	50 mA, 8 Torr	75.42	53.39	63.58	107.62	80.65	Ni 20%	Fe55Cr25Ni20	EY A/EY B
	50 mA, 9 Torr	66.28	80.79	62.37	94.51	82.75			
V constant	50 mA, 10 Torr	78.56	117.01	61.52	101.63	86.62			
	600 V, 8 Torr	109.89	83.77	68.30	89.56	78.93			
	600 V, 9 Torr	90.14	91.12	60.87	90.69	71.33			
	600 V, 10 Torr	91.54	81.99	62.71	93.80	82.81			

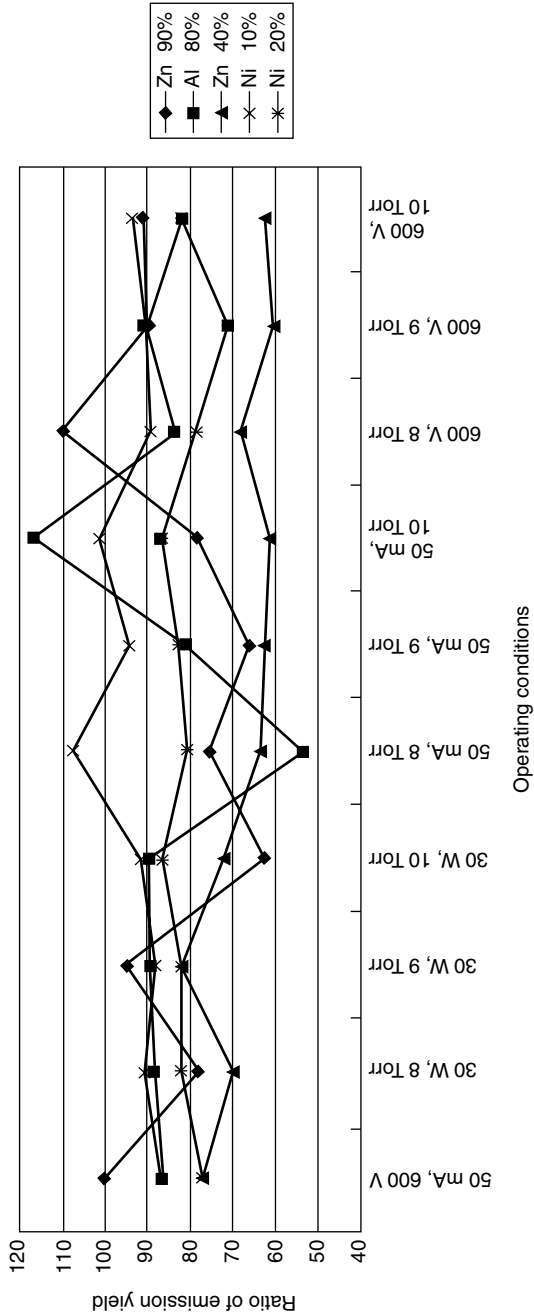


Figure 7.4 Effect of operating conditions on the ratio of elemental emission yields obtained for different matrix materials

yield and intensity is as shown in Figure 7.3b. The plot is fairly linear in spite of the very different characters of the matrices, indicating that the emission yield is an effective parameter for quantification. In practical analysis by GD-OES, emission intensities for elements are measured as a function of sputtering time, and the chemical composition of a layer sputtered for a time interval is correlated with time. By evaluating the density of each sputtered layer from the composition, the thickness of the layer is also estimated. Through these procedures, a quantitative depth profile can be obtained.

7.3.2 EFFECT OF MATRIX ON EMISSION YIELD

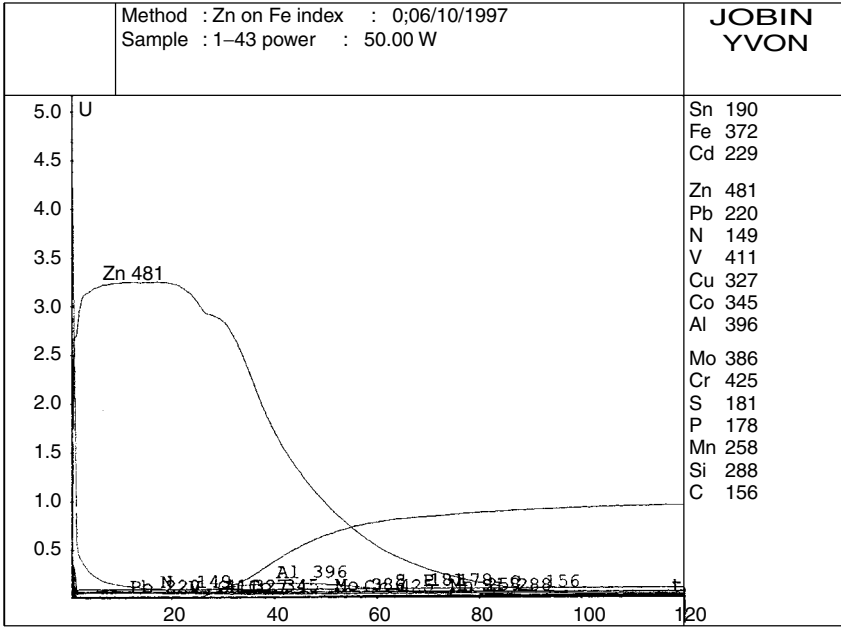
Since the operating conditions of GD-OES may be important in the quantification of coatings, emission yields have been obtained for different samples under different measurement conditions. Figure 7.4 shows the effect of operating conditions on the ratio of emission yields obtained in different kinds of matrix materials. The operating conditions tested were (a) constant current–voltage, (b) constant power and pressure, (c) constant current and (d) constant voltage conditions. Argon was used as the discharge gas in all of the measurements. Although the deviation of the ratio of emission yields from unity seems to be smaller under constant power–Ar pressure and constant current–voltage conditions than under constant current or constant voltage conditions in these cases, the effects of the matrix and operating conditions on emission yields is minimal for quantification.

7.4 DEPTH PROFILES OF COATINGS BY GD-OES

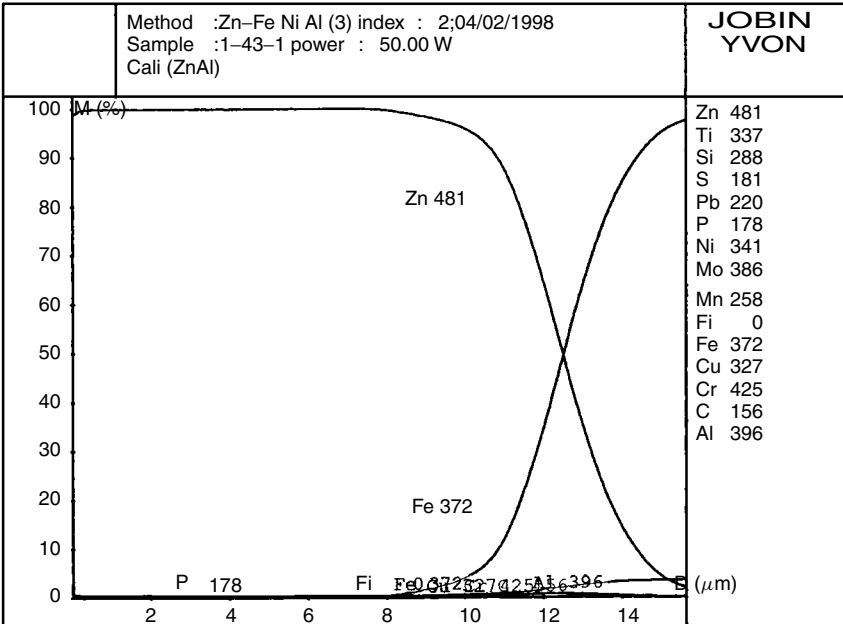
There are a number of coated steel products which are often characterized by GD-OES. Whereas electrodeposited zinc-based coatings are made electrolytically, hot-dip galvanized sheets are produced by dipping steel sheets into molten zinc. Galvannealed steel sheets are annealed to alloy a coating of zinc with iron substrates. Aluminized steels are processed by dipping steel sheets in a molten aluminum–silicon alloy. These alloys are used in the automobile industry, etc., and depth profiles and characteristic features are considered below.

7.4.1 GALVANIZED STEEL

Figure 7.5 shows the GD-OES depth profiles of a galvanized steel sheet. A depth profile of emission intensity vs sputtering time is shown in Figure 7.5a and quantitative depth profiles are shown in Figure 7.5b and c. The composition scale of Figure 7.5c is expanded. The results show that the thickness of the zinc coating is about 12 μm , and aluminum which is added to the coating alloy at less than 0.5 mass-% is enriched at the interface between the coating

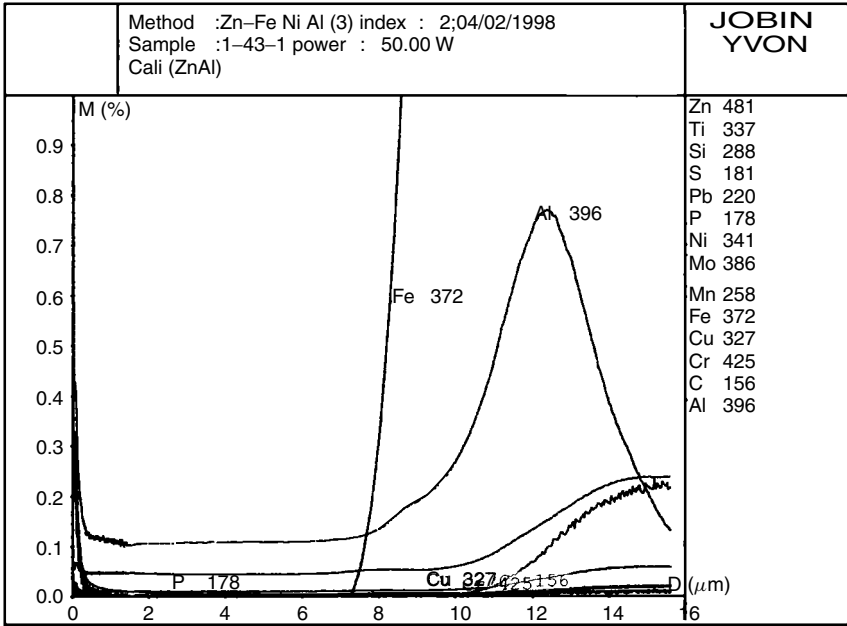


(a)

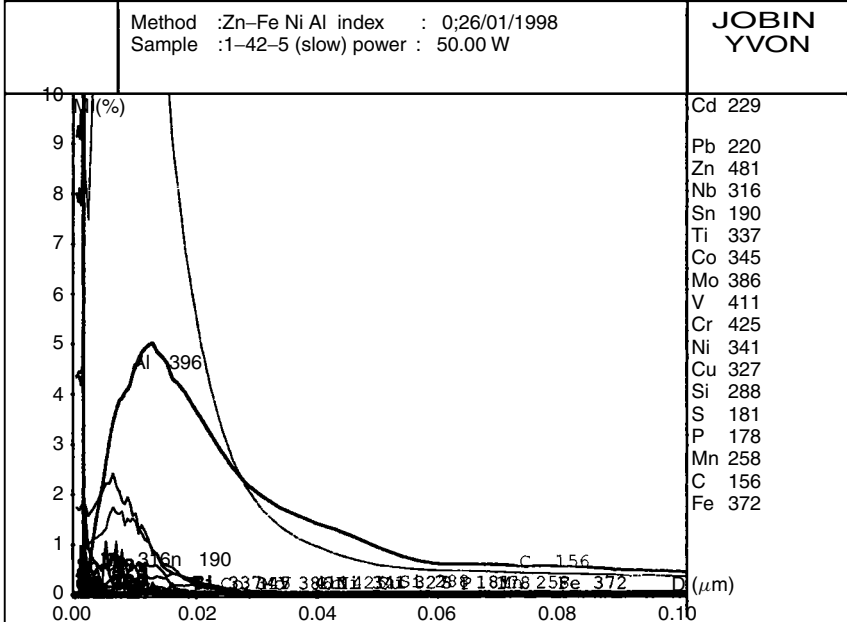


(b)

Figure 7.5 GD-OES depth profiles of a range of elements in a galvanized steel sheet



(c)



(d)

Figure 7.5 (continued)

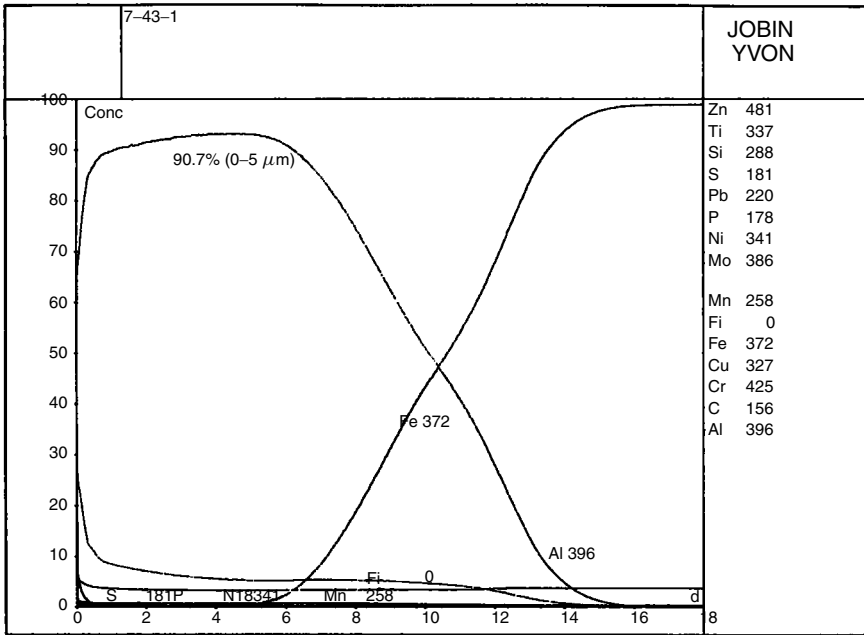


Figure 7.6 Quantitative GD-OES depth profile for an aluminized steel sheet

and matrix (quasi-maximum aluminum is 0.8 mass-%, as shown in Figure 7.5c). The enrichment of aluminum suppresses or controls alloying of the zinc coating with the steel substrate. This enrichment has been observed in previous results by X-ray photoelectron spectroscopy (XPS) and electron probe microanalysis (EPMA) [8,10]. Enrichment of aluminum is also found on the surface of the zinc coating, as shown in Figure 7.5d.

7.4.2 ALUMINIZED STEEL

A quantitative GD-OES depth profile for aluminized steel sheet is shown in Figure 7.6. The thickness of the aluminum alloy layer is about 13 μm . The profile demonstrates the heterogeneous compositional distribution of aluminum in the coating, in spite of the large area ($\sim 15 \text{ mm}^2$) analysis. This suggests that the coating alloy is decomposed into phases with some different microstructures. Information about the phase decomposition can be obtained by microstructural characterization, which will be described in Section 7.5.3.

7.4.3 GALVANNEALED STEEL

In galvanized steel, coated zinc is alloyed with the iron matrix by annealing, in order to achieve good mechanical properties of the coating. Therefore,

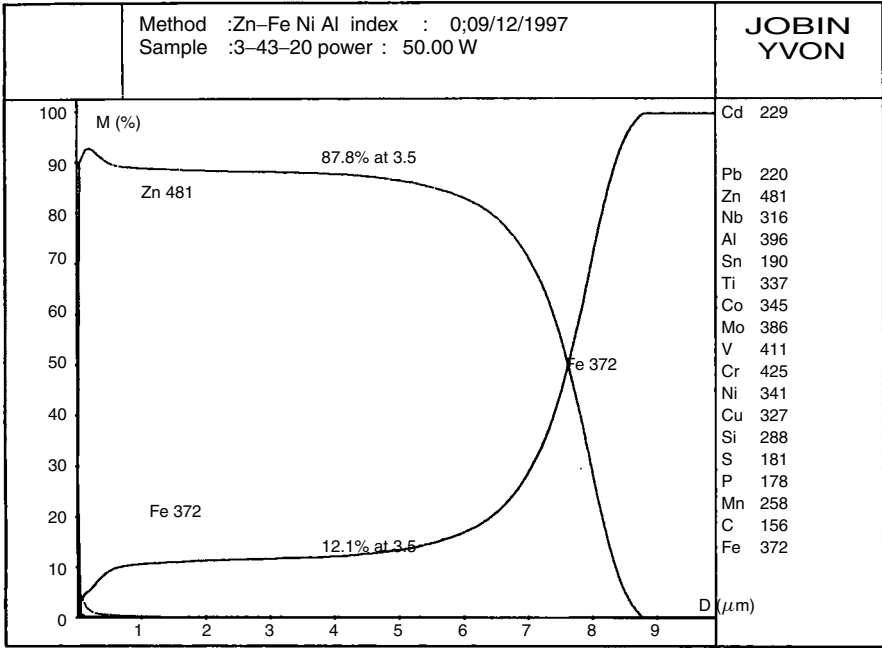


Figure 7.7 Quantitative GD-OES depth profile of a galvanized steel sheet

the concentration of iron in the coating is higher than that in galvanized steel. Figure 7.7 shows a quantitative depth profile of a galvanized steel sheet, in which the concentration of iron in the coating is 10–12 mass-% in this sample. The iron component in the coating comes from the substrate in this case, although alloy coatings such as Zn–Fe and Zn–Ni systems can be processed electrochemically.

7.5 FACTORS AFFECTING DEPTH PROFILES

GD-OES depth profiles provide the average chemical composition of coatings as a function of sputtered depth. As shown in Figures 7.5–7.7, a transition zone close to the interface between the coating and matrix, where the composition is continuously changing, is observed. Although the transition zone should be very sharp in an ideal analysis of an ideal interface, it appears to be broad. This may result from the depth resolution in the GD-OES measurement, the roughness of the interface between the coating and substrate, and microstructural changes such as alloy formation, as shown in Figure 7.8. These factors should be considered, as exemplified below.

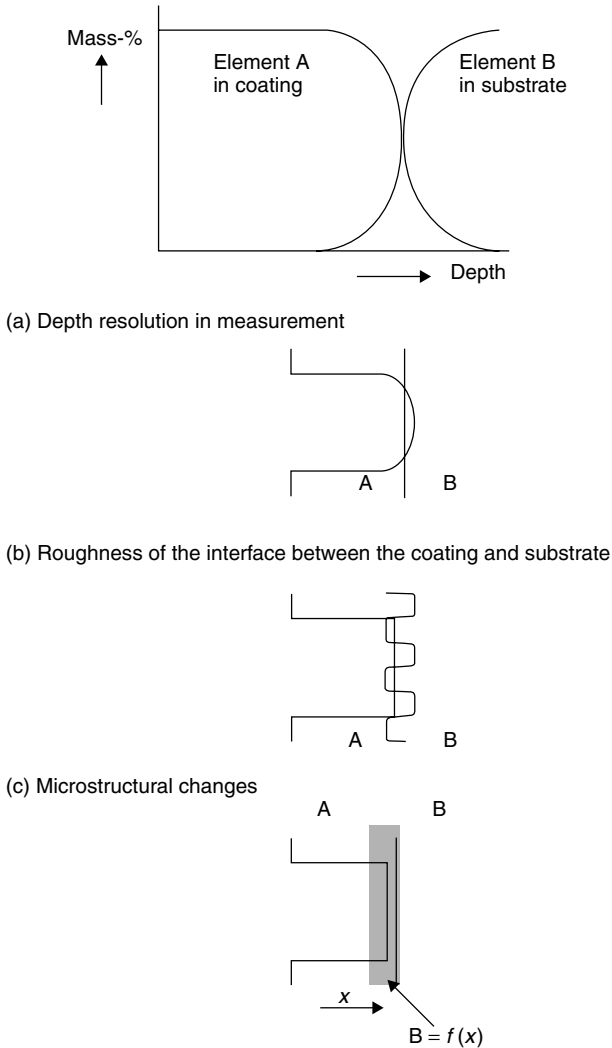


Figure 7.8 Factors affecting the quality of depth profiles: (a) fundamental resolution of the measurement, (b) roughness of the interface between the coating and substrate, and (c) microstructural changes

7.5.1 DEPTH RESOLUTION

Even if the change in composition at the interface is step-like, poor depth resolution of the measurement technique makes the depth profile broad. The depth resolution is evaluated using the depth profile shape, as illustrated in Figure 7.9. The depth resolution is typically defined as the sputtered depth traversed between

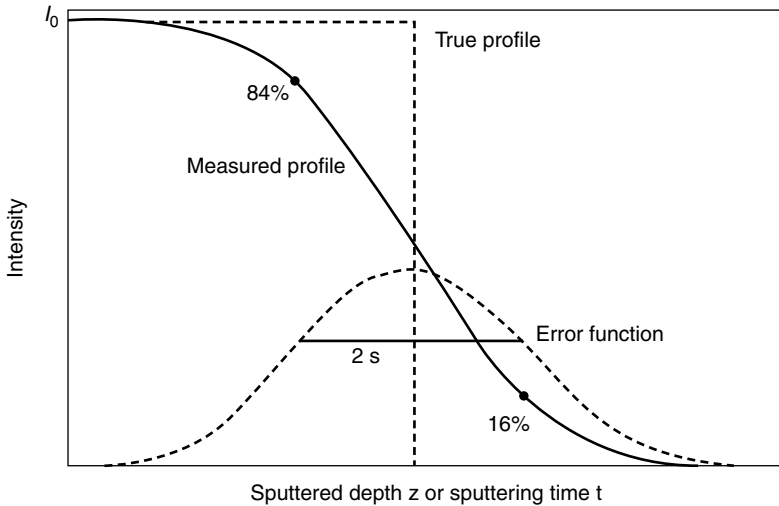


Figure 7.9 Profile distortion of a steplike interface and the basic parameters used for the definition of depth resolution

intensities of 16 and 84% in a profile. Since a sputtering crater is not always flat and the analyzed area is relatively wide in GD-OES [8], these factors may reduce the depth resolution. Figure 7.10 shows a plot of depth resolution versus thickness of different coatings produced on steel. The results show that the depth resolution increases with increasing thickness of the coating, which is a general tendency in the depth resolution vs depth relation. Some scattering in this plot may be acceptable, since coatings with different compositions are analyzed. The resolution characteristics shown in Figure 7.10 may include roughness factors as described in the following section.

7.5.2 ROUGHNESS

The roughness of the surface of the substrate steel affects the transition zone in the composition when the thickness of coatings is small. Typically, the roughness of cold rolled steel sheet is of single-micrometer order of magnitude, which is sometimes comparable to the thickness of coatings. Observation of the cross-section of a coated steel allows us to investigate roughness of the substrate and coating.

Figure 7.11a and b show a cross-sectional microphotograph of a galvanized steel sheet and the thickness of the steel and coating as a function of position of a galvanized steel. The thickness of the zinc coating on the steel is about $14 \mu\text{m}$. The results clearly show a roughness of the coating which is comparable

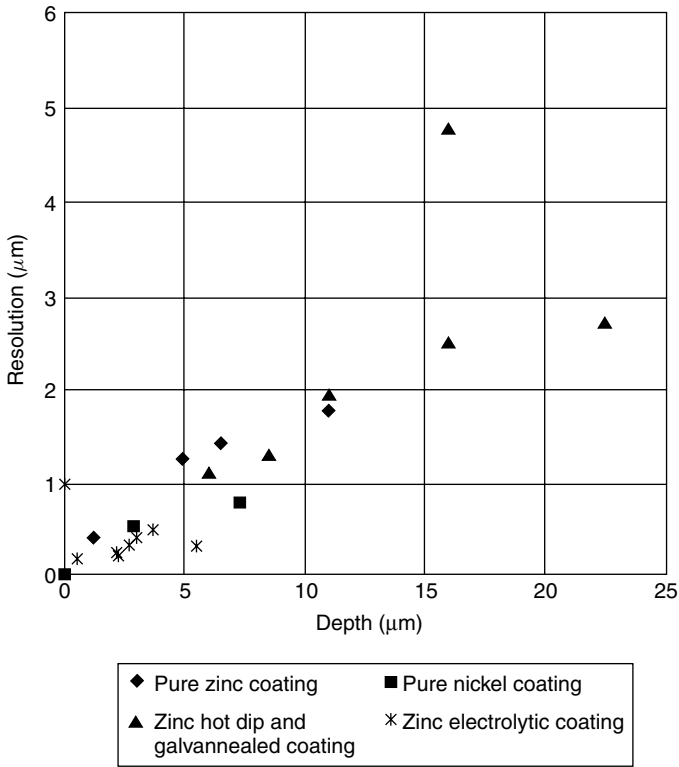


Figure 7.10 Depth resolution versus thickness for different coatings produced on steel

to the coating thickness, and therefore roughness is an important factor in discussing the sharpness of the interface (i.e. ‘resolution’ in Figure 7.10) between the coating and the matrix.

7.5.3 ALLOY FORMATION

Alloy phases with specific compositions may be formed during the coating processes. Whereas GO-OES provides compositional information about alloying, microstructural information can be obtained by the X-ray diffraction method and other micrographic methods.

Steel sheet samples on which a pure zinc layer was electrolytically deposited were annealed in hydrogen gas at 673 and 773 K for different times and then rapidly cooled to room temperature. The composition–depth relation obtained by GD-OES is shown in Figure 7.12. Changes in the X-ray diffraction patterns from a zinc coating on a steel by annealing are shown in Figure 7.13. The results show

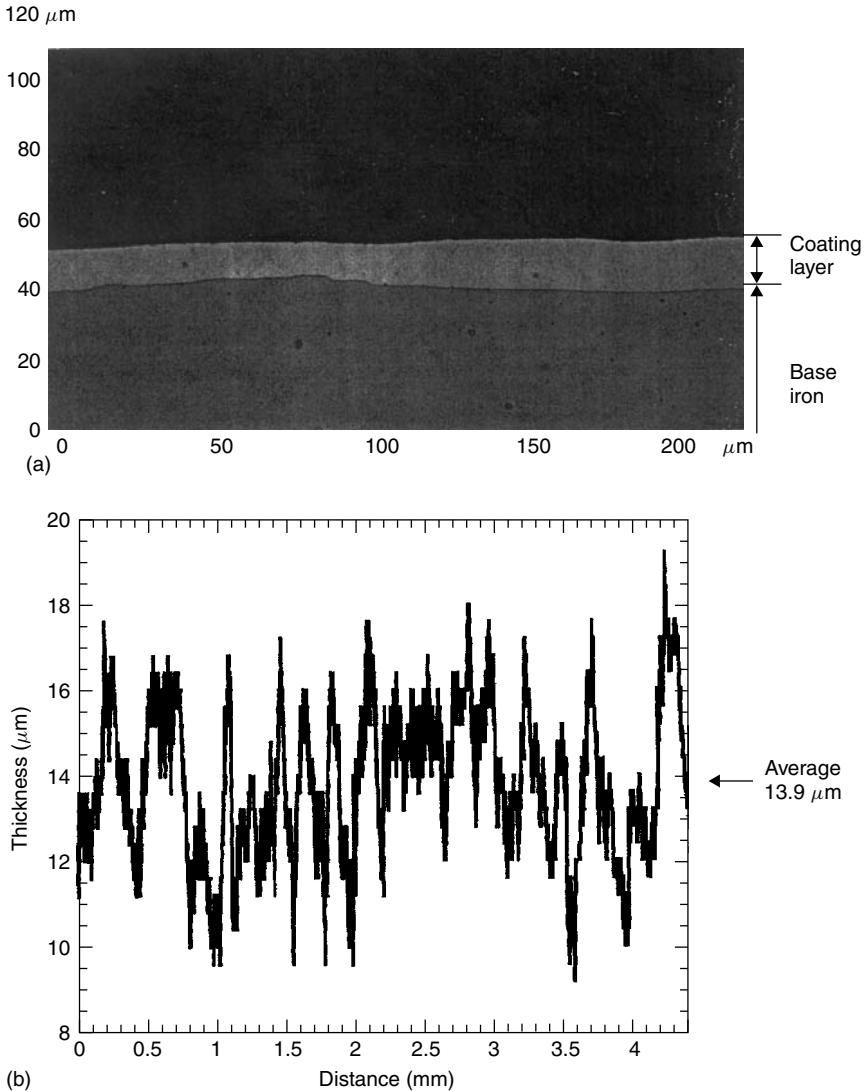


Figure 7.11 (a) Cross-sectional photomicrograph of a galvanized steel sheet and (b) the thickness of the steel and coating as a function of position on a galvanized steel

that different phases appear on annealing in this temperature range. The amount of ζ phase formed from pure zinc decreases with increasing annealing time, whereas the amount of Γ_1 phase increases. The compositions of the ζ , δ , and Γ_1 phases are 94–95%, 88–93% and 82–83% Zn, respectively. The zinc content in the Γ phase determined by GD-OES was slightly higher than 72–73%. These

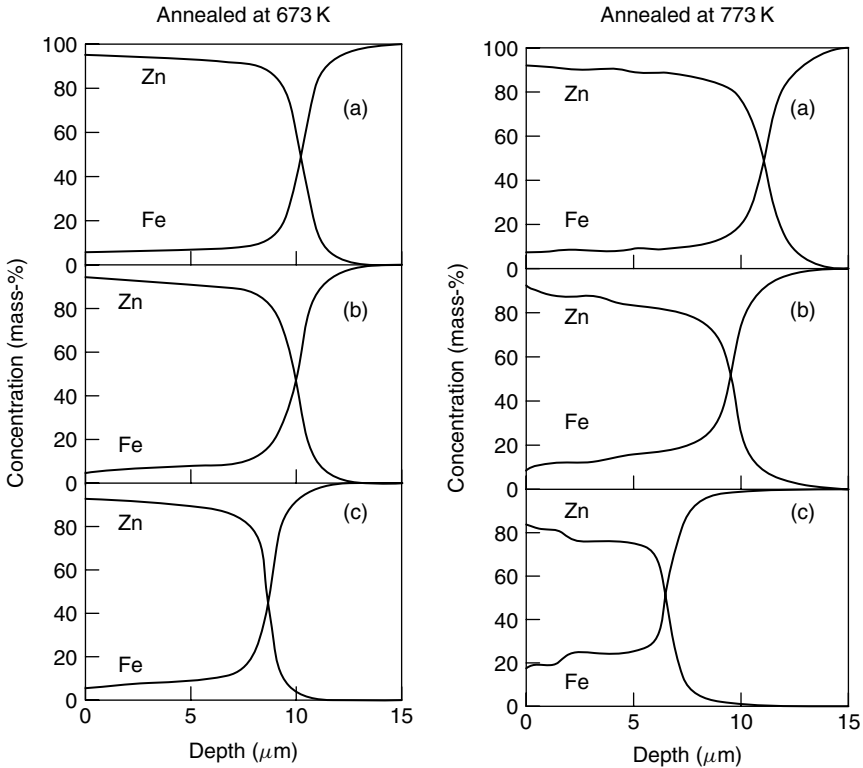


Figure 7.12 GD-OES profiles obtained from coated steel specimens annealed at 673 and 773 K for periods of (a) 300, (b) 1000, and (c) 3000 s

phases represent characteristic microstructures in the coatings, depending on the process conditions, particularly the annealing conditions after coating. In order to assist in understanding the kinetics of alloying processes, a time–temperature diagram for phase formation is shown in Figure 7.14.

Microscopic observation is also useful for investigating the microstructure of a coating. Figure 7.15 focuses on an enriched aluminum layer at the interface between the coating and substrate of galvanized steel. The enriched layer of aluminum is only $0.4 \mu\text{m}$ thick, while the GD-OES profile shows a $6\text{--}8 \mu\text{m}$ thick aluminum layer in the transition zone. This leads to the estimation that the peak value of aluminum is not the real mass-% of aluminum in the thin layer. Figure 7.16 exemplifies microstructural and compositional changes in a cross-section of a coating on aluminized steel. The results indicate that the coating, consisting of mainly aluminum and silicon, is decomposed in to two phases during processing, and the aluminum coating is alloyed with the iron substrate.

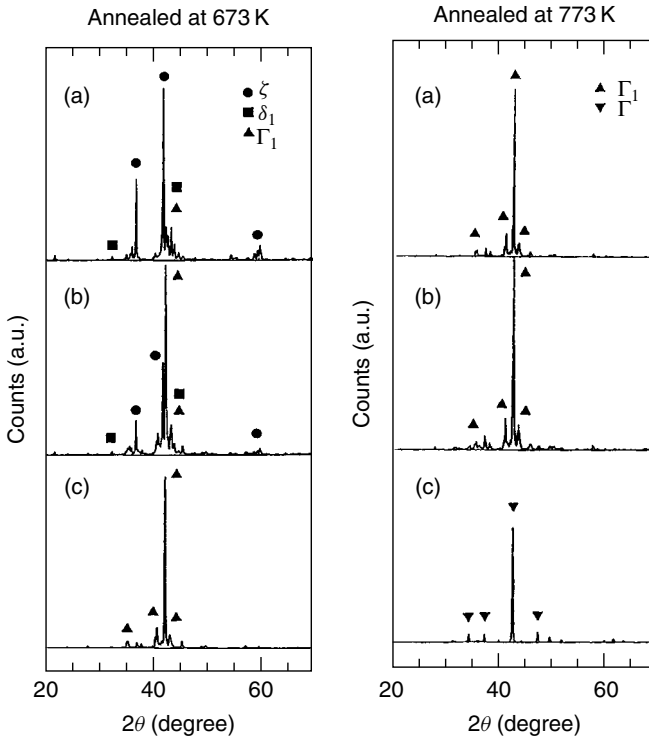


Figure 7.13 X-ray diffraction curves obtained from coated steel specimens annealed at 673 and 773 K for periods of (a) 300, (b) 1000, and (c) 3000 s

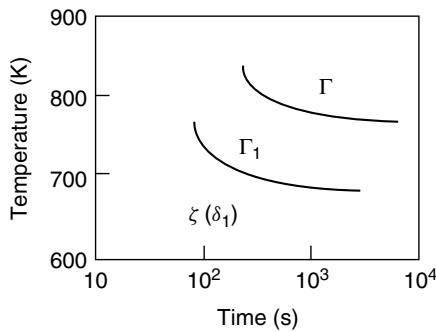


Figure 7.14 Time–temperature diagram of phase formation on the surface of the steel with a zinc coating of about 10 μm thickness

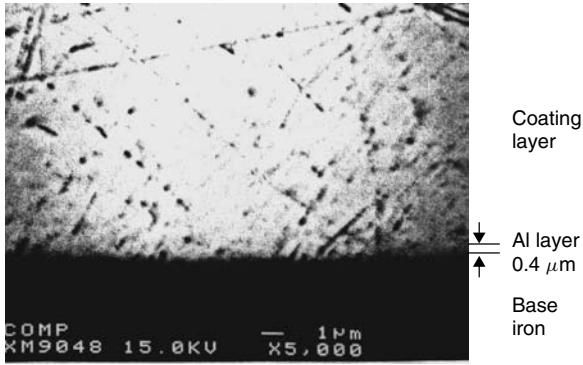


Figure 7.15 Scanning electron micrograph of an enriched aluminum layer at the boundary of a galvanized steel sheet

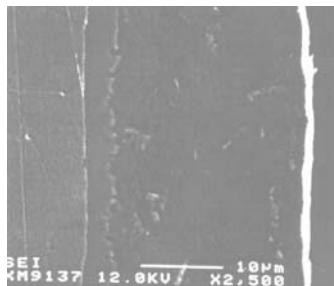
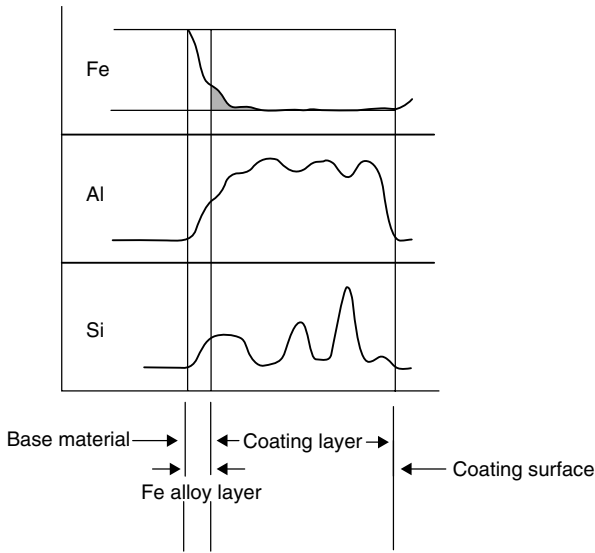


Figure 7.16 Microstructural and compositional changes in the cross-section of a coating on aluminized steel

7.6 VALIDATION AND VERIFICATION OF CALIBRATION GRAPHS

7.6.1 NECESSITY FOR VALIDATION ON CALIBRATION GRAPHS

Interlaboratory tests were carried out to compare the effects of validation using Zn and Al coating reference materials for calibration. The reference materials used were (1) Zn, Zn–Fe, Zn–Ni coating reference materials (laboratory made) and (2) Zn, Al, Cu, Fe based bulk (certified) reference materials.

Figures 7.17–7.19 show the results of quantification obtained by testing laboratories 1, 2, and 3, which established calibration graphs with coating reference materials, and by testing laboratories 4, 5, and 6, which established calibration graphs with bulk reference materials. In all cases, the laboratories that used the coated materials as reference materials found values which are near to the values assigned by chemical analyses. On the other hand, some laboratories which used bulk reference materials without validation found values which were very different from the values assigned by chemical analyses.

The quantification by GD-OES depends on the matrix of the tested samples, and the calibration graphs of GD-OES cover a very wide range from 0 to

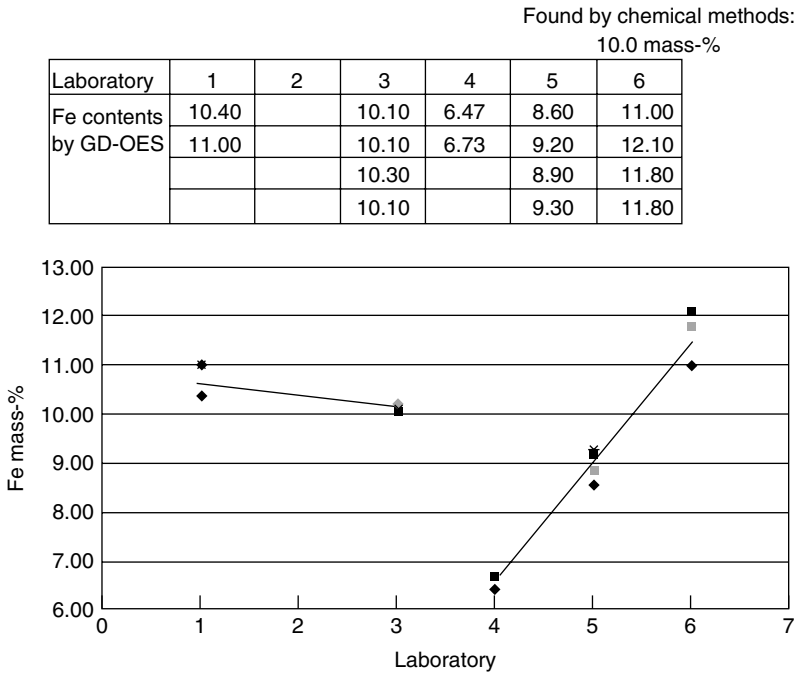


Figure 7.17 Results of interlaboratory tests by GD-OES comparing the results with those of wet chemical methods (sample: galvanized coating)

Found by chemical methods:
14.3 mass-%

Laboratory	1	2	3	4	5	6
Fe contents by GD-OES	13.60	14.40	14.60	12.60	11.50	17.26
	14.40	14.00	14.50	12.40	12.50	16.80
		13.80	14.00		11.70	16.40
		14.00	14.60		12.10	19.80

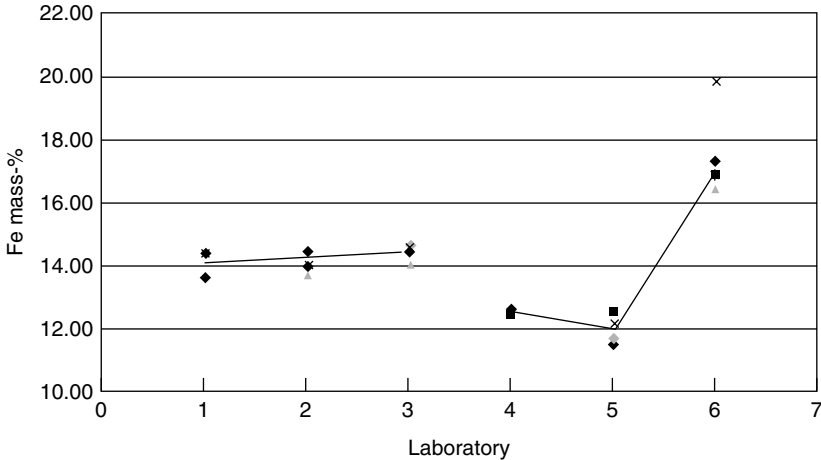


Figure 7.18 Results of interlaboratory tests by GD-OES comparing the results with those of wet chemical methods (sample: Zn-Fe electrolytic coating)

100 mass-% of the analytes. To improve the accuracy of analysis, it is essential to validate the calibration graph using coating reference materials in the area where accurate determinations are required. It is also important to verify the calibration graphs and to correct for drift in routine quality control procedures. Figure 7.20 shows the validation and verification in the measurement procedure of GD-OES.

7.6.2 PROCEDURE FOR VALIDATION AND VERIFICATION

An example of a validation procedure is as follows. After establishing the calibration graph, a few coated reference materials (RMs) are selected. The RMs should contain the relevant analytes in concentrations as close as possible to those found in the coating types to be determined and the chemical compositions are assigned by chemical methods traceable to SI units. The RMs are analyzed by GD-OES, yielding profiles of the mass fraction percentage of each analyte and depth in micrometers.

Found by chemical methods:
12.5 mass-%

Laboratory	1	2	3	4	5	6
Ni contents	12.60		13.60	10.82	11.02	13.30
by GD-OES			13.60	10.50	10.16	12.30
			13.50		10.51	11.00
			13.40			11.80

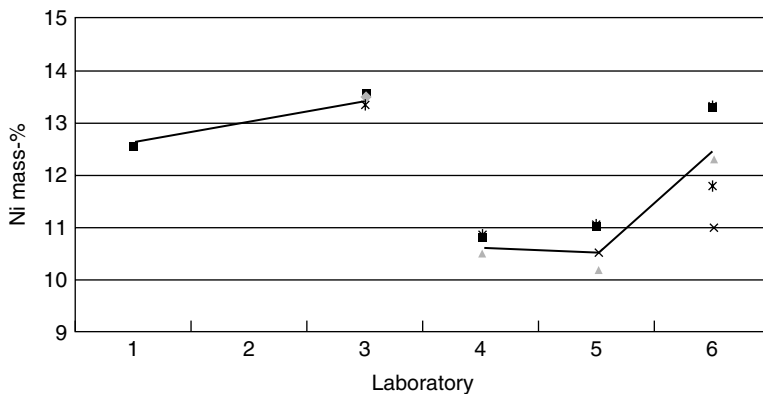


Figure 7.19 Results of interlaboratory tests by GD-OES comparing the results with those of wet chemical methods (sample: Zn–Ni electrolytic coating)

Validation of Depth

The average depth of the crater is measured by means of an optical or mechanical profilometer device, obtaining at least two profile traces in different directions across the center of the crater. The total sputtering depth in the chart is compared with the measured average depth of the crater by means of the profilometer. The coating mass is calculated using the theoretical density of the reference material, if necessary, and compared with the assigned values of the coating mass of the reference material. The average coating thickness is determined as the depth where the concentration of the major element is reduced to 50% of the average value in the coating in mass-% vs μm profile.

Validation of Chemical Composition

The average concentrations of each element are determined as the fractions of the sum of the coating weights of all elements present in the coating. In order to determine the total coating mass per element, the quantitative profile of sputtered mass for each element and the corresponding time (or depth) increment of the depth profile should be prepared (Figure 7.21). The area under each curve is

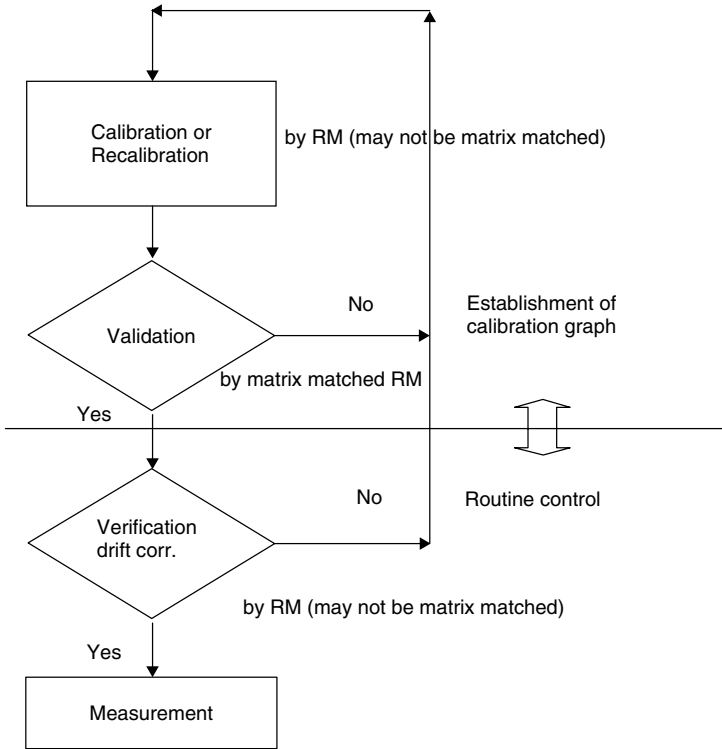


Figure 7.20 Validation and verification in the measurement procedure of GD-OES

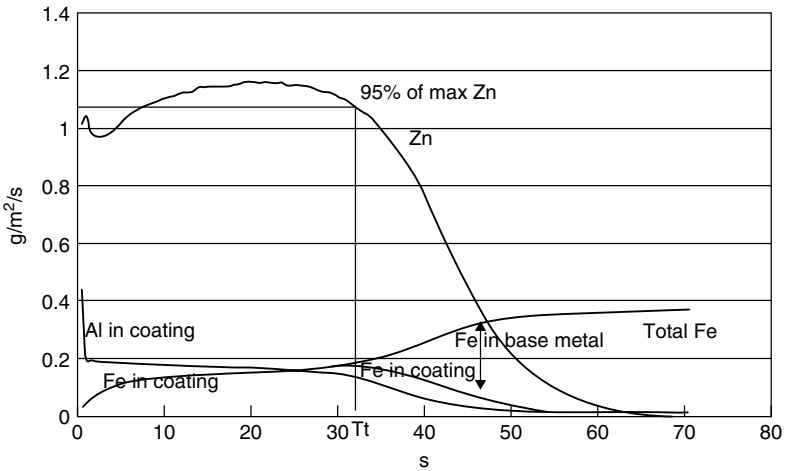


Figure 7.21 Quantitative depth profile ($g/m^2/s$ vs s) of a galvanized sheet. Note: the Al composition in the coating is multiplied by 100

integrated for the time (or depth) corresponding to the total thickness of the coating. When the coating includes the same elements as those in the substrate, the total thickness of the coating is not determined in the profile and the following integration procedure may be applied.

When the coatings include iron, it is assumed that iron in the coating begins to decrease when the signal of the iron in the base metal begins to appear in the profile (T_t s in Figure 7.21). The time T_t may be assumed as the time when the main matrix of the coating (Zn in Figure 7.21) becomes 95% of its maximum (or plateau) value. From time T_t the iron in the coating is assumed to decrease and to reach zero concentration in proportion to the main matrix of the coating. The integration of the iron in the coating transition zone is assumed to be the integral of Zn intensity from time T_t to the time when the Zn concentration becomes zero, multiplied by iron mass at T_t and divided by zinc mass at T_t . The total coating mass of iron is integrated from time zero to T_t plus the integration in the transition zone. In the case of coating elements such as zinc, aluminum, nickel, silicon and lead, which are minor components in the base metal, it is assumed that the elements in the coating reach zero when the mass profiles become same as those in the base metal. The total coating mass per element is integrated from time zero to the time when the mass profiles become the same as those in the base metal. The mass percentage of each element is calculated and compared with the assigned values of the reference material.

7.7 REFERENCES

1. *Surface Chemical Analysis—Glow Discharge Optical Emission Spectrometry (GD-OES)—Introduction to use*, ISO 14707-2000.
2. *Metallic Coatings on Steel—Determination of Mass per Unit Area and Chemical Composition—Gravimetry, Inductively Coupled Plasma Atomic Emission Spectrometry and Flame Atomic Absorption Spectrometry*, ISO/WD 17925.
3. *Surface Chemical Analysis. Determination of Thickness and Chemical Composition of Zn and/or Al Based Metallic Coatings by Glow Discharge Optical Emission Spectrometry*, ISO/WD 16962.
4. Bengtson, A.; Hanstrom, S.; Piccolo, E. L.; Zacchetti, N.; Meilland, R.; Hocquaux, H. *Surf. Interface Anal.* 1999, **27**, 743.
5. Takimoto, K.; Suzuki, K.; Nishizaka, K.; Ohtsubo, T. *Nippon Steel Tech. Rep.* 1987, **33**, 28.
6. Puomi, P.; Fagerholm, H. M.; Rosenholm, J. B.; Jyrkas, K. *Surf. Coat. Technol.* 1999, **115**, 70–78.
7. Puomi, P.; Fagerholm, H. M.; Rosenholm, J. B.; Sipila, R. *Surf. Coat. Technol.* 1999, **115**, 79–86.
8. Karlsson, J.; Hornstrom, S. E.; Klang H.; Nilsson, J. O. *Surf. Interface Anal.* 1994, **21**, 365–369.
9. Hertveldt, I.; De Cooman, B. C.; Claessens S. *Metall. Mater. Trans.* 2000, **31A**, 1225.
10. Rodnyansky, A.; Warburton, Y. J.; Hanke, L. D. *Surf. Interface Anal.* 2000, **29**, 215–220.
11. Suzuki, S.; Suzuki, T.; Kimura, M.; Imafuku, M. *J. Surf. Anal.* 1999, **5**, 282.

8

Surfaces, Thin Films and Coatings

R. PAYLING, P. CHAPON,* K. SHIMIZU,[†] R. PASSETEMPES,[‡]
A. JADIN,[§] Y. BOURGEOIS,[§] K. CRENER,[§] M. AEBERHARD[¶]
and J. MICHLER[¶]

*Department of Physics, University of Newcastle, Newcastle, NSW, Australia,
*Jobin-Yvon Horiba, Longjumeau, France, [†]University Chemical Laboratory, Keio
University, Yokohama, Japan, [‡]Direction de l'Ingénierie des Matériaux,
Technocentre Renault, Guyancourt, France, [§]Certech, Zone Industrielle C, Seneffe,
Belgium and [¶]Swiss Federal Laboratories for Materials Testing and Research
(EMPA), Thun, Switzerland*

8.1 INTRODUCTION

Glow discharge optical emission spectroscopy (GD-OES) is a widely used technique for the rapid depth profile analysis of surfaces, thin films and coatings. The fundamental aspects of these applications were discussed in Chapter 5. Glow discharge mass spectrometry (GD-MS) is also used for depth profiling, but less frequently than GD-OES, and will not be considered here. The first known depth profiles with GD-OES were of GaAs thin films [1] and of stains on steel sheet [2], in the early 1970s. For many years, the technique then developed largely in the steel and automotive industries where it found applications in surface segregation, surface treatments (such as carburizing and nitriding), oxidation and passivation, metallic coatings and polymer coatings. In more recent years, the technique has spread into other industries. Analyses of hard coatings, produced by either chemical vapour deposition (CVD) or physical vapour deposition (PVD), have become a major application area. The technique is also used in the semiconductor industry, for example, for the analysis of the boron phosphorus silicon glass (BPSG) layers on silicon wafers, and in the ceramics and glass industries.

We have chosen a series of recent studies in our respective laboratories to illustrate the capabilities of the technique. In combination with other applications presented in this book, they will give the reader a feel for what the technique is currently being used for and its current capabilities. These studies include the first nanometres of ideal surfaces, deeper industrial surfaces, thin films on glasses and thick films and coatings on steel. All of the results presented here were recorded on radio frequency glow discharge optical emission spectrometry (rf-GD-OES) instruments: either JY5000RF or JY10000RF, manufactured by Jobin-Yvon Horiba, France. They were all recorded at constant pressure in argon and with constant applied power.

GD-OES is not the only technique capable of rapid depth profiling. Its main competitors are dynamic SIMS (secondary ion mass spectrometry) and SEM (scanning electron microscopy with X-ray emission analysis). It is cheaper, faster and more quantitative than dynamic SIMS and is faster and has better depth resolution than SEM. However, like all techniques it also has some limitations, the principal ones being that it is not possible to do micro-spot analysis with GD-OES and some samples are not suitable for mounting on the GD source, e.g. screw threads, porous materials such as foams, and very low-temperature materials, e.g. low-temperature metals and some pure polymers.

GD-OES is a comparative technique, i.e. calibration against known reference materials is required for quantitative analysis. Various schemes for quantitative analysis in both rf (radio frequency) and dc (direct current) powered GD sources have been around for some years now [3]. While they are now gaining some maturity, through international interlaboratory tests ('round robins'), they are still improving. Particular examples are the recent introduction of dc bias voltage and hydrogen corrections in rf analysis [4]. Slowly these tests are showing the superiority of rf over dc methods for the analysis of both conductive and nonconductive materials and coatings.

8.2 SURFACES

8.2.1 OXIDE SURFACE ON STAINLESS STEEL

Figure 8.1 shows the rf-GD-OES depth profile of the air-formed oxide on a stainless-steel surface [5]. The stainless-steel film was formed from 304 bulk stainless steel, deposited as an $\sim 0.3 \mu\text{m}$ thick film, by room temperature magnetron sputtering on to a mirror-polished silicon wafer. Atomic force microscopy (AFM) revealed that the surface of the stainless steel was a series of hills and valleys varying in height by a few tens of nanometres, related to the columnar structure of the sputter-deposited film. Much of the film, however, was locally flat to within 1–5 nm. From XPS studies, the surface oxide on such films is about 2 nm thick [6]. Rf-GD-OES took about 0.1 s to traverse this layer. The resulting depth profile (Figure 8.1) reveals that the surface is high in O and Fe.

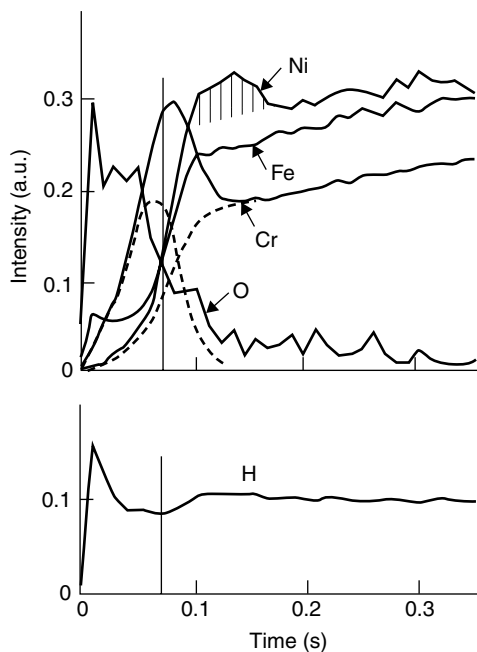


Figure 8.1 RF-GD-OES depth profile of the air-formed oxide surface on stainless steel. Reproduced with permission from Shimizu, K., Habazaki, H., Skeldon, P., Thompson, G. E. and Wood, G. C., *Surf. Interface Anal.* 2000, **29**, 743, Copyright John Wiley & Sons

The H signal is strongest at the immediate surface, indicating the surface is either hydrated or covered in a thin adsorbed water layer. Close examination of the Cr profile, as indicated by the dashed lines in Figure 8.1, suggests that the Cr is concentrated only in the inner part of the oxide. Ni was not present in the oxide layer but was segregated in the metal immediately below the oxide forming an Ni-rich layer. Taking into account the higher sputtering rate of the metal substrate compared with the oxide surface, this Ni-rich layer is less than 1 nm thick. The rf-GD-OES analysis is in agreement with XPS studies. From the rf-GD-OES results, the oxide growth on stainless steel involves the preferential oxidation of Fe and Cr in a duplex structure formed by the faster migration though the oxide of Fe^{3+} ions compared with Cr^{3+} ions.

8.2.2 OXIDE SURFACE ON GALVANIZED STEEL

The qualitative and quantitative analysis of the extreme surface of metals by GD-OES often leads to an apparent excess of oxygen [7], some surfaces having as much as 80 at.% O. Initially, it was thought this was due to the preferential

sputtering of O, but attempts to correct for preferential sputtering were not successful. Recent results suggest the O surplus may be due to the effect on emission yields of the relatively high H levels on the surfaces of metals exposed to air [8]. In particular, H appears to increase the signals from the nonmetallic elements such as C, O, N, P and S. With the development of the hydrogen correction algorithm it is now possible to correct for this effect [4,9].

The galvanized steel coating was a typical commercial product manufactured by continuous hot dipping of steel coil through a molten zinc bath. Such zinc-based coatings are typically 10–20 μm thick and contain typically about 0.5% Al. The small quantity of Al is added to control alloying between the Zn and Fe in the steel base. Some of the Al moves to the surface of the coating during solidification where it oxidizes, forming a mixed Al oxide/hydroxide [10].

Figure 8.2 shows the quantitative depth profile of the immediate surface of the galvanized steel sample with both V_{dc} and hydrogen corrections. The dc bias voltage V_{dc} is lower in the immediate surface than in the zinc substrate. The immediate surface has a very thin (<1 nm) adventitious hydrocarbon layer. Below this is a second very thin (<1 nm) rich in Zn. This second layer could be the beginnings of what is known in the industry as ‘white corrosion’, i.e. the formation of a mixed Zn oxide/Zn carbonate from exposure to moist

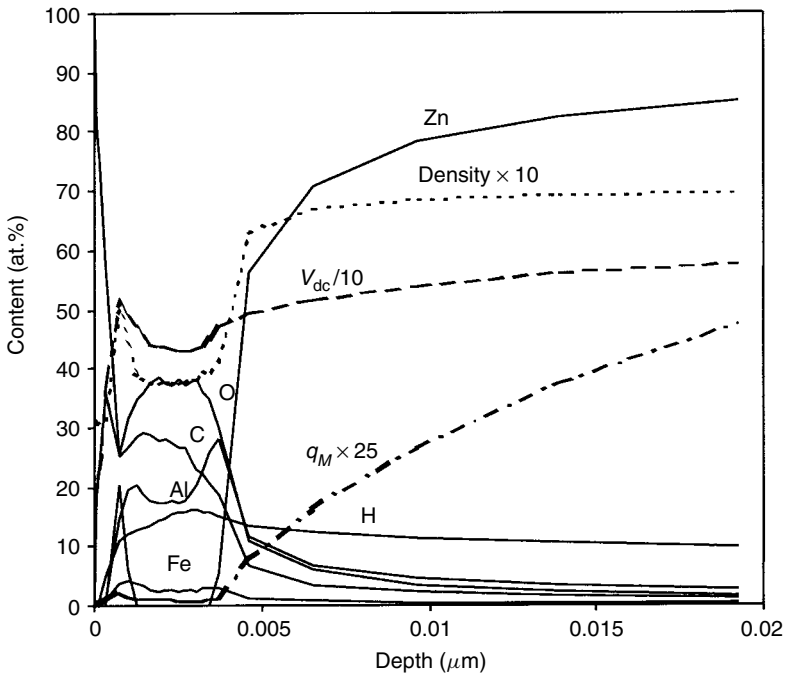


Figure 8.2 Quantitative rf-GD-OES depth profile of the surface of galvanized steel

air. The main surface layer contains C, Al, O and H, with a small amount of Fe, and is about 4 nm thick. The proportions of Al and O are close to an expected stoichiometry of hydrated Al oxide: $\text{Al}_2\text{O}_3 \cdot \text{AlOOH}$. Also shown in Figure 8.2 are the instantaneous values of density and sputtering rate, calculated as part of the quantification algorithm. The density calculation includes the new correction for oxides [9]. The densities and sputtering rates are low in the surface layer, increasing rapidly in the Zn substrate. Note: without the H correction, a 'quantitative' depth profile with these data would show that the surface layer was unrealistically 20 nm thick and predominantly O (around 70 at.%).

8.2.3 OXIDE SURFACE ON ELECTROPOLISHED ALUMINIUM

Figure 8.3 shows the rf-GD-OES depth profile of electropolished aluminium [11]. The sample was a mirror-finished, high-purity aluminium plate, electropolished

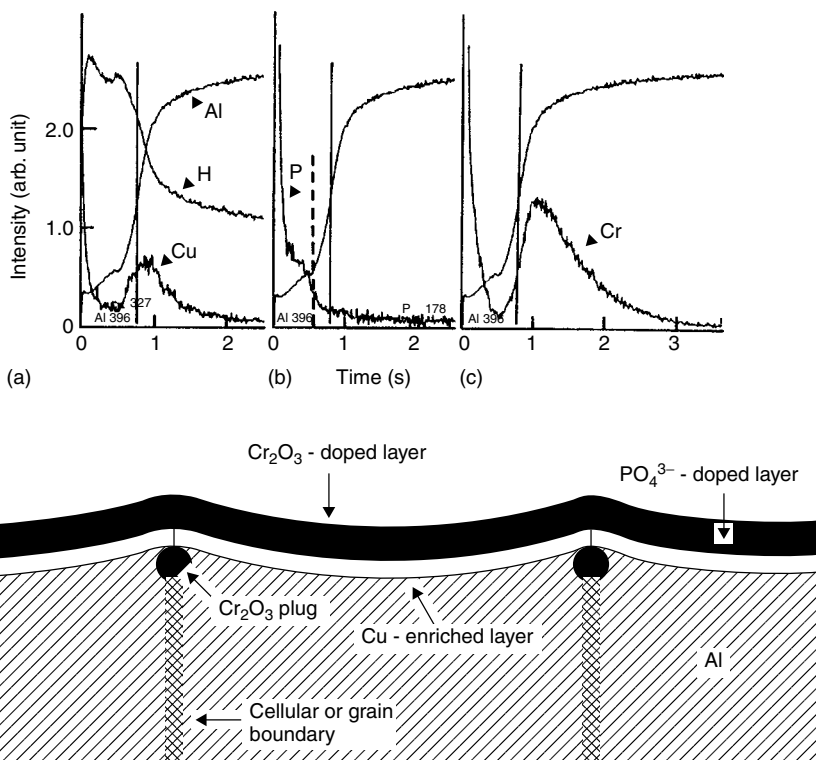


Figure 8.3 Rf-GD-OES depth profile of the oxide formed on an electropolished aluminium specimen and the proposed model of the surface topography. Reproduced with permission from Shimizu, K., Habazaki, H., Skeldon, P., Thompson, G. E. and Wood, G. C., *surf. Interface Anal.* 1999, **27**, 998–1002, Copyright John Wiley & Sons

at a constant current density of 100 mA cm^{-2} in a perchloric acid–ethanol bath held below 10°C , then rinsed in absolute ethanol and warm air dried. It was then given a post-electropolishing immersion treatment in a chromic acid–phosphoric acid solution at 95°C for 5 min, to remove the thin Cl^- doped surface film left by the polishing. Finally it was rinsed in distilled water and warm air-dried. The surface forms a new hydrated oxide surface about 4 nm thick [12]. The rf-GD-OES depth profile shows the oxide was hydrated throughout, in agreement with XPS studies. However, in addition, the temporal profile shows a Cu enrichment just beneath the oxide/metal interface. This Cu enrichment had been predicted theoretically but could not be detected by XPS or various other techniques, including SIMS, so these rf-GD-OES results are the first experimental evidence. The Cu enrichment is formed during electropolishing.

The depth profile in Figure 8.3 shows that Cr was enriched both at the immediate surface and below the surface oxide. The aluminium substrate did not contain Cr, nor did the electropolishing solution, so the Cr seen in the depth profile must come from the post-electropolishing treatment. Also of interest, P was highest at the surface and not present through the whole surface oxide. Such behaviour is similar to thick barrier oxide films formed by anodizing aluminium in neutral phosphate solutions [13]. Interpretation of these GD-OES results led to the model of the surface proposed in the lower portion of Figure 8.3. The bimodal distribution of Cr is due to a superficial oxide and deeper oxide plugs formed through flaws in the surface oxide.

8.2.4 SURFACE TREATMENTS

Automotive manufacturers use many thermal treatments to improve the mechanical properties of steels. Amongst the most frequently used are carbonitriding, carburizing, nitriding and nitrocarburizing. These different procedures are easily identified by rf-GD-OES. Quantitative depth profiles, from 0 to $\sim 100 \mu\text{m}$, provide important information for monitoring the effectiveness of these treatments, on the segregation of elements in the steel and the diffusion of elements from the gases in the controlled atmospheres used to treat the steels [14].

It is not always possible with GD-OES to go from the outer surface of the steel all the way through to the centre of the steel sample in a single measurement. During the GD analysis, some of the sputtered material redeposits on the edge of the crater. When the thickness of this redeposition reaches about $100 \mu\text{m}$, there can be a short-circuit between the anode and the cathode and the plasma stops or becomes unstable. (This is particularly problematic in the higher voltages employed in dc-powered GD sources.) One can then proceed by mechanical polishing of the sample to remove the crater, and thus, by successive measurements, construct the whole diffusion layer over several millimetres. This is time consuming but worthwhile in critical cases. Fortunately, the principal phenomena

of interest—adsorption, segregation, formation of ‘white layers’, decarburization and recarburization—are generally visible in the first 30 μm and this is possible in a single analysis.

8.2.5 CARBONITRIDING: STEEL 27 MC5R

Carbonitriding produces a C and N enrichment on the surface of low-alloy steel. The steel is introduced into an oven, with a temperature set to approximately 850 °C in an atmosphere rich in CO. Additional gases (methane or propane) can be used to control the carbon potential. N enrichment is achieved by the addition of ammonia to the furnace gas.

As can be seen in the depth profile in Figure 8.4, Cr and Mn segregate strongly in the oxidation zone, their surface contents reaching 11 and 8%, respectively, compared with about 1% in the centre of the steel. This phenomenon is caused by these elements having an oxidation potential lower than that of Fe. They are therefore more oxidizable than Fe and segregate both to the surface and to grain boundaries. Ni, on the other hand, has an oxidation potential higher than that of Fe, and so is not subject to this type of segregation. The segregation leads to a depletion layer of these elements below the surface to a depth of about 20 μm .

8.2.6 CARBURIZING: STEEL 27 MC5R

In carburizing (called gas carburizing or cementation in different parts of the industry), only carbon is enriched. The temperature is slightly higher than for

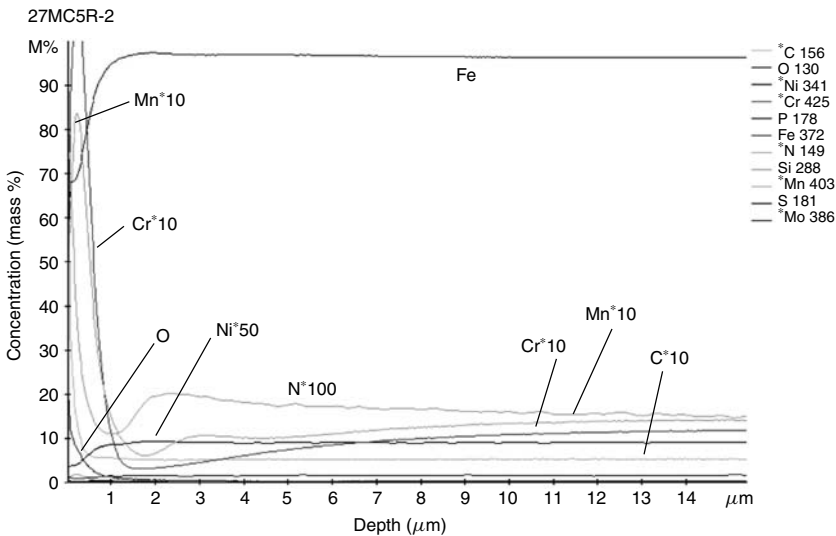


Figure 8.4 Quantitative rf-GD-OES depth profile of carbonitrided steel

carbonitriding (about 900°C). The atmosphere is the same as for carbonitriding but without the ammonia addition. Because of the controlled atmosphere (low pressure and lack of oxygen), the oxide layer is very thin, and no segregation occurs. As seen in Plate 1, there is indeed very little oxygen, while the carbon content goes through a concentration maximum of ~8% at a depth of approximately 2 μm beneath the surface.

8.2.7 NITRIDING: LOW-ALLOY STEEL AND STEEL GRADE 32CDV13

For nitriding, the oven atmosphere is composed of nitrogen, hydrogen and methane. It is therefore nonoxidizing, and manganese does not segregate to the surface. In 'ionic' nitriding of low-alloy steel, the nitride layer ('white layer') reaches a typical thickness of 5 μm as shown in Plate 2. The corresponding scanning electron micrograph illustrates the 'pore' structure formed in the alloy as a consequence of the nitrogen incorporation into the lattice.

In the nitriding of 32CDV13-grade steel, electron microscopy and GD-OES both show the presence of a 10 μm thick 'white layer' as shown in Plate 3. This is followed in the backscattered electron image by a black band (as signified with the arrow), in which microprobe analysis indicates a high degree of carburization. The GD-OES quantitative depth profile shows that the carbon content in this layer is raised from 0.9 to 3%.

8.3 THIN FILMS

8.3.1 ANODIC ALUMINA

The anodic oxidation of aluminium in suitable electrolyte solutions forms a barrier anodic oxide film less than 1 μm thick. Such films are of commercial importance as the dielectric layers of electrolytic capacitors or in the fabrication of thin film electronic devices. The films contain small quantities of species derived from the electrolyte solutions, and these significantly affect the chemical, physical and electrical properties of the films. They are therefore also of considerable scientific interest.

Figure 8.5 shows the rf-GD-OES depth profile of an anodized aluminium surface [15]. The sample was an electropolished, mirror-finished, high-purity aluminium plate, anodized at a constant current density of 5 mA cm^{-2} at 20°C in 0.1 M Na_2CrO_4 solution to 120 V, then rinsed in distilled water and warm air dried. The film was amorphous and highly uniform in thickness and microscopically flat. This can be seen in the transmission electron micrograph image of an ultramicrotomed section of the aluminium substrate and film as depicted on the left-hand side of Figure 8.5. The aluminium substrate is at the bottom of

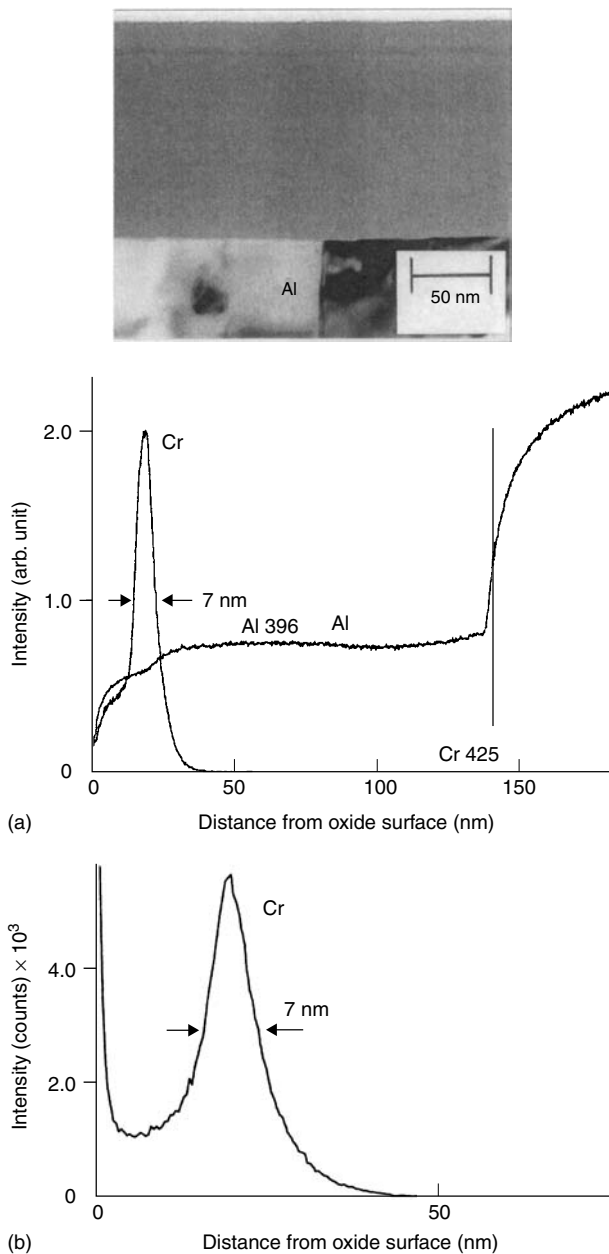


Figure 8.5 TEM image of a cross-sectional portion of anodized aluminium (top) and the corresponding (a) rf-GD-OES and (b) SIMS depth profiles. Reproduced with permission from Shimizu, K., Brown, G. M., Habazaki, H., Skeldon, P., Thompson, G. E. and Wood, G. C., *Surf. Interface Anal.* 1999, **27**, 24–28, Copyright John Wiley & Sons

the image, while the oxide is in the centre and top of the image; inside the film, 19 nm from the surface, near the top of the image, is an extremely narrow dark band about 2–3 nm thick. This band contains about 10 at.% of Cr_2O_3 . Below this band as far as the metal substrate is a pure Al_2O_3 layer, and above the band is an Al oxide layer doped in CrO_4^{2-} and Cr_2O_3 . All of these features can be seen in the rf-GD-OES depth profile (Figure 8.5a), except that the Cr-rich band appears to be about 7 nm thick. This band also appears to be about 7 nm thick in the SIMS profile (Figure 8.5b). The apparent broadening in both the rf-GD-OES and SIMS depth profiles is an artefact of the non-ideal sputtering process (i.e. crater bottoms are not atomically flat).

8.3.2 GLASSES

Several GD-OES papers have considered the analysis of glass [16–18]. The first experiments were performed with dc and were limited to bulk analysis. As glass is nonconductive, the samples were embedded in metallic powder prior to analysis. El Nady *et al.* compared their dc-GD-OES results with values obtained by ICP [16]. As rf-GD-OES allows the direct analysis of nonconductive samples, it offers a new way for characterizing glass samples. Indeed, the technique can be used for both bulk analysis and for depth profiling of multi-layer samples. On glasses, layers of only a few tens of nanometres thickness can be observed without major problems. Moreover, rf-GD-OES does not need any specific sample preparation of the glass prior to the analysis.

Comments on Specific Aspects of rf-GD-OES Glass Characterization

Careful selection of the experimental and source conditions are critical for obtaining reliable results on glass samples. As for other nonconductive samples, the sensitivity of the technique depends strongly on the thickness of the sample. However, unlike many nonconductive samples, glass has a tendency to shatter under mechanical and thermal stress. To prevent localized overheating of the sample from the plasma that can lead to fracturing of the sample, the sample should be cooled to a temperature close to 0°C while mounted on the source, both prior to and during the analysis.

Glass surfaces are generally hydroscopic and are therefore likely to be covered by a layer of water that cannot be removed easily by degassing in the source. This causes an alteration of the depth profile during the first seconds of the analysis owing to the high content of hydrogen, known to induce perturbations both in the sputtering and emission processes. Hydrocarbon contamination produces the same effect [19,20]. As a result, the discharge takes some time to reach an equilibrium situation, and so very thin superficial layers cannot be analysed accurately. In such cases, the deposition of a conducting layer on top of the sample prior to the analysis could improve the reliability of the depth profiles obtained.

For metallic layers deposited on glass substrates, the strong gradient in electrical conductivity at the metal glass interface can induce a sudden variation in the discharge conditions, leading to a possible loss of information in that region. For example, an increase in Si and Na intensities has been observed in the glass substrate close to the interface. It is then difficult to tell the difference between an experimental artefact and the migration of some elements. Another effect appearing in such samples is the decrease in intensity for some elements as the impact proceeds deeper into the sample, although the corresponding concentrations are not expected to vary significantly. Parker *et al.* suggested, for such cases, normalizing the analyte intensities to the intensity of the Ar line [18].

Optical profilometry performed on the substrates after rf-GD-OES impacts shows that the discharge conditions can be tailored to obtain relatively regular craters with a flat bottom. Owing to the small thickness of many deposited films on glass, the substrate is generally reached after only a few tens of seconds of sputtering, making it difficult to determine the shape of the crater in such films. However, the optimum source conditions can be checked by inspecting the shape of the interfaces and verifying that the succession of elements in the intensity profiles is in agreement with the deposition process.

Case Study: rf-GD-OES Analysis of Multi-layer Films Deposited on Glass Substrates

Figure 8.6 shows the rf-GD-OES depth profile of a multi-layer film consisting of three oxide layers (0.67 ZnO–0.33 SnO₂), separated by two Ag–TiO₂ bilayers,

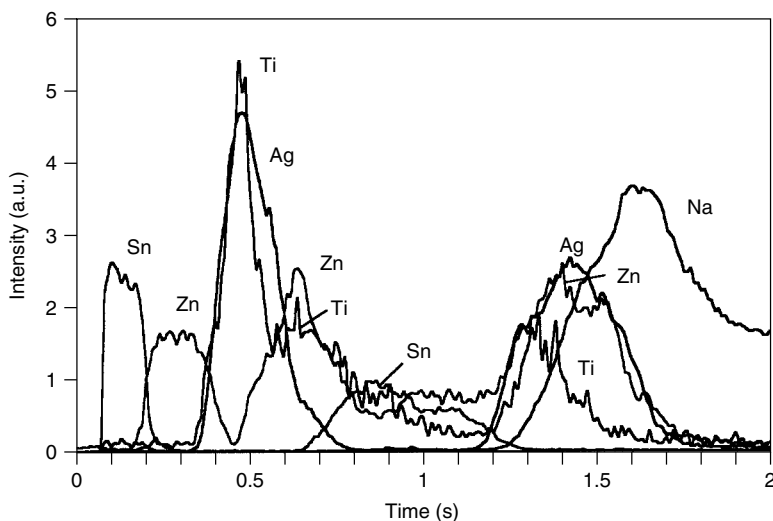


Figure 8.6 Rf-GD-OES depth profile of a multi-layer film deposited on glass

successively deposited on a glass substrate. The thicknesses of the upper and lower oxide layers were approximately 30 nm, while the thickness of the central layer was 77 nm. The lower intermediate layer (closer to the substrate) was comprised of 8.5 nm Ag and 3 nm TiO₂, and the second intermediate layer was comprised of 13.5 nm Ag and 3 nm TiO₂. In each case, Ag was the lower layer. As can be seen in the depth profiles, the top oxide layer (on the left side of the graph) is in fact a bilayer with SnO₂ on top. The Ti and Ag peaks then appear mainly superimposed, probably owing to the small thickness of the TiO₂ layer, but a closer examination shows that the Ti edge is closer to the surface, and that the Ag peak is larger in its upper part. The second oxide layer would be expected to take longer to sputter through, owing to its greater thickness, and Sn and Zn appear in the opposite order compared with that observed on the top layer. The second Ti–Ag layer is then detected, but the corresponding peaks are not well separated from the next oxide layer, where only Zn is clearly visible in the depth profile. However, an expanded view of that region shows that a very weak Sn intensity after the Zn layer. Comparing the first two Sn peaks, this effect could be attributed to the general intensity decrease with depth mentioned above for nonconductive layers. At the same time, a relatively high Na intensity appears, indicating that the film substrate interface has been reached. Normalization of the profiles using the Ar signal does not appear to correct for the Sn intensity decrease in this example. The mixing observed in the depth profiles of the layers close to the substrate could be due to several effects, among them differential sputtering, the very small thickness of the TiO₂ and Ag layers and conductivity differences between the films and the substrate.

Figure 8.7 shows the depth profile obtained on a sample composed of five bilayers (100 nm SiO₂/100 nm TiO₂) successively deposited on a borosilicate glass. In this sample, no metallic layers were present in the stack. The structure appears clearly in the figure. A surface enrichment of carbon and oxygen can also be seen, due to contamination. Another interesting feature is the evolution of the Si intensity, showing a very high value for the top layer, and a slow but continuous decrease for the later ones. As mentioned above, this effect could be due to unstable discharge conditions, mainly in the beginning of the attack. Associated with the Si signal increase at a depth of 1 μm is the onset of B and Na responses, corresponding to the film/substrate interface.

In Figure 8.7, the horizontal axis was calibrated using the known thickness of each film, to display a more realistic estimate of depth, undistorted by different sputtering rates, than is given simply by sputtering time. In the case of unknown thicknesses, a more complex calibration, involving standard samples showing a similar composition to the various layers and substrate, must be performed. This procedure has been developed for some types of materials. However, in many cases, the information supplied by raw intensity versus time profiles can be sufficient to observe the structure of multi-layer films.

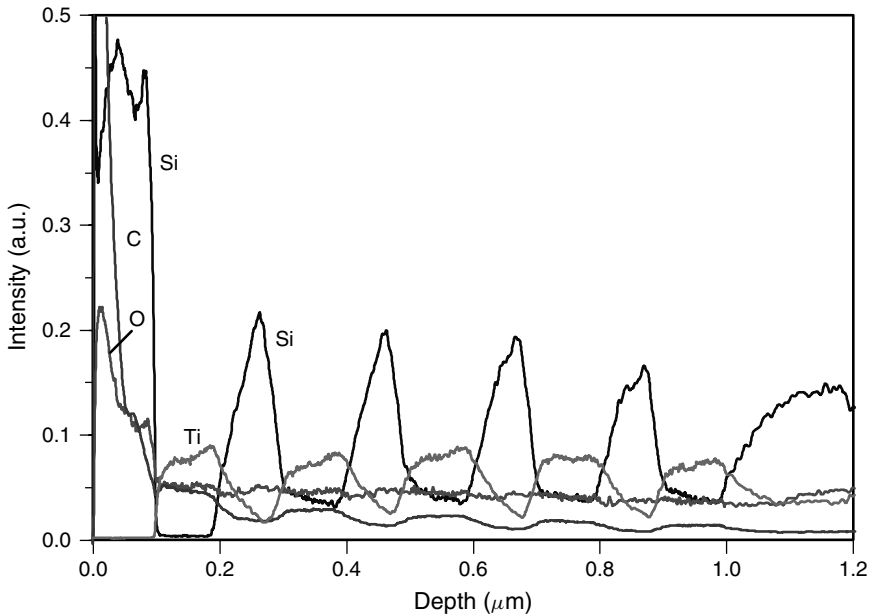


Figure 8.7 Rf-GD-OES depth profile of $\text{SiO}_2/\text{TiO}_2$ multi-layers on borosilicate glass

The results reported here show that rf-GD-OES is a suitable technique for depth-profile analysis of multi-layer films deposited on glass substrates. Indeed, the high depth resolution of this technique can allow the discrimination of nanometre-scale layers and retrieve the order in which they appear on a substrate. This can be useful, for example, in the observation of diffusion processes and in the control of diffusion barrier efficiencies. Moreover, the relative ease of use and rapidity of the analysis are advantages to be considered in quality control.

In comparison with the results obtained on conductive samples, some specific aspects must be considered, especially the effects of thickness and conductivity variations. Although qualitative results can be sufficient in many cases, a calibration can be considered if thickness or concentration information is needed. However, this involves considerable work, in each matrix type, which will probably be the subject of numerous studies in the near future.

8.4 COATINGS

8.4.1 HARD DISKS

Computer hard disks used for the magnetic storage of data are complex multi-layer systems, with layers of thickness varying from a few tens of nanometres to several tens of micrometres. From estimates in 1996, some 750 million disks are produced worldwide each year, growing at around 20% per annum. The extreme

delicacy of the structures and the need for high quality mean that production losses of 60–70% are common. Most disks (called platters in the industry) are made from aluminium alloys, but some magnesium, ceramic, glass and silicon platters have been produced. The platters are coated on both sides with a magnetic material, newer drives having the magnetic material applied as thin metal films. These multi-layer films contain numerous elements that are important to follow during production, in addition to various potential contaminants. Rf-GD-OES has been applied to the study of such materials, utilizing the excellent depth resolution of the technique, its fast sputtering rates and the high dynamic range of composition in the measurements. There is considerable interest in the plating industries in the composition of electrodeposited Ni–P layers, as the performance of hard disks depends critically on the thermal stability, flatness and presence of micro-defects, in the Ni–P layers. These qualities of the layers depend on the uniformity of the composition through the film and the presence of process-related impurities especially at interfaces.

Figure 8.8 shows the rf-GD-OES depth profile of an amorphous Ni–P plated aluminium disk as used for the fabrication of computer hard disks [21]. The disk was 1 mm thick and 3 in (~ 75 mm) in diameter, formed from an Al–4.5% Mg

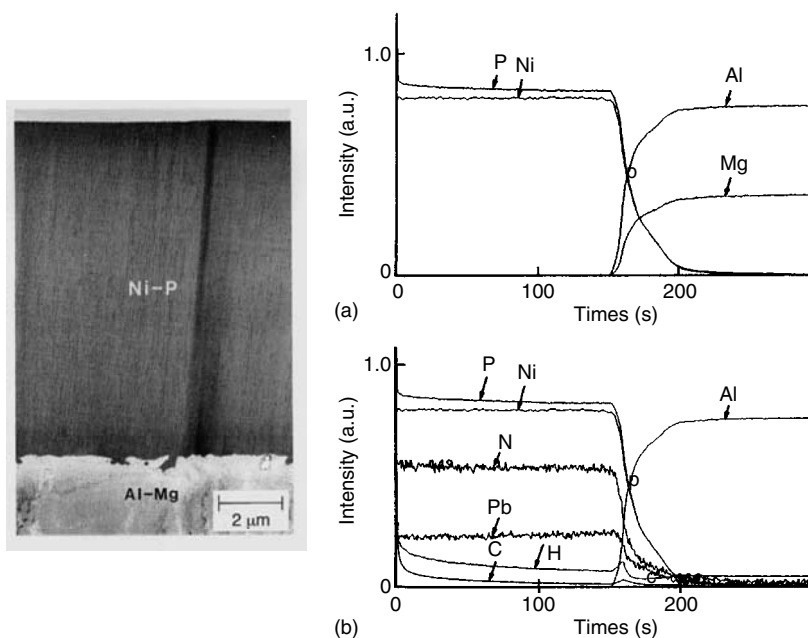


Figure 8.8 Optical micrograph of a cross-section of an Ni–P coating on an Al–Mg substrate, i.e. hard disk (left) and the corresponding rf-GD-OES depth profile of the coating (a) major elements and (b) some additional elements. Reproduced with permission from Shimizu, K., Habazaki, H., Skeldon, P., Thompson, G. E. and Wood, G. C., *Surf. Interface Anal.* 2000, **29**, 151–155, Copyright John Wiley & Sons

alloy, and polished to an average surface roughness of 5 nm. The Ni–P layer was about 12 μm thick. An optical micrograph of the coating is shown in the left-hand portion of the figure, with the substrate being at the bottom of the image and the Ni–P coating in the centre and top of the image. The micrograph shows the outer surface of the coating is flat but that the interface between the coating and substrate is fairly rough.

The major elements present — Ni, P, Al and Mg — are shown in the profile presented in Figure 8.8a. The Ni and P signals are almost constant, indicating that the composition of the Ni–P layer was uniform, although closer examination shows the P signal increases slightly towards the surface. Figure 8.8b shows that Pb and N are also present and uniform in the coating, with C and H are present but not so uniformly distributed. All of these elements are from the chemicals used in the plating bath: Ni sulphate, Na phosphate, Pb acetate and citric and lactic acids, plus ammonia used to adjust the pH of the plating bath to 4.50. Interestingly, S, although present in the bath, was not detected in the coating. The enhancement in the H signal at the interface between the Ni–P coating and Al substrate is of concern because hydrogen is implicated in the blistering of such coating.

Prior to plating, the Al substrate was degreased and etched and then given an alkaline zincate treatment containing ferric chloride. Close examination of the interface, not shown in the figure, reveals high levels of Na, Zn and Fe present at the interface. The rf-GD-OES analysis therefore reveals that residue from the zincate treatment remains at the interface.

8.4.2 CVD/PVD COATINGS

Hard coatings, including TiN, TiC, TiCN and TiAlN, are of major commercial interest as they improve the wear, friction and corrosion resistance of tools and components. Commonly these coatings are prepared by chemical vapour deposition (CVD) or by physical vapour deposition (PVD). GD-OES provides a rapid and sensitive depth profile analysis of these coatings. GD-OES therefore has much to offer this industry by assisting in the development of new coatings and the testing of new processes, and in quality assurance and production problem solving. The first qualitative GD-OES depth profiles of these coatings appeared in 1984 [22] and the first quantitative depth profiles in 1986 [23]. Since then the number of publications using GD-OES analysis of hard coatings has grown steadily [24–26].

The CVD process involves placing the sample to be coated in a furnace at a selected temperature and introducing a selected gas mixture. Given the composition of the gas and the temperature in the furnace, the coating formed is the most thermodynamically stable compound. The coating thickness depends predictably on the time in the furnace and can be predicted from known growth rates. Typically coating thicknesses can be controlled to within $\pm 15\%$ across the sample. For TiN coatings, Ti tetrachloride is added to an N_2 and H_2 carrier gas at

950 °C. For TiCN coatings, Ti tetrachloride is added to an acetonitrile (CH_3CN) and H_2 carrier gas at 850 °C.

One of the longer term aims of GD-OES analysis is the ability to analyse quantitatively any coating, including the wide variety of commercial and experimental hard coatings, with a single calibration. Currently, this is possible for conductive coatings. All of the different conductive matrices studied are combined in a single calibration. In rf-GD-OES, this can be achieved by including dc bias and H corrections. The details are explained in a recent paper [4]. The calibration for hard coatings typically includes a range of Al alloys, brass, steel and stainless-steel samples plus specially prepared reference hard coatings and bulk samples high in N and O.

Figures 8.9–8.11 show the quantitative depth profiles of three coated samples. The coatings all appear to have near-uniform compositions, as expected from their stoichiometries: a TiN-coated steel is shown in Figure 8.9a, a TiCN-coated steel in Figure 8.9b and a TiMoN-coated steel in Figure 8.9c. The depth profile of the TiN coating, in Figure 8.9a, also reveals an inner TiCN-type coating used to improve coating adhesion, while Figure 8.9b shows a thin TiN layer below the TiCN outer coating. In addition to the ability to sputter profile through these technical layers to obtain elemental profiles, one of the key features of the rf-GD-OES analysis is the inherent ability to determine elemental stoichiometry as a reflection of the reaction/treatment conditions.

8.4.3 PLASMA COATINGS

It is not possible at present to measure routinely the dc bias voltage on non-conductive samples. This is because, on a nonconductive sample, the dc bias is formed only on the inside surface of the sample facing the plasma. Hence it is not possible at present to use the dc bias correction as for conductive samples. Studies of other rf plasma parameters are under way and it is hoped that this work will lead to improved quantitative analysis of nonconductive materials [27].

Quantitative depth profiling of nonconductive coatings has, however, been possible since 1993, when Payling *et al.* reported results on pre-painted steel [28]. Their approach is called ‘matrix-matching’, as calibration samples are chosen so that they have similar matrices to the unknown samples/layers. This ensures that the emission yields are constant between calibration and analysis. This is the only successful approach for nonconductive samples to date with rf-GD-OES. A recent example of this approach is shown in Figure 8.10 for a nonconductive ZrOx–YOx plasma sprayed coating on steel.

8.4.4 ELECTRICAL COATINGS

Electrical coatings are used for parts in radio frequency applications such as radio base stations, antennas, radio telephones, lightning conductors, entertainment

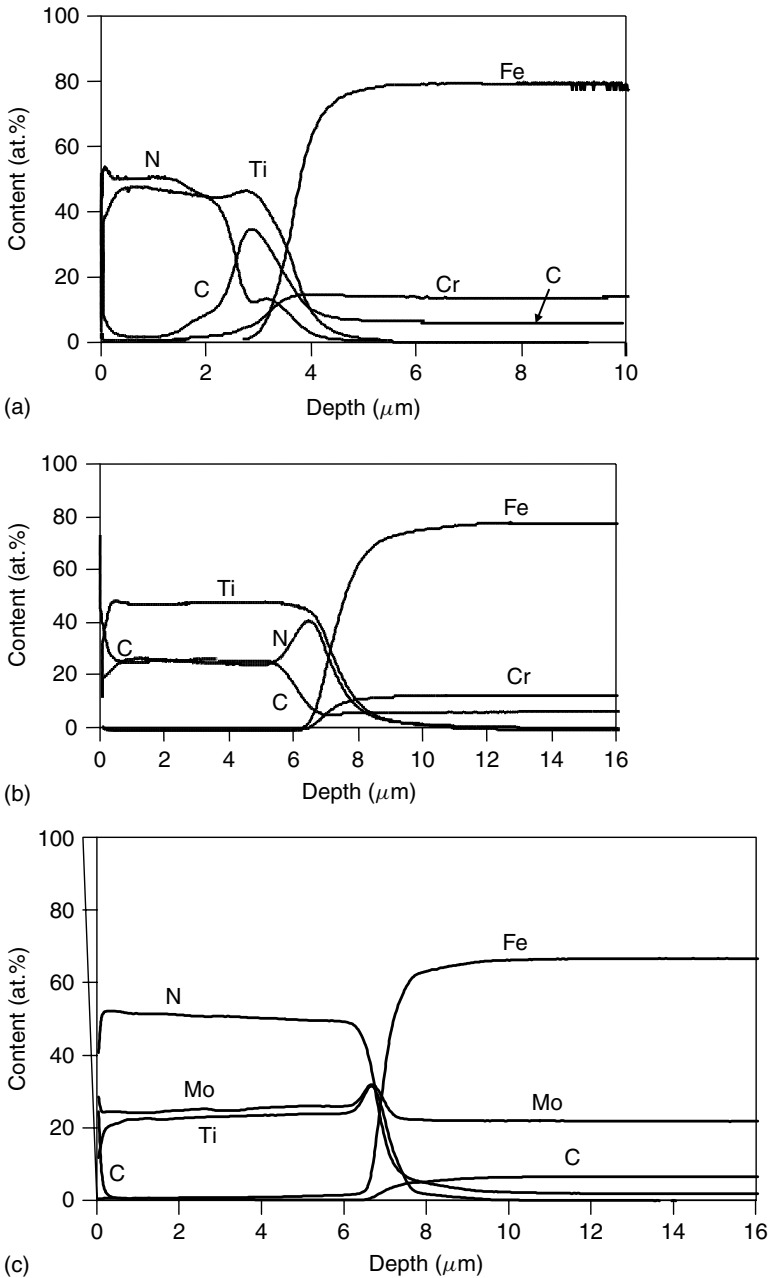


Figure 8.9 Rf-GD-OES quantitative depth profiles of a number of CVD-coated steel specimens: (a) TiN CVD-coated tool steel, (b) TiCN CVD-coated tool steel and (c) TiMoN coated steel. Reproduced by kind permission from The Iron and Steel Institute of Japan

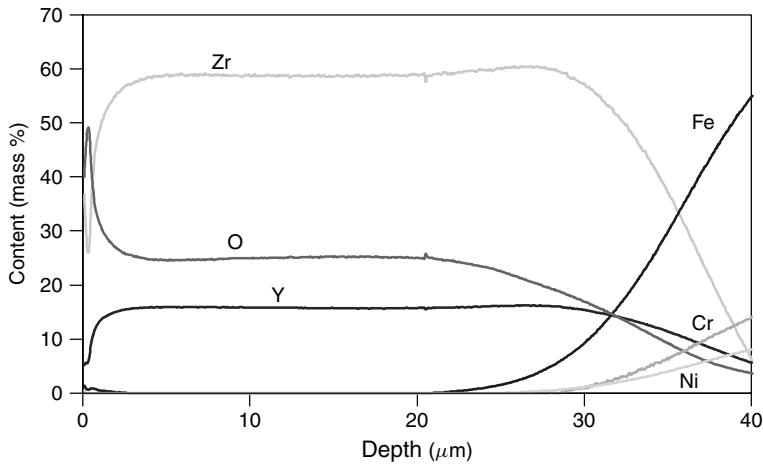


Figure 8.10 Quantitative rf-GD-OES depth profile of a ZrO_x-YO_x plasma coating on a high-alloy steel substrate

electronics, car electronics, computer boards and global positioning system (GPS) devices. A common use is for electrical contacts. The coatings are often applied electrochemically and include gold, silver, nickel or nickel phosphate layers on brass or copper. Gold is chosen for its appearance, for optical effects, corrosion resistance and for ease of soldering. Silver is used for enhanced electrical conductivity. Nickel gives excellent corrosion protection, either as a single coating or as an undercoat for various outer layers. It is also useful as a repair coating, for filling in worn areas or for reclaiming undersized parts. It is used on shafts, rolls, structural parts needing corrosion protection and electrical housings. Nickel layers may also include hard ceramic particles to form a wear-resistant composite coating. Ni-P coatings are resistant to most organic and inorganic media, except strongly oxidizing acids. Rf-GD-OES provides a rapid and sensitive depth profile analysis of all these different coatings.

Three examples of electrical coatings are shown in the rf-GD-OES profiles in Figure 8.11a–c. The first is a fresh, thin Au layer on brass (Figure 8.11a). The second example (Figure 8.11b) is an artificially aged Ag coating on brass showing significant alloying between the Ag and brass substrate related to temperature and time of ageing. The last (Figure 8.11c) is a thin Au layer on top of a Ni alloy coated brass sample, showing that some Au has diffused through the Ni alloy coating into the brass substrate. In each instance, the quantitative and qualitative aspects provide meaningful metallurgical information.

8.4.5 ELECTROPHORETIC COATINGS (CATAPHORESIS)

An electrophoretic coating (called E-coat or cataphoresis in different parts of the industry) is a special treatment for car bodies, applied after cleaning and

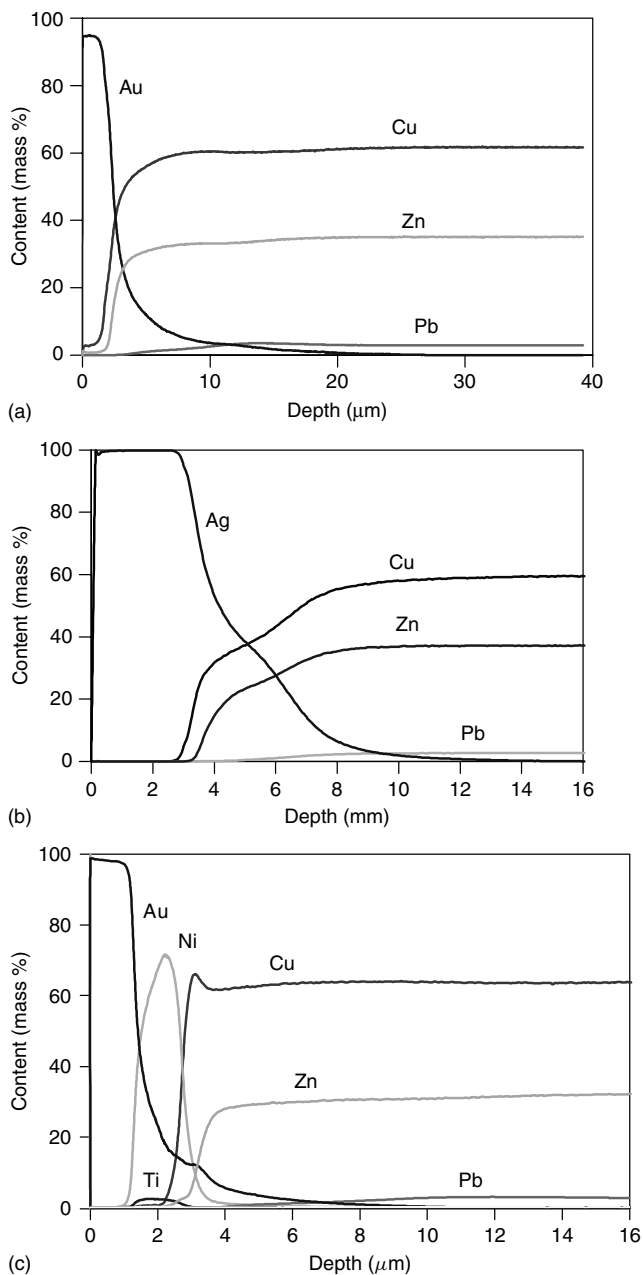


Figure 8.11 Rf-GD-OES depth profiles of precious metal coatings on various brass substrates: (a) Au-coated brass, (b) Ag-coated brass after thermal ageing and (c) Au flash-coating on an Ni alloy-coated brass. Reproduced from by kind permission from The Iron and Steel Institute of Japan

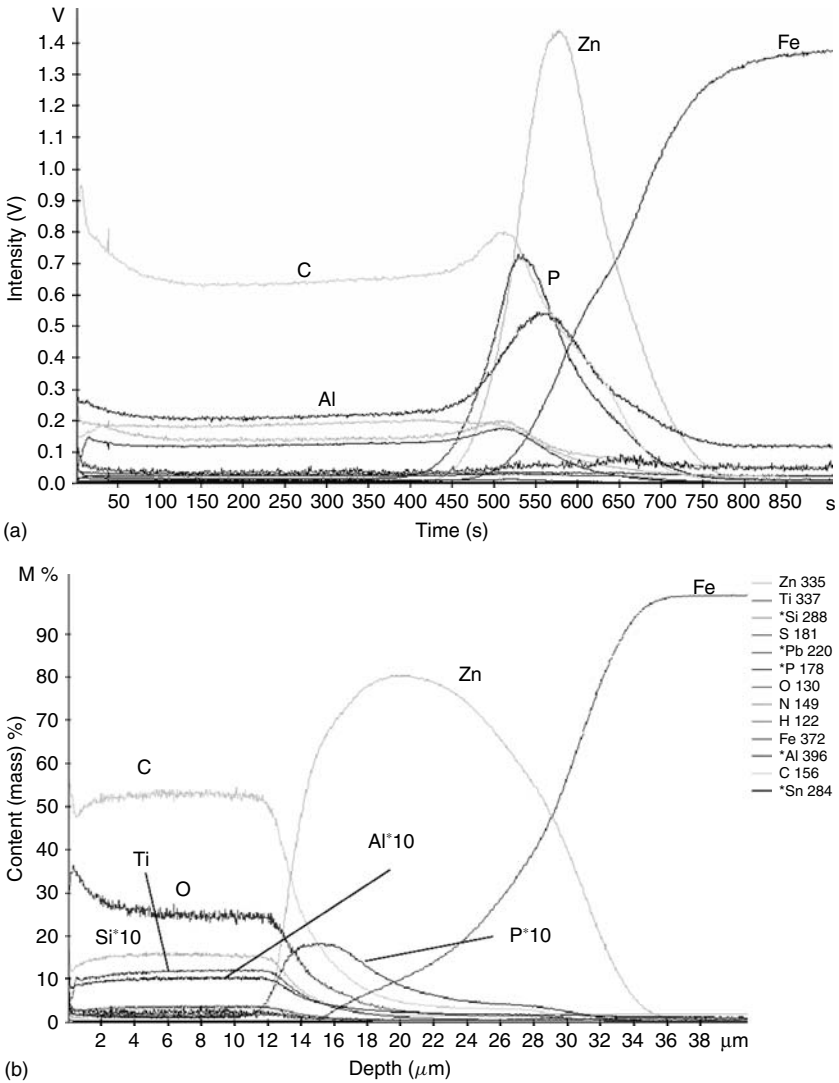


Figure 8.12 Rf-GD-OES depth profiles of electrophoretic coated, phosphated, galvanized steel: (a) qualitative analysis and (b) fully quantitative profile. Reproduced from by kind permission from The Iron and Steel Institute of Japan

phosphatation. This operation deposits a film on the entire care body. It is achieved by total immersion of the vehicle in the coating bath in which the car body is held at a negative potential. The film has a nonconductive organic matrix containing many mineral pigments, and after baking has a typical thickness of about 20 μm .

RF-GD-OES analysis the coating allows a quick determination (in about 10 min) of the chemical composition of the film, the distribution of pigments and the coating thickness, in addition to providing information on preceding coatings and treatments. A qualitative depth profile is shown in Figure 8.12a and the quantitative depth profile in Figure 8.12b. The calibration used for Figure 8.12b was multi-matrix, using solid aluminium standards, zinc alloys, cast iron, steel, ceramics and electrophoretic coatings whose compositions were determined by chemical analysis. After calibration, GD-OES quantitative depth profiles were obtained for seven electrophoretic coatings. The coating thicknesses determined by GD-OES compared well with values determined by profilometry, being within $\pm 1 \mu\text{m}$, and the average coating compositions determined by integrating the profiles for each element in the coatings compared favourably with their chemical analyses.

8.5 CONCLUSIONS

The various applications described show the versatility of rf-GD-OES: its ability to examine a variety of materials, all the way from the first nanometres on the surface of materials, through a wide range of conductive and nonconductive thin films and thick coatings. When the GD-OES results are combined with information from other techniques, the outcome is an important understanding of products and processes.

8.6 ACKNOWLEDGEMENTS

The authors thank IonBond AG, Switzerland, for providing the Bernex CVD coatings, and Huber-Suhner, Switzerland, for the electrical coatings.

8.7 REFERENCES

1. Greene, J. E.; Whelan, J. M. *Bull. Am. Phys. Soc.* 1970, **15**, 1614.
2. Ancey, M.; Berneron, R.; Parnière, P. R. C. *Met. Phys.* 1971, 582.
3. Payling, R. *Spectroscopy* 1998, **13**, 13.
4. Payling, R.; Aeberhard, M.; Delfosse, D. *J. Anal. At. Spectrom.* 2001, **50**, 16.
5. Shimizu, K.; Habazaki, H.; Skeldon, P.; Thompson, G. E.; Wood, G. C. *Surf. Interface Anal.* 2000, **29**, 743–746.
6. Kraack, M.; Bohni, H.; Muster, W. *Mater. Sci. Forum* 1995, **192–194**, 165.
7. Payling, R., in Payling, R.; Jones, D. G.; Bengtson, A. (Eds), *Glow Discharge Optical Emission Spectrometry*, John Wiley & Sons Ltd, Chichester, 1997, pp. 715–721.
8. Bengtson, A.; Payling, R., personal discussion, 2000.
9. Payling, R.; Michler, J.; Aeberhard, M., *Surf. Interface Anal.* in press.
10. Payling, R., in O'Connor, D. J.; Sexton, B. A.; St. C. Smart, R. (Eds), *Surface Analysis Methods in Materials Science*, Springer-Verlag, Berlin, pp. 387–402.

11. Shimizu, K.; Habazaki, H.; Skeldon, P.; Thompson, G. E.; Wood, G. C. *Surf. Interface Anal.* 1999, **27**, 998–1002.
12. Takahashi, H.; Nagayama, M. *J. Surf. Finish. Soc. Jpn.* 1985, **36**, 96.
13. Shimizu, K.; Brown, G. M.; Habazaki, H.; Kobayashi, K.; Skeldon, P.; Thompson, G. E.; Wood, G. C. *Electrochim. Acta* 1999, **44**, 2297–2306.
14. Kurz, M.; Ittlinger, E. *Prakt. Metallogr.* 1999, **36**, 195–205.
15. Shimizu, K.; Brown, G. M.; Habazaki, H.; Kobayashi, K.; Skeldon, P.; Thompson, G. E.; Wood, G. C. *Surf. Interface Anal.* 1999, **27**, 24–28.
16. El Nady, A. B. M.; Zimmer, K.; Zaray, G. *Spectrochim. Acta, Part B* 1985, **40**, 999.
17. Winchester, M. R.; Lazik, C.; Marcus, R. K. *Spectrochim. Acta, Part B* 1991, **46**, 483–499.
18. Parker, M.; Hartenstein, M. L.; Marcus, R. K. *Spectrochim. Acta, Part B* 1997, **52**, 567–578.
19. Dorka, R.; Kunze, R.; Hoffmann, V. *J. Anal. At. Spectrom.* 2000, **15**, 873–876.
20. Bogaerts, A.; Gijbels, R. *J. Anal. At. Spectrom.* 2000, **15**, 441–449.
21. Shimizu, K.; Habazaki, H.; Skeldon, P.; Thompson, G. E.; Wood, G. C. *Surf. Interface Anal.* 2000, **29**, 151–155.
22. Hocquaux, H.; Ohannessian, L.; Flandin-Rey, Y.; Chapon, J. *Report No. 1609*, UNIREC, Firminy, France, 1984.
23. Stock, H.-R.; Mayr, P. *Härterei-Tech. Mitt.* 1986, **41**, 145.
24. Böhm, H., in Payling, R.; Jones, D. G.; Bengtson, A. (Eds), *Glow Discharge Optical Emission Spectrometry*, John Wiley & Sons Ltd, Chichester, 1997, pp. 676–87.
25. Freire, F. L., Jr; Senna, L. F.; Achete, C. A.; Hirsch, T. *Nucl. Instrum. Methods Phys. Res. B* 1998, 136–138.
26. Jehn, H. A. *Surf. Interface Anal.* 1998, **26**, 834.
27. Payling, R.; Chapon, P.; Bonnot, O.; Belenguer, P.; Guillot, P.; Pitchford, L. C.; Therese, L.; Michler, L.; Aeberhard, M. *ISIJ Int.* 2001, **42**(suppl.), in press.
28. Payling, R.; Jones, D. G.; Gower, S. A. *Surf. Interface Anal.* 1993, **20**, 959–966.

9

Comparison of Glow Discharge Atomic Spectrometry with Other Surface Analysis Methods

K. WAGATSUMA

Institute for Materials Research, Tohoku University, Sendai, Japan

9.1 INTRODUCTION

A variety of analytical methods are available as experimental techniques for surface analysis. However, the majority of them are specified methods for particular specimens in a particular sample form, while requiring careful sample pretreatment and experimentation. This offers a pronounced contrast with the routine applications of glow discharge atomic spectrometry (GDS) covering various types of samples. The aim of this chapter is to compare GDS with other methods for surface analysis that are usually available. These methods can be classified into four categories: ion probe, electron probe, X-ray probe and laser probe methods, based on what is employed as the excitation source. Because GDS is principally directed at the elemental quantification of materials, some methods which give structural information, such as X-ray diffraction, and also vibrational spectroscopy are not mentioned here.

For these comparisons, one should recall the features of GDS (the acronyms used below will be explained in a subsequent section):

1. *Elemental quantification with high accuracy.* The glow discharge plasma is a high-performance excitation source for atomic emission spectrometry,

being very stable and emitting atomic spectra with high signal-to-background ratios. Quantitative analyses by glow discharge optical emission spectrometry (GD-OES) are carried out with a standard procedure, similar to that employed in inductively coupled plasma emission spectrometry, which is the most popular method in emission analysis. If appropriate standard reference materials can be prepared, GD-OES provides accurate analytical results from the calibration relationship. On the other hand, the quantification of other methods such as AES and XPS is generally complicated, because the reference material of which the surface is strictly defined cannot be obtained in most cases. Further, SIMS has some additional complications for quantification as the observed elemental ionization efficiencies depend dramatically not only on the composition of the surface but also on the kind of primary ions employed.

2. *Depth profiling at a relatively high erosion rate.* As is often mentioned, the sampling rate in GDS is relatively large (typically $1 \mu\text{m}/\text{min}$), mainly owing to the high density of ions bombarded into the cathode sample. As such, GDS is a suitable technique for depth profiling of relatively thick layers, such as Zn-coated steels and hot-rolled oxide layers. Ion etching guns employed with AES and XPS have much lower rates of the sputtering ranging $1\text{--}10 \text{ nm}/\text{min}$; although the in-depth resolution is generally better than that of GDS, the measuring time is prolonged. In static SIMS, ISS, and RBS, their sputtering rates are negligibly small. Dynamic SIMS is operated over a wide range of sputtering rates. A particular ion gun yielding higher sputtering rates is employed in ion microprobe analysis (IMA), having sputtering rates of several tens of $\mu\text{m}/\text{min}$.
3. *Average information over a relatively large area.* The sampling area of GDS is $0.5\text{--}2.0 \text{ cm}^2$, determined by the geometry of the discharge tube used to obtain stable glow discharge plasmas. Therefore, analytical results by GDS are the average chemical composition over a large sampling area. Unlike GDS, the lateral mapping of the composition is a particular advantage of electron probe methods such as AES and EPMA. In all microprobe methods, the excitation source can be sharply focused by an electrostatic lens. Three modes of the analysis can provide zero- to two-dimensional distribution of elements, as illustrated in Figure 9.1a–c. Such information has contributed to studies on the microscopic structure of various materials. Also in SIMS, two-dimensional imaging of the ion signals can be obtained. More recently, X-ray beams can be collimated up to a diameter of $100 \mu\text{m}$, so that the elemental mapping by photoelectrons is possible in XPS.
4. *No requirement for ultra-high vacuum and easy sample handling.* This is probably the most significant advantage of GD-OES in manufacturing applications for quality control. Most of the surface analysis methods may be operated only in a ultra-high vacuum environment in the range $10^{-6}\text{--}10^{-8} \text{ Pa}$. The reason for this is that the low-energy electrons and secondary ions monitored in some methods are easily scattered by the residual gas to decrease the signal

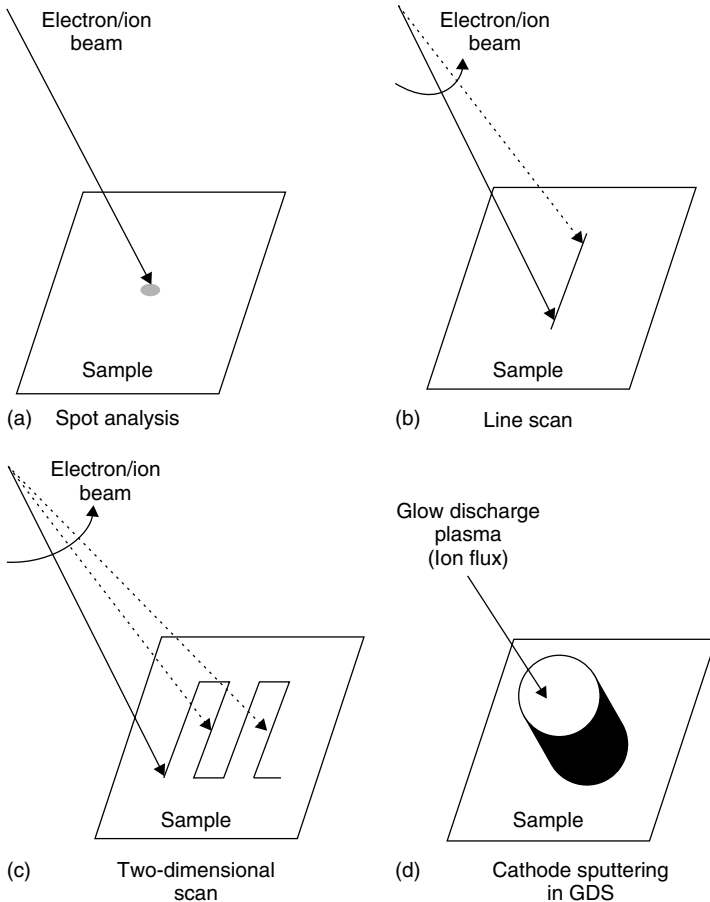


Figure 9.1 Measuring modes of electron/ion probe spectrometry

intensity drastically. In addition, the cleanliness of the sample surface must be maintained during analysis to prevent adsorption of the residual gas in the ultra-high vacuum chamber. Handling of the samples is thus complicated and a prolonged time for the measurement is needed. In routine analysis for quality inspection, GDOES is superior to the other methods because of its simplicity and rapid response.

5. *Destructive method.* Intrinsically, GDS, dynamic SIMS and IMA are destructive analytical methods to obtain the depth profiles of the chemical composition. In AES and XPS, ion bombardment with an ion etching gun is extensively employed to obtain the in-depth information at deeper portions of the sample. On the other hand, nondestructive depth profiling of the sections can be performed with angle-resolved XPS and RBS.

9.2 SURFACE ANALYSIS METHODS COMPETITIVE WITH GLOW DISCHARGE SPECTROMETRY

9.2.1 ION PROBE METHODS

Considering the similarity in the sampling process, ion probe methods could provide useful knowledge for characterizing the depth profiling in GDS. Comparison of GDS with several ion probe methods is therefore important. During the bombardment by ions or neutral atoms, several effects are caused on and near the sample surface: sample particles are ejected (sputtering) and the primary bombarding particles are implanted into the sample as well as reflected (backscattered) to the gas phase. All of the particles can yield some analytical information, which form the family called the ion probe surface analysis methods.

Secondary ion mass spectrometry (SIMS) is one of the most important surface analytical techniques [1]. The basic principle of SIMS is that charged atomic or molecular species are ejected from the sample surface bombarded by energetic ions and are subsequently analyzed with a mass spectrometer. There are two modes of operation in SIMS, as shown in Figure 9.2a and b:

1. In dynamic SIMS, the ion sputtering proceeds at fairly high densities of the primary ion current, up to several A/cm^2 , thus leading to a rapid sputtering rate. With the progress of the sputtering, depth profiling of the elemental composition can be obtained by measuring the ion intensities as a function of sputter time.
2. In static SIMS, the ion sputtering is achieved by very low ion densities, down to $\mu A/cm^2$. This mode enables the composition of the uppermost layers to be determined. These very mild conditions of sputtering are applied to the analysis of polymers, organic and biochemical materials, and so on. The major reason for this is that the precise depth profiling of such samples can be obtained as there is little damage to their structures.

A major feature of SIMS is that all elements including hydrogen can be detected with high detection sensitivities and, as the analysis is based on the mass separation of the secondary ions, their isotopes and molecular species can be also detected. On the other hand, quantification by SIMS can be difficult because the secondary ion yields are very sensitive to the composition of the surface. Therefore, quantitative analysis is generally carried out by comparison with standard reference materials close to the composition of the specimen being examined.

Imaging SIMS is an effective technique to obtain a three-dimensional analysis of the sample. As illustrated in Figure 9.1c, a fine beam of primary ions is rastered across the surface while analyte species are monitored. In addition, the entire field of view can be imaged simultaneously in the ion optics of the SIMS instrument, which is analogous to an optical microscope. In this case, the lateral resolution depends on the size of the apertures in the ion optics of the mass analyzer.

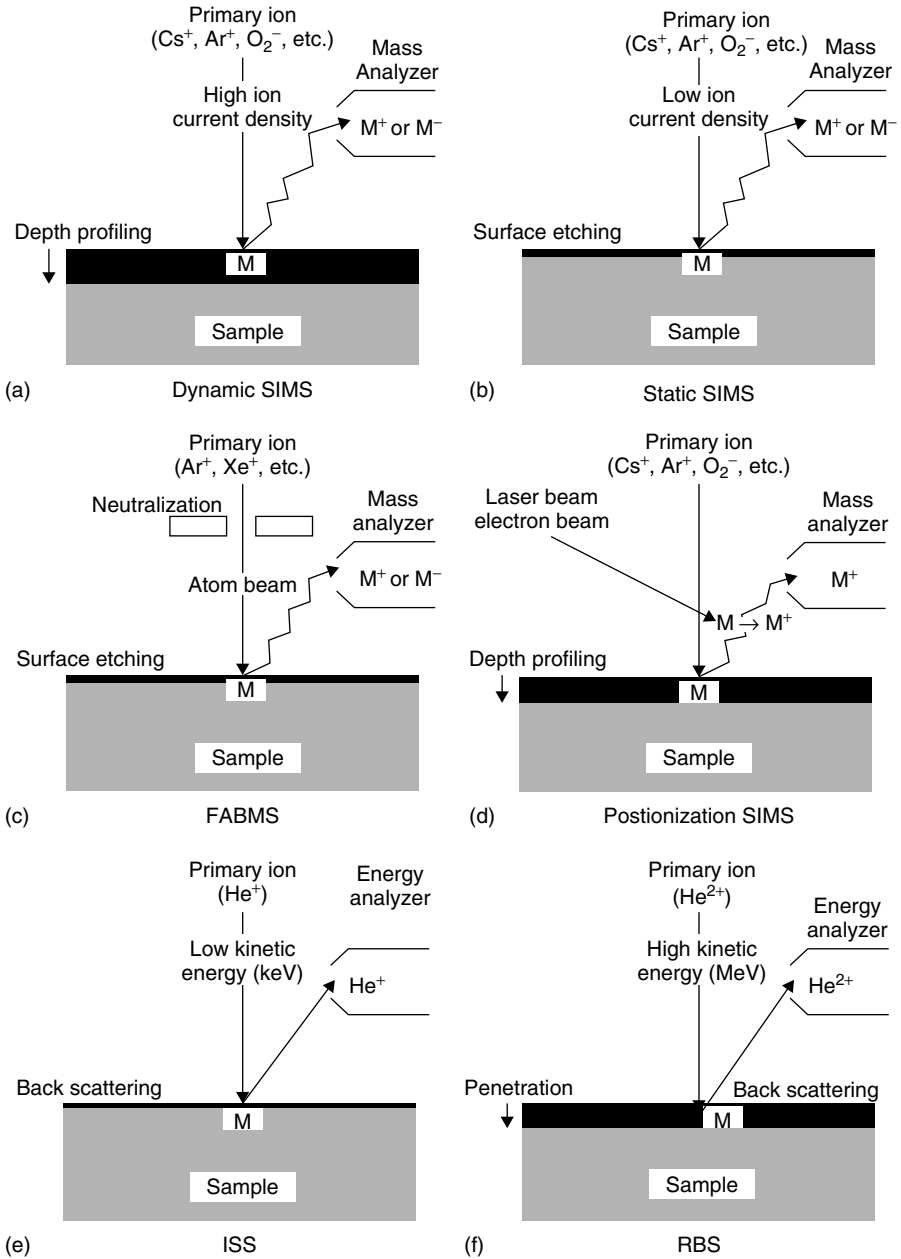


Figure 9.2 Principles of ion probe spectrometry

By developing a neutralizing method for the probing ion beam, fast atom bombardment mass spectrometry (FAB-MS) is employed as an alternative method for analysis of insulating samples to reduce charging effects (Figure 9.2c). By use of the atomic beam, sample damage can be reduced in the analysis of easily decomposed materials such as organic films. Another advanced technique in SIMS involves post-ionization methods, generally referred to as sputtered neutral mass spectrometry (SNMS). Neutral species which are a major part of the sputtered particle population are additionally ionized by laser irradiation or an electron beam so that they can be detected with a mass spectrometer (Figure 9.2d). This approach might improve the detection sensitivity. Furthermore, this can reduce matrix effects which are manifest by the large variations in the ion yields in SIMS, because a large fraction of the ionized particles are produced through the post-ionization process. This effect is similar to the plasma excitations in GDS.

Reflection of the incident ion is known as the backscattering phenomenon, which also has a good deal of analytical information [2]. In the case of low-energy ions (a few keV) the method is called ion scattering spectroscopy (ISS), whereas energy analysis of backscattered ions having higher kinetic energies (several MeV) is generally referred to as Rutherford backscattering spectroscopy (RBS), as illustrated in Figure 9.2e and f. The ISS analysis is sensitive to only the topmost monolayer of the sample surface; however, the RBS spectrum involves not only elemental information but also the depth distribution to a depth of about $1\ \mu\text{m}$. In both cases, the sample is bombarded by a monoenergetic ion beam (usually He ions), and the ions scattered from the sample surface are energy analyzed. In ISS, the energy ratio between the incident and scattered ions relates directly to the kind of the uppermost sample atoms. On the other hand, the RBS spectrum contains information not only regarding the elemental identification but also their position beneath the sample surface.

9.2.2 ELECTRON PROBE METHODS

When a sample is irradiated with high-energy electrons having acceleration energies of a few tens of kilovolts, core electrons are ejected, resulting in the ionization of sample atoms. In general, these primary electrons cannot be utilized for elemental identification because their kinetic energies are lost in various ways on traveling through in the solid-phase sample. However, the ejected electrons having a wide range of kinetic energies, called secondary electrons, are very useful for imaging purpose as in scanning electron microscopy (SEM), as illustrated in Figure 9.3a. Microstructures in shape such as defects, precipitates, grain boundaries and so on are easily observed by SEM.

Once an atom has been ionized it must return to the atomic ground state. The hole of an inner electron orbital resulting from irradiation of energetic electrons may be filled by an electron from a higher level, and the energy difference

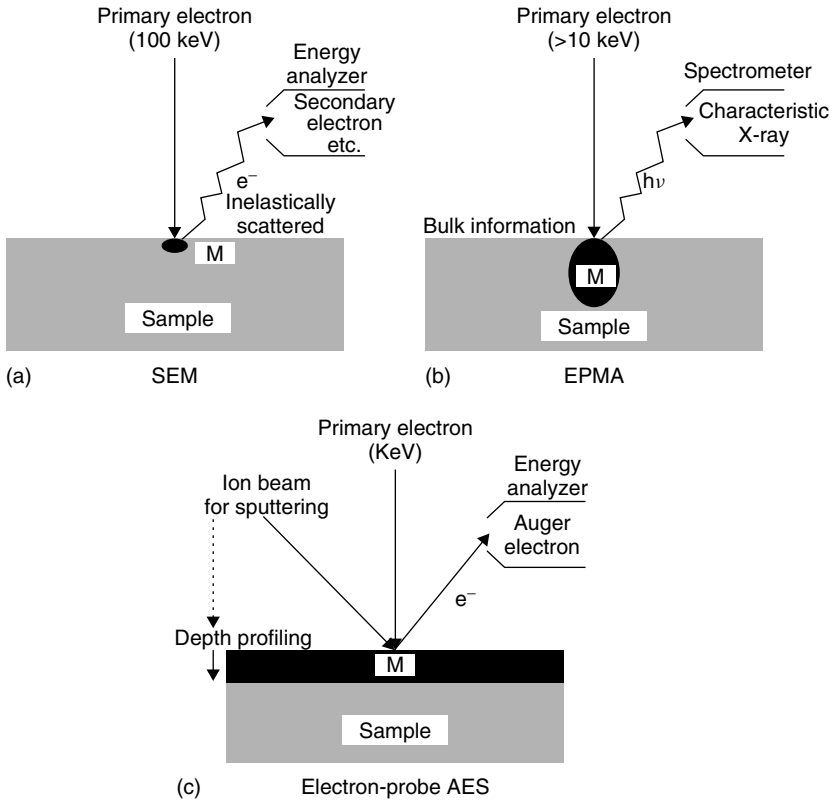


Figure 9.3 Principles of electron probe spectrometry

between the core and the higher orbitals can be released principally in two different ways [3]. One process is the emission of an X-ray photon, called the characteristic X-ray radiation for the target element:

$$h\nu = E_c - E_v \tag{9.1}$$

where $h\nu$ is the energy of the characteristic X-ray, E_c is the binding energy of the core electron and E_v is the binding energy of the higher level electron. The other possibility is an Auger transition process wherein another electron in a higher orbital can be ejected from the atom:

$$E_{c\nu\nu'} = E_c - E_v - E_{v'} \tag{9.2}$$

where $E_{c\nu\nu'}$ is the kinetic energy of the Auger electron and $E_{v'}$ is the binding energy of the emitted electron.

Both of the secondary particles contain analytical information. The photon energy of a characteristic X-ray is well defined by the energy difference between two energy levels of the corresponding electron orbitals, which is the basis of electron probe microanalysis (EPMA) (Figure 9.3b). An important feature of EPMA is that the information depth is large ($> 1 \mu\text{m}$) owing to small attenuation of the X-ray flux in the solid phase. Therefore, EPMA is an analytical method for bulk samples rather than for only surface analysis. The kinetic energy of an Auger electron is approximately equal to the difference between the energy level of the core hole and the energy levels of the two outer electrons; thus, the electron energy is characteristic of the material identity, being independent of the energy of the primary radiation electrons. In Auger electron spectroscopy (AES), the emitted electrons (including Auger electrons) are energy-analyzed when a focused beam of electrons is irradiated at a spot size of $100 \mu\text{m}$ down to several 10 nm in diameter (Figure 9.3c). AES is sensitive to only the near-surface atoms (a few nanometers) because the Auger electrons (having the kinetic energies of $2\text{--}20 \text{ keV}$) are rapidly attenuated in the solid phase. In addition to the above-mentioned process, the emission of Auger electrons can be also observed following excitation by X-rays so long as the photon energy is large enough to cause the Auger process (Figure 9.4a).

Finely focused electron guns are available for AES and EPMA measurements; therefore, point analysis of μm^2 regions can be carried out at high spatial resolution [4]. Furthermore, the focused beam of primary electrons is rastered across the sample surface, leading to a two-dimensional map of the chemical composition [scanning Auger microscope (SAM)]. As the Auger electron yield is very sensitive to the electron take-off angle, an image of Auger electron intensities could reflect the surface topography of the sample surface, which is often similar to the SEM image [4].

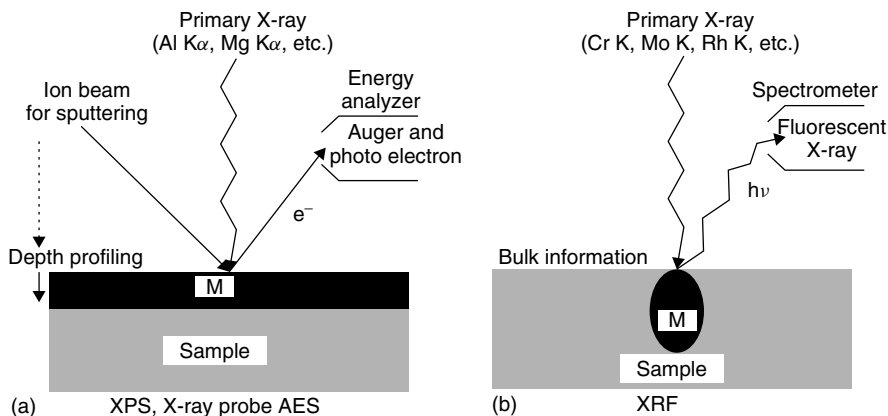


Figure 9.4 Principles of X-ray probe spectrometry

Although AES is a nondestructive method for estimating the chemical composition in the uppermost several nanometers range of the sample surface, depth analysis proceeding to a deeper region is sometimes needed in research for various material systems. For this purpose, the spectrometer for AES is usually equipped with an ion etching gun to remove materials from the sample surface. The AES analysis is then carried out sequentially with materials removal by ion sputtering and a depth profile regarding the chemical composition is gradually generated. Auger electron spectroscopy combined with the ion bombardment is a competitive method with GDS. The resulting data are recorded as elemental intensities versus sputter time. As with other sputter-based methods, the major problem in the depth profiling is the conversion of the sputtering time scale to an actual depth scale. In practice, one must calibrate the ion gun for a particular material in order to obtain the true in-depth profile. Duoplasmatron ion sources, which comprise a magnetically constricted arc plasma, have recently been employed as the ion etching gun. The gun provides an intense ion source with a narrow energy spread, making it suitable for small spot focusing. Usually, inert gas ions such as Ar having kinetic energies of 1–10 kV are employed at an ion current of several tens of microamps.

9.2.3 X-RAY PROBE METHODS

X-ray photoelectron spectroscopy (XPS) is based on the ejection of an electron from a core electron orbital when irradiating with an X-ray photon [3], as shown in Figure 9.4a. The kinetic energy of the electron (E_k) is dependent on the energy of the X-ray employed ($h\nu$) as the X-ray supplies the energy corresponding to the binding energy and then the surplus of the X-ray energy is converted into the kinetic energy of the emitted electron. Therefore, the binding energy of the electron (E_b) is the parameter which identifies the components of the material. The relationship between the parameters involved in the XPS measurement is as follows:

$$E_b = h\nu - E_k - W \quad (9.3)$$

where W is the spectrometer work function. As all three quantities on the right-hand side of the equation are measurable, it is easy to determine the binding energy of the electron by which the type of the material is determined. The X-ray source in XPS is usually chosen among those elements having soft characteristic X-rays, typically Al $K\alpha$ and Mg $K\alpha$.

One of the advantages of XPS is its ability to give the information regarding chemical state such as the oxidation number and the kind of compounds [5]. Depending on the chemical state of the sample, the peak position and the shape of XPS spectrum are changed and additional peaks appear in some cases, which are referred to as the XPS chemical shift. XPS is also known by the acronym ESCA (electron spectroscopy for chemical analysis), which emphasizes the capability

for the chemical state analysis. Data on chemical shifts have been tabulated for many elements.

XPS has a limited escape depth for the photoelectrons (typically 3 nm), for the same reason as in AES. Accordingly, XPS associated with ion sputtering to remove successive layers is also a competitive method with GDS. The depth profiling in XPS can provide variations in the chemical state as a function of the sample depth, whereas GDS provides only elemental composition. In addition to this technique, especially in XPS, the angle-resolved measurement of photoelectrons provides in-depth distribution of the sample species. It is clear that the depth of analysis is dependent on the electron take-off angle: smaller sampling depths are obtained at lower take-off angles and the maximum sampling depth at a normal take-off angle, as illustrated in Figure 9.5. The XPS measurements at different take-off angles result in a depth profile just beneath the sample surface. This depth profiling is effective for investigating compositional changes very close to the surface, e.g. passive oxide films on metals.

In X-ray fluorescence spectrometry (XRF), wavelengths and intensities of X-rays emitted by a sample are measured when the sample is irradiated with a characteristic X-ray such as Cr $K\alpha$ (Figure 9.4b). The penetration depth of the primary X-ray varies from a few to 1000 μm , depending on the type of sample material. Unlike GDS, XRF is a nondestructive method for the analysis of bulk samples rather than surface layers because the information depth exceeds micrometer-order thicknesses. Further, as such X-rays are not absorbed by air, this method does not necessarily require ultra-high vacuum conditions. This condition is similar to that of GDS, indicating that both XRF and GDS are available for rapid analysis. When analyzing thick layers and bulk samples, XRF is extensively employed to obtain the elemental compositions.

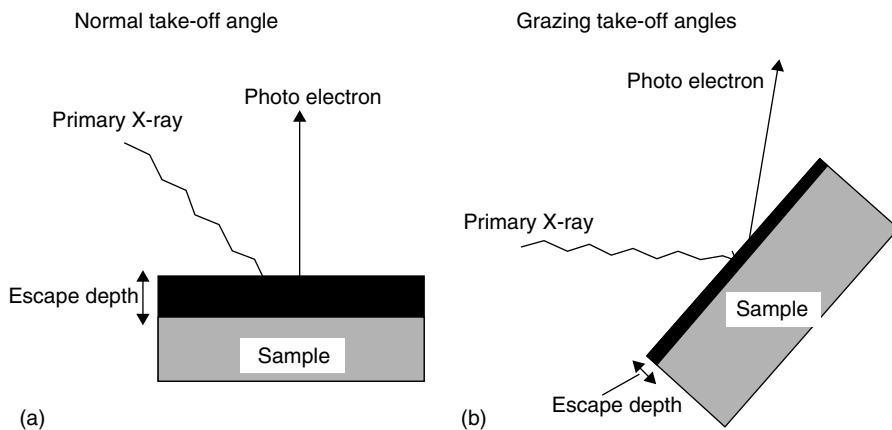


Figure 9.5 Schematic diagram of an angle-resolved method in X-ray photoelectron spectrometry

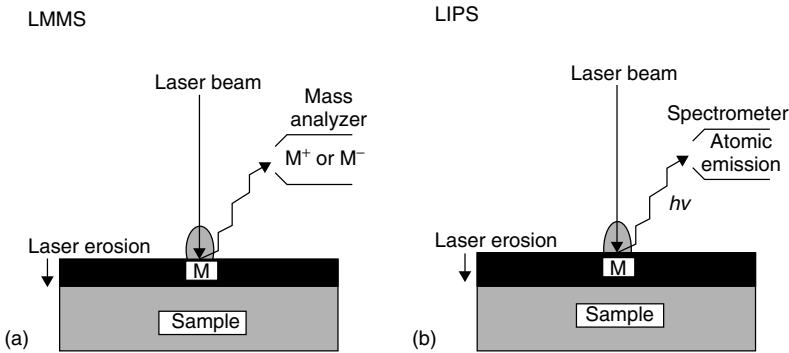


Figure 9.6 Principles of laser-probe spectrometry

9.2.4 LASER PROBE METHODS

When a laser beam is irradiated on a sample surface, a laser-induced (laser breakdown) plasma can be generated and evaporation of the sample species, called laser ablation, then occurs [6]. In laser microprobe mass spectrometry (LMMS), sample atoms ionized by the laser-induced plasma are analyzed (Figure 9.6a). On the other hand, atomic emission from the plasma is also observed, which is the basis of laser-induced plasma (atomic emission) spectrometry (LIPS) (Figure 9.6b). In particular, LIPS is very suitable for on-line/on-site elemental analysis. Although the laser ablation is much more inhomogeneous compared with ion gun sputtering and cathode sputtering in GDS, depth profiling by laser ablation is possible in some cases. Nonvolatile compounds and insulator samples can be analyzed. Inductively coupled plasma atomic emission spectrometry (ICP-AES) associated with sample introduction by laser ablation offers an analytical potential for the direct introduction of solid samples. This method is employed for samples which are difficult to dissolve in acids.

9.3 ANALYTICAL EXAMPLES

9.3.1 COMPARISONS WITH SECONDARY ION MASS SPECTROMETRY

The majority of SIMS applications are concerned with semiconductor materials and electronic devices [7]. Depth profiling by SIMS provides unique information on the distribution of the implanted and diffused dopants which principally determine the characteristics of semiconductor devices. P, As, Al, B, N, etc., implanted into Si, SiO₂ and GaAs substrates and the impurity elements have been extensively investigated by the SIMS analysis. Thin films and the interfaces building up semiconductor devices have also been studied to clarify the relation between their structures and the resultant electronic properties.

Although many studies regarding depth profiling by SIMS have been reported, few comparative studies between GDS and SIMS have appeared. Barker and Schreinlechner investigated corrosion processes of steels by liquid alkali metals such as Li and Na through the use of SIMS and GD-OES [8]. Figures 9.7 and 9.8 show depth profiles of the constituents of the steel samples exposed to liquid Li

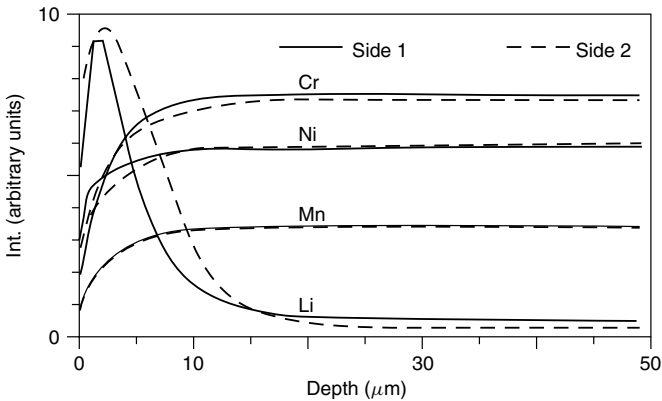


Figure 9.7 GD-OES profiles from stainless steel exposed to liquid lithium at 600 °C for 2 weeks. Sample composition: Cr 16.8, Ni 11.1 and Mn 1.5 mass-%. Reproduced with permission from Barker, M. G. and Schreinlechner, I. E., *Surf. Interface Anal.* 1986, **9**, 371–375, Copyright John Wiley & Sons

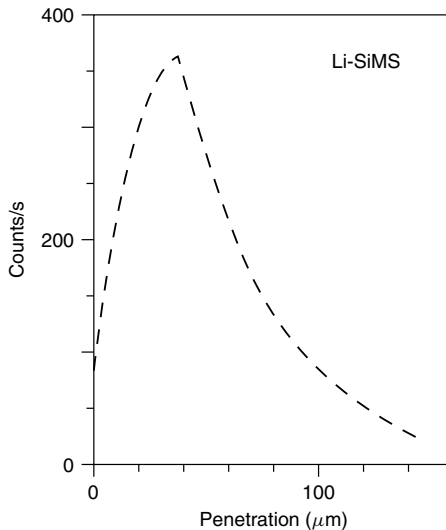


Figure 9.8 Lithium profile from stainless steel exposed to liquid lithium at 650 °C for 1 month obtained by SIMS. Reproduced with permission from Barker, M. G. and Schreinlechner, I. E., *Surf. Interface Anal.* 1986, **9**, 371–375, Copyright John Wiley & Sons

observed by GD-OES and SIMS, clearly indicating the penetration of Li into the bulk region. The in-depth distribution of Li was observed in a similar manner, whereas Li was extremely difficult to determine by the other analytical methods. It was discussed that the depth of the penetration leading to severe corrosion on the surface depends on the temperature and on the time of exposure. This study also indicated that metallic element deposition and depletion were more readily investigated using GDS.

Magee and Honig investigated depth profiling by SIMS with emphasis on three important aspects: depth resolution, dynamic range and sensitivity [9]. There are two major effects which influence the depth resolution of a profile: atomic mixing in the lattices and nonuniform sputtering within the analyzed area. Atomic mixing is an intrinsic effect in any sputtering process. The depth resolution is dependent on the energy of the primary ion, the atomic masses of the bombarding ion and the substrate and the angle of the incidence. However, the resolution is almost independent of the sample thickness if it is fairly large compared with the depths which are directly affected by the ion collision (the uppermost surface). Figure 9.9a and b show SIMS depth profiles of In for the interface of an $\text{In}_{0.05}\text{Ga}_{0.95}\text{As}/\text{GaAs}$ layer. In this specimen, the sputtering rate and the ion yield between the two layers do not change because of the small amount of In. Indium profiles for the 0.13 and 1.3 μm samples yield different interface widths. Figure 9.10 shows the variations in the interface width as a function of the sample depth (the thickness of the upper layer) under the Ar ion bombardments of 3 and 5 keV. Up to a sample depth of approximately 0.13 μm , the interface depth shows little dependence, and then increases at greater depths. The broadening of the interface at larger thicknesses is mainly due to increasing unevenness of the sputtered crater bottom, whereas the atomic mixing effect appears at depths less than 0.13 μm . It is assumed that the atomic mixing range is reduced from 5.5 to 3.5 nm by lowering the primary ion energy from 5 to 3 keV.

As is well known, the broadening in GDS profiling is mostly attributable to the nonuniform sputtering of the sample area, resulting in craters which are not parallel to the sample surface. Essentially, unlike in an ion etching gun, the sputtering parameters in GDS cannot be directly determined and it is therefore more difficult to maintain a uniform density of the bombarding ions over a large sampling area. On the other hand, the sputtering rates in GDS are high, enabling relatively thick layers to be analyzed rapidly. Furthermore, the fact that such layers are selected as the sample might emphasize the nonuniform sputtering effect rather than atomic mixing effect during the progress of the sputtering. Optimization of the crater shape should be taken into consideration to obtain a high-quality depth profile by GDS. It is known that plasma gas pressure, discharge voltage/current and the geometry of the electrodes exert complicated effects on the crater shape [10]. Hence these parameters must be optimized experimentally.

The information depth in GDS is also determined by the sputtering rate; the information depth increases with increase in sputtering rate. Hence the

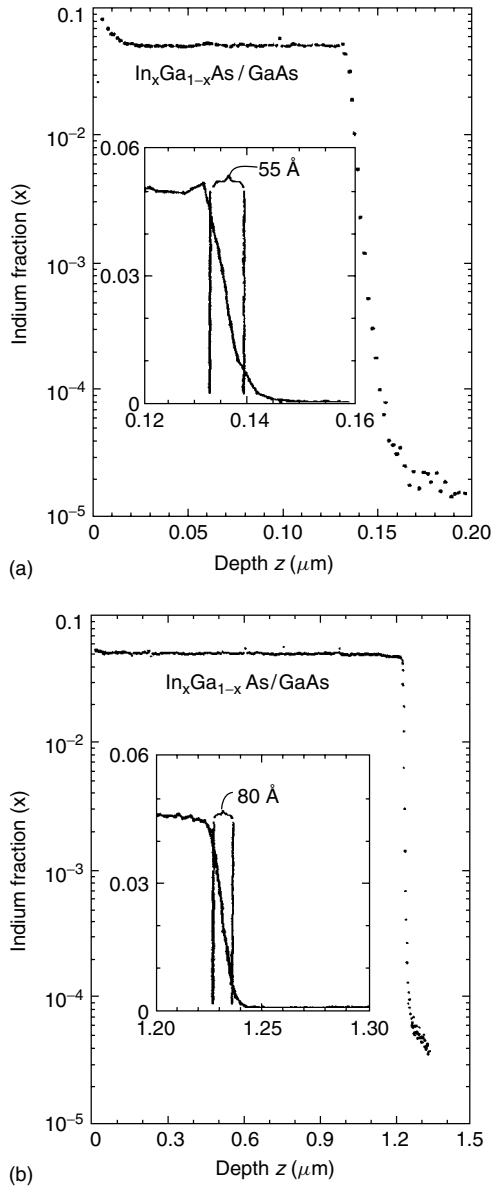


Figure 9.9 SIMS depth profiles of In for layers of $\text{In}_{0.05}\text{Ga}_{0.95}\text{As}$ grown by vapor-phase epitaxy on GaAs substrates. The linear inserts show the measured widths of the interfaces. Layer thicknesses are (a) $0.13 \mu\text{m}$ and (b) $1.3 \mu\text{m}$. Sputtering conditions are 5 keV Ar^+ and an incident angle of 60° . Reproduced with permission from Magee, C. W. and Honig, R. E., *Surf. Interface Anal.* 1982, **4**, 35–41, Copyright John Wiley & Sons

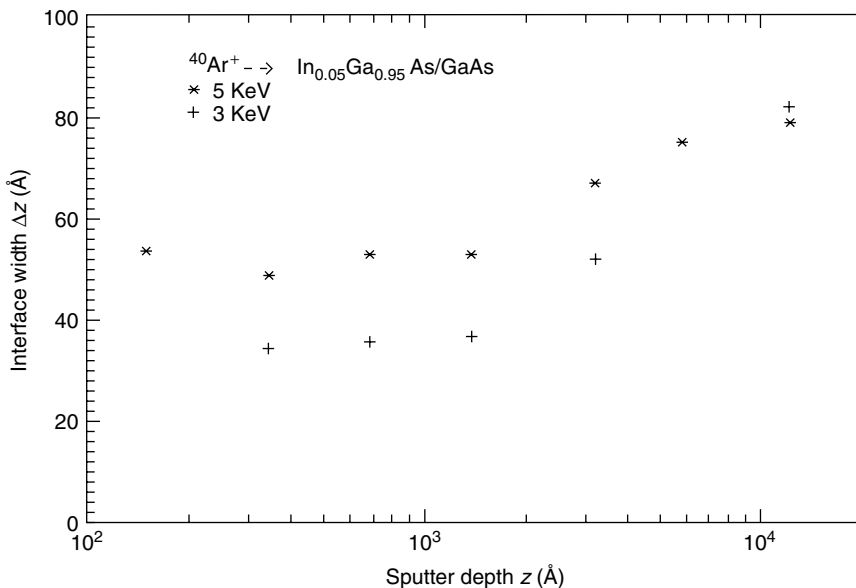


Figure 9.10 Dependence of interface width on the sputtered depth for $\text{In}_{0.05}\text{Ga}_{0.95}\text{As}/\text{GaAs}$ samples. Samples varied in thickness from 150 to 13 000 Å. Argon ion energies of 3 and 5 keV were used. Reproduced with permission from Magee, C. W. and Honig, R. E., *Surf. Interface Anal.* 1982, **4**, 35–41, Copyright John Wiley & Sons

information depth in GDS is much larger than that in SIMS, and would not seem suitable for the analysis of thinner layers. The information depth can be reduced by decreasing the sputtering rate as the discharge is operated at lower voltages/currents. However, such glow discharge plasmas lead to the decreased signal intensities from the analytes. It has been reported that modulation techniques in GD-OES are effective in obtaining better information depths without any degradation of the signal-to-noise ratios [11].

9.3.2 COMPARISONS WITH AUGER ELECTRON/PHOTOELECTRON SPECTROSCOPY

AES and XPS measurements associated with ion bombardment are often employed for the analysis of thin films having a thickness of less than 1 μm . Oxide films, electrodeposited films, surface layers treated for lubrication, abrasion, or hardening, etc., have been analyzed in-depth by this technique to give some valuable knowledge of their physical and chemical properties [12]. Several comparative studies between GDS and AES have been published.

Berneron and Charbonnier investigated the passive layers on an Fe substrate which were oxidized anodically in boric acid-buffered solutions [13]. Figure 9.11

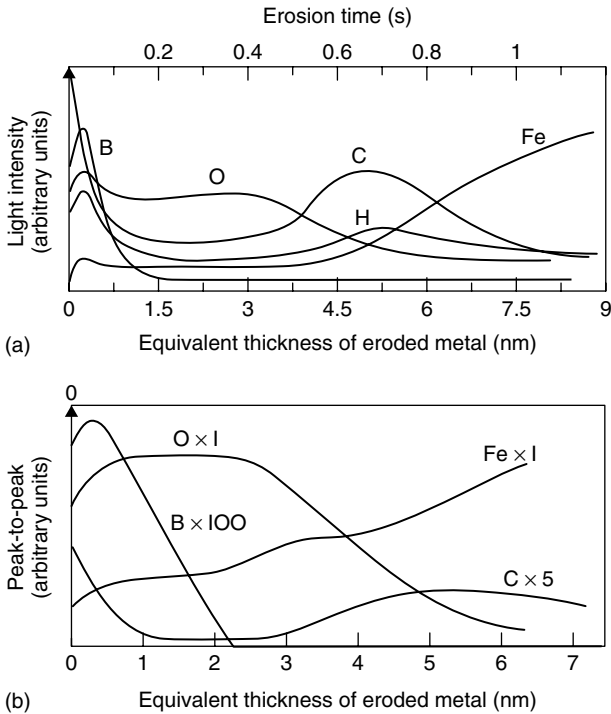


Figure 9.11 Composition profiles obtained with (a) GD-OES and (b) AES for an anodically oxidized film. Reproduced with permission from Practical Surface Analysis, D. Briggs and M. Seah (Eds), John Wiley & Sons, Chichester (1983), Copyright John Wiley & Sons

shows the depth profiles obtained with (a) GD-OES and (b) AES, indicating that the signal intensities (i.e. depths) of each element are similarly distributed. The presence of B at the uppermost layer and a more or less significant increase in C concentration toward the oxide/metal interface are also observed in the two profiles. This result implies that the profiling obtained with GD-OES is in good qualitative agreement with the AES profiling. Furthermore, GD-OES analysis allows the H profile to be followed, whereas AES provides no information about H.

Suzuki *et al.* reported the analysis of oxide films formed on steels [14]. Figure 9.12 shows the depth profiles of an oxide film formed on a 304-type stainless steel, which was oxidized at 873 K in air, obtained with (a) GD-OES and (b) AES. The quantitative GD-OES profile (concentration-to-depth relation) was obtained by use of their quantification program. The depth profile with GD-OES reveals that the film thickness is less than $0.05 \mu\text{m}$. In both of the profiles, the upper part of the oxide layer is Fe-rich with little Cr, whereas enrichment of Cr and Si is observed at a depth of about $0.02 \mu\text{m}$ beneath the surface. The

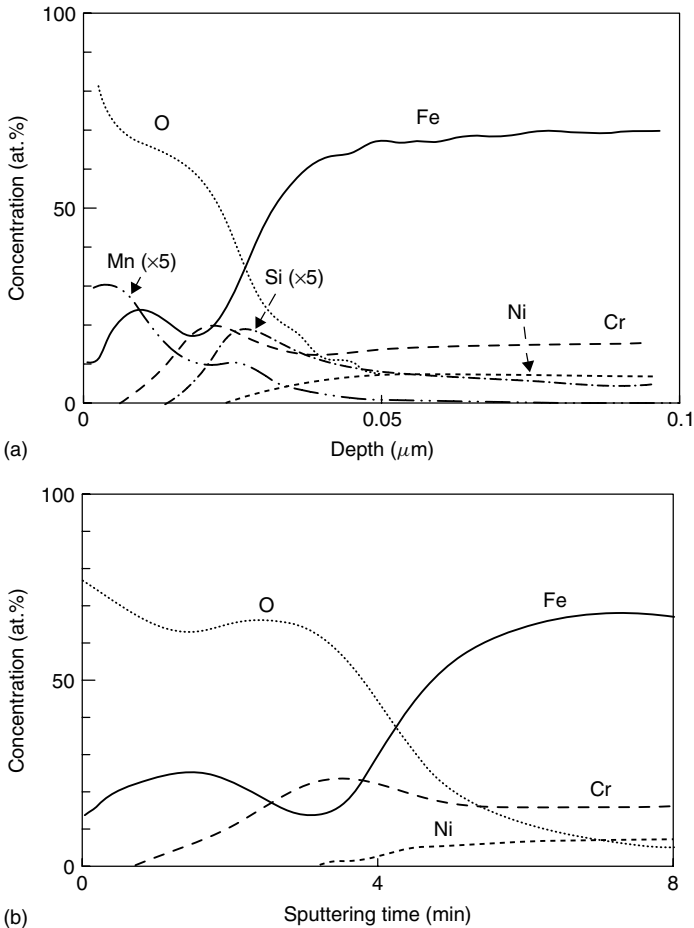


Figure 9.12 Quantitative depth profiles for the oxide film on a stainless steel obtained with (a) GD-OES and (b) AES. The sample was oxidized at 873 K in air. Reproduced with permission from Suzuki, S., Suzuki, K. and Mizuno, K., *Surf. Interface Anal.* 1994, **22**, 134–138. Copyright John Wiley & Sons

semi-quantitative results obtained with AES agree with those of GD-OES. The author also suggested oxidation mechanisms of Fe-based alloys based on the GD-OES analysis [15]. The quantitative depth profiles show that Al, Si, P, Cr and Ni are enriched at the oxide/metal interface, whereas Mn is in the oxide layer and Mo is neither at the interface nor in the oxide layer. As a result, Al, Si and Cr can suppress the growth of Fe oxides and thus reduce the thickness of the oxide layers.

Depth profiling of nitride films on Fe-based alloys has been studied using both GD-OES and AES [16]. Figure 9.13 shows the GD-OES depth profile of a

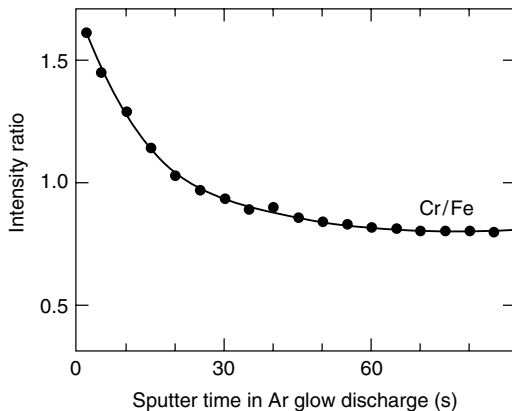


Figure 9.13 Depth profile of Cr/Fe intensity ratio obtained with GD-OES for Fe–26.8% Cr alloy sample nitrated under N_2 ion bombardment. Reproduced with permission from Wagatsuma, K. and Hirokawa, W., *Surf. Interface Anal.* 1986, **8**, 37–42, Copyright John Wiley & Sons

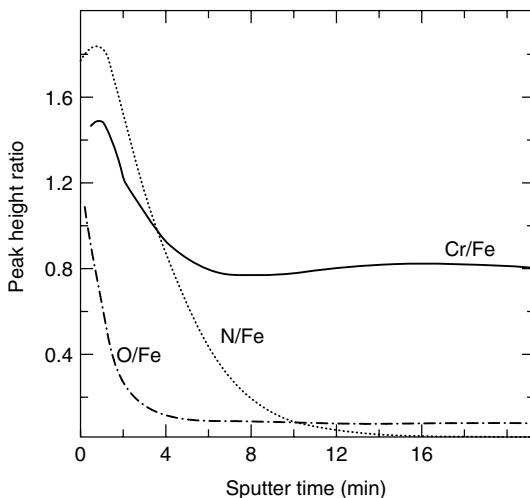


Figure 9.14 Depth profiles of Auger intensity ratios for nitrated Fe–31.5% Cr alloy. Reproduced with permission from Wagatsuma, K. and Hirokawa, W., *Surf. Interface Anal.* 1986, **8**, 37–42, Copyright John Wiley & Sons

nitrated Fe–Cr alloy sample, monitoring changes in the intensity ratio between the Cr and the Fe lines. The sample was prepared through ion nitriding in an N_2 glow discharge plasma. A decrease in the relative intensity of the Cr emission line is observed before the steady state is reached, implying that the Cr-enriched layer is present just below the surface. Figure 9.14 shows the depth profiles of

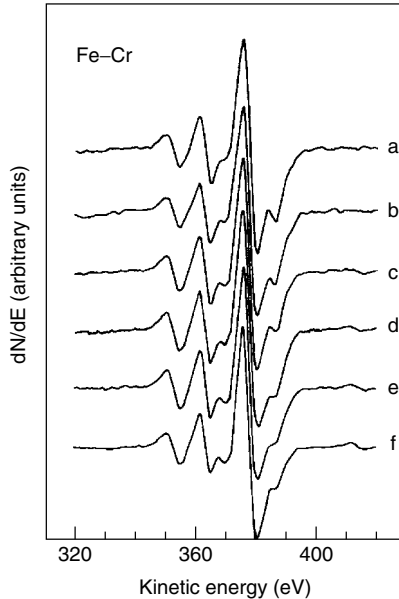


Figure 9.15 Nitrogen KLL Auger spectrum of (a) pure Fe, (b) 5.3 at.% Cr, (c) 10.7 at.% Cr, (d) 21.2 at.% Cr, (e) 31.5 at.% Cr and (f) pure Cr. Each surface was nitrided under N_2 ion bombardment. Reproduced with permission from Wagatsuma, K. and Hirokawa, W., *Surf. Interface Anal.* 1986, **8**, 37–42, Copyright John Wiley & Sons

the AES intensity ratio under the Ar ion bombardment. The variation of the N/Fe ratio is very similar to that of the Cr/Fe ratio, which also indicates the enrichment of Cr in the surface layer. The N-KLL Auger spectra include extra peaks on the high kinetic energy side when N atoms interact with transition metal atoms, called an interatomic Auger transition. Such peaks may provide information about the kind of elements in the neighborhood of the N atoms. Figure 9.15 shows the N-KLL Auger spectra for some Fe–Cr alloys of which the surface is nitrided. For comparison, the corresponding spectra for pure Fe and Cr was also measured, as shown in Figure 9.15a and f. In the alloys containing 21.2 and 31.5% Cr, the lineshape in AES is very similar to that for the pure Cr substrate. The spectral patterns can change relative to the elemental Cr form (Figure 9.15f) even though the content of the alloyed Cr is not so high. This indicates that the enrichment of Cr is caused by the N implantation. All of these results could suggest a nitriding mechanism that N particles impinging on the alloy surface preferentially interact with Cr atoms to create a Cr-enriched layer on the surface.

9.3.3 OTHER COMPARATIVE STUDIES

Depth profile analysis of Ni–Fe alloy coatings has been investigated by using GD-OES and the linescan mode in EPMA [17]. Both of the data sets exhibit

good agreement with respect to the chemical composition. In the case where the overall coating is thin or individual layers are thin, the depth resolution of GD-OES is much better than that of EPMA. Also, by use of GD-OES and EPMA linescans, depth profiles of electrolytically colored porous alumina films have been reported [18]. The depth resolution of GD-OES is superior to that of EPMA when the measuring thicknesses are in the range of several hundred nanometers. Karlsson *et al.* reported on GD-OES depth profiling of hot-dipped Zn-coated steels and the observation of the sputtered surface by SAM and SEM [19]. The GD-OES depth resolution at the interface was much worse than expected from the cross-section images of SAM. In addition, the resolution values were less reproducible. The SAM images of the crater topography reveal that the surface roughness introduced during sputtering may deteriorate the depth resolution.

9.4 REFERENCES

1. Benninghoven, A.; Rüdener, F. G.; Werner, W. H. *Secondary Ion Mass Spectrometry*, John Wiley & Sons Inc., New York, 1987, Chapter 1.
2. Chu, W. K.; Mayer, J. W.; Nicolet, M. A. *Backscattering Spectrometry*, Academic Press, New York, 1978.
3. Brundle, C. R.; Baker, A. D. *Electron Spectroscopy*, Vol. 1, Academic Press, New York, 1977, Chapter 1.
4. Briggs, D.; Seah, M. P. *Practical Surface Analysis*, John Wiley & Sons Ltd., Chichester, 1983, Chapter 4.
5. Brundle, C. R.; Baker, A. D. *Electron Spectroscopy*, Vol. 1, Academic Press, New York, 1977, Chapter 3.
6. Moenke-Blankenburg, L. *Laser Micro Analysis*, John Wiley & Sons Inc., New York, 1989, Chapter 3.
7. Benninghoven, A.; Rüdener, F. G.; Werner, W. H. *Secondary Ion Mass Spectrometry*, John Wiley & Sons Inc., New York, 1987, Chapter 6.
8. Barker, M. G.; Schreinlechner, I. E. *Surf. Interface Anal.* 1986, **9**, 371–375.
9. Magee, C. W.; Honig, R. E. *Surf. Interface Anal.* 1982, **4**, 35–41.
10. Payling, R.; Jones, D.; Bengtson, A. *Glow Discharge Optical Emission Spectrometry*, John Wiley & Sons Ltd., Chichester, 1997, Chapter 2.
11. Wagatsuma, K. *Surf. Interface Anal.* 1999, **27**, 63–69.
12. Briggs, D.; Seah, M. P. *Practical Surface Analysis*, John Wiley & Sons Ltd., Chichester, 1983, Chapter 7.
13. Berneron, R.; Charbonnier, J. C. *Surf. Interface Anal.* 1981, **3**, 134–141.
14. Suzuki, S.; Suzuki, K.; Mizuno, K. *Surf. Interface Anal.* 1994, **22**, 134–138.
15. Suzuki, S.; Wake, M.; Abe, M.; Waseda, Y. *ISIJ Int.* 1996, **36**, 700–704.
16. Wagatsuma K.; Hirokawa, W. *Surf. Interface Anal.* 1986, **8**, 37–42.
17. Ives, M.; Lewis, D. B.; Lehmerg, C. *Surf. Interface Anal.* 1997, **25**, 191–201.
18. Shimizu, K.; Habasaki, H.; Skeldon, P.; Thompson, G. E.; Wood, G. C. *Surf. Interface Anal.* 1999, **27**, 1046–1049.
19. Karlsson, J.; Hörnström, S. E.; Klang, H.; Nilsson, J.-O. *Surf. Interface Anal.* 1994, **21**, 365–369.

10

Analysis of Samples of Nuclear Concern with Glow Discharge Atomic Spectrometry

M. BETTI

*European Commission, Joint Research Centre, Institute for Transuranium
Elements, Karlsruhe, Germany*

The author dedicates this contribution to the memory of Professor Paolo Papoff, as an appreciation of his many contributions to the field of the instrumental analytical chemistry.

10.1 INTRODUCTION

The direct analysis of solid samples is very important in the nuclear field since operator exposure time to the radiation and the quantity of liquid nuclear wastes can be strongly reduced. Moreover, a nondestructive analysis allows the sample to be reused for further investigation, to be reprocessed or to be kept as an archival sample.

Compared with wet chemistry-based methods, glow discharge-based methods using optical emission spectrometry and mass spectrometry have the advantage of simpler sample preparation procedures, as a result of carrying out measurements directly on solid samples. Therefore, for nuclear samples, they meet the requirements of reducing both the exposure time of the operator and the amount of liquid waste.

Glow discharge (GD) sources have a long history in analytical chemistry, principally as sources for optical emission spectrometry. They have traditionally been involved in the determination of transition elements in steels and metals because these elements affect hardness, ductility, strength and corrosion resistance.

Glow discharge optical emission spectrometry (GD-OES) is recognized as a rapid method for depth profiling, capable of surface analysis [1–3] and interface and bulk qualitative and quantitative analysis of solids [4].

Glow discharge mass spectrometry (GDMS) is one of the most powerful solid-state analytical methods for the direct determination of impurities and depth profiling of solids [5–10].

10.2 INSTRUMENTATION

For the handling of nuclear materials, difficulties arising from the radioactive nature of the samples have to be overcome. First, the operator has to be protected from the radioactive material, which means that the use of glove-boxes (α - and β -radiation protection) and hot cells (α -, β - and γ -radiation protection) with master–slave telemanipulators is a necessity. Second, in order to avoid contamination of the working area, the analytical instruments have to be modified so that containment is assured and no radioactive material leaks either into the laboratory or into the environment. Complete instruments cannot be introduced into a glove-box because electronics are very sensitive to radiation. Therefore, in practice, electronics and parts that might need special maintenance normally have to be kept outside the glove-box and only sampling stages are contained inside.

10.2.1 INSTALLATION OF A DC-GDMS IN A GLOVE-BOX

With regard to GD spectrometers, only a GDMS [11] and a GD-OES [12] have so far been integrated in a glove-box for the characterization of radioactive samples. In the case of the GD mass spectrometer (VG 9000 GDMS), the glove-box enclosed the ion source chamber, the sample interlock and the associated pumped system. In Figure 10.1 a schematic diagram of the installation of the GD source housing in the frame of the glove-box is given. All supplies to the ion sources (argon discharge support gas and liquid nitrogen for the cryogenic cooling of the discharge cell) and the pumping ports should be fitted with absolute filters to eliminate any external contamination.

For the case of the VG 9000 GDMS, as described elsewhere in detail [11], stainless-steel filters (3 μm porosity) were installed in the argon, compressed air and liquid nitrogen inlets. Absolute filters (0.3 μm porosity) were used for the vacuum line.

The ion source was re-designed to minimize the number of operations and to simplify routine maintenance inside the glove-box area. This was achieved by

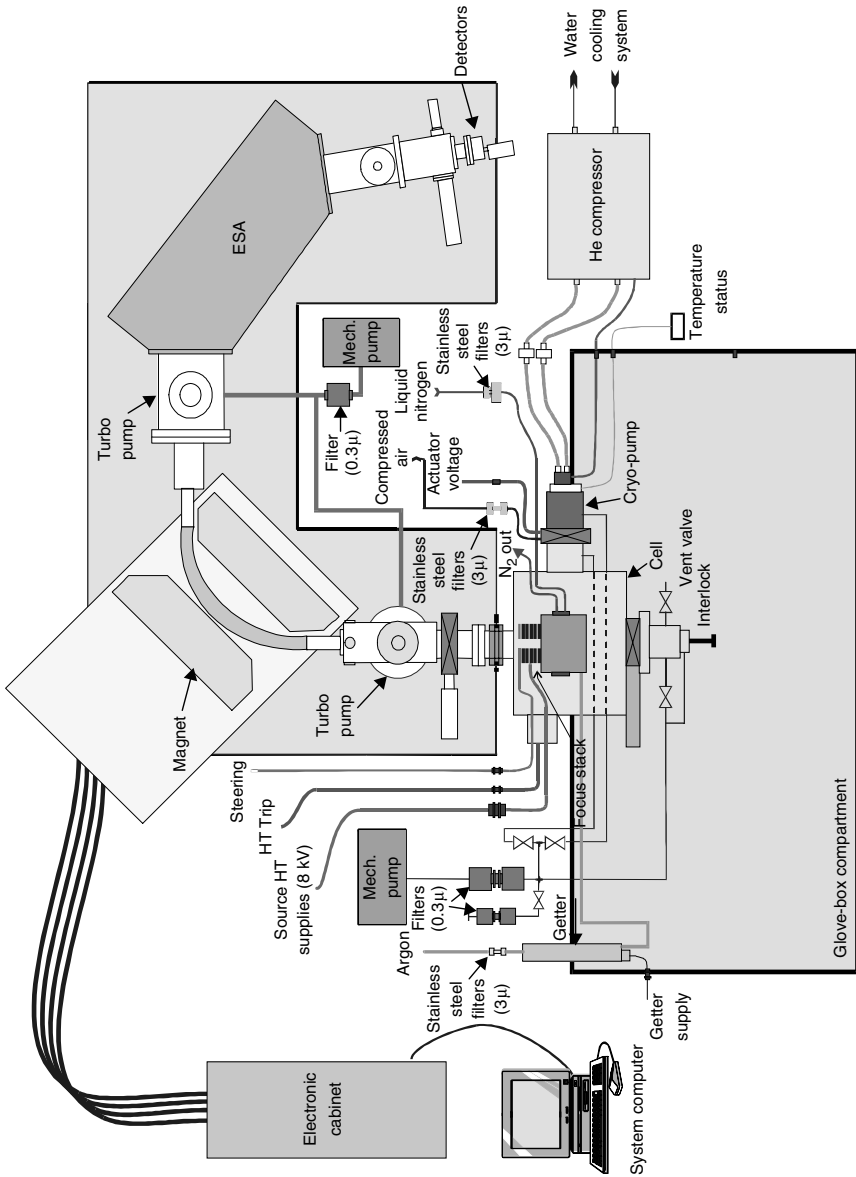


Figure 10.1 Schematic diagram of the installation of a GDMS in a glove-box

utilizing a 'universal' cell for the analysis of both pin-shaped and flat samples and a 'plug-in' focus stack. The source itself has been split into various components comprising a measurable plate with removable cell and focus stack assemblies. The source mounting position remains fixed to the back wall of the source's housing chamber. The focus stack then plugs into a recess in the mounting plate and is held in place by four fixing rods. Electrical contact to the plates of the focus stack is made by a series of copper–beryllium contacts. This eliminates the need to disconnect any wire when removing the focus stack, thus simplifying its removal.

The focus stack assembly consists of a series of tantalum plates, separated by PEEK spacers, mounted in a base containing the source-defining slit from the mass spectrometer. The focus stack provides deflection and focusing of the ion beam in the *y*- and *z*-directions to give the best image on the source-defining slit. The plates are shaped so that when the focus stack is in position, they make electrical contact with the appropriate connector on the contact assembly. The focus stack assembly also contains a mounting bracket for the location of the cell and sample holder.

The 'universal' cell has been designed to accommodate a large range of pin-shaped and flat samples. The cell itself consists of a universal body that plugs into the focus stack. This cell body, based around the existing flat geometry, remains located in position. The 'universal pin holder' can be used for the analysis of a wide range of pin samples. The analysis of flat samples is performed with the aid of the flat sample holder [13]. Changing the sample geometry from pin to flat simply requires changing the appropriate sample holder when loading the sample. It is no longer necessary to break the vacuum to do this, thus reducing the number of operations required inside the glove-box.

10.2.2 INSTALLATION OF AN RF-GD-OES IN A GLOVE-BOX

A new set-up for the integration of a radio frequency (rf)-powered GD-OES system in a glove-box has also been recently described [12].

The GD lamp used in this system was specially designed for the rf powering and is based on a previously developed concept [14]. The sample needs to be flat enough to form a vacuum seal when being pressed against a PTFE O-ring by means of a pneumatically controlled piston and the rf potential is applied to the back of the sample. The discharge is powered with the aid of an rf power supply operating at a frequency of 13.56 MHz. Only one pump is required to provide a vacuum in the lamp instead of two as in a Grimm-type lamp. The window of the lamp through which the radiation passes consists of magnesium fluoride to ensure transmission also in the wavelength range 120–180 nm. The optical path passes through a closed construction of stainless-steel tubes and bellows. A small, circular, flat mirror deviates a small part of the radiation beam perpendicularly to the optical axis towards a window, through which the radiation

of the GD sources can be observed. The main beam enters the optical detection system.

As with the previous case, in order to prevent contamination, all parts of the instrument that will come in contact with the radioactive samples have been enclosed in a glove-box divided into three separate parts. The first compartment of the glove-box contained a polishing machine. Then the GD lamp and the UV polychromator were installed separately in the second and third compartments, respectively. To avoid contamination of the pumps, HEPA filters were used for evacuation.

10.3 PRACTICAL ASPECTS AND RESULTS

In the field of nuclear research and technology, the chemical characterization of different types of fuel, cladding materials, nuclear-waste glasses and smuggled nuclear samples, from the point of view of trace, major and minor elements, and also from their isotopic composition, are of great importance. GD-based techniques have been exploited since the mid-1990s for the characterization of nuclear materials. In particular, dc-GDMS has been utilized for the detection of trace elements and for bulk and isotopic analysis. Rf-GD-OES is envisaged for the detection of light elements, namely carbon, oxygen, nitrogen, sulphur and hydrogen. So far no applications have been published.

10.3.1 APPLICATIONS FOR TRACES AND BULK ANALYSIS IN NUCLEAR SAMPLES

In the past few years, instrumental analytical techniques based on mass spectrometry have become predominant for the characterization of samples of nuclear concern. GDMS has found extensive application for trace element determination in a variety of conducting and nonconducting solids [15], and has also been used for the chemical characterization of samples of nuclear concern. In fact, GDMS provides information on the chemical composition of the material much faster than other methods, presenting an opportunity to change fuel production procedures, modify reactor operations or rapidly recognize smuggled materials. In our laboratory, a great deal of experience has been acquired in the use of GDMS for the chemical and isotopic characterization of samples of nuclear concern. Plutonium and uranium oxide specimens, mixed uranium and plutonium oxide (MOX) and metallic fuels, simulated high burn-up nuclear fuels (simfuel), zircaloy cladding materials, nuclear-waste glasses and smuggled nuclear materials have been investigated by GDMS. A number of examples of the analysis of conducting and nonconducting samples of nuclear concern characterized by a dc-GDMS are reported below.

Conductive Nuclear Samples

Metallic Alloy Fuels

The metallic alloy fuels discussed here consisted of two matrices, UNdZr and UPuZr, the major component of which was uranium at 81% and 71%, respectively. By GDMS, semiquantitative analysis could be performed using the signal intensity of the analyte and considering the element sensitivity of uranium. Using the relative sensitivity factor (RSF) values obtained for the analytes of interest in a matrix of uranium metal, the results could be improved in terms of accuracy. Since no uranium metal sample certified for the elements of interest was available, the strategy consisted of analysing uranium metal specimens of different origins by other methods, such as ICP-MS and ICP-AES. From these results, RSF values were obtained for GDMS and UNdZr and UPuZr samples could be analysed. The results of GDMS were found to be in good agreement with the theoretical values. Accuracies of better than 10% and a precision of better than 5% were obtained in runs consisting of 10 measurements. Owing to the fabrication method of the alloys investigated, these figures of merit were expected.

Several specimens of these metallic fuels were analysed with the aid of other analytical methods. For instance, tritiation (TITR) was used for the determination of the total uranium and plutonium and thermal ionization mass spectrometry (TIMS) and inductively coupled plasma mass spectrometry (ICP-MS), both combined with isotopic dilution analysis, were employed for the determination of the zirconium and neodymium contents. As shown in Table 10.1, the agreement between the concentrations determined by GDMS and those by the other techniques was always good, the ratios between the results of the two methods being always close to one. GDMS was, therefore, the appropriate technique to be used for the determination of the chemical composition of these metal fuel alloys, using the RSF values obtained for pure uranium metal matrix.

For the determination of certain trace elements in UZrNd and UPuZr alloys, RSFs obtained for uranium metal matrices were employed. The GDMS results obtained using this approach were in good agreement with those obtained by measurement with ICP-MS [6].

Zircaloy Cladding Materials

GDMS has often been used for the analysis of zirconium alloys [5]. In the nuclear industry, zircaloy is an important material constituting the cladding of the nuclear fuel during irradiation in the reactor. RSF values were obtained from reference materials and used for the analysis of zircaloy cladding materials [6]. Quantitative analysis of zircaloy cladding material was performed by applying RSF matrix-specific samples and also RSF values obtained for a uranium metal sample. Using both RSF values good accuracy was obtained. This indicates that for metallic samples the matrix effects are negligible, and the technique is applicable for quantitative analysis without using matrix-specific reference samples.

Table 10.1 Ratios of the concentrations of the constituents of UZrNd and UPuZr alloys obtained by titration (TITR), TIMS and ICP-MS with the concentrations obtained from GDMS.

Sample	TITR:GDMS		TIMS:GDMS		ICP-MS:GDMS	
	U	Pu	U	Pu	Zr	Nd
1	1.03	1.06	1.00	1.02	1.01	—
2	1.03	1.01	1.01	1.00	0.99	—
3	0.99	0.99	0.99	1.03	1.03	—
4	0.98	1.01	1.03	1.04	1.02	—
5	1.03	0.98	1.00	0.98	0.98	—
6	0.99	—	1.00	—	—	1.02
7	1.04	—	1.02	—	—	0.98
8	1.03	—	1.03	—	—	1.04
9	0.99	—	1.02	—	—	1.00
10	1.00	—	1.02	—	—	1.00

Nonconductive Nuclear Samples

As compared with other analytical methods for direct solid analysis, some advantages of GDMS are the intense, steady beam of ions with a narrow energy distribution produced from the low-pressure discharge and the physical separation of the atomization and the ionization steps of the sample material in the discharge. However, the main restricting parameter is the conductivity of the samples. To overcome this drawback, the use of an rf discharge source has been investigated [16–19], but unfortunately the sources are not yet commercially available. For dc discharges, two methods are applied for the analysis of non-conducting materials. For flat samples a ‘secondary cathode’ [8,20–24] placed directly in front of the nonconducting sample surface is used to meet the requirements of conductivity. The second approach, used for powdered samples, consists of mixing the sample with a pure conducting host matrix in an appropriate ratio to obtain sufficient conductivity for analysis [25,26].

In our laboratory, several oxide-based nuclear samples containing oxygen in a concentration varying from 12 to 18% (m/m) have been analysed as for trace elements. Oxygen, as a major matrix element, causes severe problems owing its release from the oxide during the discharge processes. Once released into the GD plasma, it influences the analytical signal by quenching excitation and ionization agents [27]. Moreover, in GDMS problems also arise from the presence of polyatomic oxides that create spectral interferences and give lower analytical sensitivity. ‘Getter metals’ such as titanium or tantalum bond strongly with oxygen and reduce its availability to form oxides with the analytes or to quench metastable argon atoms.

In order to analyse uranium and plutonium oxide samples by dc-GDMS, the use of a host matrix and a secondary cathode has been applied. As host matrix,

pure silver, tantalum and titanium were employed. It was observed that when employing tantalum and titanium, the formation of UO^+ and PuO^+ species is hindered. For a secondary cathode, tantalum was chosen and it was found that its property as a getter for oxygen is also an advantage. Indeed, it is found that the $\text{U}^+:\text{UO}^+$ and $\text{Pu}^+:\text{PuO}^+$ ratios obtained with a tantalum secondary cathode are of the same order of magnitude as those obtained with tantalum and titanium binders. The main result of the investigation is that for several elements the RSFs were found to depend on the oxygen content in the sample [6]. Therefore, a specific matrix reference sample for the quantitative analysis of oxygen-containing samples is necessary.

Rf-GD-AES has been exploited for the analysis of plutonium oxide and nuclear-waste glasses [28]. The goals of these applications included the parametric evaluation of the plasma operating conditions, an assessment of the limits of detection for trace analysis in simulated vitrified waste samples and the quantification for this type of samples. The final goal was to design a contained rf-GD-AES system for remote sampling of radioactive materials. The results demonstrate the ability of rf-GD-AES to analyse nonconductive simulated waste glasses with various inorganic components.

Nuclear-waste glasses could also be successfully analysed by GDMS applying a secondary cathode in front of the sample [6].

Comparison of dc-GDMS and Quadrupole ICP-MS for Trace Element Determination in Nuclear Samples

Materials for nuclear reactor fuel preparation need to be characterized for the isotopic composition of the major elements and the concentration of trace elements. The acceptable levels of impurities in fresh nuclear fuels vary according to the characteristics of the reactor. In order to monitor contaminations during the fabrication process, the determination of the trace elements should be performed in the starting material as well as in the final pellets of fresh fuels. For these measurements, analytical methods with proven reliability, accuracy and precision are necessary. Among currently available techniques, dc-GDMS and quadrupole ICP-MS have been used successfully [7]. The advantages of GDMS lie in its low limits of detection, uniform elemental sensitivity and the capability to determine all elements and even isotopes. One of the main challenges for GDS to overcome, as already mentioned, is the intrinsic requirement for the sample to be electrically conducting. The main characteristics of the comparison of GDMS and ICP-MS techniques are summarized in Table 10.2.

In Table 10.3, some examples of possible polyatomic interferences in ICP-MS and in GDMS determinations in U/Pu matrix samples are summarized.

ICP-MS is a well established and widely used method for the analysis of nuclear materials [29–32]. Owing to its high sensitivity and quasi-simultaneous multi-element analysis capability, ICP-MS is particularly suited

Table 10.2 Advantages and disadvantages of GDMS and ICP-MS.

Method	Advantages	Disadvantages
GDMS	Multi-element with high sensitivity	Expensive as high-resolution MS required to avoid isobaric interferences
	Low sample consumption (1–100 mg)	Not suitable for high sample throughput
	Limited matrix effects	Accurate calibration requires matrix matched standards
	No digestion problems for refractory materials	Does not lend itself to isotopic dilution MS experiments
	Depth profile analysis	Sample preparation can be problematic for nonconducting materials (risk for contamination)
	Wide linear dynamic range	
ICP-MS	High sensitivity for a wide range of analytes	Solution steps necessary Requires sample pretreatment to remove matrix interferences
	Medium cost of quadrupole instruments	Resolution of quadrupole MS insufficient to separate isobaric interferences
	Wide linear dynamic range	Requires dissolution of sample
	Multi-element calibration readily achieved	
	Easy to use for isotopic dilution analysis	
	High sample throughput	

to the determination of a large number of elements at very low concentration ranges. ICP-MS provides information on the isotopic composition and is able to determine both stable and radioactive nuclides with similar sensitivity. Unfortunately, sample preparation is needed and when using an ICP quadrupole mass spectrometer for trace analysis, numerous mass spectral interferences caused by matrix-induced ions can occur, in addition to nonspectral interferences, which are usually defined as matrix-induced signal variation [33].

In multi-element analysis of uranium and plutonium by ICP-MS, few spectroscopic interferences, as a result of the formation of doubly charged and oxide species arise from the U and Pu matrices. More serious are the nonspectroscopic matrix effects. In fact, a 1000 mg l^{-1} U or Pu matrix causes significant signal suppression for most elements. However, most of these matrix effects can be corrected by using an internal standard, matrix-matched standards, standard additions or separations of the analyte from the matrix.

GDMS is relatively free from matrix effects owing to the separation of atomization and ionization phenomena in time and space during the sputtering of the sample. Qualitative data or screening analyses can be obtained by GDMS even

Table 10.3 Some examples of possible isobaric and polyatomic interferences in GDMS and ICP-MS determinations in U/PU matrix samples.

Element	Polyatomic interferences	Element	Polyatomic interferences	Element	Isobaric interferences
²⁷ Al	¹² C ¹⁴ NH ⁺	⁶² Ni	⁴⁶ Ca ¹⁶ O ⁺ ; ⁴⁶ Ti ¹⁶ O ⁺	⁶ Li	¹² C ²⁺
²⁸ Si	²⁷ AlH ⁺ ; ¹² C ¹⁶ O ⁺	⁶³ Cu	²³ Na ⁴⁰ Ar ⁺ ; ⁴⁷ Ti ¹⁶ O ⁺	⁷ Li	¹⁴ N ²⁺
	¹⁴ N ₂ ⁺	⁶⁴ Zn	³⁶ Ar ¹² C ¹⁶ O ⁺ ; ³² S ₂ ⁺	⁹ Be	³⁶ Ar ⁴⁺
²⁹ Si	²⁸ SiH ⁺ ; ²⁷ AlH ₂ ⁺		³² S ¹⁶ O ₂ ⁺	¹⁰ B	⁴⁰ Ar ⁴⁺
	¹² C ¹⁶ OH ⁺	⁶⁵ Cu	⁴⁹ Ti ¹⁶ O ⁺		³⁰ Si ³⁺
³⁰ Si	¹⁴ N ¹⁶ O ⁺	⁶⁶ Zn	³⁸ Ar ¹² C ¹⁶ O ⁺ ; ⁵⁰ Cr ¹⁶ O ⁺	⁴⁰ Ca	⁴⁰ Ar ⁺
⁴² Ca	⁴⁰ ArH ₂ ⁺ ; ²⁶ Mg ¹⁶ O ⁺	⁶⁷ Zn	¹³⁴ Ba ²⁺	⁵⁸ Ni	⁵⁸ Fe ⁺
⁴⁴ Ca	¹² C ¹⁶ O ₂ ⁺	⁶⁸ Zn	⁴⁰ Ar ¹² C ¹⁶ O ⁺ ; ⁴⁰ Ar ¹⁴ N ⁺	⁹² Zr	⁹² Mo ⁺
⁴⁶ Ti	¹⁴ N ¹⁶ O ₂ ⁺		⁴⁸ Ti ¹⁶ O ⁺ ; ¹³⁶ Ba ²⁺	⁹⁴ Zr	⁹⁴ Mo ⁺
⁴⁸ Ti	³⁶ Ar ¹² C ⁺			⁹⁶ Mo	⁹⁶ Zr ⁺
⁵⁰ Ti, ⁵⁰ V	³⁶ Ar ¹⁴ N ⁺	¹⁰⁷ Ag	⁹¹ Zr ¹⁶ O ⁺	¹¹³ Cd	¹¹³ In ⁺
⁵¹ V	³⁶ Ar ¹⁴ NH ⁺	¹⁰⁹ Ag	⁹³ Nb ¹⁶ O ⁺	¹⁶⁰ Dy	¹⁶⁰ Gd ⁺
⁵² Cr	⁴⁰ Ar ¹² C ⁺ ; ³⁶ Ar ¹⁶ O ⁺	¹¹⁰ Cd	⁹⁴ Zr ¹⁶ O ⁺ ; ⁹⁴ Mo ¹⁶ O ⁺	¹⁶⁴ Dy	¹⁶⁴ Er ⁺
⁵³ Cr	³⁶ Ar ¹⁶ OH ⁺	¹¹¹ Cd	⁹⁴ Mo ¹⁶ O ⁺	¹¹⁶ Sn	²³² Th ²⁺
⁵⁴ Fe	⁴⁰ Ar ¹⁴ N ⁺ ; ³⁸ Ar ¹⁶ O ⁺	¹¹² Cd	⁹⁵ Mo ¹⁶ O ⁺ ; ⁹⁶ Zr ¹⁶ O ⁺	¹¹⁷ Sn	²³⁴ U ²⁺
⁵⁵ Mn	⁴⁰ Ar ¹⁴ N ¹ H ⁺ ; ³⁸ Ar ¹⁶ O ¹ H ⁺	¹¹³ Cd	⁹⁷ Mo ¹⁶ O ⁺	¹¹⁸ Sn	²³⁶ U ²⁺
⁵⁶ Fe	⁴⁰ Ar ¹⁶ O ⁺ ; ²⁸ Si ₂ ⁺	¹¹⁴ Cd	⁹⁸ Mo ¹⁶ O ⁺	¹¹⁹ Sn	²³⁸ U ²⁺
	⁴⁰ Ca ¹⁶ O ⁺	¹¹⁴ Sn	⁹⁸ Mo ¹⁶ O ⁺		
⁵⁷ Fe	⁴⁰ Ar ¹⁶ OH ⁺	¹¹⁶ Sn	¹⁰⁰ Mo ¹⁶ O ⁺		
⁵⁸ Ni	⁴⁰ Ar ¹⁸ O ⁺	¹⁵³ Eu	¹³⁷ Ba ¹⁶ O ⁺		
	⁴⁰ Ar ¹⁶ OH ₂ ⁺	¹⁵⁵ Gd	¹³⁸ Ba ¹⁶ OH ⁺		
⁵⁹ Co	⁴⁰ Ar ¹⁶ OH ₃ ⁺	¹⁸¹ W	¹⁸⁰ TaH ⁺		
⁶⁰ Ni	⁴² Ca ¹⁶ O ⁺	¹⁸² W	¹⁸¹ TaH ⁺		

when reference materials are not available. A simple comparison of the element signal of the analyte with the element sensitivity of a reference element, defined as the ratio between the signal and the elemental concentration, results in an accuracy of about 30% [34]. However, since RSF values exhibit variations with the discharge conditions, matrix type and instrumental configuration, it is necessary to determine experimental RSFs for full quantitative analysis using the conditions employed in the analysis of unknown samples. This is particularly true for the quantitative analysis of nonconducting nuclear samples, which are oxide-based [6]. As already described, in GDMS problems may arise from the presence of polyatomic oxides. However, tantalum, used as a secondary cathode, binds strongly with oxygen and reduces the oxygen available that can form oxides with the analytes or can quench metastable argon atoms.

In Table 10.4, the analysis results for an uranium oxide reference sample (Morille, CEA, France) using standard and matched-matrix RSFs are reported. To obtain results with the highest accuracy, matrix-specified RSFs values are required.

Table 10.4 GDMS quantitative analysis of Morille uranium oxide reference sample based on matrix-specific and standard RSF.

Element	Certified value ($\mu\text{g g}^{-1}$)	Matrix-specific RSF ($\mu\text{g g}^{-1}$)	Bias (%)	RSD (%) $n = 6$	Standard RSF ($\mu\text{g g}^{-1}$)	Bias (%)	Detection limit ($\mu\text{g g}^{-1}$)
Ag	10.4 ± 1.6	10.2 ± 1.3	1.9	12.1	9.3 ± 2.3	10.8	0.1
Al	99 ± 6	87 ± 5	12.1	5.5	87 ± 3	11.9	0.5
B ^a	3.8 ± 1.6	3.5 ± 1.5	7.9	40.8	2.5 ± 0.8	35.5	0.2
Ba	9.6 ± 0.4	^b			11.4 ± 0.3	-18.8	0.7
Be ^a	5.4 ± 0.6	3.8 ± 0.4	29.6	10	^b		0.5
Bi	24.4 ± 1.9	20.9 ± 1.7	14.3	7.7	41 ± 3	-68	0.6
Ca ^a	93 ± 8	94 ± 9	-1.1	9.1	95.8 ± 4.2	-3.0	0.4
Cd	4.9 ± 0.7	5 ± 0.4	-2	7.6	3.4 ± 1	30.6	0.5
Co	9.8 ± 2	11.1 ± 0.8	-13.3	6.9	9.5 ± 0.3	3.0	1.3
Cr	99 ± 2	102 ± 5	-3	4.7	94 ± 11	4.7	1.9
Cu	50.2 ± 1	52.1 ± 3.3	-3.8	6	63 ± 7	-25.6	0.6
Dy	0.5 ± 0.06	^c					0.7
Eu	0.52 ± 0.03	^c					0.5
Fe	211.6 ± 6.5	207.2 ± 10.8	2.1	5	313 ± 22	-47.9	2.4
Gd	0.56 ± 0.06	^c					0.9
In	9.4 ± 1	10.4 ± 0.5	-10.6	4.6	8.1 ± 0.3	14.3	1
Mg	19.3 ± 1.5	19.4 ± 1.6	-0.5	7.9	12.2 ± 1	36.8	0.1
Mn	24.5 ± 0.5	29.3 ± 1.1	-19.6	3.6	30 ± 1	-22.4	1.4
Mo	147 ± 5	144 ± 9	2	6	175 ± 11	-19	0.9
Ni	147 ± 3	142 ± 4	3.4	2.7	143 ± 25	2.7	6.2
Pb	101 ± 3	103 ± 9	-2	8.3	111 ± 7	-9.9	0.4
Si ^a	100 ± 8	93 ± 6	7	6.1	245 ± 11	-145	0.1
Sm	0.5 ± 0.12	^c					0.9
Sn	18.5 ± 5.6	20.8 ± 3	-12.4	13.7	15.3 ± 4.6	17.3	0.4
Th	6.2 ± 0.8	^b					0.4
Ti	49.2 ± 2.6	48.6 ± 8	1.2	15.7	^b		1.4
V	48.7 ± 2.8	47 ± 2	3.5	4.1	50 ± 1	-2.6	0.7
W	100 ± 9	106 ± 11	-6	9.9	95 ± 3	4.8	2.1
Zn	98.6 ± 5.5	102 ± 10	-3.4	9.3	148 ± 8	-50	0.8
Zr	59.9 ± 4.1	64 ± 7	-6.8	10.4	^b		0.9

Bias(%) = (certified value — GDMS value) × 100/certified value.

^aPossible interferences: ⁹Be, ³⁶Ar⁴⁺, ^{10,11}B, ⁴⁰Ar⁴⁺H, ⁴⁰Ar⁴⁺, ^{40,41,42,43,44}Ca, ⁴⁰Ar⁺, ⁴⁰ArH⁺, ¹²C¹⁴N¹⁶O⁺, ¹²C¹⁶O₂⁺, ^{28,29,30}Si, ⁵⁶Fe²⁺, ²⁷AlH⁺, ¹⁴N²⁺, ¹²C¹⁴N, ¹²C¹⁶OH⁺, ¹⁴N¹⁶O⁺.

^bNot determined.

^cBelow detection limit.

The data presented in Table 10.4 demonstrate the high stability of the discharge when using the secondary cathode technique for the analysis of uranium oxide samples. Typical precisions of the order of 10% RSD or better can be obtained. For elements with concentrations of 5–10 $\mu\text{g g}^{-1}$, an analytical precision higher than 10% RSD was obtained. Using matrix-specific RSFs, an accuracy of 5% was generally obtained.

In GDMS, detection limits, in absence of any interference, are calculated from signals equalling three times the noise of the background signal. For uranium and plutonium oxides analysed with the secondary cathode technique, detection limits for several trace elements are at the low $\mu\text{g g}^{-1}$ level, as shown in Table 10.4, when using an integration time of 120 ms per isotope. As can be seen from this table, the detection limits for Fe, Cu, Ni, Mo, Ti, W and Zr are higher because the blank contribution of these elements stemming from the tantalum mask has to be taken into account.

In ICP-MS, the detection limits were calculated from the signal equalling three times the standard deviation for nine replicates of an acid blank. For most of the elements, they are in the range 0.01–1 $\mu\text{g g}^{-1}$ with respect to the dissolved solid. However, for elements such as Fe, Zn and Ca, higher values due to isotopic interferences and to the strong dilution of samples are found. Generally, comparable detection limits for both methods were obtained [7].

In Table 10.5, the analytical precisions for the determination of trace elements in a uranium oxide reference sample by GDMS and ICP-MS are compared.

Table 10.5 Analytical precision in the analysis of Morille uranium oxide reference sample by GDMS and ICPMS.

Element	GDMS			ICP-MS		
	Mean value ($\mu\text{g g}^{-1}$)	SD ($n = 6$) ($\mu\text{g g}^{-1}$)	RSD (%)	Mean value ($\mu\text{g g}^{-1}$)	SD ($n = 9$) ($\mu\text{g g}^{-1}$)	RSD (%)
Ag	9.3	1.0	10.2	10.8	3.9	36.2
Al	87	3.8	4.3	100	12.1	12.1
B	2.5	0.2	8.6	Below detection limit		
Ba	11.4	0.4	3.5	9.6	3	31.2
Bi	41.0	3.0	7.2	24.1	2.3	9.4
Ca	95.8	3.6	3.8	94.9	13.5	14.3
Cd	3.4	0.5	15.6	4.9	3	60.7
Co	9.5	0.5	5.3	10.1	1.4	14.1
Cr	94	9.7	10.2	99.2	5.3	5.3
Cu	63	6.5	10.2	52.1	4.8	9.2
Fe	313	19.2	6.1	212.1	14.4	6.8
In	8.1	0.1	1.2	9.8	2	19.8
Mg	12.2	0.9	7.1	17.2	1.7	10.1
Mn	30	0.9	3.0	25	2.5	9.9
Mo	175	10.0	5.7	146.3	13	8.9
Ni	143	7.5	5.2	143.8	3.8	2.7
Pb	111	6.7	6.1	101.1	2.6	2.6
Si	245	11.9	4.8	Not detectable; isobaric interference		
Sn	15.3	1.8	11.6	18.1	5.6	30.9
V	50	1.1	2.2	54.5	4.1	7.5
W	95	1.3	1.3	100.3	15.5	15.4
Zn	148	7.2	4.9	95	6.9	7.3

10.3.2 DETERMINATION OF TRACES OF RADIOISOTOPES IN CONTAMINATED ENVIRONMENTAL SAMPLES

The movement of radionuclides in the environment has been studied for many years, with the principle objective of tracing the routes by which they accumulate in the food chain and become available for human consumption. The explosions in Reactor No. 4 at the nuclear power station in Chernobyl provided a point source for distribution of radionuclides and a unique opportunity to trace the mechanisms by which they are distributed. GDMS has been used for the determination of uranium in soil samples [35]; sediments and vegetation have also been investigated [20]. Very recently, dc-GDMS has been exploited for the determination of ^{237}Np in Irish Sea sediments [36]. For these matrices the major problem to overcome was the sample preparation procedure. Being nonconductive samples, they need to be blended with a conductive host matrix. Some authors [35] have used silver powder at a concentration of up to 90% of the total sample weight and after homogenization the mixture was pressed into the shape of a pin electrode. For the determination of trace elements at concentration levels of ng g^{-1} or even less, the use of this much silver can dilute the samples to such a degree that the analyte signal becomes very weak.

The method applied to the analysis of nonconducting samples, using a secondary cathode, has also been employed for environmental samples. According to this method, the samples (soils, vegetation and sediments) need to be pressed into disc-shaped electrodes. Discs obtained without blending with silver powder were found to be too fragile, so 5% of silver powder was added to the samples. This concentration was the minimum amount necessary to obtain stable disc electrodes without too much dilution. Stable discharge was obtained using a tantalum secondary cathode during the analysis. The combination of the use of blending material and a secondary cathode has been used for all environmental types of samples mentioned above.

In the determination of elements and radioisotopes at the trace level, the sensitivity is an important parameter. The procedures based on GDMS are mainly affected by interferences arising from the sample matrix, the blending material and the discharge gas. Interferences from the matrix and discharge gas can be eliminated by using a high mass resolution. This normally results in a decrease in sensitivity, and hence is not suitable for trace element determinations. The blending material (the so-called conductive host matrix) can be chosen according to the specific sample requirements or the latter can be neglected.

For example, in the analysis of traces of Th the addition of silver can be a necessity. Silver produces a spectral interference due to the formation of $^{107}\text{Ag}^{109}\text{Ag}^{16}\text{O}^+$ and a mass resolution of at least 1000 is necessary to separate the peak of this species from the Th peak. With the uranium isotopes silver does not produce interferences. Tantalum, however, gives rise to the formation of $^{180}\text{Ta}^{40}\text{Ar}^{16}\text{O}^+$ (mass 235.90) and $^{181}\text{Ta}^{40}\text{Ar}^{16}\text{O}^+$ (mass 236.90). These two

polyatomic ions interfere with $^{235}\text{U}^+$ and $^{236}\text{U}^+$. When working at a mass resolution of 300, $^{180}\text{Ta}^{40}\text{Ar}^{16}\text{O}^+$ can be resolved from those of $^{235}\text{U}^+$ and also $^{181}\text{Ta}^{40}\text{Ar}^{16}\text{O}^+$ from $^{236}\text{U}^+$. For the separation of signal from $^{180}\text{Ta}^{40}\text{Ar}^{16}\text{O}^+$ and $^{236}\text{U}^+$, respectively, a mass resolution of 1700 is necessary. The determination of ^{236}U is of great importance because this isotope indicates the presence of irradiated uranium in the sample. For ^{236}U detection limits in the pg g^{-1} range or even less are often requested. They can be obtained by the use of a secondary cathode consisting of gold. Fortunately, plutonium isotopes were found not to be affected by interferences from silver or tantalum.

10.3.3 DETERMINATION OF THE ISOTOPIC COMPOSITION FOR NUCLEAR SAMPLES

In nuclear technology and generally in nuclear research, the precise and accurate measurement of isotope ratios is of great interest. For their determination the widely accepted method is TIMS. In this method the sample must be dissolved and chemical separation of the analyte of interest is required before the analysis. GDMS has also been exploited for the determination of the isotopic composition in samples of nuclear concern [37–40]. By comparison with TIMS, it has been demonstrated that GDMS is a competitive technique for the determination of the isotopic abundance of B, Li and U, in terms of precision and accuracy. GDMS has the advantage of reduced handling of the sample before the analysis. As for the determination of the isotopic composition of Pu, corrections for ^{238}U and ^{241}Am are necessary.

10.3.4 DEPTH PROFILING OF ZrO_2 LAYERS DEPOSITED ON ZIRCALOY NUCLEAR FUEL CLADDING MATERIAL

In Europe, 36% of the electrical energy produced comes from nuclear power plants [41]. The major issues are the competitiveness of nuclear energy compared with other energy sources, the safety of nuclear reactors and the management of nuclear waste. The actual trend is to increase the burn-up of the nuclear fuel for economic reasons and to reduce the production of waste. One of the major effects encountered is the corrosion of the zircaloy cladding used for containment of the fuel pellets.

In pressurized water reactors (PWR), the lithium hydroxide added as alkaliizer to the primary coolant, at concentrations varying between 2 and 4 $\mu\text{g g}^{-1}$ depending on the number of the reactor cycles [42], may increase the oxidation rate of the zircaloy [43]. In addition, boric acid is introduced at a concentration level of 1000 $\mu\text{g g}^{-1}$ of boron in the cooling water of Western PWR to control the core reactivity at the beginning of each reactor cycle. It has been found that this additive has a retarding effect on the formation of the ZrO_2 corrosion layer [44]. More recently, the addition of zinc in some boiling water reactors (BWR) to reduce the

activation of the coolant has shown beneficial effects concerning the corrosion of zircaloy by reducing the oxide layer thickness [45,46]. In order to evaluate the influence of different additives on the corrosion induced by the lithium, it is necessary to study their incorporation in the layer of ZrO_2 formed during reactor operation.

The study of diffusion mechanisms for trace elements can be exploited in different fields of environmental processes, such as sorption/desorption of radioactive nuclides from granitic rocks. In the industrial field, the changes in physical and chemical properties of a specific material can be correlated with the concentration of dopants or surface impurities. Their diffusion mechanisms can be studied by depth profiling [34,47]. GD techniques have been used for depth profiling in several matrices [10,47–52].

GDMS has also been used for the study of the mechanisms of corrosion of zircaloy cladding of nuclear fuels, measuring the diffusion of the impurities in ZrO_2 layers by depth profiling [53]. It has been found that the use of a secondary cathode is essential. As shown in Figure 10.2, representing a depth profile for zirconium oxide layer deposited on aluminium, an anomalous peak of zirconium appears centred at about 600 s in the metal/oxide interface. This behaviour was found to be due to instability of the plasma arising from the change in electrical conductivity of the system on passing from the insulating nature of the oxide layer to the conductive oxide/metal interface. By applying a secondary cathode, this problem was overcome. In Figure 10.3a, three well-defined zones are shown to be present: the oxide layer (0–1100 s), the metal oxide interface (1100–1700 s) and the metallic support (1700–3000 s). The profile for lithium was also registered. In Figure 10.3b it can be seen that a fairly constant concentration of Li is found in the oxide layer, then it decreases in the interface zone and falls to zero in the metallic phase.

By GDMS depth profiling, the effect of B on Li diffusion has been also studied.

The influence of boron solution additions considerably reduces the oxidation of zircaloy induced by lithium [53]. The large reduction of the sample weight gain has now been corroborated with the depth profiles obtained by GDMS.

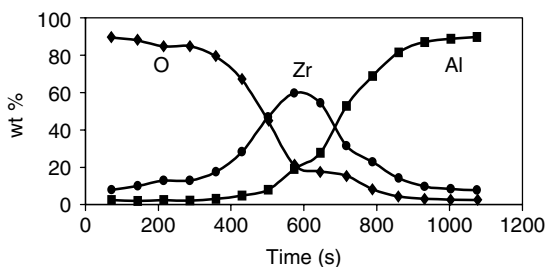


Figure 10.2 GDMS depth profile of a thin layer of ZrO_2 deposited on Al

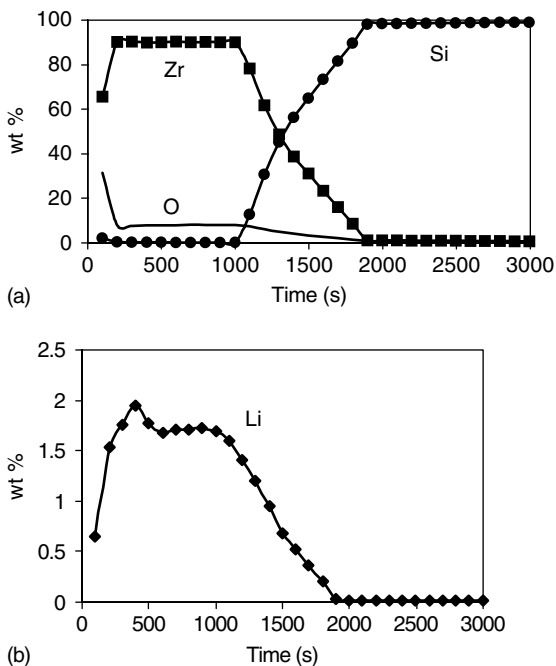


Figure 10.3 GDMS depth profiles for the major elements of a thin layer of ZrO_2 deposited on silicon and doped with lithium. (a) Zr, O and Si profiles; (b) lithium profile

Figure 10.4a and b compare the profiles of lithium incorporated in the oxide layer after 7 days of reaction in an autoclave with $1000 \mu\text{g g}^{-1}$ of Li and $1000 \mu\text{g g}^{-1}$ of Li + $1000 \mu\text{g g}^{-1}$ of B respectively. The depth profiles show a reduction of lithium uptake of one order of magnitude during corrosion in the presence of boron. An interesting property noted for boron is that this element does not penetrate into the oxide layer, as is evident from Figure 10.4b. This indicates an external protective effect, e.g. poisoning of adsorption sites or the formation of a thin protective overlayer on the surface. The possible buffering effect of the boric acid controlling the pH of the solution seems less probable for the simple fact that any other pH buffer could also produce the same beneficial effect on the oxide growth.

10.4 CONCLUSIONS

GD-based techniques have been shown to be of great use for bulk and depth profiling measurements in the case of both conductive and nonconductive samples, with an unrivalled flexibility of applications. In particular, GDMS has been

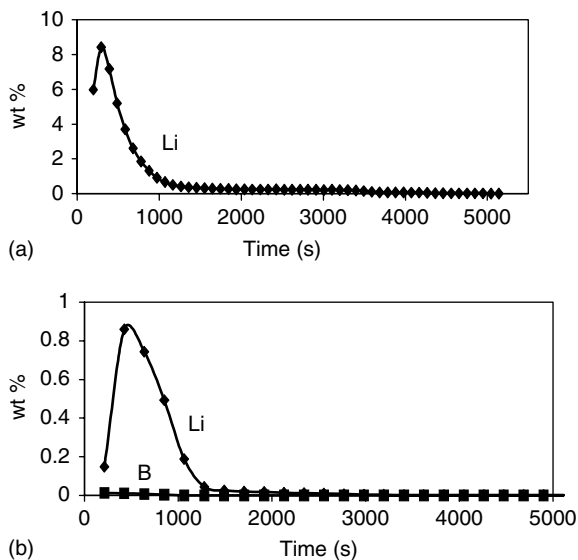


Figure 10.4 Lithium profile for a ZrO₂ layer obtained in autoclave simulating nuclear reactor operating conditions (a) without and (b) with addition of boron to the corrosive media at a concentration of 1000 μg g⁻¹

successfully applied to the characterization of samples of nuclear concern. Its nondestructive nature and the fast sample preparation make the technique very attractive for the characterization of radioactive samples. Moreover, major, minor and trace elements can be determined in the same analysis. GDMS has been demonstrated to be competitive with TIMS for determination of the isotopic compositions of matrix elements. The method can also be used for the determination of traces of radioisotopes in environmental matrices, exploiting the secondary cathode technique. Mechanisms of the diffusion of trace elements can be followed by depth profiling analysis.

10.5 ACKNOWLEDGEMENTS

The author acknowledges the valuable collaboration of Fabio Bocci in the preparation of this chapter and thanks Stefania Giannarelli, Laura Aldave de las Heras and Olivier Louis Actis-Dato for their contributions to this research. H. Ruhmann and W. Goll (FRAMATOME Advanced Nuclear Power GmbH) are acknowledged for making available the material for the depth profiling of zircaloy and for useful discussions on this subject, along with Enrique Toscano.

10.6 REFERENCES

- [1] Pons-Corbeau J., Cazet J. P., Moreau J. P., Berneron R. and Charbonnier J. C. (1986) Quantitative analysis by glow discharge optical spectrometry. *Surf Interface Anal* **9**: 21–25.
- [2] Bengtson A. (1994) Quantitative depth profile analysis by glow discharge. *Spectrochim. Acta, Part B* **49**: 411–429.
- [3] Payling R. and Jones D. G. (1993) Fundamental parameters in quantitative depth profiling and bulk analysis with glow discharge spectrometry. *Surf Interface Anal* **20**: 787–795.
- [4] Grimm W. (1968) Eine neue Glimmentladungslampe für die optische Emissionsspektralanalyse. *Spectrochim. Acta, Part B* **23**: 443–454.
- [5] Robinson K. and Hall E. F. H. (1987) Glow discharge mass spectrometry for nuclear materials. *J Metal* **39**: 14–16.
- [6] Betti M. (1996) Use of a direct current glow discharge mass spectrometer for the chemical characterisation of samples of nuclear concern. *J Anal At Spectrom* **11**: 855–860.
- [7] Aldave de las Heras L., Bocci F., Betti M. and Actis-Dato L. O. (2000) Comparison between the use of direct current glow discharge mass spectrometry and inductively coupled plasma quadrupole mass spectrometry for the analysis of trace elements in nuclear samples. *Fresenius' J Anal Chem* **368**: 95–102.
- [8] Behn U., Gerbig F. A. and Albrecht H. (1994) Depth profiling of frictional brass coated steel samples by glow discharge mass spectrometry. *Fresenius' J Anal Chem* **349**: 209–210.
- [9] Jakubowsky N., Stuewer D. and Toelg G. (1986) Improvement of ion source performance in glow discharge mass spectrometry. *Int J Mass Spectrom Ion Processes* **71**: 183–197.
- [10] Chu P. K., Huneke J. C. and Blattner R. J. (1987) Application of glow discharge mass spectrometry and sputtered neutral mass spectrometry to materials characterization. *J Vac Sci Technol* **5**: 295–301.
- [11] Betti M., Rasmussen G., Hiernaut T., Koch L., Milton D. M. P. and Hutton R. C. (1994) Adaptation of a glow discharge mass spectrometer in a glove-box for the analysis of nuclear materials. *J Anal At Spectrom* **9**: 385–391.
- [12] Hubinois J. C., Morin A., Marty P., Larpin J. P. and Perdereau M. (1999). A new integrated in glove box glow discharge optical emission spectrometer—application to carbon, nitrogen and oxygen bulk determinations in low alloy steels as a preliminary study. *J Anal Atom Spectrom* **14**: 1405–1411.
- [13] Milton D. M. P., Hutton R. C. and Ronan G. A. (1992) Optimisation of discharge parameters for the analysis of high purity silicon wafer by magnetic sector glow discharge mass spectrometry. *Fresenius' J. Anal Chem* **343**: 773–777.
- [14] Winchester M. R., Lazik C. and Marcus R. K. (1991) Characterization of radio frequency glow discharge emission source. *Spectrochim Acta Part B* **46**: 483–499.
- [15] Winchester M. R., Duckworth D. C. and Marcus R. K., in *Glow Discharge Mass Spectroscopies*, Marcus R. K. (Ed), Plenum Press, New York, 1990, ch 7.
- [16] Duckworth D. C. and Marcus R. K. (1989) Radio frequency powered glow discharge atomization/ionization source for solids mass spectrometry. *Anal Chem* **61**: 1879–1886.
- [17] Shick C. R., Raith A. and Marcus R. K. (1993) Complementary radio frequency glow discharge source for a commercial quadrupole mass spectrometry system. *J Anal At Spectrom* **8**: 1043–1048.
- [18] Marcus R. K. (1993) Operating principles and design considerations for radiofrequency powered glow discharge devices. Review. *J Anal At Spectrom* **8**: 935–943.

- [19] De Gendt S., Van Grieken R. E., Ohorodnik S. K. and Harrison W. W. (1995) Parameter evaluation for the analysis of oxide based samples with radio frequency glow discharge mass spectrometry. *Anal Chem* **67**: 1026–1033.
- [20] Betti M., Giannarelli S., Hiernaut T., Rasmussen G. and Koch L. (1996). Detection of trace radioisotopes in soil, sediment and vegetation by glow discharge mass spectrometry (1996). *Fresenius' J Anal Chem* **355**: 642–646.
- [21] Milton D. and Hutton J. C. (1993) Investigation into the suitability of using a secondary cathode to analyse glass using glow discharge mass spectrometry. *Spectrochim Acta Part B* **48**: 39–52.
- [22] Schelles W., De Gendt S., Müller V. and Van Grieken R. (1995) Evaluation of secondary cathodes for glow discharge mass spectrometry of different nonconducting sample types. *Appl Spectrosc* **49**: 939–944.
- [23] Schelles W. and Van Grieken R. E. (1996) Direct Current GDMS analysis of a Macor ceramic using a secondary cathode. *Anal Chem* **68**: 3570–3574.
- [24] Schelles W., De Gent S., Van Grieken R. E. (1996) Optimization of secondary cathode thickness for direct current glow discharge mass spectrometric analysis of glass. *J Anal At Spectrom* **10**: 937–941.
- [25] Winchester M. R. and Marcus R. K. (1988) Glow discharge sputtering atomization for atomic absorption analysis of nonconducting powder. *Appl Spectrosc* **42**: 941–944.
- [26] Tong S. L. and Harrison W. W. (1993) Glow discharge mass spectrometric analysis of non-conducting materials. *Spectrochim Acta Part B* **48**: 1237–1245.
- [27] Velazco J. C., Kolts J. H. and Setser J. W. (1978) Rate constants and quenching mechanisms for the metastable states of argon, krypton and xenon. *J Chem Phys* **69**: 4357–4373.
- [28] Marcus R. K. (1995) *Glow Discharge Optical Emission of Plutonium and Plutonium Waste*. WSRC-RP-96 -16, DOE contract No. DE-AC09-89SR18035.
- [29] Garcia Alonso J. I., Thoby-Schultendorff D., Givannone B. and Koch L. (1993) Performance characteristics of a glove-box inductively coupled plasma mass spectrometer for the analysis of nuclear materials. *J Anal At Spectrom* **8**: 673–679.
- [30] Crain J. S., Smith L. L., Yaeger J. S., Alvarado J. A. (1995) Determination of long-lived actinides in soil leachates by Inductively coupled plasma mass spectrometry. *J Radioanal Nucl Chem* **194**: 133–139.
- [31] Smith M. R., Wyse E. J., Koppelaar D. W. (1992) Radionuclide detection by inductively coupled plasma mass spectrometry: a comparison of atomic and radiation methods. *J Radioanal Nucl Chem* **160**: 341–354.
- [32] Ross R. R., Noyse J. R., Lardy M. M. (1993) Inductively coupled plasma mass spectrometry: an emerging method for analysis of long-lived radionuclides. *Radioact Radiochem* **4**: 24–37.
- [33] Schramel P. (1997) *Analytiker Taschenbuch 15*, Springer, Berlin.
- [34] Sanderson N. E., Hall E., Clark J., Charalambous P. and Hall D. (1987) Glow discharge mass spectrometry—a powerful technique for the elemental analysis of solids. *Mikrochim Acta* **1**: 275–290.
- [35] Duckworth D. C., Barshick C. M. and Smith D. H. (1993) Analysis of soils by glow discharge mass spectrometry. *J Anal At Spectrom* **8**: 875–879.
- [36] Aldave de las Heras, L., Hrneck, E., Bildstein, O. and Betti, M. (2002) Neptunium determination by dc glow discharge mass spectrometry (dc-GDMS) in Irish Sea sediment samples. *J Anal At Spectrom* in press.
- [37] Betti M., Rasmussen G. and Koch L. (1996) Isotopic abundance measurements in solid nuclear-type samples by glow discharge mass spectrometry. *Fresenius' J Anal Chem* **355**: 808–812.

- [38] Young J. P., Show R. W., Barshick C. M., and Ramsey J. M. (1998) Determination of actinide isotope ratios using glow discharge optogalvanic spectroscopy. *J Alloys Compd* **271–273**: 62–65.
- [39] Barshick C. M., Goodner K. L., Clifford H. W. and Eyley J. R. (1998) Application of glow discharge Fourier-transform ion cyclotron resonance mass spectrometry to isotope ratio measurements. *Int. J Mass Spectrom* **178**: 73–79.
- [40] Chartier F. and Tabarant M. (1997) Comparison of the performance of a Laboratory-built high resolution glow discharge mass spectrometer with that of a quadrupole inductively coupled plasma (glow discharge) mass spectrometer for boron and gadolinium isotopic analysis. *J Anal At Spectrom* **12**: 1187–1193.
- [41] *World Nuclear Industry Handbook*, Nuclear Engineering International, 1999.
- [42] Pecheur D., Godlewski J., Billot P. and Thomazet J. (1996) in *Zirconium in the Nuclear Industry, Eleventh International Symposium*, ASTM STP 1295, ASTM, Philadelphia, PA, 94–113.
- [43] Lemaignan C. and Motta T. (1994) in *Materials Science and Technology, Vol. 10B, Nuclear Materials Part II*, Frost BRT (Ed), VCH, Weinheim.
- [44] Branwell I. L., Parson P. D. and Tice D. R. (1991) in *Zirconium in the Nuclear Industry, Ninth International Symposium*, ASTM STP 1132, ASTM, Philadelphia, PA, 628–642.
- [45] Allsop H. A., Miller D. G. and Godin M. S. (1994) in *Proceedings of the SFEN International Conference on Chemistry in Water Reactors*, Société Française pour l'Énergie Nucléaire, Nice, 321–328.
- [46] Bergmann C. A., Kunig R. H. and Corpora G. J. (1994) in *Proceedings of the SFEN International Conference on Chemistry in Water Reactors*, Société Française pour l'Énergie Nucléaire, Nice, 80–81.
- [47] Jakubowski N. and Stuewer D. (1992) Application of glow discharge mass spectrometry with low mass resolution for in-depth analysis of technical surface layers. *J Anal At Spectrom* **7**: 951–958.
- [48] Marcus R. K. (1993) *Glow Discharge Spectroscopies*, Plenum Press, New York.
- [49] Nickel H., Guntur D., Mazurkiewicz M. and Naoumidis A. (1991) Contribution to the quantification of glow discharge emission depth profiles for oxide scales on Ni-base alloys. *Spectrochim Acta Part B* **46**: 125–135.
- [50] Payling R., Jones D., Bengston A. (Eds), *Glow Discharge Optical Emission Spectrometry*, Wiley, New York, 1997, chaps 12, 13, 14.
- [51] Coburn J. M. and Kay E. (1971) A new technique for elemental analysis of thin surface layers of solids. *Appl Phys Lett* **19**: 350–359.
- [52] Schelles W. and van Grieken R. (1997) Quantitative analysis of zirconium oxide by direct current glow discharge mass spectrometry using a secondary cathode. *J Anal At Spectrom* **12**: 49–52.
- [53] Actis-Dato L. O., Aldave de las Heras L., Betti M., Toscano E. H., Miserque F. and Gouder T. (2000) Investigation of mechanism of corrosion due to diffusion of Impurities by direct current glow discharge mass spectrometry depth profiling. *J Anal At Spectrom* **15**: 1479–1484.

11

Analysis of Nonconducting Materials by dc Glow Discharge Spectrometry

ANNEMIE BOGAERTS, WIM SCHELLES
and RENÉ VAN GRIEKEN

*University of Antwerp, Department of Chemistry,
Wilrijk, Belgium*

11.1 INTRODUCTION

The concept of an analytical glow discharge, in which the material to be analyzed acts as the cathode of the glow discharge cell, seems to restrict the field of application to the analysis of conducting materials. This is, indeed, the most straightforward and routine application, but nonconducting materials can also be analyzed. Three different methods have successfully been applied for the analysis of nonconductors by glow discharges, namely:

- The use of a radio frequency (rf) glow discharge instead of the direct current (dc) source. In a dc glow discharge source, a constant voltage is applied between the cathode and anode, leading to a constant current to the cathode, which yields charging-up of the nonconducting sample, preventing it from further being sputtered. In an rf source, however, a time-varying voltage (with rf frequency) is applied between the electrodes. This protects the nonconducting sample from charging-up, since the positive charge accumulated due to positive ion bombardment is neutralized by negative charge accumulation due to electron bombardment during one half of the rf cycle. This method was first applied to analytical glow discharges in 1971 by Coburn and Kay [1], but it

received much wider attention in the late 1980s, mainly as a result of work of Marcus's group [2].

- The mixing of a nonconducting powder with a conducting host matrix, which was developed in 1972 for glow discharge optical emission spectrometry (GD-OES), by Dogan *et al.* [3] and later also applied to glow discharge mass spectrometry (GDMS) and glow discharge atomic absorption spectrometry (GD-AAS).
- The use of a conducting secondary cathode in front of the nonconducting solid sample, which was first introduced in 1993 for GDMS by Milton and Hutton [4].

Since the basic principles and applications of rf discharges will be discussed in detail in another chapter, we will focus here on the two other techniques, which can be used in the case of dc glow discharges.

11.2 USE OF A CONDUCTING HOST MATRIX

11.2.1 METHODOLOGY

When the nonconducting sample is in powder form, it can readily be mixed with a conducting host matrix (mostly also in powder form), according to a certain sample-to-host mass ratio (see below). The mixing is usually accomplished by means of a mechanical shaker or grinder. A detailed description of this sample preparation procedure is given, among others, in ref. [5]. In our laboratory [6], a fraction of the sample + host mixture (e.g. 0.5 g) is usually inserted in a polystyrene vial with a glass ball pestle added. Thorough homogenization of the mixture is achieved by use of a Wig-L-Bug (Spex, Edison, NJ, USA) for several minutes. About 0.15 g of the homogenized mixture is then transferred into a polyethylene slug and pressed at a pressure of several tons per square centimeter, usually into the form of a pin (or a disk). The latter can then be directly inserted as the cathode in the glow discharge. This approach originates from experience gained with arc and spark discharges [7,8], and is relatively straightforward. However, several parameters have to be taken into account in order to perform successful measurements.

The Host Material

It is obvious that only high-purity powder can be used as the host matrix. Indeed, the host material is also sputtered and is introduced into the discharge, together with the material to be analyzed, and this results in a blank spectrum. Further, it has been proved that host materials with a good sputter yield are desirable to obtain a good overall sputtering of the compacted sample [5]. Other favorable characteristics of the host matrix include good mechanical strength upon pressing,

low cost and availability in a variety of particle sizes (see below). In addition, interferences as a result of the matrix material should be avoided.

A number of materials have been evaluated as host matrix, such as Cu [2,9–27], Ag [2,9–12,28–34], Al [2,9,35,36], Ta [9,10,29–31,37], Ti [10,29–31], Fe [9,21], graphite [9,12,29,38], W [2,9], Bi [10], In [10,39], Pb [10], Sn [10], Zn [10], Ni [21] and Ga [40]. Gallium has the advantage of being available in extremely high-purity grade. Moreover, gallium has a melting-point of 30°C. Therefore, if the gallium is mixed in the liquid state with the nonconducting material, it has been proved that only little gallium (<20% of the weight of the sample) is needed to produce a conducting electrode. It is believed that a very thin conducting gallium film is formed around each nonconducting particle. To obtain this effect, extremely thorough mixing is needed [40]. Experiments in our laboratory, however, have indicated that this sample preparation technique is not always reproducible. Another innovative technique has been applied with indium as host material [39]. Indium was used as a solid in which the nonconducting powder migrated in a high pressure vessel, thereby avoiding the trapping of residual gases.

The more classical technique, however, is based on the use of powdered host materials. The effect of different kinds of host materials has been investigated [e.g. 9,10,29]. From all these materials, tantalum has the advantage of being a getter material [9,29,30]. This means that it tends to form strong oxide bonds, effectively removing oxygen from the discharge, and therefore reducing molecular oxide interferences. Tantalum powder, however, generally is not available in such a pure form as, for example, silver and copper [41]. That explains why the latter materials are more often used as the host matrix [2,9–34]. Copper, in particular, is very suitable, because of its wide availability, relatively low cost and high sputter rate [14]. Moreover, its high thermal conductivity and an excellent suitability for blending of finely dispersed powders are additional factors for choosing copper as the host material [42]. De Gendt [6] found for an albite sample (oxide-based geological material) comparable analytical signals for a copper and a silver matrix, but lower analyte signals were obtained with graphite as a binder (see Figure 11.1) [6]. This could be due to the very low sputter rate of graphite, resulting in a very low overall sputtering of the compacted sample. In some cases [35,36], aluminum was preferred as a host matrix, because it gives rise to relatively few interferences in the mass spectrum, e.g., in the vicinity of Pd, Rh and Pt [36]. Generally, one can state that the choice of the host material has to be made for each specific analytical problem, depending on, among others, the presence of spectral interferences for the elements of interest.

Relative Percentages of Sample and Host in the Mixture

It is clear that the electrode has to contain enough conducting material to avoid instabilities in the discharge and to create enough sputtering, since high relative

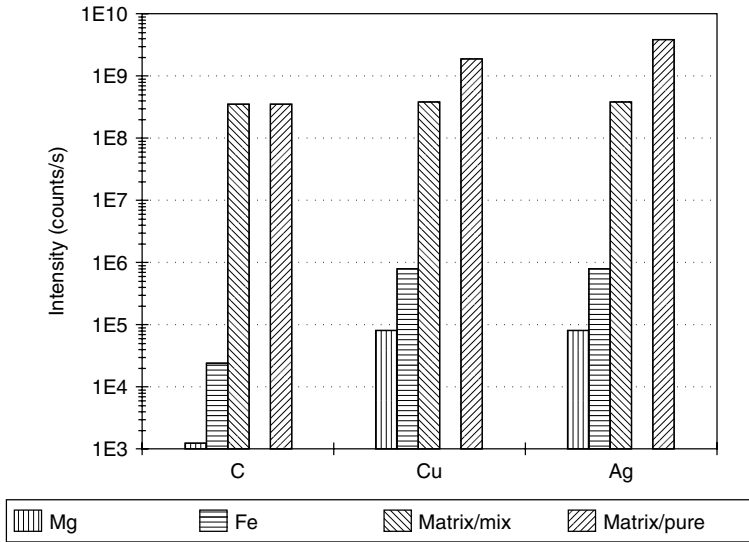


Figure 11.1 Comparison of the analyte (Mg and Fe) and host matrix ion intensities in compacted samples, in the VG9000 glow discharge mass spectrometer, for various conducting binders (graphite, copper and silver). The three bars on the left for each matrix are the analyte and matrix ion intensities in the compacted sample (nonconducting sample (albite) to conducting binder mixture of 1 + 4). The right bar for each matrix represents the matrix ion intensity in the pure matrix [6]

amounts of the sample result in low sputter yields, and thus in low signal intensities. In practice, this means that an excess of host material is needed [5,6], unless gallium is used, as discussed above. On the other hand, it is also obvious that a too high dilution of the nonconducting sample also results in low signal intensities.

Woo *et al.* [15] investigated the use of various mass ratios for an Al_2O_3 powder mixed with Cu powder, in analyses with a laboratory-built Grimm-type glow discharge quadrupole mass spectrometer.

Ratios of sample-to-host of 1 + 1 and 1 + 3 appeared to give unstable samples or unstable discharge conditions. Ratios of 1 + 5 and 1 + 10 yielded a stable discharge, and therefore a ratio of 1 + 5 (i.e. 17% sample content) was finally chosen to keep the dilution factor as low as possible [15]. In ref. [19], sample-to-host ratios were varied from 1 + 4 to 1 + 19 with some intermediate values, and the smallest sample content (i.e. 5%, in the ratio 1 + 19) was observed to give the highest sensitivity in GD-AAS. In most papers, mass ratios are reported to vary between 1 + 4 (i.e. 20% sample content) and 1 + 19 (i.e. 5% sample content).

In our laboratory, De Gendt investigated the use of various sample-to-host ratios (i.e. blank, 1 + 19, 1 + 9, 1 + 4, 1 + 2 and 1 + 1) in the analysis of a nonconducting sample (albite), mixed with high-purity copper [6]. The 1 + 1 mixture, which has the highest content of nonconducting material, led to problems

when compacting the mixture into electrodes, and was not considered further. The 1 + 4 mixture (i.e. 20% of nonconducting sample) appeared to result in the highest analyte signal in GDMS (see Table 11.1), although the sensitivity in the case of the 1 + 19 mixture was found to be only about a factor of two lower. This conclusion is in line with observations of most other researchers for analogous analyses by means of GD-OES [43–45]. On the other hand, De Gendt also emphasized that the relative amount of nonconducting sample has an influence on the time required for stabilization [6]. As could be expected, in the case of a higher nonconducting fraction in the sample, the stabilization time is longer. For SiO₂ contents (in a copper host matrix) of 33, 17 and 9% (i.e. mixing ratios of 1 + 2, 1 + 5 and 1 + 10, respectively), stabilization times of about 3, 2 and 1 h, respectively, were found (see Figure 11.2) [6]. Although from the analyte

Table 11.1 Influence of the nonconducting material content in compacted samples on the sputtering rates and the ion intensities (Cu host matrix, and Mg and Fe analyte intensities) for various albite–Cu mixtures [6].

Mixing ratio in Cu	Sputtering rate ($\mu\text{g/s}$)	Ion intensity (counts/s)		
		Cu (host)	Mg (analyte)	Fe (analyte)
Pure Cu	2.4 ± 0.4	$(2.0 \pm 0.2) \times 10^9$	—	—
1 + 19	1.25 ± 0.01	$(6.6 \pm 0.6) \times 10^8$	$(3.5 \pm 0.4) \times 10^4$	$(2.9 \pm 0.2) \times 10^5$
1 + 9	1.13 ± 0.02	$(4.5 \pm 0.5) \times 10^8$	$(4.8 \pm 0.6) \times 10^4$	$(4.2 \pm 0.2) \times 10^5$
1 + 4	0.83 ± 0.09	$(3.8 \pm 0.6) \times 10^8$	$(8.1 \pm 0.2) \times 10^4$	$(7.7 \pm 0.9) \times 10^5$
1 + 2	0.65 ± 0.02	$(2.2 \pm 0.5) \times 10^8$	$(8.5 \pm 0.5) \times 10^4$	$(7.1 \pm 0.9) \times 10^5$

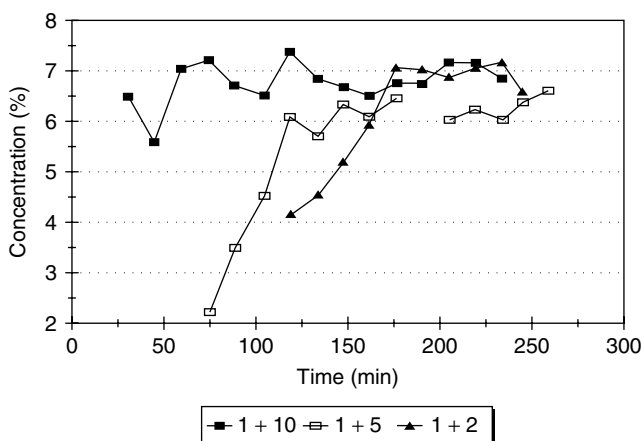


Figure 11.2 Calculated Si concentration as a function of sputter time, using Al as an internal standard, for compacted samples in a 1 + 10, 1 + 5 and 1 + 2 mixing ratio of a calcareous loam soil and Cu. The stabilization times appear to be of the order of 1, 2 and 3 h, respectively, in the VG9000 glow discharge mass spectrometer, at 3 mA and 1 kV [6]

signal (see Table 11.1) a 20% content was found to be optimum, the study on stabilization times demonstrated that, in practice, a 10% content of nonconducting material (i.e. a 1 + 9 mixture), or even less, was more convenient [6]. It should be mentioned, however, that these long stabilization times must also be partly attributed to the press, which was probably not working satisfactorily. Moreover, stabilization times in GD-OES are also typically shorter (see below).

Discharge Conditions

It is obvious that the discharge voltage, which is a measure for the energy of the particles bombarding the sample, and the discharge current, which is proportional to the number of bombarding collisions on the sample and to the number of ionization/excitation collisions in the plasma, have an influence on the sputter rate and the analyte signal intensity. Generally, one can state that a higher discharge power yields higher signal intensities. De Gendt [6] found a certain threshold for the power, under GDMS conditions, which is needed to achieve reproducible results for the concentrations of components in the nonconductor. It is clear from Figure 11.3 that below a discharge power of ca 1.5 W, the concentration of Mg obtained in the nonconducting sample (i.e. albite mixed with Cu) is not very reproducible [6]. At higher power levels, more or less reproducible concentrations at the level of 40–50 ppm were obtained, for different conditions of pressure and power (ranging from 1.5 to 5 W). This threshold for reproducible quantitative

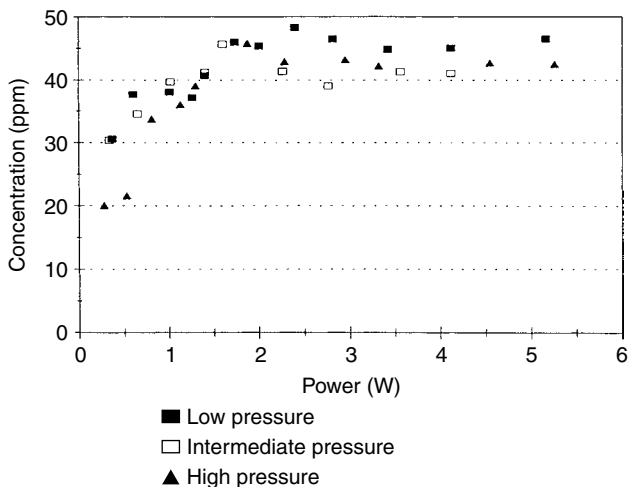


Figure 11.3 Calculated Mg concentration as a function of discharge power at three different pressures, for a 1 + 19 albite + Cu compacted electrode in the VG9000 glow discharge mass spectrometer. The calculated concentration appears to be reproducible only for power levels above 1.5 W [6]

results might be understood from the lower kinetic energy of plasma particles bombarding the cathode at low power, and hence low voltage. Indeed, it is likely that the conducting host and the nonconducting oxide-based sample have different threshold values for sputtering, and that at low power and voltage the conducting components are being sputtered more efficiently than the nonconducting sample components, which results in a too low calculated concentration of analytes [6].

Furthermore, Mai and Scholze demonstrated for compacted powder samples that a higher discharge power required a shorter stabilization time [46,47]. At 100 W, stable signals were obtained after a few minutes of sputtering only, whereas at lower power levels increasing stabilization times were required (e.g. ca 11 min at 30 W and more than 30 min at 14 W). It should be mentioned, however, that a power of 100 W might be a realistic value for Grimm-type GD-OES, but commercial GDMS instruments usually operate at much lower power levels (e.g. 3 W), so that typical GDMS stabilization times will rather be of the order of 1 h [6] (see Figure 11.2). In practice, one can state that the time required for reaching steady-state sputtering conditions can be somewhat reduced by optimizing the power, mixing ratio, etc., but a certain stabilization time appears to be inherent to the sputtering of compacted and multi-component samples.

Particle Size

It is stated that the particle sizes in the compacted sample must be small compared with the sputtering rate of surface layers, in order to obtain a discharge with gas-phase compositions which are representative of the bulk sample [5]. Moreover, small particles appear to result in more stable discharge conditions [5,46]. Generally, small particle sizes are therefore preferable, with respect to both the achievable accuracy and precision. On the other hand, a disadvantage of small particles is that they imply a larger surface area and thus a greater chance of trapping of gases in the final compacted sample. Nevertheless, most researchers agree that small particle sizes (i.e. below 50–60 μm in diameter) are preferable [16,20,21,26].

Presence of Trapped Gases

It is obvious that the sample preparation method of mixing a nonconducting sample with a conducting host matrix can give rise to contamination problems, most commonly due to the trapping of gases such as N_2 , O_2 , H_2 , H_2O , CO_2 , CO , NO , N_2O and CH_4 . These gas species often result in a lower sputtering. Moreover, they can cause quenching of metastable argon atoms, thereby reducing the efficiency of Penning ionization. Both effects will result in lower analyte intensities [48]. Furthermore, the presence of residual gas species is a source of interferences in the mass spectrum. Not only the molecular species itself, but also clusters

(hydrides, nitrides, oxides, etc.) can affect the determination of certain elements. Finally, the trapped gases generally lead also to longer stabilization times.

Some precautions during sample preparation can help in preventing the trapping of gases, e.g. heating of the sample materials before mixing, applying a mild vacuum to the sample mixture during pressing, and outgassing of the compacted sample under vacuum and/or mild heat treatment prior to analysis [5,14,26]. Furthermore, the use of host materials with gettering abilities has also been demonstrated to be useful [9,29]. Cryogenic cooling of the glow discharge cell has also been found to be successful in reducing the effects of the inevitable residual gases [49]. The most effective and generally usable method to limit the effects of trapped gases is to apply a suitable presputtering period prior to data acquisition [14]. If high discharge currents and powers are necessary to attain acceptable sensitivities [14], it is usually advantageous to increase the current from an initially low value to the desired analysis value in several steps. The presputtering sequence employed in ref. [14], for example, was as follows: (i) 60 mA during 20 s, (ii) 150 mA during 20 s, (iii) 225 mA during 15 s and (iv) 300 mA during 210 s.

11.2.2 SOME APPLICATIONS AND ANALYTICAL FIGURES OF MERIT

The host matrix technique has been used extensively since the 1970s, first mainly in GD-OES and later also in GDMS and GD-AAS. Various kinds of nonconducting materials have been analyzed, such as iron ore materials [6,11], rare earth oxides [6,9,29,31,32], other oxides [13,21], soils [10,28,34,35], rock sediments [9,22,34], marine sediments [17,18], vegetation [34], ceramic samples [15,24,25], automotive catalyst materials [14,36], medieval glass relics [26], historical ferrous ore and slag samples [27], nuclear samples [30] and biological materials [44]. Moreover, the technique might also be particularly suitable in cases where limited amounts of samples are available (e.g., archeological findings or meteoritic residues) [39]. Finally, the host matrix technique has also been applied to solution residues, e.g. for the determination of trace metals in petroleum [33], where 50–500 μl of the solution (which corresponds approximately to 0.05–0.5 g) were pipetted into 1.0 g of Ag powder. The resulting slurry was then dried at 100 °C for at least 2 h, mixed to obtain homogeneity and then pressed into a pin [33].

As mentioned above, the sample + host mixture is most often pressed in the form of a pin or disk, to be used in standard commercial GDMS cells, in Grimm-type GD-OES cells or in coaxial cathode source configurations. However, the technique has also been applied in hollow cathode glow discharge configurations, either as a pellet placed at the bottom of the cathode cavity [17] or directly pressed into the form of a hollow cylinder [44]. Moreover, Marcus and Harrison

also used the host matrix technique for the analysis of geological samples with GD-OES in the hollow cathode plume configuration [12].

In general, internal precisions were found to be better than 10% RSD, whereas external precisions below 20% RSD are commonly reported [11,13,14,21,25,36,44]. Concerning the accuracy, the suitability of the use of relative sensitivity factors (RSFs) in GDMS has been investigated. Duckworth *et al.* [28] applied a set of standard RSFs (based on metal analysis) and reported errors up to ca 100% for the obtained concentrations adjusted by the RSFs. De Gendt *et al.* thoroughly investigated the influence of several parameters on the RSFs for iron-rich and other oxide-based samples in GDMS: the effect of cryo-cooling, the nonconducting matrix, sample geometry and conducting binder were evaluated [6,11]. With the exception of the sample geometry (pin or flat cathode), the RSFs hardly seemed to be affected. However, significant differences have been found between the set of RSFs for nonconductors and the 'standard' set of RSFs, such as that used in ref. [28]. In practice, this suggests that RSFs have to be determined for each type of nonconducting matrix in order to obtain accurate results. In ref. [14], typical accuracies for GD-AAS were reported to be in the range 2–3%, whereas Wayne [36] reported GDMS precisions and accuracies better than 10% [36]. Detection limits are generally in the ppm range for GD-OES [25] and in the sub-ppm to ppb range for GDMS [34].

11.3 USE OF A CONDUCTING SECONDARY CATHODE

11.3.1 METHODOLOGY

The above-mentioned mixing technique requires samples in powder form. Certain types of samples, such as geological samples and ceramic precursors, are available in this form, but many others are available as a compact solid, e.g. a glass plate, sintered ceramic material, polymer foils, etc. These types of samples can hardly be ground and, if so, serious contamination can be introduced. A direct solid sampling technique for the analysis of nonconductors by dc glow discharges was therefore sought. The so-called 'secondary cathode technique', used for this purpose, was introduced by Milton and Hutton in 1993 for dc-GDMS [4]. To our knowledge, it has not yet been applied to other glow discharge spectrometric detection systems (GD-OES, GD-AAS, GD-AFS). Since this is a rather new technique, which has not yet been described in other recent books about glow discharge spectrometry [5,42], it is necessary to explain this concept in some more detail.

The secondary cathode is a thin conducting diaphragm (or mask) placed in front of the sample. The nonconductor is thus exposed to the discharge through the aperture (typically 3–10 mm in diameter) of the secondary cathode. A similar concept was used before for the analysis of nonconducting materials with secondary ion mass spectrometry (SIMS) and sputtered neutrals mass spectrometry

(SNMS) [50], although in this case the aperture had a maximum diameter of $500\ \mu\text{m}$. Secondary electron emission from the conducting mask, induced by ion bombardment, then provided charge compensation. Hence, in the case of SIMS and SNMS, the diaphragm acts as a bombardment-induced electron source.

The principle of the secondary cathode technique for GDMS, as described by Milton and Hutton [4], differs significantly from that described for SIMS and SNMS [50], since it relies on the fundamental processes in the glow discharge. Indeed, the secondary cathode is (partially) exposed to the glow discharge and, consequently, it is sputtered and atoms are released. It has been found that more than 60% of the sputtered atoms are redeposited on the sample surface [4,51]. In the case of a secondary cathode, this means that mask atoms are being redeposited not only on the secondary cathode, but also on the part of the nonconductor that is exposed to the discharge. This results in the formation of a nonconducting film on the surface of the insulating sample. Consequently, this area will also attract bombarding ions and does not suffer from charge building-up. It is suggested [4] that the sputtering process is energetic enough to penetrate through the thin metallic film and to remove atoms from the underlying insulator. This sputtering–redeposition process is presented schematically in Figure 11.4. As soon as an equilibrium is established between the redeposition of metal atoms and the removal of sample atoms by sputtering, the glow discharge reaches a steady state. The plasma, and consequently also the obtained mass spectrum, is comprised of ions representative of both the insulating material and of the metallic secondary cathode. Successful application of this technique relies, therefore, on the appropriate thickness of the deposited metallic layer. When the layer is too thin or incomplete, discharge instabilities may occur. On the other hand, when the metallic layer is too thick, it prevents the underlying nonconductor from being sputtered.

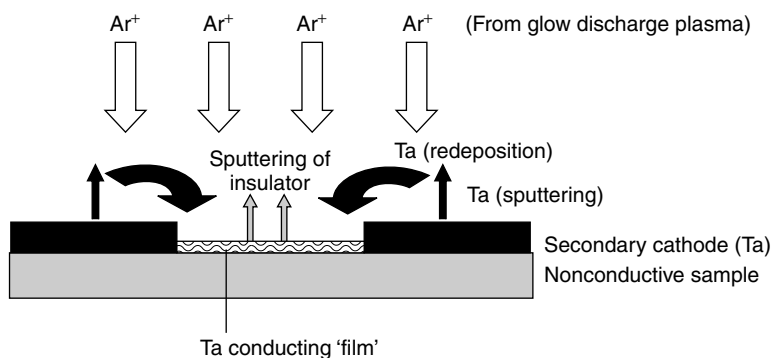


Figure 11.4 Schematic representation of the formation of the film by sputtering and redeposition of a film on the nonconducting sample surface, with the secondary cathode technique [55]

It should be emphasized, however, that the picture of a thin conducting film on top of the insulator may be not very appropriate, and that it should rather be interpreted as 'islands' of conducting material, as is described in the literature for the deposition of thin films [52]. Indeed, material arrives at a substrate mostly in atomic form. Atoms can be adsorbed and possibly also re-evaporated. After a certain time, the atom will combine with another atom, forming an atom pair, which is more stable and therefore it tends less to re-evaporate. The doublets will be joined by other single atoms to form triplets and so on. This is the *nucleation stage*, leading to the formation of relatively stable islands, each containing tens or hundreds of atoms. During the next stage, i.e. the *island growth stage*, the islands grow in size, rather than in number. Eventually, they grow large enough to touch each other, in the *agglomeration stage*. This proceeds until the film reaches continuity. It has been reported that this mostly happens after the film has reached an average thickness of several tens of nanometers. This would already be too thick to enable the underlying nonconducting sample to be sputtered, since the sampling depth is reported to be ca 0.5 nm [53]. Accordingly, one can assume that, in the case of a successful use of the secondary cathode technique, the 'thin film' that allows sputtering of the underlying nonconducting sample actually consists of hills and valleys, and that the nonconducting samples are not necessarily covered completely [54,55].

Wayne *et al.* [54] tried to obtain more insight into the sputtering of non-conductors in a dc glow discharge using the secondary cathode technique, by characterization of the conducting film of the secondary cathode material (Ta in this case) on the analytical surface. Examination of the sample surface by micro-X-ray fluorescence and scanning electron microscopy indicated that the Ta film formed by sputtering and redeposition is nonuniform, with a thicker accumulation of sputtered Ta in the outermost 0.25–0.5 mm of the sputtered area, where the Ta cathode is in physical contact with the nonconducting sample under it. Rutherford backscattering spectrometry was then used to characterize the thickness of the Ta film, and it was found that this may vary from $<10^{15}$ to $\sim 9 \times 10^{15}$ atoms/cm² for different materials. The results indicated that both crater shape and film thickness depend on the glow discharge sputtering parameters and on the nature of the material being sputtered. Finally, it was speculated that the electrical properties at the analytical surface may be very different from those expected in the bulk material [54].

Since the secondary cathode technique is a relatively young technique, which, to our knowledge, has only been used in GDMS up to now, only a few groups have been working in this field. A thorough methodological evaluation was, as far as we know, mainly carried out by Milton and Hutton [4] and in our laboratory by Schelles and co-workers [55–58]. The results of these investigations, with respect to the parameters which need to be optimized for good analytical practice, are described below. It may be important to note first that the three major criteria for a good analysis are (i) a stable (steady-state) atomization of the nonconducting

sample, (ii) high signal intensities of the nonconducting sample and (iii) a low blank contribution due to the sputtering of the secondary cathode material.

Secondary Cathode Material

The choice of the secondary cathode material is important for several reasons. First, it must be sufficiently pure to avoid too high blank levels due to the secondary cathode material. Second, its sputtering characteristics have an influence on the formation of the metallic layer: the sputtering efficiency should be high enough to produce a stable discharge, but it should not be too high, in order to avoid a complete coating which would protect the underlying nonconducting sample from being sputtered. Finally, the price and mechanical properties of the secondary cathode material, such as its suitability to machine a diaphragm out of it, are also of importance.

Various materials have been evaluated by Milton and Hutton [4]. Al, Cu and Ag, which are characterized by a high sputter rate, resulted in a rapid coating of the glass sample, under all discharge conditions. Also Pb and In were subject to too much sputtering and, moreover, they were found to be too soft, causing a short circuit. Finally, it was concluded that only a Ta secondary cathode, which has a low sputter rate, produced a stable discharge [4].

Schelles and co-workers [55,56] also investigated the use of several secondary cathode materials. Mo, Ni and Al were characterized by too much sputtering and consequently by too much redeposition. Both Ta and W appeared to be suitable as secondary cathode materials, as they have a similar sputtering efficiency and price, but Ta was favored because it yields better detection limits than W, as a result of higher sample-to-mask intensity ratios, and W appeared to be more brittle than Ta and therefore more difficult to machine.

Secondary Cathode Geometry

Given the cylindrical geometry of the discharge cell, a circularly symmetric secondary cathode resulting from a hole in a metal plate is the most obvious geometry. However, the use of a grid secondary cathode, as in SIMS [50], has also been evaluated [55]. It always resulted in vacuum leaks, because the edges of the front plate of the sample holder were not suitably sealed. Multi-aperture secondary cathodes, consisting of a metal plate with, for example, three symmetrically drilled holes, were also evaluated, but mostly an unstable discharge and low sample signal intensities were found. Therefore, a circular secondary cathode was found to be the best geometry.

In addition to the geometry, the size of the hole and the thickness of the secondary cathode also affect the analytical performance. A hole size of 4 mm diameter was found to be optimal in the investigations both of Milton and Hutton [4] and of Schelles [55]. Larger hole sizes appeared to give rise to discharge

instabilities, whereas smaller sizes resulted in high blank values due to the sputtering of the mask. The thickness of the secondary cathode was varied [55,58] between 0.12 and 1 mm. It appeared to have only a minor effect on the sample signal intensity obtained. However, the weight of the blank values due to the sputtering of the secondary cathode appeared to be more pronounced for thick secondary cathodes. Therefore, the use of a thin secondary cathode (i.e. 0.12–0.25 mm thick) was preferred to reach low detection limits [55,58]. On the other hand, it was also found that the thickness of the secondary cathode indirectly affects the obtained crater shape, and a thick secondary cathode (1 mm) appeared to favor a flat crater [55,58]. Because the secondary cathode technique works only under restricted discharge conditions (see below), which are not necessarily the best for obtaining a flat crater, it should be mentioned that rf-GDMS or GD-OES seem to be more appealing for depth profiling analysis.

Discharge Conditions

Milton and Hutton [4] investigated the effect of the gas pressure in the secondary cathode technique, and they found that only a limited pressure regime yielded a good balance between a stable discharge, because for enough redeposition the pressure should not be too low, and a sufficiently high sample-to-mask intensity ratio, because for not too much redeposition the pressure should not be too high. Schelles and co-workers [55–57] found that, in addition to the gas pressure, the discharge current and voltage are also of crucial importance for the amount of redeposition of secondary cathode material. They found that only specific combinations of voltage, pressure and current yielded stable discharge conditions. Since these combinations may depend on the type of sample to be analyzed, the optimum discharge conditions need to be investigated prior to analysis, which is considered a disadvantage of the secondary cathode technique.

Electrical Resistivity of the Sample

It is obvious that the general term ‘nonconducting samples’ includes sample types of varying electrical resistivity, and that the latter characteristic has some effect on the analytical performance of the secondary cathode technique. Schelles and co-workers [55,56] investigated samples of varying electrical resistivity. They found that samples with a resistivity higher than the critical barrier of about $10^{10} \Omega \text{ cm}$, such as glass and most soils (see Table 11.2) [55,56], can be considered as ‘nonconducting’. For these types of samples, the secondary cathode is essential to create a stable discharge. Only Ta and W could be used as a secondary cathode material, and the aperture diameter was limited to 4 mm. This results in low sample-to-mask intensity ratios, and hence a high blank contribution for certain elements. Samples with a resistivity lower than the critical barrier

Table 11.2 The specific electrical resistivity and the behavior of different materials when used directly as a cathode (i.e. without secondary cathode) in the VG9000 glow discharge [55].

Material	Electrical resistivity (Ω cm)	Behavior in the glow discharge
Aluminum	2×10^{-6}	Normal intensity (5×10^{-10} A) at 3 mA, 1 kV
SiC	1×10^3	Lower intensity (5×10^{-11} A) at 3 mA, 1 kV
Iron ore sinter	4×10^9	Very low intensity (5×10^{-16} A) at 3 mA, 1 kV
Soil	4×10^{10}	Stable discharge
Glass	3×10^{11}	Unstable discharge
		No discharge

of 10^{10} Ω cm, such as specific iron ore sinters, should be classified as 'poorly conducting'. A stable discharge here could be created without the secondary cathode, but the sample signal intensity was extremely low. This intensity could, however, be increased significantly by the use of a secondary cathode, leading to signal intensities which were comparable to those of conducting samples [55,56]. In this case, larger hole sizes could be applied, and a detailed knowledge of the properties of the nonconducting material was not so crucial.

Surface Characteristics of the Sample

Because the deposition of metal atoms on the surface of the nonconducting sample is essential in the secondary cathode concept, it is straightforward that the surface of the sample can have an influence on the operating conditions required for stable atomization. First, it appears that the surface roughness has a distinct effect [57], i.e. rough surfaces require clearly more redeposited metal atoms, and hence a higher pressure, than smooth surfaces, so as to ensure a certain conductivity. This is illustrated in Figure 11.5 and in Table 11.3. Second, samples with a similar electrical resistivity and a similar surface roughness, such as Macor, which is a glass ceramic, and glass, can still require different optimum discharge conditions. This can be understood from differences in the affinity between the metal atoms and the nonconducting sample [55].

11.3.2 SOME APPLICATIONS AND ANALYTICAL FIGURES OF MERIT

As mentioned before, the secondary cathode technique was developed for GDMS only in 1993, and we are not yet aware of its use in GD-OES and GD-AAS. A

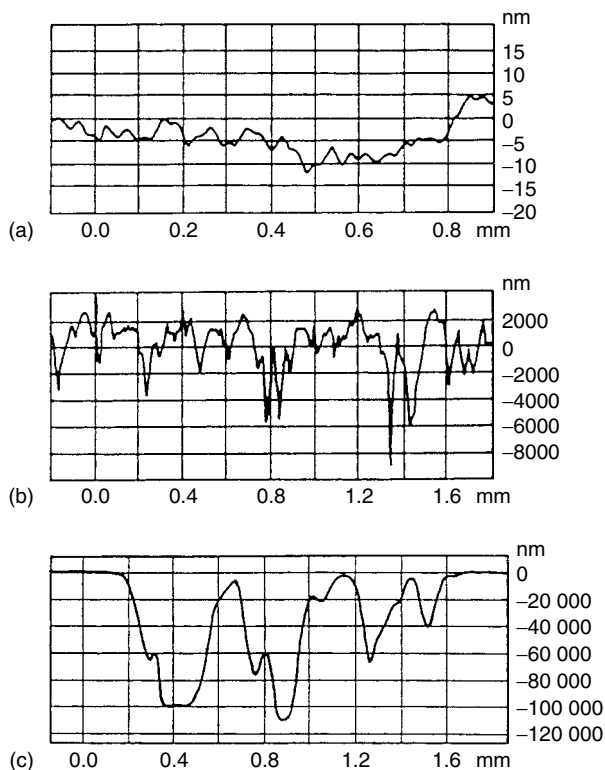


Figure 11.5 The surface roughnesses of three different sample types: (a) glass; (b) marble; (c) limestone [55]

Table 11.3 Overview of the influence of the surface roughness on the required discharge conditions in the VG9000 glow discharge mass spectrometer with a Ta secondary cathode with 4 mm aperture, for glass, marble and limestone [55].

Material	Surface roughness	Optimum discharge conditions	Pressure, % redeposition
Glass	Smooth	3 mA, 600 V	Normal
Marble	Rough	3 mA, 400 V	High
Limestone	Very rough	3 mA, <300 V	Very high

possible reason for the fact that this technique has not yet been applied in GD-OES might be the generally higher pressure in GD-OES, which yields too much redeposition of secondary cathode material, preventing the underlying nonconductor from being sputtered. On the other hand, commercial rf-GD-OES instruments are also available, which can be used for the analysis of nonconductors,

and therefore the need for using the secondary cathode technique is not as high as for GDMS, where no commercial rf-GDMS instrument is yet available.

Based on the above considerations, it is obvious that the number of papers describing applications of the secondary cathode technique is much more limited than for the host matrix technique. Nevertheless, the technique has been shown to be successful for the analysis of glass [4,54–58], iron ore sinter [55,56], marble [55,57], Teflon [55,57], ceramic materials [54,55,57,59–61], atmospheric particulate matter [62], polymers [63], soil [34], sediment [34], vegetation [34] and nuclear samples [30,64]. Most of these applications have been performed with the VG9000 double-focusing glow discharge mass spectrometer (VG Elemental, Thermo Instruments) [4,30,34,55–64], although the technique has also been used with the double-focusing magnetic sector instrument manufactured by Kratos [54].

Milton and Hutton [4] developed the secondary cathode technique for glass samples. They obtained an analytical precision of typically 5% RSD at ppm levels and detection limits in the sub-ppb to ppb range [4]. Also Schelles and co-workers [55–58] performed most of their methodological work with solid glass samples. They found internal precisions (without changing the samples) of 2–10% and external precisions (with changing the samples) of 5–25%. The practical detection limits were between 0.1 and 1 ppm, but they could be further improved by working in the low-resolution mode. If no interfering peaks were present, detection limits down to 10 ppb could then be obtained.

A comparison between the analysis of massive, solid glass samples, which are really nonconducting, and compacted iron ore sinters, which are poorly conducting, has also been described [56], showing the influence of electrical resistivity of the samples. It was found that iron ore sinters could in principle also be analyzed without the use of a secondary cathode, but the latter enhanced the signal intensity to a level comparable to that commonly reached for conducting samples. The high sensitivity and the negligible blank values as a result of a very low mask-to-sample signal intensity ratio, because a mask with larger aperture could be used, made it possible to determine concentrations of ca 100 ppb on a routine basis [55,56].

The suitability of the secondary cathode technique for the analysis of ceramic materials has been demonstrated for Nd:YAG [54], for potassium titanyl phosphate [54], for Al_2O_3 [55,57], for Macor [55,59] and for ZrO_2 [55,60,61]. Although sample characteristics such as the electrical conductivity and surface roughness for Macor are closely comparable to those of glass, the optimum discharge conditions for Macor analysis were found to be significantly different from those of glass [59]. This illustrates that the discharge conditions need to be optimized for each new type of sample. The limits of detection were found to be in the sub-ppm range. The internal precision was found to be 5.7% RSD, whereas the external precision was typically better than 10% RSD [59]. For ZrO_2 , the internal and external precisions were also found to be better than 10%

RSD in most cases, and the accuracy without using standards, and thus assuming 'uniform sensitivity', was within a factor of 2–3 the known concentration. Limits of detection for most elements were in the range between 10 ppb and 10 ppm, depending on high or low elemental sensitivity and the integration times. In practice, blank contributions due to the Ta secondary cathode material restricted the detection limits to a level of about 100 ppb or even higher. Generally, it could be concluded that 85% of the elements could routinely be determined at the sub-ppm level [60].

An interesting application of the secondary cathode technique has been reported [62] for the analysis of atmospheric particulate matter. The sample preparation was simple and time-saving. The air was sucked by a pump through a single-orifice impactor stage, in which the aerosols were impacted on a metal support, forming a central spot (see Figure 11.6) [62]. This metal plate was directly used as a cathode in the VG9000 glow discharge mass spectrometer,

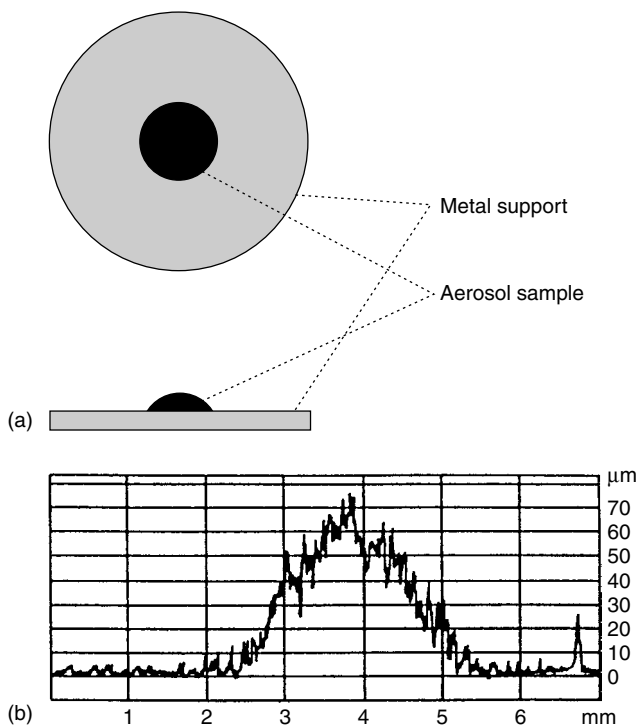


Figure 11.6 Aerosol sample spot, impacted on the metal support. (a) Schematic front view and side view; (b) thickness of the sample spot, as measured with the aid of a mechanical profilometer (Dektak 3030, Veeco Instruments, USA) [55,62]. Reprinted with permission from Schelles, W., Maes, K. J. R., De Gendt, S. and Van Grieken, R. E., *Anal. Chem.*, 1996, **68** 1136–1142. Copyright 1996 American Chemical Society

and it played the role of secondary cathode for the analysis of the atmospheric particulate matter. By careful evaluation of the sample loading and of the discharge parameters, the signal could be optimized and the drop in intensity as a consequence of its consumption during continuous sputtering could be minimized. The available aerosol analysis time could be prolonged to more than 3 h, a time span necessary to perform a multi-element analysis with the VG9000 instrument. A NIST reference aerosol was analyzed to evaluate the potential for quantitative analysis. The internal reproducibility was better than 10% RSD, and the limits of detection were estimated to be in the low-ppm or sub-ppm region [62].

The secondary cathode technique has also been applied in our laboratory for the elemental characterization of different types of polymers [63], i.e. polytetrafluoroethylene (PTFE), polycarbonate (PC), and poly(vinyl chloride) (PVC). The mass spectra obtained were predominantly characterized as atomic (see Table 11.4) [63]. It should be mentioned that the VG9000 cell here was generally cryogenically cooled, to reduce molecular peaks in the mass spectra due to residual gases. The mainly atomic mass spectra obtained with the secondary cathode technique are clearly different from the spectra of polymers obtained with rf-GDMS [65], which have a definite molecular character. Therefore, it appears that the dc- and rf-GDMS spectra are complementary: the rf spectrum shows molecular cluster peaks forming a fingerprint, and is therefore particularly suitable for characterizing and distinguishing different polymers, whereas the dc spectrum facilitates quantitative elemental analysis, because of less interferences from cluster peaks.

Betti and co-workers [30,34,64] demonstrated the capability of the secondary cathode technique for the detection of trace radioisotopes in soil, sediment and vegetation [34], and for the analysis of samples of nuclear concern [30,64]. For the latter purpose, the VG9000 instrument was placed in a glove-box [30,64]. Depending on the type of samples, a combination of the host matrix method and the secondary cathode technique was applied [30,34], in order to decrease the dilution effect of the host matrix material for determinations at the trace

Table 11.4 Average abundances for the main clusters present in the VG9000 glow discharge mass spectrum of various polymers, relative to the elemental matrix signal intensities, measured with the secondary cathode technique [55,63]. Reprinted with permission from Schelles, W. and Van Grieken, R. E., *Anal. Chem.*, 1997, **69** 2931–2934. Copyright 1997 American Chemical Society.

PTFE (relative to C ⁺ + F ⁺)		PVC (relative to C ⁺ + Cl ⁺)		PC (relative to C ⁺ + O ⁺)	
²⁴ C ₂ ⁺	1.8 × 10 ⁻³	¹³ CH ⁺	4.9 × 10 ⁻²	¹³ CH ⁺	1.3 × 10 ⁻²
³¹ CF ⁺	3.4 × 10 ⁻²	²⁴ C ₂ ⁺	3.3 × 10 ⁻³	²⁴ C ₂ ⁺	1.2 × 10 ⁻³
⁴³ C ₂ F ⁺	2.4 × 10 ⁻⁵	⁴⁷ CCl ⁺	6.3 × 10 ⁻⁴	²⁸ CO ⁺	3.2 × 10 ⁻³
⁵⁰ CF ₂ ⁺	2.4 × 10 ⁻³	⁵⁹ C ₂ Cl ⁺	1.0 × 10 ⁻⁵	⁴⁴ CO ₂ ⁺	1.6 × 10 ⁻⁴
⁶² C ₂ F ₂ ⁺	7.0 × 10 ⁻⁵				
¹⁰⁰ C ₂ F ₄ ⁺	1.3 × 10 ⁻³				

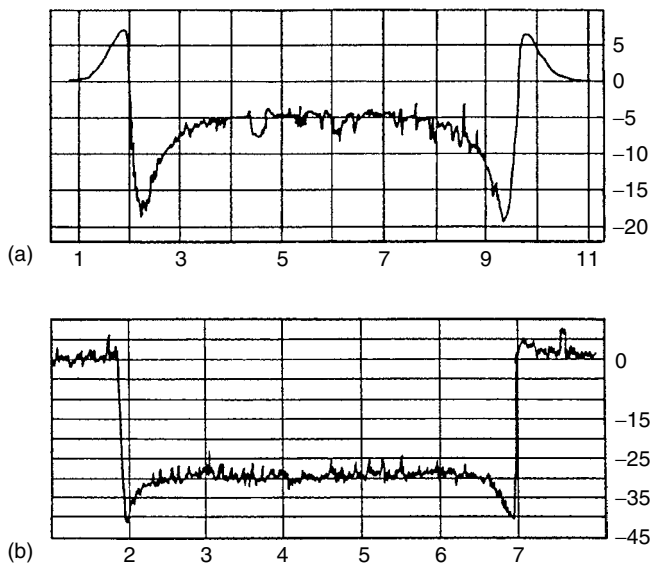


Figure 11.7 Optimized crater profile for a Cu CRM 074 sample obtained with the VG9000 glow discharge mass spectrometer. (a) Without Ta mask (850 V, 1.9 mA); (b) with Ta mask (850 V, 3.5 mA) [67]

level and to obtain a stable discharge. Detection limits in the ppb range could be obtained when integrating up to 1 h. By optimizing the integration time and mass resolution, e.g. by selecting the low-resolution mode, the detection limits could be reduced down to ppt levels for U and Th [34]. However, it should be mentioned that there are virtually no interferences in this high-mass range, and that these excellent detection limits therefore cannot be generalized. The obtained accuracy was typically 9–30%, whereas the internal and external precisions amounted to 3–7 and 5–20%, respectively [34].

Finally, it should be mentioned that a Ta secondary cathode or mask has also been applied successfully in GDMS depth profiling analysis of conducting [66,67] and nonconducting [61] samples. The mask appears to reduce significantly the crater edge effect, by which the crater is much deeper at the sides than in the center [66,67], as is illustrated in Figure 11.7 [67]. Moreover, the crater side walls become steeper and there is no deposition of material outside the crater, since the back-diffusing sputtered atoms are redeposited on the mask instead of on the sample [67].

11.4 CONCLUSION

The two techniques which can be applied with dc glow discharges to analyze nonconducting samples have been discussed in this chapter.

The host matrix technique, which consists of mixing a nonconducting powder with a conducting host matrix and pressing the mixture into an electrode, was first applied to GD-OES about 30 years ago and is nowadays being used routinely for the bulk analysis of nonconductors in GD-OES, GDMS and GD-AAS. Different kinds of host materials have been proposed in the literature, but Cu powder is most widely used, mainly because of its availability in pure form, its relatively low cost and its high sputter yield. On the other hand, Ta powder was used in some studies because it has the advantage of being a getter material, and accordingly removing oxygen from the discharge and reducing molecular oxide spectral interferences. The compacted electrode must contain an excess of conducting host material to avoid instabilities in the discharge and to ensure enough sputtering. Sample-to-host mass ratios reported in the literature usually vary between 1 + 4 and 1 + 19. The choice of discharge conditions necessary for good analytical practice is not so strict as in the secondary cathode technique (see below), but it is found that a high discharge power yields higher analyte signal intensities and more reproducible concentration results, as well as a shorter stabilization time. Moreover, most authors agree that the particle sizes in the compacted sample should be small and, of course, that the mixture should be homogeneous, to obtain good precision and accuracy. The major problem with the host matrix technique is the contamination which can occur during the mixing procedure. Further, trapped gases in the compacted sample, which yield lower signal intensities, can be a source of spectral interferences, and generally give rise to longer stabilization times (several minutes to hours). Therefore, some precautions should be taken during sample preparation and during the measurement in order to reduce the effect of these trapped gases. Another disadvantage of the host matrix method is the analyte dilution due to the mixing with the metal powder, which results in losses of sensitivity and, if the metal powder is not sufficiently pure, it may mask analyte trace element peaks. Finally, the powder compaction precludes the acquisition of certain types of data, such as concentration depth profiles.

The secondary cathode technique is a direct solid sampling technique, so that the above-mentioned type of information can in principle be acquired. It should be mentioned, however, that the secondary cathode technique can only be used for the analysis of flat samples and not for pin samples. It is a rather new approach, developed about a decade ago for GDMS, and is based on placing a thin conducting diaphragm (i.e. the 'secondary cathode') in front of the massive nonconducting sample before exposing it to the discharge. Since the secondary cathode is also partly exposed to the discharge, it is subject to sputtering and the sputtered atoms can be redeposited on the nonconducting sample, forming a conducting 'film' on the surface of the nonconductor. This film avoids electrical charging of the nonconductor, but it should be 'thin' enough to permit sputtering from the underlying insulator. Because it is a direct solid sampling technique, it is suitable for the analysis of solid samples, which are difficult to grind. Moreover,

there are no problems of contamination during sample preparation, as in the case of the host matrix technique. The technique does, however, still suffer from dilution due to sputtering of the secondary cathode material. In addition, the latter should be sufficiently pure, to reduce the blank contribution and spectral interferences. Indeed, the detection limits in the case of this technique are mainly determined by the possible blank contribution of the secondary cathode material. Further, the sputtering rate of the secondary cathode material should be low enough to avoid complete coating of the insulator, which would prevent the latter from being sputtered. Therefore, Ta has been favored as secondary cathode material, also based on its price and mechanical properties.

The hole size and thickness of the secondary cathode also play an important role, in order to achieve sufficient redeposition to produce a stable discharge, and on the other hand, not too much redeposition to limit the 'mask' blank contributions. Generally, a hole size of 4 mm diameter and a thickness of 0.25 mm are preferred. In contrast to the host matrix technique, the discharge conditions appear to be crucial for a successful measurement. It was found that only specific combinations of voltage, pressure and current yield stable discharge conditions. Obviously, sample characteristics such as electrical resistivity, surface roughness, etc., have a distinct effect on the choice of the operating conditions. It appears that the latter need to be optimized, or at least 'fine-tuned', for each new matrix under investigation. Therefore, it cannot be guaranteed that a novel matrix can immediately be analyzed, which has to be considered a disadvantage of the secondary cathode technique. On the other hand, repeated experiments have indicated that, once the required measurement conditions have been found for a specific matrix in a given instrument, they are reproducible, even over a long time such as more than 1 year. Moreover, several types of matrices have already been successfully investigated with the secondary cathode technique, and except for porous materials and low-melting-point polymers, all materials which have been studied could be successfully analyzed. Nevertheless, it should be mentioned that with the secondary cathode technique, in principle, depth profiling analysis of nonconducting samples is possible, but practical realization is not straightforward because of the restricted discharge conditions for a stable discharge. Indeed, it is possible that the conditions which would yield a flat crater profile do not coincide with the conditions necessary for stable atomization of the nonconducting sample, and therefore a perfect depth profile might be difficult to achieve. The latter application is undoubtedly more possible with rf-GDMS or rf-GD-OES. On the other hand, a definite advantage compared with rf glow discharge analysis seems to be that the signal intensities do not depend on the thickness of the sample, a problem that, up to now, is inherent to most types of rf glow discharges. In summary, we can conclude that the secondary cathode technique, because of its simplicity and low cost, can be of interest, especially to those researchers who have no rf-GDMS or rf-GD-OES instrumentation available, and who want to extend their field of application towards nonconducting materials.

11.5 REFERENCES

- [1] Coburn, J. W.; Kay, E. *Appl. Phys. Lett.*, 1971, **19**, 350–352.
- [2] Duckworth, D. C.; Marcus, R. K. *Anal. Chem.*, 1989, **61**, 1879–1886.
- [3] Dogan, M.; Laqua, K.; Massmann, H. *Spectrochim. Acta, Part B*, 1972, **27**, 65–88.
- [4] Milton, D. M. P.; Hutton, R. C. *Spectrochim. Acta, Part B*, 1993, **48**, 39–52.
- [5] Winchester, M. R.; Duckworth, D. C.; Marcus, R. K. 'Analysis of nonconducting sample types', in *Glow Discharge Spectroscopies*, Marcus, R. K. (Ed.), Plenum Press: New York, 1993, Chapt. 7, pp. 263–328.
- [6] De Gendt, S. PhD Dissertation, University of Antwerp, 1996.
- [7] Beske, H. E.; Gijbels, R.; Hurrle, A.; Jochum, K. P. *Fresenius' J. Anal. Chem.*, 1981, **309**, 329–341.
- [8] Ramendik, G.; Verlinden, J.; Gijbels, R. 'Spark source mass spectrometry', in *Inorganic Mass Spectrometry*, Adams, F.; Gijbels, R.; Van Grieken, R. (Eds), Wiley: New York, 1988, Chapt. 2, pp. 17–84.
- [9] Tong, S. L.; Harrison W. W. *Spectrochim. Acta, Part B*, 1993, **48**, 1237–1245.
- [10] Teng, J.; Barshick, C. M.; Duckworth, D. C.; Morton, S. J.; Smith, D. H.; King, F. L.; *Appl. Spectrosc.*, 1995, **49**, 1361–1366.
- [11] De Gendt, S.; Schelles, W.; Van Grieken, R.; Muller, V. *J. Anal. At. Spectrom.*, 1995, **10**, 681–687.
- [12] Marcus R. K.; Harrison, W. W. *Anal. Chem.*, 1987, **59**, 2369–2373.
- [13] Winchester, M.; Marcus, R. K. *Appl. Spectrosc.*, 1988, **42**, 941–944.
- [14] Winchester, M.; Hayes, S. M.; Marcus R. K. *Spectrochim. Acta, Part B*, 1991, **46**, 615–627.
- [15] Woo, J. C.; Jakubowski, N.; Stuewer, D. *J. Anal. At. Spectrom.*, 1993, **8**, 881–889.
- [16] Brenner, I. B.; Laqua, K.; Dvorachek, M. *J. Anal. At. Spectrom.*, 1987, **2**, 623–627.
- [17] Caroli, S.; Senofonte, O.; Del Monte Tamba, M. G.; Cilia, M.; Brenner, I. B.; Dvorachek, M. *Spectrochim. Acta, Part B*, 1993, **48**, 877–891.
- [18] Caroli, S.; Senofonte, O.; Caimi, S.; Karpati, P. *J. Anal. At. Spectrom.*, 1996, **11**, 773–777.
- [19] O'Gram, S. J.; Dean, J. R.; Tomlinson, W. R.; Marshall, J. *Anal. Chim. Acta*, 1994, **294**, 95–102.
- [20] Ehrlich, G.; Stahlberg, U.; Hoffmann, V.; Scholze, H. *Spectrochim. Acta, Part B*, 1991, **46**, 115–124.
- [21] Lomdahl, G. S.; McPherson, R.; Sullivan, J. V. *Anal. Chim. Acta*, 1983, **148**, 171–180.
- [22] Lomdahl, G. S.; Sullivan, J. V. *Spectrochim. Acta, Part B*, 1984, **39**, 1395–1403.
- [23] O'Gram, S. J.; Dean, J. R.; Marshall, J. *Anal. Proc.*, 1993, **30**, 135–136.
- [24] Flórián, K.; Fischer, W.; Nickel, H. *J. Anal. At. Spectrom.*, 1994, **9**, 257–262.
- [25] Flórián, K.; Fischer, W.; Nickel, H. *Fresenius' J. Anal. Chem.*, 1994, **349**, 174–175.
- [26] El Nady, A. B. M.; Zimmer, K.; Zárny, G. *Spectrochim. Acta, Part B*, 1985, **40**, 999–1003.
- [27] Dietrich, D.; Heger, P.; Bäucker, E.; Nuys, G. J.; Grafe, T.; Urban, G. *Fresenius' J. Anal. Chem.*, 1998, **361**, 701–703.
- [28] Duckworth, D. C.; Barshick, C. M.; Smith, D. H. *J. Anal. At. Spectrom.*, 1993, **8**, 875–879.
- [29] Mei, Y.; Harrison, W. W. *Spectrochim. Acta, Part B*, 1991, **46**, 175–182.
- [30] Betti, M. *J. Anal. At. Spectrom.*, 1996, **11**, 855–860.
- [31] Mei, Y.; Harrison, W. W. *Anal. Chem.*, 1993, **65**, 3337–3342.
- [32] De Gendt, S.; Van Grieken, R.; Hang, W.; Harrison, W. W.; *J. Anal. At. Spectrom.*, 1995, **10**, 689–695.

- [33] Barshick, C. M.; Smith, D. H.; Hackney, J. H., Cole, B. A.; Wade, J. W. *Anal. Chem.*, 1994, **66**, 730–734.
- [34] Betti, M.; Giannarelli, S.; Hiernaut, T.; Rasmussen, G.; Koch, L. *Fresenius' J. Anal. Chem.*, 1996, **355**, 642–646.
- [35] Barshick, C. M.; Barshick, S.-A.; Mohill, M. L.; Britt, P. F.; Smith, D. H. *Rapid Commun. Mass Spectrom.*, 1996, **10**, 341–346.
- [36] Wayne, D. M. *J. Anal. At. Spectrom.*, 1997, **12**, 1195–1202.
- [37] King, F. L.; McCormack, A. L.; Harrison, W. W. *J. Anal. At. Spectrom.*, 1988, **3**, 883–886.
- [38] Loving, T. J.; Harrison W. W. *Anal. Chem.*, 1983, **55**, 1526–1530.
- [39] Battagliarin, M.; Sentimenti, E.; Scattolin, R. *Spectrochim. Acta, Part B*, 1995, **50**, 13–25.
- [40] Venzago, C. personal communication.
- [41] Catalogue 1996–1997, Goodfellow Ltd.
- [42] Hoffmann, V.; Mai, H., 'Compacted powders', in *Glow Discharge Optical Emission Spectrometry*, Payling, R.; Jones, D.; Bengtson, A. (Eds), Wiley: Chichester, 1997, Chapt. 11.9, pp. 551–562.
- [43] El Alfy, S.; Laqua, K.; Massmann, H. *Z. Anal. Chem.*, 1973, **263**, 1–14.
- [44] Caroli, S.; Alimonti, A.; Zimmer, K. *Spectrochim. Acta, Part B*, 1983, **38**, 625–631.
- [45] Caroli, S.; Senofonte, O.; Violante, N.; Petrucci, F.; Alimonti, A. *Spectrochim. Acta, Part B*, 1994, **39**, 1425–1430.
- [46] Mai, H.; Scholze, H. *Spectrochim. Acta, Part B*, 1986, **41**, 797–815.
- [47] Mai, H.; Scholze, H. *Spectrochim. Acta, Part B*, 1987, **42**, 1187–1204.
- [48] Larkins, P. L. *Spectrochim. Acta, Part B*, 1991, **46**, 291–299.
- [49] Ohorodnik, S. K.; De Gendt, S.; Tong, S. L.; Harrison, W. W. *J. Anal. At. Spectrom.*, 1993, **8**, 859–865.
- [50] Jede, R.; Ganschow, O.; Kaiser, U., 'Sputtered neutrals mass spectrometry', in *Practical Surface Analysis, Ion and Neutral Spectroscopy*, Briggs, D.; Seah, M. P. (Eds), Wiley: New York, 1992, Chapt. 8, pp. 425–506.
- [51] Bogaerts, A.; van Straaten, M.; Gijbels, R. *J. Appl. Phys.*, 1995, **77**, 1868–1874.
- [52] Chapman, B. *Glow Discharge Processes*, Wiley: New York, 1980, pp. 201–204.
- [53] Harrison, W. W.; Bentz, B. L. *Prog. Anal. Spectrosc.*, 1988, **11**, 53–110.
- [54] Wayne, D. M.; Schulze, R. K.; Maggiore, C.; Cooke, D. W.; Havrilla, G. *Appl. Spectrosc.*, 1999, **53**, 266–277.
- [55] Schelles, W., PhD Dissertation, University of Antwerp, 1996.
- [56] Schelles, W.; De Gendt, S.; Muller, V.; Van Grieken, R. *Appl. Spectrosc.*, 1995, **49**, 939–944.
- [57] Schelles, W.; De Gendt, S.; Maes, K.; Van Grieken, R. *Fresenius' J. Anal. Chem.*, 1996, **355**, 858–860.
- [58] Schelles, W.; De Gendt, S.; Van Grieken, R. E. *J. Anal. At. Spectrom.*, 1996, **11**, 937–941.
- [59] Schelles, W.; Van Grieken, R. E. *Anal. Chem.*, 1996, **68**, 3570–3574.
- [60] Schelles, W.; Van Grieken, R. E. *J. Anal. At. Spectrom.*, 1997, **12**, 49–52.
- [61] Actis-Dato, L. O., PhD Dissertation, Université de Paris XI Orsay, 2000.
- [62] Schelles, W.; Maes, K. J. R.; De Gendt, S.; Van Grieken, R. E. *Anal. Chem.*, 1996, **68**, 1136–1142.
- [63] Schelles, W.; Van Grieken, R. E. *Anal. Chem.*, 1997, **69**, 2931–2934.
- [64] Betti, M.; Rasmussen, G.; Koch, L. *Fresenius' J. Anal. Chem.*, 1996, **355**, 808–812.
- [65] Shick, C. R., Jr.; DePalma, P. A., Jr.; Marcus, R. K. *Anal. Chem.*, 1996, **68**, 2113–2121.
- [66] Raith, A.; Hutton, R. C.; Huneke, J. C. *J. Anal. At. Spectrom.*, 1993, **8**, 867–873.
- [67] Jonkers, C., PhD Dissertation, University of Antwerp, 1995.

12

Standards and Reference Materials for Glow Discharge Spectroscopies

M. R. WINCHESTER

*National Institute of Standards and Technology, Chemical Science and Technology
Laboratory, Analytical Chemistry Division, Gaithersburg, MD, USA*

12.1 INTRODUCTION

The successful and widespread use of glow discharge spectroscopic analytical methods on a routine basis depends critically on the availability of appropriate standards¹ and reference materials. While it is possible to employ glow discharge methods without standards, the importance of appropriate standards for aiding the glow discharge practitioner in obtaining meaningful analytical results from day to day should not be underestimated. It has been stated that ‘technology without standards is only research and development’ [1]. The truth of this statement is borne out in the field of glow discharge spectroscopies. Likewise, reference materials are extremely important for the routine application of glow discharge analytical methods, because reference materials must be used for calibration and are also needed for other purposes. Additionally, reference materials naturally become a vital component in the development of standards.

The purpose of this chapter is to elucidate the roles played by standards and reference materials in the practice of glow discharge analytical methods. Standardization activities are described, illustrating the maturity of glow discharge

¹The term *standard* is sometimes used to refer to samples employed for calibration and other purposes. In this chapter, the term *standard* is used exclusively to refer to the documentary type of standard.

spectroscopies and the growing interest in glow discharge methods for industrial and commercial applications. Availabilities of reference materials relevant to chemical analysis through glow discharge spectroscopies are also discussed. Finally, the prospects for the future development of both appropriate standards and reference materials are explored.

12.2 PRACTICAL ASPECTS

12.2.1 STANDARDS

Standards and the Process of Standardization

The term *standard* can be formally defined as ‘a document, established by consensus and approved by a recognized body, that provides, for common and repeated use, rules, guidelines or characteristics for activities or their results, aimed at the achievement of the optimum degree of order in a given context’ (definition 3.2 in ref. 2). Stated more plainly, a *standard* is a document that describes how things should be, in order to achieve a desirable outcome. Standards are varied in type and in the range of ‘things’ described, as illustrated by Table 12.1 [3]. While each type of standard listed in the table may have some applicability to the subject of chemical analysis through glow discharge spectroscopies, three should in principle be considered more pertinent than the others. These three are the standard guide, the standard practice and the standard test method, or simply the standard method. Examples of some of these will be discussed later in this chapter.

Table 12.1 Several types of standards as defined by one standards development organization (SDO), ASTM International (formerly the American Society for Testing and Materials) (nomenclature and precise definitions may vary among SDOs). Reproduced from *Annual Book of ASTM Standards*, Vol. 03.06, American Society for Testing and Materials, West Conshohocken, PA, 2000, pp. iii–iv. Copyright ASTM International. Reprinted with permission.

Type of standard	Definition
Classification	A systematic arrangement or division of materials, products, systems, or services into groups based on similar characteristics such as origin, composition, properties or use
Guide	A compendium of information or series of options that does not recommend a specific course of action
Practice	A definitive set of instructions for performing one or more specific operations or functions that does not produce a test result
Specification	An explicit set of requirements to be satisfied by a material, product, system or service
Terminology	A document comprising definitions of terms, explanations of symbols, abbreviations or acronyms
Test method	A definitive procedure that produces a test result

At a foundational level, standardization activities relating to glow discharge spectroscopies enable glow discharge practitioners to perform more meaningful analyses on a routine basis. This is possible, because a given standard essentially distills into easily digestible form the vast knowledge and experience of the panel of experts who produced it. As a result, one may not need to be an expert in chemical analysis through glow discharge spectroscopies to obtain valid analytical results, provided that appropriate standards are available, although some basic understanding is obviously required.

The enhanced capability for more meaningful routine glow discharge analyses afforded through standardization potentially provides many benefits of industrial, technological and economic importance. For example, quality control and quality assurance activities that rely on glow discharge methods may be improved, resulting in better products and services. A related point is that the availability of standards can facilitate the implementation of quality management systems (e.g. ISO 9000), because the standards can be incorporated within the implementation plan. This in turn can make laboratory certification and accreditation relative to the quality system easier.

Another potential benefit of standardization is that commercial transactions and business relationships may be facilitated. For instance, a manufacturer of glow discharge instrumentation may find it easier to sell an instrument to a potential customer who has no prior experience with glow discharge methods, if appropriate standards, especially standard methods, are available. This is because, from the viewpoint of the potential customer, the availability of standards would largely obviate the need for extensive methods development, thereby allowing startup to be accomplished with a minimal investment of time and money. For this reason, when appropriate standards are unavailable or not widely accepted, instrument and equipment manufacturers often develop their own methods that can be provided to customers. As another example, a contract laboratory performing glow discharge analyses might find that potential customers are more likely to purchase services if they know in advance that a relevant standard method is to be used. The use of appropriate standards also places the provider in a better position to demonstrate the quality of the analytical results, therefore helping to mitigate or resolve potential disputes. In fact, standards can be cited in commercial contracts to prevent possible disputes and may be utilized in courts of law to litigate disputes when they occur. Finally, manufacturers of products that are evaluated by glow discharge methods during production may experience similar benefits of standardization. Owing to these sorts of factors, standardization actually aids the widespread diffusion of glow discharge equipment and methods into the marketplace.

Unfortunately, standardization activities can also produce significant undesirable effects. Probably the most important of these is that individual companies (or nations in international standardization activities) can effectively be locked out of specific markets, because their products or services do not conform to standards

accepted within those markets. This might occur, for example, if a particular glow discharge standard method included a mandatory procedure requiring an instrument capability not offered by a given instrument manufacturer. Even though that manufacturer might have a different way to accomplish the same goal with equivalent or even superior effectiveness, their instrument could still be considered unacceptable within the affected markets, owing to the presence of the standard method. It is believed that this has not yet happened in standardization work pertaining to glow discharge spectroscopies, but it has certainly happened in other fields. Hopefully, most such occurrences are honest oversights on the part of those participating in the standards development process. However, there have undoubtedly been cases where standardization was intentionally used to disadvantage competitors. This is why it is vitally important for all stakeholders to be involved in the standardization process.

Another potential disadvantage of standardization is that the presence of standards can sometimes have the effect of 'freezing' technology, by making more difficult the introduction and widespread acceptance of technical innovations that do not comply with accepted standards [4]. The increased difficulty can be manifested in a greater reluctance of potential customers or users to employ a particular innovation. For instrumentation and equipment manufacturers, as well as for service laboratories, the increased reluctance may result in higher marketing costs that may cause the price of the innovative product or service to be too high to be competitive with common approaches. Whatever the precise manifestation, the overall result is that technological progress may be slower than it would have been without standards. For this reason, it is often advisable to delay writing standards pertaining to a given area of technology until that technological area has reached an appropriate level of maturity.

Standardization activities have traditionally taken place within standards development organizations (SDOs). There are currently hundreds of SDOs in operation around the world (approximately 400 in the United States alone) [5–8]. Some of the largest and most influential with regard to chemical analysis are the International Organization for Standardization (ISO), ASTM International (formerly the American Society for Testing and Materials) and AOAC International (formerly the Association of Official Analytical Chemists International). While each SDO may have a somewhat unique structure and set of detailed procedures, they are all generally based on the fundamental principles of consensus, transparency, openness, balance and due process. Together, these principles help to ensure that the interests of all stakeholders will be heard during the standardization process. For standardization activities related specifically to glow discharge work, the list of stakeholders includes primarily the instrument and equipment manufacturers and users.

The traditional process of standards development is very rigorous and formal. Generally, the task of developing a given standard is undertaken by a group of experts, ideally representing the interests of all stakeholders, operating within

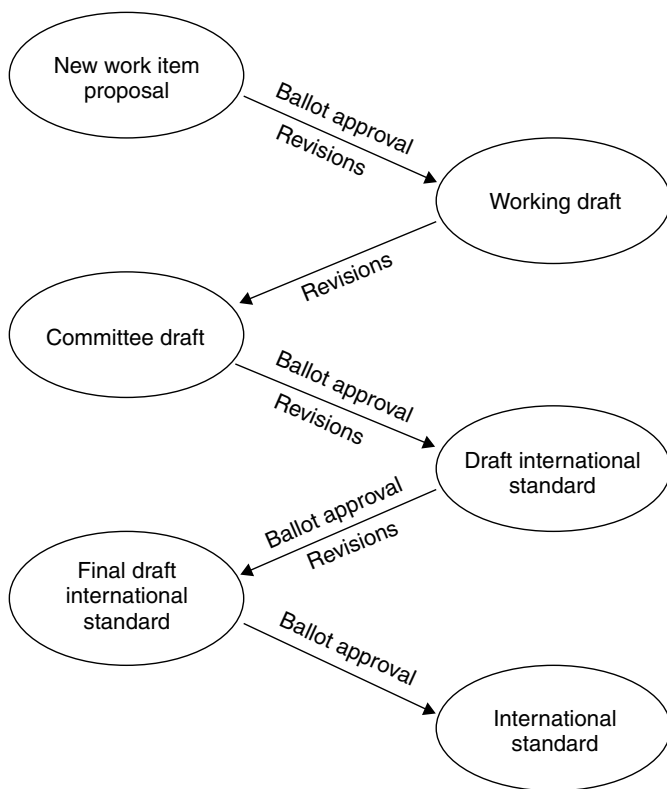


Figure 12.1 Graphical depiction of the traditional standards development process as it takes place within the International Organization for Standardization (ISO). Each ellipse represents a different stage of development for the prospective ISO standard. As shown, ballot approval may be required for a document to pass between one stage and the next.

the framework of the SDO. The candidate standard progresses through a series of developmental stages, with appropriate revisions at various stages, until it is finally approved for publication (e.g. see Figure 12.1). Usually, voting occurs at multiple stages, and ballot approval may be required for the candidate standard to be passed from one stage to the next. Although every effort is made to conduct the work expeditiously, the development of a typical standard may take several years. In response to the need for faster development of standards, especially within rapidly growing technology areas, some standards development is now being undertaken by consortia, rather than through the traditional SDO. While such consortia are indeed able to develop standards much more quickly, the interests of all stakeholders are less likely to be represented adequately [9]. As of this writing, it is believed that all standards related to glow discharge methods have been developed through traditional SDOs.

Standardization Work Pertaining to Glow Discharge Spectroscopies

A search for standards relevant to chemical analysis through glow discharge spectroscopies was recently conducted (July 2002) using the Worldwide Standards Plus database [Information Handling Services, Englewood, CO, USA].² This database lists standards produced by approximately 450 SDOs around the globe. While there is no guarantee, the search is thought to be exhaustive. As expected, the search indicated that the work of standardization to support chemical analysis through glow discharge spectroscopies is still in the beginning stages, in that very few relevant standards exist. Those that do exist have been developed only for glow discharge mass spectrometry (GDMS) and glow discharge optical emission spectrometry (GD-OES). Standards for other glow discharge techniques (e.g. glow discharge atomic absorption spectrometry) may be forthcoming as such methods gain wider acceptance within commercial laboratories. In the following subsections, the extant standards relating to glow discharge spectrochemical analysis (see Table 12.2), as well as the pertinent standards that are currently under development, are reviewed.

Standards for Glow Discharge Mass Spectrometry

At present, there are four standards pertaining directly to GDMS. The first of these to consider is an Australian Standard[®] (AS 3685-1998), entitled 'Recommended Procedures and Principles of Glow Discharge Mass Spectrometry (GD-MS)' [10]. As the title suggests, this document provides general guidelines for GDMS practice, including descriptions of common sample preparation approaches, instrumentation, operation, calibration and analysis. Specific analytical applications are not discussed. This standard, which might be best described as a standard practice, adhering to the nomenclature of Table 12.1, was developed to serve as a foundation for the later development and application of standard test methods for GDMS. However, no such Australian standard methods have yet been produced. The document was prepared by Standards Australia Committee CH/16, Spectroscopy.

The remaining three standards for GDMS are standard test methods developed by ASTM International Committee F-1 on Electronics. One of these is entitled 'Standard Test Method for Trace Metallic Impurities in Electronic Grade Aluminum by High Mass-Resolution Glow-Discharge Mass Spectrometer' (ASTM F 1593-97) [11]. The titles of the other two standard test methods are identical with the first, except that 'Aluminum' is replaced with 'Titanium' (ASTM F 1710-97) [12] and 'Aluminum-Copper, Aluminum-Silicon, and Aluminum-Copper-Silicon

² In order to describe experimental procedures adequately, it is occasionally necessary to identify commercial products by a manufacturer's name or label. In no instance does such identification imply endorsement by the National Institute of Standards and Technology, nor does it imply that the particular products or equipment are necessarily the best available for that purpose.

Table 12.2 Standards pertinent to glow discharge spectroscopies.

Standard	Title	Type ^a	Standardization body
AS 3685-1998 [10]	Recommended Procedures and Principles of Glow Discharge Mass Spectrometry (GD-MS)	Standard practice	Standards Australia Committee CH/16, Spectroscopy
F 1593-97 [11]	Standard Test Method for Trace Metallic Impurities in Electronic Grade Aluminum by High Mass-Resolution Glow-Discharge Mass Spectrometer	Standard test method	ASTM Committee F-1 on Electronics
F 1710-97 [12]	Standard Test Method for Trace Metallic Impurities in Electronic Grade Titanium by High Mass-Resolution Glow-Discharge Mass Spectrometer	Standard test method	ASTM Committee F-1 on Electronics
F 1845-97 [13]	Standard Test Method for Trace Metallic Impurities in Electronic Grade Aluminum-Copper, Aluminum-Silicon, and Aluminum-Copper-Silicon Alloys by High-Mass-Resolution Glow-Discharge Mass Spectrometer	Standard test method	ASTM Committee F-1 on Electronics
ISO 14707:2000 [14]	Surface Chemical Analysis—Glow Discharge Optical Emission Spectrometry (GD-OES)—Introduction to Use	Standard practice	ISO/TC201/SC8 Glow Discharge Spectrometry

^a Adhering to the nomenclature of Table 12.1.

Alloys' (ASTM F 1845-97) [13]. As is obvious from the titles, these standard methods provide precise instructions for the effective GDMS analyses of the solid materials indicated.

As of this writing, there are no ISO standards developed for GDMS. However, there is an ISO group that is now developing GDMS standards. This group is ISO/TC201/SC8, the Glow Discharge Spectrometry Subcommittee (SC8) under the ISO Technical Committee 201 on Surface Chemical Analysis (TC201). The Australian standard discussed above has recently been adopted by ISO/TC201/SC8 as a working draft (see Figure 12.1).

Standards for Glow Discharge Optical Emission Spectrometry

To date, only one standard pertaining to GD-OES has been issued. This document, which is an ISO standard developed by ISO/TC201/SC8, is entitled 'Surface Chemical Analysis—Glow Discharge Optical Emission Spectrometry (GD-OES)—Introduction to Use' (ISO 14707:2000) [14]. This document provides general guidelines on the use of GDOES for analysis of solid samples. Descriptions of basic principles and instrumentation, as well as common procedures for sample preparation and other pertinent topics, are presented. Specific analytical applications are outside the scope of the standard. Similarly to the Australian GDMS standard described above, this document is intended to serve as a foundation for the later development and application of standard test methods, and can be best described as a standard practice, again employing the nomenclature of Table 12.1.

ISO/TC201/SC8 is now in the process of developing a standard test method relating to GD-OES. This candidate standard method, which is currently at the Committee Draft stage (see Figure 12.1), is tentatively entitled 'Surface Chemical Analysis—Determination of Thickness and Chemical Composition of Zinc and/or Aluminium Based Metallic Coatings by Glow Discharge Optical Emission Spectrometry (GD-OES)'. As suggested by the title, the document provides precise instructions for quantitative GD-OES depth profile analysis of these industrially important coatings, with calculations of coating thicknesses and elemental mass fractions of selected elements. Both dc and rf glow discharge approaches are covered within the scope. The standard is expected to be published in 2003.

Interestingly, the candidate ISO standard method just described is actually based on a very similar European standard method now being developed by Technical Committee 20 of the European Committee on Iron and Steel Standardisation (ECISS). The main difference between the ISO and ECISS standards is that the ECISS standard allows for the use of dc glow discharge sources only. Provision for the use of rf sources may be added later. The development of the ECISS standard method has been described in a recent publication [15].

12.2.2 REFERENCE MATERIALS

Types of Reference Materials

Reference materials are most often classified according to the quality of the metrological information provided for them by the reference material supplier. The most common classes are *reference material (RM)* and *certified reference material (CRM)*, as defined in Table 12.3, although other classes also exist [16,17].³ Generally, CRMs are superior to RMs in terms of metrological properties. For example, the certified elemental mass fractions provided for bulk CRMs are believed to be more accurate on average than the noncertified mass fractions provided for bulk RMs. Moreover, the uncertainties associated with the mass fractions have often been evaluated more completely and correctly for CRMs than for RMs [18]. Similar comments could be made concerning CRMs and RMs that are characterized for properties other than elemental mass fraction (e.g. coating weights of layered materials). For these reasons, CRMs are usually preferred over RMs for use as calibration and check samples⁴ in glow discharge analyses. Nonetheless, because of practicality and availability issues, RMs are often used

Table 12.3 Official ISO definitions of *reference material* and *certified reference material* (definitions 2.1 and 2.2, respectively, taken from ISO Guide 30:1992 [16], have been reproduced with the permission of the International Organization for Standardization, ISO. This ISO Guide can be obtained from any member body or directly from the Central Secretariat, ISO, Case Postal 56, 1211 Geneva 20, Switzerland. Copyright remains with ISO).

Term	Definition
Reference material (RM)	Material or substance one or more of whose property values are sufficiently homogeneous, stable and well established to be used for the calibration of an apparatus, the assessment of a measurement method, or for assigning values to materials
Certified reference material (CRM)	Reference material, accompanied by a certificate, one or more of whose property values are certified by a procedure which establishes its traceability to an accurate realization of the unit in which the property values are expressed, and for which each certified value is accompanied by an uncertainty at a stated level of confidence

³ A Standard Reference Material[®] (SRM[®]) is considered to be a CRM issued by the National Institute of Standards and Technology (NIST). However, one potential difference between SRMs and CRMs is that SRMs must meet NIST-specified certification criteria that may not be required by other CRM producers. Nonetheless, in the practice of glow discharge analytical methods SRMs and CRMs are commonly used interchangeably. For this reason, no distinction between SRMs and CRMs is made in this chapter.

⁴ In this discussion, a sample used as a *type standard* is considered a calibration sample, and samples used for instrument validation or calibration verification are considered check samples.

for these purposes. Either CRMs or RMs may be used for drift correction, also known as recalibration, in the day-to-day practice of glow discharge analytical methods. However, reference materials producers often provide *setting-up samples (SUSs)* intended specifically for this purpose. Technically, SUSs are neither CRMs nor RMs, and only approximate elemental composition information may be provided. As a result, SUSs may not be suitable for use as calibration or check samples.

Availability of Reference Materials Pertinent to Glow Discharge Spectroscopies

Many thousands of reference materials are available from various producers, and reference materials can be found in all physical forms, including gases, solutions, powders, bulk solids and layered materials. However, because glow discharge methods are primarily used in industrial and commercial laboratories for bulk or depth profile analysis of solids, reference materials that take the form of either bulk or layered solid materials are most relevant to the present discussion. In the future, other reference materials may become more important with regard to glow discharge spectroscopies, as continuing research and development expands further the range of sample types amenable to routine glow discharge analysis. In the following subsections, the availabilities of bulk and layered reference materials relevant to chemical analysis through glow discharge spectroscopies are reviewed.

Bulk Solid Reference Materials

Hundreds of bulk solid reference materials that are useful for glow discharge applications exist, including CRMs, RMs and SUSs. Notably, most of these materials are metals and alloys. This is probably due to the combination of the long-term, widespread use of metals and alloys in industry and the fact that arc/spark and X-ray fluorescence spectroscopies have been extensively used for the industrial analysis of such materials. This situation has been advantageous for glow discharge practitioners over the years, because analysis of metallic samples has historically been the primary application for glow discharge methods. However, electrically nonconductive materials, such as glasses, ceramics and polymers, are now amenable to glow discharge analysis. There are some reference materials of these matrices that could be effectively used, but there are not many. Consequently, if glow discharge methods for the characterization of electrically nonconductive materials become widely accepted commercially, then there will likely be a growing need for additional reference materials of these types.

While there are currently many bulk metallic reference materials that are useful for glow discharge applications, there is always a need for more. Additionally, there is at least one major shortcoming of these and other reference materials

that should be noted. Mass fractions for nonmetallic elements, especially N, O and H, are often not provided by the reference materials producers. When such information is provided, it is often questionable in terms of accuracy. This unfortunate situation is partly due to the fact that the nonmetallic elements are very difficult to determine accurately. The practical result is that determination of the mass fractions of these elements through glow discharge spectroscopies is often either impossible or inaccurate. For quantitative depth profiling, the accuracy of the depth axis may also be affected in addition to the accuracy of the mass fraction axis. This is because the algorithms used to establish the depth axis are founded upon reliable estimates of the elemental composition of surface layers as a function of depth [19–21]. For these reasons, there is a need for more and better information regarding nonmetal content in reference materials.

Layered Reference Materials

Obviously, layered reference materials are needed for glow discharge depth profiling applications, rather than for bulk analysis. Specifically, they are needed primarily as check samples, rather than for calibration or drift correction. This is because calibration and drift correction for glow discharge depth profiling are usually accomplished using bulk solid reference materials only [19–21]. However, there is now increasing interest in the use of layered reference materials for these purposes. The increasing interest is founded on the fact that a given bulk solid and a coating of identical elemental composition may differ substantially in important properties, such as density.

In 1998, a survey was conducted by an advisory group formed as part of the work of ISO/TC201/SC8 to evaluate the availability of layered reference materials suitable for use in glow discharge depth profiling applications, as reported in a recent paper [22]. Owing to the fact that layered reference materials are needed primarily as check samples, and given the fact that CRMs are preferable for such purposes, the focus of the survey was to identify potentially useful layered CRMs rather than RMs. One intention was to provide a list of useful materials to the glow discharge depth profiling community, in order to aid practitioners in their day-to-day work. An additional purpose was to focus attention on the need for such CRMs, hopefully serving as an impetus for the development of materials with appropriate characteristics.

A list of characteristics that layered CRMs should have to be useful for glow discharge depth profiling was formulated by the advisory group:

1. The layered surface should have a surface area of at least several square centimeters. This is necessary so that multiple spots can be examined.
2. The CRM should be rigid enough to enable easy mounting on to the glow discharge device without fracturing or deforming.
3. The layered surface should be flat, in order to obtain adequate vacuum, because most glow discharge devices are designed to accept flat samples only.

4. The layered surface should be smooth, because the smoothness of the surface in part determines the obtainable depth resolution. Smoothness is also needed for enabling adequate vacuum quality.
5. The layered surface should be laterally uniform over the usable area, in terms of both elemental mass fractions and depth distributions.
6. At least some of the quantitative information attainable with GDS depth profiling must be certified. Examples include coating thickness, coating weight and elemental composition. However, the type of information that must be certified could not be specified, because applications of GDS depth profiling in industry are broad and continually increasing.
7. The CRM should be stable in all respects over long periods of time.

Existing CRMs were evaluated relative to this list of desirable characteristics. Attention was not limited to CRMs resembling samples of industrial importance, but all layered CRMs that could be found were considered. This included CRMs with either single-layer or multi-layer structures and those with either 'thick' ($>1 \mu\text{m}$) or 'thin' ($<1 \mu\text{m}$) layers. Moreover, CRMs incorporating either electrically conductive or nonconductive layers and/or substrates were evaluated. This approach was taken, so that the results of the survey would remain useful for many years amid the changing roles played by glow discharge spectrochemical methods in industry.

The primary tool used to conduct the CRM survey was the COMAR (CODE MAteriaux Reference) Certified Reference Materials Database, an international database that listed approximately 9000 CRMs of various types at the time the survey was taken. Both major and minor CRM producers in more than 20 countries were represented in this database, including most if not all of the major producers. As a result, the survey conducted in this way was thought to be thorough. Nonetheless, many major and minor CRM producers worldwide were individually contacted, in a further effort to avoid overlooking relevant materials.

More than 40 layered CRMs were identified through the survey. Unfortunately, none had all of the desirable characteristics listed by the advisory group. The most common inadequacy was that the physical characteristics were inappropriate for glow discharge use. For instance, many were so thin and fragile that they could not be easily mounted on to a glow discharge device. As another example, only one or two glow discharge burns could be placed on some of the CRMs, owing to the fact that the surface areas of the layered surfaces were so small. The reason for these sorts of shortcomings is that the CRMs were originally designed specifically for use with other measurement methods.

Even though no CRMs with all of the desirable characteristics were found, a number of CRMs that could be of some limited utility in glow discharge depth profiling applications were identified. Many of those CRMs are still available at the time of this writing and are listed in Table 12.4, along with additional CRMs that have become available since the survey was conducted. Importantly, none of the materials given in Table 12.4 are similar to samples which are now commonly

Table 12.4 CRMs with limited usefulness for GDS depth profiling.

Producer	CRM	Description	Certified parameter(s)	Nominal certified value(s) ^a
UNIIM ^b	1180–89	Ag on bronze	Coating mass (kg m^{-2})	0.004 and 0.850
	4982–89	Si doped with B	B depth distribution	Not applicable
	4983–89	Si doped with P	P depth distribution	Not applicable
	5441–90	GaAs doped with Si	Si depth distribution	Not applicable
	5442–90	GaAs doped with Cr	Cr depth distribution	Not applicable
IRMM ^c	CRM 261S	Ta ₂ O ₅ on Ta	Layer thickness, nm	30 and 100
	CRM 328	Au on Ni	Coating mass (mg cm^{-2})	0.863, 1.570, 5.823 and 9.597
	CRM 564	SiO ₂ on Si	Layer thickness (nm)	10, 50 and 120
NIST ^d	SRM 1358a	Cu on steel ^e	Layer thickness (μm)	80, 225 and 1000
	SRM 1359b	Cu on steel ^e	Layer thickness (μm)	48, 140, 505 and 800
	SRM 1361b	Cu on steel ^e	Layer thickness (μm)	6, 12, 25 and 48
	SRM 1362b	Cu on steel ^e	Layer thickness (μm)	40, 80, 140 and 205
	SRM 1363b	Cu on steel ^e	Layer thickness (μm)	255, 385, 505 and 635
	SRM 1364b	Cu on steel ^e	Layer thickness (μm)	800, 1000, 1525 and 1935
	SRM 2134	As implant in Si depth profile standard	Retained dose of ⁷⁵ As ($\mu\text{g cm}^{-2}$)	0.09120
	SRM 2135c	Ni/Cr multilayer stack	Overall Ni coating mass ($\mu\text{g cm}^{-2}$) Overall Cr coating mass ($\mu\text{g cm}^{-2}$)	226 190

(continued overleaf)

Table 12.4 (continued)

Producer	CRM	Description	Certified parameter(s)	Nominal certified value(s) ^a
			Individual Ni layer coating mass ($\mu\text{g cm}^{-2}$)	56.5
			Individual Cr layer coating mass ($\mu\text{g cm}^{-2}$)	38.0
			Individual Ni layer coating mass uniformity (% relative)	± 3.8
			Individual Cr layer coating mass uniformity (% relative)	± 4.0
			Individual Ni/Cr bilayer coating mass uniformity (% relative)	± 3.3
	SRM 2137	Si doped with ^{10}B	Retained dose of ^{10}B ($\mu\text{g cm}^{-2}$)	0.017
	SRM 2321	Sn-Pb alloy on Cu	Coating mass (mg cm^{-2})	6.8
			Sn mass fraction in coating (%)	60

^aAs given in either the COMAR citation or the Certificate of Analysis.

^bUNIIM, Mr. Leonov, Krasnoarmeiskaya St. 4, 620219 Ekaterinburg, GSP-824, Russia. Tel. 343 2 55 26 18. Telex 721911 PSB-SU. Fax 343 2 55 20 39.

^cIRMM, Management of Reference Materials Unit, Retieseweg, 2440 Geel, Belgium. Tel. +32 14 571 722. Fax +32 14 590 406.

^dNIST, Standard Reference Materials Program, Building 202, Mailstop 2322, Gaithersburg, MD 20899, USA. Tel. 301 975 6776. Telex TRT 197674. Fax 301 948 3730.

^eOvercoated with a thin layer of Cr for wear resistance.

characterized using glow discharge depth profiling in industry (e.g. galvanized coatings on steels), and so they are not very relevant to the current commercial use of glow discharge methods. However, the relevance may change as the scope of applicability of glow discharge depth profiling continues to expand. The fact that the listed materials are not very relevant at the time of this writing emphasizes the need for the development of new layered CRMs with the appropriate characteristics. Considering the current industrial applications of glow discharge depth profiling, some important candidate materials are galvanized and hard coatings on steel, oxide scales on steel and high-temperature alloys and surface-hardened steels, as well as Sn, Ni and Cr platings on various metals.

The development of two CRMs intended specifically for use in glow discharge depth profiling has been undertaken by the Federal Institute for Materials Research and Testing [Bundesanstalt für Materialforschung und Prüfung (BAM)] in Berlin, Germany. The first of these is a Ti/Al multilayer stack [$5 \times (50 \text{ nm Ti}/250 \text{ nm Al})$] on (100Cr6) steel, and the second is an $\text{SiO}_2/\text{TiO}_2$ multilayer stack [$5 \times (100 \text{ nm TiO}_2/100 \text{ nm SiO}_2)$] on borosilicate glass (BK7). These stack materials were chosen because of their importance in modern technology. As part of the development process, these candidate CRMs have been evaluated through a project of the Surface Chemical Analysis Technical Working Area (TWA 2) of the Versailles Project on Advanced Materials and Standards (VAMAS) [23].

The survey conducted by the ISO/TC201/SC8 advisory group has been a helpful and informative exercise. While it would certainly be useful to conduct a similar survey to search for suitable layered RMs, it is believed that no such survey has been conducted. Because of the enormous complexity and cost associated with officially certifying pertinent characteristics of layered reference materials, layered RMs, which are uncertified by definition, might be more readily available than layered CRMs. However, it is probably true that few suitable layered RMs exist.

12.3 CONCLUSIONS

Standards and reference materials are extremely important for the routine practice of glow discharge spectrochemical analysis, and there is a growing need for the continued development of both. There is every reason to believe that the development of standards relevant to glow discharge spectroscopies will not only continue, but expand, in the foreseeable future. For example, the number of glow discharge practitioners participating in the standardization work of ISO/TC201/SC8 more than tripled from 1994 to 2002, including representation from government, academia, instrument manufacturers and industrial users. The increased participation is very desirable, because it is vitally important that all affected stakeholders take part in the standardization process.

Development of reference materials relevant to the practice of glow discharge methods will undoubtedly also continue in the future. However, it is unclear whether many reference materials with useful information regarding nonmetal content or layered reference materials with appropriate characteristics for glow discharge depth profiling will be produced. This is partly because the development and production of both of these types of reference materials present special technical challenges. Moreover, developing reference materials of any sort tends to be a complex and expensive process. As a result, reference materials producers must be very selective in terms of which reference materials to develop. This is true not only for commercial reference materials producers, but also for national metrological institutes (NMIs), such as NIST, which normally have very limited human and financial resources relative to the expressed needs of industry for reference materials. NMIs typically receive many more requests for the production of various types of RMs and CRMs than can possibly be addressed. Consequently, many factors must be carefully considered in deciding which new reference materials to produce. Some of the factors that must be balanced are (1) the range of application of the proposed reference material, (2) the monetary significance, including prediction of economic impact, (3) scientific and technological significance and (4) the uniqueness of the capabilities of the NMI.

12.4 REFERENCES

1. Krechmer, K. *The Fundamental Nature of Standards: Technical and Economic Perspective*, seminar presented at the National Institute of Standards and Technology, Gaithersburg, MD, October 20, 2000.
2. *Standardization and Related Activities—General Vocabulary*, ISO Guide 2:1996, International Organization for Standardization: Geneva, 1996.
3. *Annual Book of ASTM Standards*, Vol. 03.06, American Society for Testing and Materials: West Conshohocken, PA, 2000, pp. iii–iv.
4. Spanner, J. *ASTM Stand. News*, 1995, **23**(1), 56–59.
5. *Standards Activities of Organizations in the United States*, Toth, R. B. (Ed.), NIST Special Publication 806, US Government Printing Office: Washington, DC, 1991.
6. *Profiles of National Standards-Related Activities*, Toth, R. B. (Ed.), NIST Special Publication 912, US Government Printing Office: Washington, DC, 1997.
7. *Directory of European Regional Standards-Related Organizations*, Breitenberg, M. (Ed.), NIST Special Publication 795, US Government Printing Office: Washington, DC, 1990.
8. *Directory of International and Regional Organizations Conducting Standards-Related Activities*, Breitenberg, M. (Ed.), NIST Special Publication 767, US Government Printing Office: Washington, DC, 1989.
9. Lowell, S. C. *ASTM Stand. News*, 1999, **27**(12), 30–35.
10. *Recommended Procedures and Principles of Glow Discharge Mass Spectrometry (GD-MS)*, Australian Standard® AS 3685-1998, Standards Australia: Sydney, 1998.
11. *Standard Test Method for Trace Metallic Impurities in Electronic Grade Aluminum by High Mass-Resolution Glow-Discharge Mass Spectrometer*, ASTM Standard F 1593-97, in *Annual Book of ASTM Standards*, Vol. 10.04, American Society for Testing and Materials: West Conshohocken, PA, 2000, pp. 379–385.

12. *Standard Test Method for Trace Metallic Impurities in Electronic Grade Titanium by High Mass-Resolution Glow Discharge Mass Spectrometer*, ASTM Standard F 1710-97, in *Annual Book of ASTM Standards*, Vol. 10.04, American Society for Testing and Materials: West Conshohocken, PA, 2000, pp. 397–402.
13. *Standard Test Method for Trace Metallic Impurities in Electronic Grade Aluminum–Copper, Aluminum–Silicon, and Aluminum–Copper–Silicon Alloys by High-Mass-Resolution Glow Discharge Mass Spectrometer*, ASTM Standard F 1845-97, in *Annual Book of ASTM Standards*, Vol. 10.04, American Society for Testing and Materials: West Conshohocken, PA, 2000, pp. 426–429.
14. *Surface Chemical Analysis—Glow Discharge Optical Emission Spectrometry (GD-OES)—Introduction to Use*, ISO 14707:2000, International Organization for Standardization: Geneva, 2000.
15. Bengtson, A.; Hånström, S.; Lo Piccolo, E.; Zacchetti, N.; Meilland, R.; Hocquaux, H. *Surf. Interface Anal.*, 1999, **27**, 743–752.
16. *Terms and Definitions Used in Connection with Reference Materials*, ISO Guide 30:1992, International Organization for Standardization: Geneva, 1992.
17. May, W.; Parris, P.; Beck, C.; Fassett, J.; Greenberg, R.; Guenther, F.; Kramer, G.; Wise, S.; Gills, T.; Colbert, J.; Gettings, R.; MacDonald, B. *Definitions of Terms and Modes Used at NIST for Value Assignment of Reference Materials for Chemical Measurements*, NIST Special Publication 260-136, US Government Printing Office: Washington, DC, 2000.
18. *Guide to the Expression of Uncertainty in Measurement*, International Organization for Standardization: Geneva, 1995.
19. *Glow Discharge Optical Emission Spectrometry*; Payling, R., Jones, D., Bengtson, A. (Eds.), John Wiley & Sons Ltd: Chichester, 1997, Chapt. 10.
20. Bengtson, A. *Spectrochim. Acta, Part B*, 1994, **49**, 411–429.
21. Payling, R. *Spectroscopy*, 1998, **13**, 36–44.
22. Winchester, M. R.; Beck, U. *Surf. Interface Anal.*, 1999, **27**, 930–935.
23. *Evaluation of Multilayer Reference Coatings for Quantitative GDOES Depth Profiling*, Project A4 of the Surface Chemical Analysis Technical Working Area (TWA 2), Versailles Project on Advanced Materials and Standards (VAMAS), initiated 1 January 1998.

13

Analysis of Liquid Samples Using Glow Discharge Spectroscopies

R. K. MARCUS

Department of Chemistry, Clemson University, Clemson, SC, USA

13.1 INTRODUCTION

The preceding chapters of this book have dealt almost exclusively with the application of glow discharge (GD) sources to the analysis of materials directly in the solid state. It is this basic capability that sets the GD apart from other common spectrochemical methods, wherein the sample is usually introduced as a solution. By the same token, GDs possess certain properties that might be applied advantageously in the analysis of solution-based samples. The most obvious of these possible advantages is the simplicity of the sources relative to atmospheric pressure plasmas that operate at powers above 1 kW. Two less apparent traits are the capability to work with minute sample volumes and the ability to produce detailed molecular species information. Specifically, as will be shown in the following sections, empirical formulae can be deduced through optical emission and molecular weight/fragmentation information may be obtained by mass spectrometry.

The reason why GD devices are not widely employed for bulk solution analysis is very simple: as a result of the low gas temperature and a low density plasma, GDs do not have sufficient energy to desolvate liquid analyte species. If analytes in solution cannot be obtained in the isolated atom/molecule form, then obviously the desired information cannot be derived. Even if analytes could be desolvated to dry particle form, the presence of residual solvent vapors would

quench the energetic species in the plasmas to the point where no useful analytical information could be obtained [1,2]. Therefore, it is implicit in the use of GD sources for solution sample analyses that the analytes must be completely desolvated prior to admission to the discharge volume. Three approaches to this end are presented herein: analysis of dry solution residues, continuous introduction of desolvated aerosols, and the use of transport-type liquid chromatography/mass spectrometry (LC/MS) interfaces.

13.2 INSTRUMENTATION

13.2.1 SOLUTION RESIDUE ANALYSIS

The analysis of dry solution residues by glow discharge optical and mass spectrometries has been pursued for almost five decades [3]. The gist of the experiment involves the deposition of an aliquot (1–100 μL) of analyte containing solution in or on the cathode of the GD and evaporating the solvent to produce a dry residue. The cathode is then placed in the discharge source, and the plasma is ignited to effect sample atomization through the normal cathodic sputtering process. Analyte species can be determined by atomic absorption, emission, or mass spectrometries. While flat (planar) disk cathodes have been employed successfully in this approach, the use of hollow cathodes yields benefits in terms of convenient handling of volume-limited solution samples and production of a more energetic plasma. On the other hand, direct application of solutions onto flat cathodes while still mounted in the source can reduce sample turnaround times. The two basic configurations of GD systems employed for solution residue analysis are shown in Figure 13.1.

The source dimensions and cathode materials employed in this procedure have varied considerably through the literature. The primary considerations in choosing the cathode material include the absence of the desired analytes (i.e. low blank values) and a very high sputtering rate. For example, there are tradeoffs between the ready availability of high purity (i.e. low contamination) graphite versus its inherently low sputtering rate. By the same token, there have been a wide number of source/cathode geometries employed. As noted above, both hollow and planar cathodes have been utilized, with the former finding wider use. This is particularly true in the case where optical emission detection is practiced. In this instance, the benefits of the hollow cathode effect, wherein very high current densities can be derived at nominal discharge voltages, yields a far more effective analyte excitation environment than the more open planar geometry. Hollow cathode (HC) dimensions are typically 1–5 mm in diameter, with lengths of 10–25 mm. An inert discharge gas at pressures of 1–10 Torr and discharge currents of up to 200 mA are common. In general, there is a tendency toward the use cathodes of small diameter to obtain high analytical sensitivity and the ability to operate well with very small sample volumes. Discharge sources employing planar cathodes

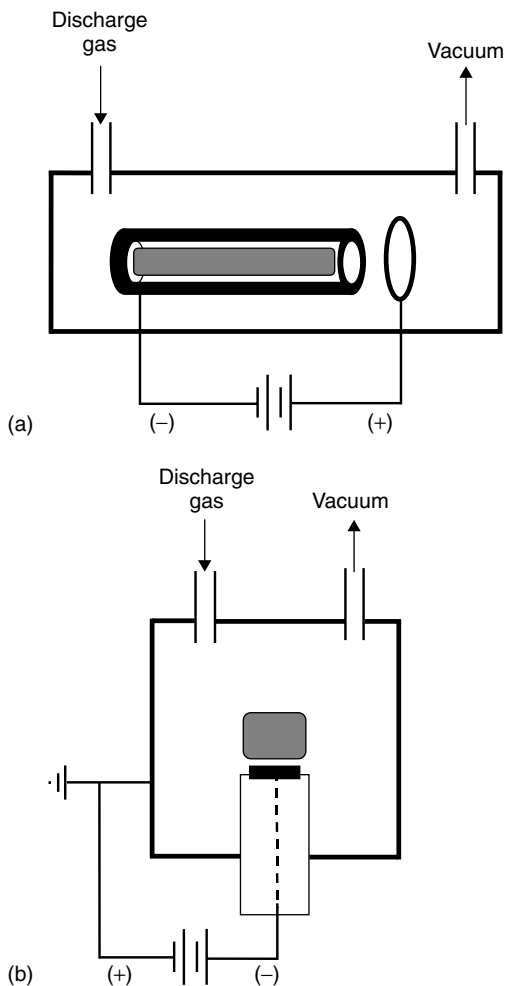


Figure 13.1 Two basic configurations of GD systems employed for dry solution residue analysis: (a) hollow cathode; (b) planar (disk) cathode

tend to operate in the single torr, single milliamp range. Pertinent figures of merit and applications of the various means of solution residue analysis will be described in the subsequent sections.

13.2.2 DIRECT SAMPLE ASPIRATION

As described previously, the glow discharge itself is not capable of affecting solution-sample desolvation. In addition, the gas-phase collision excitation

processes are severely quenched by the presence of molecular vapors such as water [1,2]. There has been only a single description of a system with direct introduction of a vaporized analyte solution in the literature [4]. Figure 13.2 illustrates the basic elements of the device developed by Schroeder and Horlick [4] for continuous solution introduction into a hollow cathode emission source. Very simply, aerosol production with a conventional pneumatic nebulizer operating at a flow rate of 0.3–1.2 mL/min and employing He as the nebulizer gas was used in combination with a heated desolvation chamber and a cooled condenser prior to introduction of the analyte into the HC source. The discharge was sustained by the He nebulizer/carrier gas at pressures of ~ 20 Torr and at currents of up to 295 mA. The major impetus for developing such a system was the ability to sample the effluents of liquid chromatographic separations, which is not possible by the ‘discrete’ sampling employed in the solution residue methods. The performance of this unique system will be described in subsequent sections.

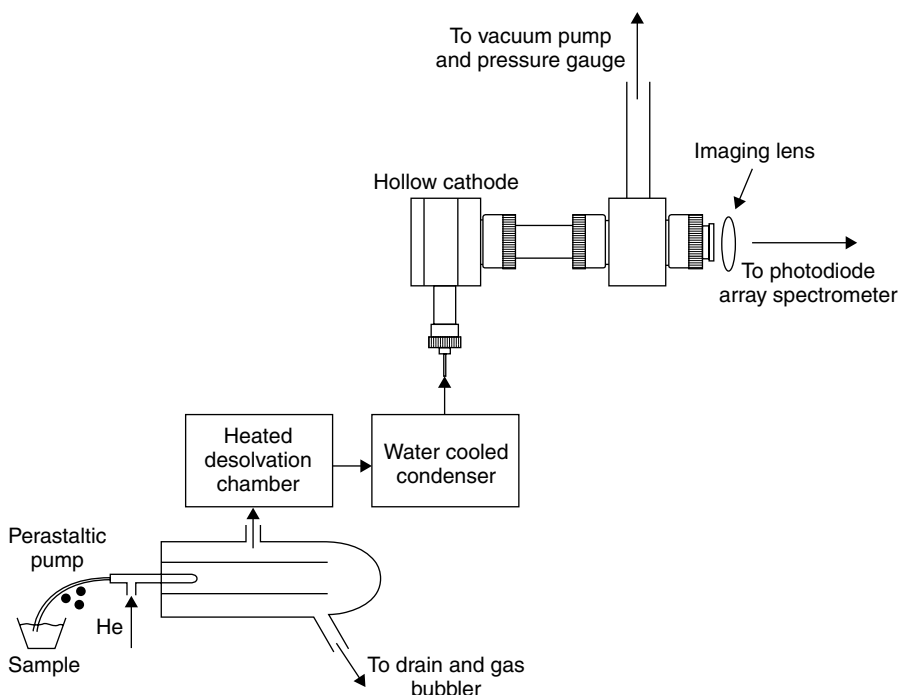


Figure 13.2 System components of the apparatus employed for continuous solution introduction into a hollow cathode discharge. Reprinted from Schroeder, S. G. and Horlick, G., *Spectrochim. Acta, Part B*, 1994, **49**, 1759–1773, with permission from Elsevier Science

13.2.3 TRANSPORT-TYPE LC/MS INTERFACES

To a first approximation, the challenges posed in the introduction of solution-phase samples into glow discharge sources are very similar to those faced in the introduction of liquid samples into the low-pressure ion sources used in organic mass spectrometry. Traditional electron impact and chemical ionization sources are incapable of effecting desolvation and the presence of residual solvent vapors causes severe depression of analyte ion signals and leads to high levels of spectral interference. As alluded to above, the ultimate embodiment of any solution-phase analysis system is the on-line detection of species separated by liquid chromatography. By analogy, then, it is not surprising that two liquid chromatography/mass spectrometry (LC/MS) interfaces, the moving belt [5,6] and the particle beam [7,8], have also been implemented for sample introduction into GD devices. The moving belt and particle beam devices fall into the category of 'transport-type' LC/MS interfaces. While achieved by different means, these interfaces include aspects of on-line sampling, desolvation, solvent vapor removal, and analyte delivery into low-pressure environments. In LC/MS applications, analytes are delivered solvent-free to ion sources operating at pressures $<10^{-4}$ Torr, at solution flow rates in the case of conventional LC separations in the range 0.2–2.0 mL/min. Thus, the use of these interfaces with GD sources would provide an environment wherein the analyte should have no memory of its solution-phase heritage.

The use of a moving belt transport device has been described by Brackett and Vickers [9] and is shown in schematic form in Figure 13.3. Very simply, the liquid flow through a restricted capillary (~ 100 – $300 \mu\text{L}/\text{min}$) is deposited on the 0.125 in diameter beads of a stainless-steel conveyor chain moving at a velocity of ~ 140 mm/min. The chain passes through a resistively heated tube (27 W electric power, no temperature provided) at reduced pressure (not specified), affecting desolvation along the path to the discharge region. As seen in the expanded view of the cathode region, the metallic chain comes in contact with the cathode of the GD, and as such sputtering of the residue from the beads is realized. While simple wire and linked chain conveyors were also investigated, the best reproducibility was obtained with the bead chain geometry.

A more widely used transport-type LC/MS interface is the particle beam (PB), shown schematically in Figure 13.4. Particle beam interfaces, as first described by Willoughby and Browner [7], all include some form of a nebulizer housed in a heated chamber where desolvation of the aerosol takes place, followed by a multistage momentum separator which affects particle enrichment by removal of nebulizer gases and solvent vapors through the vacuum. In simple terms, mixtures of gas and particulate matter passing through small (≤ 1 mm diameter) orifices across pressure differentials produce an expansion based on the relative momenta of the stream components. Light weight species (gases) tend to expand radially and are skimmed from the beam, while more massive analyte particles continue to pass through successive orifices. Use of two or more stages of differential

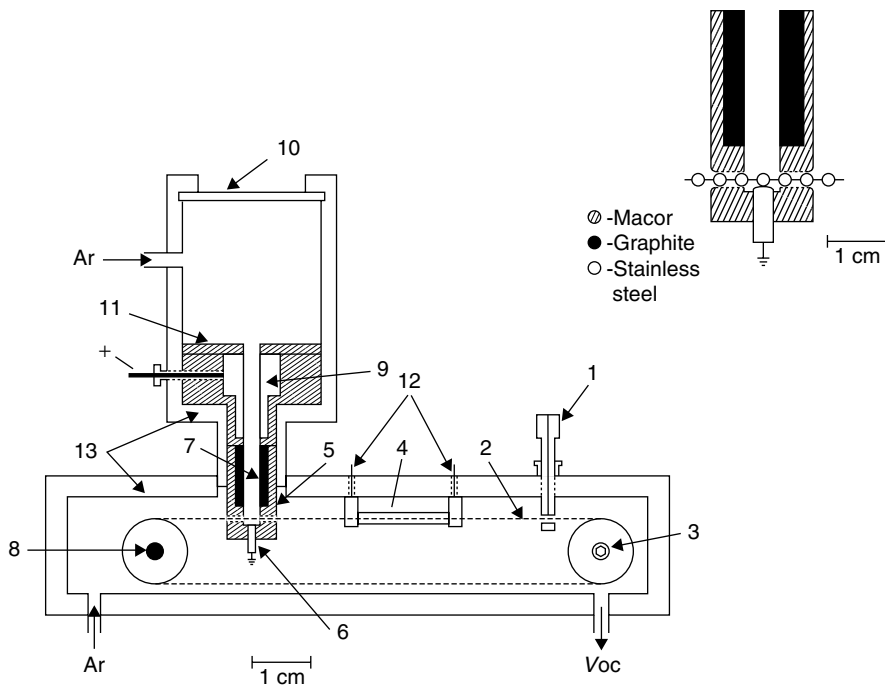


Figure 13.3 Moving belt apparatus developed for solution residue introduction into a Grimm-type glow discharge lamp. Reprinted from Brackett, J. M. and Vickers, T. J., *Spectrochim. Acta, Part B*, 1983, **38**, 979–985, with permission from Elsevier Science

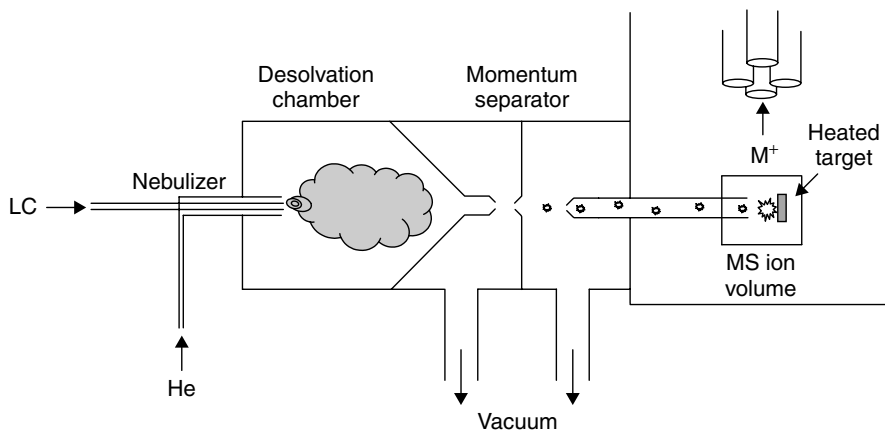


Figure 13.4 Basic components of a particle beam LC/MS interface

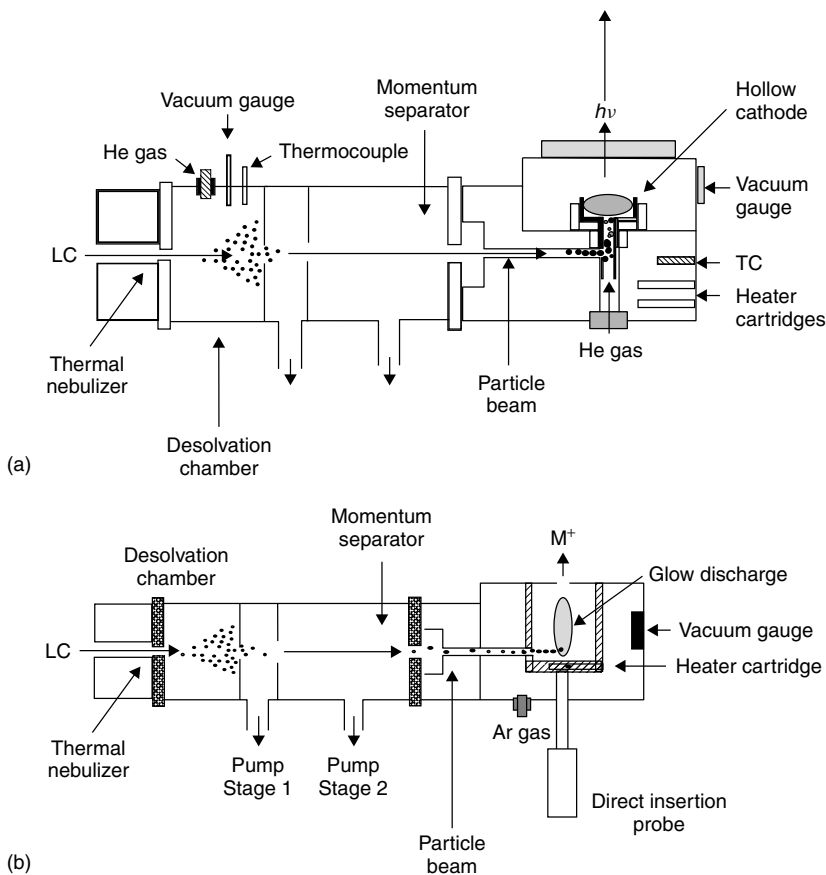


Figure 13.5 Particle beam sample introduction coupled to (a) glow discharge atomic emission and (b) mass spectrometry sources

pumping yields a true beam of particles free from residual gases, allowing their delivery to ionization volumes operating at pressures of $\sim 10^{-4}$ Torr where they are flash vaporized into the gas phase. The PB interface provides a means of sampling liquids at flow rates of up to ~ 1.5 mL/min, while allowing ionization by electron impact, chemical ionization and many other methods. Strange and Marcus used this approach to introduce particles into GD sources for analysis by optical emission [10] and mass spectrometries as depicted in Figure 13.5.

13.3 PRACTICAL ASPECTS AND APPLICATIONS

While the application of glow discharge spectroscopies to the analysis of solution-phase samples may seem very foreign to most readers, there have in fact

been many (>50) such publications in the scientific literature. Many of these reports describe analytical characteristics that are unique relative to capabilities of 'traditional', commercially available instrumentation/techniques. Therefore, the following discussions will not only concentrate on providing representative traits, but also highlight the possibilities not provided by other methods.

13.3.1 SOLUTION RESIDUE ANALYSIS

Far and away, the analysis of solution residues represents the most widely applied means of GD analysis of liquid samples, with the earliest example appearing in a report by Birks in 1954 [3]. In fact, that work showed some of the basic characteristics still realized to date when using HC emission sources. This work went largely unnoticed until the 1960s, when papers by Pevtsov and Krasil'shchik [11] and Büger and Fink [12] seemingly re-introduced the technique. Interestingly, some of the earliest applications were probably far before their time as Rudnevskii and co-workers [13] and Berezin [14] each illustrated the use of the technique for the determination of sulfur and cadmium in solution in the first case and sulfur and halogens in the latter. Thus, the flexibility of the use of low-pressure plasmas for solution analysis was demonstrated long before their use found widespread application.

The dry residue analysis approach extends by analogy from longstanding methods developed for arc and spark emission spectrometries. In the case of the glow discharge, though, a cathodic sputtering mechanism is employed for sample atomization rather than volatilization at temperatures of >5000 K as in the arc and spark sources. On a first principle basis, this should provide a more stable analytical signal for glow discharge analysis. Early workers also recognized the fact that small volume samples could most effectively be deposited into HCs while also maintaining the well characterized advantages of HC excitation over more open geometries [15]. In this regard, the review article by Slevin and Harrison [16] stands as the seminal work in concisely describing the potential analytical advantages of the use of HC geometries. The volume edited by Caroli [17] describes variations from basic HC geometries and operation modes that can be used to advantage in particular circumstances. Analytical developments in the area of solution residue analysis can be divided into families of papers based on the detection mode: atomic emission, atomic absorption, and mass spectrometry.

Atomic Emission Spectroscopy

Harrison and Prakash [18] described a demountable hollow cathode source which permitted the analysis of solution residues and a thorough evaluation of the pertinent discharge parameters that affect analytical performance of HC sources in general. Stainless-steel and graphite cathodes of ~4 mm i.d. were employed in

the basic evaluation of the method, the former chosen for its relative robustness and the latter allowing absorption of the analyte solutions into the cathode matrix. In the case of the steel cathodes, rapid sputtering of the dried residues was found to reduce analyte residence times in the plasma and thus deteriorating the precision. Addition of a spectroscopic buffer (i.e. $\sim 50\times$ excess of a carrier salt) was found to extend the sputtering lifetime and thus improved the precision. Use of graphite cathodes achieved the same end, although the total evolution of the analyte was not realized in a given run and so the cathodes were suitable for only a single analysis. Stainless-steel cathodes, however, could be cleaned and used multiple times. Figure 13.6 illustrates the temporal profile for 0.1 ppm B in the presence of 50 ppm Li_2SO_4 (0.45 mL volume) and that of the carrier blank using a stainless-steel cathode. Note that the relatively slow evolution of the analyte signal is due to the fact that the current could only be increased stably over the course of 30–60 s. Argon, neon and helium were evaluated as discharge gases, with Ar yielding the best analytical responses owing to its better sputtering characteristics. Analytical working curves for solutions of Pb, Cu, B, and Sn over the nominal concentration range of 0.1–5 ppm each exhibited very good linearity and precision ($\pm 3\text{--}5\%$). Unfortunately no limits of detection were presented. The high sensitivity obtained for lead in the presence of the carrier

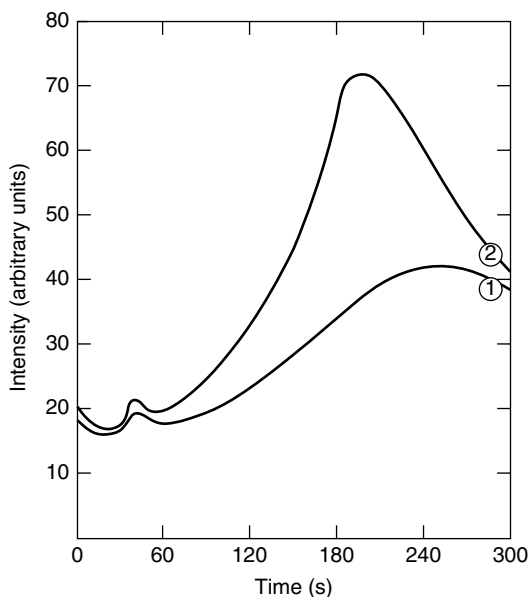


Figure 13.6 Temporal profile of B (I) 249.7 nm emission intensity for (1) the carrier salt (50 ppm Li_2SO_4) blank and (2) 0.1 ppm B in the presence the carrier using a stainless-steel cathode. Reprinted from Harrison, W. W. and Prakash, N. J., *Anal. Chim. Acta*, 1970, **49**, 151–159, with permission from Elsevier Science

salt permits the application of the method to the determination of Pb in biological materials (hair and liver tissue) as a natural extension [19]. In this case, carrier salts of thousands of ppm concentration could be tolerated to yield a precision and accuracy of ~6% for Pb at the 0.1 ppm level for aqueous solutions. Analysis of the biological material digests yielded recoveries of >92% for Pb concentrations of 2–8 ppm in the original samples.

Harrison and Daughtrey extended the work on HC-AES analysis of solution residues by the use of a commercial, demountable hollow cathode lamp. Discharge parameters (current, pressure, and gas identity) were evaluated for the new source [20], with conditions of 50 mA discharge current and a source pressure of 1 Torr Ar chosen as optimum for the determination of gold in the anti-inflammatory drug myochrosine. Detection limits at the single nanogram level for 100 μL solutions are apparent, although not explicitly stated. The same apparatus, with slight modifications, was employed for the determination of boron in aqueous solution [21]. In that work, a 100 mA discharge current and an Ar pressure of 0.7 Torr were employed. Both molecular (BO_2) bands and boron atomic lines were monitored, yielding detection limits of ~20 ng and 10 pg (i.e. 0.1 ppb in the 100 μL solution sample), respectively. The determination of boron in a variety of biological matrices is complicated by interferences from the organic and inorganic residues. To alleviate these problems, a combination of anion- and cation-exchange resins were used to extract the extraneous species from the solutions obtained by an initial radio frequency (rf) sample ashing steps [22]. NBS orchid leaves and bovine liver standards, and human hair samples were used as test matrices. High precision (± 10 –20% RSD) determinations were obtained for boron concentrations at the single ppm level in the raw samples. Detection limits at the single ppb level were obtained for a variety of natural and process water specimens.

One of the interesting properties of hollow cathode discharges is an enhancement of plasma excitation efficiencies as the diameters are reduced to below 2 mm, particularly when the depth to diameter ratios exceed 3:1. Extensive studies by Williams and co-workers have demonstrated the power of the use of so-called microcavity HCs for analysis of volume-limited (<1 μL) samples [23–26]. In these applications, typified in the analysis of renal fluids, the target is high absolute sensitivity (picogram levels) rather than concentration-based figures of merit. Early studies involved the determination of Li, Na, K, and Ca producing limits of detection at the sub-picogram level in ~5 nL sample volumes [23]. High sensitivity was also obtained in the determination of P and Cl, yielding detection limits of 9 and 20 pg, respectively [24]. The roles of the discharge gas identity and pressure and the hollow cathode size and composition were evaluated with respect to their effects on analyte responses. The influence of the cathode cleaning processes and aging of metallic cathodes was studied in detail. As shown in earlier studies by Daughtrey and Harrison for solids analysis using HC sources [27], they found that cathodes tended to develop rounded

bottoms, which produce increased precision relative to new, flat-bottomed cathodes [26]. That group also developed some very interesting diagnostic tools to study the discharge power delivery as well as new power supply designs for operating stably with both continuous and pulsed HC sources [25,26]. Rapid power switching and stabilization are crucial in volume-limited sample applications, where the emission responses for the analytes last for less than 2 s. Also contributing in the area of microcavity hollow cathode use was the group of Winefordner [28], who obtained detection limits by optical emission spectroscopy for Cu and Pb at the level of 10 pg and 210 fg, respectively. The work to date indicates that the use of HC-AES could be a powerful tool in microsample analyses. Perhaps the use of simultaneous, multielement analysis would be an implementation that would lead to wider application.

Atomic Absorption Spectrometry

While the use of GD-AES to analyze solution residues has a long history, there is a large body of literature on the use of both atomic absorption (GD-AAS) and mass spectrometry (GDMS) to determine the sputtered species. Following on early work by Walsh and co-workers at the Australian CSIRO [29], which suggested that a glow discharge would be an ideal atomization/absorption volume, Gandrud and Skogerboe employed a GD cell in-line with the optical path of a commercial atomic absorption spectrometer [30]. Neat metal salt solutions (volumes not provided) were deposited on either graphite or aluminum 'platrodes'. The sputtered atom transients were much longer than shown for the HC emission sources, tending to last from 1.5 to 2 min. Residence times, atomization rates, and degree of matrix effects were found to depend on the cathode identity. Use of an Al platrode yielded detection limits ranging from 5 to 40 ng for a wide range of elements. Kirkbright and co-workers employed a similar arrangement to determine iodine [31]. Absorption transients for 5 μ L injections lasted for more than 30 s, an advantage over other non-flame methods of iodine determination. The detection limit when measuring the absorbance for the I (I) 183.0 nm line was found to be 30 ng, with a high level of reproducibility and low levels of matrix effects.

Bruhn and Harrison presented perhaps the most detailed study on the roles of the discharge conditions, discharge gas identity, and sputtering time on the performance of GD in solution dry residue analysis applications [32]. Hemicylindrical cathodes were prepared by first forming hollow cathodes of Cu and graphite, then milling away half of the cathode tube. Scanning electron micrographs were used to illustrate the effect of sputtering on the structure of the cathode surfaces. The size and density of hillocks and spires on the surfaces clearly indicated the extent of sputtering. Those studies supported all of the previous empirical data regarding the choice of cathode identity, etc., to achieve high analyte ablation rates in solution residue analysis. Trade-offs between sputtering

characteristics, blank values, and memory efforts were also discussed. Analytical response curves were generated for a range of elements using 10 μL aliquots of aqueous solutions. Under the conditions of 30 mA discharge current and an Ar pressure of 1.5 Torr, the duration of the transients varied between 0.5 and 1.5 min. Detection limits varied from 2 to 100 ng, with reproducibilities ranging from ~ 3 to 10% RSD, depending on the cathode identity and the surface treatment method.

The most extensive use of GD-AAS has been made by Chakrabarti and co-workers at Carleton University [33–38]. This work was initiated as a result of the commercial introduction of the Analyte Atomsources device for sputter production of atoms for analysis of bulk solids [39]. The high atomization rates of that system, and the coincident production of six ‘divits’ in the sample surface as a result of the placement of the gas jets, suggested that these depressions might be used to deposit aliquots of analyte solution conveniently. Extensive experiments were undertaken to understand the dynamics of the production of the transient atom population as solution residues were sputtered from the surface [33,34], an example of which is shown in Figure 13.7a for an Ag analyte solution [34].

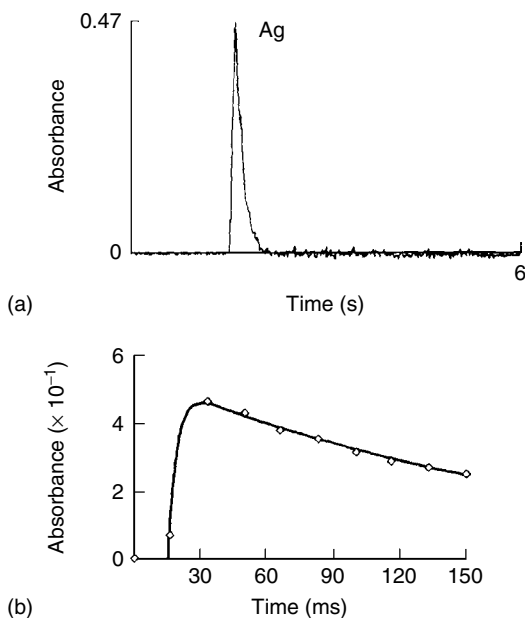


Figure 13.7 Transient atom populations of silver solution residues sputtered in a GD-AAS atomizer. (a) Transient optical absorption signal obtained for 50 ng of silver deposited as the nitrate salt and (b) calculated profile based on determined rate equations. Reprinted from Chakrabarti, C. L., Headrick, K. L., Hutton, J. C. and Marchand, B., *Spectrochim. Acta, Part B*, 1989, **44**, 385–394, with permission from Elsevier Science

Table 13.1 Rate constants for the transient mode of atomization of solution residues and AAS detection. Reprinted from Chakrabarti, C. L., Headrick, K. L., Hutton, J. C. and Marchand, B., *Spectrochim. Acta, Part B*, 1989, **44**, 385–394, with permission of Elsevier Science.

Element	Wavelength (nm)	k_a (s^{-1})	k_b (s^{-1})	k_a/k_b ratio
Ag	328.1	255 ± 20	5.4 ± 0.3	47
Al	309.3	24 ± 1	0.7 ± 0.1	34
Au	242.8	100 ± 10	21.7 ± 0.4	5
Cd	228.9	127 ± 13	9 ± 1	4
Co	240.7	235 ± 24	9.0 ± 0.6	26
Cu	324.8	132 ± 10	6.3 ± 0.1	21
Fe	248.3	44 ± 8	4.6 ± 0.5	10
Mn	279.5	110 ± 5	5.2 ± 0.2	21
Ni	232.0	51.8 ± 0.4	2.06 ± 0.08	25
Pb	283.4	393 ± 39	40.2 ± 0.3	10
V	318.4	28.6 ± 0.6	3.2 ± 0.3	9

The ablation rates of solution residues were compared with those of bulk metals, indicating that the former process was far more efficient than the latter. The production of the transient atom population and subsequent diffusion from the atomizer was modeled as a series of first-order rate equations of component k_a and k_b , respectively. Table 13.1 illustrates how the temporal characteristics vary across a range of elements. The resultant computation of the transient for Ag is shown in Figure 13.7b, for the first 150 ms of the discharge pulse. Ultimately, the use of short duration (50 ms), high instantaneous power pulses yielded the best analytical sensitivity as this produces the densest atom clouds [34]. In Table 13.2, the very impressive limits of detection and characteristic masses (1 μ L volumes) obtained in the pulsed mode of atomization for GD-AAS are listed [35]. Many of these values are comparable to those obtained by graphite furnace AAS.

Further developments by Chakrabarti and co-workers in the use of the GD-AAS method for solution sample analysis were directed at improving the hydrodynamics of the source as well as evaluations of matrix effects. Based on the previous modeling experiments, the researchers found that better gas/vacuum control led to higher sample ablation rates and longer residence times than realized in the commercial atomizer [37]. The result was a 5-fold improvement in peak-height absorbance sensitivity and a 1–2 orders of magnitude improvement in peak-area sensitivity [36]. All atomic spectrochemical methods are prone to matrix effects of one form or another. The presence of easily ionized salt species would be expected to be problematic in the GD source, particularly when operating in the conventional continuous dc discharge mode. Use of the pulsed mode of operation was found to eliminate these problems effectively [38]. The same results were obtained when continuous rf powering was employed. This suggests that the matrix effect is indeed related to the conductivity of the salt residue,

Table 13.2 Characteristic masses and limits of detection for the transient mode of atomization of solution residues and AAS detection. Reprinted with permission from Chakrabarti, C. L., Headrick, K. L., Hutton, J. C., Zhang, B., Bertels, P. C. and Back, M. H., *Anal. Chem.*, 1990, **62**, 574–586. Copyright 1990 American Chemical Society.

Element	Detection limit ^a (pg)	Characteristic mass (pg)	
		Transient atomization	GFAAS
Al	7.0	2.9	11.8
Ag	140	26	1.2
Au	550	47	7.3
Cd	27	4.9	0.39
Co	3000	130	5.4
Cr	0.5	0.25	1.8
Cu	43	8.0	3.0
Fe	210	30	2.8
Mg	0.5	0.11	0.30
Mn	68	25	1.7
Mo	0.34	0.041	5.4
Ni	1500	210	0.5
Pb	1600	210	7.7
V	185	68	69

^aMass giving a signal = 3σ /slope of the analytical calibration curve ($\sigma = 1$ standard deviation).

to which rf powering is immune. Both pulsed dc and continuous rf modes of operation were virtually immune to salt concentrations of up to 10% (w/v).

Mass Spectrometry

In terms of sensitivity, mass spectrometry is the most powerful of the GD sampling methods. In fact, GDMS is generally acknowledged as being the most sensitive of the bulk elemental analysis methods. Unfortunately, this high sensitivity, coupled with the ability also to gain isotopic information, has not translated to a large number of papers describing applications to solution residue analysis. This is due to a combination of reasons, including a smaller GDMS user base, the difficulties associated with sample interchange, and the very high level of deleterious effects resultant from residual water on ion source performance. The applications that have appeared, however, set out very well the possible scope of the methodology.

Daughtrey and Harrison [40] extended their HC-AES work to mass spectrometric detection with a modified spark source mass spectrometer system. Sampling of discharge ions through the base of the HC (cathode sampling) and the open end of the tube (anode sampling) were evaluated. The former showed

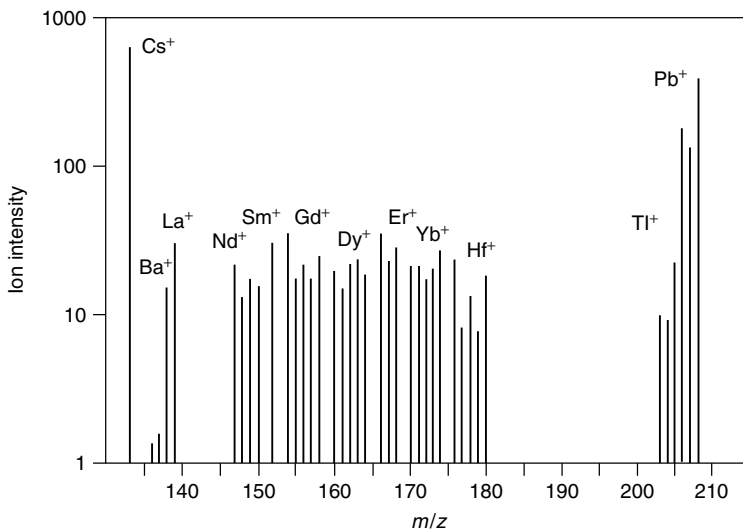


Figure 13.8 Glow discharge mass spectrum for rare earth elements obtained for a solution residue deposited within the Cu hollow cathode. 0.2 mL solution volume, 200 ppm concentration for each element. Reprinted with permission from Daughtrey, E. H. Jr and Harrison, W. W., *Anal. Chem.*, 1975, **47**, 1024–1028. Copyright 1975 American Chemical Society

substantial advantages in terms of signal intensity, stability, and ease of sample interchange, and so was adopted for all subsequent work by this group. The types of mass spectra that can be generated from solution residues deposited within the Cu hollow cathodes are illustrated in Figure 13.8. Sample-to-sample precision for four firings of 200 ppm multielement solutions (200 μ L volumes) showed variations of $\sim 17\%$ RSD, which are much better than the typical 30–35% RSD seen in spark source MS analyses. Donohue and Harrison [41] extended the HC source development through the implementation of rf powering provided by the spark source generator. Rf powering, of course, provides a means of direct sputtering of insulating materials, which includes solution residues deposited on metals or glass substrates. Sensitivities down to the 10–100 ng level were observed for many elements, with the respective elemental responses being fairly uniform except in a few instances. Conzemius and co-workers also investigated the use of HC ion sources, but with the unique feature of cryogenically cooling the solution residue, essentially analyzing an ice matrix [42]. High ion beam currents and good stability were reported. This approach, however, promoted excess amounts of oxide and water-related spectral interferences and no further reports of this methodology have been found.

Although hollow cathode GD geometries have certain advantages in sample handling and sensitivity in AES analysis of residues, the difficulty in sample

interchange with HCs in mass spectrometry makes them unattractive. Harrison and co-workers introduced the use of 'coaxial' discharge geometries as an easy means of sample introduction [43]. This geometry employs pin- or disk-shaped cathodes. Solution residues are prepared by applying the solution to the electrode surface and drying under an IR lamp. Different from HC sources, solutions deposited on coaxial cathodes produce long-lived signals, up to 1 h at sputtering currents of <1 mA. The precision (2–5% RSD) was equivalent to that on the same instrument when an HC source was employed, but at a sacrifice in sensitivity. Jakubowski and co-workers demonstrated the high sensitivity of GDMS analysis of dry solution residue analysis by using a quadrupole mass analyzer and disk- and pin-shaped electrodes [44]. The precious metals Pt and Ir were the target analytes. While disk-shape cathodes produce longer lived signals, the pin-shaped cathodes provide higher ion yields. Single ion monitoring of the transients enabled detection limits of <1 pg for these elements. Mason and co-workers applied this basic methodology to study the mobilization of Pb by the chemotherapy agent cisplatin [45]. Urine specimens were treated with nitric acid to destroy the organic constituents, a Bi spike was added to the reconstituted solution, and 10 μL of solution were applied to graphite disk electrodes. Linear calibration curves for Pb and Pt were obtained when using the Bi internal standard, with detection limits at the level of single ppb (tens of picograms) observed for both analytes.

The most extensive use of the solution deposition methodology in GDMS has been made at the Oak Ridge National Laboratory using a commercial, double-focusing GDMS instrument [46–50]. Rather than simply depositing solutions on solid metal electrodes, it was found that mixing the solution sample (200 μL) with 1 g of high-purity silver powder, drying the slurry, and then pressing the sample in pin form produced long-lived, intense analyte ion signals [46]. One advantage of using solution samples over direct solids analysis is the ability to generate calibration curves easily through serial dilution. Ratioing of the analyte signals to that of the Ag matrix also permits the use of relative sensitivity factors (RSFs). Use of solution-generated RSFs produced average relative errors of 14% at concentrations of 10–500 ppm, with detection limits of ~ 2 ppm in the sample volume. The precision and accuracy were greatly improved through the use of the isotope dilution methodology [47]. In this case, Pb isotopes in waste water could be determined at concentrations ranging from 2 to 80 ppm, with a sample-to-sample precision of <3% RSD and relative concentration errors of $\sim 2\%$.

Based on the success of the slurry-based sample preparation method, new applications and fundamental studies have been undertaken at Oak Ridge National Laboratory [48–50]. An extension of the isotope dilution determinations of Pb in waste water was the use of the method for raw and leached petroleum samples [48]. Elemental analysis of such samples by ICP sources is problematic owing to extensive extraction and matrix conversion requirements. Aqueous leachates prepared according to the EPA SW846 Method 3050 (an 8 h process)

were mixed with the Ag powder and pressed into pin form. Raw oil samples were mixed with the Ag powder, subjected to a low-temperature ashing step and then pressed into the form of pins. While many of the analytes showed comparable RSFs, the presence of large amounts of spectral background due to carbonaceous residues in the case of the non-digested samples caused large disparities for low-mass (<80 amu) elements. Use of standards prepared by the two respective sampling methods yielded high-quality results, with both the precision and accuracy of the GDMS analyses being equivalent to those of ICP-AES for the analysis of the same samples [48].

The differences in RSFs noted above for solution and bulk samples were investigated as a matrix effect by use of different anionic species for analytes with the solutions both dried on bulk metals and the compacted Ag powders [49]. Relative ion yields (RIYs) were found to be 'anion specific' and likely to be related to surface chemistries. Quantification through standard addition or use of matrix-matched standards compensate for such discrepancies. Finally, electrochemical deposition in combination with the compacted sample technology was investigated as a means of producing 'bulk' standards for GDMS [50]. In this approach, electrochemical reduction of aqueous ions on a compacted Ag electrode, followed by grinding, re-mixing, and pressing of a new pin specimen, showed promise as a way to prepare standards in a controlled fashion. Standard addition or isotope dilution could be employed. Encouraging preliminary results were presented, also suggesting that electrochemical preconcentration prior to GDMS may hold promise as an analytical method in itself.

13.3.2 DIRECT SAMPLE ASPIRATION

While there is but a single publication in the literature describing the direct aspiration of solutions into glow discharge sources [4], it is instructional to be aware of the approach, considering its pros and cons. Different from the use of a solution deposition approach, direct aspiration has the advantage of possibly being used in element-specific detection for liquid chromatography or in the simple flow injection mode. Schroeder and Horlick [4] demonstrated that (following desolvation) an HC discharge can be sustained in the presence of residual water vapors of a nebulized solution introduced at a flow rate of ~ 1 mL/min. As expected, the presence of water vapor effects the discharge conditions, requiring ~ 30 – 50% higher voltages to operate at comparable currents (e.g. ~ 350 vs 250 V at 150 mA). Evidence of incomplete removal of water vapor is shown in Figure 13.9 through the presence of the OH \cdot band in the spectral region of 310 nm in the optical emission spectrum. Also illustrated in the figure is the ability to subtract this continuous background through the use of a photodiode array (PDA) detector as a result of the high temporal stability of the plasma. Figure 13.10 demonstrates the temporal response of the Li (I) 670.8 nm atomic emission line upon introduction of a 1 $\mu\text{g}/\text{mL}$ concentration to the 1 mL/min

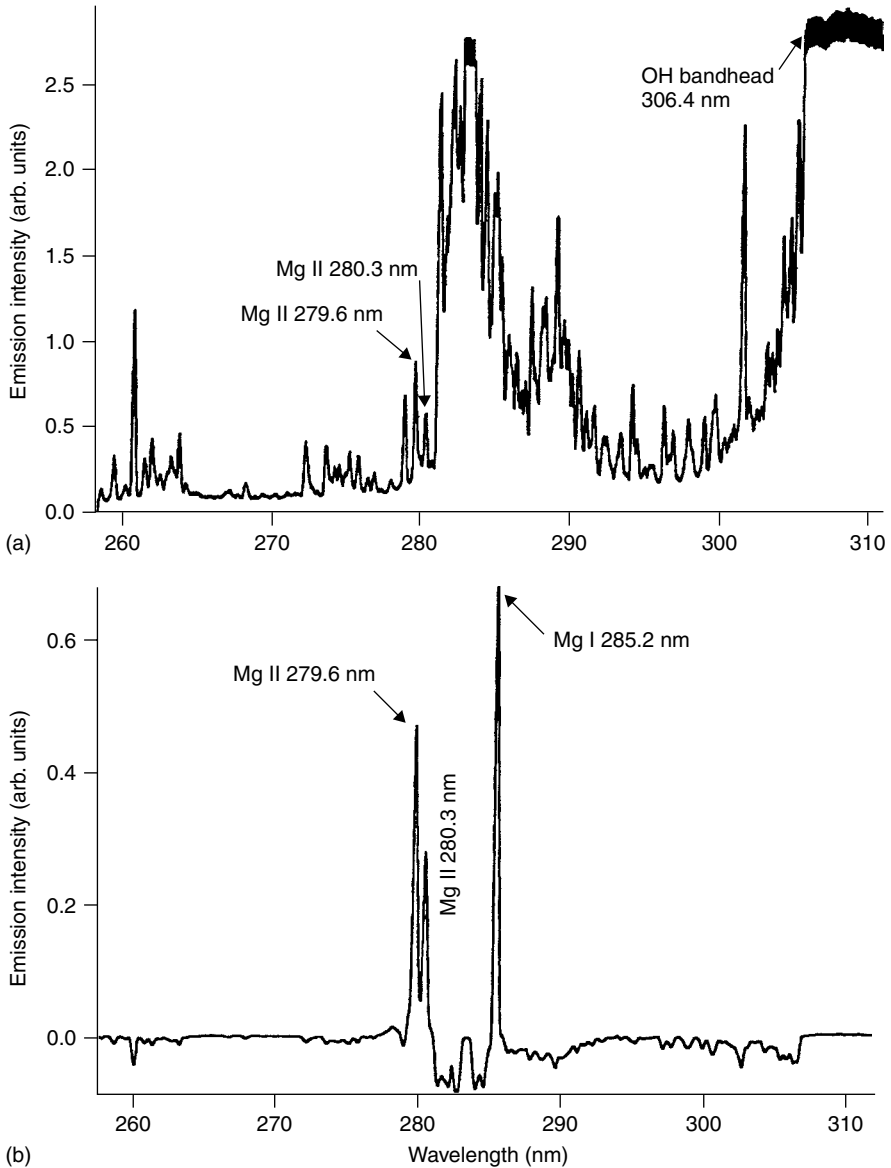


Figure 13.9 Optical emission spectra obtained for the continuous introduction of solutions into a hollow cathode source. (a) A solvent blank (background) emission spectrum and (b) the background subtracted signal for a 10 µg/mL Mg solution. Reprinted from Schroeder, S. G. and Horlick, G., *Spectrochim. Acta, Part B*, 1994, **49**, 1759–1773, with permission from Elsevier Science

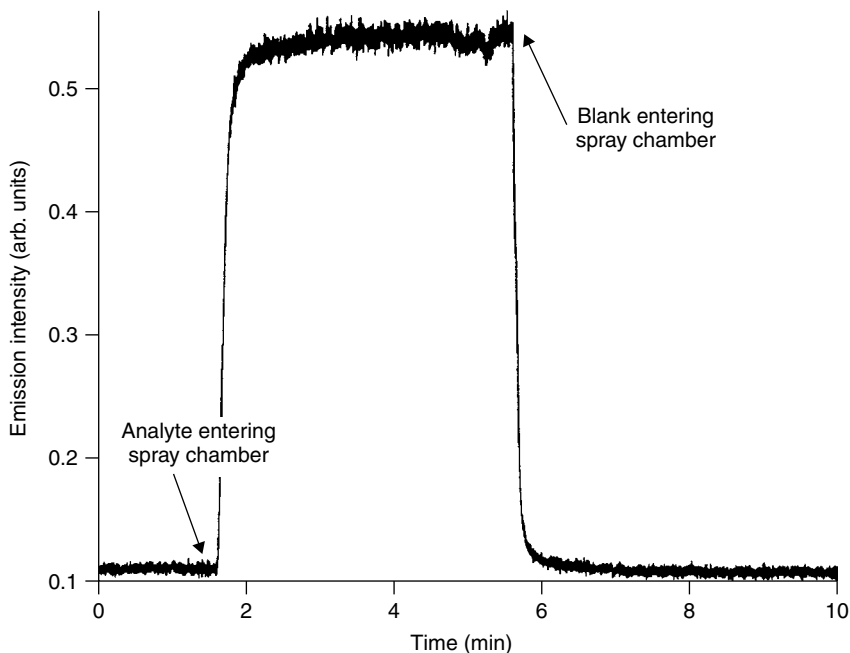


Figure 13.10 Temporal response of Li (I) 670.8 nm emission intensity obtained for the introduction of a $1 \mu\text{g/mL}$ concentration of Li to the 1 mL/min aqueous flow. Reprinted from Schroeder, S. G. and Horlick, G., *Spectrochim. Acta, Part B*, 1994, **49**, 1759–1773, with permission from Elsevier Science

aqueous flow. As can be seen, the analyte response rapidly reaches its maximum value and reflects a stable plasma. Unfortunately, the washout characteristics of the system are such that >20 s are required for the signal to reach 10% of its steady-state value upon reintroduction of blank solution. This behavior would need to be addressed for LC applications.

The detection limits for the device were evaluated for a number of alkali, alkaline earth, and transition metal analytes. Values ranged from 0.03 ng/mL for Li to 200 ng/mL for Zn, with the transition metals having higher excited state energies and the highest detection limits. The elevated values for the elements emitting in the UV–VIS region of the spectrum were partly attributed to the lower sensitivity of the PDA detector. A calibration curve for Li was found to have a high degree of linearity ($r^2 = 0.999$ for log-log) over three orders of magnitude (0.01–10 ppm). Future studies were suggested to include improved independent control of the carrier gas flow rates and the discharge gas pressure and ways to achieve better water vapor removal. Although no subsequent publications have appeared on this topic, there are a number of qualities demonstrated here which warrant further consideration.

13.3.3 TRANSPORT-TYPE LC/MS INTERFACES

The discussions in the previous section are a good introduction to the use of transport-type interfaces for solution introduction into GD sources. In fact, these devices are something of a hybrid between solution deposition (i.e. dry residue analysis) and the continuous aspiration (i.e. flowing system) approaches. As described in Section 13.2.3, the moving belt (MB) and particle beam (PB) LC/MS interfaces are explicitly designed to sample flowing liquid systems. They effect total analyte desolvation and solvent vapor removal, and delivery of analyte residues/particles into low pressure ($<10^{-3}$ Torr) ionization regions. In the case of GD excitation and ionization sources, the analytes are easily delivered to 1–10 Torr discharge environments.

The use of transport-type devices for liquid sample introduction was pioneered by Brackett and Vickers [9,51], who previously worked with solution residue analysis through the use of a wound filament sampling stage [52]. Their moving belt ‘flow glow’, shown in Figure 13.3, was designed specifically to address the throughput limitations of solution residue analysis, with an eye for its use as an element-specific detector for liquid chromatography. Initial evaluation of the apparatus was undertaken using aqueous $\text{Pb}(\text{NO}_3)_2$ solutions. Based on prior publications on the use of MB interfaces in organic mass spectrometry [5,6], the relevant performance parameters were evaluated [9]. The ability of the desolvation furnace to remove all remnants of the solvent is crucial to the performance of the GD source in terms of stability and net analytical signal. In Figure 13.11 the compromise between total analyte delivery and the addition of excess solvent for the introduction of a $83 \mu\text{g}/\text{mL}$ Pb solution is illustrated. As can be seen, increases in solution delivery rate increase the chain loading and consequently also the Pb (I) response (actually signal-to-noise ratio) up to a flow rate of $\sim 200 \mu\text{L}/\text{min}$. Beyond this point, the analyte response decreases and the discharge stability degrades. This response, along with a change in the appearance of the plasma glow, reflects the influence of excess solvent loading on the plasma. The available heat for desolvation is the controlling factor of the range of applicable flow rates. Furnace powers of $>25 \text{ W}$ were required for stable operation at the $200 \mu\text{L}/\text{min}$ flow rate, and lower applied powers were found to lead to noticeable perturbations of the discharge. Unfortunately, no temperature measurements in the desolvation region were reported and the maximum heating power of the system used was limited to 27 W .

The potential occurrence of memory effects in the MB interface was tested by the use of a discrete $5.0 \mu\text{L}$ aliquot of $17 \mu\text{g}/\text{mL}$ of a Pb solution to a single bead. During a single pass of the chain through the discharge region at a discharge current of 52 mA , the residue could be removed to undetectable levels. In a preliminary evaluation of the analytical characteristics of flow glow system, an exponential dilution apparatus was used to deliver the aqueous Pb solutions to the system. The resultant calibration curve showed excellent linearity over two

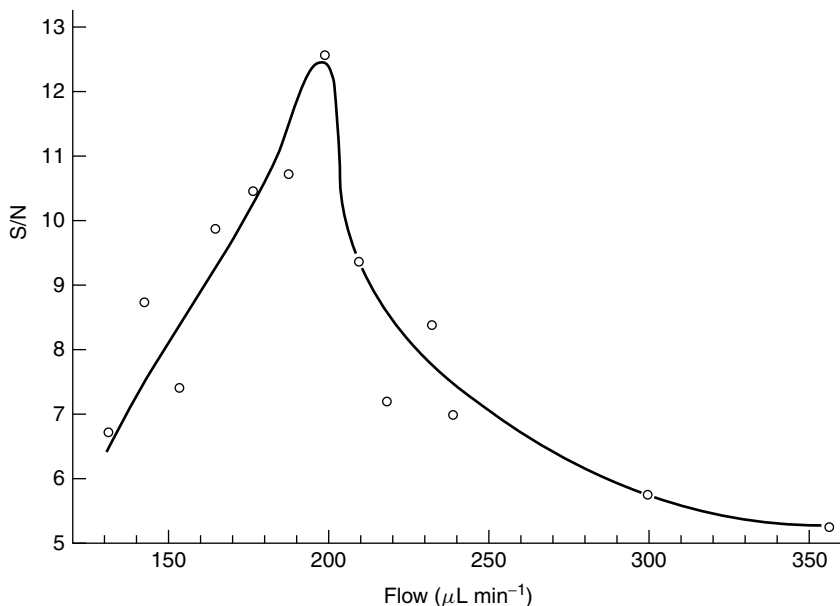


Figure 13.11 Influence of the solution delivery rate on the measured signal-to-noise ratio of the Pb (I) 405.8 nm line intensity for a Pb concentration of $83 \mu\text{g/mL}$. Reprinted from Brackett, J. M. and Vickers, T. J., *Spectrochim. Acta, Part B*, 1983, **38**, 979–985, with permission from Elsevier Science

orders of magnitude, and a detection limit of $0.9 \mu\text{g/mL}$ was obtained, with a precision of 8% RSD for multiple injections of $10 \mu\text{g/mL}$ Pb solutions.

Further characterization of the moving belt interface involved the study of the response characteristics for a number of elements having different excitation energy, compounds with different vaporization characteristics and a study of the influence of solvent identity on the source performance [51]. The detection limits for the elements Pb, Cd, B, and Cu ranged from 0.8 to $3.2 \mu\text{g/mL}$, with an unexpectedly high value for Cu attributed to the fact that the discharge anode, made of copper, contributed a significant background copper atom population. Pb, Cd, and Cu at concentrations of $50 \mu\text{g/mL}$ could be removed quantitatively from the bead chain in a single pass at a discharge current 58 mA, while B in the form of boric acid required a discharge current of 90 mA. Serious memory effects were found for Ca, Sr, and Ba introduced as aqueous chloride solutions. These compounds had the lowest volatilities of the suite of compounds studied. Although not specifically addressed by the authors, this indicates that vaporization, and not simple cathodic sputtering, plays a role in removing the analyte residues from the chain in the GD region. The fact that vaporization may be important was further illustrated as after an addition of $\text{Ba}(\text{NO}_3)_2$ to a Pb solution the Pb (I) response was severely suppressed. Analyte compound identity was shown

to be very important by the introduction of the volatile 2,4-pentanedione (acac) derivative of Al and the highly functionalized diphenylthiocarbazone derivative of Cd. In the former case, no Al (I) emission was observed as the compound apparently sublimed in the desolvation chamber. The heat-sensitive organo-Cd compound produced an adequate Cd (I) response as the metal was released from the organic matrix upon heating, although residual buildup of the carbonaceous material on the chain led to plasma instability and a complicated spectral background. Finally, the role of solvent composition was investigated for a number of common organics [51]. The plasma was shown to remain unaffected when introducing samples in acetonitrile, hexane, and carbon tetrachloride, but methanol and ethanol were found to lead to the extinction of the plasma. These results fall in line with the prior work with moving belt interfaces for mass spectrometry, setting design and operation challenges for future work. Unfortunately, no subsequent work has been published up to now.

Similar to that observed with transport-type interfaces for organic LC/MS, the noted difficulties with the MB interface eventually led the exploration of new interface approaches for solution introduction, specifically the particle beam (PB) interface [7,8]. The ability to work within a wide range of solution-phase compositions and flow rates, while still delivering dry analyte particles to the mass spectrometer ionization volume, are the advantages of the PB approach. Strange and Marcus [10] first described the use of a PB interface for the introduction of liquids into GD plasmas. In that work, Cu and Al disks were employed as the cathode in the discharge and the target at which the particle beam impinged. The observed optical emission spectra indicated that there was little or no water solvent carried over from the momentum separator at solution flow rates of 0.1–1.0 mL/min. Scanning electron micrographs of particles collected at the cathode surface indicated that particles ranging from 0.5 to 10 μm diameter were delivered to the source. While these studies established the feasibility of the PB-GD approach, two definite points of improvement were suggested. First, some means of target heating was needed for achieving sample vaporization, rather than relying on atomization by the GD sputtering. Second, the use of a hollow cathode geometry would clearly provide a more energetic excitation environment than the diffuse glow in the case of a planar cathode geometry.

A series of papers by You and Marcus [53–56] described the design aspects, the sample introduction characteristics, and the analytical performance of the particle beam–hollow cathode–atomic emission spectrometry (PB–HC–AES) system. As expected, the response in optical emission of the introduced analyte species depended on the discharge operating conditions of discharge gas pressure and identity and current [53]. The results were in general agreement with those obtained with other HC sources, such as He was found to be a better excitation environment than Ar, and the optimum discharge gas pressure was in the 2–4 Torr range. Furthermore, the analyte emission intensity was found to be

roughly proportional to the discharge current (up to 100 mA). A cursory evaluation of the roles of the nebulizer tip temperature, the solution flow rate, and the cathode block (vaporization) temperature was also presented. A key observation in that first work was the fact that introduction of a discrete volume of analyte solution (i.e. flow injection) into the solvent stream produced an analyte response profile with little or no dispersion. This type of response suggests that the memory effects are low and that the device can be effectively used as a chromatographic detector. For the case of analytical calibration curves obtained for Na and Cs (nitrates) with neat aqueous solutions, detection limits of 0.05 and 0.1 $\mu\text{g/mL}$ for 200 μL injections were achieved, which are about two orders of magnitude lower than those in the case of the planar cathode PB-GD geometry. When determining Cs in more complex media (5 M NaNO_3 /0.1 M KOH, pH = 14) representative of nuclear waste separation solutions, a severe suppression in the Cs (I) response was found to occur, even at a 1000 \times dilution. It was assumed that owing to the chemical form of Cs in solution, particulates were formed that were highly involatile. By a simple addition of an aliquot of HCl (5 : 1, sample:HCl), the Cs (I) response could be improved by two orders of magnitude over that for the neat aqueous solution. With nitric acid such an effect was not found and so it seems to be driven more by particle vaporization than by the pH, as the CsCl salt is more volatile than the nitrate form. With addition of HCl to the mock waste solutions the observed suppression could be overcome, and detection limits of 10 ng/mL for Cs could be obtained.

Detailed studies on the nebulization and particle transport characteristics in PB-HC-AES have been performed by Marcus and co-workers [54,55]. The respective roles of the nebulizer tip temperature, the He nebulizer gas flow rate, and the use of a supplemental He gas flow in the desolvation chamber were studied as a function of the analyte solution flow rate. Each of these parameters was found to contribute directly to the nebulization and vaporization processes in a more or less straightforward manner. It was important for the use of the device for LC applications to find that the Cu (I) analyte emission was insensitive to the water-methanol solvent composition, ranging from 100% water to 100% methanol. As with other pneumatic nebulizer systems, they obtained the highest analyte responses with the use of small ($\sim 50 \mu\text{m}$) inner diameter silica capillaries and high He nebulizer gas flow rates. Calibration curves for aqueous Cu, Pb, Fe, and Mg (including the aforementioned HCl addition) exhibited very good linearity, and the detection limits were found to range from 12 to 25 ng/mL for 200 μL injections.

One of the key advantages of the use of low-pressure, inert gas plasmas lies in the fact that there is no continuous emission background from atmospheric species such as C, N, O, H, etc. Of course, these are also components of most liquid sample matrices and LC mobile phases. Therefore, the determination of such elements depends on the use of highly efficient solvent removal methods; such as the PB interface. The use of standard flame and furnace atomic absorption

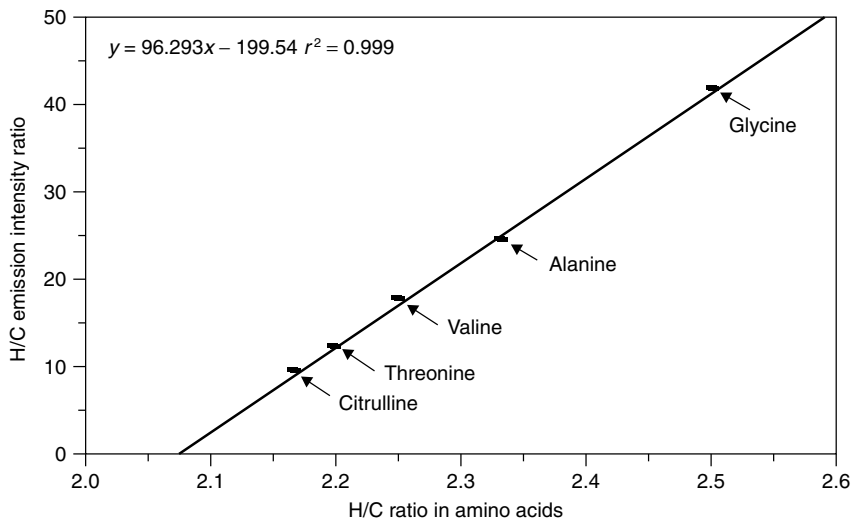


Figure 13.12 Comparison of experimentally obtained H (I) 656.3 nm/C (I) 193.0 nm emission intensity ratios to the actual atom ratios (H/C) for a number of amino acids. Reprinted with permission from You, J., Dempster, M. A. and Marcus, R. K., *Anal. Chem.*, 1997, **69**, 3419–3426. Copyright 1997 American Chemical Society

and ICP sources for such determinations is less attractive owing to low desolvation efficiencies and constant atmospheric background. The access to the above ‘gaseous’ elements enables some level of molecular information to be obtained in elemental speciation experiments. It is possible to determine atomic ratios of these elements and to elucidate the empirical formula of a compound eluting from a liquid chromatography column. The application of the PB–GD–AES approach to empirical formula determinations, and by extension to elemental speciation, is demonstrated in Figure 13.12 [56]. A plot of the ratio of the H (I) optical emission signal to that of C (I) as a function of the molar ratios of those elements for a range of aliphatic amino acids is shown. It can be seen that the agreement is excellent. A response curve for the H (I)/N (I) ratio has also been used to distinguish between a number of aromatic amino acids [57]. Elemental detection limits for H, C, and N in amino acid specimens can be established in the range ~0.1–3 ppm for 200 μL injection volumes. This corresponds to molecular detection limits of 10^{-9} M! In Table 13.3 the analytical figures of merit for the application of LC/PB–GD–AES for the analysis of a pair of organomercury compounds are shown, illustrating both the sensitivity and versatility of the methodology [57]. It is envisioned that this approach has great potential for applications in elemental speciation.

In order to obtain the most comprehensive information in elemental speciation, one would want unambiguous molecular weight and structural information

Table 13.3 Analytical response characteristics for organomercury compounds by PB–HC–AES. Reproduced by permission of The Royal Society of Chemistry from Dempster, M. A. and Marcus, R. K., *J. Anal. At. Spectrom.*, 2000, **15**, 43–48.

Analyte	Wavelength	r^2	Detection limit (in 200 μL injections)
Hg in thimerosal	435.8	0.9979	2.9×10^{-11} mol thimerosal (0.03 ppm Hg)
Hg in merbromin	435.8	0.9995	4.1×10^{-11} mol merbromin (0.04 ppm Hg)
C in thimerosal	538.0	0.9834	3.5×10^{-8} mol thimerosal (19 ppm C)
C in merbromin	538.0	0.9934	5.2×10^{-8} mol merbromin (63 ppm C)
Na in thimerosal	589.0	0.9943	1.4×10^{-10} mol thimerosal (0.02 ppm Na)
Br in merbromin	614.9	0.9997	1.3×10^{-10} mol merbromin (0.1 ppm Br)
H in thimerosal	656.3	0.9877	2.2×10^{-9} mol thimerosal (0.1 ppm H)

on compounds eluting from the separation column. Thus, ideally, one would have a mass spectrometry ion source capable of accepting LC flows and still produce meaningful molecular and elemental mass spectra. Traditional ‘organic’ ionization sources such as electron impact (EI) and chemical ionization (CI), while excellent at providing information on the molecular level, are virtually useless for the ionization of free metal atoms and small inorganic complexes. By the same token, ICP-MS is a very powerful means of performing elemental analysis of liquid specimens, but by its nature all molecules are decomposed down to the atomic level. One accordingly needs an ionization source of modest energy such that organic compounds can still be kept intact, while some atomic species yield simple ‘elemental’ mass spectra.

Gibeau and Marcus used the same approach as described above, namely a particle beam interface and a glow discharge ionization source, to realize a versatile LC detector [58]. Different from the AES application, the beam of particles impinges directly on a disk-type cathode where they are vaporized/sputtered into the gas phase for subsequent ionization. Although not nearly as efficient as a hollow cathode source (to be pursued in the future), working with this geometry has demonstrated that the basic approach provides the sorts of information desired in elemental speciation. As in the case of AES, experiments with amino acids have been done to characterize this technique. In Figure 13.13 the PB–GD mass spectrum for a 200 μL injection of 10^{-2} M tryptophan is shown. As in all other ‘small’ molecules examined to date, the structure of this spectrum is *very* similar to those generated with traditional EI sources, and in fact identification with the aid of standard databases is possible. One observes signals representative of the molecular weight of the molecule, and the successive loss of organic functional groups. The mass spectra obtained with ‘elemental’ solutions are very simple in structure, with little or no evidence of oxide species or the like. The sensitivity of the method at an early stage of development is comparable to that obtained when coupling PB interfaces to EI sources, and the detection limits for both organic molecules and elemental species are at the single nanogram level.

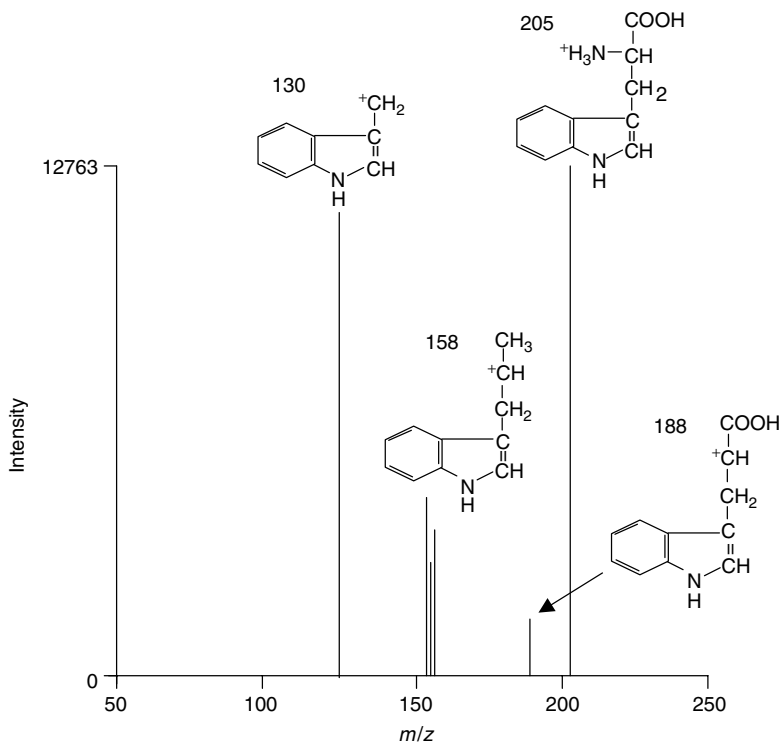


Figure 13.13 Particle beam–glow discharge (PB–GD) mass spectrum obtained for a 200 μL injection of 10^{-2} M tryptophan. Reprinted with permission from Gibeau, T. E. and Marcus, R. K., *Anal. Chem.*, 2000, **72**, 3833–3840. Copyright 2000 American Chemical Society

Surprisingly, this value is in line with commercial ICP-MS instrumentation. The flexibility of the LC/PB–GDMS technique is shown by the separation and speciation of mixtures of inorganic and organo-lead compounds; as with the GD ionization source, spectra are produced which accurately represent both types of species [59]. Also, a separation and identification of mixtures of polycyclic aromatic hydrocarbons (PAHs), steroids, and selenoamino acids has been carried out. It is believed that this methodology holds great promise in providing more comprehensive speciation information than any other MS source.

13.4 REFERENCES

1. Loving, T. J.; Harrison, W. W. *Anal. Chem.* 1983, **55**, 1526–1530.
2. Ratliff, P. H.; Harrison, W. W. *Appl. Spectrosc.* 1995, **49**, 863–871.
3. Birks, F. T. *Spectrochim. Acta* 1954, **6**, 169–179.

4. Schroeder, S. G.; Horlick, G. *Spectrochim. Acta, Part B* 1994, **49**, 1759–1773.
5. Scott, R. P. W.; Scott, C. G.; Munroe, M.; Hess, J. Jr. *J. Chromatogr.* 1974, **99**, 395–405.
6. Games, M. B. *Adv. Mass Spectrom.* 1986, **10B**, 323.
7. Willoughby, R. C.; Browner, R. F. *Anal. Chem.* 1984, **56**, 2626–2631.
8. Creaser, C. S.; Stygall, J. W. *Analyst* 1993, **118**, 1467–1480.
9. Brackett, J. M.; Vickers, T. J. *Spectrochim. Acta, Part B* 1983, **38**, 979–985.
10. Strange, C. M.; Marcus, R. K. *Spectrochim. Acta, Part B* 1991, **46**, 517–526.
11. Pevtsov, G. A.; Krasil'shchik, V. Z. *J. Anal. Chem. USSR (Engl. transl.)* 1963, **18**, 1140–1142.
12. Büger, P. A.; Fink, W. *Fresenius' J. Anal. Chem.* 1969, **244**, 314–315.
13. Rudnevskii, N. K.; Maksimov, D. E.; Vysotskii, V. V. *Spectrosc. At. Mol.* 1969, **72**, 880–882.
14. Berezin, I. A. *Zavod. Lab.* 1961, **27**, 862–863.
15. Little, P. F.; Engel, A. V. *Proc. R. Soc. London, Ser. A* 1954, **224**, 209–230.
16. Slevin, P. J.; Harrison, W. W. *Appl. Spectrosc. Rev.* 1975, **10**, 201–255.
17. Caroli, S. *Improved Hollow Cathode Lamps for Atomic Spectroscopy*, Ellis Horwood, Chichester, 1985.
18. Harrison, W. W.; Prakash, N. J. *Anal. Chim. Acta* 1970, **49**, 151–159.
19. Prakash, N. J.; Harrison, W. W. *Anal. Chim. Acta* 1971, **53**, 421–427.
20. Harrison, W. W.; Daughtrey, E. H. *Anal. Chim. Acta* 1973, **65**, 35–40.
21. Daughtrey, E. H.; Harrison, W. W. *Anal. Chim. Acta* 1973, **67**, 253–258.
22. Daughtrey, E. H. Jr.; Harrison, W. W. *Anal. Chim. Acta* 1974, **72**, 225–230.
23. Ryu, J. Y.; Davis, R. L.; Williams, J. C.; Williams, J. C. Jr. *Appl. Spectrosc.* 1988, **42**, 1379–1387.
24. Chen, F.; Williams, J. C. *Anal. Chem.* 1990, **62**, 489–495.
25. Tseng, J.; Williams, J. C. *Anal. Chem.* 1991, **63**, 1933–1942.
26. Cai, X.; Williams, J. C. *Appl. Spectrosc.* 1995, **49**, 890–899.
27. Daughtrey, E. H.; Donohue, D. L. Jr.; Slevin, P. J.; Harrison, W. W. *Anal. Chem.* 1975, **47**, 683–688.
28. Morgan, C. A.; Davis, C. L.; Smith, B. W.; Winfordner, J. D. *Appl. Spectrosc.* 1994, **48**, 261–264.
29. Gatehouse, B. M.; Walsh, A. *Spectrochim. Acta* 1960, **16**, 602–604.
30. Gandrud, B. W.; Skogerboe, R. K. *Appl. Spectrosc.* 1971, **25**, 243–246.
31. Kirkbright, G. F.; West, T. S.; Wilson, P. J. *Anal. Chim. Acta* 1974, **68**, 462–465.
32. Bruhn, C. G.; Harrison, W. W. *Anal. Chem.* 1978, **50**, 16–21.
33. Chakrabarti, C. L.; Headrick, K. L.; Bertels, P. C.; Back, M. H. *J. Anal. At. Spectrom.* 1988, **3**, 713–723.
34. Chakrabarti, C. L.; Headrick, K. L.; Hutton, J. C.; Marchand, B. *Spectrochim. Acta, Part B* 1989, **44**, 385–394.
35. Chakrabarti, C. L.; Headrick, K. L.; Hutton, J. C.; Zhang, B.; Bertels, P. C.; Back, M. H. *Anal. Chem.* 1990, **62**, 574–586.
36. Chakrabarti, C. L.; Headrick, K. L.; Hutton, J. C.; Bertels, P. C.; Back, M. H. *Spectrochim. Acta, Part B* 1991, **46**, 183–192.
37. Hutton, J. C.; Chakrabarti, C. L.; Bertels, P. C.; Back, M. H. *Spectrochim. Acta, Part B* 1991, **46**, 193–202.
38. Absalan, G.; Chakrabarti, C. L.; Headrick, K. L. *Can. J. Appl. Spectrosc.* 1996, **41**, 51–60.
39. *Atom Source*, Analyte Corp., Grants Pass, OR.
40. Daughtrey, E. H. Jr.; Harrison, W. W. *Anal. Chem.* 1975, **47**, 1024–1028.
41. Donohue, D. L.; Harrison, W. W. *Anal. Chem.* 1975, **47**, 1528–1531.
42. Foss, G. O.; Svec, H. J.; Conzemius, R. J. *Anal. Chim. Acta* 1983, **147**, 151–162.

43. Mattson, W. A.; Bentz, B. L.; Harrison, W. W. *Anal. Chem.* 1976, **48**, 489–491.
44. Jakubowski, N.; Stuewer, D.; Toelg, G. *Spectrochim. Acta, Part B* 1991, **46**, 155–163.
45. Evetts, I.; Milton, D.; Mason, R. *Biol. Mass Spectrom.* 1991, **20**, 153–159.
46. Barshick, C. M.; Duckworth, D. C.; Smith, D. H. *J. Am. Soc. Mass Spectrom.* 1993, **4**, 47–53.
47. Barshick, C. M.; Smith, D. H.; Wade, J. W.; Bayne, C. K. *J. Anal. At. Spectrom.* 1994, **9**, 83–87.
48. Barshick, C. M.; Smith, D. H.; Hackney, J. H.; Cole, B. A.; Wade, J. W.; *Anal. Chem.* 1994, **66**, 730–734.
49. Hess, K. R.; Barshick, C. M.; Duckworth, D. C.; Smith, D. H.; *Appl. Spectrosc.* 1994, **48**, 1307–1315.
50. Day, D. A.; Zook, A. L.; Barshick, C. M.; Hess, K. R. *Microchem. J.* 1997, **55**, 208–221.
51. Brackett, J. M.; Vickers, T. J. *Spectrochim. Acta, Part B* 1984, **39**, 837–841.
52. Brackett, J. M.; Vickers, T. J. *Spectrochim. Acta, Part B* 1982, **37**, 841–847.
53. You, J.; Fanning, J. C.; Marcus, R. K. *Anal. Chem.* 1994, **66**, 3916–3924.
54. You, J.; Depalma, P. A. Jr.; Marcus, R. K. *J. Anal. At. Spectrom.* 1996, **11**, 483–490.
55. You, J.; Dempster, M. A.; Marcus, R. K. *J. Anal. At. Spectrom.* 1997, **12**, 807–815.
56. You, J.; Dempster, M. A.; Marcus, R. K. *Anal. Chem.* 1997, **69**, 3419–3426.
57. Dempster, M. A.; Marcus, R. K. *J. Anal. At. Spectrom.* 2000, **15**, 43–48.
58. Gibeau, T. E.; Marcus, R. K. *Anal. Chem.* 2000, **72**, 3833–3840.
59. Gibeau, T. E.; Marcus, R. K. *J. Chromatogr. A* 2001, **915**, 117–128.

14

GC Speciation with GDMS Detection

J. A. CARUSO and L. MILSTEIN*

University of Cincinnati, Department of Chemistry, Cincinnati, OH, USA

14.1 INTRODUCTION

Glow discharge sources, owing to their low operating powers and pressures, are excellent detectors for elemental speciation studies, particularly when coupled to mass spectrometers (GDMS). GDMS can provide structural information for gaseous samples, for which there are no existing standard reference materials. The instrumentation involved in gas chromatography (GC)–rf-GDMS speciation studies was examined through several modifications.

Quantitative information was obtained for organotin compounds and tetraethyl-lead from a certified reference material (CRM) that was GC introduced into a helium glow discharge MS source. Mass spectra resembling electron impact ionization were also obtained for these compounds. Tunable mass spectral fragmentation is demonstrated with respect to source pressure and helium–argon mixed gas composition of the glow discharge source. Rf-glow discharges have been coupled to quadrupole mass analyzers for elemental speciation studies. Elemental speciation studies were performed with a dc gas sampling glow discharge ionization source and a pulsed glow discharge, both coupled to a time-of-flight (TOF) mass spectrometer. Elemental and molecular information were obtained concurrently with these sources. Both of these sources have the potential to be interfaced with gas chromatography.

* Present address: RTI International, Research Triangle Park, NC, USA.

14.2 ELEMENTAL SPECIATION

Speciation, or the technique associated with detection of different ‘forms’ of an element, is mandatory for assessing potential biological, geological, toxicological and environmental hazards. Element-selective detectors, particularly inductively coupled plasma mass spectrometry (ICP-MS), coupled to liquid chromatography (LC), have been used for some time for this purpose. ICP-MS provides excellent detection limits, has multielemental and isotopic capabilities, and is easily interfaced with LC [1]. The limit to this technique, however, is the inability of the detector to provide any molecular or structural information about the chemical species of interest. ICP-MS only detects the monitored element (s), because the high powers and pressures needed to operate the ICP destroy the nebulized species and render it to the elemental state.

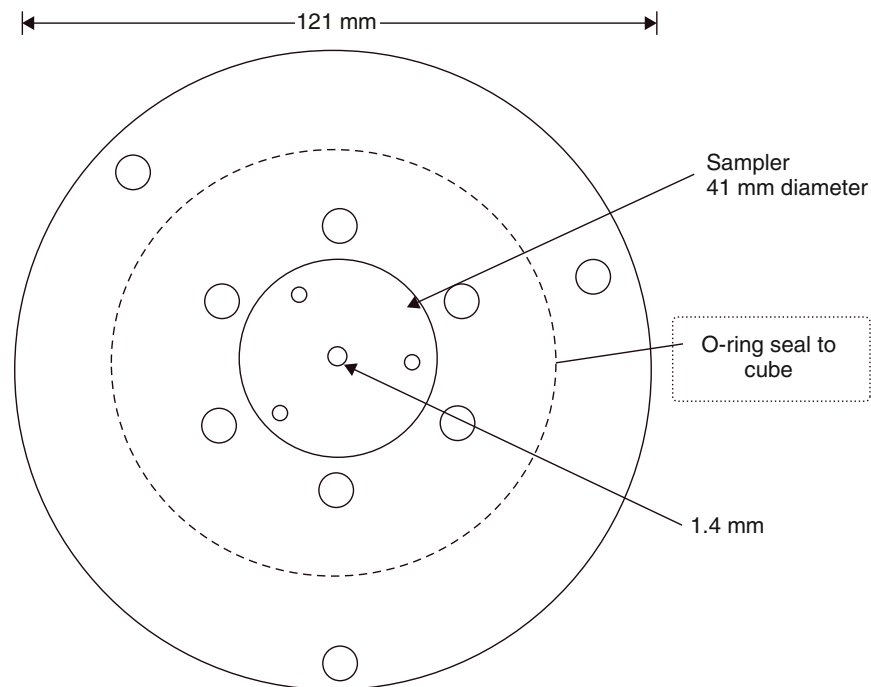
A current goal in the field of elemental speciation studies is to obtain elemental and molecular information about a chemical species with the same ionization source. Glow discharge mass spectrometry (GDMS) is one possible alternative to providing such information in addition to its counterpart, low-pressure ICP-MS [2–6]. These ‘softer’ ionization sources, unlike the ICP operated in its atmospheric pressure mode, provide information about the element (usually a metal) of interest while forming the metal species’ fragments. Thus, identification of chemical species can be obtained even when standard reference materials (CRMs) are absent for these substances.

14.3 INSTRUMENTATION

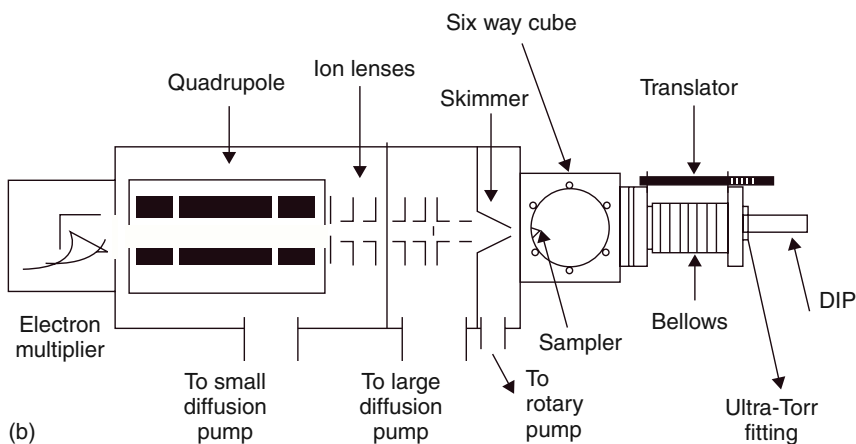
14.3.1 GLOW DISCHARGE SOURCES

The initial design of the rf-GDMS used for gas chromatographic speciation analyses was developed by Giglio and Caruso [7]. It was mounted on an ICP-MS instrument (VG Elemental) in place of the original torchbox, after appropriate interlocks had been bypassed. The rf-GD plasma was formed in a stainless-steel shaped cube chamber mounted on the sampling cone (Figure 14.1) and equipped with a larger orifice than the sampler used for the ICP-MS. The plasma interface had the same dimensions as the aluminum front plate on the ICP-MS.

This same source was then interfaced with gas chromatography [8]. High-purity Al 6161 T6 served as the cathode. A direct GD insertion probe, based on the design by Duckworth and Marcus [9], fit into the cube and was connected to the rf matching network and generator. The probe was placed 1 cm away from the sampling orifice. Helium was used as the discharge gas as it has a low molecular weight ($m/z = 4$), exhibits fewer mass spectrometric interferences with the analytes, and contributes to small amounts of cathodic sputtering and scattering. Importantly, its high ionization potential contributes favourably to analyte ionization. Helium gas was passed through a heated copper coil before being introduced into the GD plasma. A tee was used to connect the stainless-steel tube containing the GC column, orthogonal to the heated helium flow.



(a)



(b)

Figure 14.1 Experimental setup of the GDMS with an expanded view of the stainless-steel cube chamber mounted on a sampling cone. Reprinted from Giglio, J. J. and Caruso, J. A., *Appl. Spectrosc.*, 1995, **49**, 900–906, with permission of The Society of Applied Spectroscopy

This design was further improved [10] by using a cell body in place of the cube, which served as the anode. The probe, which was inserted inside the cell limiting the cell volume to 1.8 cm^3 , was mounted on a translational stage in order for the aluminum cathode to be positioned reproducibly at a fixed distance from the orifice opening. This allowed optimization of the sampling distance with respect to the studied analyte species. Radiofrequency power was supplied by a 13.56 MHz generator and impedance matched by an automated matching network. The source operated at powers ranging from 10 to 40 W and pressures from 6 to 30 Torr.

The design of the GDMS source was modified further [11] to make it applicable to controllable fragmentation studies. In place of the insertion probe, an aluminum cathode was cemented inside the ceramic tube with a $\frac{1}{16}$ in stainless-steel (SS) tube securely fitted into it providing electrical contact. The grounded sampler plate, in this case, served as the anode. This new design allowed viewing the glow discharge, which was not possible before. Also, the position of the transfer line capillary tube relative to the sampling orifice was not critical due to the cell symmetry. Figure 14.2 shows a close-up of the GD cell. The plasma can be seen with this design since the discharge tube is visually accessible. Helium was used for initial tunable source pressure studies [11] and mixed helium–argon gas was the discharge gas for the gas mixture studies [6]. Once again, a 13.56 MHz impedance matched generator was used.

The dc gas-sampling glow discharge (GSGD) and the dc pulsed glow discharge are some of the most recent sources that have not been interfaced with GC, but have high potential for such. The GSGD source, as depicted in Figure 14.3, designed by Hieftje and co-workers [12,13], replaced the sampling plate on the right-angle ICP-TOFMS. The discharge source was of the hollow cathode type and constructed from 314 stainless steel; $\frac{1}{16}$ in i.d. SS chromatographic tubing was inserted into the cathode and positioned flush with the bottom of the hollow cavity. A Macor™ (electrically insulating) spacer and insert were used to restrict the discharge to the area between the cathode and the grounded skimmer, yielding a more stable plasma. The optimal distance between the cathode surface and skimmer was found to be 11.0 mm. A copper cooling coil was connected to the front of the GSGD and spectrometric interface. The coil, and also the interface, were chilled to 5°C during glow discharge operation. In the original design [12], helium gas was the source gas used for the elemental studies and argon for the molecular studies. For the modified design [13], helium was exclusively used because the ionization mode could be ‘switched’ by changing the polarity of voltage applied to the sample-introduction plate. This modulator produced reproducible waveforms that could detect signals from a transient signal generator such as the gas chromatograph [13].

In the latter design, the GSGD atomic mode current, voltage and pressure were 25 mA, 350 V and 5.50 Torr, respectively, and the molecular mode conditions were 15 mA, 210 V and 5.50 Torr.

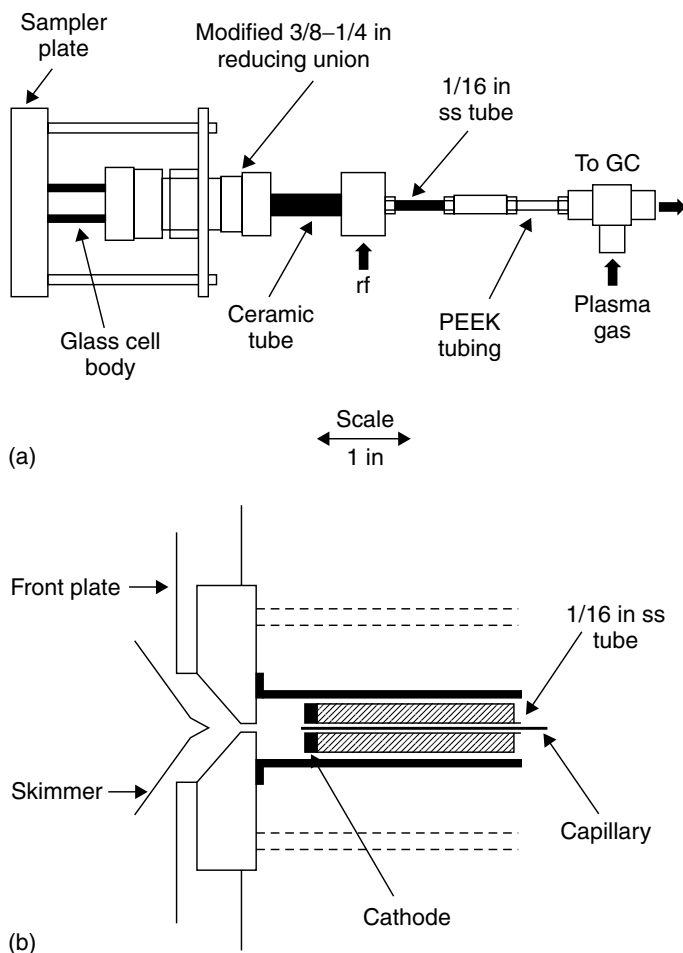


Figure 14.2 (a) Schematic diagram of the GD cell illustrating the cell symmetry and the replacement of the direct insertion probe with an aluminum cathode. (b) Close-up of the cell. Reproduced with permission of The Royal Society of Chemistry from Belkin, M., Waggoner, J. W. and Caruso, J. A., *Anal. Comm.*, 1998, **35**, 281–283

A microsecond pulsed dc glow discharge source was studied by Majidi and co-workers [14,15]. The schematic diagram in Figure 14.4 depicts the glow discharge chamber equipped with a $\frac{1}{2}$ in diameter direct insertion probe inlet and a 1 mm exit orifice for the ions to be extracted into the TOF mass spectrometer. The high-voltage microsecond pulses, which control the fragmentation process, were maintained by a digital delay generator. The source operated at pressures between 0.4 and 0.5 Torr, an applied potential of 1.0 kV, a pulse duration of 20 μ s and a frequency of 100 Hz.

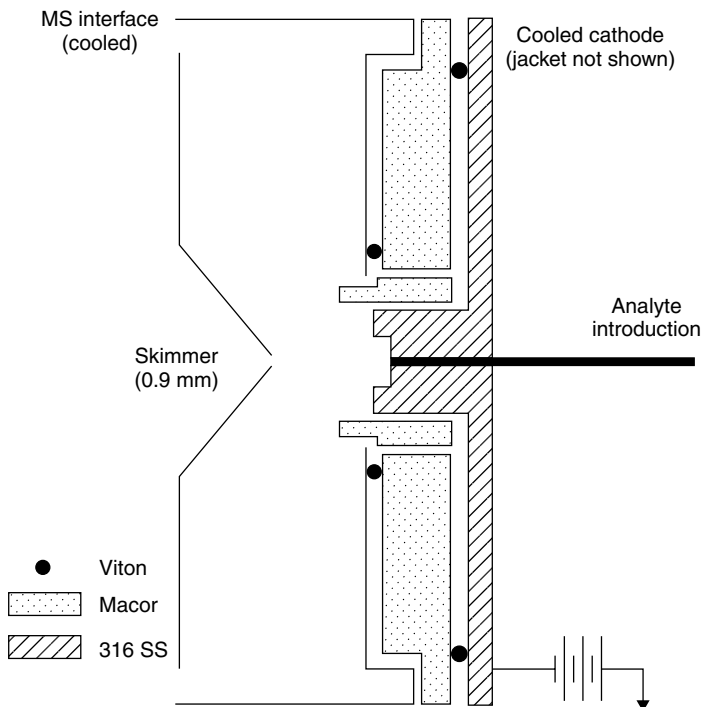


Figure 14.3 Schematic diagram of the GSGD source. Reproduced with permission of The Royal Society of Chemistry from Steiner, R. E., Lewis C. L. and Majidi, V., *J. Anal. At. Spectrom.*, 1999, **14**, 1537–1541

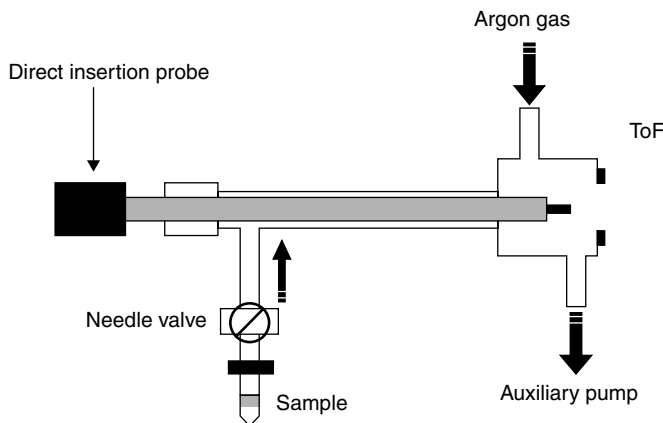


Figure 14.4 Schematic diagram of the microsecond pulsed dc glow discharge source interfaced with the TOF mass spectrometer. Reproduced with permission of The Royal Society of Chemistry from Majidi, V., Moser, M., Lewis, C., Hang, W. and King, F. J., *Anal. At. Spectrom.*, 1997, **12**, 1255–1261

14.3.2 GAS CHROMATOGRAPHY–GLOW DISCHARGE INTERFACES

In the first two GC–GDMS studies, the fused-silica capillary transfer line, extending from the GC oven in which it is connected to the column, met the direct insertion probe and sampler orifice on the mass spectrometer at an angle. In the modified design, ('Design 3'), the $\frac{1}{16}$ in i.d. SS tube and the cathode are together so the transfer line is threaded through the tube and positioned directly in front of the orifice (Figure 14.2). This latter design was found to eliminate discharge asymmetry.

As mentioned before, the GSGD employed SS chromatographic tubing which contained the fused-silica capillary tubing leading from the sample introduction methods used: flow cell and exponential dilution cell [13]. GC could conceivably be employed in the future as the sample introduction method. For the pulsed GD source, volatile and semi-volatile samples were contained in vials and attached to a metering leak valve extending from the GD [14].

14.3.3 MASS SPECTROMETER SYSTEMS

For all of the Caruso group studies [7,8,10,11], the GD apparatus was used in place of the ICP torchbox, providing ions to the quadrupole mass spectrometer. The six-way cube was designed to be interfaced with the sampling cone already present on the ICP-MS instrument [7,8] whereas the latter sources were equipped with their own sampling cones [10,11].

Time-of-flight mass spectrometry (TOFMS) was used for the GSGD and pulsed glow discharge studies. For the latest GSGD studies (of the switched dc design), steering plates were used to direct the ion packets into the TOF tube [13]. The polarity of the electrode was changed to obtain either atomic or molecular information. The TOF used for the pulsed glow discharge [14] was an angular-type instrument, operated in the reflectron mode. It was positioned orthogonal to the GD ion beam to facilitate the pulsed injection of sample ions into the TOFMS system.

14.3.4 GAS CHROMATOGRAPHY

Gas chromatographs utilizing capillary columns were interfaced with rf-GDMS sources [8,10,11]. These columns were connected to a deactivated fused-silica retention gap on one end and a deactivated fused-silica transfer line on the other end. The transfer line was inserted into a $\frac{1}{16}$ in SS tube. When information about high boiling-point analytes was desired (e.g. tetrabutyltin), the transfer line was heated and monitored with several thermocouples and transformers at a high temperature ($\sim 250^\circ\text{C}$). This high temperature was chosen to prevent analyte condensation in the transfer line or cell interior. In the latest set of experiments,

the column itself served as the transfer line [6] to eliminate dead volume and peak band broadening.

Guzowski and Hieftje mentioned that GC will be interfaced with the switched dc-GSGD to obtain detection limits for their analytes [13]. Majidi and co-workers also indicated that chromatography will be interfaced with the pulsed glow discharge source to analyze multi-component samples [14].

14.4 PRACTICAL ASPECTS AND RESULTS

14.4.1 QUANTITATIVE INFORMATION

One of the advantages of using ICP-MS in its regular atmospheric pressure mode is that it yields low limits of detection (sub-nanogram to sub-picogram) for elemental analysis studies of liquid samples [1]. The rf-GDMS yields comparable detection limits for analytes introduced by GC. Detection limits were determined based on the signal for the major element (metal) only in the single ion monitoring (SIM) mode. Volatile organotin compounds were introduced into each GD source. The detection limits for tetramethyltin (TMT) improved only slightly as the GD design source changed, whereas the sensitivity (indicated by the slopes of the calibration curves) improved by a factor of three on going from the second to the third GC-GDMS design [11] (Table 14.1). This suggests that the calculation of the limits of detection (three times the standard deviation of the background) was hampered by the high variation of the capillary column's background noise. Hence the third GC-GD design is more favorable for improved elemental sensitivity of trace-level analytes.

For GSGD-MS, atomic and molecular detection limits were reported for several halogenated compounds as shown in Table 14.2. These compounds were introduced by the exponential dilution system. The values are expressed in the units of pg s^{-1} . A linear calibration graph over more than two orders of magnitude of concentration was achieved. Hieftje and co-workers demonstrated that the

Table 14.1 Figures of merit for tetramethyltin (TMT): a comparison using the second and third GC-GD-MS designs (adapted from ref. 11).

Parameter	Design 2	Design 3
Linear range (decades)	2.5	2
Slope (counts pg^{-1})	681	2237
Correlation coefficient	0.9950	0.9997
Log-log slope	1.011	0.973
MDA (pg)	1.2	1.0
Detection limit (pg)	0.6	0.6
RSD (%)	<5	3.5

Table 14.2 Detection limits (pg s^{-1}) obtained with a modulated GSGD source at a switching frequency of 10 Hz (the values in parenthesis represent the m/z values used for quantification) (adapted from ref. 13).

Compound	Atomic detection limit	Molecular detection limit
Chloroform	36 (35)	148 (83)
Carbon tetrachloride	24 (35)	184 (117)
Methylene chloride	91 (35)	197 (84)
Trichloroethylene	98 (35)	247 (95)
1-Chlorohexane	40 (35)	122 (27)
Bromoform	3.9 (79)	14 (93)
1,2-Dibromoethane	52 (79)	44 (27)

atomic detection limits for the GSGD are comparable to those for other plasma-based ionization sources; however, plasma switching slightly compromised the detection limits for the halogens compared with the microwave-induced plasma (MIP) coupled to mass spectrometry [13].

14.4.2 ANALYSIS OF A REAL WORLD SAMPLE

NIST SRM 2715 Lead in Reference Fuel was diluted in hexane (1 + 9) and injected into the GD cell [8]. The GD was operated at 40 W and a source pressure of 0.8 mbar. The calculated concentration (as lead) was $760 \pm 50 \text{ mg g}^{-1}$, which was in agreement with the certificate value of $784 \pm 4.00 \text{ mg g}^{-1}$. High background noise may also have contributed to the high uncertainty of the calculated concentration value.

14.4.3 QUALITATIVE INFORMATION: MOLECULAR STRUCTURAL INFORMATION

The lower powers and pressures of GDMS promote 'softer' ionization than atmospheric pressure ICP-MS, allowing mass spectral fragmentation patterns to be generated. For example, quadrupole mass spectral data were collected using time-resolved data acquisition software (TRA), which generated the full mass spectral pattern of each analyte. Organotin compounds introduced into the previously described GDMS sources [8,10,11] exhibit mass spectral fragmentation patterns similar to electron impact ionization (EI) library spectra. The elemental tin ions, as well as the methylated and ethylated fragment ions, observed for each compound are the same as those seen from the EI spectra from the NIST library. Figure 14.5 shows a comparison of tetramethyltin (TMT) mass spectra obtained from the GDMS vs EI spectra from the NIST library. Viewing the fragment ion

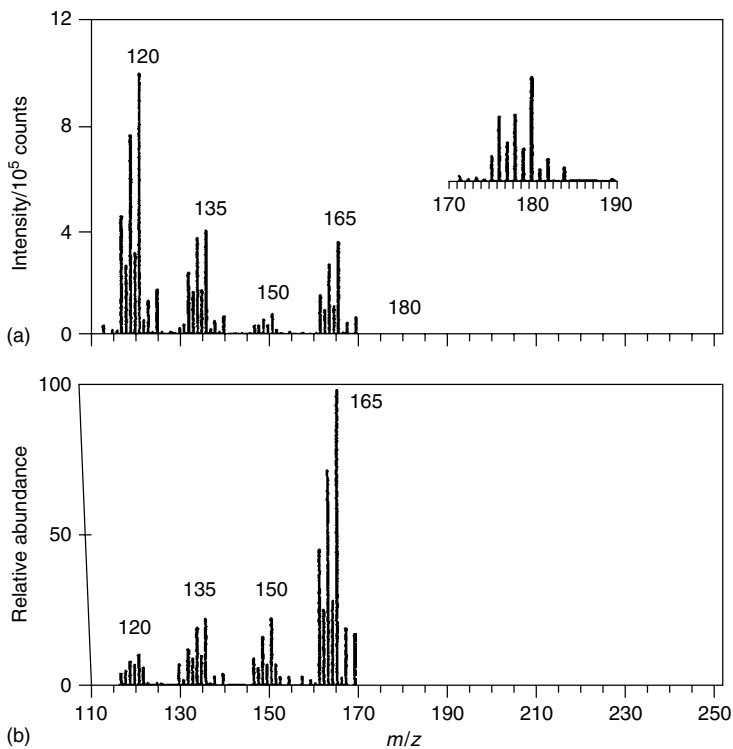


Figure 14.5 Comparison of the mass spectrum of tetramethyltin (TMT), as obtained with the modified symmetric GC–GDMS set-up, vs EI spectra from the NIST library. Reproduced with permission of The Royal Society of Chemistry from Belkin, M. A., Olson, L. K. and Caruso, J. A., *J. Anal. At. Spectrom.*, 1997, **12**, 1255–1261

patterns as well as the elemental isotope ratios proves that both quantitative and qualitative information can be obtained with the same source; however, the fragment ions were not intense enough to perform trace quantitative analysis. Thus, the reported detection limits for tin are high since the contribution of tin from the fragment ions was neglected. In order to obtain a more accurate report of the detection limits, it would be necessary to account for the tin present in the fragment ions as well as the elemental tin contribution obtained in the SIM mode.

14.4.4 TUNABLE FRAGMENTATION USING GD PARAMETERS

By varying one or more of the plasma ionization source parameters, mass spectra can be ‘tuned’ to obtain desired information about the analyte. Pressure was one plasma parameter used to tune the mass spectral fragmentation for the modified helium rf-GDMS, as illustrated in Figure 14.6. The ion signal ratio (Sn^+ ion

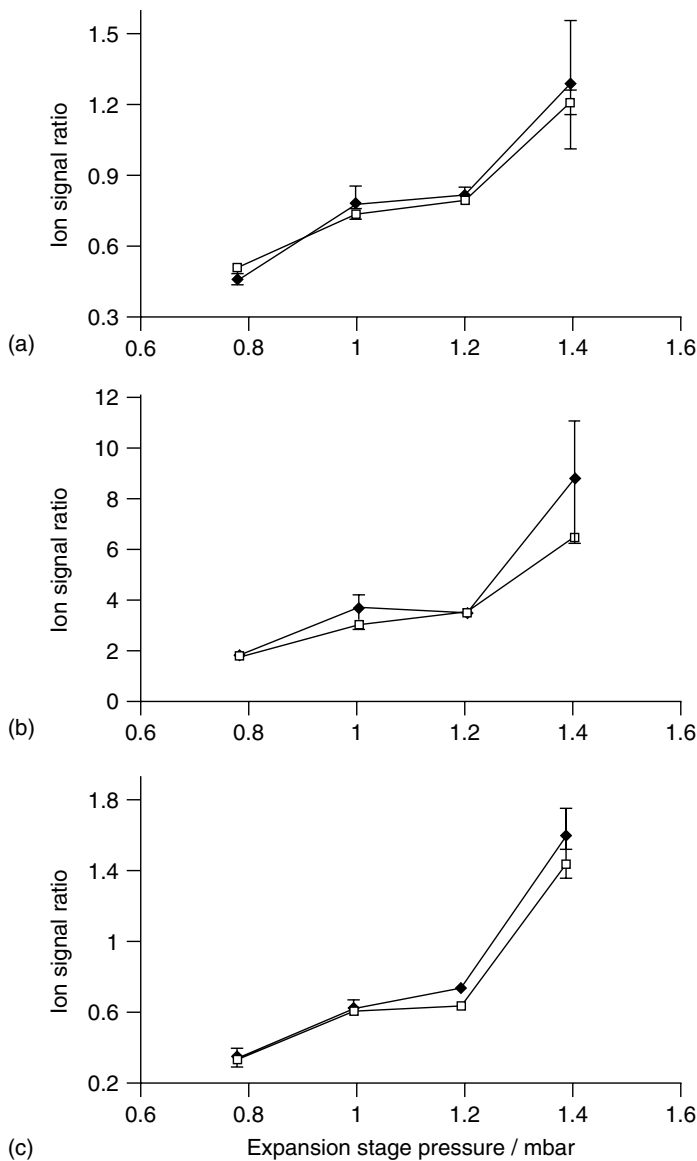


Figure 14.6 Effect of expansion stage pressure on TMT mass spectral fragmentation for ion signal ratios of m/z (a) 120:135, (b) 120:150 and (c) 120:165 for the modified helium rf-GDMS. The symbol \blacklozenge represents maximum ion signals and \square represents ion signals averaged across chromatographic peaks. Reproduced with permission of The Royal Society of Chemistry from Belkin, M., Waggoner, J. W. and Caruso, J. A., *Anal. Comm.*, **35**, 1998, 281–283

intensity/fragment ion intensity) was plotted against the expansion stage pressure of the mass spectrometer for different fragments. At higher pressures, for GC-introduced TMT, there are more elemental ions present and at lower pressures there are more molecular ions present [11]. Langmuir probe studies of a GD source showed that the average electron energy decreased with increasing discharge pressure [16]. Assuming that EI is the predominant ionization mechanism in an rf-GD source, changing electron energy may account for the increase or decrease of molecular ions present [16].

Adding argon to the helium GD was another plasma parameter that was investigated. The ion signal ratios became higher with the addition of argon gas to a helium plasma. As shown in Figure 14.7a [6], the addition of 4% by mass of argon resulted in virtually no fragment ions of structural significance for TMT as compared with the mass spectra of TMT introduced into a 100% helium GDMS (Figure 14.7b).

For the original GSGD-MS design, atomic and molecular modes of operation are dependent on the discharge gas (helium for atomic, argon for molecular), source pressure, current and cathode geometry [12] (see Table 14.3). In the elemental mode, speciation was performed for several chlorinated hydrocarbons based on their $^{35}\text{Cl}^+ / ^{12}\text{C}^+$ ratios. In a more recent study, switching the voltage polarity to the sample introduction plate modulated the atomic and molecular ionization for the switched dc-GDMS [13]. To improve the ionization sensitivity in the molecular mode, several input-electrode geometries were used. Figure 14.8 shows several mass spectra for bromoform using different electrode geometries. The fragment patterns are different for each geometric design. The planar electrode used in Figure 14.8a shows a higher percentage of the lower molecular weight fragments. The mass spectrum depicted in Figure 14.8b shows an equal distribution of fragmentation species with a hollow anode electrode (the anode surface and the skimmer sampling distance being 9 mm apart). The mass spectrum in Figure 14.8c, which was also generated from a hollow anode electrode (the anode surface and skimmer sampling distance 11 mm

Table 14.3 GSGD (original design) operating conditions (adapted from ref. 12).

Parameter	Atomic	Molecular
Cathode geometry	Hollow	Planar
Discharge gas	Helium	Argon
Current (mA)	10–130	3–20
Dc voltage (V)	200–4000	30–300
Pressure (Torr)	1–10	0.1–3

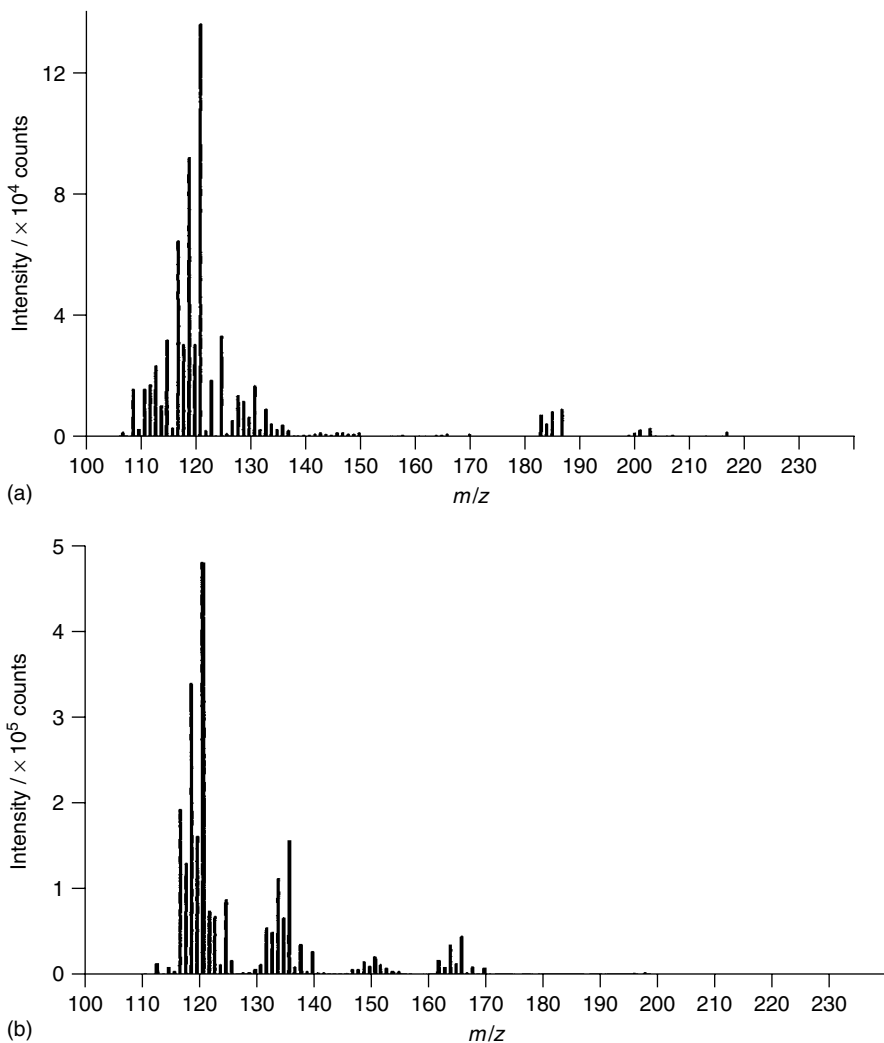


Figure 14.7 (a) Mass spectral fragmentation of TMT for an He GD source containing 4% by mass argon. (b) Mass spectral fragmentation of TMT in 100% helium GD

apart) compares most favorably with the 70 eV EI mass spectrum for bromoform (Figure 14.8d). Guzowski and Hieftje continued to use the hollow anode electrode with an 11 mm sampling distance for the remainder of their halogen studies because of the correlation of the mass spectra with the EI mass spectra [13].

For the microsecond pulsed glow discharge coupled to TOFMS, elemental information is obtained during plasma ignition, followed by EI molecular fragmentation and after termination of the electrical pulse (ca. 200 μ s), molecular ion information (Penning ionization and charge exchange) [14]. This entire

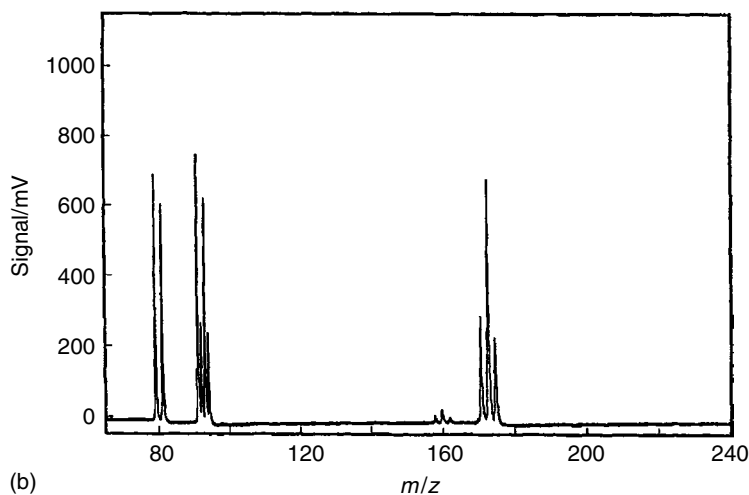
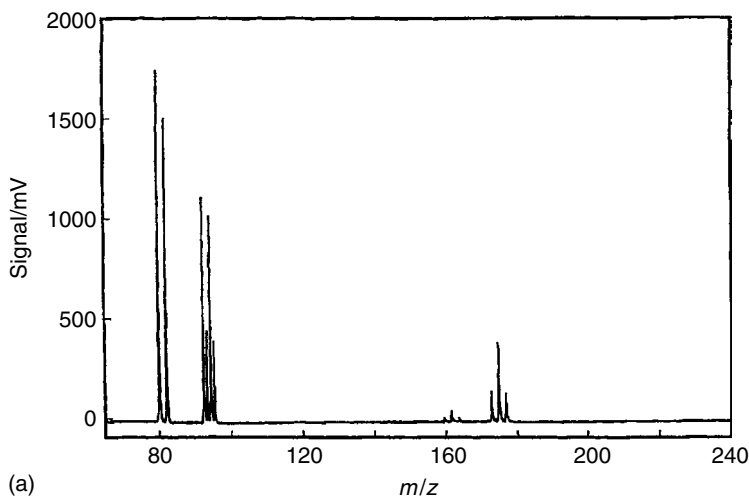
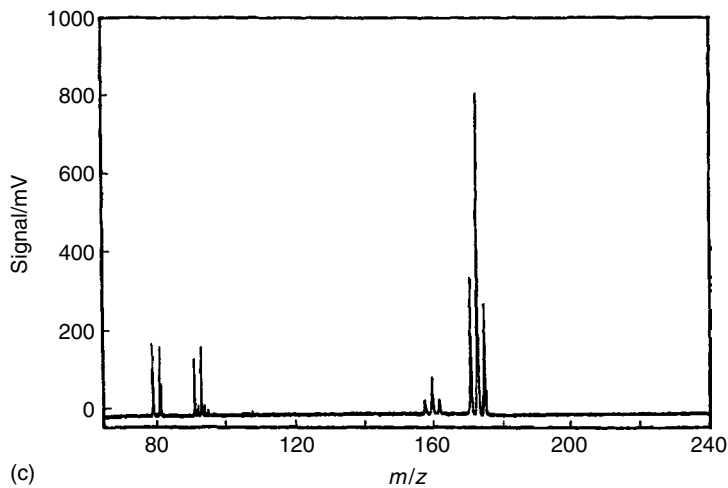
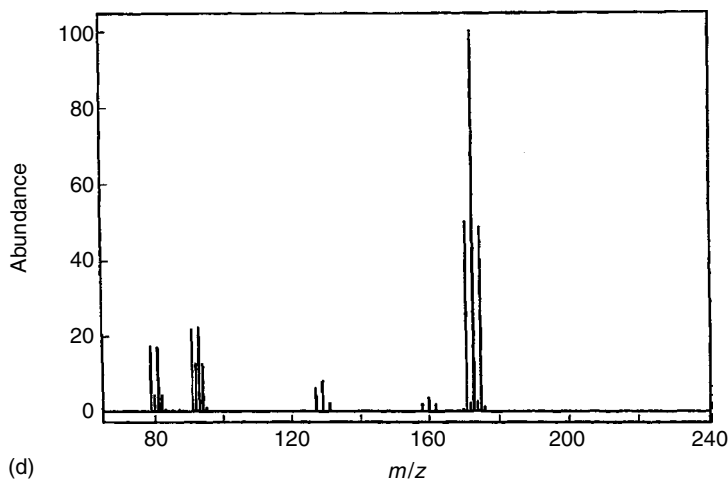


Figure 14.8 Mass spectra for bromoform using different electrode geometries for the GSGD source. (a) Planar electrode; (b) hollow anode (sampling distance between input electron and skimmer 9 mm); (c) hollow anode (sampling distance between input electron and skimmer 11 mm); and (d) reconstructed 70 eV EI mass spectrum for bromoform as a comparison. Reproduced with permission of The Royal Society of Chemistry from Guzowski, J. P. and Hieftje, G. M., *J. Anal. At. Spectrom.*, 2000, **15**, 27–36



(c)



(d)

process spans less than 1 ms. Therefore, when an analyte is introduced continuously into the pulsed plasma chamber, one may obtain elemental, structural and molecular information concurrently by using the TOFMS for time-gated detection. When this technique is combined with chromatography in the future, 'true' sample speciation, within a chromatographic time frame, can be achieved. In Figure 14.9, the mass spectrum of ethylbenzene is shown after 45 μs (b) and after 305 μs (c) of plasma ignition and compared with the NIST electron ionization reference spectrum (a). Part (b) shows much structural information about the compound (i.e. C_6H_5^+ at 77 u) and part (c) illustrates the molecular ion has a mass of 106 amu.

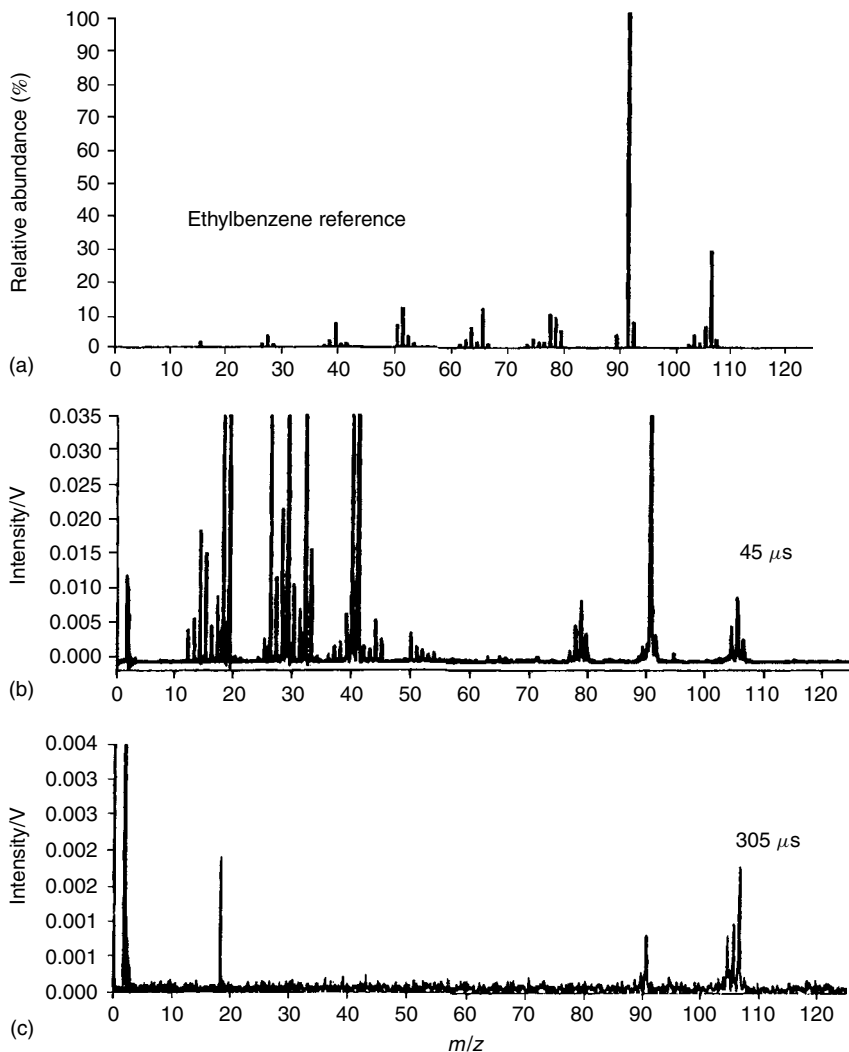


Figure 14.9 Mass spectra of ethylbenzene: (a) NIST EI reference spectra obtained at 70 eV; (b) microsecond-pulsed GD profile obtained 45 μ s after the plasma ignition; and (c) microsecond-pulsed GD profile obtained 305 μ s after the plasma ignition. Reproduced with permission of The Royal Society of Chemistry from Majidi, V., Moser, M., Lewis, C., Hang, W. and King, F. J., *Anal. At. Spectrom.*, 2000, **15**, 19–25

14.5 CONCLUSIONS

Using GC coupled to rf-GDMS allows quantitative information in the low-picogram range to be obtained for volatile metal species. Qualitative information

in the form of mass spectral fragmentation patterns provides identification of these same species. As stated before, interfacing GC with dc gas sampling GD and microsecond pulsed GD is likely. Another future goal is to interface GD sources that have already been successfully interfaced with GC to liquid chromatography (LC) in order to analyze a larger variety of samples. Marcus and co-workers have successfully interfaced LC with particle beam (PB)-GDMS [17,18]. This is discussed in Chapter 13.

14.6 REFERENCES

1. Montaser, A. *Inductively Coupled Plasma Mass Spectrometry*, Wiley-VCH: New York, 1998.
2. Evans, E. H.; Caruso, J. A. *J. Anal. At. Spectrom.* 1993, **8**, 427–431.
3. Evans, E. H.; Pretorius, W.; Ebdon, L.; Rowland, S. *Anal. Chem.* 1994, **66**, 3400–3407.
4. Waggoner, J. W.; Belkin, M.; Sutton, K. L.; Caruso, J. A.; Fannin, H. B. *J. Anal. At. Spectrom.* 1998, **13**, 879–883.
5. Waggoner, J. W.; Milstein, L. S.; Belkin, M.; Sutton, K. L.; Caruso, J. A.; Fannin, H. B. *J. Anal. At. Spectrom.* 2000, **15**, 13–18.
6. Milstein, L. S.; Waggoner, J. W.; Sutton, K. L.; Caruso, J. A. *Appl. Spectrosc.* 2000, **54**, 1286–1290.
7. Giglio, J. J.; Caruso, J. A. *Appl. Spectrosc.* 1995, **49**, 900–906.
8. Olson, L. K.; Belkin, M.; Caruso, J. A. *J. Anal. At. Spectrom.* 1996, **11**, 491–496.
9. Duckworth, D. C.; Marcus, R. K. *J. Anal. At. Spectrom.* 1992, **7**, 711–715.
10. Belkin, M. A.; Olson, L. K.; Caruso, J. A. *J. Anal. At. Spectrom.* 1997, **12**, 1255–1261.
11. Belkin, M.; Waggoner, J. W.; Caruso, J. A. *Anal. Commun.* 1998, **35**, 281–283.
12. Guzowski, J. P.; Broekaert, J. A. C.; Ray, S. J.; Hieftje, G. M. *J. Anal. At. Spectrom.* 1999, **14**, 1121–1127.
13. Guzowski, J. P.; Hieftje, G. M. *J. Anal. At. Spectrom.* 2000, **15**, 27–36.
14. Majidi, V.; Moser, M.; Lewis, C.; Hang, W.; King, F. *J. Anal. At. Spectrom.* 2000, **15**, 19–25.
15. Steiner, R. E.; Lewis, C. L.; Majidi, V. *J. Anal. At. Spectrom.* 1999, **14**, 1537–1541.
16. Belkin, M.; Caruso, J. A.; Christopher, S. J.; Marcus, R. K., *Spectrochim. Acta, Part B*, 1998, **53**, 1197–1208.
17. Marcus, R.; Demster, M.; Gibeau, T.; Reynolds, E. *Anal. Chem.* 1999, **71**, 3061–3069.
18. Gibeau, T. E.; Marcus, R. K. *Anal. Chem.* 2000, **72**, 3833–3840.

15

Glow Discharge Atomic Emission Spectrometry for the Analysis of Gases and as an Alternative Gas Chromatographic Detector

ROSARIO PEREIRO, NESTOR G. ORELLANA-VELADO
and ALFREDO SANZ-MEDEL

*Department of Physical and Analytical Chemistry, Faculty of Chemistry,
University of Oviedo, Oviedo, Spain*

15.1 INTRODUCTION

So far, most analytical applications of the glow discharge (GD) have dealt with direct solid samples analysis, and this technique has remained almost unexplored for the analysis of gaseous samples. However, the physical features of a low-pressure GD as a spectrochemical source (gas-kinetic temperatures are low, implying that the continuum background emission should be relatively weak; yet electronic excitation temperatures in GDs are very high [1,2]) along with the low costs of acquisition and maintenance of this source, make it also a promising detector for the analysis of gaseous analytes. In this context, different types of samples and different ways to introduce the analytes in gaseous form into the GD have been investigated, including the direct introduction of volatile or easily volatilized organic compounds, the introduction after a chemical derivatization where the analyte is converted into a volatile species derivative, and on-line introduction of the separated analyte through a gas chromatograph.

Most of the GDs used for such purposes employ helium as plasma gas. The advantages of using helium in this type of application are twofold: first, the good excitation properties of the helium plasmas are well known (of special interest for the analysis of non metals); and second, helium produces a much lower cathode erosion rate than other inert gases (e.g. argon), allowing the discharge to be kept stable over long periods of time.

Both flat cathode (FC) and hollow cathode (HC) glow discharges have been used for the analysis of gaseous species by atomic emission spectrometry (AES); however, most of the research has been carried out with HC-GDs because of the high emission intensities obtained when using very small cathode cavities of HC-GD (microcavity effect). Thus, HC-GD could offer special advantages for gas analysis [3] and in particular for gas chromatographic (GC) detection (band broadening in the detector would be minimized because of the small, well-defined dimensions of the plasma).

On the other hand, it should also be emphasized that most of the work on gas analysis with GDs has been carried out using dc-GDs; however, in recent years rf-GD-AES has emerged as an interesting detection technique worth evaluating for the analysis of gases.

In this chapter, the main features of the three sample introduction modes to GDs will be reviewed.

15.1.1 DIRECT INTRODUCTION OF GASEOUS SAMPLES OR THERMALLY VAPORIZED LIQUID ORGANIC SAMPLES

Several papers have described the use of modified GDs, adapted for the analysis of gaseous samples or thermally vaporized organic compounds by AES. Here, the GD serves to decompose the gaseous compounds and to excite or ionize the resulting atoms. The determination of trace amounts of nonmetals by AES is difficult owing to the high excitation energy of the transitions of some of these elements in the visible spectral region; however, several helium plasmas have been proposed for the determination of these analytes, including He microwave induced plasma (MIP) [4], He stabilized capacitive plasma (SCP) [5] and He inductively coupled plasma (ICP) [6].

Using He as plasma gas, different approaches have been reported for determinations of nonmetallic elements (e.g. C, I, Br, Cl, F and S) in gases and in liquids (organic compounds thermally vaporized) by GD-AES. Most of the experiments carried out in this direction were oriented to assess the potential, or interest, of an eventual coupling of a gas chromatograph to GD-AES detection.

Using a helium hollow cathode dc-GD, Puig and Sacks [7] reported the determination of F, Cl and Br by AES in fluorocarbon compounds. In this case, controlled volumes of samples were introduced with a gas-tight Hamilton syringe into the carrier gas through a septum. Winefordner and co-workers [8] also

proposed the use of helium dc-HC-GD-AES for the elemental analysis of CCl_4 , CS_2 , HF, CH_2Br_2 and CH_3I using methanol for dilution of the analytes.

Hieftje and co-workers investigated a dc-GD flat design [9,10], which they called 'gas sampling glow discharge' (GSGD), for the determination of the non-metals C, F, Cl and S in molecular gases and organic vapours by AES. The utility of the He GSGD for the determination of elemental ratios involving carbon, chlorine and sulphur was successfully investigated with this GD design for several simple organic compounds; in other words, the GD seems to be able reproducibly to atomize organic compounds and excite their constituent atoms without noticeable influence of the structure of the original molecule.

Later, Hieftje's group described the use of a different design of a GSGD, in this case based on the Grimm source, for the determination of chlorine in halogenated organic compounds [11]. Vapours from both aliphatic as well as aromatic hydrocarbons were introduced into the discharge. To a first approximation, the signals were found to be proportional to the amount of both chlorine and carbon released into the discharge, enabling the ratio of carbon to chlorine to be determined.

The analytical potential of a helium rf-GD for the determination of Cl, C, S and Br in low boiling-point organic compounds has also been reported with very good prospects in terms of sensitivity [12] and reliable determinations of elemental ratios in simple chlorinated hydrocarbons have already been demonstrated.

In the light of all the reports so far, it appears that the GDs, simple to build and operate, are fairly robust to the introduction of organic vapours, offer good sensitivity for nonmetals and are able to provide elemental information regardless of the original molecular form of the analytes; in other words, reliable formula determinations of organic compounds are possible.

15.1.2 CHEMICAL DERIVATIZATIONS TO CONVERT THE ANALYTE FROM A LIQUID SAMPLE INTO A VOLATILE DERIVATIVE, PRIOR TO ITS EVENTUAL INTRODUCTION INTO THE GLOW DISCHARGE

The generation of analyte vapour from a liquid sample allows dramatic increases in sensitivity in atomic spectrometry (usually 100% of the analyte is transported to the atomiser as a vapour and this compares most favourably with the 1–5% introduced when using conventional nebulization systems for plasma spectrometry). Of course, selective volatilization also permits the elimination of the sample matrix, thus circumventing the problem of chemical interferences in the spectrochemical source. Moreover, this approach can be an appropriate mode to avoid the influence of liquid samples on plasmas with very low resistance to aqueous aerosols (as is the case with GDs).

The formation of volatile covalent hydrides of analytes such as arsenic, antimony, selenium, tin, germanium, etc., prior to their introduction into an atomic

detector is a common approach used so far when a chemical reaction is used to produce a volatile derivative [13]. In the case of helium plasmas, approaches based on strong oxidation of some halides, such as chloride or bromide, to yield the volatile covalent halines (e.g. Cl_2 , Br_2) [4,5] should also be mentioned.

The most common chemical reducing agent used in hydride generation is tetrahydroborate in acidic media. After reaction, molecular hydrogen, carbon dioxide and water vapour usually accompany the volatile hydride of the analyte. Hydride generation has been attempted as a sample introduction mode into the GD, using both batch and continuous introduction manifolds. Concerning batch systems, Feldman [14] reported the use of a series of traps prior to the GD in the determination of arsenic in biological samples by helium dc-GD-AES: a liquid nitrogen trap to accumulate arsine and separate it from the excess of hydrogen produced during the reaction, sodium hydroxide to trap carbon dioxide and phosphoric acid to desiccate the sample. Also, Matsumoto and co-workers proposed a helium dc-GD-AES for the determination of lead, selenium, germanium, arsenic, antimony and tin after their hydride generation [15]. In this case, a carbon dioxide trap (column packed with NaOH), a water trap (dry ice–2-propanol bath) and a liquid nitrogen trap (to eliminate the excess of hydrogen) were used.

Despite their well-known advantages, batch volatile species generation procedures have a number of drawbacks, such as (a) relatively modest throughputs, (b) poor precision due to difficult control of the reaction conditions, (c) requirement for fairly large amounts of sample, and (d) in the case of hydride generation processes, molecular hydrogen is generated which can extinguish the plasma when it is released in a sudden burst as in the batch mode. These drawbacks can be lowered or eliminated by changing to continuous systems [16].

A gas sampling dc-GD coupled on-line to a continuous hydride generation system was described for the determination of arsenic by AES [17]; argon, helium and neon were investigated as plasma gases, 20 ng ml^{-1} being the best detection limit (DL) reported. A continuous hydride system was also coupled on-line to an alternative He GD design. The performances of dc and rf sources were compared, and also the analytical characteristics attainable using a flat cathode and a hollow cathode design [18]; detection limits of tenths of ng ml^{-1} for arsenic and antimony were achieved by GD-AES with such a design.

The helium MIP is the most commonly used plasma for the determination of nonmetals; however, to overcome the low resistance of most low-power MIP devices to aqueous aerosols, approaches based on the chemical oxidation to volatile molecular chlorine were successfully reported using potassium permanganate in sulphuric acid media as oxidizing agent [4,5]. Based on this approach, rf- and dc-GD-AES were investigated for the determination of aqueous chloride, after on-line conversion into volatile chlorine by continuous chemical oxidation in a flow system [19]. Using this on-line continuous approach and GD-AES detection, both the visible and the near-infrared (NIR) regions were investigated. It has been reported for other plasma sources that some NIR transitions offer

better sensitivity than those in the visible region [6,20,21]. Detection limits for chlorine with the rf-GD-AES system were as low as 0.14 ng ml^{-1} when using the 837.60 nm line [19]. The method was applied to the determination of the absorbable organic halogen (AOX) parameter in wastewater from a cellulose factory [19].

15.1.3 GLOW DISCHARGE ATOMIC EMISSION SPECTROMETRY AS ALTERNATIVE GAS CHROMATOGRAPHIC DETECTOR

An ideal elemental detector for gas chromatography should exhibit the following properties: capability for detection of most elements of the periodic table, specificity, high sensitivity, stability over long periods of time, low costs of acquisition and low costs of maintenance. The good analytical properties offered by the GD for the analysis of gases prompted the investigation of GD sources as gas chromatographic detectors, even though a few papers have been published so far dealing with this GC-GD hyphenated technique. Harley and Pretorius [22] back into 1956 investigated the first GD detector for GC, which was based on voltage changes across the detector when eluting compounds from the chromatographic column. More recently, GC-GD has been coupled to more selective detection principles such as the specific AES and mass spectrometry (MS). Detailed information about the use of GC-GD with MS detection is given in Chapter 14. Hence we will restrict the discussion here to optical emission systems.

The two main types of applications pursued by coupling GC to GD-AES have been trace metal speciation and the determination of nonmetals in organic compounds. The importance of metal speciation cannot be overemphasized, as information provided by total concentration determinations of a given toxic metal offered by atomic spectrometric detectors is no longer sufficient to evaluate its impact on the environment, its bioavailability or its actual toxicity. More and more information about the identity and concentration of the different species of a given trace element of interest in the sample (speciation information) is demanded in the most diverse fields [23,24]. Metal speciation requires the combination of a powerful separation technique with a sensitive element-specific detector. The on-line coupling of GC to a plasma source and optical or mass spectrometric detection constitutes a very powerful approach for the speciation of volatile analytes.

The use of flat cathode and hollow cathode designs for coupling capillary GC to GD-AES has been investigated with dc and rf discharges for mercury speciation (methylmercury, ethylmercury and inorganic mercury) [25,26]; recent studies with GC coupled to rf-GD-AES have expanded applications to the speciation of lead and tin by using solid-phase microextraction as a means for sample introduction [27]. Particularly good detection limits were obtained with a GC-rf-HC-GD-AES hybrid arrangement, with which the detection limit for

methylmercury is as low as 0.2 ng ml^{-1} (as mercury). This methodology was successfully applied to the speciation of methylmercury in marine certified reference materials [26].

Also, the use of a dc-HC-GD for gas chromatographic detection of chlorinated and brominated hydrocarbons has been investigated [28]. Different cathode materials and cathode dimensions were investigated in order to reach maximum sensitivity and a cathode of graphite, with a cavity depth of 20 mm, was finally selected. Using this system, the possibility of the reliable detection of 1-bromo-3-chloropropane, 1-bromo-2-chloroethane and dichloromethane at the low pg s^{-1} level was demonstrated.

15.2 INSTRUMENTATION FOR THE ANALYSIS OF GASES AND GAS CHROMATOGRAPHIC DETECTION BY GD-AES

In this section, we consider only those particular aspects by which the GD-AES systems for the analysis of gases differ from those traditionally used for the direct analysis of solids. Therefore, we will deal with aspects such as differences in the design of the discharge chambers, the manifolds used for gas sample introduction into the discharge chamber and the interfaces between the gas chromatograph and the GD.

15.2.1 DESIGN OF THE GLOW DISCHARGE CHAMBER: CHAMBER BODY AND CATHODES

Different discharge chamber designs have been used for the determination of compounds introduced as gases into the discharge; these include, for example, chamber bodies constructed according to the Grimm design [11] or the Marcus design [12,18,19,25,26] or even similar to the interface designed for ICP-MS [9,10]. Concerning cathode geometry, both hollow cathode and flat cathode designs have been proposed. In some studies, the two cathode geometries were tested with the same chamber body [18], thus allowing some conclusions to be drawn about the convenience of one cathode design over the other.

An important factor to be taken into account for the type of analysis considered in this chapter is the selection of the optimum location in the chamber to introduce the gaseous analyte into the plasma. In most of the designs, the analyte transported to the discharge by plasma gas flow (carrier gas) is introduced through the cathode, whereas in others it is introduced very close to the cathode, for example through the so-called 'limiting disc' which separates the body chamber from the cathode [12,25]. In fact, it has been proved that much better sensitivity is obtained when the analytes are introduced in such a way that they are forced to pass through the whole length of the plasma instead of introducing them through the main discharge chamber body.

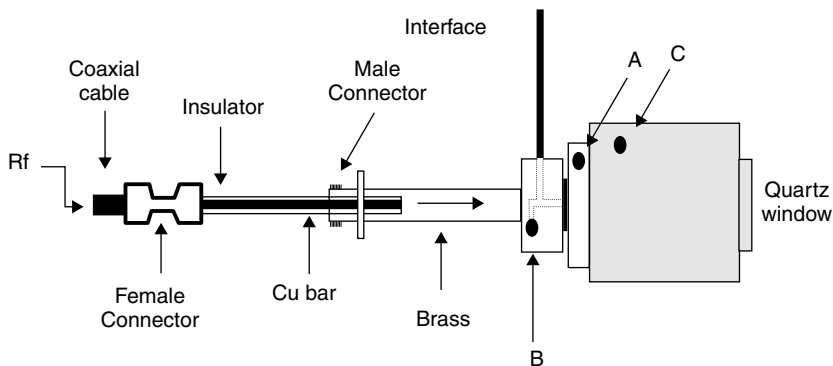


Figure 15.1 Designs investigated for the introduction of a make-up gas into the discharge for mercury speciation by GC coupled to rf-HC-GD-AES. (A) Introduction through the limiting disc; (B) introduction through the cathode; and (C) introduction through the discharge chamber. Reproduced by permission of The Royal Society of Chemistry from Orellana-Velado, N. G., Pereiro, R., and Sanz-Medel, A., *J. Anal. At. Spectrom.* 2000, **15**, 49–53

For some introduction systems, the use of a plasma make-up gas has been investigated [26]: for mercury speciation using gas chromatography coupled to rf-HC-GD-AES, three different ways of plasma make-up gas introduction in the discharge chamber were evaluated (Figure 15.1): (A) through the limiting disc, (B) through the hollow cathode body and (C) by the discharge chamber. Similar detection limits were observed when the He make-up flow was introduced either through the body of the discharge chamber or through the limiting disc, but they were poorer for design B. Probably the mercury species suffer higher dilution when they are carried to the plasma by the make-up He flow introduced through the hollow cathode.

15.2.2 APPROACHES FOR THE DIRECT INTRODUCTION OF GASEOUS SAMPLES INTO THE DISCHARGE

Two principal approaches have been described for the introduction of a plug of the sample (gases, volatile or thermally volatilized organic vapours) into the GD-AES: the direct introduction of the gas sample in the He carrier stream with a syringe through a septum [7,8] and the use of the exponential dilutor [9,10,12], as described by Lovelock [29].

In the exponential dilutor technique, discrete volumes of sample are introduced into a flask called an 'exponential dilution chamber'. It contains a magnetically driven stirrer to allow gas homogeneity. The exponential dilution chamber is provided with a three-way stopcock (Figure 15.2), which allows the He carrier gas to pass directly to the GD or to pass through the vessel dragging the sample

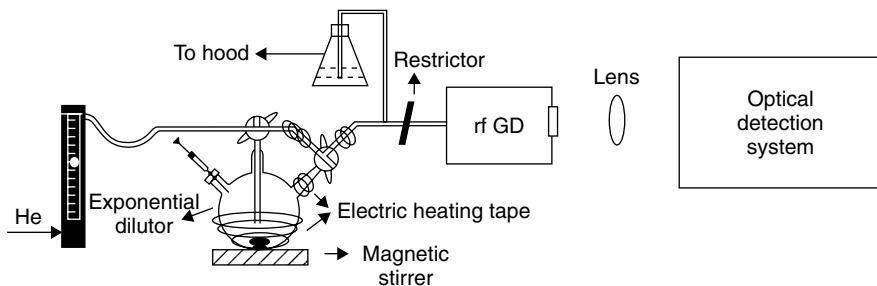


Figure 15.2 Experimental set-up used for the determination of nonmetals in organic vapours by rf-GD-AES using an exponential dilution chamber for sample introduction. Reprinted with permission from Centineo, G., Fernández, M., Pereiro, R. and Sanz-Medel, A., *Anal. Chem.*, 1997, **69**, 3702–3707. Copyright 1997 American Chemical Society

to the plasma. In the latter case, the initial concentration C_0 in the vessel is diluted continuously according to

$$C(t) = C_0 \exp(-Ft/V) \quad (15.1)$$

where $C(t)$ is the concentration at time t , F the flow rate of the helium carrier gas, t the time spent after the stopcock was turned and V the volume of the vessel.

With the aid of the above relationship, it is possible to obtain calibration graphs with a single sample injection (exponential decay calibration) by following, for each individual sample plug injection, the decay profile of the emission intensity versus the time elapsed after the stopcock was turned and considering the exponential dilution in concentration that takes place in the flask.

It is important to note that this exponential chamber can be heated (e.g. with electric heating tape) to guarantee the vaporization of organic compounds. Also, the interface between the exponential dilution flask and the GD can be heated.

15.2.3 MANIFOLDS FOR THE CHEMICAL FORMATION OF VOLATILE ANALYTE DERIVATIVES FROM LIQUID SAMPLES

A typical on-line sampling introduction device for the determination of halides in water samples by GD-AES [19] is shown in Figure 15.3. It consists of two channels driven by a peristaltic pump, one of them containing the sample diluted in sulphuric acid and the other the oxidant (0.05 M KMnO_4 in concentrated sulphuric acid). Sample and oxidant are merged at a T-piece. The volatile halogen generated is passed through a gas–liquid separator, where the volatile chlorine is stripped off continuously to the GD with the aid of a constant flow of helium

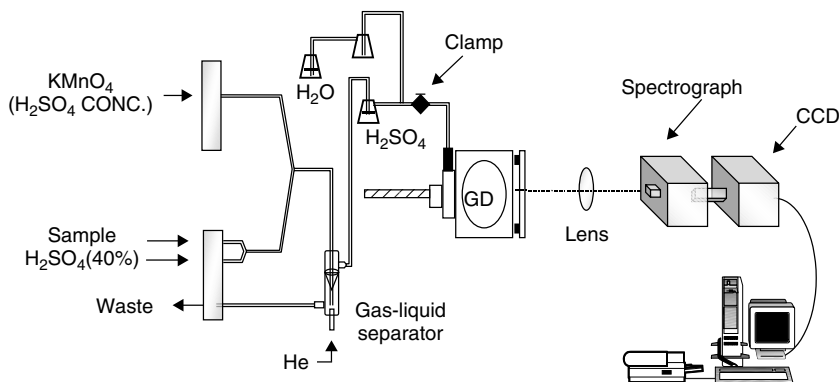


Figure 15.3 Schematic diagram of the experimental set-up for the determination of chloride in water samples by GD-AES. Reproduced by permission of The Royal Society of Chemistry from Rodriguez, J., Pereiro, R. and Sanz-Medel, A., *J. Anal. At. Spectrom.*, 1998, **13**, 911–915

carrier gas. Residual moisture is removed on-line by bubbling the reaction gases through a desiccator flask filled with concentrated sulphuric acid.

To match the aspiration rate of the GD vacuum pump to the flow rate of the carrier gas, a restriction was provided by placing a throttling clamp on the plastic sampling tube located at the entrance of the GD. Also, a side arm directed into two connected Erlenmeyer flasks was incorporated into the sampling line as a means of controlling the equilibration of these two gas flow rates. The second flask was filled with water while the first flask was empty and it was used to ensure that no water from the second flask was introduced into the GD.

In the case of the generation of covalent hydrides of elements such as arsenic or antimony, the initial work with GD-AES made use of batch hydride generation procedures [14,15]. However, considering the advantages of continuous flow hydride generation systems [16], in more recent papers continuous flow hydride generation in combination with GD-AES detection was used [17,18]. The manifold for the on-line introduction of hydrides was similar to that used for the determination of chloride described previously, except that here the two channels of the peristaltic pump were used for simultaneous pumping of the sample (in 2 M HCl) and the reducing agent (sodium tetrahydroborate), respectively. Flow injection (FI) experiments were also carried out; therefore, a six-way valve was connected before the mixing tee and the sample was injected into a 2 M HCl carrier solution and then merged with the tetrahydroborate reagent [18].

15.2.4 DESIGN OF INTERFACES BETWEEN GAS CHROMATOGRAPHY AND GLOW DISCHARGES

Different designs of transfer lines between GC and the GD have been reported. In the Marcus design with a flat cathode GD, a stainless-steel tube (200 mm

long, 10 mm o.d.) was welded to the limiting disc of the GD [25]. The tube of the interface had an inner hollow of 5 mm through which the capillary from the GC passed and it was positioned 1 mm from the plasma discharge. The temperature of this transfer line was maintained at approximately 150 °C, so as to prevent analyte condensation. With this interface, dc and rf powering of the Marcus GD were compared. A detailed view of this transfer line is shown in Figure 15.4a.

In another design, proposed for mercury speciation by rf-HC-GD-AES [26], the stainless-steel GC–GD interface (150 mm long, 10 mm o.d. and 5 mm i.d.) was welded to the hollow cathode body (Figure 15.4b). The capillary column was connected with the hollow cathode through a 1 mm i.d. orifice and various distances between one end of the capillary column and the plasma discharge were tested. A position was finally selected where the capillary was closest to the hollow cathode cavity (1 mm from the plasma discharge). In some experiments, a helium make-up discharge gas was introduced in the cathode through

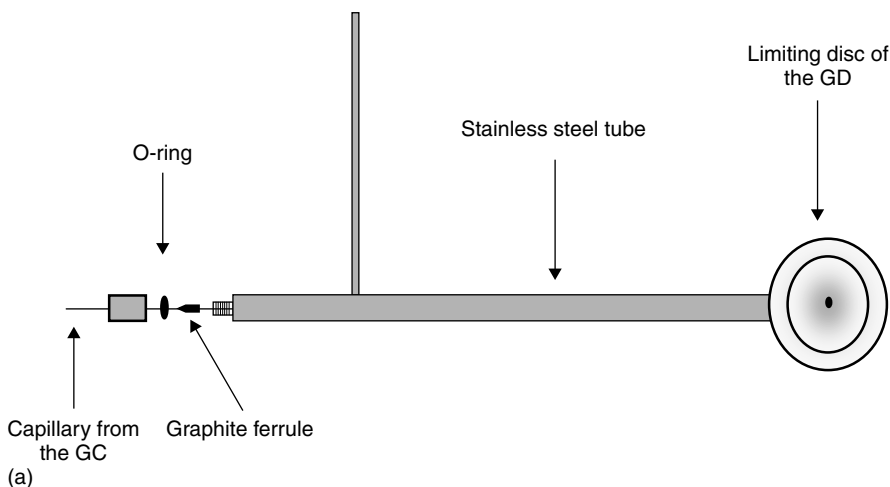


Figure 15.4 Different designs proposed as interfaces between the gas chromatograph and the glow discharge. (a) External view of the transfer line between the GC and GD-AES with a flat cathode as used for mercury speciation. In this case the transfer line was welded to a limiting disc. Reproduced by permission of The Royal Society of Chemistry from Orellana-Velado, N. G., Pereiro, R., and Sanz-Medel, A., *J. Anal. At. Spectrom.*, 1998, **13** 905–909. (b) Diagram of the transversal section of a hollow cathode welded to the transfer line of a GC. The system was used for mercury speciation by GC–rf-HC-GD-AES. The entrance called ‘He inlet’ was used in some experiments only. Reproduced by permission of The Royal Society of Chemistry from Orellana-Velado, N. G., Pereiro, R., and Sanz-Medel, A., *J. Anal. At. Spectrom.* 2000, **15**, 49–53. (c) Interface between the gas supply and an HC-GD-AES system proposed for organochloride and organobromide determinations. Reproduced by permission of The Royal Society of Chemistry from Schepers, C. and Broekaert, J. A. C., *J. Anal. At. Spectrom.*, 2000, **15**, 61–65

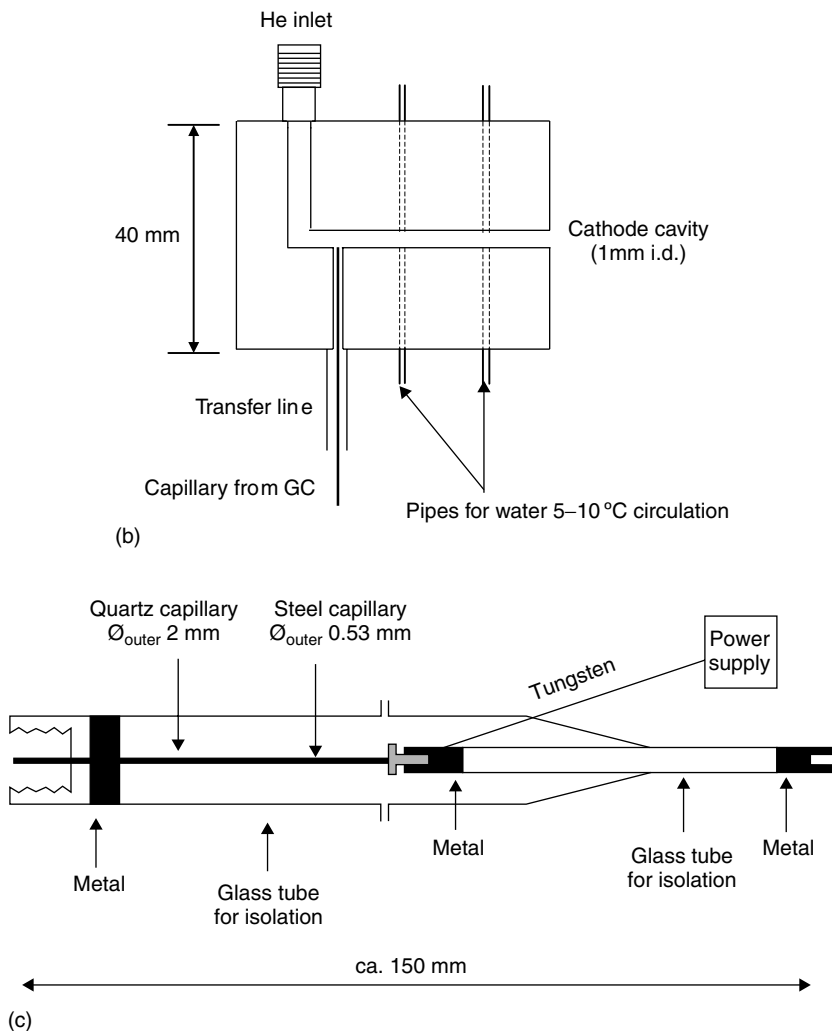


Figure 15.4 (continued)

an inlet placed 5 mm from one end of the cathode. The cathode was refrigerated by circulating cooling water (5–10 °C) through laterally located holes of 3 mm diameter crossing from one side of the hollow cathode to the other, in which pipes were welded together to the external part of the holes (Figure 15.4b).

Recently, GC has also been coupled to a dc-HC-GD-AES system for organohalogen determination [28]. In this case, the interface (Figure 15.4c) consisted of a glass enclosure around a steel capillary used to lead the gas sample into the discharge and to couple the power to the discharge (a quartz tube was used to insulate the

steel capillary). At the end of the capillary a glass tube, bearing a conventional GC fitting at the other end, was used for the sample inlet.

15.3 PRACTICAL ASPECTS AND RESULTS

Some brief general comments about the most frequently selected operating conditions in GD-AES for the type of samples and analytes mentioned throughout this chapter will be given in this section together with the analytical performance characteristics for several illustrative examples. Finally, some selected applications to real sample analysis will be discussed.

15.3.1 OPERATING FEATURES AND ANALYTICAL PERFORMANCE OF GD-AES FOR THE DIRECT ANALYSIS OF GASES

The selection of the operating conditions, including pressure and power, has been investigated for the determination of nonmetals and thermally volatilized organic compounds with different source designs. Experiments showed that optimum values for pressure are in the interval 20–40 Torr. For example, in Figure 15.5 the ratio of

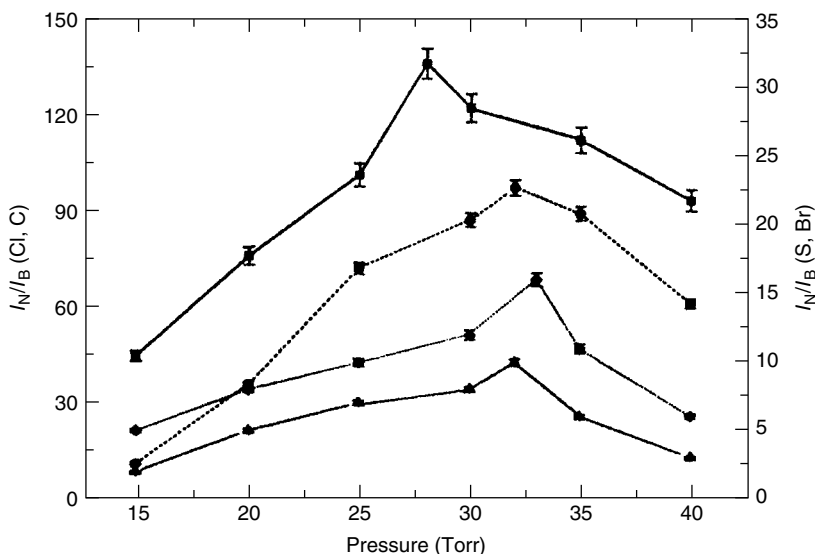


Figure 15.5 Plots of I_N/I_B versus pressure for the determination of Cl, C, Br and S in volatilized organic liquids by rf-GD-AES. (■) Chlorine; (▲) bromine; (◆) sulphur; and (●) carbon. Reprinted with permission from Centineo, G., Fernández, M., Pereiro, R. and Sanz-Medel, A., *Anal. Chem.*, 1997, **69**, 3702–3707. Copyright 1997 of the American Chemical Society

Table 15.1 Analytical performance of rf-GD-AES for the determination of nonmetals in volatilized organic compounds. Reprinted with permission from Centineo, G., Fernández, M., Pereiro, R. and Sanz-Medel, A., *Anal. Chem.*, 1997, **69**, 3702–3707. Copyright 1997 American Chemical Society.

Element	Wavelength (nm)	DL (pg s ⁻¹) ^a	RSD (%) ^b	Upper value in linear range (ng s ⁻¹)
Cl	479.45	0.7	3.9 (2.2)	1000
C	247.86	0.3	2.0 (0.7)	360
Br	470.49	11	4.6 (3.0)	900
S	545.38	6	3.2 (4.4)	900

^aDL calculations are based on three times the standard deviation of 10 independent readings.

^bRSD = relative standard deviation. The analyte concentration in ng s⁻¹ at which the RSD was evaluated is given in parentheses.

net intensity (I_N)/background intensity (I_B) is plotted versus pressure for the case of chlorine (introduced as 1,2-dichloroethane), bromine (as 1,2-dibromoethane), carbon (as 1,2-dichloroethane) and sulphur (as carbon disulphide). Previous work with other plasma discharges well known for gas analysis, such as the MIP, showed similar patterns for the effect of pressure on the analytical signals [30,31]. For the MIP the influence of pressure has been attributed to a balance between the atomization of the molecules, which is promoted by high gas temperatures (and subsequently high pressure) and the excitation, which could be promoted by the high electron temperatures that occur at low pressures [30,31]. The effect of the power dissipated in the discharge has been also examined and it should be noted that the power used is usually lower than 100 W.

In Table 15.1 the analytical figures of merit for Cl, C, Br and S in rf-GD-AES (flat cathode) at 80 W of rf-delivered power are listed [12]. The detection limits for the four nonmetals are of the order of low picograms per second.

The capabilities of GDs for elemental ratio determinations of simple organohalogens also have been investigated with satisfactory results [10–12]. To carry out this type of experiment, a ‘model’ molecule is chosen so as to define a standard heteroatom/carbon intensity ratio. All other organic compounds within each series are referenced to this standard. The results obtained for chlorine and sulphur are given in Table 15.2 for the case of dc-GD-AES (flat cathode) and they were shown to be correct after rounding to integers [10].

15.3.2 PERFORMANCE OF GD-AES FOR THE DETERMINATION OF CHEMICALLY VOLATILIZED ANALYTES FROM LIQUID SAMPLES: SOME REAL APPLICATIONS

With the aid of the experimental set-up depicted in Figure 15.3, chloride could be detected in water samples. The system for the generation of volatile chlorine is

Table 15.2 Elemental ratio determinations with dc-GD-AES (normalized to carbon). Reprinted from Pereiro, R., Starn, T. K. and Hieftje, G. M., *Appl. Spectrosc.* 1995, **49**, 616–622, with permission of The Society for Applied Spectroscopy

Compound	Chlorine	
	Cl _{theor}	Cl _{cal}
Dichloromethane ^a	2	
Chloroform	3	3.01
Trichloroethylene	3	2.82
Tetrachloromethane	4	4.00
	Sulfur	
	S _{theor}	S _{cal}
Thiophene ^a	1	
Carbon disulphide	2	2.12

^aDenotes standard compound in each group.

based on a continuous on-line manifold. The dc-GD and rf-GD operating parameters (flat cathode devices) were investigated for AES detection [19] and values of 25 Torr and 1500 V for dc-GD and 25 Torr and delivered power of 80 W for rf-GD were selected. Delivered rf powers higher than 80 W were not tested as above these powers the plasma becomes unstable owing to the lack of effective cooling of the cathode (several minutes after ignition of the discharge such instabilities started to be observed). Table 15.3 shows a comparison of the characteristics of GDs for the determination of chloride in aqueous samples with those of a similar sample introduction system for other helium plasmas [4,5]. It can be seen that the detection limits obtained with GDs are at least one order of magnitude lower than those published for alternative plasmas. Moreover, the rf-GD with NIR detection provides an extremely sensitive method for the determination of chloride at the tenths of ng ml⁻¹ level.

GD-AES has been applied to the determination of the well-known AOX parameter [4]. AOX has been accepted as a parameter which allows one to assess the total amount of organically bound chlorine in environmental pollution. In conventional AOX methods, organochlorides are combusted to yield hydrogen chloride, which is finally determined by microcoulometric titration, whereas in the case of rf-GD, the chloride is introduced into the continuous system for chlorine generation and on-line GD-AES detection [19]. Results of comparative analyses of three different wastewater samples from a cellulose factory in Asturias (Spain) using either rf-GD-AES(NIR) or microcoulometric titration are given in Table 15.4; the results of the two techniques are shown to be in good agreement.

Table 15.3 Critical comparison of the determination of chloride with different plasma sources using similar introduction system and AES detection (the emission lines are given in parentheses). Reproduced by permission of The Royal Society of Chemistry from Rodriguez, J., Pereiro, R. and Sanz-Medel, A., *J. Anal. At. Spectrom.*, 1998, **13**, 911–915

	DL (ng ml ⁻¹)	Linear range	RSD (%)	Ref.
<i>Microwave induced plasmas</i>				
Beenakker, axial torch (479.45 nm)	37	—	3	[4]
Beenakker, tangential torch (479.45 nm)	17	Up to 100 ppm	3	[5]
Atmospheric surfatron (479.45 nm)	6	Up to 100 ppm	2	[4]
Low-pressure surfatron (479.45 nm)	3	—	5	[4]
Microwave plasma torch (479.45 nm)	3	Up to 1300 ppm	2	[4]
<i>Stabilized capacitive plasma</i>				
Stabilized capacitive plasma (837.60 nm)	1.4	3 orders of magnitude	3	[5]
Stabilized capacitive plasma (479.45 nm)	45	2 orders of magnitude	1	[5]
<i>Glow discharges</i>				
dc-GD (837.60 nm)	0.5	—	1.8	[19]
dc-GD (479.45 nm)	2.5	—	2.4	[19]
rf-GD (837.60 nm)	0.14	Up to 5 ppm ^a	4.3	[19]
rf-GD (479.45 nm)	1.0	Up to 5 ppm ^a	1.0	[19]

^aMaximum concentration assayed.

Table 15.4 Comparative AOX determination in a real wastewater sample from a cellulose factory: results expressed as ng ml⁻¹ of chlorine bound to organics. Reproduced by permission of The Royal Society of Chemistry from Rodriguez, J., Pereiro, R. and Sanz-Medel, A., *J. Anal. At. Spectrom.*, 1998, **13**, 911–915

Sample	Coulometric detection ^a	rf-GD-AES ^a
1	105.0 (±2.9%)	110.7 (±4.8%)
2	356.3 (±2.4%)	350.8 (±4.1%)
3	159.3 (±2.2%)	157.5 (±4.3%)

^aValues in parentheses are the RSDs (%) of five replicates.

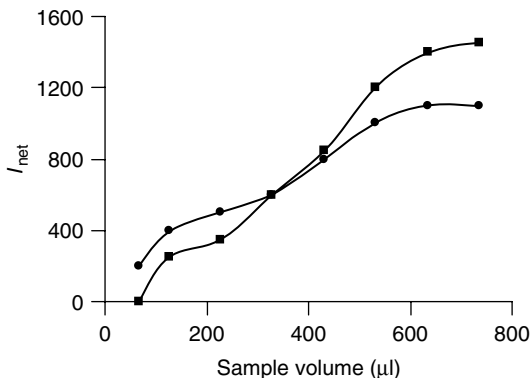


Figure 15.6 Influence of the sample volume when using a dc-HC (●) and a dc-FC-GD-AES (■) for the determination of arsenic with an FI system. Reprinted from Orellana-Velado, N. G., Fernández, M., Pereiro, R., and Sanz-Medel, A., *Spectrochim. Acta, Part B*, 2001, **56**, 113–122, with permission of Elsevier Science

Arsenic and antimony determinations by continuous and FI on-line hydride generation and GD-AES detection were also performed with different emission lines, using both HC and FC geometries and dc and rf sources [18]. A pressure of 30 Torr was used in all the experiments, while the delivered power was 80 W for rf-FC, 30 W for rf-HC, 32 W for dc-FC and 23 W for dc-HC. With continuous flow sampling and a flat cathode device, detection limits of 0.2 ng ml^{-1} for arsenic (at 228.8 nm) and 0.7 ng ml^{-1} for antimony (at 252.7 nm) were achieved with dc-GD-AES.

The performance of the HC compared with the FC for small sample volumes injected (flow injection) was investigated in the case of arsenic determination by on-line hydride generation. Results obtained with the HC and FC systems and different sample volumes using FI-GD-AES are plotted in Figure 15.6 [18]. It can be seen that for lower sample volumes injected, the HC design seems to provide higher analytical signals than GD-AES with an FC. This could be probably attributed to the ‘microcavity effect’ in the HC, which produces high emission intensity and reduces band broadening when small sample sizes are used.

15.3.3 OPERATING CHARACTERISTICS AND ANALYTICAL PERFORMANCE OF GC-GD-AES: APPLICATIONS TO REAL SAMPLES

The use of GD-AES for element-specific detection in capillary GD was explored for metal speciation. In dc-GD-AES [25] and rf-GD-AES [25,26], mercury was selected as the ‘model’ for these studies. Inorganic mercury, methylmercury and ethylmercury were the species to be determined, after derivatization with

a Grignard reagent (butylmagnesium chloride). Later, this approach was also tested for tin and lead speciation [27].

The use of an FC-GD and an HC-GD as GC detectors for the determination of mercury by GD-AES [25] was evaluated. Dc and rf discharges were compared for the case of the flat design. The following operating conditions were selected: a pressure of 25 Torr (pressures higher than 30 Torr produced overheating in the cathode and the limiting disc, which leads to an unstable discharge), voltage 1200 V and current 13 mA for the dc-FC-GD and an rf delivered power of 70 W for the rf-FC-GD. Concerning the hollow cathode device, an rf delivered power of 25 W was used because with higher powers, the reflected power produced overheating in the cathode, which increases the emission background and gives rise to discharge instabilities. The He flow rates selected for sample introduction were 40 ml min^{-1} for the flat geometry and 10 ml min^{-1} for the hollow cathode.

In Figure 15.7, a typical chromatogram obtained with the rf-HC-GD-AES detector for the injection of $1 \mu\text{l}$ of a 10 ng ml^{-1} solution containing the three

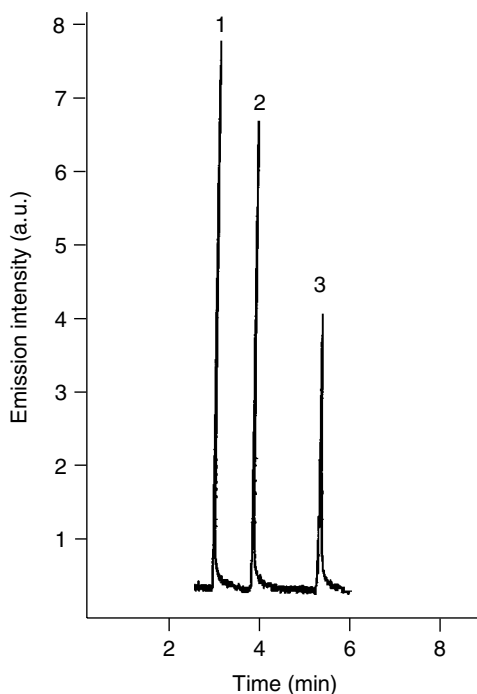


Figure 15.7 Typical chromatogram obtained in the case of the injection of a 10 ng ml^{-1} mixture of the mercury species in a GC-rf-HC-GD-AES system. 1, Methylmercury; 2, ethylmercury; and 3, inorganic mercury. Reproduced by permission of The Royal Society of Chemistry from Orellana-Velado, N. G., Pereiro, R., and Sanz-Medel, A., *J. Anal. At. Spectrom.* 2000, **15**, 49–53

mercury species under investigation is shown. The analytical performance of this hyphenated technique is given in Table 15.5 where it is compared with the figures of merit obtained for the flat cathode geometry and those of an MIP, which is the plasma more frequently used as a GC specific detector for mercury speciation studies. It is important to emphasize that the detection limits obtained with rf-HC-GD-AES were 5–10 times better than those obtained with a flat cathode [25] and that they are also better than those obtained with MIP-AES [32].

To demonstrate the practical utility of coupling GC with GD-AES, mercury species were extracted from marine certified reference materials (dogfish muscle and liver) of the National Research Council of Canada (DORM-2 and DOLT-2). The extraction of the complexes with diethyldithiocarbamate was carried out with toluene. The analytes were derivatized with a Grignard reagent in the organic phase and determined by GC coupled to GD-AES. For the GC-rf-HC-GD-AES technique, results for the determination of the certified methylmercury in these two materials are given in Table 15.6. Ethylmercury, added before the extraction of the analyte, was used as an internal standard. It can be seen in Table 15.6 that the analytical results obtained are in good agreement with the certified values.

The determination of halogenated hydrocarbons (Cl and Br) by gas chromatography coupled to dc-HC-GD-AES has also been investigated recently using a plasma of 10–20 W [28]. Detection limits of 3 pg s⁻¹ for chlorine and 5 pg s⁻¹

Table 15.5 Analytical characteristics of GC-rf-GD-AES. Reproduced by permission of The Royal Society of Chemistry from Orellana-Velado, N. G., Pereiro, R., and Sanz-Medel, A., *J. Anal. At. Spectrom.* 2000, **15**, 49–53

Method	Detection Limit (3σ) ($\mu\text{g l}^{-1}$)			Repeatability (% RSD)		
	MeHg	EtHg	Inorg. Hg	MeHg	EtHg	Inorg. Hg
GC-rf-HC-GD-AES	0.2	0.2	0.3	5.0	7.9	7.5
GC-GD-AES [25] (flat cathode)	1.0	1.0	3.0	4.2	5.0	7.0
GC-MIP-AES [32]	0.8	1.3	—	—	—	—

Table 15.6 Speciation of mercury in certified reference material by GC-rf-GD-AES. Reproduced by permission of The Royal Society of Chemistry from Orellana-Velado, N. G., Pereiro, R., and Sanz-Medel, A., *J. Anal. At. Spectrom.* 2000, **15**, 49–53

	Methylmercury (mg kg^{-1} as Hg)	
	DORM-2	DOLT-2
Obtained	5.01 ± 0.35	0.620 ± 0.041
Certified	4.47 ± 0.32	0.693 ± 0.053

for bromine were obtained. The linear dynamic ranges were found to extend from 50 to 1500 pg s^{-1} for Cl and from 100 to 3500 pg s^{-1} for Br.

15.4 CONCLUSIONS

The results presented show that rf-GD and dc-GD sources are a favourable alternative to other low-power plasmas, such as the MIP and the SCP, which have been more frequently employed to date for the analysis of gases or volatilized analytes by AES.

Detection limits achieved by GD-AES for the determination of nonmetals present either in gases, in thermally vaporized organic liquids or even in volatile halines which are chemically produced from aqueous halides can even be lower than those obtained with other more common plasma sources for gas analysis and AES detection. Similarly, the determination of analytes that form volatile covalent hydrides, such as arsenic or antimony, by GD-AES and on-line flow procedures has been demonstrated to be feasible and even very promising.

On the other hand, the great potential of hyphenated systems involving GC and GD-AES detection with different source designs (HC and FC), and also for different modes of powering the discharge (rf and dc), has been definitely proved. In fact, in the case of mercury speciation better detection limits were obtained when using GC-rf-HC-GD-AES than those typical of MIP-AES. Further, the technique has been validated for the determination of methylmercury in real samples. Finally, it also has to be emphasized that the GC-GD-AES hybrid technique has the major advantage that the construction and maintenance costs of the system are low. Indeed, the consumption of He discharge gas (10 ml min^{-1} for the HC device) is about 10 times lower than that needed in MIP-AES.

15.5 REFERENCES

- [1] Broekaert, J. A. C. *J. Anal. At. Spectrom.* 1987, **2**, 537–542.
- [2] Marcus, R. K. *J. Anal. At. Spectrom.* 1993, **8**, 935–943.
- [3] Caroli, S. *J. Anal. At. Spectrom.* 1988, **3**, 887–891.
- [4] Koschuh, B.; Montes, M.; Camuña, J. F.; Pereiro, R.; Sanz-Medel, A. *Mikrochim. Acta* 1998, **129**, 217–223.
- [5] Camuña, J. F.; Montes, M.; Pereiro, R.; Sanz-Medel, A.; Katschthaler, C.; Gross, R.; Knapp, G. *Talanta* 1997, **44**, 535–544.
- [6] Chan, S. K.; Montaser, A. *Spectrochim. Acta, Part B* 1987, **42**, 591–597.
- [7] Puig, L.; Sacks, R. *Appl. Spectrosc.* 1989, **43**, 801–809.
- [8] Ng, K. C.; Ali, A. H.; Winefordner, J. D. *Spectrochim. Acta, Part B* 1991, **56**, 309–314.
- [9] Starn, T. K.; Pereiro, R.; Hieftje, G. M. *Appl. Spectrosc.* 1993, **47**, 1555–1561.
- [10] Pereiro, R.; Starn, T. K.; Hieftje, G. M. *Appl. Spectrosc.* 1995, **49**, 616–622.
- [11] Broekaert, J. A. C.; Starn, T. K.; Wright, L. J.; Hieftje, G. M. *Spectrochim. Acta, Part B* 1998, **53**, 1723–1735.

- [12] Centineo, G.; Fernández, M.; Pereiro, R.; Sanz-Medel, A. *Anal. Chem.* 1997, **69**, 3702–3707.
- [13] Nakahara, T. *Spectrochim. Acta Rev.* 1991, **14**, 95–109.
- [14] Feldman, C. *Anal. Chem.* 1979, **51**, 664–669.
- [15] Matsumoto, K.; Ishiwatari, T.; Fuwa, K. *Anal. Chem.* 1985, **56**, 1545–1548.
- [16] Sanz-Medel, A. (Ed.). *Flow Analysis with Atomic Spectrometric Detectors*, Elsevier, Amsterdam, 1999.
- [17] Broekaert, J. A. C.; Pereiro, R.; Starn, T. K.; Hieftje, G. M. *Spectrochim. Acta, Part B* 1993, **48**, 1207–1220.
- [18] Orellana-Velado, N. G.; Fernández, M.; Pereiro, R.; Sanz-Medel, A. *Spectrochim. Acta, Part B*, 2001, **56**, 113–122.
- [19] Rodríguez, J.; Pereiro, R.; Sanz-Medel, A. *J. Anal. At. Spectrom.* 1998, **13**, 911–915.
- [20] Freeman, J. E.; Hieftje, G. M. *Spectrochim. Acta, Part B* 1985, **40**, 475–492.
- [21] Freeman, J. E.; Hieftje, G. M. *Spectrochim. Acta, Part B* 1985, **40**, 653–664.
- [22] Harley, J.; Pretorius, V. *Nature*, 1956, **178**, 1244.
- [23] Lobinski, R.; Adams, F. C. *Spectrochim. Acta, Part B* 1997, **52**, 1865–1903.
- [24] Sanz-Medel, A. *Spectrochim. Acta, Part B* 1998, **53**, 197–211
- [25] Orellana-Velado, N. G.; Pereiro, R.; Sanz-Medel, A. *J. Anal. At. Spectrom.* 1998, **13**, 905–909.
- [26] Orellana-Velado, N. G.; Pereiro, R.; Sanz-Medel, A. *J. Anal. At. Spectrom.* 2000, **15**, 49–53.
- [27] Orellana-Velado, N. G.; Pereiro, R.; Sanz-Medel, A. *J. Anal. At. Spectrom.* 2001, **16**, 376–381.
- [28] Schepers, C.; Broekaert, J. A. C. *J. Anal. At. Spectrom.* 2000, **15**, 61–65.
- [29] Lovelock, J. E. *Anal. Chem.* 1961, **33**, 162–178.
- [30] Rivière, B.; Mermet, J.-M.; Deruaz, D. *J. Anal. At. Spectrom.* 1987, **2**, 705–709.
- [31] Costa-Fernández, J. M.; Lunzer, F.; Pereiro-García, R.; Sanz-Medel, A.; Bordel-García, N. *J. Anal. At. Spectrom.* 1995, **10**, 1019–1025.
- [32] Bulska, E.; Baxter, D. C.; Frech, W. *Anal. Chim. Acta* 1991, **249**, 545–554.

16

Low-pressure Inductively Coupled Plasmas

E. H. EVANS

Plymouth Analytical Chemistry Research Unit, Department of Environmental Sciences, University of Plymouth, Plymouth, UK

16.1 INTRODUCTION

The argon inductively coupled plasma (ICP), operated at atmospheric pressure, has been used widely as an ion source for mass spectrometry and as an excitation source for optical spectroscopy [1,2]. Its main advantages are:

- high thermal temperature, which ensures almost complete dissociation of all but the most refractory compounds, resulting in fewer chemical interferences;
- efficient excitation and ionization of the majority of the elements in the periodic table due to its high excitation and ionization temperatures;
- inert atmosphere resulting in fewer chemical interferences.

However, there are some applications in optical and mass spectrometry for which the atmospheric pressure, argon ICP is not ideal, the principal disadvantages being:

- it cannot be used for qualitative analysis because it breaks down compounds into their constituent atoms;
- it is expensive to purchase and running costs are high, especially in the developing world where the price of argon is high and it may not be readily available;
- in optical spectroscopy, lines with high excitation energies are not efficiently excited;
- in mass spectrometry there are a number of disadvantages:

- i. ionization is less efficient for elements with an ionization energy greater than ~ 9 eV, specifically the metalloids, chalcogens and halogens;
- ii. the determination of ^{39}K and ^{40}Ca , which are the major isotopes of these elements, suffers from interferences due to the major isotope of Ar at m/z 40;
- iii. N, C and O cannot be determined because of the high background caused by water and entrained atmospheric air;
- iv. the major isotopes of several important elements suffer from serious polyatomic ion interferences, e.g. the interferences of $^{14}\text{N}_2$ on ^{28}Si , $^{16}\text{O}_2$ on ^{32}S , $^{14}\text{N}^{16}\text{OH}$ on ^{31}P , $^{40}\text{Ar}^{16}\text{O}$ on ^{56}Fe and $^{40}\text{Ar}^{35}\text{Cl}$ on ^{75}As .

A number of approaches have been adopted in order to overcome these disadvantages, focusing on improving the excitation and/or ionization properties of the plasma, removing interferences, reducing running costs, improving the qualitative analysis capability, or all of these. The approaches are often facilitated by operating the ICP at low pressure, for the following main reasons:

- it is easier to form plasmas in gases other than argon, e.g. helium plasmas can be generated, which offer greater excitation and ionization energy and fewer interferences in mass spectrometry;
- atmospheric gases are excluded, thereby reducing the propensity for polyatomic ion interferences in mass spectrometry and molecular band emission in optical spectroscopy;
- the nonequilibrium nature of the plasma at low pressure results in higher excitation and ionization temperatures;
- lower gas flows and power consumption result in simpler construction and lower operating costs.

There are also several major disadvantages of reduced pressure plasma operation, namely that sample introduction is more problematic because of the requirement to maintain the plasmas at lower than atmospheric pressure and intolerance of solvents. Hence, low-pressure ICPs have found their major application when coupled with gas chromatography, vapour generation or electrothermal vaporization, and special measures must be adopted if liquid samples are to be introduced.

This chapter primarily describes instrumentation and applications of low-pressure inductively coupled plasmas (LP-ICPs) when used as sources for mass and optical spectrometry; however, for completeness, short sections on other related radio frequency (rf) and microwave plasmas are also included. Advantages and disadvantages of the LP-ICP for optical and mass spectrometry are discussed in comparison with the more commonly used atmospheric argon ICP. The fundamental characteristics and physical properties of low-pressure ICPs are discussed, followed by a treatment of the instrumentation and analytical requirements for coupling with optical and mass spectrometry. Likewise, short sections covering low-pressure microwave and other rf plasmas are also included. There

then follows a treatment of applications using these plasmas as element-selective and atomic/molecular detectors for gas chromatography, plus a separate section on reduced pressure afterglows and tandem sources.

16.2 FUNDAMENTALS

Fundamental studies of low-pressure rf plasmas fall broadly into the following two categories: studies of plasmas used as sources in optical emission or mass spectrometry, and studies of plasmas used as sources for processing applications in the semiconductor industry. It is the first category which primarily interests us as analytical spectroscopists; however, the second category contains much fundamental work on the physics of rf plasma sources very similar to those used in analytical spectroscopy, so this area will also be briefly reviewed.

The most comprehensive study of low-pressure ICPs used for atomic spectroscopy has been undertaken by Seliskar and co-workers [3–11], who designed a ‘reduced pressure’ ICP torch initially to be used for hydrogen isotope analysis [9]. This torch, the design of which is shown in Figure 16.1, was used to generate discharges in He, Ar, Ne, H₂ and N₂ at 27 MHz, power 5–500 W and pressure 0.01–10 Torr. Most of their studies concentrated on an He plasma for which they identified two modes of operation, dependent on power and pressure [10]. At low power a diffuse and dim plasma was observed, caused by capacitive (electrical) coupling of the rectified rf energy, called the *E-mode*. At higher power the plasma suddenly switched to a much brighter and denser plasma confined within the load coil, caused by inductive (magnetic) coupling of the rf energy, termed the *H-mode*. The power at which the E–H transition occurred (for He) varied with pressure, being 150 W at 4.8 Torr and 300 W at 38.5 Torr, and was accompanied by a large increase in the continuum radiation intensity. The E–H transition occurred at 15 W when the plasma was sustained in Ar. Subsequently, they studied the fundamental characteristics of Ar and He plasmas (primarily H-mode) by doping with other gases. The general conclusions were that (a) some species, notably the monovalent ions Cl⁺ and Ar⁺, exhibited a Boltzmann distribution and so possibly existed in partial local thermodynamic equilibrium (LTE) [4]; (b) neutral species of Ne, Ar and Kr were non-Boltzmann [5]; (c) rotational temperatures calculated using N₂, N₂⁺ and OH bandheads offered conflicting evidence, but tended to suggest a nonequilibrium system due to the curved nature of the Boltzmann plots [8,11]; (d) in the helium plasma there was a large distribution of excited state energies [10] up to and slightly beyond the first ionization energy of He (24.59 eV). The temperature measurements resulting from these studies are summarized in Table 16.1, although it should be remembered that these were not calculated in order to determine the temperature but rather as an indication of whether LTE existed.

Fannin *et al.* [7] studied the same (He) plasma using Fermi–Dirac statistics and argued that this, or any other plasma, should not be considered in terms of

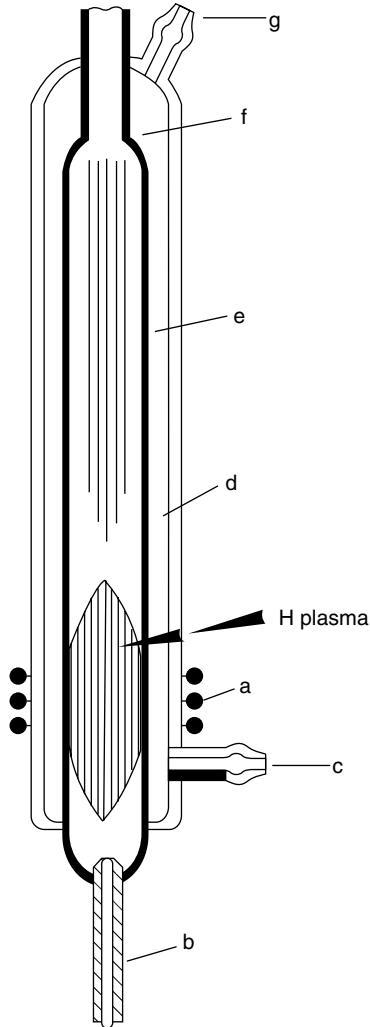


Figure 16.1 Reduced pressure ICP torch designed by Seliskar and co-workers. Reprinted from Miller, D. C., Fannin, H. B., Fleitz, P. A. and Seliskar, C. J., *Appl. Spectrosc.*, 1986, **40**, 611–617, with permission of The Society for Applied Spectroscopy

LTE, but rather in terms of different distributions for different probe species (e.g. Fermi–Dirac for He I species and Boltzmann for monovalent ions) and a single spectroscopic temperature.

Ishii *et al.* [12] studied a reduced pressure ICP based on the design of Seliskar and Warner [3] and found that, for a helium plasma operated at 0.6 Torr and 260 W, $n_e = 4 \times 10^{14} \text{ cm}^{-3}$ (estimated using the series limit of the He $^3\text{S}-^3\text{P}$

Table 16.1 Summary of results of fundamental studies of reduced pressure ICPs used for analytical atomic spectrometry.

Plasma gas	Power (W)	Pressure (Torr)	Thermometric species	n_e (cm^{-3})	Temperature (K)	Ref.	
He	350	4.67	Ne I	4×10^{14}	8800 ± 800^a	5	
			Ar I		6300 ± 600^a		
			Kr I		5700 ± 500^a		
			Ar II		9400 ± 700^a		
			Kr II		$10\,000 \pm 1000^a$		
Ar (1–50% He)	250	—	Ar II	2.63×10^{14}	7800 ± 600	6	
			Ar II		8820 ± 970		
Ar	250	—	N ₂ 337.1 nm system	5.75×10^{14}	1650 ± 100	8	
			N ₂ ⁺ 391.4 nm system		1750 ± 50		
He	260	0.6	He ³ S– ³ P transition	4×10^{14}		12	
Ar	170	0.5	H _{β} Stark broadening	2.63×10^{14}		13	
	170	5		5.75×10^{14}			
	150	0.6	Fe lines				4430^b
							4300^c
							4400^b
	1.4				4300^c		
He	150	1.0			4250^b		
					4400^c		
					4250^b		
		1.6			4400^c		

^aDopant concentration of 1%.^b27.12 MHz.^c13.56 MHz.

transition and the Inglis–Teller equation). These results were obtained for a H-mode plasma residing within the load coil.

Choi *et al.* [13] characterized a low-pressure ICP-AES system used for laser ablation analysis. They used the Stark broadening of the H _{β} line at 486.13 nm to determine the electron number density (n_e) and excitation temperature (T_{exc}) for Ar and He plasmas over a range of pressure (0.5–5 Torr for Ar and 1.0–1.6 Torr for He) and power (50–200 W) resulting in values of $n_e = (2.63\text{--}5.75) \times 10^{14}$ (Ar plasma only) and $T_{\text{exc}} = 4200\text{--}4500$ K (for Ar and He using Fe lines). Yan *et al.* [14] characterized a reduced pressure ICP used for mass spectrometry, using a Langmuir probe to study the effect of pressure (7.5 and 17 Torr), power (225–450 W) and electrostatic shielding on plasma potential (V_p) for an

Ar plasma. V_p varied from 12–20 V (over the power range studied) without shielding to 5–6 V with shielding.

Recently, there has been considerable interest in the development of rf plasma sources for processing applications, such as reactive ion etching, in the semiconductor industry. Originally, rf capacitive discharges were used, but it soon became apparent that higher density plasmas could be maintained at lower gas pressures using inductively coupled or microwave induced discharges. Consequently, there has been an explosion in interest in the fundamental characterization of low-pressure ICP discharges formed with noble and molecular gases in the 5–500 mTorr pressure range. The literature is extensive so no attempt will be made to review it here other than mention of a few key references. Low-pressure ICP sources used for this type of work generally share several common characteristics since the introduction of the Gaseous Electronics Conference (GEC) RF Reference Cell [15], which was introduced in order to facilitate comparison of

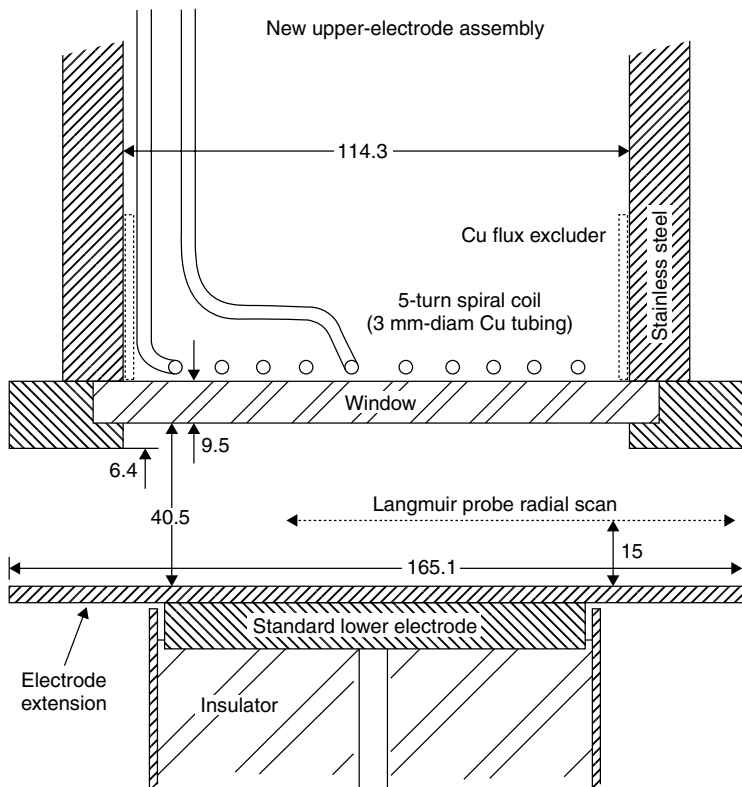


Figure 16.2 Schematic of the GEC rf reference cell. Reprinted from Miller, P. A., Heberner, G. A., Greenberg, K. E., Pochan, P. D. and Aragon, B. P., *J. Res. Natl. Inst. Stand. Technol.*, 1995, **100**, 427–439, with permission of the US Department of Commerce

results of plasma diagnostic experiments between researchers. The GEC reference cell is comprised of a five-turn planar coil that is pressed against a silica window through which it couples to the plasma (Figure 16.2). The plasma was operated in Ar (10 mTorr and between 34 and 250 W power) and Langmuir probe measurements yielded values of $n_e = 10^{12} \text{ cm}^{-3}$, $V_p = 21 \text{ V}$ and $T_e = 4 \text{ eV}$. In common with Miller *et al.* [10], the E–H transition was observed at very low power in Ar, but at higher powers in other gases. For example, for a nitrogen plasma operated at 20 mTorr the E-mode persisted up to 175 W input power (of which 150 W was dissipated resistively and only 25 W went into the plasma), then switched to the H-mode, which could be maintained down to 200 W (of which 77.5 W was dissipated resistively and 122.5 W went into the plasma).

Other workers [16] have modified the cell by electrostatically shielding the coil from the plasma to prevent capacitive coupling, so that the plasma only operates in the H-mode, which is preferred for ion etching owing to the greater plasma density. With the shield in place the plasma would no longer self-ignite in the E-mode, so a Tesla coil was used to ignite the inductive discharges at minimum powers of 30 W (Xe), 60 W (Ar), 130 W (Ne) and 320 W (N₂) between pressures of 7.6 and 76 mTorr. It was not possible to operate discharges in pure He or H₂. The GEC reference cell utilizes a planar rf coil; however, Okada *et al.* [17] studied a plasma cell with a three-turn, helical rf coil with an electrostatic shield between the coil and plasma cell (similar to coils used in analytical spectroscopy). They reported $n_e = 1.2 \times 10^{12} \text{ cm}^{-3}$, $T_e = 2.1 \text{ eV}$ and $V_p = 12 \text{ V}$ for a 1 kW Ar plasma operated at 50 mTorr. They also studied the electron energy distribution function (EEDF) using a Langmuir probe and showed that it was predominantly Maxwellian at pressures above 10 mTorr, but changed to a Druyvesteyn distribution below 10 mTorr. This finding is supported by Hori *et al.* [18], who observed a Maxwellian distribution above 20 mTorr using Thompson scattering.

So, in summary, reduced pressure ICPs can be operated in two modes: a low-power E-mode, caused by capacitive (electrical) coupling of the rectified rf energy, which gives rise to a dim, diffuse plasma, and a high-power H-mode, caused by inductive (magnetic) coupling of the rf energy. The power at which the E–H transition occurs varies with pressure and the nature of the plasma gas.

16.3 INSTRUMENTATION

16.3.1 LOW-PRESSURE INDUCTIVELY COUPLED PLASMAS

The principles of plasma formation for LP-ICPs are similar to those at atmospheric pressure, with the exception that the plasma is contained in a quartz discharge tube at reduced pressure. The pressure can be reduced sufficiently using a rotary vacuum pump. Most of the LP-ICPs to-date have been sustained using commercially available rf generators, which operate at 27 MHz, with the only alterations been made to the impedance matching network and load coil.

One of the main advantages of LP-ICPs is that stable plasmas can be formed in a variety of plasma gases with relative ease. An example of this is the fact that many of the LP-ICPs will self-ignite on the application of rf power to the load coil, whereas atmospheric pressure plasmas need to be 'seeded' with free electrons before ignition by use of a Tesla coil. LP-ICPs have been sustained in argon, helium, air, nitrogen and mixtures of these gases with chemical ionization reagent gases such as isobutane and ammonia. These plasmas have been sustained between 5 and 750 W forward power and between 0.01 and 10 mbar pressure.

Optical Emission Spectrometry

A low-pressure ICP torch for optical emission spectroscopy was originally designed by Seliskar and Warner [3] and subsequently adapted for use by Ishii *et al.* [12], as shown in Figure 16.1. This shows the H-mode plasma which is contained within the load coil. The E-mode plasma is more diffuse and is contained along the whole length of the discharge tube. More recently, a simple design was reported by Jerrel *et al.* [19], who utilized a 48-turn load-coil, wound around a quartz discharge tube, and coupled to a 35 MHz rf generator with an estimated power output of 15 W. They introduced helium gas to obtain a pressure of 8 Torr, 70 cm downstream from the plasma source. A gas chromatograph was coupled to the discharge and atomic emission was monitored with several spectrometric systems, the most convenient of which was an Ocean Optics plug-in spectrometer with a 1200 lines mm^{-1} grating connected via a 50 μm diameter fibre optic.

Mass Spectrometry

Evans and Caruso [20] initially designed an LP-ICP torch constructed of three concentric quartz tubes, not dissimilar to an atmospheric pressure torch. This torch was water-cooled and fitted inside the load coil of a commercial instrument. The water cooling was a precautionary measure to prevent the torch from melting because no outer cooling gas flow was present. This torch was later simplified to a single quartz tube of $\frac{1}{4}$, $\frac{1}{2}$ or $\frac{3}{4}$ in outer diameter for use under conditions of low power and gas flow [21]. The plasma gas in these cases was supplied via an ultra-torr T-piece or by an additional $\frac{1}{4}$ in side arm. The dimensions of the torches were chosen because of the availability of standard vacuum fittings which coupled the torch to the mass spectrometer interface and sample introduction method. The low-pressure torch was coupled to the first-stage expansion chamber of a commercially available ICP-MS instrument by replacing the original sampling cone with a specially constructed low-pressure sampler similar to that designed by Creed *et al.* [22], as shown in Figure 16.3. This consisted of a solid aluminium sampler cone which was machined with

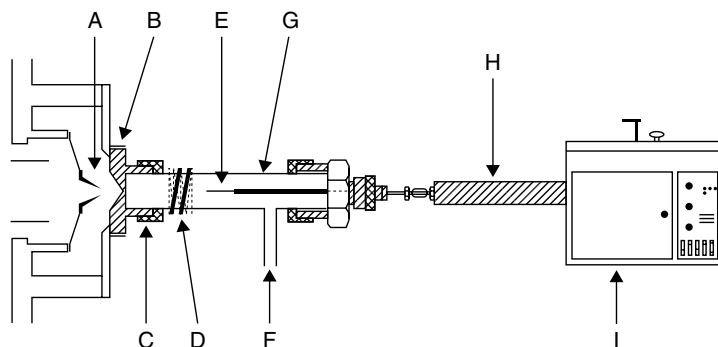


Figure 16.3 Diagram of the LP-ICP-MS interface. A, skimmer; B, low-pressure sampler; C, vacuum fitting; D, ICP load coil; E, tip of GC column; F, plasma gas; G, quartz torch; H, heated transfer line; I, gas chromatograph. Reprinted with permission from Evans, E. H., Pretorius, W., Ebdon, L. and Rowland, S., *Anal. Chem.*, 1994, **66**, 3400–3407. Copyright 1994 American Chemical Society

an ultra-torr vacuum fitting of the required size. This enabled the low-pressure torch to be vacuum sealed to the expansion chamber. The sampler orifice on the LP sampler had a diameter of 2.5 mm, which permitted effective pumping of the LP torch via the vacuum pump present on the expansion stage of the mass spectrometer. It is usually necessary to improve the pumping capacity of the interface (e.g. if high gas flows are used or if helium is used as the plasma gas), either by the addition of a second vacuum port or by use of a large vacuum pump.

Although it is a relatively straightforward matter to convert a commercial atmospheric ICP for low-pressure operation, several problems may be encountered:

- the tuning networks on commercial instruments do not have the range to tune plasmas sustained at low-pressure and/or in gases other than argon, hence high reflected power will result unless the capacitors in the torch box are modified;
- the plasma sampling interface on commercial instruments has been optimized for sampling ions at atmospheric pressure, so sampler and skimmer orifices and spacings require optimization;
- the ion lenses have been designed to focus ions extracted from an argon ICP, with energies in the range ca 1–20 eV, whereas helium plasmas may result in ions with a larger energy spread, so compromise tuning conditions may be difficult to obtain;
- the mass analyser of the commercial instruments had a mass range from m/z 5 to 255, which is disadvantageous for applications where high-mass molecular ions may be formed.

These problems have resulted in the design and construction of a prototype LP-ICP-MS [23]. This was achieved by adapting an old GC-MS instrument, with an upper mass range of m/z 800, to sample ions from an LP-ICP. A modified rf generator and impedance matching network were used to form a stable 6 W, 3 ml min⁻¹, helium LP-ICP with no reflected power. Waggoner *et al.* [24] used a similar interface design but manufactured their own rf generator to sustain an LP-ICP. The generator operated at a frequency of 35 MHz and used a 48-turn load coil to sustain a 12 W LP-ICP. This novel generator was a considerably cheaper method of sustaining an LP-ICP, but it had the disadvantage of operating at a fixed power output.

One of the major advantages of the designs of the LP-ICPs described above is that there is no need to vent the GC solvent or add oxygen as a scavenger gas as is commonly the case with physically smaller microwave induced plasmas. Also, the requirement to introduce hydrogen as a scavenger gas to prevent refractory metal oxide formation on the torch walls is much reduced.

16.3.2 LOW-PRESSURE MICROWAVE INDUCED PLASMAS

Optical Emission Spectrometry

Originally, microwave plasmas were operated at pressures of less than 100 Torr in order to sustain the plasma [25]. With the advent of the TM₀₁₀ Beenakker cavity [26] it was possible to operate MIPs at atmospheric pressure in a variety of gases, so relatively little recent research has been undertaken with low-pressure microwave plasmas using this type of cavity. In this design the cavity is made of a highly conducting metal such as copper, and microwave energy, generated using a magnetron operating at a frequency of 2.45 GHz, is supplied via a coaxial cable and coupling loop. The diameter of the cavity should be equivalent to one wavelength and tuning is achieved using screws or slides set into the cavity. The quartz discharge tube is placed in the centre of the cavity where the oscillating electric field is at a maximum, the plasma gas passing through the tube is seeded with electrons using a Tesla coil, and a collisional ionization process is established between the oscillating electrons, ions and gaseous atoms. The MIP can be operated at powers between 50 and 3000 W, but high-power operation requires the use of a waveguide to deliver the microwave energy, water cooling of the cavity, careful tuning to prevent overheating and high gas flows to prevent the torch melting. Typical operating conditions are power 50–200 W and gas flow 0.2–1.0 l min⁻¹. The influence of pressure on the properties of an MIP formed with a TM₀₁₀ cavity has been studied by Goode *et al.* [27], who found that pressure had no significant effect on the excitation and rotational temperature of Ar and He plasmas.

Surfatron plasmas, introduced by Moisan *et al.* [28], have attracted some interest [29–32], yielding enhanced analyte emission and improved detection

limits at low pressures [33]. Theoretical and technical aspects of surfatron generation have been reviewed by Moisan and Zakrzewski [30] and Selby and Hieftje [29]. A typical surfatron design for spectrochemical analysis is shown in Figure 16.4. Microwave power is transferred into the plasma via a coaxial coupler and the length of the excitation structure is varied, after ignition, to achieve minimum reflected power. The resultant plasma can be several tens of centimetres long, requires no further tuning and can be operated over a wide range of frequency, power and gas flow. However, like the Beenakker cavity, this design cannot tolerate large amounts of solvent.

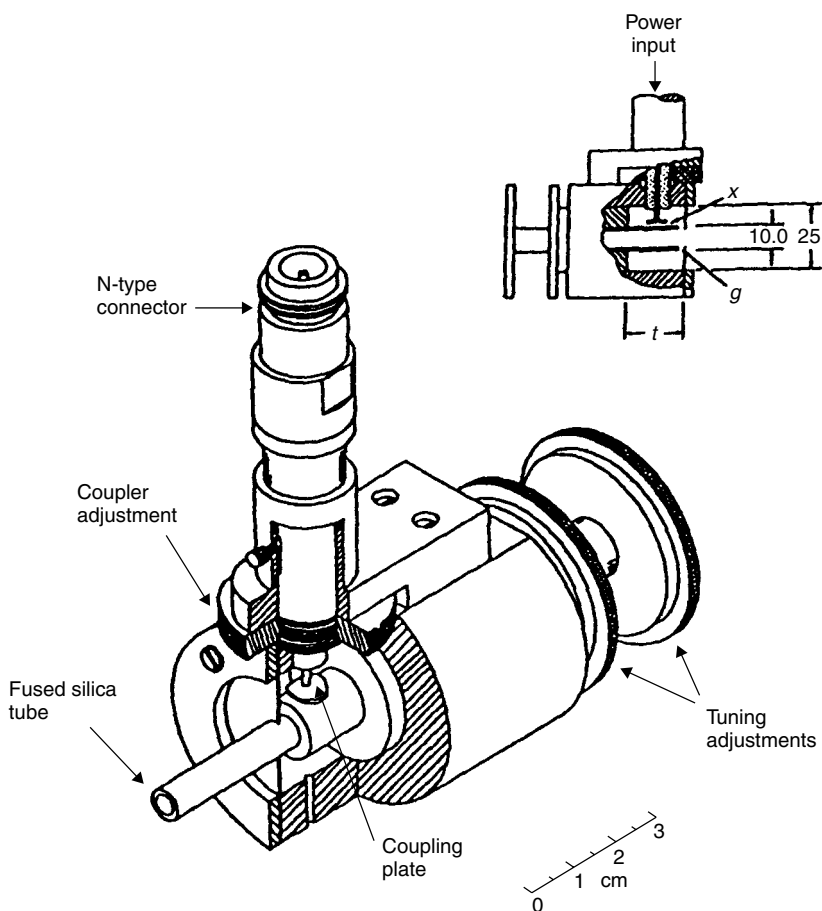


Figure 16.4 Surfatron designed for spectrochemical analysis. Reprinted from Selby, M. and Hieftje, G. M., *Spectrochim. Acta, Part B*, 1987, **42**, 285–298, with permission of Elsevier Science

Mass Spectrometry

The major application of the low-pressure MIP has been in combination with mass spectrometry, for the following reasons:

- it is relatively simple to interface a low-pressure torch to a low-pressure mass spectrometer, so the LP-MIP lends itself to this application;
- the axial nature of the ion sampling process is well suited to the type of interface necessary for LP-MIP-MS;
- air entrainment is reduced, resulting in the reduction of a number of troublesome polyatomic ion interferences, e.g. NOH^+ on P^+ at m/z 31;
- at low pressures thermal dis-equilibrium results in higher T_{exc} and n_e values compared with atmospheric pressure [34,35], hence MIPs are more efficient ionization sources at lower pressures;
- plasma ignition is easy, stabilization of the plasma occurs quickly, tuning is easier, reflected power is low and tube erosion is less of a problem compared with operation at higher power and plasma density [36];
- there is the possibility of using the source for both element-selective detection and molecular fragmentation.

A simple and effective interface between an MIP and mass spectrometer was originally described by Creed *et al.* [22], as shown in Figure 16.5, and has been widely adopted for LP-MIP-MS and LP-ICP-MS studies. The interface comprises a sampler machined from aluminium and incorporating a $\frac{1}{2}$ in ultra-torr vacuum fitting, into which the low-pressure MIP torch is inserted. A TM_{010} Beenakker cavity surrounded the discharge tube, and the rear of the torch was interfaced with a GC.

16.3.3 RF MICROPLASMA

Brede and co-workers [37–41] have developed an rf microplasma coupled with GC and mass spectrometry for element-selective detection shown in Figure 16.6. The source is effectively an rf capacitively coupled plasma, formed by twisting one rf and two grounded ring electrodes around a 4 cm long, 1.65 mm o.d., 0.35 mm i.d. quartz tube which forms a sheath around the GC capillary (Figure 16.6). The source is mounted inside the low-pressure housing of the mass spectrometer, which removes the need for a molecular beam interface, provided that sufficiently low gas flows are used. Helium is introduced into the torch at typical GC flow rates ($1\text{--}3 \text{ ml min}^{-1}$) and an rf field of 2–150 W and 100–500 kHz is applied to the central ring electrode to generate the plasma. Using this type of plasma, it is generally necessary to introduce oxygen or hydrogen to act as scavenger gases that prevent carbon deposition or the formation of refractory analyte oxides, respectively.

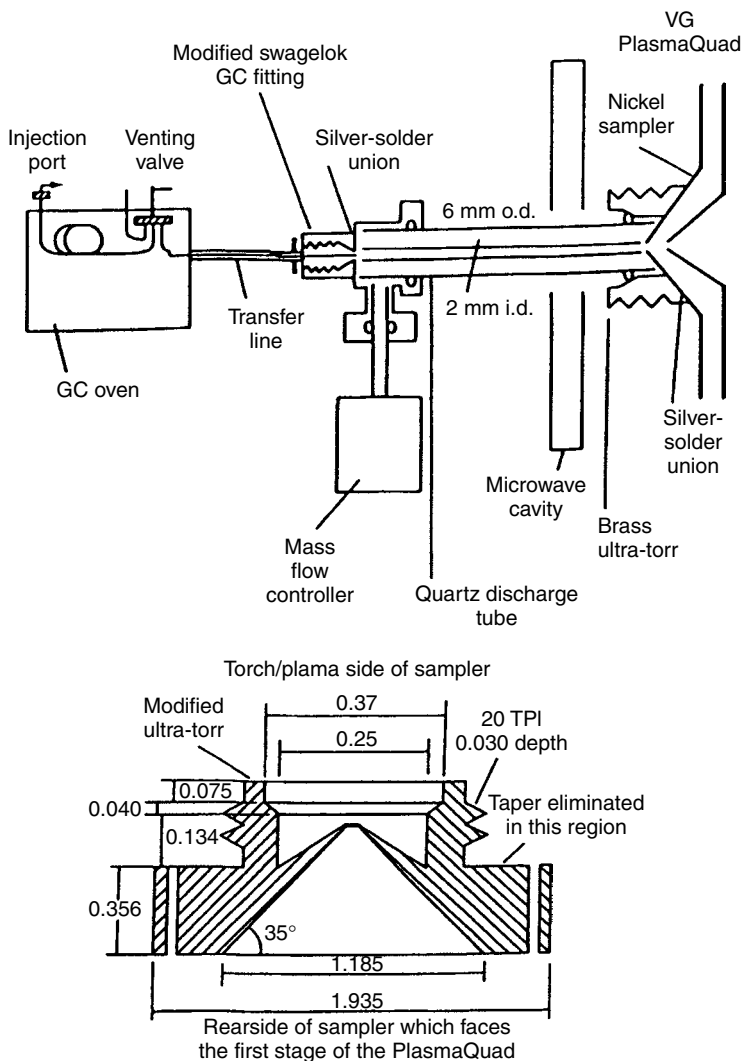


Figure 16.5 Interface for LP-MIP-MS: top, GC, torch and aluminium sampler; bottom, cross-sectional drawing of aluminium sampler. Reproduced by permission of The Royal Society of Chemistry from Creed, J. T., Davidson, T. M., Shen, W. and Caruso, J. A., *J. Anal. At. Spectrom.*, 1990, **5**, 109–113

16.3.4 REDUCED PRESSURE AFTERGLOWS AND TANDEM SOURCES

Reduced pressure afterglows extracted from an atmospheric ICP have been studied by Houk and co-workers [42–47] in order to understand better the

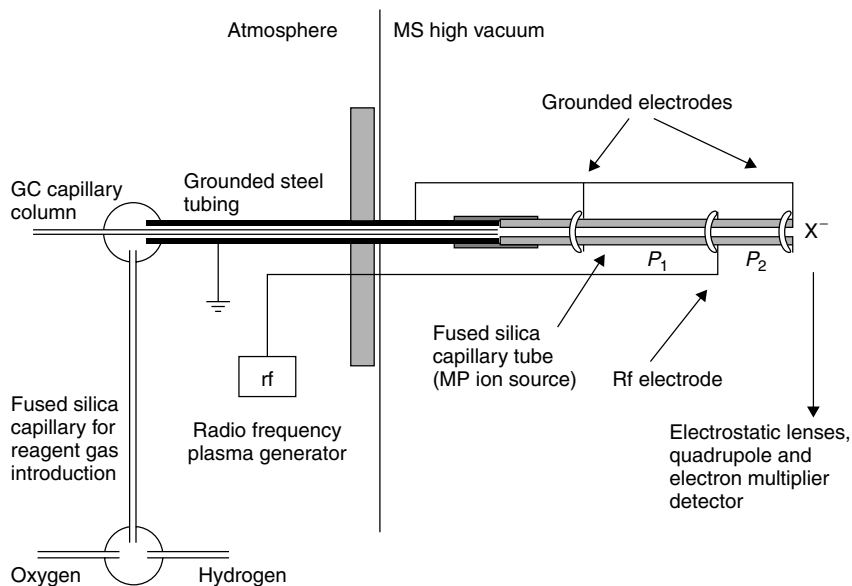


Figure 16.6 Microplasma ion source for mass spectrometry. Reproduced by permission of The Royal Society of Chemistry from Brede, C., Pedersen-Bjergaard, S., Lundanes, E. and Greibrokk, T., *J. Anal. At. Spectrom.*, 2000, **15**, 55–60

processes occurring in ion extraction for ICP-MS, and also as sources for AES. Two main types of extraction discharges have been studied, utilizing either a copper sampling cone [43,45] or flat plate [42,44,46,47]. The latter design was studied most extensively and comprised a water-cooled copper plate with a 0.53–1.06 mm orifice through which an argon ICP, operated at ca 1100 W, was extracted into a reduced pressure quartz chamber, as shown in Figure 16.7. The quartz chamber was maintained at a pressure of 1.8–9.5 Torr and atomic emission from the discharge was viewed through the side wall using various spectrometers, although typically an échelle spectrometer with a segmented array charge-coupled device (SCD) detector was used.

Borer and Hieftje [48,49] have developed a tandem source where the sample is nebulized into an atmospheric pressure ICP where it is vaporized, atomized, then extracted into a reduced pressure MIP where atomic emission is excited. The design of the tandem source is shown in Figure 16.8. The theoretical advantages of such a combination rely on ease of sample introduction into the ICP and its high atomization efficiency, coupled with the better ionization and excitation efficiency of the reduced pressure MIP. Most significantly, they found that the increase in excitation temperature (T_{exc} increased from ~ 5500 K at 660 Torr to ~ 6700 K at 60 Torr) was barely sufficient to offset the decrease in analyte number density caused by extraction into the low-pressure MIP.

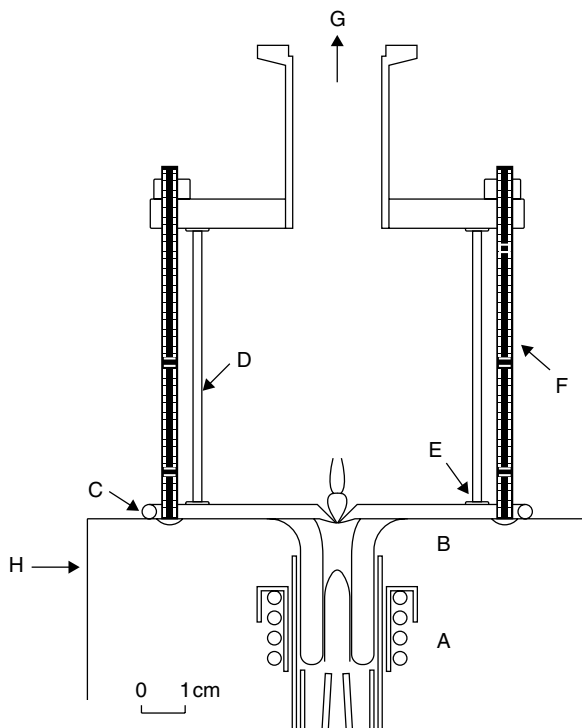


Figure 16.7 Apparatus used to study a reduced pressure afterglow extracted from an argon ICP. Reproduced by permission of The Royal Society of Chemistry from Luan, S., Pang, H. M. and Houk, R. S., *J. Anal. At. Spectrom.*, 1996, **11**, 247–252

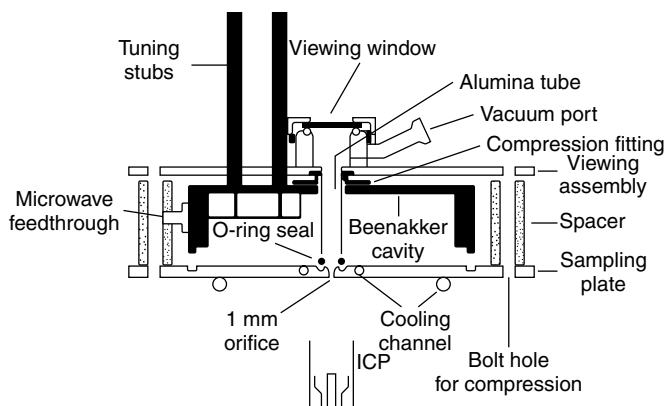


Figure 16.8 Tandem ICP-MIP source. Reproduced by permission of The Royal Society of Chemistry from Borer, M. W. and Hieftje, G. M., *J. Anal. At. Spectrom.*, 1993, **8**, 339–348

16.4 PRACTICAL ASPECTS AND RESULTS

Most of the low-pressure plasmas described in Section 16.3 have been used either for fundamental studies of plasma properties or in conjunction with gaseous sample introduction. Most of these plasmas have been used as detectors for GC, hence the following discussion concentrates primarily on this application of these sources. The main exception to this are the reduced pressure afterglows, such as extracted discharges and tandem sources used for atomic emission spectrometry, so these are dealt with separately at the end of this section.

16.4.1 ELEMENT-SELECTIVE DETECTION FOR GC SEPARATIONS

The principle advantage of plasma sources, whether they be atmospheric or low-pressure, is their selectivity, i.e. the unequivocal identification of the element of interest. The technique is also extremely sensitive, with detection limits for most elements in the picogram range, and has a large linear dynamic range of 100–10 000. However, such plasmas are relatively intolerant of solvent vapour, so they have been used most extensively as element-selective detectors for GC because of their selectivity advantage compared with flame ionization and electron capture detectors. In this context, selectivity is defined by the selectivity ratio, which is the ratio of the molar concentration of carbon to the molar concentration of the element of interest, which would give the same signal at the analysis wavelength or m/z .

Low-pressure Inductively Coupled Plasmas

Low-pressure ICPs have been used as sources for element-selective detection with both optical and mass spectrometry. As already mentioned, the LP-ICP is relatively intolerant of solvent vapour so applications have generally concentrated on the analysis of gaseous samples [9,50], gas chromatographic eluates [20,21,51], or dry aerosols from electrothermal vaporization [52], laser ablation [13] or hydride generation [53]. One publication has described liquid sample introduction [54].

Early publications by Seliskar and co-workers identified the suitability of a helium LP-ICP as an excitation source for optical emission spectroscopy and element-selective detection with gas chromatography [4], although they only reported on fundamental studies of this plasma. Later, Jerrell *et al.* [19] designed a simple system, utilizing a 15 W fixed-power plasma and a plug-in spectrometer, for the element-selective detection of halogenated compounds, and obtained the figures of merit shown in Table 16.2.

Table 16.2 Figures of merit obtained for GC–LP-ICP-AES for the element-selective detection of organohalide compounds (adapted from Ref. 19).

Analyte	Emission line (nm)	LOD (pg s ⁻¹)
Fluorobenzene	F 820.9	240
	F 867.9	550
	F 891.3	1110
Carbon tetrachloride	Cl 837.6	49
	Cl 912.1	80
Dibromobenzene	Br 826.5	117
	Br 881.995	370
	Br 889.8	155
Ethyl iodide	I 905.8	52

The groups of Evans and Caruso have developed argon [20,21,55] and helium [51] LP-ICPs (operated at powers between 90 and 1000 W and gas flows between 450 and 1000 ml min⁻¹) coupled with mass spectrometry for element-selective detection with GC (Table 16.3). The main advantage of these sources (and plasma sources in general) is their excellent selectivity and sensitivity, with the added advantages that gas usage and power consumption are low so that cost and instrument complexity are reduced. The excellent selectivity and sensitivity are clearly demonstrated in Figure 16.9, where it is apparent that element-selective detection for Pb at m/z 208, using argon LP-ICP-MS, yielded a much more selective chromatogram than that obtained by nonselective detection with FID. Another useful attribute of the technique is that nonselective chromatograms can also be obtained by monitoring the ion signal at m/z 12, thereby opening up the possibility of empirical formulae determinations. This application was pursued further by O'Connor *et al.* [55], who investigated the potential of the technique for the determination of volatile organic compounds (VOCs) in foods. They were able to analyse the headspace of olive oil samples spiked with a cocktail of VOCs using element-selective detection at m/z 35 and 13 for Cl and C, respectively (Figure 16.10). One of the problems that they encountered was a high background signal at m/z 12, which saturated the pulse-counting detector, so m/z 13 had to be used for carbon-selective detection; however, they were still able to obtain Cl/C ratios. Figures of merit for GC coupled with LP-ICP-MS used for element-selective detection are shown in Table 16.3.

The introduction of liquid samples by solution nebulization followed by desolvation has been investigated by Castellano *et al.* [54]. The low-pressure plasma in this instance was a 2 l min⁻¹ helium plasma operated at a forward power of 750 W. The solution was introduced by first forming a small aerosol mist by using either ultrasonic or glass frit nebulizers. The ultrasonic nebulizer was

Table 16.3 Selected figures of merit obtained for GC-LP-ICP-MS for the element-selective detection of organometallic and organohalide compounds.

Element, <i>m/z</i>	Compound	Detection limit (3σ) for element of interest (pg)	Power (W)	Gas/flow rate (ml min ⁻¹)	Plasma torch pressure (mbar)	Ref.
Br, 79	Bromobenzene	3.8	100	He/460	nd	51
Br, 79	Benzyl bromide	3.0				
Cl, 35	Chlorobenzene	2.9				
Cl, 35	Chloroheptane	8.1				
Cl, 35	Lindane	14				
Cl, 35	Chlorobenzene	500	200	Ar/1000	13	21
Fe, 56	Ferrocene	33				
Br, 79	Bromobenzene	50				
Sn, 120	Tetrabutyltin	35				
I, 127	Iodobenzene	25				
Pb, 208	Tetraethyllead	13				
Sn, 120	Tetraethyltin	11	90	He/562	nd	23
Sn, 120	Tetrabutyltin	2				
Pb, 208	Tetraethyllead	14				
Sn, 120	Tetraethyltin	0.12	12–15	He/375	nd	24
Sn, 120	Trimethylphenyltin	0.35				
Sn, 120	Tetrabutyltin	0.56				
I, 127	Iodobenzene	4	6	He/6	0.3	78
Br, 81	Dibromobenzene	76				
Hg, 202	Dimethylmercury	8	9	He/6	0.3	80
Cl, 35	Carbon tetrachloride	408	6	He/6	0.3	55
Cl, 35	Hexachlorobenzene	156				
Cl, 35	Tetrachloroethylene	105				
Cl, 35	1,4-Dichlorobenzene	72				
Cl, 35	Pentachlorobenzene	91				
Cl, 35	1,3,5-Trichlorobenzene	150				
Cl, 35	Chloroform	451				
Cl, 35	1,1,1-Trichloroethane	1				
Cl, 35	Carbon tetrachloride	45	100	Ar/450	nd	
Cl, 35	Hexachlorobenzene	19				
Cl, 35	Tetrachloroethylene	206				
Cl, 35	1,4-Dichlorobenzene	10				
Cl, 35	Pentachlorobenzene	14				
Cl, 35	1,2,3-Trichlorobenzene	7				
Cl, 35	Trichloroethylene	141				
Cl, 35	Chloroform	46				
Cl, 35	1,2-Dichloroethane	0.1				
C, 13	1,2,3-Trichlorobenzene	692				

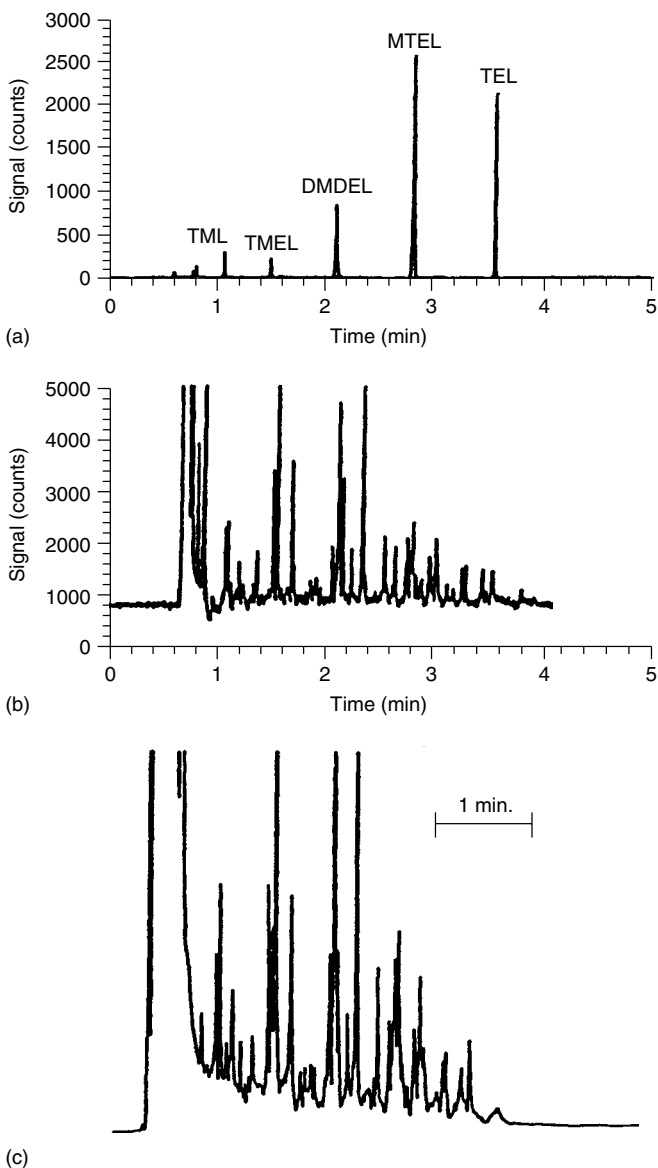


Figure 16.9 Element-selective chromatograms obtained for a sample of naphtha in hexane containing tetraethyllead (TEL), methyltriethyllead (MTEL), dimethyldiethyllead (DMDEL), trimethylethyllead (TMEL) and tetramethyllead (TML). The chromatograms were obtained using GC coupled with LP-ICP-MS detection with selective ion monitoring at (a) m/z 208 and (b) m/z 12, and (c) flame ionization detection (FID). Reprinted with permission from Evans, E. H., Pretorius, W., Ebdon, L. and Rowland, S., *Anal. Chem.*, 1994, **66**, 3400–3407. Copyright 1994 American Chemical Society

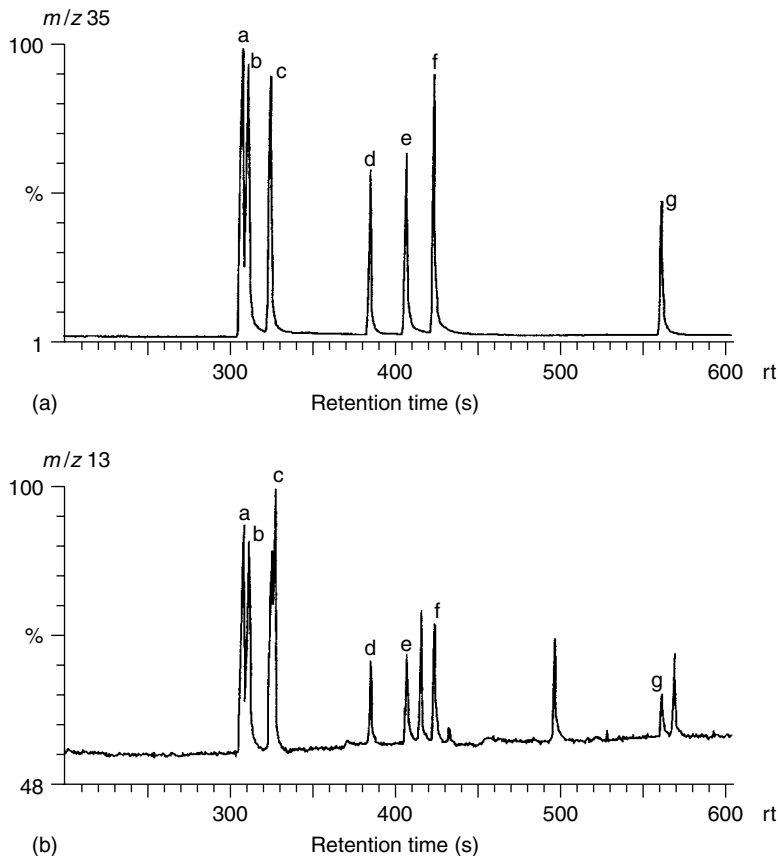


Figure 16.10 Selected ion chromatograms for 50 μl headspace of spiked oil monitored at (a) m/z 35; and (b) m/z 13. GC conditions: 0 $^{\circ}\text{C}$ for 3 min, increased to 220 $^{\circ}\text{C}$ at 20 $^{\circ}\text{C min}^{-1}$. (a) 1,2-Dichlorobenzene; (b) 1,3-dichlorobenzene; (c) 1,4-dichlorobenzene; (d) 1,2,3-trichlorobenzene; (e) 1,2,4-trichlorobenzene; (f) 1,3,5-trichlorobenzene; (g) pentachlorobenzene. Reproduced with permission from O'Connor, G., Rowland, S. J. and Evans, E. H., *J. Sep. Sci.* in press

shown to be ineffective at producing a stable aerosol at low pressure and therefore most of the solutions were nebulized using the glass frit design. A solution flow rate of 60 $\mu\text{l min}^{-1}$ was continuously nebulized and was then passed through a desolvation device before entering the plasma. Figures of merit for analytes directly nebulized into the LP-ICP are shown in Table 16.4.

Electrothermal vaporization (ETV) has been used to introduce liquid samples into an LP-ICP [52]. A 5 μl sample solution was placed on the filament of an ETV unit that was isolated from the LP-ICP via a series of valves. The water was then driven off in a desolvation step, which was seen to cause plasma fluctuations,

Table 16.4 Figures of merit for different types of sample introduction into LP-ICP-MS.

Element, <i>m/z</i>	Detection limit (3σ) for element of interest ($\text{ng ml}^{-1}/\text{pg}^{-1}$)	Power (W)	Gas/flow rate (l min^{-1})	Expansion pressure (mbar)	Sample introduction	Ref.
As, 75	12	750	He/2	1.4	Glass frit nebulizer	54
Br, 79	1.6/8	600	He/230	17	ETV, 5 μl sample	52
Cl, 35	5.3/26.5	600			ETV, 5 μl sample	
Se, 80	21	750	He/2	1.4	Glass frit nebulizer	54
I, 127	2.2/11	600			ETV, 5 μl sample	52
In, 115	15	750	He/2	1.4	Glass frit nebulizer	54
Cs, 133	12	750	He/2	1.4	Glass frit nebulizer	54
Pb, 208	6	750	He/2	1.4	Glass frit nebulizer	54

before the analyte was vaporized and ionized by the LP-ICP. The same group also reported briefly on the interfacing of hydride generation with helium LP-ICP-MS for the determination of Se [53]. Hydrides were generated with 2 mol l^{-1} HCl and 1% (w/v) NaBH_4 and swept into the plasma in a carrier gas of He at 100 ml min^{-1} . The major advantage of this approach is the interference-free determination of Se at m/z 80 because of the absence of $^{40}\text{Ar}^{40}\text{Ar}^+$. Figures of merit are given in Table 16.4.

Low-pressure Microwave Induced Plasmas

The greatest application of the microwave induced plasma (MIP) has been as an excitation source in an element-selective detector for gas chromatography, first described by McCormack *et al.* [25] and Bache and Lisk [56]. Originally, microwave plasmas were operated at pressures less than 100 Torr in order to sustain the plasma. With the advent of the Beenakker cavity [26], it was possible to operate MIPs at atmospheric pressure in a variety of gases, so that LP-MIPs have been otherwise largely ignored as excitation sources for AES. The role of microwave plasmas in atomic (optical) spectrometry has been comprehensively reviewed by Ebdon *et al.* [57,58] up to 1987, and more recently by Croslyn *et al.* [59] for the period 1985–97. The use of microwave plasmas in atomic (both optical and mass) spectrometry has been reviewed by Evans and O'Connor [60], Uden [61] and Jin *et al.* [62]. The surfatron microwave plasma operated at

reduced pressure has attracted some interest as an element-selective detector for gaseous sample introduction [63–65] for gas chromatography [33,66], liquid chromatography [67] and hydride generation [68]. Figures of merit obtained using low-pressure surfatron microwave plasmas as element-selective detectors are given in Table 16.5.

Coupling of an LP-MIP with mass spectrometry for element-selective detection of gas chromatographic eluates was first performed by Heppner [69], who investigated an MIP formed with helium or hydrogen at between 30 and 150 W forward power and at a pressure between 10 and 200 Torr. Compounds such as hexane and toluene were injected into an MIP using GC, although no actual chromatography was performed. The compounds were almost totally destroyed in the MIP, and broken down to constituent elements which recombined to form simple polyatomic forms such as CH, CH₄ and CO in the MIP tail-flame. These compounds were then extracted into a mass spectrometer where they were ionized using EI and analysed mass spectrometrically.

Subsequently, GC–LP-MIP-MS has been investigated by Caruso and co-workers [22,70,71] and O'Connor *et al.* [55]. In the original report by Creed *et al.* [22], the plasma was generated with helium at 60 W power, in a quartz tube interfaced directly to the first-stage expansion of the mass spectrometer, for element-selective detection of the halogens. This torch design was later modified by Caruso and co-workers [70,71], who compared different types of plasma torches for the detection of phosphorus- and sulphur-containing GC

Table 16.5 Figures of merit for different types of sample introduction into LP surfatron microwave plasma AES.

Element	λ (nm)	Compound	LOD (3σ) (ng ml ⁻¹)	LOD (3σ) (pg s ⁻¹)	Comments	Ref.
Cl	479.5	Lindane		3	GC, 50 Torr,	33
S	545.39	Malathion		35	170 W He	
P	253.56	Malathion		12	plasma	
Br	470.48	4-Bromo- acetophenone		10		
C	247.86	Lindane		3		
As	228.81		0.7		Hydride	68
Sb	231.15		0.9		generation,	
Se	259.81		1.2		30–60 Torr, 115 W Ar plasma	
As	228.8	Dimethylarsenic acid	6		HPLC and hydride	67
As	228.8	As(III)	1		generation,	
Hg	253.6	Methylmercury	0.35		50 Torr, 75–115 W Ar plasma	

eluates. The first was an air-cooled torch (low air flow), wherein the cooling gas was blown over the outer surface of the torch with a wall thickness of 2 mm, and the second was an improved design wherein cooling gas circulated around the periphery of a thin-walled (approximately 1 mm) torch. Detection of phosphorus at m/z 31 was possible using both types of plasma torch, but, a marked increase in sensitivity was observed using the second torch because the formation of refractory oxides of phosphorus at the torch walls was reduced. Detection of phosphorus would be difficult with an atmospheric MIP owing to the interference of NOH^+ at m/z 31. Water cooling of the torch and the addition of hydrogen as a scavenger gas further improved the sensitivity for phosphorus [71]. Also, in order to determine sulphur at m/z 32, it was better to use a nitrogen LP-MIP, rather than He, in order to minimize ionization of interfering O_2^+ , present in the plasma from ablation of the quartz tube and from impurities in the plasma gas. A summary of results obtained using low-pressure MIP-MS as an element-selective detector for GC eluates is given in Table 16.6.

Table 16.6 Figures of merit obtained for GC-LP-MIP-MS used for element-selective detection.

Compound	Element	LOD as mass of element (pg)	Comments	Ref.
1,2-Dichlorobenzene	Cl	31	He plasma, straight quartz torch	55
1,4-Dichlorobenzene	Cl	72		
Iodobenzene	I	0.1	60 W He plasma, 2 mm i.d. straight quartz torch	22
Bromononane	Br	3.5		
<i>p</i> -Chlorotoluene	Cl	24		
Chlorotoluene	Cl	22	450 W He plasma with 0.87% H_2 at 0.75 Torr, water-cooled torch	71
Chloronaphthalene	Cl	36		
Triethyl phosphate	P	90 000	90 W, He plasma at 2.1 Torr, air-cooled torch	70
	P	1000		
	P	86	450 W He plasma with 0.87% H_2 at 0.75 Torr, water-cooled torch	71
Diazinon	P	97	450 W He plasma with 0.87% H_2 at 0.75 Torr, water-cooled torch	71
	P	790		
	S	510	90 W N_2 plasma at 5.3 Torr, improved air-cooled torch	70
Malathion	P	229	He plasma, water-cooled torch	71
	P	570	90 W N_2 plasma at 5.3 Torr, improved air-cooled torch	70
	S	150		

Rf Microplasma

The rf microplasma of Brede has been coupled with GC and MS for element-selective detection of organohalides in positive [37–39] and negative ion [41] modes, and of organotin compounds [40]. One of the major advantages of this plasma is that there is no need for a molecular beam-type interface with the mass spectrometer because the plasma is compact enough and has sufficiently low gas flow that it can be contained entirely within the mass spectrometer. The device exhibits excellent detection limits and selectivity, as shown in Table 16.7 and Figure 16.11.

16.4.2 ATOMIC AND MOLECULAR DETECTION FOR GC SEPARATIONS

Low-pressure (and atmospheric pressure) ICPs and MIPs have proved extremely effective as sources for element-selective detection with mass and optical spectrometry, with excellent selectivity and sensitivity. When used in this way as a chromatographic detector, they have found considerable application for speciation studies of organometallic and other heteroatomic compounds. However, qualitative analysis can only be achieved by co-injection of a known standard compound because co-eluting compounds cannot be differentiated. Unknown compounds can only be identified by resort to an alternative technique such as electron ionization (EI), chemical ionization (CI), fast atom bombardment (FAB), thermospray and electrospray. Hence, it would be advantageous if a single ion source could fulfil all of these roles, i.e. sensitive and element-selective quantitative analysis and qualitative analysis of unknowns [72]. The following discussion relates to

Table 16.7 Figures of merit obtained for GC–microplasma-MS for the element-selective detection of organometallic and organohalide compounds.

Compound	Element, <i>m/z</i>	Detection limit (pg s ⁻¹)	Power (W)	Gas flows (ml min ⁻¹)			Ref.
				He	O ₂	H ₂	
1-Fluoronaphthalene	F, 19	6.1	5.2	2.3	0.001	0.016	38
1,3,5-Trichlorobenzene	Cl, 35	9.7					
1,4-Dibromobenzene	Br, 79	37					
Iodobenzene	I, 127	53					
1-Fluoronaphthalene	C, 12	13					
Tetraethyltin	Sn, 120	8.9	1.1	2.2	0.76	0	40
1-Fluoronaphthalene	F, 19	12	0.97	2.0	0.021	0.002	41
Hexachloroethane	Cl, 35	0.27					
1,4-Dibromobenzene	Br, 79	0.25					
Iodoheptane	I, 127	0.13					

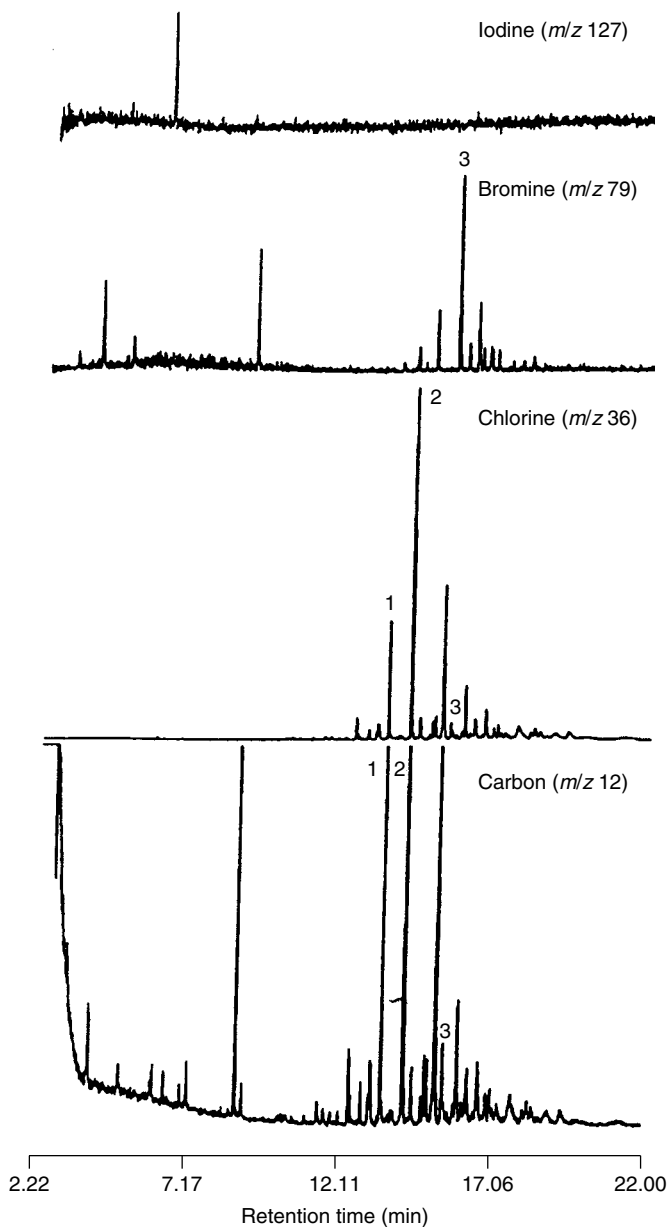


Figure 16.11 I-, Br-, Cl- and C-selective chromatograms of a Soxhlet extract in hexane of a deposited sludge from a nickel refinery. Reproduced by permission from Brede, C., Lundanes, E., Greibrokk, T., Pedersen-Bjergaard, S., *HRC-J. High Resolut. Chromatogr.*, 1998, **21**, 633–639, Copyright John Wiley & Sons

the use of low-pressure ICPs and MIPs in this regard; however, complementary research on the use of glow discharges (GDs) has also been undertaken (see Chapters 13 and 14).

Early work on the use of the microwave induced plasma as a possible 'soft' ionization source for molecular MS was undertaken by Heppner [69], as described above. Subsequently, Poussel *et al.* [73] utilized an MIP formed with argon, xenon or krypton, and maintained at a power of between 25–50 W, at pressures between 2×10^{-2} and 6×10^{-2} mbar. Compounds such as cyclohexane and dodecane were introduced directly into the tail-flame of the MIP discharge, where they were fragmented and ionized. These species were extracted into a mass spectrometer through a skimmer cone of 1.2 mm diameter, and yielded spectra similar to those obtained using EI. Similar work was performed by Olson *et al.* [74], who obtained spectra for chlorobenzene and toluene which were comparable to EI spectra. They also introduced compounds through the base of the MIP discharge and found that the molecular ions disappeared, with a consequent increase in the intensity of the monoatomic ions. These studies were followed up by Togashi *et al.* [75] in a fundamental investigation of the ionization processes. They investigated four possible ionization mechanisms in the low-pressure argon afterglow in the interface, namely:

- electron impact ionization;
- photoionization by argon resonance emission (internal energy 11.62, 11.83 eV);
- Penning ionization by argon atoms in a metastable state (internal energy 11.55, 11.72 eV);
- charge exchange with Ar^+ ions (internal energy 15.76 eV).

Methanol, methane and benzene were introduced into the interface of a conventional argon ICP-MS and the mass spectra were compared with those predicted using breakdown graphs, obtained by photoelectron-photoion coincidence spectroscopy, to estimate the internal energies of the molecules formed. This confirmed that charge exchange with Ar^+ was the predominant mechanism of ionization. Atmospheric pressure ionization (API) sources have also been developed utilizing an MIP [76,77]. The headspace vapour of perfluorotributylamine and tetramethyltin was introduced into an MIP and fragment ions produced, and the degree of fragmentation could be varied by changing the MIP power and carrier gas flow. A direct injection nebulizer (DIN) was also used to introduce a solution of tributylammonium hydroxide at a flow rate of 20–30 $\mu\text{l min}^{-1}$.

All of the studies discussed above were performed by introducing the pure compound or headspace vapour into the respective ion sources, so were not representative of analysis at concentrations found in most real samples. The first report of molecular fragmentation of ultra-trace level analytes with discrete sample introduction was by Evans *et al.* [21], who coupled gas chromatography (GC) with a low-pressure inductively coupled plasma (LP-ICP) and mass spectrometry

(MS) as shown in Figure 16.3. At 6–50 W power and 1 mbar He pressure (i.e. when operated in the E-mode), the source produced molecular ions and fragmentation spectra similar to an EI source. At 150 W power and 10 mbar Ar pressure (H-mode plasma), complete dissociation and hence element-selective detection were achieved for a variety of organohalogen and organometallic compounds. Subsequently, the groups of Evans and Caruso published a series of papers on the use of the LP-ICP-MS [23,24,78–81] and/or radio frequency glow discharge (rf-GD) [82–84] as ion sources for molecular and atomic mass spectrometry using GC sample introduction [23]. Figures of merit for LP-ICP-MS operated in both atomic and molecular modes are shown in Table 16.8.

Despite the obvious potential of plasma sources for atomic and molecular mass spectrometry, one of the problems encountered is the tendency for molecular fragment ions to form only when a large mass of analyte is injected, typically between 5 and 50 ng. In order to compete with established techniques such as EI or CI, gaseous detection limits of between 0.005 and 0.05 ng are required. O'Connor *et al.* [78] addressed this problem by introducing a reagent gas into the plasma. In this study it was observed that a helium plasma produced only elemental ion signals; however, the introduction of isobutane enabled the plasma to be operated in a tunable mode. The addition of 0.07 ml min⁻¹ of isobutane to a 3 ml min⁻¹ helium plasma produced mass spectra similar to EI spectra

Table 16.8 Figures of merit for GC–LP-ICP-MS operated at low power in atomic and molecular modes.

Analyte	<i>m/z</i> (ion) monitored	Mode of operation	LOD (pg)	Ref.
Dimethylmercury	202 (Hg ⁺)	Atomic	8	80
	202 (Hg ⁺)	Molecular	20	
Methylmercury chloride	217 (MeHg ⁺)	Molecular	48	
Methylethylmercury	217 (MeHg ⁺)	Molecular	18	
Tetraethyllead	208 (Pb ⁺)	Molecular	20	79
	237 (EtPb ⁺)		70	
	295 (Et ₃ Pb ⁺)		70	
Chlorobenzene	112 (ClPh ⁺)	Molecular	100	78
Iodobenzene	204 (IPh ⁺)	Molecular	140	
		127 (I ⁺)	Atomic	4
Dibromobenzene	236 (Br ₂ Ph ⁺)	Molecular	229	
	81 (Br ⁺)	Atomic	76	
Tetraethyltin	120 (Sn ⁺)	Atomic	0.12	24
Trimethylphenyltin			0.35	
Tetrabutyltin			0.56	
Bromobenzene	79 (Br ⁺)	Atomic	11	81
1-Bromoheptane			6.4	
Benzylbromide			4.2	

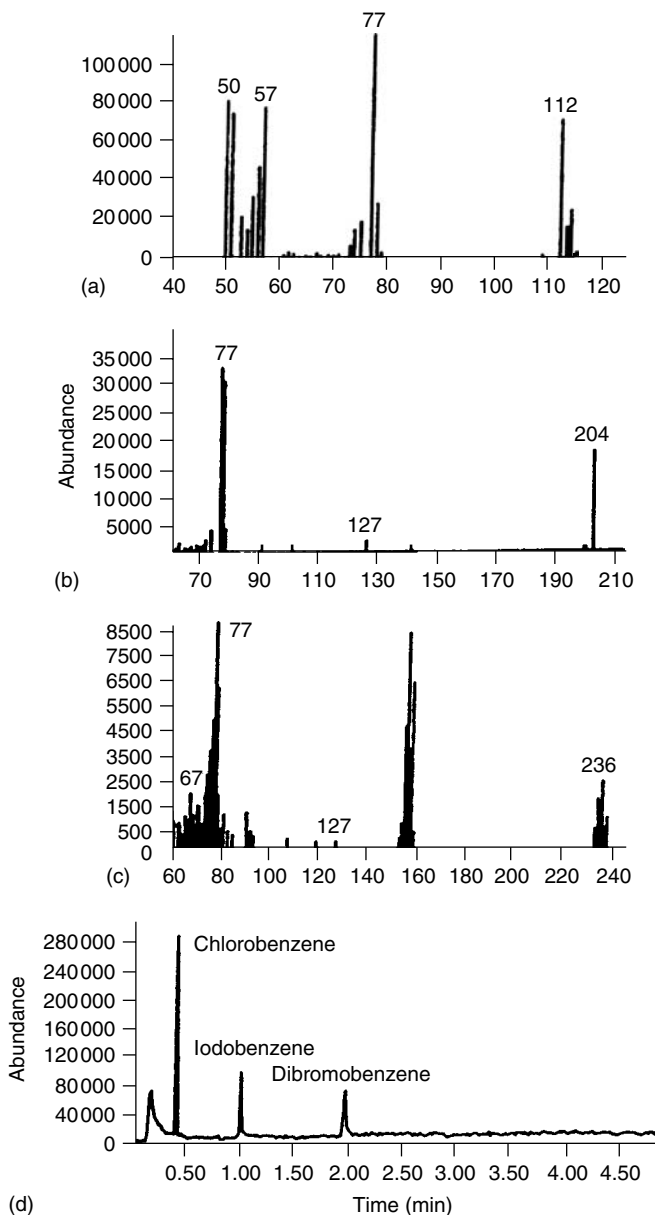


Figure 16.12 Mass spectra scans obtained from an isobutane–helium (0.07 and 3.0 ml min⁻¹) LP-ICP operated in ‘molecular’ mode for 10 ng on-column injection of (a) chlorobenzene, (b) iodobenzene and (c) dibromobenzene, and (d) total ion chromatogram. Reproduced by permission of The Royal Society of Chemistry from O’Connor, G., Ebdon, L. and Evans, E. H., *J. Anal. At. Spectrom.*, 1997, **12**, 1263–1269

for a series of organohalide compounds (Figure 16.12). Upon the addition of 0.2 ml min^{-1} of isobutane to the LP-ICP only the molecular ion of the analyte compound was visible with detection limits between 100 and $200 \text{ pg } \mu\text{l}^{-1}$ for the molecular ions. They defined the two modes of operation as 'atomic' (i.e. element-selective detection) and 'molecular' (i.e. qualitative analysis of unknowns). The same workers optimized the system for the determination of tetraethyllead in fuel [79], and achieved detection limits of $7 \text{ pg } \mu\text{l}^{-1}$ for the total ion signal and 20 and $70 \text{ pg } \mu\text{l}^{-1}$ for the fragment ions at m/z 208 and 295, respectively, when operating in the 'molecular' mode. It was possible to match almost exactly the mass spectrum for tetraethyllead in NBS CRM 1637 II gasoline with an EI source library spectrum. Similar qualitative results were obtained using an LP-ICP by Waggoner *et al.* [24,81], who found a match between empirical and library mass spectra of organotin and organohalide compounds. The technique has also been applied to the determination of methylmercury in marine samples and sediments [80] using ammonia as a reagent gas.

Other workers have utilized GD sources for atomic and molecular mass spectrometry [82–88], as discussed in Chapters 13 and 14.

16.4.3 REDUCED PRESSURE AFTERGLOWS AND TANDEM SOURCES

The reduced pressure afterglow developed by Houk and co-workers was used to study the ion extraction processes for ICP-MS and as a possible source for AES. In one publication [44], a number of fundamental studies to determine the temperature of the Mach disc of a reduced pressure afterglow at 0.9 Torr pressure were reported (Figure 16.7). Boltzmann plots of OH bandheads (305–325 nm) yielded straight-line relationships, indicating that the Mach disc was close to thermal equilibrium, with $T_{\text{rot}} = 2400 \pm 300 \text{ K}$. The Doppler temperature was determined from the Doppler broadening of the atomic emission lines of Ca (II, 393.4 nm) and Sr (II, 407.7 nm), and laser-induced atomic fluorescence of Na (I, 589.592 nm), to give $T_{\text{Dopp}} = 2200\text{--}2800$ and 2300 K, respectively, in the Mach disc. Subsequent reports [46,47] concentrated on the utility of the afterglow as a source for AES, with a number of optimization experiments performed to this end. In summary, they found that inducing a mild secondary discharge in the afterglow, by adjusting the operating conditions, resulted in maximum analyte emission from the Mach disc, although this was still $100\text{--}1000 \times$ lower than for an atmospheric pressure ICP. Nevertheless, the continuum background was much lower than in atmospheric pressure ICP-AES (equivalent to the shot noise), so low detection limits were still obtainable (Table 16.9).

In contrast, using an ICP-MIP tandem source, Borer and Hieftje [48,49] found that, despite a more uncluttered spectrum (with the exception of OH bands) and lower noise, poor signal-to-background ratios resulted in poorer detection limits and linear dynamic ranges compared with ICP-AES.

Table 16.9 Detection limits obtained for the reduced pressure afterglow compared with atmospheric pressure ICP-AES.

Species	Line (nm)	Detection limit (ng ml ⁻¹)		
		Without discharge ^a	With discharge ^b	Atmospheric pressure ^b
Ca II	393.366	2	0.1	0.4
Mg II	279.553	6	0.4	0.4
Sr II	407.771	4	0.1	0.1
Mn II	257.610	n/d	2	2

^aRef. 46.^bRef. 47.

16.5 CONCLUSIONS

Low-pressure plasmas have proved to be very successful when used as element-selective detectors for gas chromatography, whether coupled to optical emission or mass spectrometric detection. Their main advantages are that plasmas can be easily formed in a wide variety of gases, they are more portable and less expensive to operate than atmospheric pressure plasmas owing to low gas and power consumption and the excitation efficiency is generally enhanced at low pressure. However, they also suffer from the drawbacks that they have low gas kinetic temperatures and do not readily accept liquid samples. Perhaps the most promising uses for such plasmas are as tuneable or pulsed sources for atomic and molecular mass spectrometry, or possibly as tandem excitation sources.

16.6 REFERENCES

1. Ebdon, L.; Evans, E. H.; Fisher, A.; Hill, S. J. *An Introduction to Analytical Atomic Spectrometry*, Wiley: Chichester, 1998.
2. Evans, E. H.; Giglio, J. J.; Castellano, T. M.; Caruso, J. *Inductively Coupled and Microwave Induced Plasma Sources for Mass Spectrometry*, Royal Society of Chemistry: Cambridge, 1995.
3. Seliskar, C. J.; Warner, D. K. *Appl. Spectrosc.* 1985, **39**, 181–183.
4. Wolnik, K. A.; Miller, D. C.; Seliskar, C. J.; Fricke, F. L. *Appl. Spectrosc.* 1985, **39**, 930–935.
5. Fannin, H. B.; Seliskar, C. J.; Miller, D. C. *Appl. Spectrosc.* 1987, **41**, 621–624.
6. Fannin, H. B.; Seliskar, C. J. *Appl. Spectrosc.* 1987, **41**, 1216–1219.
7. Fannin, H. B.; Hurly, J. J.; Meeks, F. R. *Appl. Spectrosc.* 1988, **42**, 1181–1186.
8. Seliskar, C. J.; Miller, D. C.; Fleitz, P. A. *Appl. Spectrosc.* 1987, **41**, 658–660.
9. Miller, D. C.; Seliskar, C. J.; Davidson, T. M. *Appl. Spectrosc.* 1985, **39**, 13–19.
10. Miller, D. C.; Fannin, H. B.; Fleitz, P. A.; Seliskar, C. J. *Appl. Spectrosc.* 1986, **40**, 611–617.
11. Fleitz, P. A.; Seliskar, C. J. *Appl. Spectrosc.* 1987, **41**, 679–682.
12. Ishii, I.; Tan, H. M.; Chan, S. K.; Montaser, A. *Spectrochim. Acta, Part B* 1991, **46**, 901–916.

13. Choi, Y. S.; Lee, S. C.; Im, H. S.; Park, C. J. *Microchem J.* 1999, **63**, 24–33.
14. Yan, X. M.; Huang, B. L.; Tanaka, T.; Kawaguchi, H. *J. Anal. At. Spectrom.* 1997, **12**, 697–701.
15. Miller, P. A.; Hebnner, G. A.; Greenberg, K. E.; Pochan, P. D.; Aragon, B. P. *J. Res. Natl. Inst. Stand. Technol.* 1995, **100**, 427–439.
16. Schwabedissen, A.; Benck, E. C.; Roberts, J. R. *Phys. Rev. E* 1997, **55**, 3450–3459.
17. Okada, K.; Komatsu, S.; Matsumoto, S. *J. Vac. Sci. Technol. A* 1999, **17**, 721–725.
18. Hori, T.; Bowden, M. D.; Uchino, K.; Muraoka, K. *Appl. Phys. Lett.* 1996, **69**, 3683–3685.
19. Jerrell, L. J.; Dunn, M. R.; Anderson, J. E.; Fannin, H. B. *Appl. Spectrosc.* 1999, **53**, 245–248.
20. Evans, E. H.; Caruso, J. A. *J. Anal. At. Spectrom.* 1993, **8**, 427–431.
21. Evans, E. H.; Pretorius, W.; Ebdon, L.; Rowland, S. *Anal. Chem.* 1994, **66**, 3400–3407.
22. Creed, J. T.; Davidson, T. M.; Shen, W.; Caruso, J. A. *J. Anal. At. Spectrom.* 1990, **5**, 109–113.
23. O'Connor, G.; Ebdon, L.; Evans, E. H.; Ding, H.; Olson, L. K.; Caruso, J. A. *J. Anal. At. Spectrom.* 1996, **11**, 1151–1161.
24. Waggoner, J. W.; Belkin, M.; Sutton, K. L.; Caruso, J. A.; Fannin, H. B. *J. Anal. At. Spectrom.* 1998, **13**, 879–883.
25. McCormack, A. J.; Tong, S. C.; Cooke, W. D. *Anal. Chem.* 1965, **37**, 147.
26. Beenakker, C. I. M. *Spectrochim. Acta, Part B* 1976, **31**, 483.
27. Goode, S. R.; Buddin, N. P.; Chambers, B.; Baughman, K. W.; Deavor, J. P. *Spectrochim. Acta, Part B* 1985, **40**, 317–328.
28. Moisan, M.; Beaudry, C.; Leprince, P. *IEEE Trans. Plasma Sci.* 1975, **PS-3**, 55–59.
29. Selby, M.; Hieftje, G. M. *Spectrochim. Acta, Part B* 1987, **42**, 285–298.
30. Moisan, M.; Zakrzewski, Z. *J. Phys. D: Appl. Phys.* 1991, **24**, 1025–1048.
31. Timmermans, E. A. H.; Jonkers, J.; Rodero, A.; Quintero, M. C.; Sola, A.; Gamero, A.; Schram, D. C.; van der Mullen, J. A. M. *Spectrochim. Acta, Part B* 1999, **54**, 1085–1098.
32. Abdallah, M. H.; Mermet, J. M. *Spectrochim. Acta, Part B* 1982, **37**, 391.
33. Riviere, B.; Mermet, J. M.; Deruaz, D. *J. Anal. At. Spectrom.* 1987, **2**, 705–709.
34. Busch, K. W.; Vickers, T. J. *Spectrochim. Acta, Part B* 1973, **28**, 85.
35. Brassemer, P.; Maessen, F. J. M. *J. Spectrochim. Acta, Part B* 1974, **29**, 203.
36. Evans, J. C.; Olsen, K. B.; Sklarew, D. S. *Anal. Chim. Acta* 1987, **194**, 247.
37. Brede, C.; Lundanes, E.; Greibrokk, T.; Pedersen-Bjergaard, S. *HRC–J. High Resolution Chromatogr.* 1998, **21**, 282–286.
38. Brede, C.; Lundanes, E.; Greibrokk, T.; Pedersen-Bjergaard, S. *HRC–J. High Resolution Chromatogr.* 1998, **21**, 633–639.
39. Brede, C.; Pedersen-Bjergaard, S.; Lundanes, E.; Greibrokk, T. *Anal. Chem.* 1998, **70**, 513–518.
40. Brede, C.; Pedersen-Bjergaard, S.; Lundanes, E.; Greibrokk, T. *J. Chromatogr. A* 1999, **849**, 553–562.
41. Brede, C.; Pedersen-Bjergaard, S.; Lundanes, E.; Greibrokk, T. *J. Anal. At. Spectrom.* 2000, **15**, 55–60.
42. Houk, R. S.; Lim, H. B. *Anal. Chem.* 1986, **58**, 3244–3248.
43. Houk, R. S.; Lafreniere, B. R.; Lim, H. B.; Fassel, V. A. *Appl. Spectrosc.* 1987, **41**, 391–395.
44. Lim, H. B.; Houk, R. S.; Edelson, M. C.; Carney, K. P. *J. Anal. At. Spectrom.* 1989, **4**, 365–370.
45. Lim, H. B.; Carney, K. P.; Edelson, M. C.; Houk, R. S.; Brenner, I. B. *Spectrochim. Acta, Part B* 1993, **48**, 1617–1623.

46. Luan, S.; Pang, H. M.; Houk, R. S. *J. Anal. At. Spectrom.* 1996, **11**, 247–252.
47. Amad, M. H.; Houk, R. S. *J. Anal. At. Spectrom.* 1998, **13**, 223–228.
48. Borer, M. W.; Hieftje, G. M. *J. Anal. At. Spectrom.* 1993, **8**, 333–338.
49. Borer, M. W.; Hieftje, G. M. *J. Anal. At. Spectrom.* 1993, **8**, 339–348.
50. Yan, X. M.; Tanaka, T.; Kawaguchi, H. *Appl. Spectrosc.* 1996, **50**, 182–187.
51. Castellano, T. M.; Giglio, J. J.; Evans, E. H.; Caruso, J. A. *J. Anal. At. Spectrom.* 1994, **9**, 1335–1340.
52. Yan, X. M.; Tanaka, T.; Kawaguchi, H. *Spectrochim. Acta, Part B* 1996, **51**, 1345–1353.
53. Tanaka, T.; Kobayashi, K.; Hiraide, M. *Nippon Kagaku Kaishi* 1999, 463–466.
54. Castellano, T. M.; Giglio, J. J.; Evans, E. H.; Caruso, J. A. *J. Anal. At. Spectrom.* 1997, **12**, 383–385.
55. O'Connor, G.; Rowland, S. J.; Evans, E. H. *J. Sep. Sci.* in press.
56. Bache, C. A.; Lisk, D. J. *Anal. Chem.* 1965, **37**, 1477.
57. Ebdon, L.; Hill, S. J.; Ward *Analyst* 1986, **111**, 1113–1138.
58. Ebdon, L.; Hill, S. J.; Ward *Analyst* 1987, **112**, 1–16.
59. Croslyn, A. E.; Smith, B. W.; Winefordner, J. D. *Crit. Rev. Anal. Chem.* 1997, **27**, 199–255.
60. Evans, E. H.; O'Connor, G. In *Speciation*, Caruso, J. A., Sutton, K. (Eds), Elsevier: Amsterdam, 2000.
61. Uden, P. C. *J. Chromatogr. A* 1995, **703**, 393–416.
62. Jin, Q.; Duan, Y.; Olivares, J. A. *Spectrochim. Acta, Part B* 1997, **52**, 131–161.
63. Riviere, B.; Mermet, J. M.; Deruaz, D. *J. Anal. At. Spectrom.* 1988, **3**, 551–555.
64. Granier, A.; Bloyet, E.; Leprince, P.; Marec, J. *Spectrochim. Acta, Part B* 1988, **43**, 963–970.
65. Montes Bayon, M.; Camuna Aguilar, F.; Pereiro, R.; Sanchez Uria, J. E.; Sanz-Medel, A. *Spectrochim. Acta, Part B* 1996, **51**, 685–695.
66. Riviere, B.; Mermet, J. M.; Deruaz, D. *J. Anal. At. Spectrom.* 1989, **4**, 519–523.
67. Costa Fernandez, J. M.; Lunzer, F.; Pereiro Garcia, R.; Sanz-Medel, A. *J. Anal. At. Spectrom.* 1995, **10**, 1019–1025.
68. Lunzer, F.; Pereiro Garcia, R.; Bordel Garcia, N.; Sanz-Medel, A. *J. Anal. At. Spectrom.* 1995, **10**, 311–315.
69. Heppner, R. A. *Anal. Chem.* 1983, **55**, 2170–2174.
70. Story, W. C.; Olson, L. K.; Shen, W.; Creed, J. T.; Caruso, J. A. *J. Anal. At. Spectrom.* 1990, **5**, 467–470.
71. Story, W. C.; Caruso, J. A. *J. Anal. At. Spectrom.* 1993, **8**, 571–575.
72. Marcus, R. K.; Evans, E. H.; Caruso, J. A. *J. Anal. At. Spectrom.* 2000, **15**, 1–5.
73. Poussel, E.; Mermet, J. M.; Deruaz, D.; Beaugrand, C. *Anal. Chem.* 1988, **60**, 923–927.
74. Olson, L. K.; Story, C. W.; Creed, J. T.; Shen, W.; Caruso, J. A. *J. Anal. At. Spectrom.* 1990, **5**, 471–475.
75. Togashi, H.; Hashizume, A.; Niwa, Y. *Spectrochim. Acta, Part B* 1992, **47**, 561–568.
76. Shen, W.; Satzger, R. D. *Anal. Chem.* 1991, **63**, 1960–1964.
77. Vela, N. P.; Caruso, J. A.; Satzger, R. D. *Appl. Spectrosc.* 1997, **51**, 1500–1503.
78. O'Connor, G.; Ebdon, L.; Evans, E. H. *J. Anal. At. Spectrom.* 1997, **12**, 1263–1269.
79. O'Connor, G.; Ebdon, L.; Evans, E. H. *J. Anal. At. Spectrom.* 1999, **14**, 1303–1306.
80. Rosenkranz, B.; O'Connor, G.; Evans, E. H. *J. Anal. At. Spectrom.* 2000, **15**, 7–12.
81. Waggoner, J. W.; Milstein, L. S.; Belkin, M.; Sutton, K. L.; Caruso, J. A.; Fannin, H. B. *J. Anal. At. Spectrom.* 2000, **15**, 13–18.
82. Belkin, M.; Waggoner, J. W.; Caruso, J. A. *Anal. Commun.* 1998, **35**, 281–283.
83. Belkin, M. A.; Olson, L. K.; Caruso, J. A. *J. Anal. At. Spectrom.* 1997, **12**, 1255–1261.

84. Gorecki, T.; Belkin, M.; Caruso, J.; Pawliszyn, J. *Anal. Commun.* 1997, **34**, 275–277.
85. Guzowski, J. P.; Broekaert, J. A. C.; Ray, S. J.; Hieftje, G. M. *J. Anal. At. Spectrom.* 1999, **14**, 1121–1127.
86. Guzowski, J. P.; Hieftje, G. M. *J. Anal. At. Spectrom.* 2000, **15**, 27–36.
87. Majidi, V.; Moser, M.; Lewis, C.; Hang, W.; King, F. L. *J. Anal. At. Spectrom.* 2000, **15**, 19–26.
88. Marcus, R. K.; Dempster, M. A.; Gibeau, T. E.; Reynolds, E. M. *Anal. Chem.* 1999, **71**, 3061–3069.

17

Multidimensional Ionization Sources for Plasma-source Mass Spectrometry

JOHN P. GUZOWSKI, JR and GARY M. HIEFTJE

Department of Chemistry, Indiana University, Bloomington, IN, USA

17.1 INTRODUCTION

The role of plasma-source mass spectrometry (PSMS) historically has been to provide an elemental inventory for the sample under investigation. One of the most powerful and popular atomic ionization sources for this purpose is the argon inductively coupled plasma (ICP), which was used first as a radiation source in optical emission spectroscopy and later as an ion source for a mass spectrometer [1,2]. The ICP comes close to fulfilling many of the characteristics of an ideal source for atomic spectrometry [3]; it is an efficient atomization and ionization (i.e. a ‘hard’) device, both liquids and gases can be introduced into it, and a large fraction of elements in the periodic table can be measured with the aid of this tool. Moreover, many different separation techniques and spectrometer geometries have been interfaced to the ICP, thereby adding to its flexibility and analytical utility [1].

Inductively coupled plasma mass spectrometry (ICP-MS) yields information about the elemental composition of a sample rapidly and reliably, even for analytes present at the sub-ng/L level [1]. However, it is now recognized that the chemical form of an element is an important factor in determining how the species will be received, transported, utilized, and eliminated from a biological or environmental system [4–10]; an accurate estimate of an analyte’s impact will require more than just a simple determination of its atomic constituents. The

process of identifying the chemical form of an element has been termed 'chemical speciation'; numerous review articles have discussed the experimental methodologies and approaches used to differentiate and identify chemical complexes and compounds [4,10–14]. Speciation is a very important task in analytical sciences. Chromium(VI) is toxic to humans, whereas Cr(III) is considered an essential nutrient [4,15,16]. Likewise, the fate of metals in the environment is strongly influenced by their chemical form. Heavy metal ions easily can move from one geographic location to another if complexed with humic acids, which are commonly found in the presence of decaying leaves and organic matter. These acids can transport this toxic cargo into drinking water aquifers located many miles from the original source of contamination [17].

Element-specific detectors for chromatography are important tools in chemical speciation [1,16,18,19]; excellent limits of detection (below picogram levels) can be achieved and the high degree of selectivity provides compensation for incomplete separations and elevated background levels. In these devices, an energetic source atomizes and ionizes constituents in the chromatographic effluents that are then measured by optical or mass spectrometry. Some of the more commonly applied devices include the microwave induced plasma (MIP) [20], microwave plasma torch (MPT) [21,22], inductively coupled plasma [2], and glow discharge (GD) [18,23]. A wide range of compounds can be analyzed with the separation methods that are commonly interfaced with these ion sources [1,18,19,22,24,25].

Conventional gas chromatography–mass spectrometry (GC–MS) relies primarily upon the electron impact (EI) ionization source to generate a reproducible molecular fragmentation pattern of an eluate [26]. Mass spectral reference libraries and search algorithms have been developed around these EI patterns, making them useful for identifying unknown components in chromatographic effluents. Analysis by GC–MS is restricted to thermally volatile or derivatized species, thus precluding its use for most biologically significant compounds. Moreover, EI and chemical ionization (CI) sources cannot be interfaced directly with LC or electrophoretic methods because of complications arising from the copious amount of solvent vapor that they generate. Fortunately, atmospheric pressure ionization sources such as electrospray ionization (ESI) [27], nanospray, and thermospray [28–30] can be used to convert ions and molecules in solution into gas-phase ions that can then be mass analyzed. More importantly, these atmospheric pressure ionization (API) devices produce 'soft' ionization, which makes them useful for studying thermally labile compounds such as proteins and carbohydrates. Very little atomic information ordinarily can be obtained from these low-power sources, so an alternative technique must be used to obtain elemental data.

A complete and virtually unambiguous identification strategy might involve producing a molecular fragmentation pattern, a molecular weight, and an elemental inventory for each component of a sample. This information, along with

a chromatographic retention time, would practically ensure that each unknown molecule or atomic species could be identified. The methods available to perform such an analysis already exist; however, it is necessary to analyze the sample on several different instruments, each of which provides a single kind of information. Unfortunately, the properties that make a device an ideal (or even useful) ionization source for elemental mass spectrometry [3] also make it a poor tool for generating molecular fragmentation patterns, and vice versa. Obviously, it would be desirable to obtain all of the information in a single measurement.

The development of multidimensional, or multipurpose, ion sources that can provide more than one sort of information would bridge the gap that now exists between conventional atomic and molecular ionization sources. This goal might be realized through the coupling of two or more devices in tandem, although this could be an expensive and complex solution. A simpler approach would be to use a single source operated under two or more sets of conditions, each corresponding to a specific (atomic or molecular) ionization mode [31]. Moreover, it would be desirable to capture the several types of information sequentially, and in real time, for a rapidly changing signal such as those produced by elution-based separation strategies.

In this overview, plasma-source mass spectrometric techniques that have been employed for the collection of atomic, molecular, and molecular fragmentation spectra will be outlined. Special emphasis will be placed on those methods that use plasma-based ionization sources in nontraditional and unique ways. Examples from the authors' laboratory will serve to illustrate several different approaches that might be useful in the further development of multidimensional ionization sources for mass spectrometry.

17.2 TANDEM SOURCES IN PSMS

Some of the intrinsic limitations of plasma-based ionization sources can be overcome by operating them in a tandem fashion [32,33]. In a tandem configuration, two or more sources are coupled in an attempt to take advantage of the most desirable characteristics of each. This integrated union is designed to achieve the properties of an ideal ionization source [3].

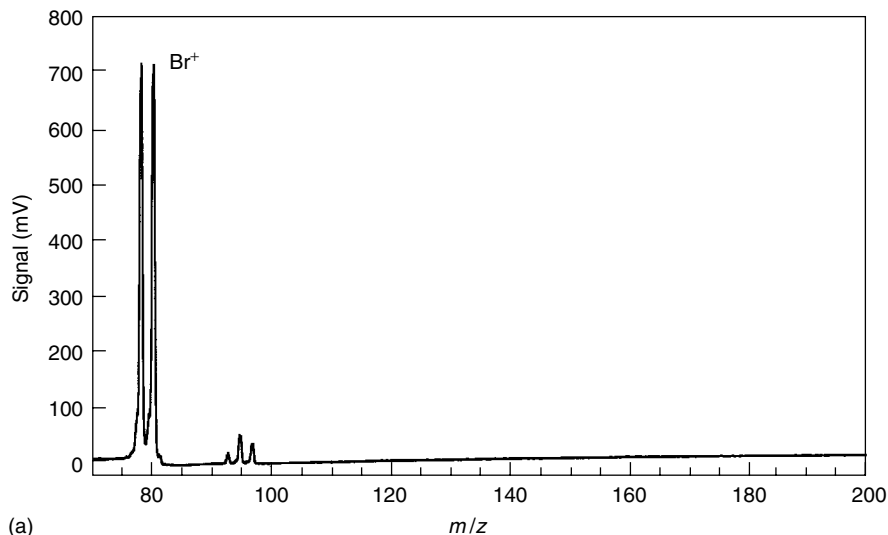
The first source of a tandem pair is often selected for its ability to convert the sample into a form that can be most effectively used by the second device, thereby maximizing the yield of chemical information [32]. In the first source, a sample component is atomized or molecular fragments produced and these products transported into the second unit. The primary function of the second source is to ionize (or excite) the atoms or molecules that have been generated in the previous step. If the second source operates at a significantly lower pressure than the first, sample vapor can be conveniently and efficiently transferred between partners [33]. Ideally, each source can be operated independently, which facilitates their optimization and eliminates the need to

work under compromise conditions. A classification system for tandem sources has been developed and used to categorize a variety of combinations for atomic spectrometry [32]. A few notable tandem sources for PSMS include laser ablation (sampling)—ICP (atomization/ionization)—MS [34], and electrothermal volatilization (vaporization)—ICP (atomization/ionization)—MS [35]. The definition of a tandem source (TS) recently has been revised to include combinations of sampling systems and atomization cells [36].

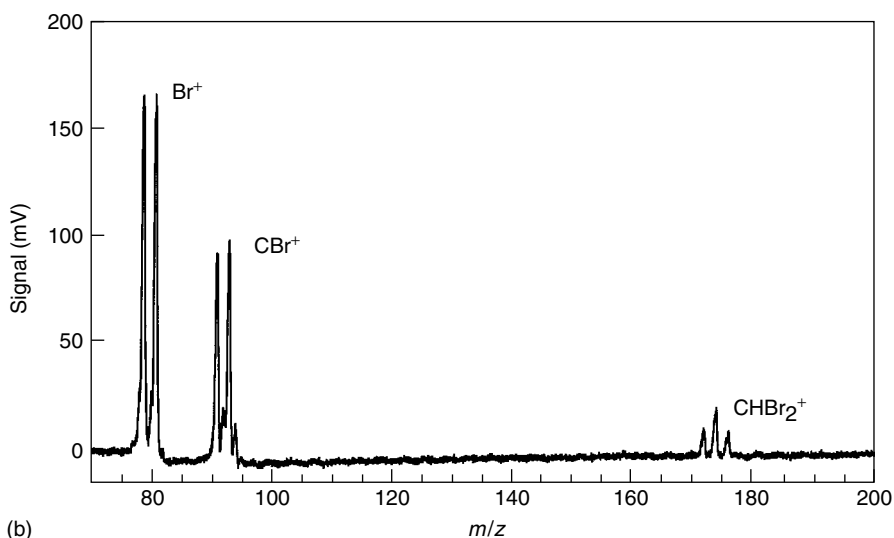
The development of combined sources has focused principally on the generation of atomic vapor. However, the tandem-source concept can be extended to include molecular–atomic ion generators, representing a departure from the definition first formulated by Borer and Hieftje [32]. In a tandem configuration described by Ray and Hieftje [37], an MPT constitutes the first source and an atmospheric sampling glow discharge (ASGDI) serves as the second device. Separately, the MPT [21,22] and ASGDI [38,39] effectively produce atomic and molecular ions, respectively. The atmospheric pressure helium MPT is an especially attractive ion source because it provides access to species such as nonmetals and halogens that possess high ionization potentials [21]. The reduced pressure ASGDI has been used to produce molecular fragmentation ions for organic compounds such as trinitrotoluene and bromobenzene [38,40].

This tandem pair was used to generate atomic and molecular fragment spectra for brominated hydrocarbons. The glow discharge was sustained in the first vacuum stage of a Balzers PAM 150 quadrupole mass spectrometer. The atomic mass spectrum was collected while both sources were operational, whereas the molecular spectrum was generated by extinguishing the MPT and sweeping sample vapor through its cavity and into the ASGDI. The GD sample introduction plate was biased at +350 V in these experiments and the grounded skimmer served as the cathode. This biasing arrangement is different from that employed by McLuckey *et al.* [39]; however, molecular fragmentation patterns could not be generated with the ASGDI unless it was ‘reverse-biased’. The first source operated at atmospheric pressure and the second at 5 Torr, which facilitates the transport of sample vapor between them [32].

The atomic and molecular fragmentation spectra of bromoform vapor produced in the MPT–ASGDI tandem source are presented in Figure 17.1a and b, respectively. The standard 70 eV EI pattern is depicted in Figure 17.1c for comparison [41]. The predominant species signal in the atomic mass spectrum is bromine; however, signals were observed at lower m/z (below 20 amu) and likely result from the ionization of entrained atmospheric gases [22]. Features in the atomic spectrum (m/z 93) also suggest the formation of polyatomic species such as $^{79}\text{Br}^{14}\text{N}^+$. The molecular fragmentation pattern (Figure 17.1b) contains a higher fraction of smaller m/z species than does the reference spectrum (Figure 17.1c). Nevertheless, a significant number of key fragment ions are present in Figure 17.1b and structural information could be obtained from such a plot.



(a)



(b)

Figure 17.1 Mass spectra collected from the microwave plasma torch (MPT)/atmospheric sampling glow discharge (ASGDI) tandem source combination for bromoform. The MPT gas flow rate was 25 ml/min and a forward power of 120 W was used. The ASGDI pressure was nominally 2 Torr, and the front plate was biased at +350 V (30 mA, current limited). (a) Atomic mass spectrum; (b) molecular mass spectrum, collected when the MPT was extinguished; (c) standard 70 eV EI mass spectrum. Adapted with permission from The Royal Society of Chemistry from Ray, S. J. and Hieftje, G. M., *Anal. Chim. Acta*, 2001, **445**, 35–45

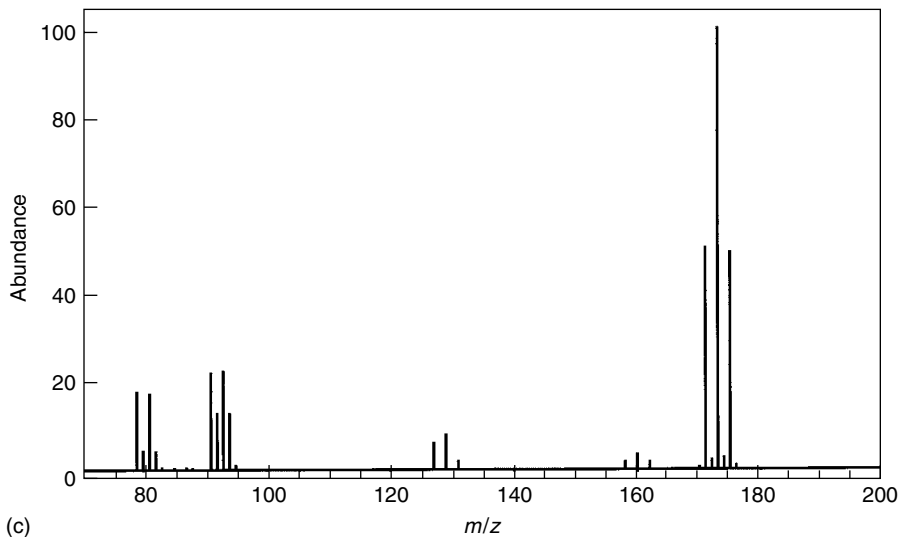


Figure 17.1 (continued)

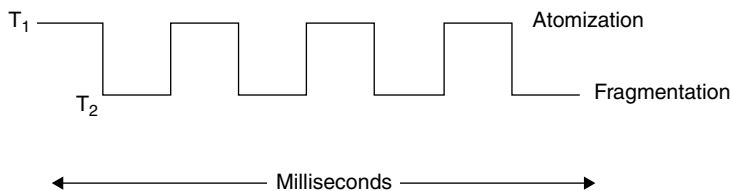


Figure 17.2 The modulated (or switched) source concept. In the low-power mode (T_2), the molecular fragmentation pattern could be collected. The plasma is then switched to a high-power mode (T_1) and the sample is atomized and ionized, and the elemental mass spectrum is obtained. A 50% duty cycle is presented; however, the best ratio should be experimentally determined for the source(s) used. Adapted with permission from Ref. [31]

The results presented by Ray [37] suggest that it might be possible to modulate the source(s) between two different power levels in an attempt to collect sequentially atomic and molecular fragmentation spectra; this concept is illustrated in Figure 17.2 [31]. The commercial microwave generator employed in the study by Ray and Hieftje [37] (Micotron 200, Oxfordshire, UK) has provisions for switching between two different power levels, so ideally a low (or zero) power mode could be established that would reduce the MPT efficiency, allowing the second source to generate molecular fragment ions. Several groups have shown that a glow discharge can be pulsed on and off at high rates (>100 Hz) [42–44]. It would seem possible to produce both types of patterns in rapid succession by synchronizing the power modulation of these two devices.

Several unique tandem sources can be envisioned: electrospray (molecular) and pulsed glow discharge (atomic) [42,43,45]; electrospray and power-modulated ICP [46] (or MPT); modulated glow discharge (atomic) [43,45] and electron impact (molecular) ionization. Separately, these sources have been successfully used to generate either atomic or molecular fragmentation spectra. Future efforts will certainly leverage the attractive features of each of these sources through novel tandem combinations.

17.3 MULTIPURPOSE IONIZATION SOURCES FOR PSMS

Ion source developments in PSMS have been fueled by an interest in overcoming some of the limitations of current atomic devices (such as spectroscopic and nonspectroscopic interferences) [1,2,31] and a desire to measure more than simply the elemental composition of a sample. The former issue is being addressed by studying the fundamental processes that occur during the generation and transport of sample vapor through PS instrumentation [3,31]; application-driven forces serve to advance the latter [4].

The information content obtained from PS mass spectrometric instrumentation can be enhanced by:

1. the development of hyphenated techniques such as GC-ICP-MS [4] or CE-ESI-TOFMS [47] that can provide complementary or orthogonal information;
2. operating the ion sources in unconventional or novel modes [32,43,45,48] as a means of enriching the information content of the analysis, which includes accessing alternative modes of ionization;
3. employing combinations of the above two strategies.

Classical ion sources configured to operate in nontraditional modes, and those that are capable of providing both atomic and molecular kinds of information, are highlighted below.

17.3.1 INDUCTIVELY COUPLED PLASMAS

The ICP is an efficient atomization and ionization device for atomic mass spectrometry [2]. Its high gas-kinetic temperature can easily desolvate and fragment species introduced into the plasma, yielding a relatively simple atomic mass spectrum. The ICP has been used less commonly to generate molecular fragmentation patterns.

Houk *et al.* [49] early described the production of molecular fragmentation spectra for an amino acid and a saccharide that were introduced into an atmospheric pressure ICP coupled to a quadrupole mass spectrometer. The 'cool' plasma was operated with a higher than usual central channel flow rate and

a slightly diminished forward power (1.0–0.9 kW). Accordingly, the analyte residence time in the plasma was reduced and the ICP gas-kinetic temperature lowered; these combined effects reduced atomization and enhanced the molecular fragmentation process. Many small m/z species were identified and attributed to the analyte, some of which were probably water-molecule clusters. The patterns were not compared with standard 70 eV EI spectra.

The most successful use of the ICP for the production of EI-like molecular fragmentation patterns involves its operation at reduced pressure (RP) and low power (LP) [48,50–52]. An ICP can easily be sustained at low forward power levels when operated at reduced pressure; the lower gas-kinetic temperature then reduces atomization and enhances fragmentation. Spectral interferences arising from entrainment of atmospheric gases can be minimized [1,53] through enclosed RP operation. Moreover, RP plasmas can be ignited easily and a variety of support gases used including air, helium, and oxygen [19]. Lower flow rates are typically required, thus permitting the practical use of less common (and higher purity) gases [54].

Evans and co-workers [48,51,55,56] used a low-power RP helium ICP for the production of molecular fragmentation patterns of halogenated hydrocarbons. The RP-ICP interface developed for a Fisons PlasmaQuad 2 is presented in Figure 17.3. A gas chromatograph (GC) was used for sample introduction [55], and the discharge sustained solely by the flow of gas from the column (~ 3 ml/min, helium) at a forward power of 15 W. The mass spectral fragmentation pattern for bromobenzene vapor introduced into the helium LP-ICP is presented in Figure 17.4 [55]; qualitatively it is very similar to the standard EI spectrum (Figure 17.1c), although the relative peak intensities between the two are slightly different. Waggoner *et al.* [52] documented the performance of

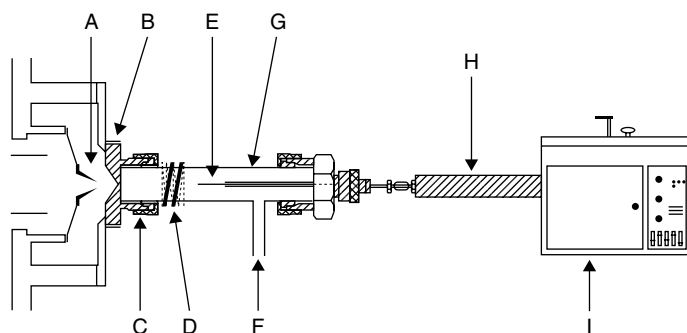


Figure 17.3 GC–LP-ICPMS interface: A, Skimmer; B, low-pressure sampler; C, vacuum fitting; D, ICP load coil; E, tip of the GC column; F, plasma gas; G, quartz torch; H, heated transfer line; I, gas chromatograph. Reprinted with permission from Evans, E. H., Pretorius, W., Ebdon, L. and Rowland, S., *Anal. Chem.*, 1994, **66**, 3400–3407. Copyright 1994 American Chemical Society

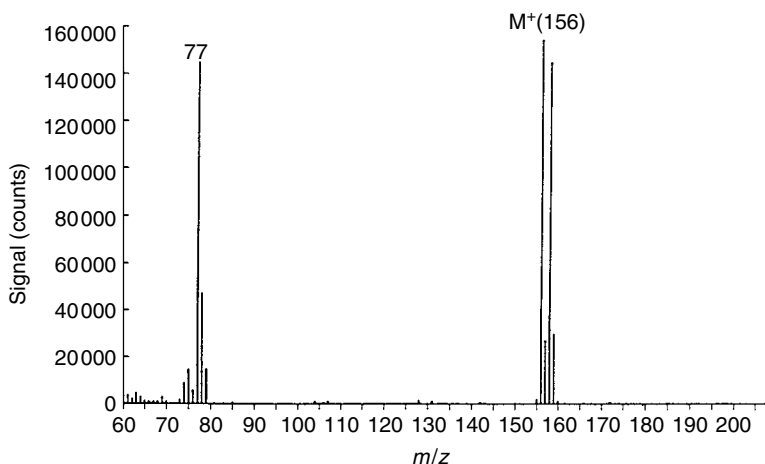


Figure 17.4 Mass spectrum for molecular fragmentation pattern of bromobenzene collected with the LP-ICP/MS. A forward power of 50 W was used, and the helium gas flow rate from the column used to sustain the plasma was ~ 3 ml/min. Reprinted with permission from Evans, E. H., Pretorius, W., Ebdon, L. and Rowland, S., *Anal. Chem.*, 1994, **66**, 3400–3407. Copyright 1994 American Chemical Society

a low-cost LP-ICP-MS, and used it to generate molecular fragmentation spectra of organic tin compounds. A gas chromatograph [52] was used to introduce tin compounds into this low-power (12–15 W) plasma; molecular detection limits were better (lower) than 1 pg. Molecular fragmentation patterns of tetraethyltin, tetramethyltin, and trimethyl(phenyl)tin resembled traditional EI spectra.

A reduced pressure ICP can be used for elemental-selective detection also if operated at a somewhat higher power (200 W) and pressure (13 mbar) [55] (Figure 17.3). In this case, atomic signal levels were strongly influenced by the flow of argon make-up gas introduced into the side arm of the interface (F in Figure 17.3); the optimal gas flow rates (0.2–1.2 L/min) appear to be element-specific. Detection limits were found to be in the range 13–500 pg for organohalogen and organometallic compounds introduced into the discharge from a gas chromatograph. The chromatographic analysis and element-selective mass spectrometric detection of a petroleum-based matrix containing several lead compounds is depicted in Figure 17.5a (Pb^+ , $m/z = 208$) and b (C^+ , $m/z = 12$) [55]. The gain in detection capability for lead can be immediately recognized by comparing Figure 17.5a and b, and underscores the importance of selective detection, especially for the analysis of complex samples.

Yan and co-workers [50] have shown that a low-pressure (132 Torr, 700 W) argon ICP can also be used for measuring elements having a high ionization potential [50]; signal levels for iodine were increased by more than one order of magnitude over similar measurements performed at atmospheric pressure.

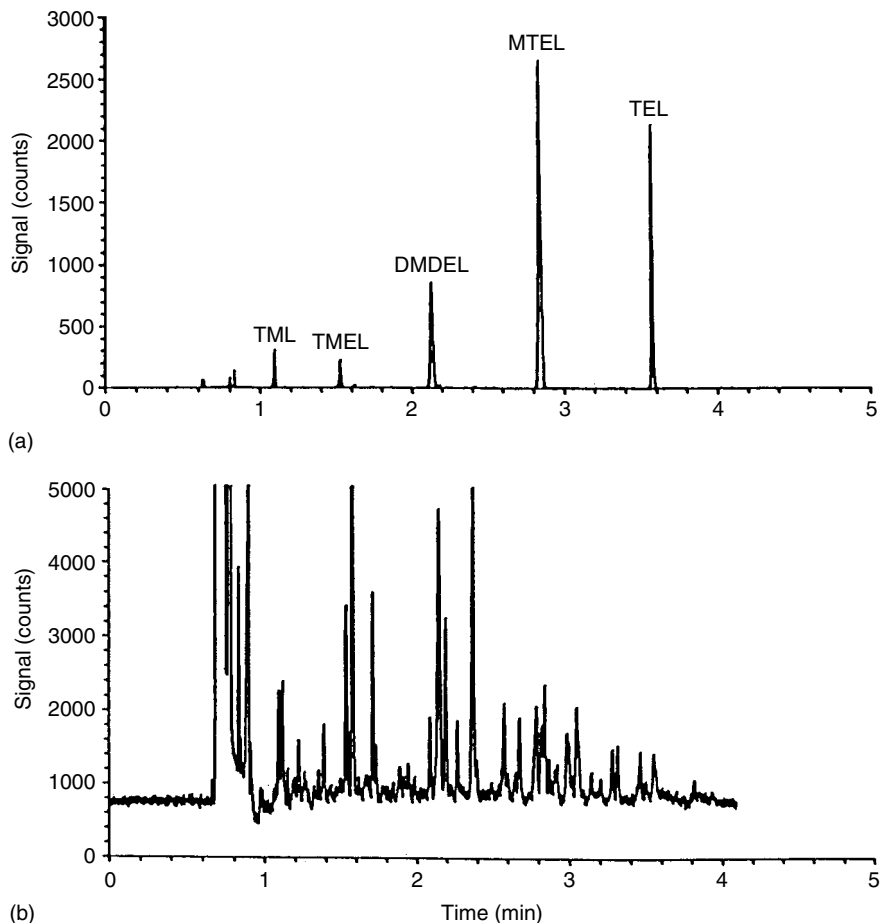


Figure 17.5 Chromatograms obtained for a sample of naphtha in hexane containing tetraethyllead (TEL), methyltriethyllead (MTEL), dimethyldiethyllead (DMDEL), trimethylethyllead (TMEL) and tetramethyllead (TML). (a) m/z 208, Pb^+ ; (b) m/z 12, C^+ . Reprinted with permission from Evans, E. H., Pretorius, W., Ebdon, L. and Rowland, S., *Anal. Chem.*, 1994, **66**, 3400–3407. Copyright 1994 American Chemical Society

More recently, O'Conner *et al.* [56] performed elemental detection with a helium RP-ICP sustained at a forward power of only 6 W and a pressure of 0.2 Torr. A detection limit of 4 pg was reported for iodobenzene with this exceptionally low-power plasma.

The ion sources described in this section have all been operated statically, that is, the conditions were adjusted manually in order to effect the desired ionization mode. However, it would appear feasible to switch the sources automatically and repetitively between two ionization modes by means of a power-modulated

rf generator[46,57]. If this switching could be done efficiently and rapidly, both types of mass spectra could be acquired for transient signals [31]. Naturally, it would be necessary to interface the ion source with a mass spectrometer that would retain signal fidelity and minimize spectral skew [58–61].

17.3.2 MICROWAVE INDUCED PLASMAS

The microwave induced plasma (MIP) has been used as both an atomic [1,18,21, 22,62–64] and molecular [19] ionization source for mass spectrometry. The preferred configuration for enhancing molecular fragmentation, and minimizing atomization, is to operate the unit at reduced pressure and low forward power. Many of the attractive features associated with the operation of the RP-ICP are also found in the MIP. In 1982, Markey and Abramson [65] reported using a GC–LP-MIP-MS system for the analysis of mixtures containing butane and hexanes; the resulting molecular type of mass spectra were attributed to the production and subsequent recombination of fragment ions in the discharge.

Heppner [66] used a helium RP-MIP to measure elemental ratios of heteroatomic compounds introduced into the plasma from a gas chromatograph. Complex molecules (e.g. 3,4-dimethylpyridine), eluting from the GC, passed through the MIP where they were quantitatively broken down to a few simple compounds or fragments (e.g. acetylene, hydrogen cyanide) that were characteristic of the original analyte. These neutral species then were transferred into a mass spectrometer and ionized by electron impact. The plasma power was adjusted over the range 30–150 W (at 2.45 GHz), at a pressure of 10–200 Torr. Elemental information for the initial molecule was obtained by measuring the breakdown products. Good correlations were found to exist between the theoretical and experimental carbon–oxygen elemental ratios over a limited range (0–8, carbon/oxygen). The sensitivity limit for elemental carbon passing through the MIP was reported to be 0.3 $\mu\text{g/s}$ with a dynamic range of 400. Unfortunately, the molecular fragments formed in the MIP were too generic and could not be used for structural identification of the analyte species.

Poussel *et al.* [67] were the first to report that EI-like molecular fragmentation spectra could be generated from analyte vapor introduced into the expansion region of a low-pressure surfatron geometry MIP interfaced to a quadrupole mass filter. Several different support gases were used, including argon, krypton and xenon; the discharge was typically operated at low power (25–70 W) and a pressure of 40 mTorr. The gas-kinetic temperature could be controlled over the range from 70 to 220 °C by altering the forward power (20–60 W) and discharge pressure (0.02–0.06 mbar). Signal levels for the fragmentation ions of perfluorotributylamine (PFTBA) were found to be higher than those in the reference spectrum. The degree of molecular fragmentation could be altered in these experiments through adjustment of the plasma power, which might provide

a future means of switching between atomic and molecular ionization modes. The detection limit for PFTBA was estimated to be 10–40 ng/s.

The Caruso group [53,68–70] also has used a low-pressure MIP for generating atomic and molecular fragmentation patterns of hydrocarbons and halogenated species. Their initial report focused on using the LP-MIP as an atomic ion generator; however, evidence presented also supports its use as a soft ionization device. Creed *et al.* [69] outlined the development of a helium LP-MIP for elemental analysis. A modified Beenakker TM₀₁₀ cavity was coupled to a quadrupole mass filter, and operated at a pressure of 0.6 mbar (helium) and a forward power of 60 W. The sample was introduced into the discharge from a capillary gas chromatograph and transported coaxially (with the discharge support gas) into the MIP cavity. This mode of analyte introduction increased the component's residence time in the plasma, which improved atomization and ionization efficiencies. Detection limits for iodine and chlorine were reported to be 0.1 and 24 pg, respectively. Story *et al.* [68] operated a modified version of this microwave cavity at a higher pressure (2.1 Torr, helium) and power (90 W) to determine sulfur and phosphorus in a chromatographic effluent. The atomic detection limit for phosphorus was in the range 1–90 ng, and depended upon how the torch was cooled. Sub-nanogram detection limits were obtained for malathion and diazinon (measured as ³¹P⁺ and ³²S⁺) when the discharge gas was switched from helium to nitrogen. In a nitrogen plasma, interaction between elemental phosphorus and the quartz torch assembly is reduced. Moreover, sulfur isobars (¹⁶O₂⁺) are not readily formed in a nitrogen discharge. A water-cooled torch and higher power (450 W) enabled Story and Caruso [70] to improve further the detection capabilities of this method for the determination of pesticides (20–100 pg).

Subsequent reports by the Caruso group expanded upon the utility of the LP-MIP for producing molecular fragmentation patterns of saturated and aromatic hydrocarbons. Olson *et al.* [53] reported that EI-like spectra could be obtained by introducing sample vapor directly into the expanding plasma plume within the low-pressure stage of an MIP-MS; this interface is depicted in Figure 17.6. This method of sample introduction closely resembles that of Poussel *et al.* [67]. The MIP forward power was set to 20 W, and spectra were collected over a range of helium gas flow rates (20–55 ml/min), corresponding to pressures from 0.13 to 0.5 mbar. The degree of fragmentation could be increased by operating the discharge at higher power (50 W); the ¹²C⁺ signal was observed under these more aggressive conditions.

The MIP has been used most successfully to produce EI-like molecular patterns when operated at low pressure. However, atmospheric pressure MIPs have also been used to generate molecular fragmentation patterns, and offer some advantage over their reduced pressure counterparts. Sampling systems that produce a heavy solvent load can easily overload and quench an RP ionization source. In contrast, atmospheric pressure devices readily handle higher solvent fluxes [54] and can be coupled with separation techniques such as SFC and LC.

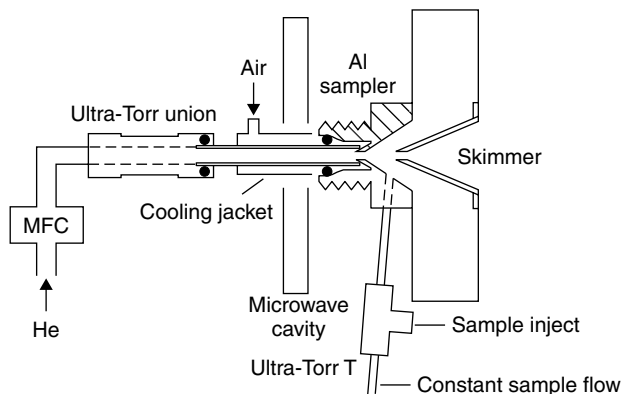


Figure 17.6 Low-pressure MIP torch interfaced to the PlasmaQuad. Reproduced by permission of The Royal Society of Chemistry from Olson, L. K., Story, W. C., Creed, J. T., Shen, W. and Caruso, J. A., *J. Anal. At. Spectrom.*, 1990, **5**, 472

Satzger and co-workers [54,71] described a Beenakker TM_{010} microwave cavity that can produce soft (EI-like) molecular fragmentation patterns at low power levels (10–30 W), and atomic mass spectra at higher power densities (60–70 W). Both liquid and gaseous samples were introduced into this API source, making it useful for both GC–MS and LC–MS. A plasma sustained in nitrogen (60–75 ml/min) at 24 W was found to yield structurally useful fragmentation patterns for PFTBA and tetramethyltin [71]. The precision was better than 6% (RSD) for replicate measurements of a gaseous sample continuously introduced into the system [54]; a slightly worse precision (9%) was obtained for the analysis of liquid samples [71].

To date, the MIP has been operated statically for both atomic and molecular ionization applications; power modulation would seem to be the next step in attempting to sequentially obtain atomic and molecular mass spectra. The versatility of this source will guarantee its continued use as a speciation tool [63].

17.3.3 GLOW DISCHARGES

The analytical utility of the glow discharge (GD) ionization source stands in stark contrast to its mechanical simplicity. The glow discharge historically has been used mostly for the analysis of solid samples; it is inherently a low-pressure (0.1–10 Torr) and low power (2–50 W) device. A less commonly adopted application of the GD is for the analysis of organic compounds; these LP plasmas can be used to produce molecular fragmentation spectra that often resemble standard EI patterns [43–45,72–75].

Several groups have used the classical GD for producing molecular fragmentation spectra. Mason and Milton [76] deposited proteins and sugars on to a GD

cathode, and used argon ions to sputter and ionize the deposits, yielding molecular fragmentation spectra. Shick *et al.* [74] used a 20 W argon rf-GD to generate molecular fragmentation patterns of polymers and polytetrafluoroethylene (PTFE) copolymers that had been affixed to a GD cathode. Distinctive fingerprint spectra were produced as a result of variations in the side-chains of these plastics [74] and allowed their differentiation.

Atmospheric Sampling GD

A conventional glow discharge is sustained at a reduced pressure of inert gas, typically argon or helium. In contrast, McLuckey and co-workers [39,40] developed a glow discharge supported in air; atmospheric gases are drawn into the system through a 0.2 mm sampling orifice at rate of about 300 ml/min. The atmospheric-sampling glow discharge ion source (ASGDI) operates over a pressure range of 0.2–0.8 Torr and requires 1–4 W of power (3–10 mA, –350 V). The source produces both positive and negative ions; voltages applied to the mass spectrometer lenses and electron multiplier determine which species will be detected in the quadrupole mass filter. Discharge current and pressure strongly influenced the fragmentation of molecules entering the source. A detection limit of 1.4 parts per trillion (ppt) was reported for the trinitrotoluene anion, with a dynamic range of at least six orders of magnitude. The authors did not report on the use of this source for elemental analysis; however, access to atomic spectra might be possible at higher power densities.

Radio Frequency Powered GD

Caruso and co-workers [24,77] used an LP radio frequency (13.56 MHz) powered helium glow discharge to generate atomic and molecular fragmentation patterns of organometallic tin and lead compounds. A capillary column GC was used to transfer analytes into the rf-GD, and a quadrupole mass spectrometer served as the detector. The column outlet was mounted in a probe assembly that was positioned between the sampler and skimmer [24]. Atomic and molecular fragmentation spectra were produced over a range of helium pressure (0.2–0.8 Torr) and power (10–40 W). This system was initially used for the determination of organometallic compounds [24]. However, several fragmentation patterns of tetraethyltin were presented, which suggest that this device might be a useful speciation tool. Atomic detection limits for tetraethyltin and tetrabutyltin were 1 pg (at 3σ), and the linear dynamic range exceeded two orders of magnitude.

In a follow-up publication, Belkin and co-workers [77] examined fragmentation processes occurring within a modified rf-GD cell. The cell pressure was higher (6–30 Torr, helium) than that used in earlier studies [24], but the power was comparable (10–40 W). A capillary gas chromatograph was used to introduce organometallic compounds into the glow discharge. Atomic signal levels

were noted to decline as the rf power was raised. The $^{120}\text{Sn}^+:(\text{Me})_3\text{Sn}^+$ signal ratio (from trimethyltin) was unaffected by changes in discharge pressure or power, suggesting that source conditions could not be used to influence the fragmentation process. A fragmentation pattern for trimethyltin produced in the rf-GD is presented in Figure 17.7a. A higher percentage of lower molecular weight fragments was formed in the rf-GD than in an EI source (Figure 17.7b). Nevertheless, this spectrum contains all of the structurally relevant ions required for identification purposes. Detection limits were lower than 1.2 pg (at 3σ) for the elemental analysis of tetramethyl-, tetraethyl- and trimethylphenyltin; the precision was better than 5% (RSD) for 10 replicate measurements of these compounds.

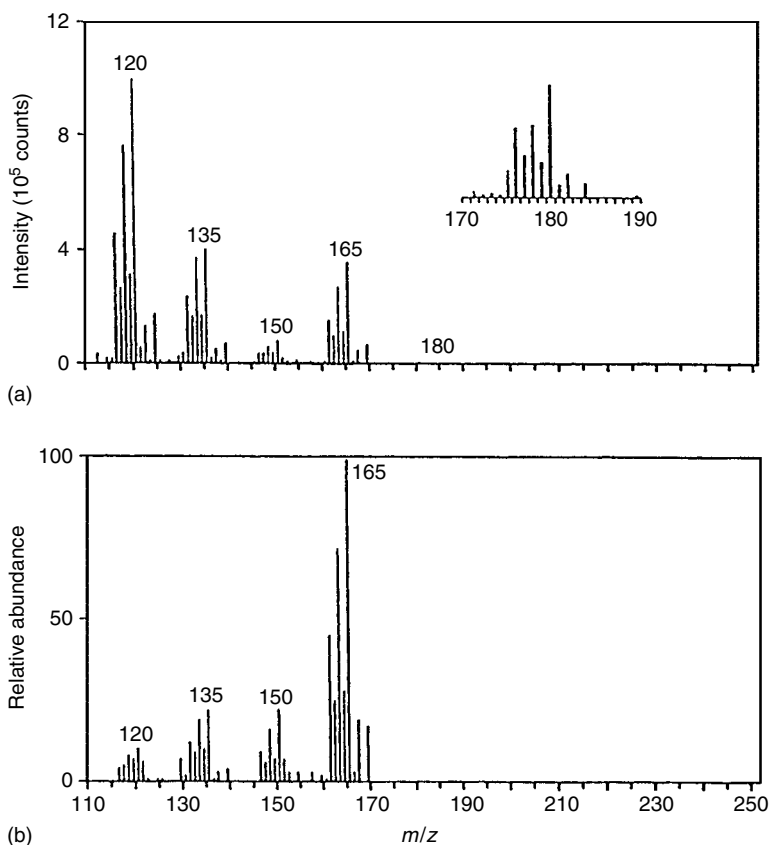


Figure 17.7 Molecular fragmentation pattern for trimethyltin. (a) Generated in the RP-LP-rf-GD. The cell power was 30 W at a helium pressure of 26 Torr. (b) Standard EI spectrum (NIST) presented for comparison. Reproduced by permission of The Royal Society of Chemistry from Belkin, M. A., Olson, L. K. and Caruso, J. A., *J. Anal. At. Spectrom.*, 1997, **12**, 1255–1261

Gas Sampling Glow Discharge

Guzowski and co-workers [23,44,45,78] reported on the use of a helium gas sampling glow discharge (GSGD) ionization source to generate atomic and molecular fragmentation patterns for halogenated hydrocarbon vapors. The GSGD was switched between ionization modes by alternating the polarity and magnitude of voltage applied to the sample introduction plate [45]. A block diagram of the GSGD ion source is reproduced in Figure 17.8. The GSGD was designed to replace the sampling plate of an ICP-TOFMS instrument and is mechanically very simple, which makes it easy to service and maintain. The TOFMS employed in these studies was originally designed for use with an inductively coupled plasma [58,60,79]; however, it easy to interface to other sources.

In the atomic mode (-300 V, 30 mA), the ‘abnormal’ discharge in the GSGD covers the entire electrode surface, and sample vapor passing through this region is

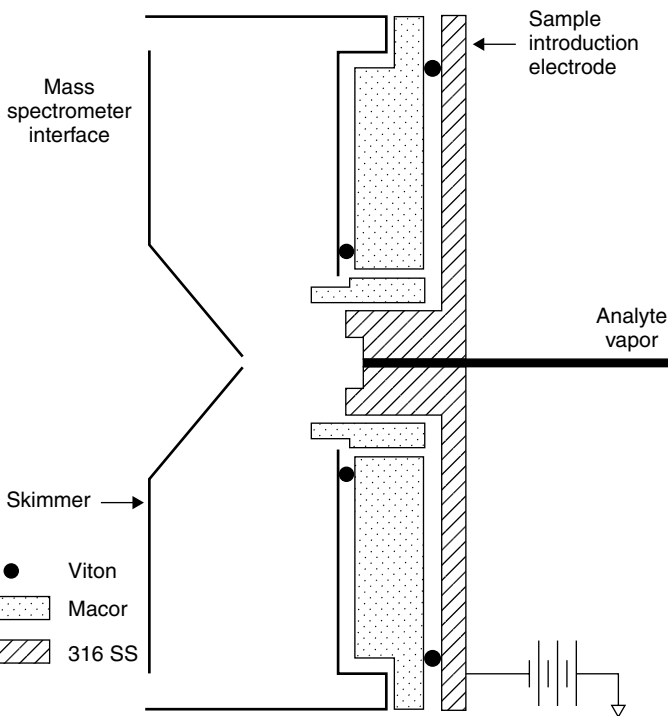


Figure 17.8 Diagram of the gas sampling glow discharge (GSGD) ionization source. The cathode is constructed from 314 stainless steel (SS). The Macor sleeve restricts the discharge to the region between the cathode and the grounded skimmer. The discharge is contained within the first vacuum stage of the mass spectrometric interface. Adapted by permission of The Royal Society of Chemistry from Guzowski, J. P., Broekaert, J. A. C., Ray, S. J. and Hieftje, G. M., *J. Anal. At. Spectrom.*, 1999, **14**, 1121–1127

efficiently atomized and ionized [44]. The molecular ionization mode is accessed by applying a positive voltage (+200 V, 20 mA) to the sampling electrode. In this reversed configuration, the grounded skimmer and instrumental cavity serve as the cathode and the discharge operates in the normal glow mode [45,80]. Although the two types of discharges are operated at similar power levels, the 'normal' plasma is distributed across a greater surface area ($>10\times$), which yields a less-energetic source. The GD is known to contain a number of discrete zones [80,81]; the location of each probably changes as the voltage polarity is switched. The analyte vapor likely experiences a different group and concentration of plasma species (electrons, helium metastables) in the two modes, which accounts for its ability to generate different types of mass spectra.

A capillary gas chromatograph was coupled to the GSGD-TOFMS for the mass spectrometric determination of halogenated hydrocarbons. The GSGD was operated separately in the atomic and molecular ionization modes. The chromatographic separation of the homologous series from n-chloropentane to n-chlorodecane is presented in Figure 17.9a ($^1\text{H}^+$), b ($^{12}\text{C}^+$), and c ($^{35}\text{Cl}^+$). Boxcar averagers were used for data collection and 2 ng of analyte deposited on the column. The hydrogen signals (Figure 17.9a) are weaker than those for either chlorine or carbon, and probably reflect a mass bias in the horizontal steering

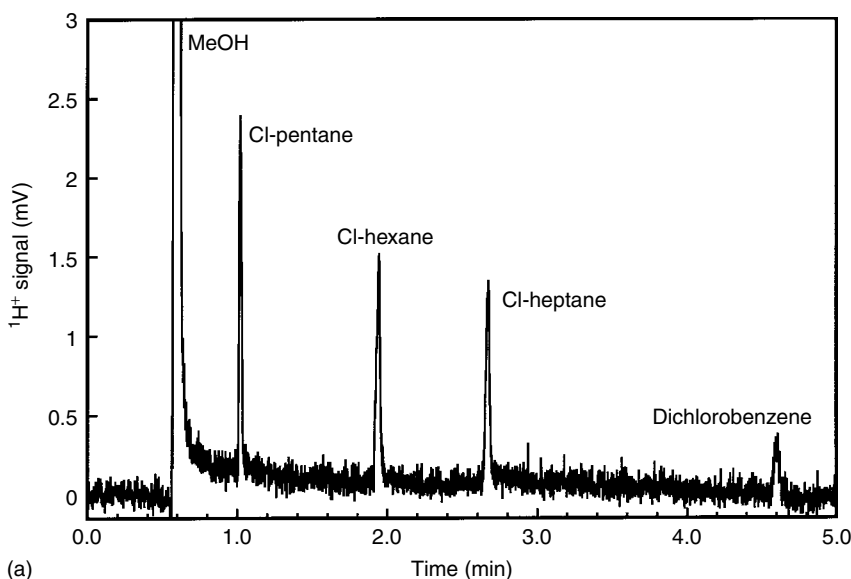
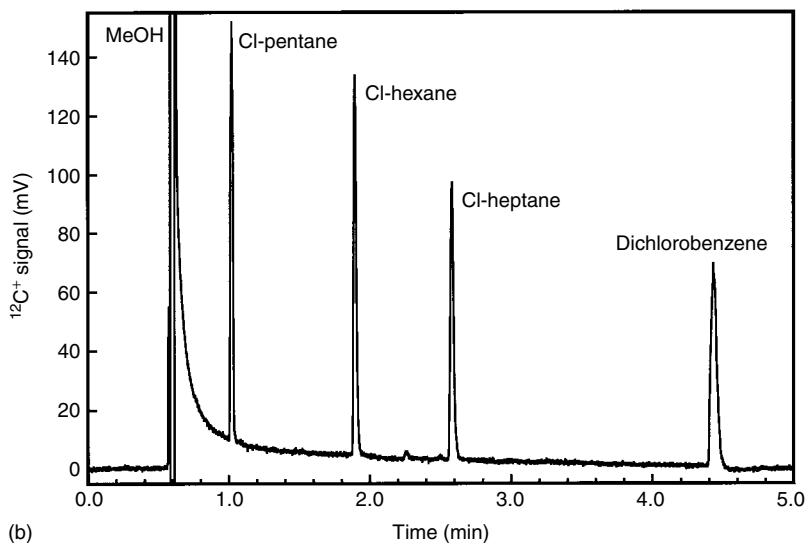
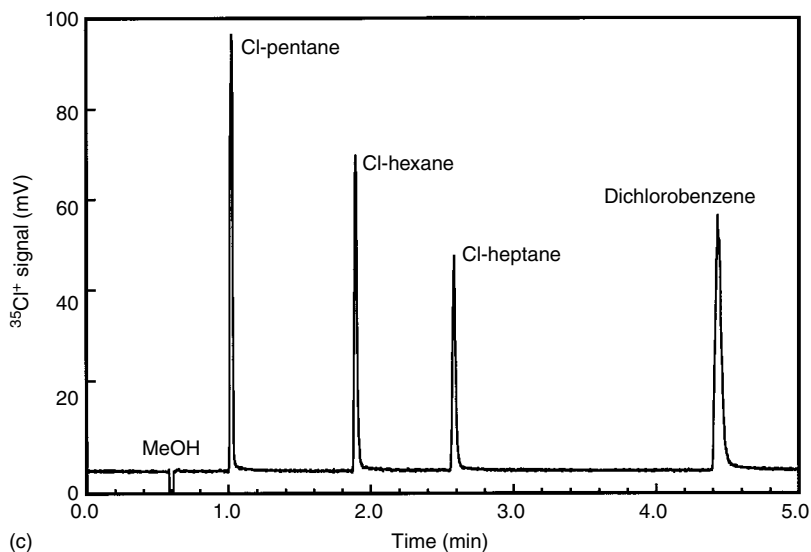


Figure 17.9 Capillary gas chromatographic separation and element-selective detection of straight-chain chlorinated hydrocarbons. The dc plasma was operated at 5.50 Torr helium and a current of 30 mA. Boxcar averagers were used to collect the data; 2 ng of each analyte were deposited on the GC column. (a) $^1\text{H}^+$; (b) $^{12}\text{C}^+$; (c) $^{35}\text{Cl}^+$



(b)



(c)

Figure 17.9 (continued)

plates [79]. The discharge appeared stable even when the solvent (methanol) eluted from the column. Simultaneous data collection was limited to two channels (boxcar averagers) with this system; however, it should be possible to obtain information for all m/z s by substituting a more powerful multichannel data collection system [61,82] such as a time array detector [26]. Single-channel

gated ion counting provided atomic detection limits better (lower) than 26 fg/s for chlorinated and brominated compounds manually introduced into the instrument, with a dynamic range of 3–4 orders of magnitude [23]. A sequence of 10 replicate injections of bromoform vapor resulted in an atomic precision of 6.5% (RSD); comparable precision was obtained for the measurement of fragment-ion signals.

The GSGD source can be used to produce EI-like mass spectra [23,45] when operated in the ‘soft’ ionization mode. Figure 17.10a depicts a molecular ionization

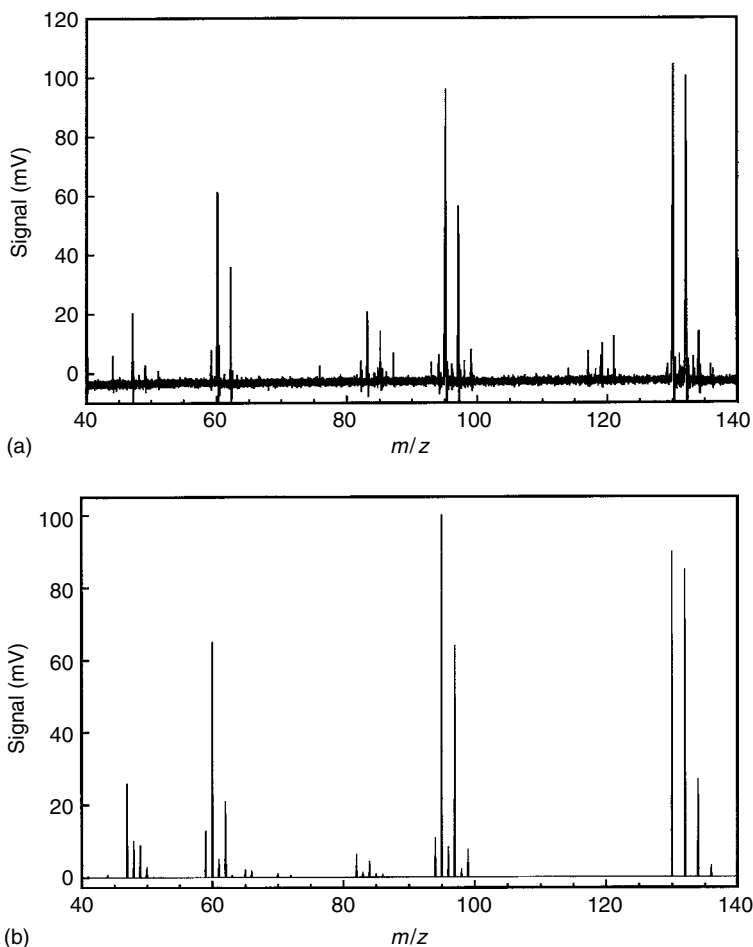


Figure 17.10 Production of molecular fragmentation spectra for trichloroethylene using the GSGD operated in the ‘soft’ ionization mode; sample introduction plate biased at +200 V, 10 mA. Discharge pressure, 5.50 Torr helium. Sample vapor was swept into the discharge from a flow cell and a Tektronix digital oscilloscope (TDS 500) was used to collect the 1000 spectral averages. (a) Experimental; (b) standard 70 eV EI spectrum

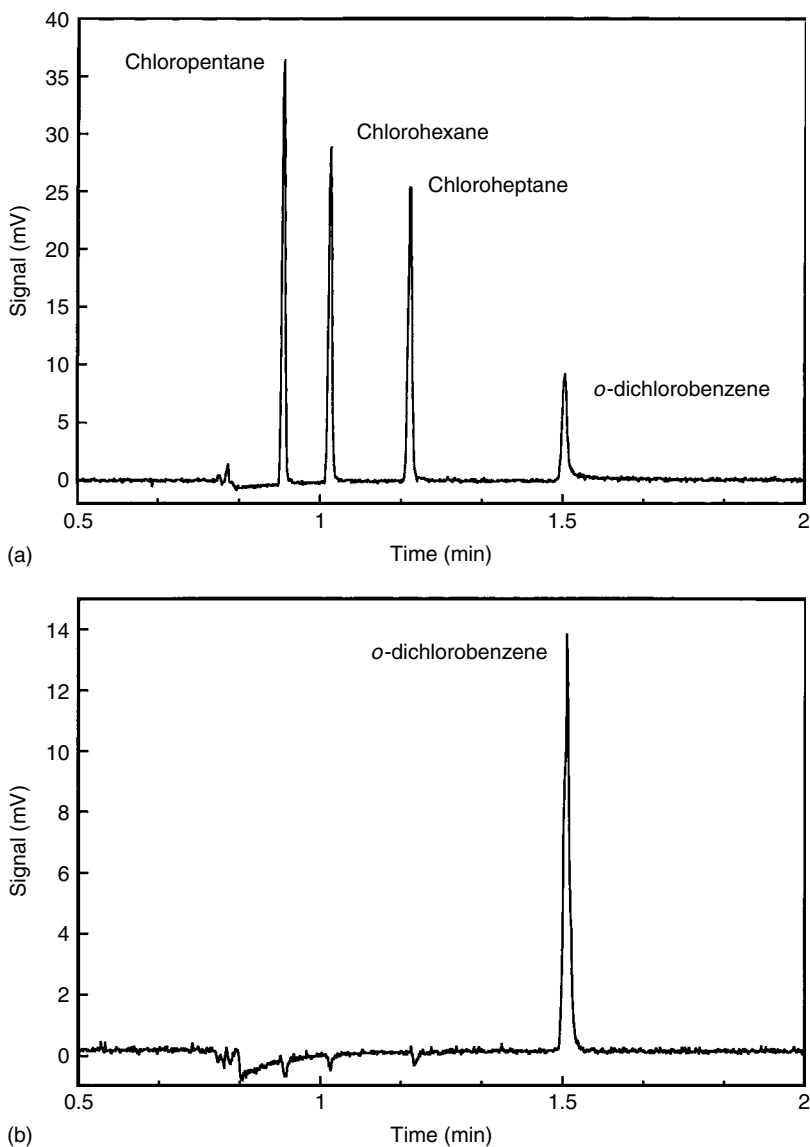


Figure 17.11 Different classes of chemical compounds will yield specific m/z fragments; these ions can be used as a discrimination tool. Capillary gas chromatographic analysis of different types of chlorinated hydrocarbons, monitored at class-specific flight times (a) A common fragment ion for all of the listed compounds, m/z 27, $C_2H_3^+$; (b) fragment ion specific for aromatic compounds, m/z 75, $C_6H_3^+$ Adapted from Ref. [23] with permission from the American Chemical Society

spectrum for trichloroethylene (TCE) that was collected as it eluted from the column. The most abundant fragment ions for TCE (Figure 17.10a) are present at levels comparable to those of the reference spectrum (Figure 17.10b) [41]; similar agreement was found for other chlorinated and brominated compounds [45]. Straight-chain hydrocarbons generally produce fragment patterns containing higher-than-expected abundances of lower m/z species, suggesting the GSGD is more energetic than a simple EI source. [23,45].

Many organic compounds produce class-specific molecular fragment ions that can be used as a tool for discrimination. Figure 17.11a presents the signal collected at m/z 27 ($C_2H_3^+$), which is a common fragmentation ion for these aliphatic and aromatic hydrocarbons [23]. The signal at m/z 75 ($C_6H_3^+$) originates from the aromatic compound (Figure 17.11b) and demonstrates the selectivity that is available with this technique. Single-ion monitoring is routinely used in GC-MS for the analysis of complex sample matrices where chromatographic resolution of every sample constituent is not possible [26].

The elemental ratio is another piece of information that can be used to distinguish between different types and classes of compounds; this information might also be used to calculate an analyte's empirical formula [18,83]. Several types of ion sources have been used to measure atomic ratios, including the MPT, MIP, and GSGD [18,22,44,84]. A good correlation ($R > 0.99$) was found between the expected and experimental carbon-chlorine elemental ratio for volatile halogenated hydrocarbons analyzed by GSGD-TOFMS; this relationship is presented in Figure 17.12. A flow cell was used to sweep the sample vapor into the discharge; signal-averaged data were collected on a digital oscilloscope. Data were not corrected for isotopic abundances and reflect the simple atomic ratios; comparable results were obtained for peak heights and areas.

Like the microwave induced and inductively coupled plasmas, the GSGD was statically operated in these studies. Although it might be easy to switch manually between the two modes of operation, it would be preferable to effect this change automatically. If this ionization source is to be a useful tool for chemical speciation studies, the switching frequency must be fast enough to track even rapidly changing signals.

17.3.4 POWER MODULATED GD SOURCES

Several recent reports have documented the development of a single ionization source that can sequentially generate atomic and molecular mass spectra [43,45]. These sources differ from those described in the previous sections because both types of mass spectra were collected at similar pressures and instrumental set points, and during a single measurement event. Both of these sources are based on GD methodology, and produce the two kinds of spectra by modulating the discharge power.

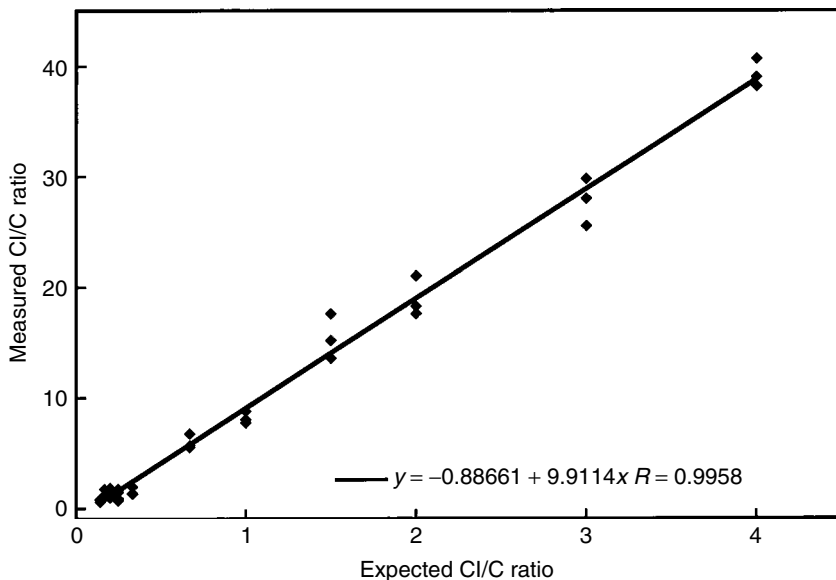


Figure 17.12 Identification of chlorinated hydrocarbons based upon the $^{35}\text{Cl}^+ / ^{12}\text{C}^+$ elemental ratio. Sample vapor was swept into the GSGD from a flow cell; 1000 co-added scans were collected on a Tektronix digital oscilloscope. Plasma operated at 5.50 Torr helium and 30 mA. The following compounds were tested (with the expected Cl:C ratio): carbon tetrachloride (4 : 1), chloroform (3 : 1), methylene chloride (2 : 1), ethylene dichloride (1 : 1), 1,2-dichloropropane (2 : 3), chloropropane (1 : 3), 2-chloro 2-Methylpropane (1 : 4), 2-chlorobutane (1 : 4), 2-chloro- 2-Methylbutane (1 : 5), 1-chloropentane (1 : 5), 1-chloroheptane (1 : 7), chlorobenzene (1 : 6). Adapted by permission from The Royal Society of Chemistry from Guzowski, J. P., Broekaert, J. A. C., Ray, S. J. and Hieftje, G. M., *J. Anal. At. Spectrom.*, 1999, **14**, 1121–1127

Millisecond Pulsed GD

Steiner and co-workers [43] exploited the unique properties of a millisecond pulsed argon GD and the high temporal resolution of a TOFMS to sequentially collect atomic and molecular mass spectra during a single analysis. The microsecond pulsed argon GD was used previously to enhance the yield of atomic species sputtered from a cathode; however, it has never been used to generate molecular fragmentation patterns [42,85]. The proposed ionization mechanisms in the millisecond pulsed GD, and their relationship to the modulation sequence, are presented in Figure 17.13 [43]. Initiation of the discharge (during the ‘prepeak’) generates a large number of electrons that can be used to produce EI-like mass spectra, as demonstrated for the introduction of xylene vapor into the discharge. Shortly after the discharge was terminated (the ‘afterpeak’), an elemental mass spectrum for tantalum (the cathode material) was collected. Interestingly, the

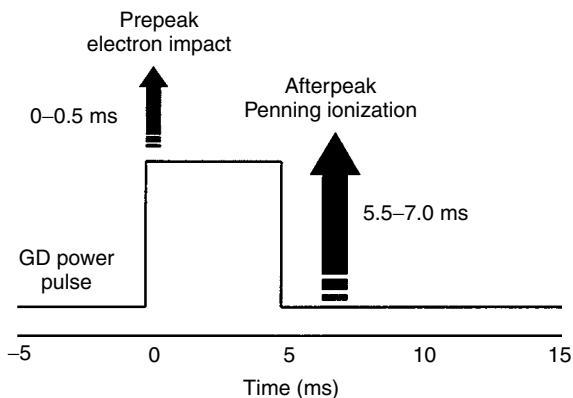


Figure 17.13 Depiction of the millisecond argon glow discharge pulse sequence, illustrating the location and duration of each analytical temporal region (prepeak and afterpeak). Adapted by permission from The Royal Society of Chemistry from Steiner, R. E., Lewis, C. L. and Majidi, V., *J. Anal. At. Spectrom.*, 1999, **14**, 1537–1541

parent ion for xylene could be collected during the ‘afterpeak’ (thereby giving the molecular weight), but an atomic mass spectrum for this compound did not appear. The plasma was pulsed at a frequency of 50 Hz with a duty cycle of 25%. Ion extraction and mass analysis were synchronized with the discharge modulation and, accordingly, specific temporal regions of the plasma could be investigated. Detection limits for the atomic and molecular modes were not reported in this preliminary investigation.

Switched GSGD Source

Guzowski and Hieftje [45] have reported that a helium gas sampling glow discharge (GSGD) ionization source, operated in a switched mode, can be used to collect sequential atomic and molecular mass spectra for sample vapors. This source differs from the millisecond (or microsecond) pulsed GD [42,85] because the duty cycle of each ionization mode is 50%, and mass spectral data can be collected during the entire respective ionization half-cycle.

The discharge cell was virtually identical with that used in their earlier study [44], except that the cathode geometry was optimized for the production of EI-like molecular fragmentation patterns. The polarity of voltage applied to the sample-inlet electrode was switched by an electromechanical relay, driven by the square-wave output of a common waveform generator. The plasma could be modulated at rates in excess of 100 Hz, with the upper limit apparently governed by the relay settling time. Logic gates were used to coordinate the timing events of the TOFMS repeller pulse, plasma switching, and triggering of the data collection

devices. Both types of mass spectra could be obtained under similar (but not the optimal) experimental conditions.

Figure 17.14a depicts an atomic mass spectrum for bromoform, and Figure 17.14b shows the molecular fragmentation pattern for the same compound collected during the opposite GSGD half-cycle. The discharge was modulated at a rate of 10 Hz for these experiments while the sample vapor was continuously swept from a flow cell into the discharge. A digital oscilloscope was used to collect the data (1000 scans) by triggering it on the appropriate plasma half-cycle. A strong correlation exists between the standard 70 eV spectrum (Figure 17.14c) and that obtained experimentally (Figure 17.14b). Moreover, both sets of spectra (atomic, molecular fragment) are indistinguishable from those obtained for static operation of the plasma. The isotopic abundance of bromine (Figure 17.1a) appears to be incorrect; this artifact is caused by saturation of the detection or amplification electronics [44] and disappears at lower analyte fluxes. The atomic (as halogen) and molecular fragment ion detection limits were found to be in the range 1–120 pg/s; the precision was better than 8% (RSD) for both modes of operation.

The atomic detection limits for the switched source are about one order of magnitude worse (higher) than when the source is operated in the static mode. This slight reduction in signal occurred because it was necessary in the pulsed mode to use ion-lens settings that were not optimal, but that permitted transmission of both types of ions (atomic and molecular). The additional information obtained with the switched source is judged to make these compromises acceptable. Future developments include modulating all of the ion lenses in concert with the plasma, which should enhance signal levels, improve detection limits, and increase spectral resolution.

From the experimental results of Steiner *et al.* [43] and others [42,85], it is known that the process of switching (or pulsing) a low-pressure plasma can enhance certain ionization mechanisms at temporally discrete periods during the power modulation sequence. Signal enhancements for the atomic and molecular ionization modes can similarly be achieved for the switched GSGD by coordinating the plasma modulation and mass analysis (ion extraction event). Specifically, signal levels can be increased by up to 50-fold if the repeller event is delayed by several milliseconds relative to the plasma switch [44]. However, only a single mass spectrum can then be collected for each plasma half-cycle, which reduces the duty factor of this measurement. Faster plasma modulation rates might be used to partially offset this loss of efficiency.

The switched source was also coupled with a capillary gas chromatograph [23] and the figures of merit for this experimental combination were found to be comparable to those of the dc plasma. Detection limits for the GC switched-GSGD-TOFMS were found to agree within one order of magnitude with static values obtained with boxcar averager data collection, and are presented in Table 17.1.

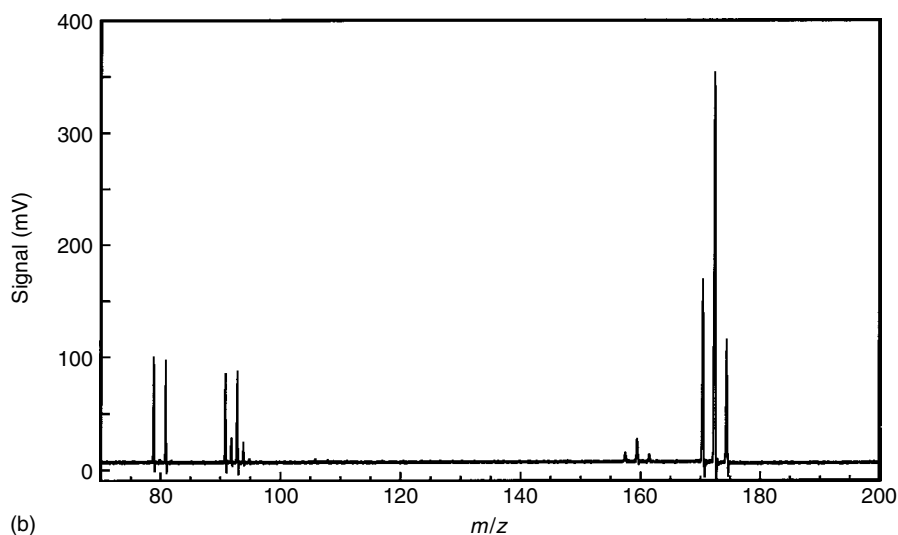
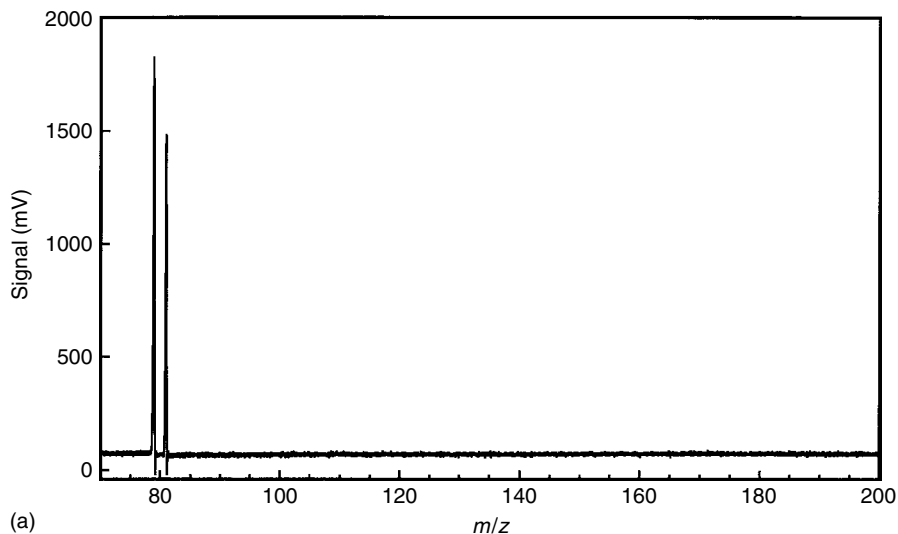


Figure 17.14 Atomic and molecular mass spectra for bromoform vapor swept into the GSGD while the plasma was modulated at 10 Hz. Data were collected on the digital oscilloscope, which was triggered on the appropriate half-cycle using simple logic gates. (a) Atomic ionization mode. Discharge conditions: 5.50 Torr helium, 30 mA, 350 V. (b) Molecular fragmentation mass spectrum; discharge conditions: 5.50 Torr helium, 20 mA, 250 V

Table 17.1 Detection limits for the switched GC–GSGD–TOFMS (10 Hz)^a. Adapted from Ref. [23].

Compound	Atomic detection limit		Molecular fragment detection limit	
1-Chloropentane	24 ^b	(35) ^c	135 ^b	(41) ^c
1-Chlorohexane	22	(35)	59	(41)
1-Chloroheptane	17	(35)	107	(41)
1-Chlorooctane	17	(35)	55	(41)
1-Chlorononane	17	(35)	63	(41)
1-Chlorodecane	34	(35)	44	(41)
Chloroform	5	(35)	7	(85)
<i>o</i> -Dichlorobenzene	6	(35)	14	(75)
Bromoform	3	(79)	19	(93)
Bromobenzene	9	(79)	10	(77)

^aPlasma conditions: atomic, 30 mA/350 V; molecular, 20 mA/250 V; boxcar averagers used for data collection.

^bReported as the analyte, expressed in units of pg/s and calculated at 3σ .

^c m/z at which measurement was made; the most intense isotope (atomic) or fragment ion (molecular).

The detection limits for static operation of the plasma were always better (lower) than for the switched mode, for reasons stated above.

The GSGD employed in these studies has been interfaced to a TOFMS which offers high temporal resolution, as one complete mass spectrum is produced every 60 μ s. Rapidly changing signals, such as those derived for a switched plasma or a fast chromatographic separation, require high spectral generation rates in order to avoid signal distortion [61,82]. Moreover, all ions that are mass analyzed in the TOF are extracted at the same instant in time, which contributes to enhanced precision in a ratioing mode [58,59]. This advantage can be used to compensate for ion-source instabilities, and provides an opportunity for improving isotope and elemental ratio measurements. The stability of the switched GSGD (10 Hz) atomic signal was monitored for 1.25 h; results of this study are presented in Figure 17.15. Bromoform vapor was swept into the cell, and the Tektronix digital oscilloscope was used to collect 5000 transients at each time interval. The atomic ($^{79}\text{Br}^+$) signal varies by 13% (RSD) over this time period, but the isotope ratio ($^{79}\text{Br}^+ / ^{81}\text{Br}^+$) is much more stable and only deviates by 1.1% (RSD). Similar results were obtained when the molecular fragment ion signals were monitored [45]. The improved precision of the atomic ratio over that of the raw signal underscores the importance of simultaneous extraction and measurement of all masses in an ion packet, and is a feature particular to TOFMS [44,58,59].

The GSGD–TOFMS has been used chiefly to analyze organic vapors. However, this system also can be used for the analysis of fine aerosols and molecular vapor, such as those produced by an electrothermal vaporization (ETV) cell [78]. It can be advantageous to use ETV when sample volumes are limited, or when

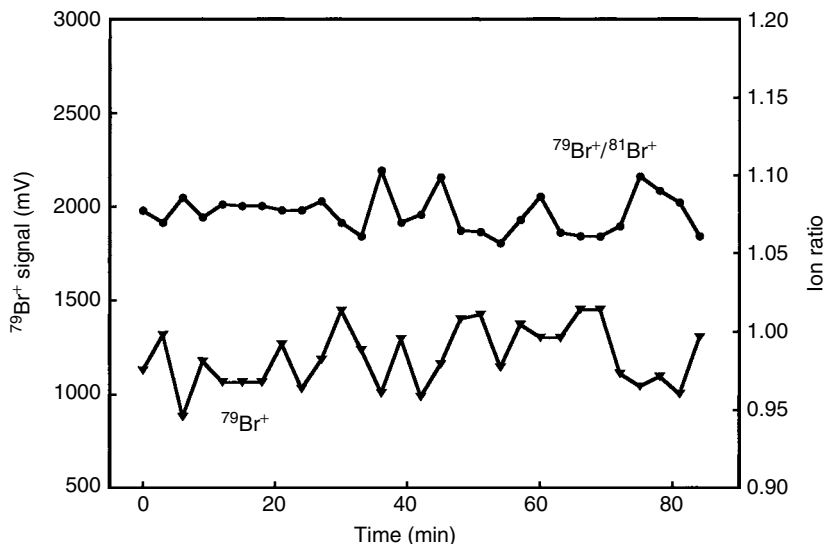


Figure 17.15 Signal stability for the GSGD-TOFMS measured over a period of 1.25 h. Bromoform vapor was swept in the discharge, which was modulated at a rate of 10 Hz. A digital oscilloscope was used to collect the 5000 co-added spectra; a minimum of three replicate measurements were made at each time interval. The raw ($^{79}\text{Br}^+$) signal and the isotope ratio ($^{79}\text{Br}^+ / ^{81}\text{Br}^+$) are presented. The stability of the raw signal was 13% (RSD), while the stability of the ratio was considerably better at 1.1% (RSD). Adapted by permission of The Royal Society of Chemistry from Guzowski, J. P., Broekaert, J. A. C., Ray, S. J. and Hieftje, G. M., *J. Anal. At. Spectrom.*, 1999, **14**, 1121–1127

it is necessary to preconcentrate a species prior to analysis [35,86,87]. With the switched GSGD-TOFMS coupled to an ETV sample introduction cell, it was possible to distinguish between an inorganic (ferrous chloride) and an organometallic (ferrocene) iron compound on the basis of differences in their thermochemical and mass spectral characteristics. In a simple mass spectral analysis, these compounds could be discerned solely by their appearance temperature, as depicted in Figure 17.16a for the $^{56}\text{Fe}^+$ signal. Ferrocene sublimates at temperatures above 100°C [88] and leaves the graphite cup at a much lower temperature than does the inorganic salt (m.p. 674°C). Of course, a more complicated sample matrix might preclude a distinction based on appearance time alone. Ferrocene can form molecular fragment ions in the GSGD, which can be monitored and used to distinguish it from the chloride salt. The signal collected at m/z 120 (FeCp^+) during the molecular half-cycle is shown in Figure 17.16b. The plasma was modulated at 10 Hz in these studies. Conventional analysis by ETV incorporates both an ‘ashing’ and a ‘charring’ step, which remove volatile species from the matrix; the switched GSGD-TOFMS might permit a more complete characterization of a specimen by providing a means of screening both the atomic and molecular

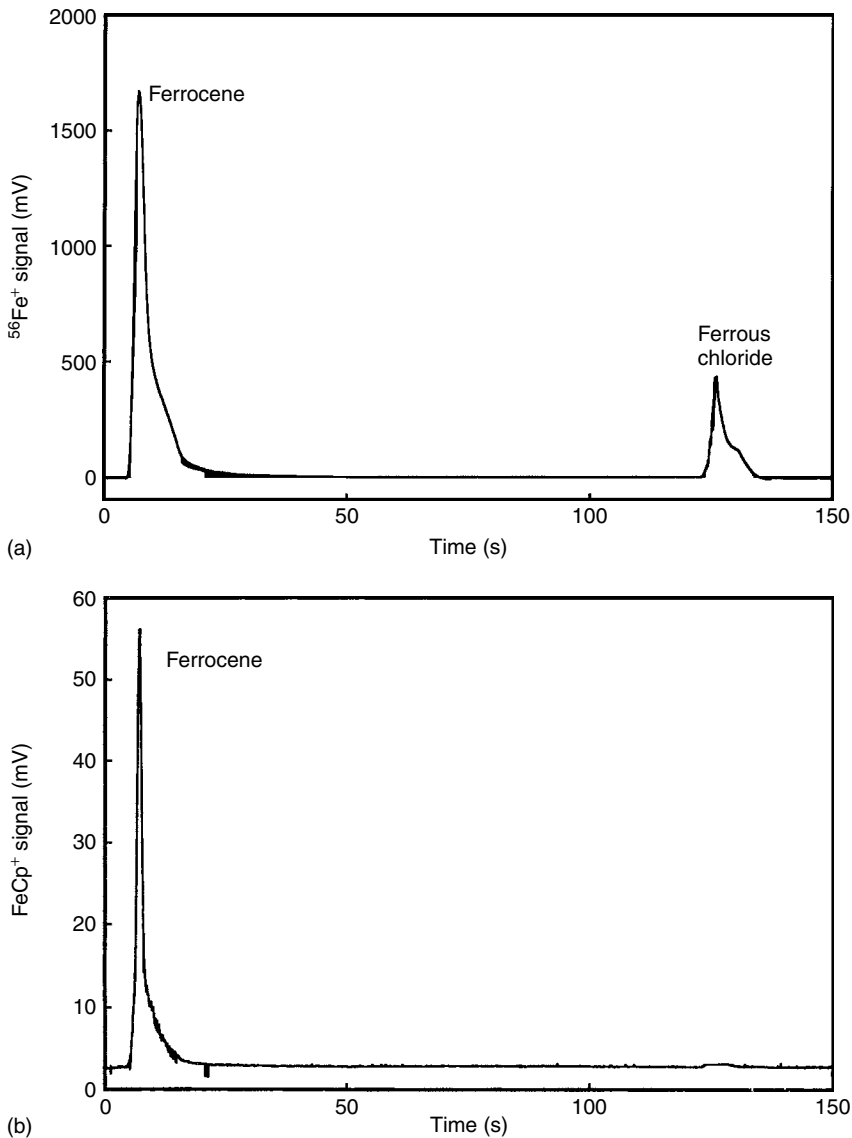


Figure 17.16 Chemical speciation of two iron compounds (ferrocene and ferrous chloride) introduced into the GSGD from an electrothermal vaporization cell. GSGD operated in the modulated mode (10 Hz). ETV parameters: ash 400 °C (120 s); ramp 300 °C/s; atomize 2200 °C (4 s); transfer line flow rate of 120 ml/min helium heated to 130 °C. (a) Atomic signal collected at m/z 56 ($^{56}\text{Fe}^+$). (b) Molecular fragment ion signal collected at m/z 120 (FeCp^+). Adapted from Guzowski, J. P., Broekaert, J. A. C. and Hieftje, G. M., *Spectrochim. Acta, Part B*, 2000, **55**, 1295–1314 with permission from Elsevier Science

components in the sample. Atomic detection limits for the ETV-GSGD-TOFMS were better (lower) than 15 pg (3σ) for zinc, copper, thallium, lead, and tin with boxcar averagers being used for data collection.

17.4 CONCLUSIONS

Great strides have been made in the nontraditional use of plasma-based ionization sources for the production of atomic and molecular mass spectra. Many classical ionization sources that operate at atmospheric pressure (ICP, MPT) cannot be sustained at sufficiently low forward power levels to yield clean fragmentation spectra. They generally must be reconfigured for low-pressure operation so that EI-like patterns can be obtained. To date the most successful attempts at developing a truly multidimensional ionization source have utilized a glow discharge plasma. Both pulsed and switched sources have been used to generate sequentially atomic and molecular fragmentation patterns in rapid succession. Furthermore, the operation and use of the GD sources have been simplified because both types of ions could be generated at similar pressures and common experimental setpoints. Of these sources, only the switched GSGD-TOFMS was capable of alternately generating atomic and EI-like molecular fragmentation spectra for an analyte vapor [45].

The examples presented in this overview have emphasized the use of plasma-based ionization sources. Another device that might be a useful partner in a tandem combination is electrospray ionization (ESI) [27,29,89]; it should be possible to couple an ES source with a switched (or pulsed) glow discharge for the rapid and sequential production of atomic and molecular ions. The ES source can ionize large, thermally labile molecules and a TS combination that incorporates ESI could provide unique information about metalloproteins and metallodrugs and might be an easy and predictable way to fragment biomolecular ions. The electrospray ion source requires a minimal sample flow ($\mu\text{l}/\text{min}$, nL/min) that is well matched with many separation techniques [47,90,91] and low-power plasmas.

Future developments will focus on ionization sources that can produce information-rich spectra quickly, using simple and reliable instrumentation. Also, the versatility and acceptance of a method will be directly related to how easily it can be interfaced with separation methods that operate on a millisecond time-scale. Lastly, the need for chemical speciation information will expand in the future, encouraging the development of information-rich sources of the sort described above.

17.5 ACKNOWLEDGMENTS

Funding was provided in part by the Department of Energy through grant No. DE-FG02-98ER14890, by ICI technologies, by Merck Research Laboratories,

and by the LECO Corporation. J.P.G. acknowledges fellowship support from Eli Lilly & Co. and the Department of Education.

17.6 REFERENCES

- [1] Montaser, A. *Inductively Coupled Plasma Mass Spectrometry*, Wiley-VCH: New York, 1998, pp. 615–771.
- [2] Jarvis, K. E.; Gray, A. L.; Houk, R. S. *Handbook of Inductively Coupled Plasma Mass Spectrometry*, Chapman and Hall: New York, 1992, pp. 1–21.
- [3] Hieftje, G. M. Critical comparisons of sources and detection methods in atomic spectrometry, *Fresenius' J. Anal. Chem.* 1990, **337**, 528–537.
- [4] Lobinski, R. Elemental speciation and coupled techniques, *Appl. Spectrosc.* 1997, **51**, 260A–278A.
- [5] Caroli, S. Chemical speciation: a decade of progress, *Chem. Anal.* 1996, **68**, 1–20.
- [6] Ellis, L. A.; Roberts, D. J. Chromatographic and hyphenated methods for elemental speciation analysis in environmental media, *J. Chromatogr. A* 1997, **774**, 3–19.
- [7] Gardiner, P. E. Chemical speciation in biology and medicine: the role of atomic spectrometric techniques, *J. Anal. At. Spectrom.* 1988, **3**, 163–168.
- [8] Liyanage, J. A.; Taylor, D. M.; Williams, D. R. Chemical speciation in wound fluid leading to enhanced bioavailability for healing, *Chem. Speciation Bioavailability* 1996, **8**, 45–52.
- [9] Shrivastava, A. K. Speciation of trace elements in environmental samples, *Rev. Anal. Chem.* 1995, **14**, 143–166.
- [10] Trojanowicz, M.; Pyrzynska, K.; Pobozy, E.; Maruszak, W. Chemical speciation — a challenge for analytical chemistry, *An. Assoc. Bras. Quim.* 1996, **45**, 158–170.
- [11] Donard, O. F. X.; Lobinski, R. Plasma spectrometry and molecular information, *J. Anal. At. Spectrom.* 1996, **11**, 871–876.
- [12] Vela, N. P.; Olson, L. K.; Caruso, J. A. Elemental speciation with plasma mass spectrometry, *Anal. Chem.* 1993, **65**, 585A–597A.
- [13] Lobinski, R.; Pereiro, I. R.; Chassaingne, H.; Wasik, A.; Szpunar, J. Elemental speciation and coupled techniques — towards faster and reliable analyses, *J. Anal. At. Spectrom.* 1998, **13**, 859–867.
- [14] Fuwa, K.; Haraguchi, H.; Morita, M.; Van Loon, J. C. A critical review of spectrochemical methods for chemical speciation using element specific detectors with chromatography, *Bunko Kenkyu* 1982, **31**, 289–305.
- [15] Cotton, A. F.; Wilkinson, G. *Advanced Inorganic Chemistry*, 5th edn, John Wiley & Sons Inc.: New York, 1988, pp. 1021–1335.
- [16] Zoorob, G. K.; McKiernan, J. W.; Caruso, J. A. ICP-MS for elemental speciation studies, *Mikrochim. Acta* 1998, **128**, 145–168.
- [17] Manahan, S. E. *Environmental Chemistry*, 5th edn, Lewis Publishers: Chelsea, MI, 1991, p. 62.
- [18] Uden, P. C. (ed.), *Element-specific Chromatographic Detection by Atomic Emission Spectroscopy*, ACS Symposium Series 479, American Chemical Society: Washington, DC, 1992.
- [19] Evans, E. H.; Giglio, J. J.; Castillano, T. M.; Caruso J. A. (Eds). *Inductively Coupled and Microwave Induced Plasma Sources for Mass Spectrometry*, Royal Society of Chemistry: Cambridge, 1995, pp. 33–95.
- [20] Camuna-Aguilar, J. F.; Pereiro-Garcia, R.; Sanchez-Uria, J. E.; Sanz-Medel, A. A comparative study of three microwave induced plasma sources for atomic emission spectrometry — II. Evaluation of their atomization/excitation capabilities for chlorinated hydrocarbons, *Spectrochim. Acta, Part B* 1994, **49**, 545–554.

- [21] Jin, Q.; Borer, M. W.; Hieftje, G. M. A microwave plasma torch assembly for atomic emission spectrometry, *Spectrochim. Acta, Part B* 1991, **46**, 417–430.
- [22] Pack, B. W.; Broekaert, J. A. C.; Guzowski, J. P.; Hieftje, G. M. Determination of halogenated hydrocarbons by helium microwave plasma torch time-of-flight mass spectrometer coupled to a gas chromatograph, *Anal. Chem.* 1998, **70**, 3957–3963.
- [23] Guzowski, J. P.; Hieftje, G. M. The gas sampling glow discharge: a versatile ionization source for gas chromatography time-of-flight mass spectrometry, *Anal. Chem.* 2000, **72**, 3812–3820.
- [24] Olson, L. K.; Belkin, M.; Caruso, J. A. Radiofrequency glow discharge mass spectrometry for gas chromatographic detection: a new departure for elemental speciation studies, *J. Anal. At. Spectrom.* 1996, **11**, 491–496.
- [25] Quimby, B. D.; Dryden, P. C.; Sullivan, J. J. Selective detection of volatile nickel, vanadium, and iron porphyrins in crude oils by gas chromatography-atomic emission spectroscopy, *J. High Resolut. Chromatogr.* 1991, **14**, 110–116.
- [26] Watson, J. T. *Introduction to Mass Spectrometry*, Lippincott-Raven: New York, 1997, pp. 139–211.
- [27] Fenn, J. B.; Mann, M.; Meng, C. K.; Wong, S. F.; Whitehouse, C. M. Electrospray ionization—principles and practice, *Mass Spectrom. Rev.* 1990, **9**, 37–70.
- [28] Covey, T. R.; Lee, E. D.; Bruins, A. P.; Henion, J. D. Liquid chromatography/mass spectrometry, *Anal. Chem.* 1986, **58**, 1451A–1461A.
- [29] Voyksner, R. D. Atmospheric pressure ionization LC/MS, *Environ. Sci. Technol.* 1994, **28**, 118A–127A.
- [30] Kebarle, P.; Tang, L. From ions in solution to ions in the gas phase, *Anal. Chem.* 1993, **65**, 972A–986A.
- [31] Hieftje, G. M.; Norman, L. A. Plasma source mass spectrometry, *Int. J. Mass Spectrom. Ion Processes* 1992, **118/119**, 519–573.
- [32] Borer, M. W.; Hieftje, G. M. Tandem sources for analytical atomic spectrometry, *Spectrochim Acta Rev.* 1991, **14**, 463–486.
- [33] Borer, M. W.; Hieftje, G. M. Design considerations for a pressure-differential tandem source for use in atomic spectrometry, *J. Anal. At. Spectrom.* 1993, **8**, 333–338.
- [34] Mahoney, P. P.; Li, G.; Hieftje, G. M. Laser ablation inductively-coupled plasma mass spectrometry with a time-of-flight mass spectrometer, *J. Anal. At. Spectrom.* 1996, **11**, 401–405.
- [35] Carey, J. M.; Caruso, J. A. Electrothermal vaporization for sample introduction in plasma source spectrometry, *Crit. Rev. Anal. Chem.* 1992, **23**, 397–439.
- [36] Kantor, T.; Hieftje, G. M. “Tandem” versus “combined” sources in atomic spectrometry, *Spectrochim Acta, Part B* 1995, **50**, 961–962.
- [37] Ray, S. J.; Hieftje, G. M. Microwave plasma torch-atmospheric sampling glow discharge modulated tandem source for the sequential acquisition of molecular fragmentation and atomic spectra, *Anal. Chim. Acta* 2001, **445**, 35–45.
- [38] McLuckey, S. A.; Glish, G. L.; Asano, K. G.; Grant, B. C. Atmospheric sampling glow discharge ionization source for the determination of trace organic compounds in ambient air, *Anal. Chem.* 1988, **60**, 2220–2227.
- [39] McLuckey, S. A.; Glish, G. L.; Asano, K. G. Coupling of an atmospheric-sampling ion source with an ion-trap mass spectrometer, *Anal. Chim. Acta* 1989, **225**, 25–35.
- [40] McLuckey, S. A.; Van Berkel, G. J.; Goeringer, D. E.; Glish, G. L. Ion trap mass spectrometry of externally generated ions, *Anal. Chem.* 1994, **66**, 689A.
- [41] Stenhagen, E., Abrahamsson, S., McLafferty, F. W. (Eds). *Atlas of Mass Spectral Data*, Interscience: New York, 1969.
- [42] King, F. L.; Pan, C. Temporal signal profiles of analytical species in modulated glow discharge plasmas, *Anal. Chem.* 1993, **65**, 735–739.

- [43] Steiner, R. E.; Lewis, C. L.; Majidi, V. Consideration of a millisecond pulsed glow discharge time-of-flight mass spectrometer for concurrent elemental and molecular analysis, *J. Anal. At. Spectrom.* 1999, **14**, 1537–1541.
- [44] Guzowski, J. P.; Broekaert, J. A. C.; Ray, S. J.; Hieftje, G. M. Development of a direct current gas sampling glow discharge ionization source for the time-of-flight mass spectrometer, *J. Anal. At. Spectrom.* 1999, **14**, 1121–1127.
- [45] Guzowski, J. P.; Hieftje, G. M. Characterization of a switched direct current gas sampling glow discharge ionization source for the time-of-flight mass spectrometer, *J. Anal. At. Spectrom.* 2000, **15**, 27–36.
- [46] Parisi, A. F., *PhD Dissertation*, Indiana University, Bloomington, IN, 1986.
- [47] Smith, R. D.; Barinaga, C. J.; Udseth, H. R. Improved electrospray ionization interface for capillary zone electrophoresis–mass spectrometry, *Anal. Chem.* 1988, **60**, 1948–1952.
- [48] Evans, E. H.; Caruso, J. A. Low pressure inductively coupled plasma source for mass spectrometry, *J. Anal. Atom. Spectrom.* 1993, **8**, 427–431.
- [49] Houk, R. S.; Fassel, V. A.; Svec, H. J. Mass spectra of polar organic compounds in aqueous solutions introduced into an inductively coupled plasma, *Org. Mass Spectrom.* 1982, **17**, 240–244.
- [50] Yan, X.; Tanaka, T.; Kawaguchi, H. Reduced-pressure inductively coupled plasma mass spectrometry for nonmetallic elements, *Appl. Spectrosc.* 1996, **50**, 182–187.
- [51] O’Connor, G.; Ebdon, L.; Evans, E. H.; Ding, H.; Olson, L. K.; Caruso, J. A. Feasibility study of low pressure inductively coupled plasma mass spectrometry for qualitative and quantitative speciation, *J. Anal. Atom. Spectrom.* 1996, **11**, 1151–1161.
- [52] Waggoner, J. W.; Belkin, M.; Sutton, K. L.; Caruso, J. A.; Fannin, H. B. Novel low power/reduced pressure inductively coupled plasma ionization source for mass spectrometric detection of organotin species, *J. Anal. Atom. Spectrom.* 1998, **13**, 879–883.
- [53] Olson, L. K.; Story, W. C.; Creed, J. T.; Shen, W.; Caruso, J. A. Fragmentation of organic compounds using low-pressure microwave induced plasma mass spectrometry, *J. Anal. At. Spectrom.* 1990, **5**, 472.
- [54] Shen, W.; Satzger, R. D. Development of a low-power microwave atmospheric pressure molecular ionization source for mass spectrometry with direct introduction of gaseous and liquid organic samples, *Anal. Chem.* 1991, **63**, 1960–1964.
- [55] Evans, E. H.; Pretorius, W.; Ebdon, L.; Rowland, S. Low-pressure inductively coupled plasma ion source for molecular and atomic mass spectrometry, *Anal. Chem.* 1994, **66**, 3400–3407.
- [56] O’Connor, G.; Ebdon, L.; Evans, H. Low pressure inductively coupled plasma ion source for molecular and atomic mass spectrometry: the effect of reagent gases, *J. Anal. At. Spectrom.* 1997, **12**, 1263–1269.
- [57] Parisi, A. F.; Rayson, G. D.; Hieftje, G. M.; Olesik, J. W. Temporally and spatially resolved studies in an amplitude modulated inductively coupled plasma, *Spectrochim Acta, Part B* 1987, **42**, 361–376.
- [58] Mahoney, P. P.; Ray, S. J.; Hieftje, G. M. Time-of-flight mass spectrometry for elemental analysis, *Appl. Spectrosc.* 1997, **51**, 16A–28A.
- [59] Guilhaus, M. Principles and instrumentation in time-of-flight mass spectrometry, *J. Mass Spectrom.* 1995, **30**, 1519–1532.
- [60] Myers, D. P.; Hieftje, G. M. Preliminary design considerations and characteristics of an inductively coupled plasma time-of-flight mass spectrometer, *Microchem. J.* 1993, **48**, 259–277.
- [61] Holland, J. F.; Enke, C. G.; Allison, J.; Stults, J. T.; Pinkston, J. D.; Newcome, B.; Watson, J. T. Mass spectrometry on the chromatographic timescale: realistic expectations, *Anal. Chem.* 1983, **55**, 997A–1012A.

- [62] Yie-ru, H.; Qing-yu, O.; Wei-le, Y. Study of gas chromatography—microwave-induced plasma atomic emission on spectrometry. Part I. Effect of the structure of a compound on the determination of its empirical formula, *J. Anal. At. Spectrom.* 1990, **5**, 115–120.
- [63] Olson, L. K.; Caruso, J. A. The helium microwave-induced plasma: an alternative ion source for plasma mass spectrometry, *Spectrochim Acta, Part B* 1994, **49**, 7–30.
- [64] Wu, M.; Duan, Y.; Jin, Q.; Hieftje, G. M. Elemental mass spectrometry using a helium microwave plasma torch as an ion source, *Spectrochim Acta, Part B* 1994, **49**, 137–148.
- [65] Markey, S. P.; Abramson, F. P. Capillary gas chromatography/mass spectrometry with a microwave discharge interface for determination of radioactive-carbon-containing compounds, *Anal. Chem.* 1982, **54**, 2375–2376.
- [66] Heppner, R. A. Elemental detection with a microwave induced plasma/gas chromatograph—mass spectrometer system, *Anal. Chem.* 1983, **55**, 2170–2174.
- [67] Poussel, E.; Mermet, J. M.; Deruaz, D.; Beaugrand, C. Evaluation of a microwave induced plasma as a soft ionization source in mass spectrometry, *Anal. Chem.* 1988, **60**, 923–927.
- [68] Story, W. C.; Olson, L. K.; Shen, W.; Creed, J. T.; Caruso, J. A. Reduced-pressure microwave-induced plasma mass spectrometric detection of phosphorus and sulphur in gas chromatographic eluates, *J. Anal. At. Spectrom.* 1990, **5**, 467–470.
- [69] Creed, J. T.; Davidson, T. M.; Shen, W.; Caruso, J. A. Low-pressure helium microwave-induced plasma mass spectrometry for the detection of halogenated gas chromatographic effluents, *J. Anal. At. Spectrom.* 1990, **5**, 109–113.
- [70] Story, W. C.; Caruso, J. A. Gas chromatographic determination of phosphorus, sulfur, and halogens using a water-cooled torch with reduced-pressure helium microwave-induced plasma mass spectrometry, *J. Anal. At. Spectrom.* 1993, **8**, 571–575.
- [71] Vela, N. P.; Caruso, J. A.; Satzger, R. D. Potential for an atmospheric-pressure low-power microwave induced plasma ionization source for mass spectrometry, *Appl. Spectrosc.* 1997, **51**, 1500–1503.
- [72] Kohler, M.; Schlunegger, U. P. Tunable degree of fragmentation of volatile organic compounds with a low-pressure Penning ion source, *J. Mass Spectrom.* 1995, **30**, 134–139.
- [73] Schuler, H. Über die emissionsspektroskopie organischer substanzen mit hilfe der elektronstossanregungen in der glimmentladung. I, *Spectrochim Acta* 1950, **4**, 85–93.
- [74] Shick, C. R.; DePalma, P. A.; Marcus, R. K. Radio frequency glow discharge mass spectrometry for the characterization of bulk polymers, *Anal. Chem.* 1996, **68**, 2113–2121.
- [75] Carazzato, D.; Bertrand, M. J. Characterization of a glow discharge ion source for the mass spectrometric analysis of organic compounds, *J. Am. Soc. Mass Spectrom.* 1994, **5**, 305–315.
- [76] Mason, R.; Milton, D. Glow discharge mass spectrometry of some organic compounds, *Int. J. Mass Spectrom. Ion Processes* 1989, **91**, 209–225.
- [77] Belkin, M. A.; Olson, L. K.; Caruso, J. A. Radiofrequency glow discharge as an ion source for gas chromatography with mass spectrometric detection, *J. Anal. At. Spectrom.* 1997, **12**, 1255–1261.
- [78] Guzowski, J. P.; Broekaert, J. A. C.; Hieftje, G. M. Studies of an electrothermal vaporizer as a sample introduction strategy for a gas sampling glow discharge time-of-flight mass spectrometer, *Spectrochim Acta, Part B* 2000, **55**, 1295–1314.
- [79] Myers, D. P.; Li, G.; Yang, P.; Hieftje, G. M. An inductively coupled plasma-time-of-flight mass spectrometer for elemental analysis. Part I: optimization and characterization, *J. Am. Soc. Mass Spectrom.* 1994, **5**, 1008–1016.

- [80] Broekaert, J. A. C. State of the art glow discharge lamp spectrometry, *J. Anal. At. Spectrom.* 1987, **2**, 537–542.
- [81] Marcus, R. K. *Glow Discharge Spectroscopies*, Plenum Press: New York, 1993, pp. 1–63.
- [82] Holland, J. F.; Allison, J.; Watson, J. T.; Enke, C. G. In *Time-of-Flight Mass Spectrometry*, Cotter, R. (Ed.), American Chemical Society: Washington, DC, 1994, pp. 157–175.
- [83] Freeman, J. E.; Hieftje, G. M. Near-infrared atomic emission from a helium microwave-induced plasma: element ratio determinations, *Spectrochim Acta, Part B* 1985, **40**, 653–664.
- [84] Sullivan, J. J.; Quimby, B. D. Detection of C, H, N, and O in capillary gas chromatography by atomic emission, *J. Chromatogr.* 1989, **12**, 282–286.
- [85] Klinger, J. A.; Barshick, C. M.; Harrison, W. W. Factors influencing ion signal profiles in pulsed glow discharge mass spectrometry, *Anal. Chem.* 1991, **63**, 2571–2576.
- [86] Ohta, K.; Koike, Y.; Mizuno, T. Determination of zinc in biological materials by sequential metal vapor elution analysis with atomic absorption detection, *Anal. Chim. Acta* 1996, **329**, 191–195.
- [87] Shen, W. L.; Caruso, J. A.; Fricke, F. L.; Satzger, R. D. Electrothermal vaporisation interface for sample introduction in inductively coupled plasma mass spectrometry, *J. Anal. At. Spectrom.* 1990, **5**, 451–455.
- [88] Windholz, M. (Ed.), *The Merck Index*, 10th edn, Merck: Rahway, NJ, 1983, p. 3961.
- [89] Ikonomou, M. G.; Blades, A. T.; Kebarle, P. Electrospray–ion spray: a comparison of mechanisms and performance, *Anal. Chem.* 1991, **63**, 1989–1998.
- [90] Olivares, J. A.; Nguyen, N. T.; Yonker, C. R.; Smith, R. D. On-line mass spectrometric detection for capillary zone electrophoresis, *Anal. Chem.* 1987, **59**, 1230–1232.
- [91] Whitehouse, C. M.; Dreyer, R. N.; Yamashita, M.; Fenn, J. B. Electrospray interface for liquid chromatographs and mass spectrometers, *Anal. Chem.* 1985, **57**, 675–679.

Index

- ablation rates 51–5
 - and sample composition 53
- abnormal glow discharge 5, 31
- absorption parameter 26
- absorption profile 26
- accuracy 66
- aerosol samples 309
- afterglow phenomena 20
- air pollution monitoring 63
- alloy characterization 2
- alloy formation during coating processes 220–2
- α -ionization 105
- aluminium, anodic oxidation 238–9
- aluminium-based coatings 207–29
- aluminium oxide coating 121
- aluminized steel 216, 222, 224
- amino acids, H/C ratio in 358
- analytical model 156
- anode dark space 32
- anode-to-cathode surface areas 100
- anodic films, depth profiles of 122
- anodic oxidation of aluminium 238–9
- anodically oxidized film 268
- antenna 29
- AOAC International 320
- AOX parameter 385, 394–5
- arc discharge 4
- argon atoms
 - energy level scheme 166
 - excited levels, collisional-radiative model for 165–7
 - ionization rates 194
 - optical emission spectra 200
 - see also* fast argon atoms
- argon density profiles 182
- argon gas atoms, heat transfer model for 165
- argon gas heating in dc glow discharges 160
- argon inductively coupled plasma (ICP) 401–2, 435
- argon ionization rate due to electron impact 105
- argon ions
 - collision processes of 191
 - density profiles 181
 - energy distribution of 191
 - fluid model for 162–4
 - Monte Carlo model 164–5
- argon spectral interferences 54
- ASTM 320, 322
- Aston cathodic dark space 31
- asymmetric charge exchange ionization 77
- atmospheric particulate matter, secondary cathode technique 309
- atmospheric pressure ionization (API) 426
- atmospheric sampling glow discharge (ASGDI) 438, 439, 448
- atomic absorption spectrometry (AAS) 16, 184, 187
 - dry residue solution analysis 345–8
- atomic detection for GC separations 424–9
- atomic emission spectrometry (AES) 16, 36–49, 55–63, 78, 254–5, 280, 359, 389, 397–8, 398
- analytical characteristics 398
- as alternative gas chromatographic detector 385–6
- basic principles 37–9
- coincidences of lines in registered spectra 38
- compact solid samples 43

- atomic emission spectrometry (AES)
 (*continued*)
 figures of merit 45–9
 gas analysis 381–400
 hybrid arrangement 385–6
 operating characteristics and analytical
 performance 392–3, 396–9
 spectral background 38–9
 trace analysis 37
- atomic energy level diagram 24
- atomic spectrometry 15
- average information over a relatively
 large area 254
- basic features of 253–5
- reduced pressure ICPs 405
- atomic spectroscopy 5
- atomization efficiency 414
- Auger electron spectroscopy (AES) 66,
 207, 260–1
- Auger electron/photoelectron spectroscopy
 267–71
- Auger neutralization 164
- Auger transition process 259
- Australian Standard 322
- background equivalent concentration
 (BEC) 37
- background intensity ratio 37
- backscattering phenomenon 258
- barrier discharge 31
- biological materials, determination of Pb
 in 344
- Boltzmann constant 18
- Boltzmann distribution 19
- Boltzmann equation 21, 35, 156
- Boltzmann plot 34
- boosted discharges 64
- boron phosphorus silicon glass (BPSG)
 231
- brominated hydrocarbons 386
- bromobenzene 442–3
 1-bromo-2-chloroethane 386
 1-bromo-3-chloropropane 386
- bromoform 375–6, 439, 458–9, 461
- bulk analysis 54–5
 mass spectrometry 123–30
 metal samples 55–60
- bulk insulators 2
- bulk solid reference materials 326–7
- bulk solution analysis 335
- burn-in times 52
- burning crater 52
- burning spots 53–4
- burning voltage 31
- butylmagnesium chloride 397
- calibration, emission yield concept
 147–8
- calibration curve 47
 lithium 353
 mass spectrometry 92–3
- calibration functions 37, 47, 48
- calibration graphs 208
 validation and verification 225–9
- carbon disulphide 393
- carbon-oxygen elemental ratios 445
- carbon tetrachloride 456
- carbonitriding of steel 27 MC5R 237
- carburizing of steel 27 MC5R 237–8
- cathode dark space (CDS) 156, 181,
 188–92
 Monte Carlo model 164–5, 168–70
- cathode dark space (CDS) and negative
 glow (NG) 180
- cathode sputtering 6, 50, 52, 101,
 167–8, 196–8
- cell geometry effect 199–200
- centrifugal force 83
- centripetal force 83
- ceramic materials, secondary cathode
 technique 308
- certified reference material (CRM) 325,
 327–32, 363
 definition 325
 depth profiling 329–31
 mercury in 398–9
- Chantarelle reference sample 94
- characteristic X-ray radiation 259
- charge-coupled device (CCD) 39–41,
 144
- charge-injection devices 39
- charge transfer 17
- chemical composition, validation 227–9
- chemical ionization (CI) 359, 424
- chemical vapour deposition (CVD) 231,
 245–6
- chloride determination
 in water samples 389
 with different plasma sources using
 similar introduction system and AES
 detection 395
- chlorinated hydrocarbons 374, 386, 451,
 454, 456

- chlorobenzene 428, 456
- 2-chlorobutane 456
- chloroform 456
- 1-chloroheptane 456
- 2-chloro-2-methylbutane 456
- 2-chloro-2-methylpropane 456
- 1-chloropentane 456
- chloropropane 456
- CIROS instrument 41
- cladding materials 277–8
 - depth profiling 286–8
- coating analysis by emission yield method 209–13
- coating weight measurement traceability 208–9
- coatings
 - depth profile analysis 213–17, 243–51
 - nonconducting materials 2
 - thickness and composition 208–9
- collision processes 157
 - argon ions 191
 - in plasma 192–6
 - overview 158–9
- collisional-radiative models 160, 199
 - argon atom excited levels 165–7
 - copper atoms and ions 168
- COMAR (COde MAteriaux Reference) Certified Reference Materials Database 328
- compact electrically nonconductive samples 61
- computer hard disks 243–5
- conducting host matrix, nonconducting materials 294–301
- conducting secondary cathode 294
 - nonconducting materials 301–11
- continuous introduction of solution into hollow cathode source, optical emission spectra 352
- continuous solution introduction into hollow cathode discharge 338
- copper atoms and ions
 - collisional-radiative model for 168
 - energy level scheme 169
- copper ions
 - flux energy distribution of 193
 - in CDS, Monte Carlo model for 168–70
- corona discharge 31
- corrosion mechanisms 287
- costs 66–7
- crater profile 197–8
 - Cu CRM 074 311
- Cr/Fe intensity ratio 270–1
- crystal water 61
- Cu CRM 074, crater profile 311
- current-pressure-voltage characteristic 173
- current-voltage characteristic 27
- current-voltage relationships of diode-type discharges 3–5
- Czerny-Turner monochromator 40
- dc bias potential 100–1
- dc discharge, potential distribution in 180
- dc gas-sampling glow discharge (GSGD) 366
- dc glow discharge 26–31, 293–4
 - argon gas heating in 160
- dc-glow discharge-AES 384–5, 394, 396–9
- dc-glow discharge-MS 374
- dc-powered glow discharge sources 101–6
- dc pulsed glow discharge 366
- degree of ionization 21
- density profiles of tantalum ions 185
- depth profile analysis 59–60, 66, 141–54
 - anodic films 122
 - by glow discharge spectroscopy 153
 - coatings 213–17, 243–51
 - CRMs 329–31
 - data acquisition parameters 145
 - factors affecting quality 217–22
 - figures of merit 145
 - high erosion rate 254
 - instrumentation 142–5
 - painted coatings on metals 116–19
 - practical aspects and results 144–53
 - presentation and interpretation of data 145–53
 - qualitative 152
 - quantitative 152
 - SIMS 265–6
 - surface layers 207
 - surfaces 232–8
 - thin films 238–43
 - very thin layers 119–23
- ZrO₂ layers deposited on zircaloy nuclear fuel cladding material 286–8

- depth resolution 218–19
- depth validation 227
- destructive vs. nondestructive methods 255
- detection limits 48, 56, 115–16, 129, 284, 384–6
 - GDMS 63
 - GSGD source at 371
 - reduced pressure afterglow 430
 - rf-glow discharge-OES 117
 - transition metal analytes 353
- diagnostics 33–6, 64
- dibromobenzene 428
- 1,2-dibromoethane 393
- 1,2-dichlorobenzene 420
- 1,3-dichlorobenzene 420
- 1,4-dichlorobenzene 420
- 1,2-dichloroethane 393
- dichloromethane 386
- 1,2-dichloropropane 456
- diffusion mechanisms for trace elements 287
- dimethyldiethyllead (DMDEL) 419, 444
- diode-array detection 47
- diode geometry 5, 77
- DIP-mounted rf-GDMS ion sources 110
- direct injection nebulizer (DIN) 426
- direct insertion probes (DIP) 78, 110–11
- direct sample aspiration 337–8, 351–3
- discharge current 5
- discharge parameters 145, 344
- discharge power delivery 345
- DOLT-2 398
- Doppler broadening 25, 33
- DORM-2 398
- Druyvenstein function 18, 20
- dry solution residue analysis 61–3, 336–7, 342–5
 - atomic absorption spectrometry 345–8
 - atomic emission spectroscopy 342–5
 - mass spectrometry 348–51
 - practical aspects and applications 342–51
 - transient mode of atomization 347
- dual-vacuum pumping 107
- duoplasmatron ion sources 261
- dynamic SIMS 256
- E-mode 403, 407, 427
- Ebert monochromator 40–1
- Echelle spectrometers 41
- ECISS standards 324
- E-H transition 403, 407
- Einstein transition probabilities 20
- electric field distributions 179–81
- electrical characteristics 173–9
 - as function of time in rf cycle 178
- electrical coatings 246–8
- electrical conductivity 97
- electrical current flowing towards rf electrode 179
- electrical discharge 16–17
- electrical parameters 31–3
- electrical potential 86
- electrical resistivity, nonconducting samples 305–6
- electromagnetic field 83
- electromagnetic radiation (EMR) 107
- electromagnetic spectrum 98
- electron energy distribution function (EEDF) 407
- electron impact ionization 73, 75–6, 195, 359, 424
 - argon ionization rate due to 105
 - collisions 6
 - library spectra 371
 - molecular fragmentation 376
- electron number density 19, 21, 35–6, 183
- electron probe methods 258–61
- electron probe microanalysis (EPMA) 260, 271–2
- electron probe spectrometry 255, 259
- electron sources 76
- electron temperature 36
- electrophoretic coatings 248–51
- electropolished aluminium, oxide surface on 235–6
- electrospray 424
- electrothermal vaporization (ETV) 420, 460–1
- element-selective chromatograms 419
- element-selective detection 436
 - figures of merit 417–18, 423–4
 - low-pressure inductively coupled plasmas for 416–21
 - reduced pressure ICP 443
- emission intensity and sputtering rate 151
- emission yield concept 146–8
 - calibration 147–8
 - coating analysis by 209–13
 - effect of matrix 213
- empirical intensity 149

- energy distribution of argon ions 191
- environmental samples 285–6
- equilibrium state 19
- ethylbenzene 377–8
- ethylene dichloride 456
- ethylmercury 397–8
- excitation and de-excitation processes 19
- excitation conditions 20
 - compensation for variations in 149–50
- excitation efficiency 64
- excitation temperature 33–4
- excited-state emission 106
- expansion stage pressure 373
- exponential dilution chamber 387–8
- exponential dilutor technique 387

- fast argon atoms
 - flux energy distribution 192
 - Monte Carlo model 164–5
- fast atom bombardment (FAB) 424
- fast atom bombardment mass spectrometry (FAB-MS) 258
- fast electrons, Monte Carlo model for 161
- fast Fourier transformation (FFT) 91
- ferrocene 462
- ferrous chloride 462
- figures of merit
 - atomic emission spectrometry 45–9
 - depth profile analysis 145
 - element-selective detection 417–18, 423–4
 - GC-LP-ICP-MS operated at low power in atomic and molecular modes 427
 - LP-ICP-MS 421
 - LP-surfatron microwave plasma AES 422
 - nonconducting materials 300–1
 - secondary cathode technique 306–11
 - solids analysis 64
 - tetramethyltin (TMT) 370
- Finnigan MAT Element instrument 128
- flame atomic absorption spectrometry (FAAS) 208
- flame ionization detection (FID) 417, 419
- flat cathode (FC) 57, 65, 382, 385–6, 389
- fluid model 156, 162
- fluorohydrocarbon polymers 132
- flux energy distribution
 - argon ions 190
 - copper ions 193
 - electrons 189
 - fast argon atoms 192–6
- Fortrat parabola 35
- Fourier transform emission spectrometry 42–3
- Fourier transform ion cyclotron resonance mass spectrometry 90–1
- Fourier transform optical emission spectrometry 26
- fundamental noise 46

- GaAs thin films 141
- galvanized coatings 2
- galvanized steel 213–16, 221, 224
 - oxide surface on 233–5
- galvannealed steel 216–17, 228
- gas analysis 63
 - atomic emission spectrometry 381–400
 - instrumentation 386
 - operating features and analytical performance 392–3
 - practical aspects and results 392–9
- gas chromatography (GC) 3, 363–79
 - coupled to rf-HC-GD-AES 387
 - detector 381–400
 - element-selective detection 416
 - elemental speciation 364
 - glow discharge hyphenated technique 385
 - glow discharge interfaces 369, 389–92
 - glow discharge sources 364–7
 - instrumentation 364–70, 386–92
 - low-pressure microwave induced plasmas 421–3
 - molecular structural information 371–2
 - practical aspects and results 370–7
 - qualitative information 371–2
 - quantitative information 370–1
- gas chromatography-LP-ICP-MS 442
- gas chromatography-LP-ICP-MS operated at low power in atomic and molecular modes, figures of merit 427
- gas chromatography-LP-MIP-MS 422
- gas discharge
 - electrical characteristics 4
 - ion source 73
- gas jet-assisted sputtering 64
- gas-liquid separator 388
- gas-phase collisions 75

- gas-phase excitation/ionization 7
- gas-phase processes 17–26
- gas pressure 54, 177
 - in secondary cathode technique 305
- gas samples
 - direct introduction 382–3, 387–8
 - introduction 3
- gas sampling glow discharge (GSGD)
 - 44, 63, 457–63, 460
 - determination of non-metals 383
 - ionization source 450–5
 - source at detection limits 371
- gas sampling glow discharge (GSGD)-MS,
 - original design 374
- gas temperature 34–5, 176
- gas temperature profiles 174–5
- Gaseous Electronics Conference (GEC)
 - RF Reference Cell 406–7
- Gauss profile 25
- glass
 - characterization 240–1
 - surface roughness 307
- glass samples 115
 - secondary cathode technique 308
- glass substrates, depth profile analysis of
 - multi-layer films deposited on 241–3
- glasses 240–3
- glove-box installations 274–7
- glow discharge
 - abnormal 5
 - analytical applications 1–2
 - operating modes 79–81
 - structure 31
 - use of term 4
- glow discharge cell 184
- glow discharge chamber, design 386–7
- glow discharge devices
 - basic operating principles 3–6
 - scope of application 6–7
- glow discharge lamp 28, 44
- glow discharge mass spectrometry *see*
 - mass spectrometry
- glow discharge-OES 38, 182–3
- glow discharge sources, gas
 - chromatography 364–7
- glow discharge spectroscopy 141
 - depth profile analysis by 153
- graphite cathodes 342
- Grimm-type glow discharge, design 386
- Grimm-type glow discharge cell 43, 44,
 - 54, 61, 63, 66, 78, 174, 176, 182–3,
186, 187, 199, 200
- Grimm-type glow discharge geometry 125
- Grimm-type glow discharge ion sources 78–9, 93, 108, 141, 143
- Grimm-type glow discharge lamp 108,
 - 119, 340
- ground-state atoms 75
- H-mode 403, 407
- H/C ratio in amino acids 358
- halogenated hydrocarbons 450–1
- halogenated species 446
- HDPE 133
- heat conduction equation 165
- heat transfer model for argon gas atoms 165
- helium dc-GD-AES 384
- helium dc-HC-GD-AES 383
- helium hollow cathode 382
- helium make-up discharge gas 390
- helium MIP 384
- helium plasma gas 382
- helium RP-MIP 445
- high-resolution spectral record 26
- high-voltage vacuum spark discharge 73–4
- Hittorf dark space 31
- hollow cathode 57, 63–5, 78–9, 337,
 - 382, 385–6, 390
 - emission source 338
- hollow cathode discharges 344
- hollow cathode lamp 28–9, 344
- hybrid model 157
- hydride generation 384
- hydrocarbons 446
- illumination system 40
- imaging SIMS 256
- impulse theory 53
- inductively coupled plasma (ICP) 382,
 - 401–33, 435
 - molecular fragmentation patterns 441–5
- inductively coupled plasma (ICP)-AES 208, 263
- inductively coupled plasma (ICP)-MS 278, 359, 364, 386, 435
- inductively coupled plasma (ICP)-TOFMS 366, 450

- inelastic collisions 17
- Ingles-Teller equation 405
- inorganic mercury 397–8
- instrumentation
 - depth profile analysis 142–5
 - developments and applications 2
 - gas analysis 386
 - gas chromatography 364–70, 386–92
 - glow discharge emission spectrometry 39–45
 - liquid sample analysis 336–41
 - low-pressure ICPs 407–14
 - mass spectrometry 74, 82–91
 - in glove box 274–6
 - optical emission spectrometry in glove box 276–7
 - rf glow discharges 106–11
- intensity normalization technique,
 - calibration function 148
- interference influences 49
- interference noise 46
- International Organization for Standardization (ISO) 320
- inverse calibration function 37
- iodobenzene 428
- ion components 80
- ion cyclotron resonance cell 91
- ion intensity 297
- ion microprobe analysis (IMA) 254
- ion probe methods 256–8
- ion probe spectrometry 255, 257
- ion sampling configuration 72
- ion scattering spectroscopy (ISS) 254, 258
- ion sources 77–81
- ion stability 88
- ion temperature 36
- ion trap mass analyzer 87–9
- ionization degree 21
- ionization mechanisms 75, 76
- ionization modes 75–7
- ionization rates
 - argon atoms 194
 - sputtered copper atoms 195
- ionization source 359
 - molecular fragmentation patterns 447–8
 - multidimensional 435–68
 - multipurpose, for PSMS 441–63
 - organic compounds 447
- iron-based alloys, nitride films on 269–71
- ISO/TC 201/SC 8 324, 327, 331
- isotope ratios 286
- kanalstrahlen 72
- Langmuir probe 36, 182, 183
- laser ablation analysis 405
- laser induced fluorescence (LIF) 184–6
- laser induced plasma spectrometry (LIPS) 263
- laser microprobe mass spectrometry (LMMS) 263
- laser probe methods 263
- layered reference materials 327–31
- LDPE 133
- Leco Corporation 144
- limestone, surface roughness 307
- limits of detection *see* detection limits
- linear dynamic range 48, 65–6
- liquid chromatography (LC) 364, 379
- liquid chromatography/mass spectrometry (LC/MS) 339–41, 354–60
- liquid nitrogen trap 384
- liquid sample analysis 335–62
 - conversion to volatile derivative 383–5
 - determination of chemically volatilized analytes from 393–6
- instrumentation 336–41
 - practical aspects and applications 341–60
 - solution nebulization 417
 - volatile analyte derivatives 388–9
- lithium, calibration curve 353
- lithium hydroxide 286
- lithium (I) 670.8 nm emission intensity 353
- lithium profiles 264, 288–9
- L-LDPE 133
- local thermal equilibrium 19
- local thermodynamic equilibrium (LTE) 403–4
- Lorentz broadening 25, 33
- Lorentz profile 25
- low-alloy steel 238
- low-power RP helium ICP 442
- low-pressure gas discharges 71, 73
- low-pressure ICP 401–33, 443
 - advantages 402
 - element-selective detection 416–21
 - fundamentals 403–7
 - instrumentation 407–14

- low-pressure ICP (*continued*)
 mass spectrometry 408–10
 figures of merit 421
 optical emission spectrometry 408
 practical aspects and results 416–29
 sources for mass and optical spectrometry 402
- low-pressure ICP-AES 405
- low-pressure MIP 414
 gas chromatography 421–3
 mass spectrometry 412
 molecular fragmentation patterns 446–7
 optical emission spectrometry 410
- low-pressure MIP torch 447
- low-pressure plasma 1–3, 357, 403
- low-pressure surfatron microwave plasma AES, figures of merit 422
- low-temperature equilibrium (LTE) 34–6
- M tryptophan, PB-GD mass spectrum 359, 360
- McPherson monochromator 47
- magnetic fields 61, 62, 64
- magnetic sector analyzer 82–5
- magnetron glow discharge sources 111
- manufacturing applications for quality control 254
- marble, surface roughness 307
- Marcus-type discharge chamber design 386, 389
- Marcus-type geometry 126
- Marcus-type sources 108, 120–1
- marine certified reference materials 386
- mass analyzers 111
- mass-selective instability trapping mode 87, 88
- mass spectrometry 7, 71–96, 182–3, 273–4, 335, 364
 analytical applications 72, 123–36
 bulk elemental analysis 123–30
 calibration curve 92–3
 current status 74–5
 detection limits 63
 dry residue solution analysis 348–51
 examination of low pressure flames 74
 fundamentals 75–82
 general considerations 71
 historical aspects 72–4
 in analytical chemistry 74
 instrumentation 74, 82–91
 internal standardization (RSF) 94
 key factors in growth 74
 low-pressure ICP 408–10
 low-pressure MIP 412
 microplasma ion source for 414
 MIP 445–7
 nonconductive materials 98
 oxide materials 130–2
 polymeric materials 132–6
 qualitative considerations 91–2
 quantitative analysis 92–5
 relative sensitivity factors (RSFs) 201–2
 rf glow discharge sources 109–11
 standards 322–4
 transport phenomena 81–2
see also liquid chromatography/mass spectrometry (LC/MS)
- mass spectrum 80, 91
- matching boxes 107
- material ablation 49–55
 sputtering 50–2
- Mathieu differential equation 87
- Mathieu stability equation 88
- mercury 397–8
 in certified reference material 398–9
 rf-HC-GD-AES 387, 390
- metal layers 2
- metal samples, bulk analysis 55–60
- metallic alloy fuels 278
- metastable collisions 105
- metastable levels 20
- methylene chloride 456
- methylmercury 386, 397–8
- methyltriethyllead (MTEL) 419, 444
- Michelson interferometer 41–2
- microchannel plates 40
- microplasma ion source for mass spectrometry 414
- microsecond-pulsed glow discharge 177
- microwave induced plasma (MIP) 382
 mass spectrometry 445–7
see also low-pressure MIP
- microwave plasma torch (MPT) 438
- millisecond pulsed glow discharge 456–7
- MIT spectral line tables 38
- modulated (or switched) source concept 440
- molecular detection for GC separations 424–9

- molecular flow 82
- molecular fragmentation patterns 438
 - ICP 441–5
 - ionization source for 447–8
 - low-pressure MIP 446–7
- molecular mode 428
- molecular weight/fragmentation information 335
- momentum analyzer 84
- monochromators 39–40
- Monte Carlo model 160
 - argon ions and fast argon atoms in CDS 164–5
 - copper ions 164–5, 168–70
 - fast electrons 161
- Monte Carlo simulations 157
- Morille reference sample 94
- moving belt apparatus 340
- multidimensional ionization sources 435–68
- multipurpose ionization sources for PSMS 441–63

- naphtha 444
 - element-selective chromatograms 419
- national metrological institutes (NMIs) 332
- National Research Council of Canada 398
- nebulization process 49, 357
- negative glow 180
- negative potential 99
- neodymium 278
- neon 54
- Newton's laws 161
- Ni-Fe alloy coatings 271–2
- Nier-Johnson geometry 84
- NIST, iron standard 104
- NIST electron ionization reference spectrum 377
- NIST library 371
- NIST SRM 1104 Free-Cutting Brass 125
- NIST SRM 1252 Phosphorized Copper 103
- NIST SRM 1259 Aluminium Alloy 124
- NIST SRM 2137 Boron Implant in Silicon standard 122
- NIST SRM 2715 Lead in Reference Fuel 371

- NIST SRM 610 Trace Elements in Glass 125, 127
- NIST SRM 612 Trace Elements in Glass 126, 128
- NIST SRM 613 Trace Elements in Glass 129
- nitride films on iron-based alloys 269–71
- nitriding of low-alloy steel and steel grade 32CDV 13 238
- nitrogen KLL Auger spectrum 271
- noise components 65
- noise limitations 46
- noise types 46
- nonconducting materials 293–315
 - coatings 2
 - conducting host matrix 294–301
 - conducting secondary cathode 301–11
 - discharge conditions 298–9
 - figures of merit 300–1
 - glow discharge methods 293–4
 - influence on sputtering rates and ion intensities 297
 - mass spectrometry 98
 - nuclear samples 279–80
 - particle size effect 299
 - powder mixed with conducting host matrix 294
 - powder samples 60–1
 - trapped gases 299–300
- nonconducting samples 61, 97
 - electrical resistivity 305–6
 - surface characteristics 306–11
- nonfundamental noise 46
- nonmetallic elements in gases and liquids 382
- nonmetals 2
 - determination in organic vapours by rf-GD-AES 388
 - determination in volatilized organic compounds 393
- non spectroscopic measurements 36
- nonuniform gas temperature 160
- normal glow discharge 31
- nuclear fuels 277
- nuclear research and technology 277
- nuclear samples 273–92
 - applications for traces and bulk analysis 277–84
 - comparison of dc-GDMS and quadrupole ICP-MS 280–4
 - isotopic composition 286

- nuclear samples (*continued*)
 - nonconductive 279–80
 - practical aspects and results 277–88
 - trace elements 280–4
- nuclear-waste glasses 280
- numerical modeling 155–205
 - overview 157–60
 - plasma species 157, 159
 - results and discussion 170–202
 - specific features and limitations 156
- optical emission intensities 199
- optical emission measurements 74
- optical emission spectra
 - argon atoms 200
 - continuous introduction of solution into hollow cathode source 352
- optical emission spectrometry 7, 15–69, 273–4, 335
 - bulk elemental analysis 112–16
 - low-pressure ICP 408
 - low-pressure MIP 410
 - quantitative analyses 254
 - standards 324
- optical emission spectroscopy 7, 33
 - rf glow discharges (in general) 107–9
- orbital angular momentum 22
- orbital quantum number 22
- organic compounds, ionization source for 447
- organohalide compounds 417–18, 424–9
- organohalogen compounds 443
- organohalogen determination,
 - GC-dc-HC-GD-AES system 391
- organometallic compounds 418, 424–9, 443, 448
- oxide film on stainless steel 269
- oxide materials, mass spectrometry 130–2
- oxide surface
 - on electropolished aluminium 235–6
 - on galvanized steel 233–5
 - on stainless steel 232–3
- painted coatings on metals, depth profiling of 116–19
- particle beam interface 340, 356, 359
- particle beam-glow discharge-AES 358
- particle beam-glow discharge mass spectrum, M tryptophan 359, 360
- particle beam-glow discharge-MS 379
- particle beam-hollow cathode-AES 356
- particle beam sample 341
- particle-in-cell method 157
- particle transport characteristics 357
- Paschen curve 28
- Paschen-Runge mounting 41
- Pauli exclusion principle 24
- Pb (I) 405.8 nm line intensity 355
- Penning ionization 32, 75–7, 299, 376
- pentachlorobenzene 420
- perfluorotributylamine (PFTBA) 445–6
- photodiode array (PDA) detector 351, 353
- photoelectrons 39
- photoexcitation 32
- photomultipliers 39, 41
- physical vapour deposition (PVD) 231, 245–6
- planar cathode 337
 - PB-glow discharge geometry 357
- Planck's law 20
- plasma 3, 5, 16–17, 32, 98
 - collision processes in 192–6
 - plasma characteristics 98, 102, 104
 - plasma chemistry 109
 - plasma coatings 246
 - plasma density 64
 - plasma environment 104
 - plasma excitation efficiencies 344
 - plasma ionization source parameters 372
 - plasma mass spectrometric methods 63
 - plasma parameters 33–6, 64, 103
 - plasma physics 109, 142
 - literature 155
 - plasma-source mass spectrometry (PSMS) 435–68
 - multipurpose ionization sources for 441–63
 - tandem sources in 437–41
 - plasma species 160, 187
 - densities and level populations 181–8
 - energies of 188–92
 - numerical modeling 157, 159
 - plasma structure 5
- plutonium 278, 281–2
- plutonium oxide 277, 280
- Poisson distribution 46
- Poisson equation 156, 164, 180
- polyatomic oxides 282
- polycyclic aromatic hydrocarbons (PAHs) 360
- polymer mass spectrometry 2, 132–6

- polymers 448
 - secondary cathode technique 310
- polytetrafluoroethylene (PTFE) 448
- poly(vinylidene fluoride) (PVDF) 134–6
- potential 179–81
- potential difference 6, 99
- potential distribution in dc discharge 180
- power modulated glow discharge sources 455–63
- power of detection 63–5
- precision 46–7, 56, 65, 284, 301
- pressurized water reactors (PWR) 286
- primary electrons 76
- PTFE-co-PFA 132
- pulsed discharges 64
- pulsed glow discharge mode 80–1

- quadrupole mass filter 85–7
- qualitative depth profile 142, 146, 151
- quality control, manufacturing applications for 254
- quantification
 - GDMS techniques 151
 - optical emission 146–8
 - rf-powered sources 150
- quantitative depth profile 153
- quantum numbers 23

- radioisotopes
 - contaminated environmental samples 285–6
 - secondary cathode technique 310
- random noise 46
- rare earth elements (REEs) 104
 - dry solution residue analysis 349
- recombination 17
- reduced pressure afterglow 413–14, 415, 429
 - detection limits 430
- reduced pressure ICP, elemental-selective detection 443
- reduced pressure ICP torch 403–4
- reduced pressure MIP 414
- reference materials 317–18, 331–2
 - definition 325
 - pertinent to glow discharge spectroscopies 326–31
 - practical aspects 325–31
 - types 325–6
 - see also* certified reference material (CRM)
- reflectron 90

- relative sensitivity factors (RSFs) 92, 94, 124–5, 126, 128, 129, 201–2, 278, 282, 283, 301
- resonance broadening 25
- reverse Nier-Johnson geometry 84
- rf amplitude 88
- rf electrode, electrical current flow towards 179
- rf frequency 88
- rf-glow discharge 26–31, 61, 80, 97–139, 293
 - atomization/excitation source 30
 - instrumentation 106–11
 - operation principles 99–101
- rf-glow discharge-AES 384–5, 396–9
- rf-glow discharge-OES 102
 - basic geometries 107
 - bulk analyses of nonconductors 114
 - calibration characteristics 113
 - elemental detection limits 116
 - limits of detection 117
 - nonmetals 114
 - quantification of capabilities 118
- rf-glow discharge sources
 - analytical applications 112–36
 - design of 101
- rf-glow discharge technology 98
- rf Grimm lamp 108
- rf-HC-GD-atomic emission spectrometry (AES)
 - gas chromatography coupled to 387
 - mercury speciation by 390
- rf microplasma 412, 424
- rf plasma sources 406
- rf power 2, 7, 29
- rf power coupling, efficiency of 101
- rf-powered glow discharges 98, 448–9
 - comparisons with dc-powered devices 101–6
- rf-powered sources, quantification using 150
- rotational quantum number 34
- Russell-Saunders coupling 23
- Rydberg's constant 22

- Saha constant 21
- Saha equation 36
- sample graininess 61
- sample volume, influence of 396
- scanning Auger microscopy (SAM) 260, 272

- scanning electron microscopy (SEM)
 - 232, 258, 272
- Scharfetter-Gummel exponential scheme
 - 164
- secondary cathode technique 98, 282
 - atmospheric particulate matter 309
 - ceramic materials 308
 - figures of merit 306–11
 - gas pressure in 305
 - geometry 304–5
 - glass samples 308
 - hole size and thickness 313
 - material 304
 - polymers 310
 - sample geometry 312
 - trace radioisotopes 310
- secondary electrons 76
- secondary ion mass spectrometry (SIMS)
 - 6, 66, 120–2, 132, 207, 232, 240, 254, 256, 263–7
- secondary neutral mass spectrometry (SNMS) 131
- segmented array charge-coupled device (SCD) detector 414
- selected ion chromatograms, spiked oil
 - 420
- selection rules 23
- selective ion monitoring 419
- self-sustaining discharge 31
- SEM-EDX maps 118
- semiconductor detectors 39
- semiconductor manufacturing 101
- sequential spectrometers 40, 102
- signal-to-background (S/B) ratio 102–3, 106, 115
- signal-to-noise (S/N) ratio 103, 355
- silicon-modified polyester-metallic coated steel sample 119
- Silsbee focusing 52
- silver solution residues, transient atom populations of 346
- SIMR method 148–50
- simultaneous spectrometers 40–1
- SiO₂/TiO₂ multi-layers on borosilicate glass 243
- skin effect 107, 109
- slow electron-argon ion fluid model 180
- slow electrons
 - density of 181
 - fluid model for 162–4
- solid oxide fuel cells (SOFC) 131
- solids analysis 2, 3, 97–8
 - figures of merit 64
- solution-based samples 335
- solution nebulization, liquid samples 417
- solution sample introduction 3
- spark source optical emission 112
- speciation experiment 3
- Spectrums Analytik 144
- spiked oil, selected ion chromatograms
 - 420
- spin quantum number 23
- sputter atomization 7
- sputtered atoms, thermalization of 167–8
- sputtered cathode 183
- sputtered copper atoms, ionization rates of
 - 195
- sputtered depth determination 148–9
- sputtered neutral mass spectrometry (SNMS) 66, 258
- sputtered tantalum atoms 184
- sputtering crater 143
- sputtering equilibrium 65
- sputtering experiments 51
- sputtering process 6, 64, 98, 141
 - artefacts from 151–3
 - material ablation 50–2
- sputtering profiles 61
- sputtering rate 54, 151, 153, 297
- sputtering rate-intensity proportionality
 - 147
- sputtering yield 51
- stabilized capacitive plasma (SCP) 382
- stainless steel
 - lithium profile from 264
 - oxide film on 269
 - oxide surface on 232–3
- stainless-steel cathode 342, 343
- stainless-steel cube chamber 365
- stainless-steel GC-GD interface 390
- Standard Reference Material (SRM) 325
- standardization
 - process 318–21
 - undesirable effects 319–20
- standards 317–24, 331–2
 - definition 318–21
 - development process 320–1
 - graphical depiction 321
 - effect of freezing technology 320
 - mass spectrometry 322–4
 - optical emission spectrometry 324

- practical aspects 318–24
 - relevant to chemical analysis through glow discharge spectroscopies 322–4
 - types 318
- standards development organizations (SDOs) 320
- Stark broadening 36, 405
- static SIMS 256
- steel 27 MC5R
 - carbonitriding of 237
 - carburizing of 237–8
- steel grade 32CDV 13 238
- steel industry application 207–29
- steel sheet, Zn-based coatings on 151
- surface analysis 253–72
 - atomic spectrometry 253–72
 - comparison with other methods 253–72
 - experimental techniques 253
- surface-improved metallurgical products 59
- surface layers, depth profiles 207
- surface roughness
 - glass, marble and limestone 307
 - substrate steel 219–20
- surface treatments 236–7
- surfaces, depth profile analysis 232–8
- surfatron plasmas 410–11
- switched glow-discharge-GSGD-TOFMS 460
- switched GSGD source 457–63
- tandem sources 413–14, 429
 - ICP-MIP 415
 - PSMS 437–41
- tantalum ions, density profiles 185, 186
- Tesla coil 407
- tetrabutyltin 448
- tetraethyllead (TEL) 419, 444
- tetraethyltin 448
- tetrahydroborate in acidic media 384
- tetramethyllead (TML) 419, 444
- tetramethyltin (TMT) 371
 - figures of merit 370
- thermal accommodation coefficient 176
- thermal ionization mass spectrometry (TIMS) 278, 286, 289
- thermal volatilization 50
- thermalization of sputtered atoms 167–8
- thermally vaporized liquid organic samples 382–3
- thermionic electron emission 5
- thermodynamic equilibrium 19
- thermospray 424
- thin films 141
 - analysis 2
 - depth profile analysis 238–43
- time-of-flight mass spectrometry (TOFMS) 89–90, 363, 366, 369, 376–7, 450, 460
- time-resolved data acquisition software (TRA) 371
- titration (TITR) 278
- total angular momentum 23
- Townsend discharge 4, 31
- trace elements, diffusion mechanisms for 287
- transient atom populations of silver solution residues 346
- transient mode of atomization of solution residues 347, 348
- transition metal analytes, detection limits for 353
- transport equations 164
- transport-type LC/MS interfaces 339–41, 354
- trapping of gases 299–300
- tributylammonium hydroxide 426
- 1,2,3-trichlorobenzene 420
- 1,2,4-trichlorobenzene 420
- 1,3,5-trichlorobenzene 420
- trichloroethylene (TCE) 453, 455
- trimethylethyllead (TMEL) 419, 444
- trimethyltin 449
- tunable fragmentation 372–7
- two-line method 33
- uranium 278, 281–2
 - uranium oxide 277
 - reference sample 283–4
- vacuum regions 82
- vacuum system 45–6
- very thin layers, depth profiling 119–23
- VG 9000 glow discharge cell 124, 173, 176, 180, 188–9, 194, 197–9, 274, 298, 307, 309–10
- VG 9000 glow discharge mass spectrometer 84–5, 94, 174, 191, 296–7
- VG 9000 glow discharge mass spectrum 182

- VG GloQuad 110, 134
- volatile analyte derivatives from liquid samples 388–9
- volatile covalent hydrides of analytes 383
- volatile organic compounds (VOCs) 417
- volatilization 29, 31, 49, 50
- volatilized organic compounds, determination of nonmetals in 393
- volatilized organic liquids, determination of Cl, C, Br and S in 392

- water samples, determination of chloride in 389
- wavelength calibration 43
- wavelength determination 22

- weighing error 47

- X-ray fluorescence spectrometry (XRF) 61, 65, 112, 207, 208, 262
- X-ray photoelectron spectrometry, angle-resolved method 262
- X-ray photoelectron spectroscopy (XPS) 120, 207, 233, 254–5, 261, 261–2
- X-ray probe methods 260–2

- Zeeman effect 23
- zinc-based coatings 151, 207–29
- zircaloy cladding materials 278, 286–8
- zirconium 278
- zirconium alloys 278
- ZrO₂ layers 286–8

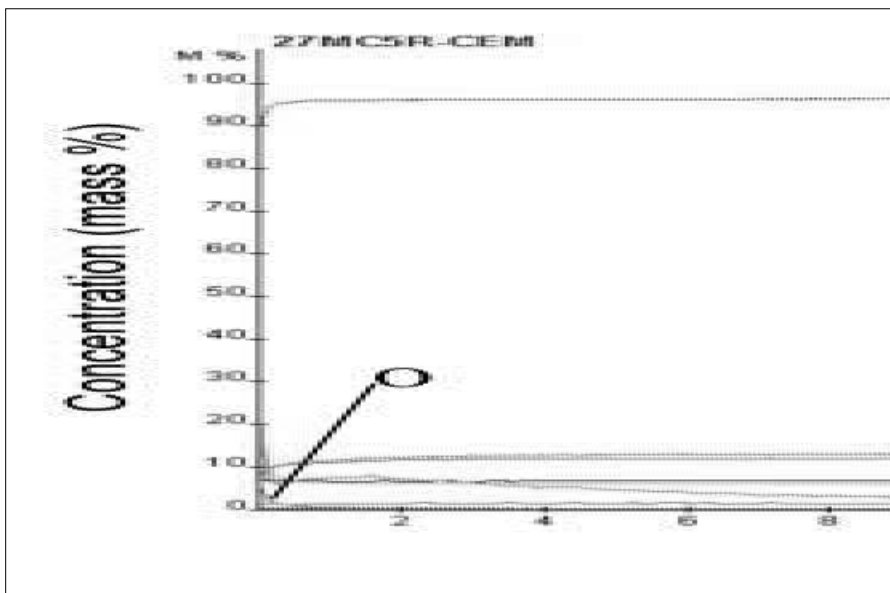


Plate 1 Quantitative rf-GD-OES depth profile of carburised steel.



Plate 2 Backscattered electron image of a cross-section of a nitrided low alloy steel (left) and quantitative rf-GD-OES depth profile of 'ionic' nitrided low alloy steel.

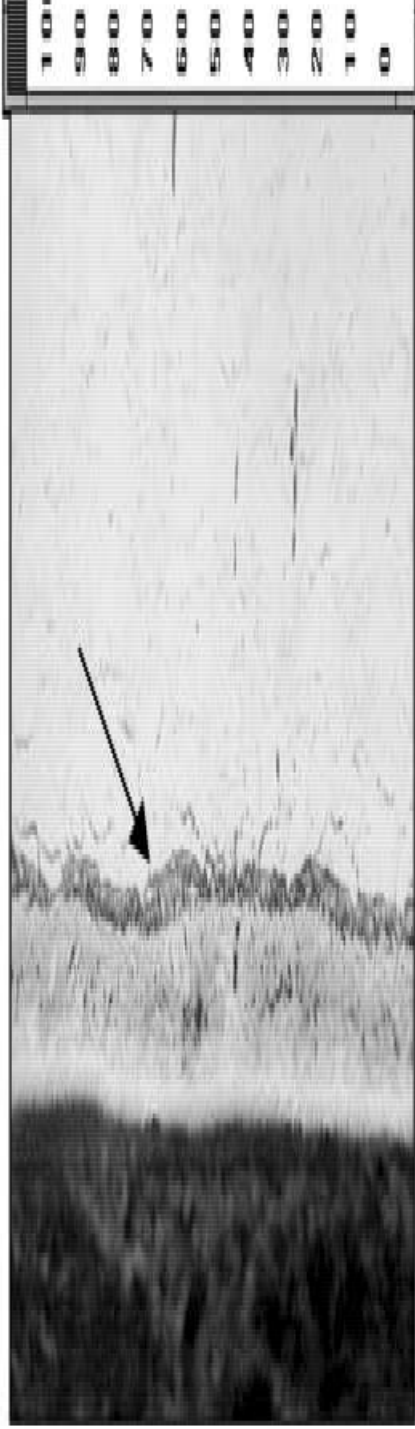


Plate 3 Scanning electron micrograph of a cross-sectional portion of a nitrided 32CDV13 steel (left) and the corresponding quantitative rf-GD-OES depth profile (right).